INTERNATIONAL DOCTORAL
SCHOOL OF THE USC

Sheila
Barrios Esteban

PhD Thesis

Polypeptide and polyphosphazene based nanosystems for anticancer gene therapy

Santiago de Compostela, 2023

Doctoral Programme in Drug Research and Development

DOCTORAL THESIS

POLYPEPTIDE AND POLYPHOSPHAZENE BASED NANOSYSTEMS FOR ANTICANCER GENE THERAPY

Sheila Barrios Esteban

INTERNATIONAL PHD SCHOOL OF THE UNIVERSITY OF SANTIAGO DE COMPOSTELA

PHD PROGRAMME IN DRUG RESEARCH AND DEVELOPMENT

SANTIAGO DE COMPOSTELA

2023

DECLARACIÓN DE LA AUTORA DE LA TESIS

Dña. **Sheila Barrios Esteban**

Título de la tesis: **Polypeptide and polyphosphazene based nanosystems for anticancer therapy**

Presento mi tesis, siguiendo el procedimiento adecuado al Reglamento y declaro que:

1) La tesis abarca los resultados de la elaboración de mi trabajo.
2) De ser el caso, en la tesis se hace referencia a las colaboraciones que tuvo este trabajo.
3) Confirmo que la tesis no incurre en ningún tipo de plagio de otros autores ni de trabajos presentados por mí para la obtención de otros títulos.
4) La tesis es la versión definitive presentada para su defensa y coincide la versión impresa con la presentada en formato electrónico.

Y me comprometo a presentar el Compromiso Documental de Supervisión en el caso que el original no esté depositado en la Escuela.

En **Santiago de Compostela**, **29 de diciembre 2022**

Firma electrónica

AUTORIZACIÓN DE LOS DIRECTORES DE LA TESIS

Polypeptide and polyphosphazene based nanosystems for anticancer gene therapy

Dra. **Noémi Csaba**, Profesora Titular del Departamento de Farmacología, Farmacia y Tecnología Farmacéutica de la Universidad de Santiago de Compostela

Dr. **Marcos García Fuentes**, Profesor Titular del Departamento de Farmacología, Farmacia y Tecnología Farmacéutica de la Universidad de Santiago de Compostela

INFORMAN:

Que la presente tesis, se corresponde con el trabajo realizado por Dª. **Sheila Barrios Esteban**, bajo nuestra dirección, y autorizamos su presentación, considerando que reúne los requisitos exigidos en el Reglamento de Estudios de Doctorado de la USC, y que como directores de esta no incurre en las causas de abstención establecidas en la Ley 40/2015.

De acuerdo con lo indicado en el Reglamento de Estudios de Doctorado, declaran también que la presente tesis doctoral es idónea para ser defendida en base a la modalidad de Monográfica con reproducción de publicaciones, en los que la participación de la doctoranda fue decisiva para su elaboración y las publicaciones se ajustan al Plan de Investigación.

En **Santiago de Compostela**, **29 de diciembre de 2022**

Fdo.: **Noémi Csaba**

Fdo.: **Marcos García Fuentes**

AUTORIZACIÓN DEL TUTOR DE LA TESIS

Polypeptide and polyphosphazene based nanosystems for anticancer gene therapy

Dra. **Noémi Csaba**, Profesora Titular del Departamento de Farmacología, Farmacia y Tecnología Farmacéutica de la Universidad de Santiago de Compostela

INFORMA:

Que la presente tesis, se corresponde con el trabajo realizado por Dª. **Sheila Barrios Esteban**, bajo mi tutorización, y autorizo su presentación, considerando que reúne los requisitos exigidos en el Reglamento de Estudios de Doctorado de la USC, y que como directora de esta no incurre en las causas de abstención establecidas en la Ley 40/2015.

De acuerdo con lo indicado en el Reglamento de Estudios de Doctorado, declaro también que la presente tesis doctoral es idónea para ser defendida en base a la modalidad de Monográfica con reproducción de publicaciones, en los que la participación de la doctoranda fue decisiva para su elaboración y las publicaciones se ajustan al Plan de Investigación.

En **Santiago de Compostela**, **29 de diciembre de 2022**

Fdo.: **Noémi Csaba**

DECLARATION OF THE AUTHOR

I, Sheila Barrios Esteban, author of this thesis, have no conflict of interest to declare.

This doctoral thesis was supported by the Center for Research in Molecular Medicine and Chronic Diseases, by the BritishSpanish Society (Santander Universities) and by Bolsas de Investigación 2021-Área de Ciencias de Saúde (Deputación provincial da Coruña).

A mi familia

"Cuando huye la suerte ¿sabes lo que hay que hacer?

Sigue nadando, sigue nadando"

Buscando a Nemo

TABLE OF CONTENTS

TABLE OF CONTENTS

ABSTRACT

ABSTRACT

Cancer remains the second cause of death worldwide. Currently, some cases can be avoided by reducing risk factors and applying preventive strategies. However, this is not enough when the tumor is aggressive and invasive, which is usually the case with glioblastoma and uveal melanoma. Although these tumors do not have a high incidence, their life expectancy is very short, between 6 and 14 months. Their treatment is based on surgical resection combined with radiation therapies and chemotherapy, which are aggressive treatments that trigger a variety of side effects. Therefore, new therapeutic approaches are required, where gene therapy has emerged as a new concept to improve the prognosis and quality of life of these patients. Nevertheless, gene medicine is still limited by the requirement of a delivery system for the protection and transport of nucleic acids. At this point, nanotechnology has become a key enabling tool for the design and development of non-viral gene delivery systems in oncology.

Considering this information, the main objective of this thesis has been the optimization of polymer-based nanosystems for the association of nucleic acids such as DNAs, siRNAs and miRNAs, and their evaluation as delivery carriers in advanced *in vitro* cancer models. In the first experimental chapter, nanoparticles with a matrix-structure, composed of protamine and dextran sulfate, were evaluated as gene delivery systems. The results confirmed the capacity of these non-viral vectors for the association and internalization of genetic material in bidimensional (2D) and spheroids models of primary glioblastoma cells. However, the moderate levels of gene expression suggest further studies to optimize their transfection capacity.

Previous studies by our research group revealed that the association of the in-house synthesized polyphosphazene substituted with 6-mercaptohexanoic acid (6MHA-PPZ), improved the endosomal escape of polycation/pDNA nanocomplexes. In the second experimental chapter, the effect of integrating 6MHA-PPZ on protamine and polyethylenimine (PEI) nanocomplexes was also studied as gene delivery systems, using advanced models of glioblastoma. The results obtained showed a general improvement in gene transfer capacity with the addition of 6MHA-PPZ, especially in protamine/pDNA nanocomplexes, with minimal cytotoxicity. In addition, the biodistribution of these nanocomplexes was also evaluated in an *in vivo* zebrafish model showing their accumulation in the yolk sac with a small number of particles diffusing to the head area, especially for PEI nanocomplexes. The addition of 6MHA-PPZ also improved the fluorescence signal due to its capacity to release the nucleic acids more easily from the endosomes.

The third experimental chapter consisted of the study of protamine nanocapsules for ocular administration in uveal cancer. The results showed that these nanocarriers presented favorable physicochemical properties for the association and intracellular transport of nucleic acids in uveal melanoma cells; however, the transfection efficiency should be further optimized to

obtain better levels of therapeutic gene expression. This nanosystem also performed favorably in a three-dimensional (3D) corneal model, without causing permanent alteration of the epithelia.

In general, the present work shows the potential of a variety of polymeric nanosystems as non-viral vectors in gene therapy against cancer. The three platforms showed adequate performance with minimal toxicity. This work also stresses the importance of moving as soon as possible towards advanced *in vitro* models to identify gene delivery formulations with the best chances for clinical translation.

RESUMEN

El cáncer sigue siendo la segunda causa de muerte a nivel mundial. Actualmente, algunos casos pueden evitarse reduciendo los factores de riesgo y aplicando estrategias preventivas. Sin embargo, esto no es suficiente cuando el tumor es agresivo e invasivo, como es el caso del glioblastoma y del melanoma uveal. Aunque estos tumores no tienen una incidencia alta, su esperanza de vida es muy corta, entre 6 y 14 meses. Su tratamiento se basa en la resección quirúrgica combinada con radioterapia y quimioterapia, los cuales, se tratan de tratamientos agresivos que desencadenan una variedad de efectos secundarios. Es por ello por lo que se requieren nuevos enfoques terapéuticos, donde la terapia génica ha surgido como un nuevo concepto para mejorar el pronóstico y la calidad de vida de estos pacientes. Sin embargo, la medicina genética todavía se ve limitada por el requisito de un sistema de entrega para la protección y el transporte de ácidos nucleicos. En este punto, la nanotecnología se ha convertido en una herramienta clave para el diseño y desarrollo de sistemas de administración de genes no virales en oncología.

Teniendo en cuenta esta información, el objetivo principal de esta tesis ha sido la optimización de nanosistemas basados en polímeros para la asociación de ácidos nucleicos como ADN, siARN y miARN, y su evaluación como transportadores en modelos *in vitro* avanzados de cáncer. En el primer capítulo experimental, se evaluaron nanopartículas con estructura de matriz, compuestas por protamina y sulfato de dextrano, como sistemas de administración de genes. Los resultados confirmaron la capacidad de estos vectores no virales para la asociación e internalización del material genético en modelos bidimensionales (2D) y esferoides de células primarias de glioblastoma. Sin embargo, los niveles moderados de expresión génica sugieren más estudios para optimizar su capacidad de transfección.

Estudios previos de nuestro grupo de investigación revelaron que la asociación del polifosfaceno sustituido con ácido 6-mercaptohexanoico (6MHA-PPZ), mejoró el escape endosómico de los nanocomplejos policatión/pADN. En el segundo capítulo experimental, se estudió el efecto de la integración de 6MHA-PPZ en nanocomplejos de protamina y polietilenimina (PEI) como sistemas de administración de genes, utilizando modelos avanzados de glioblastoma. Los resultados obtenidos mostraron una mejora general en la capacidad de transferencia génica con la adición de 6MHA-PPZ, especialmente en nanocomplejos protamina/pDNA, con mínima citotoxicidad. Además, la biodistribución de estos nanocomplejos también se evaluó en un modelo *in vivo* de pez cebra, mostrando su acumulación en el saco vitelino con el desplazamiento de una pequeña cantidad de partículas hacia el área de la cabeza, especialmente para los nanocomplejos PEI. La adición de 6MHA-PPZ mejoró la señal de fluorescencia debido a su capacidad para liberar más fácilmente los ácidos nucleicos de los endosomas.

El tercer capítulo experimental consistió en el estudio de nanocápsulas de protamina para administración ocular en cáncer de úvea. Los resultados mostraron que estos nanoportadores presentaron propiedades fisicoquímicas favorables para la asociación y transporte intracelular de ácidos nucleicos en células de melanoma uveal; sin embargo, la eficiencia de la transfección debe optimizarse aún más para obtener mejores niveles de expresión génica terapéutica. Este nanosistema también funcionó favorablemente en un modelo corneal tridimensional (3D), sin causar una alteración permanente del epitelio.

En general, el presente trabajo muestra el potencial de una variedad de nanosistemas poliméricos como vectores no virales en terapia génica contra el cáncer. Las tres plataformas mostraron un rendimiento adecuado con una toxicidad mínima. Este trabajo también destaca la importancia de avanzar lo antes posible hacia modelos *in vitro* avanzados para identificar formulaciones de administración de genes con las mejores posibilidades de traducción clínica.

RESUMEN *IN EXTENSO*

RESUMEN *IN EXTENSO*

El cáncer se considera uno de los problemas de salud más importantes a nivel mundial, siendo la segunda causa de muerte después de las enfermedades cardíacas [1, 2]. Esta enfermedad tiene una influencia negativa en el bienestar físico, social, mental y emocional del paciente, y su diagnóstico presenta varios problemas multidimensionales [3]. La Agencia Internacional para la Investigación del Cáncer (IARC) ha pronosticado que, en 2030 habrá aproximadamente entre 13 a 17 millones de muertes por esta enfermedad en todo el mundo [4]. Hoy en día, ya se han registrado más de doscientos tipos de cánceres conocidos, donde entre los más diagnosticados se encuentran el cáncer de mama, de pulmón y de próstata [5]. Según estadísticas de la Organización Mundial de la Salud (OMS), el glioblastoma y el melanoma uveal son tumores que, aunque no tienen una incidencia muy alta en comparación con los anteriores, se caracterizan por ser muy agresivos, con una esperanza de vida entre 6 y 14 meses. En el caso del glioblastoma, se trata de uno de los tumores cerebrales más violentos, con una proliferación excesiva y una angiogénesis descontrolada [6]. Presenta una incidencia global de 3,22 por 100.000 habitantes, donde representa el 57,3% de todos los gliomas y el 48,3% de todos los tumores cerebrales malignos. Se diagnostica principalmente en adultos con una edad media de 64 años [7]. Por otro lado, el melanoma uveal es el tumor intraocular primario más frecuente en adultos cuyo origen prioritario es la coroides (90%), aunque también existen casos en el cuerpo ciliar (6%) y en menor proporción en el iris (4%) [8]. Aunque su incidencia es muy baja, estimándose en 5 casos por cada 1.000.000 de habitantes, este tumor puede llegar a metastatizar en casi el 50% de los pacientes, afectando principalmente al hígado [9].

Por lo general, los tumores sólidos se vuelven más agresivos con el tiempo, incrementando su capacidad de invadir el tejido sano circundante y de diseminación metastásica. Estos procesos requieren un aumento en la rigidez del tumor y una fluidificación parcial para que las células cancerosas puedan desplazarse [10]. En diagnósticos graves, el tratamiento se basa en la resección quirúrgica seguida de terapias de irradiación, y quimioterapia [6] [11]. Éste es un tratamiento agresivo con varios efectos secundarios, y que no siempre garantiza grandes beneficios de supervivencia. En algunos tumores, ensayos clínicos han indicado que no hay un incremento significativo en la supervivencia entre pacientes que recibieron quimio-radioterapia postoperatoria y aquellos que solo se sometieron a cirugía. Una de las razones principales del fracaso de esta terapia conjunta, es que no considera la presencia de una subpoblación específica de células conocidas dentro de la masa tumoral, las células madre cancerosas (CSCs, siglas del inglés “Cancer Stem Cells”) [12]. La característica principal de estas células es su mayor resistencia a la radioterapia y a la quimioterapia, que, combinado con su capacidad de reiniciación tumoral, indican el fracaso del tratamiento con una recurrencia tumoral, llegando incluso a lesiones metastásicas [13, 14]. Es por ello que las terapias dirigidas, en especial, la terapia génica, se han postulado como un nuevo concepto para mejorar el pronóstico y la calidad de vida de los pacientes.

Históricamente, la terapia génica se basa en la transferencia de material genético a las células huésped para restaurar la función celular dañada o defectuosa [15]. Sin embargo, su traducción y éxito clínico no han sido satisfactorios debido a los desafíos asociados con su administración. Los ácidos nucleicos inyectados sistémica o localmente presentan una biodisponibilidad y una absorción celular baja. Incluso los que llegan a internalizar corren el riesgo de su degradación por enzimas o desencadenan una respuesta inmunológica. Como estos desafíos limitan su potencial para inducir la regulación génica, generalmente se requiere de un sistema de administración o vector [16].

Los vectores virales son uno de los vehículos más eficientes para la administración de genes, pero su toxicidad a altas dosis y su inmunogenicidad han llevado a investigar otras herramientas [13]. Los avances en el campo de la nanotecnología han llevado al desarrollo de nanotransportadores de genes no virales [17], considerados como seguros, fáciles de fabricar, de baja inmunogenicidad, y biodegradables [18]. En la última década, los nanosistemas a base de lípidos y/o polímeros se han investigado en el campo de la oncología. Los lípidos catiónicos son los reactivos de transfección más utilizados para el suministro de ácidos nucleicos en forma de nanoestructuras vesiculares, ya sean liposomas, sistemas lipídicos nanoestructurados (NLC, siglas del inglés "Nanostructured Lipid Carriers") o niosomas, e incluso en forma de nanopartículas (NPs) lipídicas sólidas (SLN, siglas del inglés "Solid Lipid Nanoparticles") [13]. Estos sistemas lipídicos forman la base de los primeros medicamentos de terapia génica ya comercializados como TransoPlex® y Onpattro® [19, 20], además de las vacunas contra el COVID-19 basadas en ARN mensajero de Moderna® y Pfizer/BioNTech® [21].

Sin embargo, las partículas lipídicas presentan algunas limitaciones que cuestionan su aplicabilidad, incluida su toxicidad, inducción de respuesta inmune, limitada capacidad de carga de fármacos, corto periodo de circulación, y acumulación en el hígado, pulmones y bazo [22]. En este aspecto, los polímeros catiónicos como la polietilenimina (PEI) y péptidos promotores de la penetración celular (CPP, siglas del inglés: "Cell Penetrating Peptides"), entre los que destaca la protamina de bajo peso molecular, se han convertido en excelentes candidatos. Ambos polímeros se tratan de materiales muy utilizados para la liberación de genes por su alta capacidad para condensar el material genético, además de su capacidad para atravesar la membrana celular, promoviendo un mejor escape endosomal y una mejor liberación [23, 24]. Además, estos biomateriales están aprobados por la FDA debido a su alta seguridad.

A pesar de la reciente aprobación de varios nanomedicamentos anticancerosos, ya sean virales como Gendicine®, Oncorine® y Yescarta® o no virales como Onivyde® y Vyxeos®, la tasa de éxito de la traducción clínica sigue siendo relativamente baja [25-28]. Múltiples barreras biológicas y farmacológicas evidencian la necesidad de nuevos modelos preclínicos para la innovación en la investigación traslacional del cáncer [28]. Por lo general, los compuestos anticancerígenos se prueban en modelos de cultivo celular bidimensionales (2D), pero éstos no recapitulan de forma adecuada el microambiente tumoral humano, y muestran una expresión génica alterada. Los cultivos tridimensionales (3D) han demostrado presentar unas características más cercanas y realistas a las complejas condiciones *in vivo* [29]. Estos modelos permiten el cultivo de células cancerosas de una manera que recuerdan la arquitectura estructural del tumor con interacciones célula-célula y célula-matriz extracelular [30]. La combinación de estos modelos con células primarias derivadas de pacientes tiende a dar una representación aún más realista y fenotípicamente más precisa en comparación con líneas celulares comerciales [31].

Por otra parte, los modelos murinos han sido el modelo animal más usado para los estudios básicos y preclínicos del cáncer, pero actualmente, el uso de peces cebra representa un modelo *in vivo* de gran interés. Entre sus ventajas destacan su similitud notable con los aspectos anatómicos, funcionales y bioquímicos de la enfermedad humana, una evolución rápida y una reducción en el coste, además de las consideraciones éticas [32]. En conclusión, cada modelo, ya sean los cultivos 2D/3D o el modelo de pez cebra, deben usarse para complementar, enriquecer e informar en el diseño y la optimización de nanomedicamentos, facilitando su traslación a la clínica. En vista de estos antecedentes, el principal objetivo de la tesis fue el desarrollo y la optimización de tres plataformas de nanosistemas poliméricos como vectores de administración de genes, y la evaluación de su potencial en modelos preclínicos avanzados.

En la primera parte de la tesis, se desarrollaron y optimizaron NPs poliméricas resultantes de la combinación de protamina (Pr) y un polisacárido de carga opuesta, dextrano (Dx). La estructura policatiónica de la protamina con un contenido rico en argininas, de aproximadamente 67 a 70%, le confiere la propiedad de unirse a moléculas de ADN para condensarlo formando nanocomplejos [33]. Por otra parte, el sulfato de dextrano se trata de un polímero biodegradable, de toxicidad reducida y con capacidad de aumentar la eficacia en la liberación de ciertos fármacos y genes [34]. Teniendo en cuenta estudios previos de cribado, en este trabajo se seleccionó el prototipo de ratio 4:1 (*m/m*) de Pr:Dx, ya que presentaba unas características fisicoquímicas y una capacidad de asociación de ácidos nucleicos adecuadas para su uso en terapia génica (Figura 1.). La estabilidad en el entorno fisiológico, y durante el almacenamiento representan algunas de las principales limitaciones en el desarrollo de nuevas terapias génicas. Nuestra formulación mostró resultados adecuados en ambos aspectos relacionados con la estabilidad. Por tanto, se consideró este prototipo como un candidato ideal para su evaluación *in vitro* en modelos avanzados de líneas celulares relevantes para la translación clínica.

4:1 PrDx (*m/m*)	Tamaño (nm)	PDI	Potencial Zeta (mV)
-	120 ± 7	0.2	+34 ± 2
pADN	146 ± 1	0.2	+33 ± 5
miARN	124 ± 5	0.1	+30 ± 3

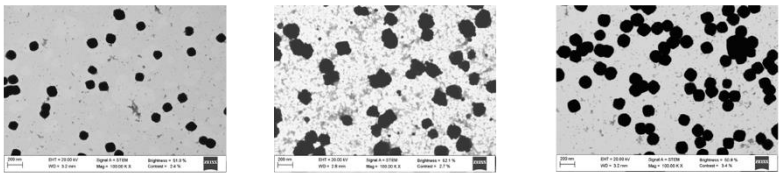

4:1 (*m/m*) Pr:Dx NPs blancas | 4:1 (*m/m*) Pr:Dx NPs + pADN | 4:1 (*m/m*) Pr:Dx NPs + miARN

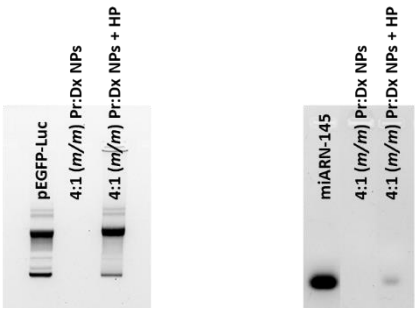

Figura 1. Características fisicoquímicas y morfológicas de las NPs de Pr:Dx con ratio 4:1 (*m/m*) sin carga y asociadas con 8% (*m/m*) de diferentes ácidos nucleicos. Evaluación de la capacidad de asociación del material genético mediante electroforesis en gel de agarosa cargando 0,5 μg de pADN y 1 μg de miARN por banda. PDI= siglas del inglés "Polydispersity Index", HP= heparina (Media ± SD (n= 3)).

La combinación de varios estudios de viabilidad de actividad metabólica celular, integridad de membrana y un ensayo de volumen de esferoides, mostraron una baja citotoxicidad de este prototipo tanto en modelos de glioblastoma 2D como 3D (Figura 2. (a)). Por otra parte, estudios de captación celular mediante microscopía confocal y de fluorescencia de lámina de luz, y su cuantificación por citometría de flujo, revelaron una internalización de las NPs de casi el 100% en ambos modelos de glioblastoma (Figura 2. (b)). Estos resultados verificaron la capacidad de este nanosistema de penetrar de forma eficiente en las células, e incluso en superestructuras multicelulares [35-38].

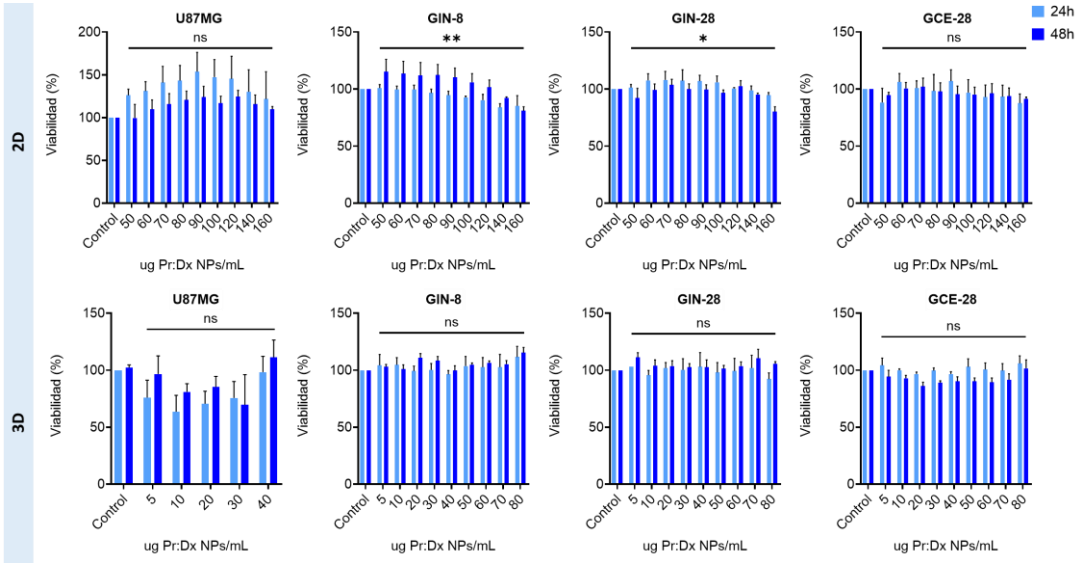

(a)

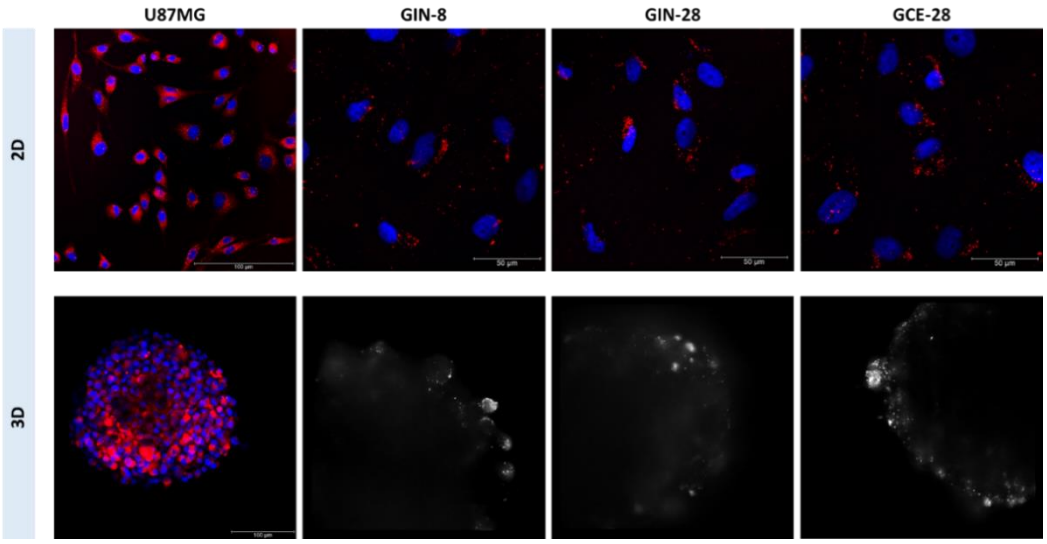

(b)

Figura 2. (**a**) Citotoxicidad *in vitro* de diferentes concentraciones de las NPs de Pr:Dx blancas en modelos de cultivo 2D y 3D de glioblastoma U87MG, GIN-8, GIN-28 y GCE-28 tras 24 h y 48 h de su retirada (Media ± SEM (n= 3)). (**b**) Imágenes de microscopía confocal y fluorescencia de lámina de luz de la capacidad de internalización de las NPs de Pr:Dx blancas marcadas con fluorescencia (canal rojo y puntos brillantes) en modelos de cultivo 2D y 3D de glioblastoma U87MG, GIN-8, GIN-28 y GCE-28, tras 4 h de su incubación. Núcleos de células teñidos con DAPI (canal azul). Barra de escala= 50 y 100 µm.

La capacidad de transfección está condicionada por la entrada y el tráfico intracelular de los vectores, que son procesos dependientes de la línea celular. En este caso, a pesar de que nuestro nanosistema promovió una expresión eficiente a partir de dosis de 1 μg de plásmido tanto en células como en esferoides de glioblastoma, no se correlacionó con los valores de captación celular (Figura 3.). En conclusión, las NPs de Pr:Dx han demostrado presentar unas propiedades adecuadas para la asociación y protección de cargas genéticas con baja citotoxicidad, alta capacidad de internalización, pero una eficiencia de transfección mejorable en modelos avanzados de glioblastoma.

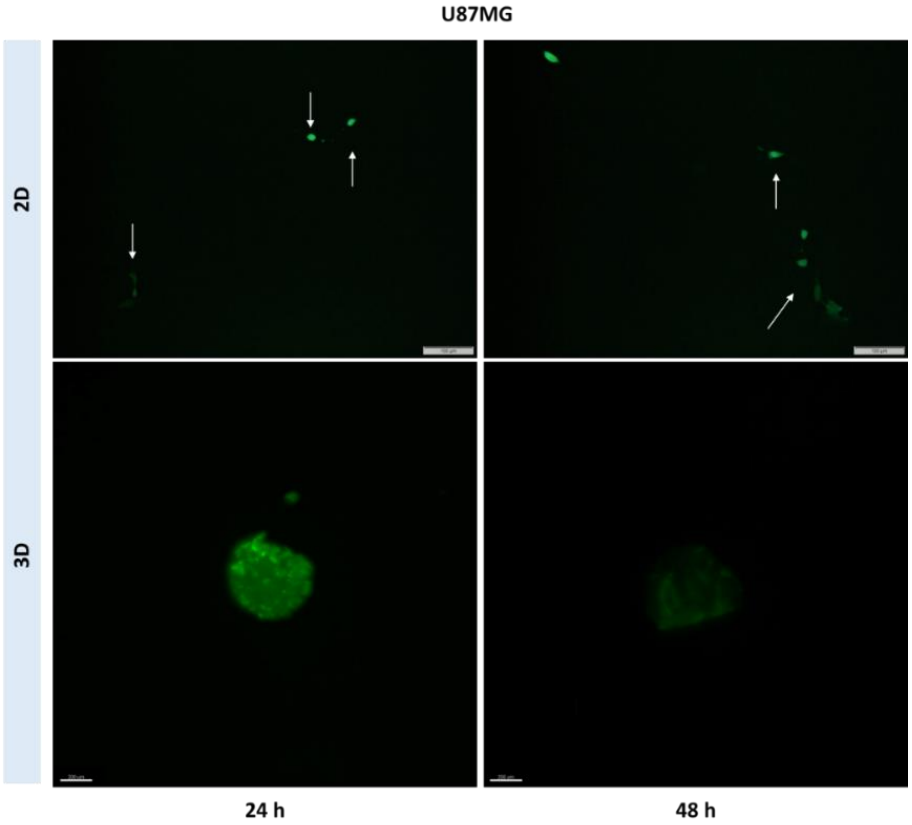

Figura 3. Imágenes de microscopía de fluorescencia y fluorescencia de lámina de luz de la expresión de la proteína verde fluorescente mejorada (EGFP= siglas del inglés: "Enhaced Green Fluorescence Protein") en modelos de cultivo 2D y 3D de glioblastoma U87MG tras 24 h y 48 h de la retirada de las NPs de Pr:Dx asociadas con 8% (*m*/*m*) de pADN, a una concentración de 2,5 μg de pADN, incubadas durante 4 h. Barra de escala= 100 y 200 μm.

Estudios recientes de nuestro grupo de investigación han demostrado que la adición del polifosfaceno aniónico 6MHA-PPZ potencia la internalización, el escape endosomal y la biodisponibilidad intracelular de una serie de nanosistemas poliméricos [39]. En base a estos resultados, la segunda parte de la tesis se centró en el desarrollo de nanocomplejos de polietilenimina (PEI) y protamina por condensación con un plásmido modelo en combinación con el polifosfaceno 6MHA-PPZ. Las formulaciones presentaron unas propiedades fisicoquímicas apropiadas en cuanto a tamaño y carga superficial para la asociación de ácidos nucleicos, sin observarse variaciones significativas con la adición del polímero aniónico (Tabla 1.). Sin embargo, cabe resaltar un aumento en el rendimiento de formación de los nanocomplejos en presencia de este polifosfaceno, concordando con los resultados de caracterización previos [39]. Las propiedades se mantuvieron estables en condiciones de almacenamiento y en medio de cultivo celular, pero sufrieron agregación en medios de cultivo

convencionales de pez cebra, especialmente para los nanocomplejos de protamina. En cambio, al incubarse en agua corriente declorada y estéril, su estabilidad coloidal no se vio afectada.

Tabla 1. Características fisicoquímicas de los nanocomplejos de PEI y protamina, con y sin el polifosfaceno aniónico 6MHA-PPZ, con diferente ratio de carga (N:C:P). PDI= siglas del inglés "Polydispersity Index", DCR= siglas del inglés "Derived Count Rate" (Media ± SD (n= 7)).

Nanocomplejos	Ratio de carga (N:C:P)	Tamaño (nm)	PDI	Potencial Zeta (mV)	DCR (kcps)
PEI:6MHA-PPZ:pADN	8:0:1	114 ± 19	0,178	+27 ± 11	532 ± 251
	8:4:1	106 ± 10	0,128	+33 ± 15	1458 ± 403
Pr:6MHA-PPZ:pADN	8:0:1	128 ± 6	0,171	+26 ± 7	887 ± 129
	8:4:1	110 ± 14	0,124	+25 ± 8	2070 ± 312

En cuanto a la evaluación de su potencial como nanosistemas de terapia génica, esto se realizó en modelos preclínicos de esferoides de glioblastoma derivados de pacientes con diferente origen de la masa tumoral, y en un modelo *in vivo* de embriones de peces cebra. En general, los nanocomplejos de PEI mostraron una citotoxicidad mayor que los de protamina, pero dicho exceso de toxicidad fue parcialmente corregido con la adición del polímero 6MHA-PPZ, concordando con resultados previos en una línea de glioblastoma altamente transformada [39] (Figura 4.).

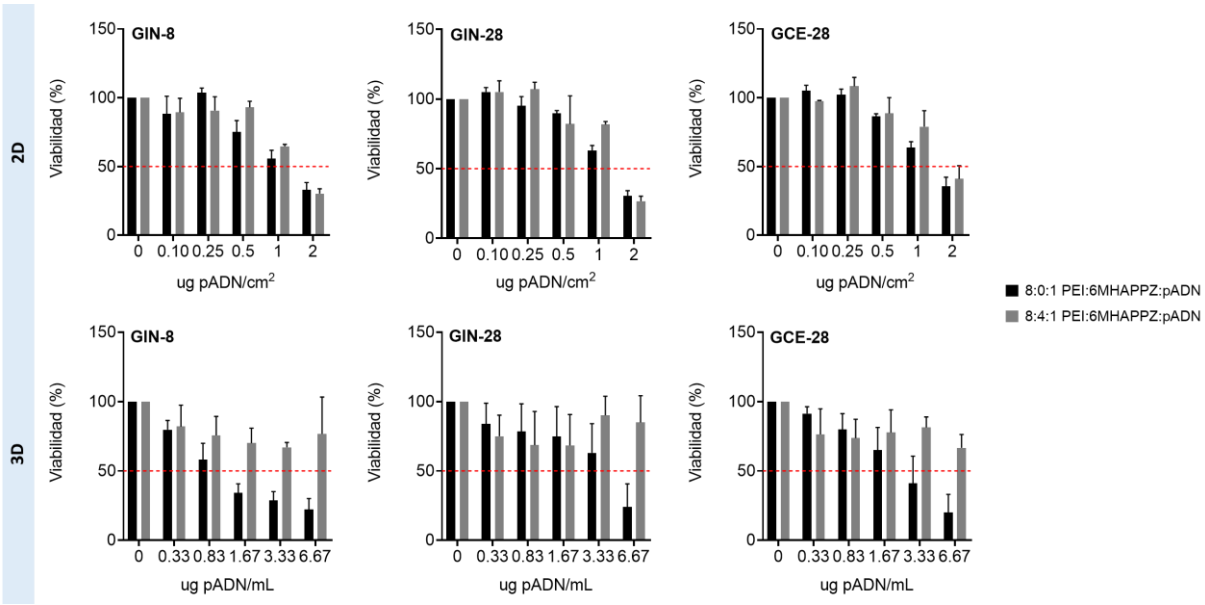

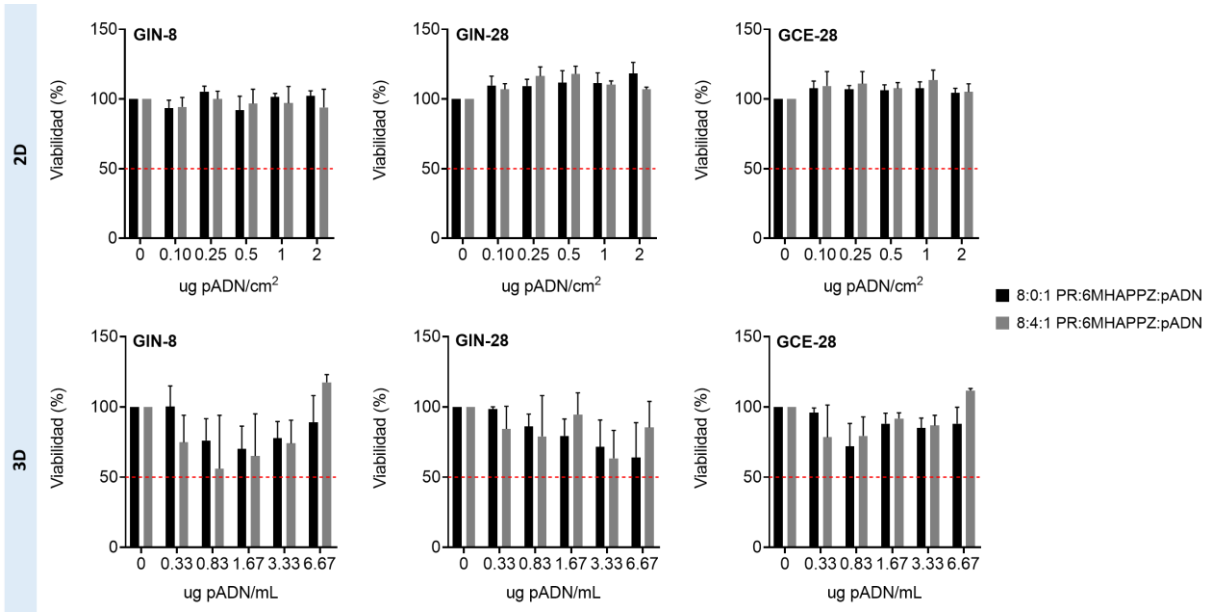

Figura 4. Citotoxicidad *in vitro* de diferentes concentraciones de los nanocomplejos de PEI y protamina, sin (barras negras) y con (barras grises) el polifosfaceno aniónico 6MHA-PPZ, a diferente ratio de carga (C:N:P), en modelos de cultivos 2D y 3D de glioblastoma GIN-8, GIN-28 y GCE-28 tras 48 h y 72 h de su retirada, respectivamente (Media ± SEM (n= 3)).

La eficiencia de transfección se determinó mediante la cuantificación de la expresión de la proteína Luciferasa. En general, la adición del polifosfaceno aniónico mejoró la transfección, aumentando el efecto del escape endosomal, especialmente en los nanocomplejos de protamina, cuyos valores de transfección alcanzaron incluso al del modelo de referencia PEI/pADN (Figura 5.). Sin embargo, en los modelos preclínicos de esferoides se observaron efectos diferentes en función de la línea celular. Se obtuvieron resultados de transfección similares a los obtenidos en los cultivos 2D en el caso de los esferoides de glioblastoma de líneas transformadas comerciales, pero no sucedió lo mismo en los esferoides de líneas primarias de glioblastoma, donde el efecto del polifosfaceno 6MHA-PPZ fue menos claro. Esto confirmó la necesidad de usar modelos clínicamente relevantes lo antes posible.

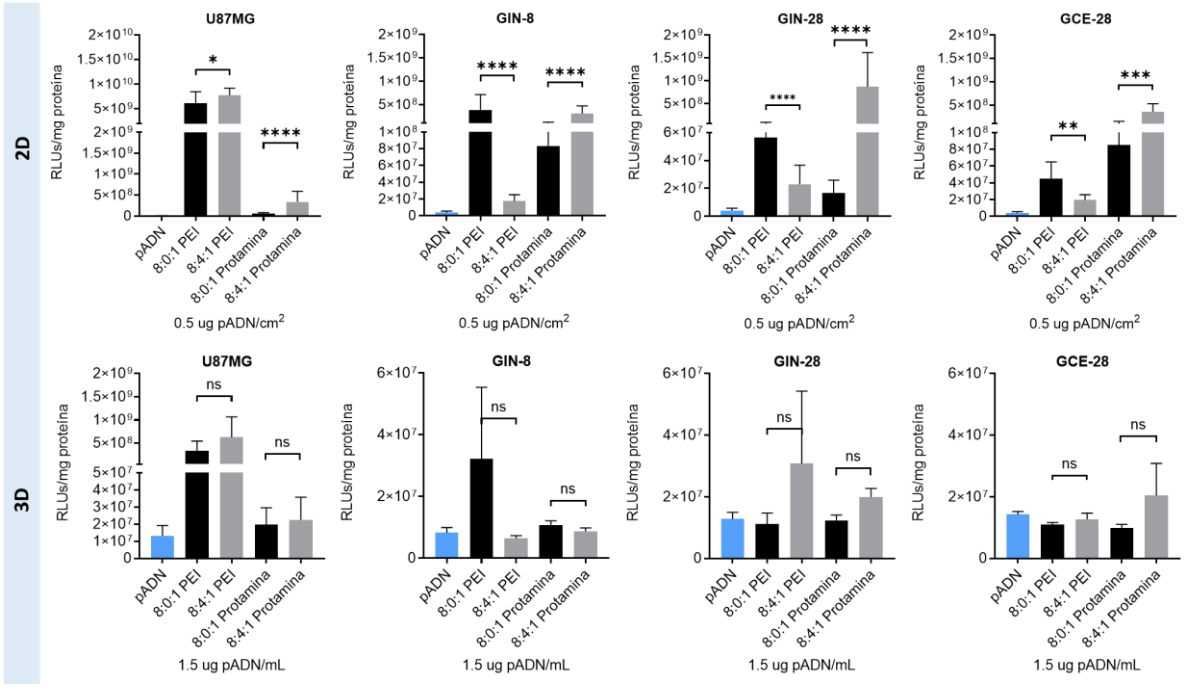

Figura 5. Ensayo de transfección en modelos de cultivo 2D y 3D de glioblastoma U87MG, GIN-8, GIN-28 y GCE-28 mediante la medida de la luminiscencia tras 48 h y 72 h de la retirada de los nanocomplejos, respectivamente (RLUs/mg de proteína (RLUs= siglas del inglés "Relative Luminiscence Units") (Media ± SEM (n= 3)).

En cuanto a su biodistribución en modelos *in vivo* de embriones de pez cebra de 48 horas post-fecundación, se obtuvo una mayor acumulación de las formulaciones en el saco vitelino, especialmente de los nanocomplejos de PEI, que, tras 5 días post-inyección, parte de estas partículas se desplazaron hacia la zona de la cabeza. Por otra parte, se observó que la adición del polifosfaceno aniónico dio lugar a una mayor intensidad de fluorescencia confirmando la capacidad de este polímero para potenciar el escape endosomal de péptidos catiónicos, como PEI, permitiendo la liberación del material génico. Para los nanocomplejos de protamina, estos valores resultaron ser más bajos como consecuencia de su fuerte capacidad de complejación de ácidos nucleicos [40], que incluso en presencia de 6MHA-PPZ, la completa liberación del material genético resultó ser más complicada (Figura 6.). En conclusión, la combinación del polifosfaceno aniónico 6MHA-PPZ con polímeros catiónicos comerciales mejoró las características de los nanocomplejos reduciendo su citotoxicidad, aumentando su eficacia de transfección en modelos avanzados de glioblastoma y consiguiendo una biodistribución en el saco vitelino hacia la cabeza en modelos de embriones de peces cebra.

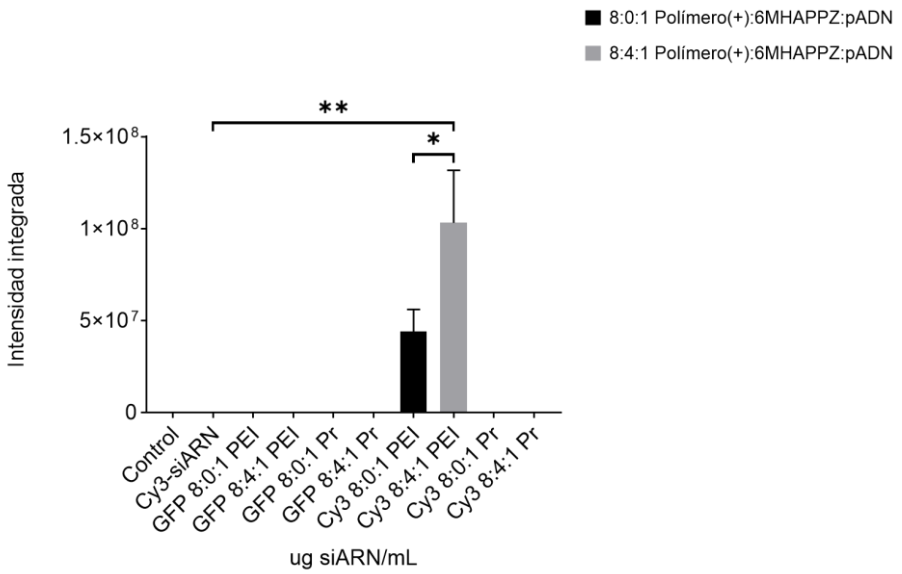

Figura 6. Cuantificación de la señal de fluorescencia en los embriones de pez cebra tratados con los controles y los nanocomplejos de PEI y protamina, sin (barras negras) y con (barras grises) el polifosfaceno aniónico 6MHA-PPZ, con diferente ratio de carga (N:C:P), a una concentración de 25 µg de siARN/mL (GFP= siglas del inglés: "Green Fluorescence Protein") (media ± SEM (n= 10/condición).

Las nanocápsulas (NCs) poliméricas tienen una utilidad potencial como nanoportadores en la vía ocular gracias a su capacidad de interacción con los epitelios de la córnea y conjuntiva [41]. Por tanto, la tercera parte de esta tesis consistió en el desarrollo y la optimización de nanocápsulas de protamina (Pr NCs) para su aplicación en terapia génica contra el cáncer ocular. La formulación fue preparada mediante el método de desplazamiento de solvente obteniendo una población homogénea de nanogotas oleosas de vitamina E, cubiertas por una capa polimérica de protamina, y estabilizadas con ayuda de surfactantes no iónicos. Su morfología esférica, sus propiedades fisicoquímicas, y su asociación reversible de macromoléculas de ADN plasmídico y miARN, las convirtió en vehículos adecuados para terapia génica (Figura 7.). Este nanosistema mostró una estabilidad adecuada en condiciones de almacenamiento durante un mes, y estabilidad coloidal en medio de cultivo celular. Considerando la vía de administración, su estabilidad también fue testada en fluido lacrimal simulado, donde las características de las Pr NCs cargadas con diferentes porcentajes de ADN se mantuvieron estables previniendo la liberación prematura del plásmido.

Pr NCs	Tamaño (nm)	PDI	Potencial Zeta (mV)
-	242 ± 40	0,121	+33 ± 11
1% pADN	345 ± 39	0,260	-31 ± 4
2,5% pADN	337 ± 31	0,227	-42 ± 3
1,5% miARN	274 ± 48	0,097	-15 ± 3

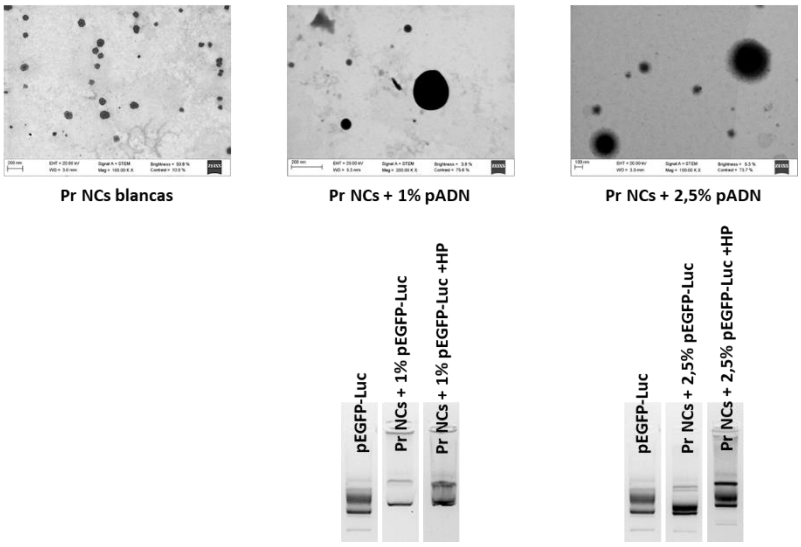

Figura 7. Características fisicoquímicas y morfológicas de las Pr NCs sin carga y asociadas con diferentes cargas de ADN plasmídico y miARN. Evaluación de la capacidad de asociación de material genético mediante electroforesis en gel de agarosa cargando 0,135 µg de pADN por banda. PDI= siglas del inglés "Polydispersity Index", HP= heparina (Media ± SEM (n= 3)).

La evaluación de su potencial como nanosistema de terapia génica se llevó a cabo en células de melanoma uveal (MU). Los resultados mostraron baja citotoxicidad a diferentes concentraciones y tiempos (Figura 8. (a)), y una eficiente internalización intracelular (Figura 8. (b)).

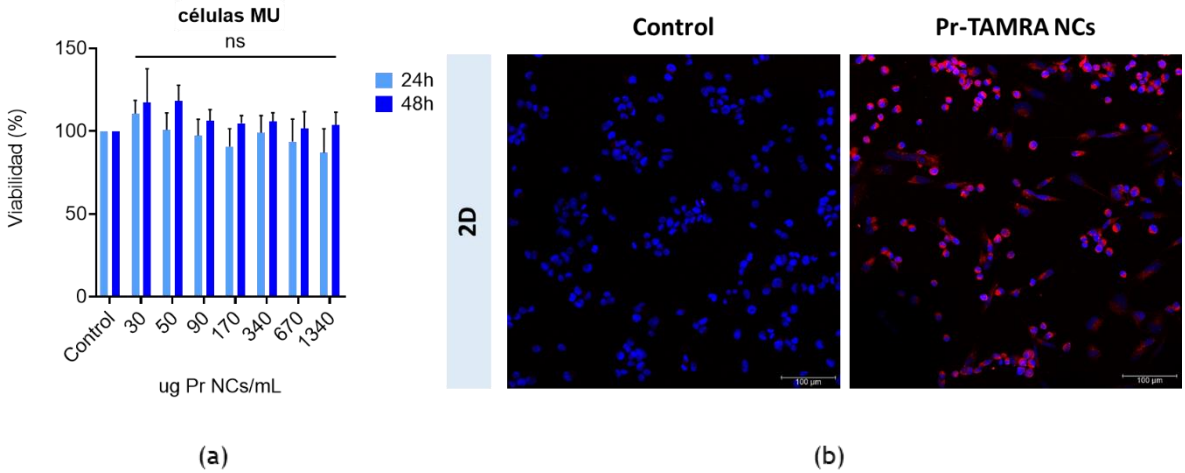

Figura 8. (**a**) Citotoxicidad *in vitro* de diferentes concentraciones de las Pr NCs blancas en células de melanoma uveal tras 24 h y 48 h de su retirada (Media ± SEM (n= 3)). (**b**) Imágenes de microscopía confocal de la internalización de las Pr NCs blancas marcadas con fluorescencia (canal rojo) en células de melanoma uveal tras 4 h de incubación. Núcleos de células teñidos con DAPI (canal azul). Barra de escala= 100 µm.

En el área de terapia génica ocular, los nanosistemas poliméricos son especialmente atractivos debido a su capacidad de interactuar íntimamente con la superficie ocular. En este aspecto, nuestro grupo de investigación fue uno de los pioneros en demostrar la capacidad de estos nanovehículos para adherirse a la superficie ocular y penetrar a través de la córnea y el epitelio conjuntival, permitiendo así una administración por vía tópica de fármacos en los que esta vía no era viable [41-47]. En base a estos estudios, se determinó la capacidad de transporte de las Pr NCs en un modelo 3D de córnea. Los resultados mostraron que la formulación, tanto con ADN plasmídico asociado como sin él, fue capaz de atravesar esta barrera epitelial (Figura 9. (a)) sin alterar su integridad y morfología (Figura 9. (b)) [48].

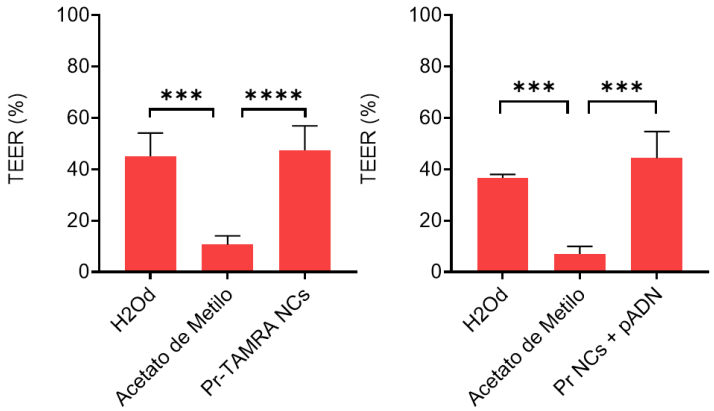

(a)

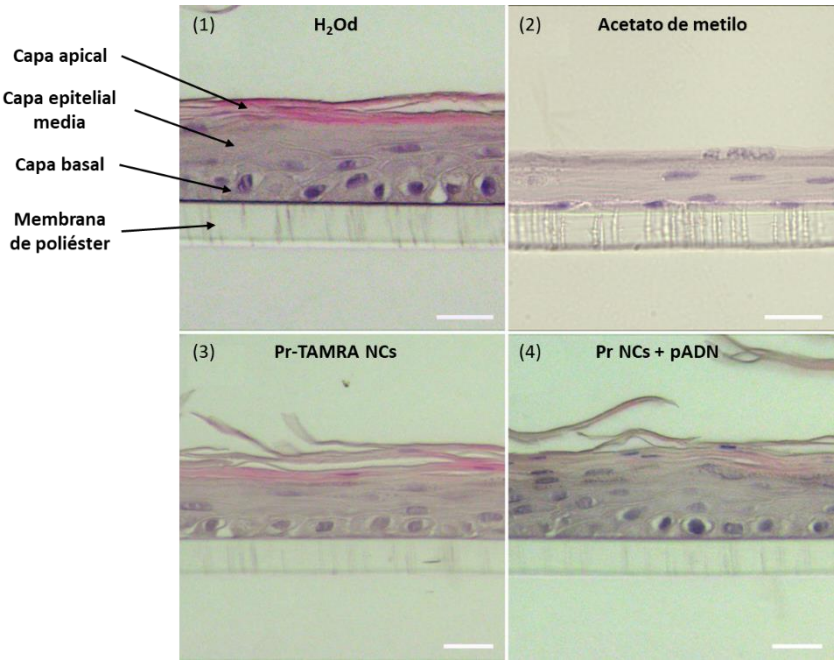

(b)

Figura 9. (**a**) Estudio de permeabilidad de las Pr NCs blancas, y asociadas con 2,5% (*m*/*m*) de pADN, en un modelo 3D de córnea (QobuR-RhCE). Resultado expresado en porcentaje de la medida de la resistencia transepitelial (TEER) tras 4 h de su retirada (Media ± SEM (n= 3)). (**b**) Imágenes histológicas teñidas con Hematoxilina y Eosina de la sección transversal de modelos 3D de córnea (QobuR-RhCE) tras 4 h de tratamiento con (1) H_2Od (control negativo), (2) acetato de metilo (control positivo), (3) Pr NCs marcadas con fluorescencia, y (4) Pr NCs asociadas con 2,5% (*m*/*m*) de pADN (2,5 μg de pADN/inserto). Barra de escala= 20 μm.

Finalmente, estos nanosistemas mostraron niveles adecuados de transfección a 48 h después de su incubación con las células (Figura 10.). En conclusión, estos resultados confirmaron que las Pr NCs podrían considerarse un nanosistema prometedor para el tratamiento del melanoma uveal en terapia génica.

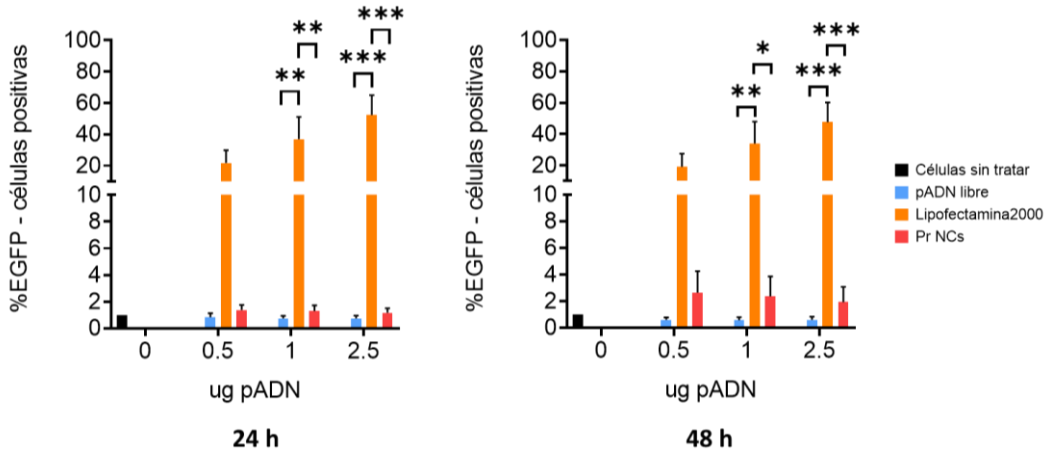

Figura 10. Cuantificación de la expresión de EGFP mediante citometría de flujo midiendo el porcentaje de células de melanoma uveal positivas para la presencia de dicha proteína, tras 24 h y 48 h de la retirada de las Pr NCs asociadas con 2,5% (*m*/*m*) de pADN (Media ± SEM (n= 3)).

En resumen, esta tesis ha demostrado el potencial de plataformas variadas de nanosistemas, ya sean NPs, nanocomplejos y NCs poliméricas, para aplicaciones de terapia génica. Los nanosistemas desarrollados tienen propiedades morfológicas y fisicoquímicas adecuadas, son biodegradables, tienen buena capacidad de asociación y transporte de genes. Los nanotransportadores tienen además una buena relación entre eficacia y citotoxicidad, confirmada mediante su evaluación en diferentes modelos preclínicos avanzados tales como esferoides y peces cebra.

RESUMO *IN EXTENSO*

RESUMO *IN EXTENSO*

O cancro considérase un dos problemas de saúde máis importantes a nivel mundial, sendo a segunda causa de morte despois das enfermidades cardíacas [1, 2]. Esta enfermidade ten unha influencia negativa no benestar físico, social, mental e emocional do paciente, e o seu diagnóstico presenta varios problemas multidimensionais [3]. A Axencia Internacional para a Investigación do Cancro (IARC) prognosticou que, en 2030 haberá aproximadamente entre 13 a 17 millóns de mortes por esta enfermidade en todo o mundo [4]. Hoxe en día, xa se rexistraron máis de douscentos tipos de cancros coñecidos, onde entre os máis diagnosticados atópanse o cancro de mama, de pulmón e de próstata [5]. Segundo as estatísticas da Organización Mundial da Saúde (OMS), o glioblastoma e o melanoma uveal son tumores que, aínda que non teñen unha incidencia moi alta en comparación cos anteriores, caracterízanse por ser moi agresivos, cunha esperanza de vida entre 6 e 14 meses. No caso do glioblastoma, trátase dun dos tumores cerebrais máis violentos, cunha proliferación excesiva e unha angiogénesis descontrolada [6]. Presenta unha incidencia global de 3,22 por 100.000 habitantes, onde representa o 57,3% de todos os gliomas e o 48,3% de todos os tumores cerebrais malignos. Diagnostícase principalmente en adultos cunha idade media de 64 anos [7]. Doutra banda, o melanoma uveal é o tumor intraocular primario máis frecuente en adultos cuxo orixe prioritaria é a coroides (90%), aínda que tamén existen casos no corpo ciliar (6%) e en menor proporción no iris (4%) [8]. Aínda que a súa incidencia é moi baixa, estimándose en 5 casos por cada 1.000.000 de habitantes, este tumor pode chegar a metastatizar en case o 50% dos pacientes, afectando principalmente o fígado [9].

Polo xeral, os tumores sólidos vólvense máis agresivos co tempo, incrementando a súa capacidade de invadir o tecijo san circundante, e producindo diseminación metastásica. Estes procesos requiren un aumento na rixidez do tumor e unha fluidificación parcial para que as células cancerosas poidan desprazarse [10]. En diagnósticos graves, o tratamento baséase na resección cirúrxica, seguida de terapias de irradiación, e quimioterapia [6] [11]. Este é un tratamento agresivo con varios efectos secundarios, e que non sempre garante grandes beneficios de supervivencia. Nalgúns tumores, ensaios clínicos indicaron que non hai un incremento significativo na supervivencia entre pacientes que recibiron quimio-radioterapia postoperatoria e aqueles que si se someteron a cirurxía. Unha das razóns principais do fracaso desta terapia conxunta é que non considera a presenza dunha subpoboación específica de células coñecidas dentro da masa tumoral, as células nai cancerosas (CSCs, siglas do inglés “Cancer Stem Cells”) [12]. A característica principal destas células é a súa maior resistencia á radioterapia e á quimioterapia, que, combinado coa súa capacidade de reiniciación tumoral, indican o fracaso do tratamento cunha recorrencia tumoral, chegando a lesións metastásicas [13, 14]. É por iso, que as terapias dirixidas, en especial, a terapia xénica, postuláronse como un novo concepto para mellorar o prognóstico e a calidade de vida dos pacientes.

Historicamente, a terapia xénica baséase na transferencia de material xenético para restaurar a función celular danada ou defectuosa [15]. Con todo, a súa tradución e éxito clínico non foron satisfactorios debido aos desafíos asociados coa súa administración. Os ácidos nucleicos inxectados sistémica ou localmente presentan unha biodispoñibilidade e absorción celular baixa. Incluso os que chegan a internalizar corren o risco da súa degradación por enzimas ou desencadean unha resposta inmunolóxica. Como estes desafíos limitan o seu potencial para inducir a regulación xénica, xeralmente requírese dun sistema de administración ou vector [16].

Os vectores virais son un dos vehículos máis eficientes para a administración de xenes, pero a súa toxicidade a altas doses e a súa inmunogenicidade levaron a investigar outras ferramentas [13]. Os avances no campo da nanotecnoloxía levaron ao desenvolvemento de nanotransportadores de xenes non virais [17], considerados como seguros, fáciles de fabricar, de baixa inmunogenicidade, e biodegradables [18]. Na última década, os nanosistemas a base de lípidos e/o polímeros investigáronse no campo da oncoloxía. Os lípidos catiónicos son os reactivos de transfección máis utilizados para a administración de ácidos nucleicos en forma de nanoestructuras vesiculares xa sexan liposomas, sistemas lipídicos nanoestructurados (NLC, siglas do inglés "Nanostructured Lipid Carriers") ou niosomas, e mesmo en forma de nanopartículas (NPs) lipídicas sólidas (SLN, siglas do inglés "Solid Lipid Nanoparticles") [13]. Estes sistemas lipídicos forman a base dos primeiros medicamentos de terapia xénica xa comercializados como TransoPlex® e Onpattro® [19, 20], ademais das vacinas contra o COVID-19 baseadas en ARN mensaxeiro de Moderna® e Pfizer/BioNTech® [21].

Con todo, as partículas lipídicas presentan algunhas limitacións que cuestionan a súa aplicabilidade, incluída a súa toxicidade, indución de resposta inmune, limitada capacidade de carga de fármacos, curto período de circulación, e acumulación no fígado, pulmóns e bazo [22]. Neste aspecto, os polímeros catiónicos como a polietilenimina (PEI) e péptidos promotores da penetración celular (CPP, siglas do inglés: "Cell Penetrating Peptides"), entre os que destaca a protamina de baixo peso molecular, convertéronse en excelentes candidatos. Ámbolos polímeros trátanse de materiais moi utilizados para a liberación de xenes pola súa alta capacidade para condensar o material xenético, ademais da súa capacidade para atravesar a membrana celular, promovendo un mellor escape endosomal e unha mellor liberación [23, 24]. Ademais, estes biomateriais están aprobados pola FDA debido á súa alta seguridade.

A pesar da recente aprobación de varios nanomedicamentos anticancerosos, xa sexan virales como Gendicine®, Oncorine® e Yescarta® ou non virais como Onivyde® e Vyxeos®, a taxa de éxito da tradución clínica segue sendo relativamente baixa [25-28]. Múltiples barreiras biolóxicas e farmacolóxicas evidencian a necesidade de novos modelos preclínicos para a innovación na investigación translacional do cancro [28]. Polo xeral, os compostos anticanceríxenos próbanse en modelos de cultivo celular bidimensionais (2D), pero estes non recapitulan de forma axeitada o microambiente tumoral humano, e mostran unha expresión xénica alterada. Os cultivos tridimensionais (3D) demostraron presentar unhas características máis próximas e realistas ás complexas condicións *in vivo* [29]. Estes modelos permiten o cultivo de células cancerosas dunha maneira que lembran á arquitectura estrutural do tumor con interaccións célula-célula e célula-matriz extracelular [30]. A combinación destes modelos con células primarias derivadas de pacientes tende a dar unha representación aínda máis realista e fenotípicamente máis precisa en comparación coas liñas celulares comerciais [31].

Por outra banda, os modelos murinos foron o modelo animal máis usado para os estudos básicos e preclínicos do cancro, pero actualmente, o uso de peces cebra representa un modelo

in vivo de gran interese. Entre as súas vantaxes destacan a súa similitude notable cos aspectos anatómicos, funcionais e bioquímicos da enfermidade humana, unha evolución rápida e unha redución no custo, ademais das consideracións éticas [32]. En conclusión, cada modelo, xa sexan os cultivos 2D/3D ou o modelo de peixe cebra, deben usarse para complementar, enriquecer e informar no deseño e a optimización de nanomedicamentos, facilitando a súa translación á clínica. En vista destes antecedentes, o principal obxectivo da tese foi o desenvolvemento e a optimización de tres plataformas de nanosistemas poliméricos como vectores de administración de xenes, e a avaliación do seu potencial en modelos preclínicos avanzados.

Na primeira parte da tese, desenvolvéronse e optimizaron NPs poliméricas resultantes da combinación de protamina (Pr) e un polisacárido de carga oposta, o dextrano (Dx). A estrutura policatiónica da protamina cun contido rico en argininas, de aproximadamente 67 a 70%, confírelle a propiedade de unirse a moléculas de ADN para condensalos formando nanocomplexos [33]. Por outra banda, o sulfato de dextrano trátase dun polímero biodegradable, de toxicidade reducida e con capacidade de aumentar a eficacia na liberación de certos fármacos e xenes [34]. Tendo en conta estudos previos de cribado, neste traballo seleccionouse o prototipo de ratio 4:1 (*m/m*) de Pr:Dx, xa que presentaba unhas características fisicoquímicas e unha capacidade de asociación de ácidos nucleicos adecuadas para o seu uso en terapia xénica (Figura 1.). A estabilidade no medio fisiolóxico, e durante o almacenamento representan algúns das principais limitacións no desenvolvemento de novas terapias xénicas. A nosa formulación mostrou resultados adecuados en ámbolos aspectos relacionados coa estabilidade. Por tanto, considerouse este prototipo como un candidato ideal para a súa avaliación *in vitro* en modelos avanzados de liñas celulares relevantes para a translación clínica.

A combinación de varios estudos de viabilidade de actividade metabólica celular, integridade de membrana e un ensaio de volume de esferoides, mostraron unha baixa citotoxicidade deste prototipo tanto en modelos de glioblastoma 2D como 3D (Figura 2. (a)). Por outra banda, estudos de captación celular mediante microscopía confocal e de fluorescencia de lámina de luz, e a súa cuantificación por citometría de fluxo, revelaron unha internalización das NPs de case o 100% en ambos os modelos de glioblastoma (Figura 2. (b)). Estes resultados verificaron a capacidade deste nanosistema de penetrar de forma eficiente nas células e mesmo en supraestruturas multicelulares [35-38].

A capacidade de transfección está condicionada pola entrada e o tráfico intracelular dos vectores, que son procesos dependentes da liña celular. Neste caso, a pesar de que o noso nanosistema promoveu unha expresión eficiente a partir de doses de 1 µg de plásmido tanto en células como en esferoides de glioblastoma, non se correlacionou cos valores de captación celular (Figura 3.). En conclusión, as NPs de Pr:Dx demostraron presentar unhas propiedades adecuadas para a asociación e protección de cargas xenéticas con baixa citotoxicidad, alta capacidade de internalización, pero unha eficiencia de transfección mellorable en modelos avanzados de glioblastoma.

Estudos recentes do noso grupo de investigación demostraron que a adición do polifosfaceno aniónico 6MHA-PPZ potencia a internalización, o escape endosomal e a biodispoñibilidade intracelular dunha serie de nanosistemas poliméricos [39]. En base a estes resultados, a segunda parte da tese centrouse no desenvolvemento de nanocomplexos de polietilenimina (PEI) e protamina por condensación cun plásmido modelo en combinación co polifosfaceno 6MHA-PPZ. As formulacións presentaron unhas propiedades fisicoquímicas apropiadas en canto a tamaño e carga superficial para a asociación de ácidos nucleicos, sen

observarse variacións significativas coa adición do polímero aniónico (Táboa 1.). Con todo, cabe resaltar un aumento no rendemento de formación dos nanocomplexos en presenza deste polifosfaceno, concordando cos resultados de caracterización previos [39]. As propiedades mantivéronse estables en condicións de almacenamento e no medio de cultivo celular, pero sufriron agregación en medios de cultivo convencionais de peixe cebra, especialmente no caso dos nanocomplejos de protamina. En cambio, ao incubarse en auga corrente declorada e estéril, a súa estabilidade coloidal non se viu afectada.

En canto á avaliación do seu potencial como nanosistemas de terapia xénica, isto realizouse en modelos preclínicos de esferoides de glioblastoma derivados de pacientes con diferente orixe da masa tumoral, e nun modelo *in vivo* de embrións de peces cebra. En xeral, os nanocomplexos de PEI mostraron unha citotoxicidade maior que os de protamina, pero o exceso de toxicidade foi parcialmente corrixido coa adición do polímero 6MHA-PPZ, concordando con resultados previos nunha liña de glioblastoma altamente transformada [39] (Figura 4.). A eficiencia de transfección determinouse mediante a cuantificación da expresión da proteína Luciferasa. En xeral, a adición do polifosfaceno aniónico mellorou a transfección, aumentando o efecto do escape endosomal, especialmente nos nanocomplexos de protamina, cuxos valores de transfección alcanzaron mesmo ao do modelo de referencia PEI/pADN (Figura 5.). Con todo, nos modelos preclínicos de esferoides observáronse efectos diferentes en función da liña celular. Obtivéronse resultados de transfección similares aos obtidos nos cultivos 2D no caso dos esferoides de glioblastoma de liñas transformadas comerciais, pero non sucedeu o mesmo nos esferoides de liñas primarias de glioblastoma, onde o efecto do polifosfaceno 6MHA-PPZ foi menos claro. Isto confirmou a necesidade de usar modelos clínicamente relevantes canto antes.

En canto a súa biodistribución en modelos *in vivo* de embrións de peixe cebra de 48 horas post-fecundación, obtívose unha maior acumulación das formulacións no saco vitelino, especialmente dos nanocomplexos de PEI, onde tras 5 días post-inxección, parte destas partículas desprazáronse cara á zona da cabeza. Por outra banda, observouse que a adición do polifosfaceno aniónico deu lugar a unha maior intensidade de fluorescencia confirmando a capacidade deste polímero para potenciar o escape endosomal de péptidos catiónicos, como PEI, permitindo a liberación do material xénico. Para os nanocomplexos de protamina, estes valores resultaron ser máis baixos como consecuencia da súa forte capacidade de complexación de ácidos nucleicos [40], que mesmo en presenza de 6MHA-PPZ, a completa liberación do material xenético resultou ser máis complicada (Figura 6.). En conclusión, a combinación do polifosfaceno aniónico 6MHA-PPZ con polímeros catiónicos comerciais mellorou as características dos nanocomplexos reducindo a súa citotoxicidade, aumentando a súa eficacia de transfección en modelos avanzados de glioblastoma e conseguindo unha biodistribución no saco vitelino cara á cabeza en modelos de embrións de peixes cebra.

As nanocápsulas (NCs) poliméricas teñen unha utilidade potencial como nanoportadores na vía ocular grazas á súa capacidade de interacción cos epitelios da córnea e conjuntiva [41]. Por tanto, a terceira parte desta tese consistiu no desenvolvemento e a optimización de nanocápsulas de protamina (Pr NCs) para a súa aplicación en terapia xénica contra o cancro ocular. A formulación foi preparada mediante o método de desprazamento de solvente obtendo unha poboación homoxénea de nanogotículas oleosas de vitamina E, cubertas por unha capa polimérica de protamina, e estabilizadas coa axuda de surfactantes non iónicos. A súa morfoloxía esférica, as súas propiedades fisicoquímicas, e a súa asociación reversible de macromoléculas de ADN plasmídico e miARN, converteunas en vehículos adecuados para

terapia xénica (Figura 7.). Este nanosistema mostrou unha estabilidade adecuada en condicións de almacenamento durante un mes, e estabilidade coloidal no medio de cultivo celular. Considerando a vía de administración, a súa estabilidade tamén foi testada en fluído lacrimal simulado, onde as características das Pr NCs cargadas con diferentes porcentaxes de ADN mantivéronse estables previndo a liberación prematura do plásmido. A avaliación do seu potencial como nanosistema de terapia xénica levouse a cabo en células de melanoma uveal (MU). Os resultados mostraron baixa citotoxicidade a diferentes concentracións e tempos (Figura 8. (a)), e unha eficiente internalización intracelular (Figura 8. (b)).

Na área de terapia xénica ocular, os nanosistemas poliméricos son especialmente atractivos debido á súa capacidade de interactuar intimamente coa superficie ocular. Neste aspecto, o noso grupo de investigación foi un dos pioneiros en demostrar a capacidade destes nanovehículos para adherirse á superficie ocular e penetrar a través da córnea e o epitelio conjuntival, permitindo así unha administración por vía tópica de fármacos nos que esta vía non era viable [41-47]. En base a estes estudos, determinouse a capacidade de transporte das Pr NCs nun modelo 3D de córnea. Os resultados mostraron que a formulación, tanto con ADN plasmídico asociado como sen el, foi capaz de atravesar esta barreira epitelial (Figura 9. (a)) sen alterar a súa integridade e morfoloxía (Figura 9. (b)) [48]. Finalmente, estes nanosistemas mostraron niveis adecuados de transfección a 48 h despois da súa incubación coas células (Figura 10.). En conclusión, estes resultados confirmaron que as Pr NCs poderían considerarse un nanosistema prometedor para o tratamento do melanoma uveal en terapia xénica.

En resumo, esta tese demostrou o potencial de plataformas variadas de nanosistemas, xa sexan NPs, nanocomplexos e NCs poliméricas, para aplicacións de terapia xénica. Os nanosistemas desenvolvidos teñen propiedades morfolóxicas e fisicoquímicas adecuadas, son biodegradables, teñen boa capacidade de asociación e transporte de xenes. Os nanotransportadores teñen ademais unha boa relación entre eficacia e citotoxicidade, confirmada mediante a súa avaliación en diferentes modelos preclínicos avanzados tales como esferoides e peces cebra.

REFERENCIAS

[1] E.B. Yahya, A.M. Alqadhi, Recent trends in cancer therapy: a review on the current state of gene delivery, Life Science 269 (2021) 1-15. https://doi.org/10.1016/j.lfs.2021.119087.

[2] L. Torresano, C. Nuevo-Tapioles, F. Santacatterina, J.M. Cuezva, Metabolic reprogramming and disease progression in cancer patients, Biochim. Biophys. Acta – Mol. Basis Dis. 1866 (2020) 1-16. https://doi.org/10.1016/j.bbadis.2020.165721.

[3] Y. ElMokhallalati, E. Alaloul, M. Shatat, T. Shneewra, S. El Massri, O. Shaer, S. Relton, H. Abu-Odah, M.J. Allsop, The symptom burden and quality of life in cancer patients in the Gaza Strip, Palestine: a cross-sectional study, PloS ONE 17 (2022) 1-15. https://doi.org/10.1371/journal.pone.0262512.

[4] O.L. Gobbo, K. Sjaastad, M.W. Radomski, Y. Volkov, A. Prina-Mello, Magnetic nanoparticles in cancer theranostics, Theranostics 5 (2015) 1249-1263. http://doi.org/10.7150/thno.11544.

[5] J. Ferlay, M. Colombet, I. Soerjomataram, D.M. Parkin, M. Piñeros, A. Znaor, F. Bray, Cancer statistics for the year 2020: an overview, J. Cancer 149 (2021) 778-789. https://doi.org/10.1002/ijc.33588.

[6] N. Irrera, A. D'Ascola, G. Pallio, A. Bitto, F. Mannino, V. Arcoraci, M. Rottura, A. Leni, L. Minutoli, D. Metro, M. Vaccaro, D. Altavilla, F. Squadrio, β-caryophyllene inhibits cell proliferation through a direct modulation of CB2 receptors in Glioblastoma cells, Cancers as (2020) 1-14. https://doi.org/10.3390/cancers12041038.

[7] B. Chen, C. Chen, Y. Zhang, J. Xu, Recent incidence train of elderly patients with glioblastoma in the United States, 2000-2017, BMC Cancer 21 (2021) 1-10. https://doi.org/10.1186/s12885-020-07778-1.

[8] K.N. Smit, J. Chang, K. Derks, J. Vaarwater, T. Brands, R.M. Verdijk, E.A.C. Wiemer, H.W. Mensink, J. Pothof, A. de Klein, E. Kilic, Aberrant microRNA expression and its implications for uveal melanoma metastasis, Cancers 11 (2019) 1-14. https://doi.org/10.3390/cancers11060815.

[9] N.J. Lamas, A. Martel, S. Nahon-Estève, S. Goffinet, A. Macocco, C. Bertolotto, S. Lassalle, P. Hofman, Prognostic biomarkers in uveal melanoma: the status quo, recent advances, and future directions, Cancers 14 (2022) 1-44 https://doi.org/10.3390/cancers14010096.

[10] K.J. Streitberger, L. Lilaj, F. Schrank, J. Braun, K.T. Hoffman, M. Reiss-Zimmermann, J.A. Käs, I. Sack, How tissue fluidity influences brain tumor progression, PNAS 117 (2020) 128-134. https://doi.org/10.1073/pnas.1913511116.

[11] D.C. Branisteanu, C.M. Bogdanici, D.E. Branisteanu, M.A. Maranduca, M. Zemba, F. Balta, C.L. Branisteanu, A.D. Moraru, Uveal melanoma diagnosis and current treatment options (review), Exp. Ther. Med. 22 (2021) 1-8. https://doi.org/10.3892/etm.2021.10863.

[12] L. Abballe, E, Miele, Epigenetic modulators for brain cancer stem cells: implications for anticancer treatment, World J. Stem Cells 13 (2021) 670-684. http://doi.org/10.4252/wjsc.v13.i7.670.

[13] C. Garcia-Mazas, S. Barrios-Esteban, N. Csaba, M. Garcia-Fuentes, Chapter13-Suppression of cancer stem cells, Woodhead Publ. Ser. Biomater. (2020) 365-398. https://doi.org/10.1016/B978-0-08-102983-1.00013-2.

[14] Y.P. Liu, C.C. Zheng, Y.N. Huang, M.L. He, W.W. Xu, B. Li, Molecular mechanisms on chemo- and radiotherapy resistance and the potential implications for cancer, MedComm 2 (2021) 315-340. https://doi.org/10.1002/mco2.55.

[15] L. Duan, L. Xu, X. Xu, Z. Qin, X. Zhou, Y. Xiao, Y. Liang, J. Xia, Exome-mediated delivery of gene vectors for gene therapy, Nanoscale 13 (2021) 1387-1397. http://doi.org/10.1039/D0NR07622H.

[16] C.H. Kapadia, J.R. Melamed, E.S. Day, Spherical nucleic acid nanoparticles: therapeutic potential, BioDrugs 32 (2018) 297-309. https://doi.org/10.1007/s40259-018-0290-5.

[17] M.L. Borrajo, M.J. Alonso, Using nanotechnology to delivery biomolecules from nose to brain- peptides, proteins, monoclonal antibodies, and RNA, Drug Deliv. and Transl. Res. 12 (2022) 862-880. https://doi.org/10.1007/s13346-021-01086-2.

[18] L. Zhu, R.I. Mahato, Lipid, and polymeric carrier-mediated nucleic acid delivery, Expert Opin. Drug Deliv. 7 (2010) 1209-1226. https://doi.org/10.1517/17425247.2010.513969.

[19] C. Olbrich, U. Bakowsky, C-M. Lehr, R.H. Müller, C. Kneuer, Cationic solid-lipid nanoparticles can efficiently bind and transfect plasmid DNA, JCR 77 (2001) 345-355. https://doi.org/10.1016/S0168-3659(01)00506-5.

[20] C. Horejs, From lipids to nanoparticles to mRNA vaccines, Nat. Rev. Mater. 6 (2021) 1075-1076. https://doi.org/10.1038/s41578-021-00379-9.

[21] M.J. Mulligan, K.E. Lyke, N. Kitchin, J. Absalon, A. gurtman, S. Lockhart, K. Neuzil, V. Raabe, R. bailey, K.A. Swanson, P. Li, K. Koury, W. Kalina, D. Cooper, C. Fontes-Garfias, P.Y. Shi, Ö. Türeci, K.R. Tompkins, E.E. Walsh, R. Frenck, A.R. Falsey, P.R. Dormitzer, W.C. Gruber, U. Sahin, K.U. Jansen, PhaseI/II study of COVID-19 RNA vaccine BNT162b1 in adults, Nature 586 (2020) 589-593. https://doi.org/10.1038/s41586-020-2639-4.

[22] K.H. Moss, P. Popova, S.R. Hadrup, K. Astakhova, M. Taskova, Lipid nanoparticles for delivery of therapeutic RNA oligonucleotides, Mol. Pharmaceutics 16 (2019) 2265-2277. https://doi.org/10.1021/acs.molpharmaceut.8b01290.

[23] J.V. González-Aramundiz, M. Peleteiro, A. González-Fernández M.J. Alonso, N.S. Csaba, Protamine nanocapsules for the development of thermostable adjuvanted nanovaccines, Mol. Pharmaceutics, 15 (2018) 5653-5664. https://doi.org/10.1021/acs.molpharmaceut.8b00852.

[24] H. Rilo-Alvarez, A.M. Ledo, A. Vidal, M. Garcia-Fuentes, Delivery of transcription factors as modulators of cell differentiation, Drug Deliv. Transl. Res. 11 (2021) 426-444. https://doi.org/10.1007/s13346-021-00931-8.

[25] M. Germain, F. Caputo, S. Metcalfe, G. Tosi, K. Spring, A.K.O. Aslund, A. Pottier, R. Schiffelers, A. Ceccaldi, Delivering the power of nanomedicine to patients today, JCR. 326 (2020) 164-171. https://doi.org/10.1016/j.jconrel.2020.07.007.

[26] J.L. Shierley, Y.P. de Jong, C. Terhorst, R.W. Herzog, Immune responses to viral gene therapy vectors, Mol. Ther. 28 (2020) 709-722. https://doi.org/10.1016/j.ymthe.2020.01.001.

[27] J.T. Bulcha, Y. Wang, H. MA, P.W.L. Tai, G. Gao, Viral vector platforms within the gene therapy landscape, Sig. Transduct. Target. Ther 53 (2021) 1-24. https://doi.org/10.1038/s41392-021-00487-6

[28] R. van der Meel, E. Sulheim, Y. Shi, F. Kiessling, W.J.M. Mulder, T. Lammers, Smart cancer nanomedicine, Nat. Nanotechnol. 14 (2019) 1007-1017. https://doi.org/10.1038/s41565-019-0567-y.

[29] C.C. Jayme, A.F. Pires, D.S. Fernandez, H. Bi, A.C. Tedesco, DNA polymer films used as drug delivery systems to early-stage diagnose and treatment of breast cancer using 3D tumor spheroids as a model, Photodiagnosis Photodyn. Ther. 37 (2022) 1-12. https://doi.org/10.1016/j.pdpdt.2021.102575.

[30] B. Pinto, A.C. Herniques, P.M.A. Silva, H. Bousbaa, Three-dimensional spheroids as in vitro preclinical models for cancer research, Pharmaceutics 12 (2020) 1-38. https://doi.org/10.3390/pharmaceutics12121186.

[31] C.E. Vasey, R.J. Cavanagh, V. Taresco, C. Moloney, S. Smith, R. Rahman, C. Alexander, Polymer pro-drug nanoparticles for sustained release of cytotoxic drugs evaluated in patient-derived glioblastoma cell lines and in situ gelling formulations, Pharmaceutics 13 (2021) 1-17. https://doi.org/10.3390/pharmaceutics13020208.

[32] M. Hason, P. Bartunek, Zebrafish models of cancer-new insights on modeling human cancer in a non-mammalian vertebrate, Genes 10 (2019) 1-30. https://doi.org/10.3390/genes10110935.

[33] R. Hadianamrei, X. Zhao, Current state of the art in peptide-based gene delivery, JCR. 343 (2022) 600-619. https://doi.org/10.1016/j.jconrel.2022.02.010.

[34] J.M. Ageitos, A. Pulgar, N. Csaba, M. Garcia-Fuentes, Study of nanostructured fibroin/dextran matrixes for controlled protein release, Eur. Polym. J. 114 (2019) 197-205. https://doi.org/10.1016/j.eurpolymj.2019.02.028.

[35] D. Delgado, A. del Pozo-Rodríguez, M.A. Solinís, A. Rofríguez-Gascón, Understanding the mechanism of protamine in solid lipid nanoparticle-based lipofection: the importance of the entry pathway, Eur. J. Pharm, Biopharm. 79 (2011) 495-502. https://doi.org/10.1016/j.ejpb.2011.06.005.

[36] D. Delgado, A.R. Gascón, A. del Pozo-Trodríguez, E. Evhevarría, A.P.R. De Garibay, J.M. Rodríguez, M.A. Solinís, Dextran-protamine-solid lipid nanoparticles as a non-viral vector for gene therapy: *in vitro* characterization and *in vivo* transfection after intravenous administration to mice, Int. J. Pharm. 425 (2012) 35-43. https://doi.org/10.1016/j.ijpharm.2011.12.052.

[37] A.P.R. de Garibay, D. Delgado, A. del Pozo-Rodríguez, M.A. Solinís, A.R. Gascón, Multicomponent nanoparticles as nonviral vectors for the treatment of fabry disease by gene therapy, Drug Des. Devel. Ther. 6 (2012) 303-310. https://doi.org/10.2147/DDDT.S36131.

[38] D. Delgado, A. del Pozo-Rodríguez, M.A. Solinís, M. Avilés-Triqueros, B.H.F. Weber, E. Fernández, A.R. Gascón, Dextran and protamine based solid lipid nanoparticles as potential vectors for the treatment of X-linked juvenile retinoschisis, Hum. Gene Ther. 23 (2012) 345-355. https://doi.org/10.1089/hum.2011.115.

[39] W.H. Hsu, P. Sánchez-Gómez, E. Gomez-Ibarlucea, D.P. Ivanov, R. Rahman, A.M. Grabowska, N. Csaba, C. Alexander, M. Garcia-Fuentes, Structure-optimized interpolymer polyphosphazenes complexes for effective gene delivery against glioblastoma, Adv. Ther. 2 (2018) 1-15. https://doi.org/10.1002/adtp.201800126.

[40] H. Al-Azzawi, W. Alshaer, E. Esawi, Z. Lafi, D. Abuarqoub, R. Zaza, M. Zraikat, A. Battah, A. Awidi, Multifunctional nanoparticles recruiting hyaluronic acid ligand and polyplexes containing low molecular weight protamine and ATP-sensitive DNA motif for doxorubicin delivery, J. Drug Deliv. Sci. Technol. 69 (2022) 1-11. https://doi.org/10.1016/j.jddst.2022.103169.

[41] S. Reimondez-Troitiño, I. Alcalde, N. Csaba, A. Íñigo-Portugués, M. de la Fuente, F. Bech, A.C. Riestra, J. Merayo-Lloves, M.J. Alonso, Polymeric nanocapsules: a potential

new therapy for corneal wound healing, Drug Deliv. and Transl. Res. 6 (2016) 708-721. https://doi.org/10.1007/s13346-016-0312-0.

[42] C. Losa, L. Marchal-Heussler, F. Orallo, J.L.V. Jato, M.J. Alonso, Design of new formulations for topical ocular administration: polymeric nanocapsules containing metipranolol, Pharm. Res. 10 (1993) 80-87. https://doi.org/10.1023/A:1018977130559.

[43] P. Calvo, C. Thomas, M.J. Alonso, J.L. Vila-Jato, J.R. Robinson, Study of mechanism of interaction of poly(ϵ-caprolactone) nanocapsules with the corneal by confocal laser scanning microscopy, Inter. J. Pharm. 103 (1994) 283-291. https://doi.org/10.1016/0378-5173(94)90179-1.

[44] P. Calvo, J.L. Vila-Jato, M.J. Alonso, Evaluation of cationic polymer-coated nanocapsules as ocular drug carriers, Inter. J. Pharm. 153 (1997) 41-50. https://doi.org/10.1016/S0378-5173(97)00083-5.

[45] A.M. de Campos, Y. Diebold, E.L.S. Carvalho, A. Sánchez, M.J. Alonso, Chitosan nanoparticles as new ocular drug delivery systems: *in vitro* stability, *in vivo* fate, and cellular toxicity, Pharm. Res. 21 (2004) 803-810. https://doi.org/10.1023/B:PHAM.0000026432.75781.cb.

[46] M. de la Fuente, M.J. Alonso, Bioadhesive hyaluronic-chitosan nanoparticles can transport genes across the ocular mucosa and transfect ocular tissue, Gene Ther. 15 (2008) 668-676. https://doi.org/10.1038/gt.2008.16.

[47] C. Losa, M.J. Alonso, J.L. Vila, F. Orallo, J. Martinez, J.A. Saavedra, J.C. Pastor, Reduction of cardiovascular side effects associated with ocular administration of metipranolol by inclusion in polymeric nanocapsules, J. Ocul. Pharmacol. Ther. 8 (2009) 191-198. https://doi.org/10.1089/jop.1992.8.191.

[48] M. Chacón, N. Vázquez, M. Persinal-Medina, S. Alonso-Alonso, I. Alcalde, J. Merayo-Lloves, A. Meana, In-house performance assessment of 3D QobuR-reconstructed human cornea-like epithelium (RhCE) for the evaluation of eye hazard, Toxicol. In Vitro 82 (2022) 1-7. https://doi.org/10.1016/j.tiv.2022.105390.

DISCLOSURE REGARDING ANNEX I

In the introduction of this doctoral thesis, the Annex I corresponding to the following publication, is referenced as:

CHAPTER-13: SUPPRESSION OF CANCER STEM CELLS

Carla Garcia-Mazas*, **Sheila Barrios-Esteban***, Noemi Csaba and Marcos Garcia-Fuentes

*These authors contributed equally.

Biomaterials for Cancer Therapeutics (Second Edition) in Woodhead Publishing Series in Biomaterials. Chapter 13. pp. 365-398. ISBN 9780081029831

DOI: https://doi.org/10.1016/B978-0-08-102983-1.00013-2

Department of Pharmacology, Pharmacy and Pharmaceutical Technology, Center for Research in Molecular Medicine, and Chronic Diseases (CiMUS), University of Santiago de Compostela, Santiago de Compostela, Spain.

WHERE:

Dr. Carla García Mazás and Ms. Sheila Barrios Esteban have contributed equally to this publication.

The sections related to the work written by Ms. Sheila Barrios Esteban in this publication are enlisted below:

13.1 Introduction

13.1.1 Models of cancer origin

13.1.2 Characteristics of cancer stem cells

13.1.3 The cancer stem cell niche

13.1.4 Cancer stem cell drug resistance

13.3 Nanomedicines for cancer stem cell therapy

13.3.2 Gene delivery to cancer stem cells

13.3.3 Targeting to cancer stem cells

13.4 Concluding remarks

INTRODUCTION

INTRODUCTION

1. GENE THERAPY AND CANCER

Cancer is considered the second leading cause of death after heart diseases [1], where the International Agency for Research on Cancer (IARC) has predicted 13 to 17 million deaths in 2030 worldwide [2]. From our current understanding of the biology of cancer [3], this pathology could be considered a hereditary disease caused by genetic and epigenetic alterations that affect normal cellular processes. The physiopathology behind involves somatic mutations in upstream cell signaling pathways and/or genetic lesions in genes encoding cell cycle proteins responsible for growth, differentiation, and apoptosis [1]. Therefore, malignant cells can change in size, structure, and function, and can spread to other tissues and organs to obtain their nutrients [4]. Currently, there are more than 200 types of known cancers [5], where those commonly diagnosed worldwide are female breast cancer (2.26 million cases/year), lung (2.21 million cases/year) and prostate cancers (1.41 million cases/year). The leading causes of death are lung (1.79 million deaths), liver (830,000 deaths), and stomach cancers (769,000 deaths) [6]. It is true that a reduction in mortality rates has been perceived due to preventive measures, early detection, immunotherapy, and other advances in chemotherapy. Unfortunately, patients diagnosed with more aggressive tumors, such as small cell lung cancer, triple negative breast cancer, pancreatic ductal adenocarcinoma, glioblastoma, metastatic melanoma, and ovarian cancer still show a low survival rate, and most medicines and treatments are ineffective. Highly aggressive tumors are characterized by a highly invasive phenotype, chemoresistance, and lack of biomarkers for targeted therapies [7]. In the present work, two aggressive tumors such as glioblastoma and uveal melanoma will be highlight.

Glioblastoma is the most common and aggressive primary tumor of the central nervous system feared by both patients and doctors due to its classification as malignant grade IV [8]. In addition, the transcriptomic studies of human glioblastoma biopsies demonstrated that these tumors are highly heterogeneous and invasive [9]. Ninety percent of glioblastomas are primary tumors that develop rapidly without the appearance of malignant lesions, while 10% are secondary tumors originated through the progression of pre-existing gliomas [10]. Despite being one of the least frequent tumors with a global incidence of 3.22 per 100,000 inhabitants, its poor prognosis makes it an important public health problem. This tumor represents 57.3% of all gliomas and 48.3% of all malignant brain tumors, with a mean age of 64 years in adults for primary glioblastoma, and of 10 to 15 years in young people for secondary glioblastoma [8]. According to data collected in the National Cancer Database (NCDB), its incidence is higher in males, in developed countries, and in white people [11].

Regarding ocular tumors, they are less frequent, and their peculiarity is they are difficult to diagnose [12]. Ocular melanoma is the second most common type of melanoma after cutaneous

melanoma, with 83% arising from the uvea, 5% from the conjunctiva, and 10% from other sites. Considering this information, **uveal melanoma** (UM) can be considered the second most common form of melanoma, originated from melanocytes located in the uveal tract of the eye and in the conjunctival membrane [13, 14]. This tumor is located mainly in the choroid (90%), although there are cases in the ciliary body (6%) and in the iris (4%) [13]. Despite being considered a relatively rare cancer with an incidence of 5 cases per 1,000,000 people, it also has an unfavorable prognosis with a high tendency to metastasize, mainly to the liver [15]. Patients could present symptoms such as blurred vision, or no symptoms at all, and the tumor is frequently detected by routine eye exams. Metastases may develop in almost 50% of patients [16].

Patients diagnosed with any of these tumors have a survival less than 2 years, being 14 months for glioblastoma [17] and 10-13 months for UM [18]. In addition to their poor prognosis, their conventional treatment is a combination of surgical resection, radiotherapy and, in the case of glioblastoma, temozolomide-based chemotherapy [19, 20]. Surgery is essential for the treatment of aggressive solid tumors as it allows mass reduction and access to tissue samples for pathology. In glioblastoma, as long as neurological functions are not compromised, maximal resection is beneficial [21], and for UM, enucleation is the historical approach for definitive local treatment and remains appropriate in the presence of large tumors and extensive extraocular growth [20]. However, the efficacy of surgical resection is limited by the intrinsic malignant nature of these tumors. The invasive nature of glioblastoma makes complete resection challenging because of the potential recurrence of cancer cells close to the resection cavity [9]. In UM, local recurrence can occur after enucleation, mostly associated to the appearance of systemic metastases [22]. Radiotherapy not only attacks tumor cells, but also healthy cells can be affected [23], causing side effects such as optic neuropathy, cataracts, radiation retinopathy or even toxic tumor syndrome in the case of UM [24], and neuro-cognitive decline in glioblastoma [25]. Regarding chemotherapy, high doses of drug are generally required to affect rapidly proliferating cells, causing high levels of toxicity, and the possibility of tumor chemoresistance [23]. For this reason, more effective and less invasive therapies are being investigated mainly focused on targeting genetic and epigenetic alterations that make tumors more resistant to conventional pharmacological treatment [26, 27].

Gene therapy is considered as a promising tool to transfer nucleic acids with the objective of treating a wide range of disorders from infectious and hereditary diseases, including cancer [28]. The concept dates back to the 1960s when the first studies showed that DNA sequences could be introduced into mammalian cells for gene repair [29]. However, it was in 1990 when gene therapy trials gained impetus. French Anderson, Michael Blaese, and Steve Rosenberg performed the first successful gene transfer study at the National Institutes of Health. In this research, lymphocytes were harvested from patient-infiltrating tumors, genetically tagged using a retroviral vector, and finally reinfused to genetically screen for their ability to localize to the tumor [30, 31]. Current methodologies for gene therapy include direct mutation, correction, or application of DNA to encode protein-based therapeutic drugs. However, the most common strategy is encoding a functional therapeutic gene to replace a mutated one [8]. This has already been used clinically to correct the genetic alteration of some disorders. In ***ex vivo* gene therapy**, defective cells are removed from the body, modified with a therapeutic gene, cultured *ex vivo*, and transferred back to the host where the corrected gene will replicate. In ***in vivo* gene therapy**, a vector is injected to transport the therapeutic gene to host cells. In cancer gene therapy, the aim is to eliminate or reduce the size of the tumor through different mechanisms [28, 29] [32] Gene therapy for malignant tumors has three modalities: suicide gene therapy, is a therapeutic

approach based on introducing a suicide gene that encodes an enzyme that is able to convert a prodrug into its active pharmacological variant resulting in cell death [33], corrective gene therapy, is a method applying therapeutic agents such as siRNAs, miRNAs or gene-editing tools into tumor cells to change their gene expression to inhibit their proliferation and the toxin/apoptosis-induced gene therapy which involves the production of cytotoxic proteins that are desired to cause apoptosis in the transduced cells [34]. Currently, the main strategy adopted in cancer field is to deliver the corrected gene into the primary tumor cells and its subsequent autologous transplantation into the host's target organs [35]. Regarding therapeutic nucleic acids used in gene therapy against cancer, some of the most recent examples are described in detail in Annex I of this thesis. In conclusion, for gene therapy to be successful, it become imperative to select a safe and efficient procedure to transfer these engineered nucleic acids into target cells.

1.1. Multiple biological barriers to overcome

Delivery of nucleic acids remains a significant challenge because the need to overcome several highly complex physiological barriers [36]. Nucleic acids cannot enter the cells directly due to their inherent properties, such as hydrophilicity, large size, and negative charge [37]. Moreover, they must avoid intracellular biological barriers and other extracellular defense mechanisms [38] (Figure 1.).

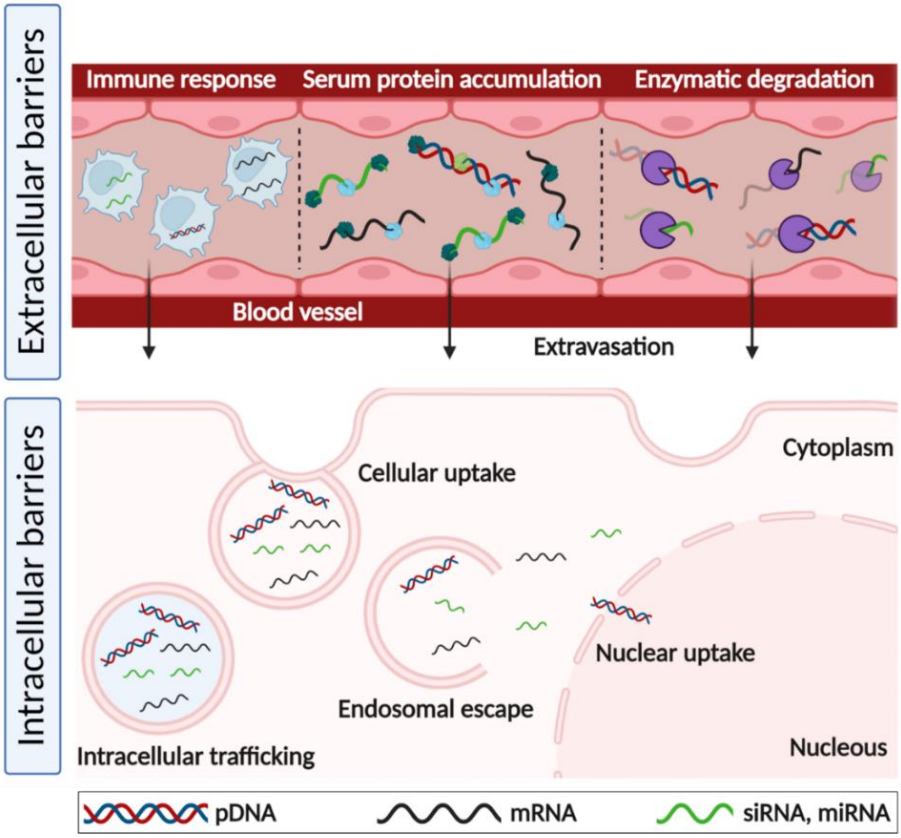

Figure 1. Extra- and intracellular barriers to nucleic acid delivery. Created in BioRender.com.

The **enzymatic degradation by nucleases** is a fundamental problem for any gene therapy approach [39]. Systemically administered nucleic acids are highly susceptible to degradation by plasma enzymes. The phosphate bonds are split by exonucleases and removed by **renal filtration**, being another limitation. On the other hand, locally administered nucleic acids have

low intracellular concentrations due to their inherent properties previously mentioned. In addition, intracellular endosomal compartments must be avoided to prevent degradation by intracellular enzymes. In extracellular environment, the half-life of naked nucleic acids ranges from a few minutes to hours, leading to off-site accumulation and inadequate therapeutic levels [38]. Moreover, in this environment there are also **serum proteins** whose accumulation and agglomeration constitute another limiting barrier for nucleic acid therapy [40]. Nucleic acids can also trigger **immune responses** by inducing cytokine release that can lead to severe inflammatory responses. This involves that, when designing gene expression therapies, the potential for immunogenicity and toxicity must be evaluated in order to avoid the incidence of adverse toxic responses in patients [41].

Once past the extracellular barriers, several intracellular barriers obstruct the way to efficient gene delivery. In order to reach the intracellular environment, the **difficulty to cross the plasma membrane** is a major obstacle. Small, neutral, and slightly hydrophobic molecules can passively diffuse across the cell membranes, but large and negatively charged molecules such as DNAs and RNAs rely on active transport mechanisms based in endocytosis [42]. Following endocytic uptake, polynucleotides are localized in early endosomes which mature via late endosomes into endolysosomes. This maturation is accompanied by intraluminal acidification and activation of several degradative enzymes, so the **endosomal escape** before their degradation constitutes another limiting factor. Even if endosomal escape occurs, the nucleic acids reside in the cytosol, where they have to avoid being removed from the cell by autophagy or degraded by cytoplasmic nucleases [43]. While siRNA, miRNA and mRNA have their site of action in the cytosol, the pDNA needs to be delivered to the nucleus, with the nuclear envelope another major barrier. Moreover, the **intracellular trafficking** to the nucleus is critical as a consequence of pDNA degradation by cytoplasmic enzymes [44]. Finally, genetic perturbations such as inhibition or overexpression of a non-target gene (**Off-Target effect**) are another major intracellular setback [45]. Nucleic acids can be targeted to cause specific gene-silencing mainly induced by siRNAs and CRISPR technology, [38], gene-knockout by the CRISPC-Cas9 gene editing system [46] and gene-overexpression by cloning a transgene cDNA [47], but can further exert severe off-target effects leading to gene mutations and unwanted cellular transformations.

Therefore, to achieve efficient and safe gene delivery, it is necessary to design and develop carriers that are capable of overcoming these barriers to transport and release nucleic acids in target tumor cells. Here, nanotechnology has emerged as a promising way to improve gene delivery.

2. NANOSYSTEMS FOR NUCLEIC ACID DELIVERY

Nanomedicine is an essential technology of the 21st century with the objective to exploit nanotechnology for several biomedical applications. Oncology has been one of the major therapeutic targets of nanomedicine research [48]. In this field, nanosystems are designed to have unique properties: (i) high capacity to incorporate different therapeutic agents, either drugs or nucleic acids, (ii) high capacity to deliver their cargo specifically to target cells, reducing unwanted secondary effects, and (iii) controlled release properties [23].

Clinical gene therapy depends on the delivery vectors, whether viral or non-viral. **Viral vectors** are effective for transferring genetic cargo, making them a reliable option in cancer

treatment and hereditary diseases. They have the natural ability to infect efficiently host cells, a process that can be used for transporting genes [32] [49]. Several cancer gene therapies based on viral vectors have come to market approval by Food and Drug Administration (FDA) and the European Medicines Agency (EMA) (Table 1.). However, these vectors have some limitations, especially those related to undesired immune responses [49, 50].

Table 1. Examples of approved products for cancer gene therapy. Table adapted from 32, 51.

Product	Approved country	Year	Vector	Cancer
Gendicine	China	2003	Adeno-associated virus	Head and neck
Oncorine	China	2005	Oncolytic virus	Nasopharyngeal
Rexin-G	USA	2010	Retrovirus	Metastatic
Imlygic	USA	2015	HSV	Melanoma
Kymriah	Switzerland/USA	2017	Lentivirus	Lymphoblastic leukemia
Yescarta	USA		Retrovirus	Lymphoma
Tecartus	USA	2020	Retrovirus	Prostate
Breyanzi	USA/Canada/UE/UK/Japan	2021	Lentivirus	Follicular lymphoma
Abecma	USA/Canada/EU/UK/Japan		Lentivirus	Multiple myeloma
Relma-cel	China		Lentivirus	Lymphoma
Delytact	Japan		Onclytic HSV	Glioma

A large number of studies have shown that **non-viral nanocarriers** have several advantages: low intrinsic immunogenicity, biocompatibility and biodegradability, low-cost industry-friendly production, and no clear upper on the molecular size of the cargo (i.e., packaging limit) [52, 53]. However, their application has been limited by their insufficient transfection efficiency due to poor serum stability, high endosomal entrapment, limited intracellular release, and low accumulation in target organelle [54]. Therefore, specific properties are required to increase the efficacy and clinical translation of non-viral gene nanocarriers [55]. In the last decade, nanosystems based on polymers and/or lipids have been extensively investigated to treat cancer (Figure 2.). In the following paragraphs, we describe some of the most used non-viral nanosystems for the administration of nucleic acids, with a special focus on the field of oncology.

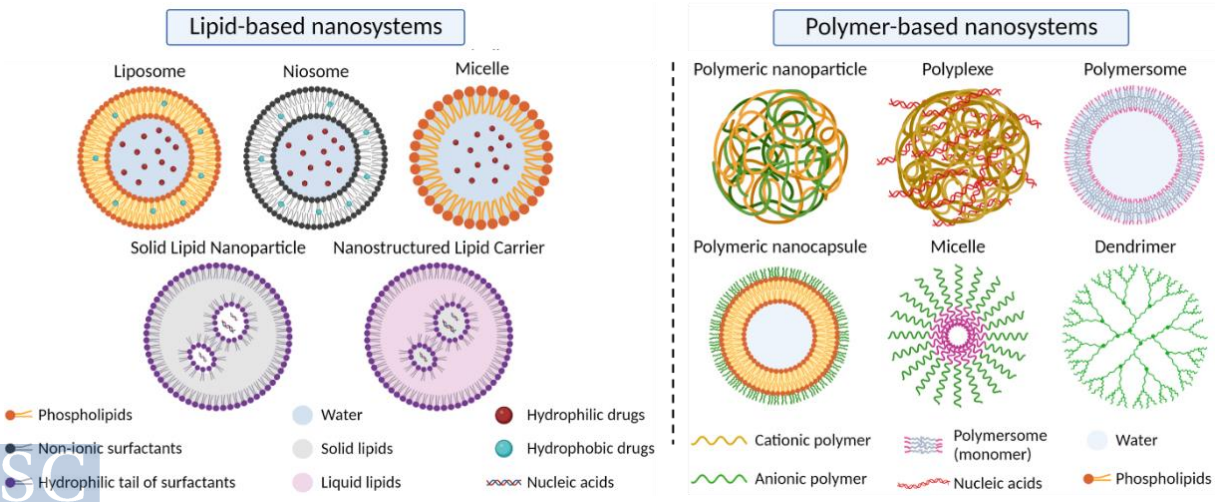

Figure 2. Lipid- and polymer-based nanosystems used to deliver nucleic acids. Created in BioRender.com.

Cationic lipids are the most investigated biomaterials in gene therapy. They have an active role in DNA binding and transfection due to their positive charge, and can facilitate endosomal escape. In Annex I, we provide a more exhaustive description of these lipids (Figure 3.), and their most common nanosystems (Figure 2.). Briefly, most lipidic nanosystems have a spherical vesicular structure organized in a bilayer, such as liposomes [56] or composed by a mixed solid and liquid matrix and an oily nucleus, such as nanostructured lipid carriers (NLC) [57]. Solid lipid nanoparticles (SLN) represent one of the most promising technologies for gene therapy because they have good gene-transfer efficiency in *in vitro* and *in vivo* models, together with good biocompatibility [58].

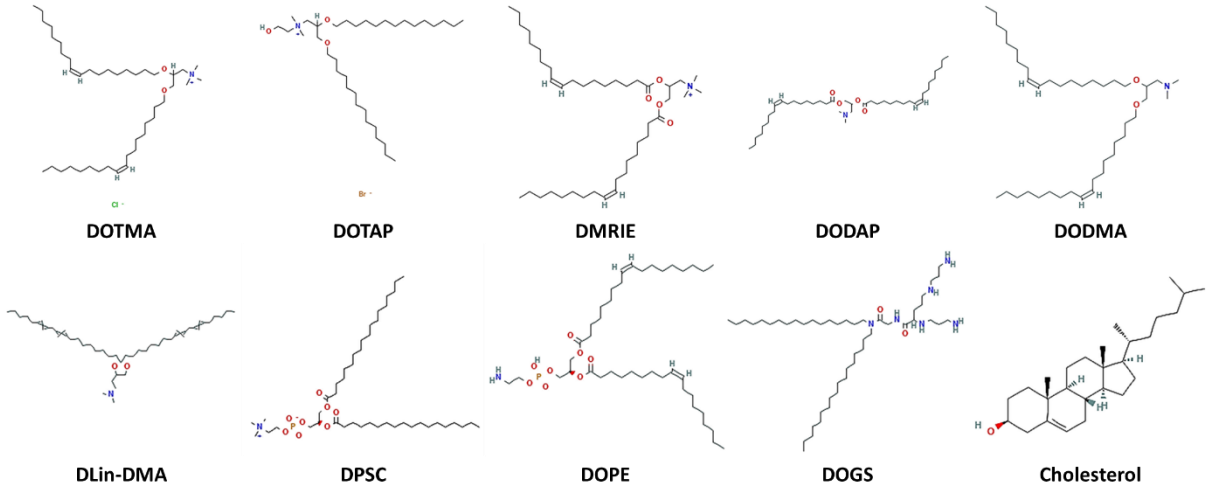

Figure 3. Lipid chemical structure of most important lipids to formulate non-viral nanosystems for their use in gene therapy. DOTMA: N-[1-(2,3-dioleyloxy)propyl]-N,N,N-trimethylammonium, DOTAP: N-[1-(2,3-dioleoyloxy)propyl]-N,N,N-trimethylammonium chloride, DMRIE: 1,2-dimyristyloxypropyl-3-dimethyl-hydroxyethylammonium bromide, DODAP: 1,2-dioleoyl-3-dimethylammonium propane, DODMA: 1,2-dioleoyl-3-dimethylaminopropane, DLin-DMA: 4-(dimethylamine)-butanoic acid, DPSC: 1,2-distearoyl-sn-glycero-3-phosphorylcholine, DOPE: 1,2-dioleoyl-phosphatidyl-ethanolamine, and DOGS: 2,5-bis(3-aminopropylamino)-N-[2-(di(heptadecyl)amino)-2-oxoethylpentanamide lipid. Images from PubChem 2023 update.

Currently, there are a few similar platforms based on lipid nanoparticles (NPs) for gene delivery that have reached the market. Those are TransoPlex® for DNA transfer [59] and Onpattro® for siRNA [60]. In addition, lipid NPs are also in the marketed formulations of Moderna® and Pfizer/BioNTech® mRNA-based vaccines against COVID-19 [61]. However, in general, non-viral lipid nanosystems still have the drawbacks of potential toxicity, and suboptimal gene transfer. These limitations fuel further research in non-viral systems, including polymeric ones.

Polymeric vectors are another attractive alternative for gene delivery due to their structural diversity, tunable physicochemical properties, stability under storage, higher genetic cargo capacity, and simple low-cost preparation [62] (Figure 2.). NPs based on cationic polymers are some of the most used for gene therapy, and important examples are described in Annex I (Figure 4.). Natural or synthetic cationic polymers with positively charged primary, secondary and/or tertiary amine groups can condense nucleic acids forming polyplexes. They have the ability to neutralize the anionic charges of nucleic acids, protecting them from enzymatic degradation, and thus facilitating their intracellular release [63]. Polyplexes with positive surface charge are more efficient in cell interaction due to their ability to bind to the cell membrane, promoting intracellular uptake [64]. Several polycations exhibit adequate transfection efficiency, but the presence of positive charges can also confer them undesirable

toxicity. Therefore, the surface charge, the NP-size, the ratio between amino and phosphate groups (N/P ratio), and the molecular weight are important factors in the formulation behavior *in vivo* [64, 65]. Polypeptides and polyaminoacids are some of the most used and flexible materials for the preparation of gene delivery systems, and polyphosphazenes are other materials of interest since they considered as "peptide mimics". The following sections will explore the potential of these polymer classes in gene delivery.

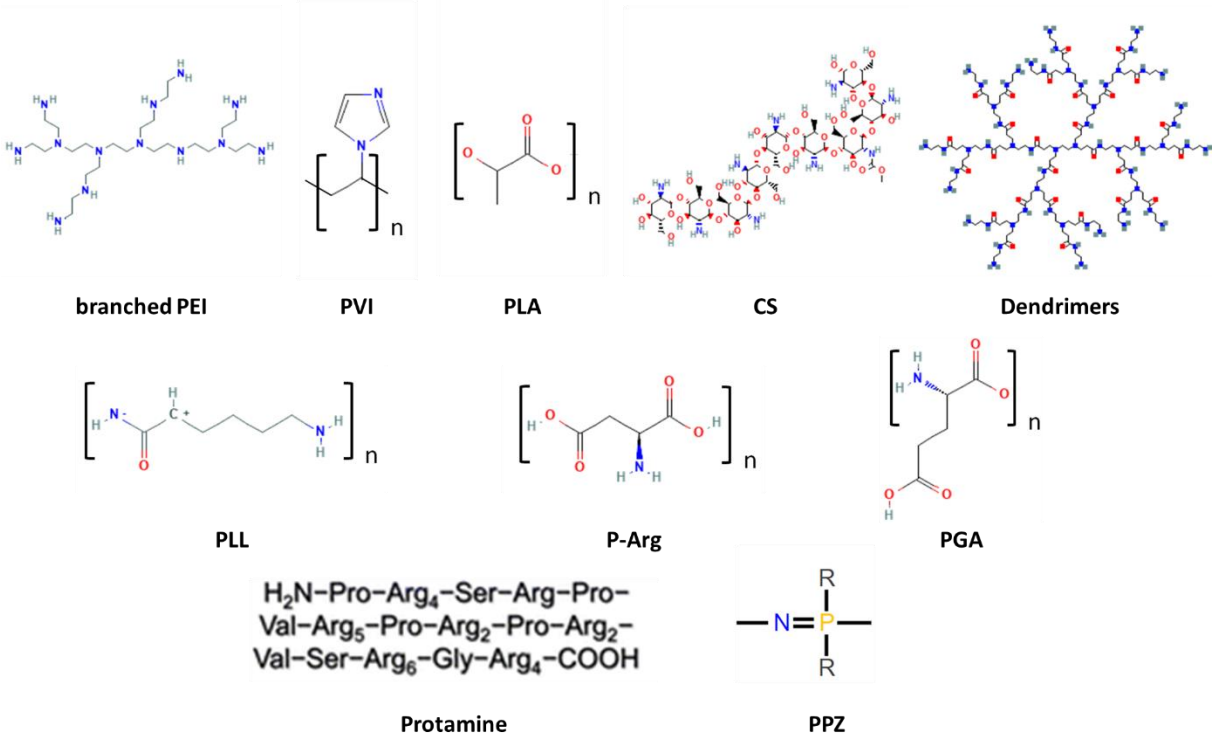

Figure 4. Polymeric chemical structure of most important polymers to formulate non-viral nanosystems for their use in gene delivery. PEI: polyethylenimine, PVI: poly(vinyl imidazole), PLA: polylactic acid, CS: chitosan, PLL: poly-L-Lysine, P-Arg: poly-L-arginine, PGA: polyglutamic acid, and PPZ: polyphosphazenes. Images from PubChem 2023 update.

2.1. Polypeptides and polyaminoacids in drug delivery

To overcome the above detailed limitations of current gene delivery technologies, new nanostructures based on the use of polyaminoacids, and polypeptides are being explored. Cell penetrating peptides (CPPs) have been investigated for the delivery of DNA, RNA, and antibodies for over the past two decades [66]. They are synthetic or biological small peptides composed of 7 to 30 amino acids that show enhanced penetration through the plasma membrane [67]. Based on their physical characteristics, CPPs can be classified as amphipathic, hydrophobic, and cationic, where the latter have become a promising tool for gene delivery. Cationic CPPs are composed by short sequences of amino acids, mainly arginine, lysine, and histidine, being the residues involved in cellular penetration. In addition, a special group of them are nuclear localization sequences (NLS) composed by lysine, arginine and proline residues which enter the nucleus via the nuclear pore complexes (NPC) [68]. In this context, some polyaminoacids such as poly-L-lysine (PLL) and poly-L-arginine (P-Arg) have generated growing interest due to their high capacity to condense the genetic material [69, 70], being the first polymers commonly used in gene delivery [70, 71] (Figure 4.). They are cationic, biodegradable, biocompatible, and non-immunogenic homopolymers [72] that penetrate cell

membranes [73]. However, their major limitations are their toxicity and relatively low transfection efficiency [71], which can be improved by combination with other polymers. Especially, their conjugation with polyethylene glycol (PEG) has been used to provide increased stability in salt and serum, reduce toxicity and lower immunogenicity [74]. Several studies have focused on the synthesis of di- or tri-block copolymers combining PLL and P-Arg with PEG [75-77] that form cationic micellar NPs [74]. Moreover, the conjugation of PLL with PEI polymer has shown higher transfection efficiency, and a significant reduction in toxicity [78, 79].

Besides PLL and P-Arg, the natural polypeptide **protamine** (Pr) is one of the most used delivery agents in gene therapy. At the end of the 19th century, Albrecht Kossel described its composition as a natural peptide derived from fish sperm with high content of arginines and low molecular weight (Mw= 4 to 5 kDa, LMWP) [80] (Figure 4.). Salt forms of protamine sulfate are considered biologically safe, and they have been approved for clinical use by the FDA as drug and as pharmaceutical excipient [81]. Sixty years ago, Harold Amos published the first report of its use as a transporter of nucleic acids for eukaryotic cells [82]. Since then, different protamine-based nanosystems have been developed for multiple therapeutic modalities with high efficacy. In fact, the use of protamine as a polymeric shell on nanocapsules (NCs) [83-86] or, simply, its combination with other polysaccharides such as hyaluronic acid [87], alginate [88] or dextran sulfate [89] to form NPs, can be a tool to promote the delivery of diverse biomacromolecules, such as antigens [83] [86] [88, 89], peptides [90], or nucleic acids [91]. Regarding the latter, beyond providing enhanced penetration capacity, the natural condensing function of this polypeptide is also a useful tool for delivery applications [92]. In the field of cancer, several studies describe the use of protamine nanocarriers for the delivery of different nucleic acids for tumor treatment. For instance, Pr NPs showed efficient encapsulation of shRNA, effectively protecting it from degradation by nucleases and serum. Furthermore, protamine improves *in vitro* transfection levels and shBcl-2-loaded NPs showed increased antitumoral effect in a A549 model [93]. Moreover, it was observed that lipidic systems and PAMAM dendrimers functionalized with protamine are promising therapeutic options for plasmid DNA [94], siRNA [95, 96], and miRNA [91] delivery, as observed in variety of tumor models. The protamine in these nanosystems acted as a DNA condenser preventing the enzymatic degradation and as transporter to the nucleus [97]. Considering this information, Pr NPs could be a promising non-viral nanodevice for improving targeted gene delivery in cancer therapy.

2.2. Polyphosphazenes: a new platform for gene delivery.

Polyphosphazenes (PPZ) are a relatively new class of polymers with certain similarities with polyaminoacids: biodegradability, polymer elasticity, chemical versatility, and design flexibility [98]. PPZ with organic side chains are referred as poly(organo)phosphazenes, and stand out among biomedical materials as organic-inorganic hybrids. Their chemical structure is formed by a backbone connected by alternating single and double bonds of phosphorus and nitrogen atoms, a chemical bound structure with some similarities to natural polyaminoacids, (Figure 4.). Moreover, their side chains could be replaced by different organic groups giving rise to a wide diversity of PPZ with their own physical and chemical properties [99]. These polymers were considered attractive in a variety of biomedical applications, especially, for controlled release of anticancer drugs [100-103], gene delivery [104-107], and tissue engineering [108, 109]. In gene therapy, PPZ stand out for their good performance parameters [98]. Hennink's research group pioneered the development of PPZ as gene delivery systems.

They synthetized PPZ with side chains of tertiary amines, 2-dimethylaminoethanol (DMAE) and 2-dimethylaminoethylamine (DMAEA), and found that both polymers effectively complexed plasmid DNA, where DMAEA-PPZ had higher gene transfer efficiency. Furthermore, they also studied the relationship between polymer molecular weight and gene delivery efficiency [110]. Based on these studies, our research group has recently developed a variety of PPZ with ionic nature, synthesized by thiol-ene click chemistry. Among this variety of PPZ, the inclusion of 6-mercaptohexanoic acid (6MHA) side chains resulted in most interesting material, as it could improve the transfection efficiency of polyphosphazene polyplexes while reducing the toxicity of the nanocarrier. Furthermore, they showed higher transgene expression in three-dimensional (3D) models and subcutaneous glioblastoma xenograft models compared to a simple polycation/pDNA nanocomplex [107]. Overall, this information established PPZ as a new biodegradable and versatile polymeric gene delivery strategy due to their high capacity for gene-transfer efficacy.

3. ADVANCED MODELS FOR *IN VITRO* TESTING OF GENE DELIVERY CARRIERS

In general, the clinical success of cancer nanomedicines is still slowed down by the challenges in formulation, batch-to-batch consistency, scale-up, lack of adapted characterization and detection methods, as well as, regulatory barriers [111]. In addition to this, the physiological barriers imposed by the tumor microenvironment also hinder the effective administration of therapeutic nanomedicines [112]. For this reason, the choice of appropriate preclinical models reflecting tumor complexity is critical for preclinical evaluation of new therapies [113]. The most common experimental models to study human tumors include cancer cell lines, 3D culture models, and a great variety of *in vivo* models ranging from *Drosophila melanogaster*, *Danio rerio* to genetically modified mouse models, pigs, and patient-derived xenografts. More recently, new *in silico* computational models have also been implemented, having important contributions in combination with *in vitro* and *in vivo* models [114] (Figure 5.).

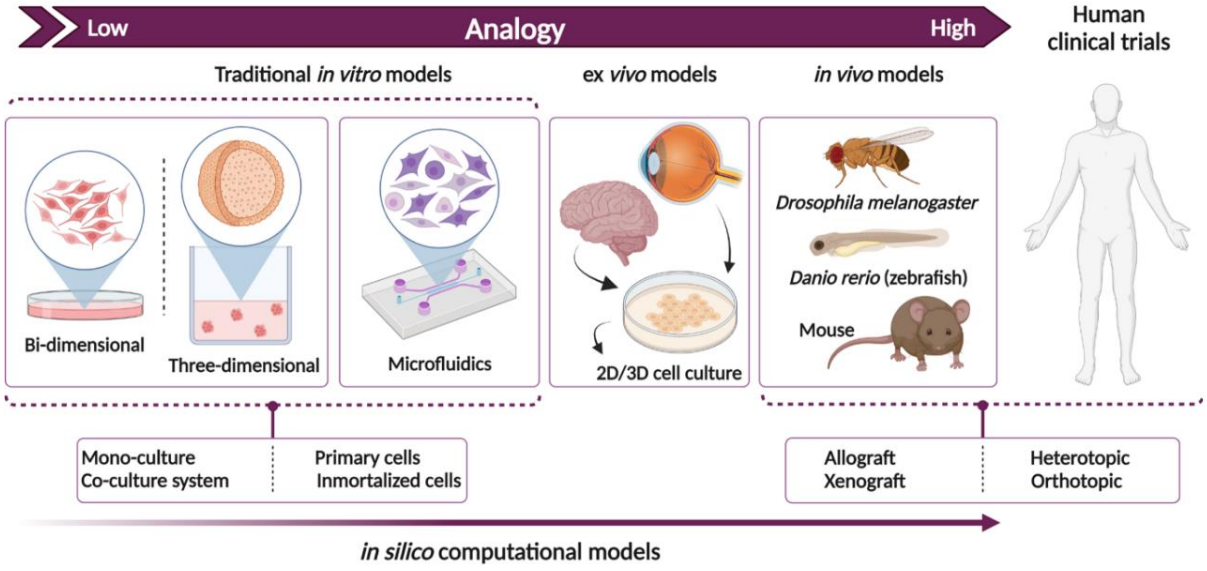

Figure 5. Representation of experimental models currently available for cancer gene therapy classified as traditional *in vitro*, *in vivo*, and *in silico* models. Created in BioRender.com.

All these models have their own particular characteristics, advantages, and disadvantages. Thanks to their simplicity and ease of use, **conventional two-dimensional** (**2D**) cancer cell cultures have contributed importantly to nanomedicine research. However, these models do not imitate tumor structure, they lack cellular heterogeneity and tumor microenvironment [115]. In this context, **3D models** represent more reliably tumor physiology. For instance, tumor spheroids may contain an outer layer of proliferating cells, a middle layer of quiescent cells, and an inner necrotic core [116]. Our research group has benefited from the use of 3D models as an evaluation tool for gene delivery. For example, glioblastoma spheroids were used to assess the toxicity and transfection ability of different polyphosphazene nanocomplexes. Those experiments supported good correlation between 3D spheroid data and in *in vivo* gene delivery experiments [107].

Another step further is the use of **primary cell lines** derived directly from patients. These cells better retain the molecular characteristics of patient tumors and showcase tumor interpatient variability. They are considered a better alternative to study cancer biology and drug sensitivity. The combination of primary cultures and 3D models has particular importance for studies guiding decision-making in the clinic due to their capacity measure drug sensitivity in a personalized way [117]. For example, the previous work of Vasey et al., studied the effects of a range of PEGylated poly(lactide)-poly(carbonate)-doxorubicin polymer NPs in a primary human astrocyte cell line and in a panel of primary infiltrating margin glioblastoma cells. The release studies showed that sufficient doxorubicin was released from the NPs to achieve a cytotoxic dose *in vitro*, being an adequate profile for the pharmacological therapies required in patients with glioblastoma. In addition, the results warranted the translational evaluation when using xenograft models for post-surgical drug delivery [118]. However, experimental evidence that spheroid technologies reliably reflect *in vivo* conditions is scarce, so their validation still requires comparative analysis with *in vivo* models [116].

Undoubtedly, *in vivo* models continue being the key for comprehensive analysis of nanomedicines. In this sense, murine tumor models have proven to be useful for the understanding of the biological processes causing tumor growth and for preclinical development of antitumor therapies. All experimental mouse models must meet the Animal Research Reporting of *In Vivo* Experiments (ARRIVE) criteria and the ethical standards of animal experimentation. In recent decades, the **zebrafish model** (*Danio rerio*) has emerged as a first screening alternative to murine models, helping the scientific community in their pursuit of the 3R principles (Replacement, Reduction, and Refinement). The reduction of time and the use of resources, the greater informative and predictive capacity compared to *in vitro* results, and the ability to refine the findings are some of the advantages of this model. Therefore, using the zebrafish model, it is possible to replace and reduce the use of rodents in research and mitigate problems related to the welfare of these animals [119, 120].

Overall, the development of a successful nanosystem requires extensive physicochemical characterization in combination with several preclinical studies from *in vitro* to *in vivo* models to understand its future behavior. This approach is what is intended to be addressed over the present work.

REFERENCES

[1] E.B. Yahya, A.M. Alqadhi, Recent trends in cancer therapy: a review on the current state of gene delivery, Life Science 269 (2021) 1-15. https://doi.org/10.1016/j.lfs.2021.119087.

[2] O.L. Gobbo, K. Sjaastad, M.W. Radomski, Y. Volkow, A. Prina-Mello, Magnetic nanoparticles in cancer theranostics, Theranostics 5 (2015) 1249-1263. https://doi.org/10.7150%2Fthno.11544

[3] L. Torresano, C. Nuevo-Tapioles, F. Santacatterina, J.M. Cuezva, Metabolic reprogramming and disease progression in cancer patients, Biochim. Biophys. Acta – Mol. Basis Dis. 1866 (2020) 1-16. https://doi.org/10.1016/j.bbadis.2020.165721.

[4] N. Hinge, M.M. Pandey, G. Singhvi, G. Gupta, M. Mehta, S. Satija, M. Gulati, H. Dureja, K. Dua, Nanomedicine advances in cancer therapy, Woodhead Publ. Ser. Biomater. (2020) 219-253. https://doi.org/10.1016/B978-0-12-818471-4.00008-X.

[5] C. Shen, Y. Zhou, J. Zhan, S.N. REske, A.K. Buck, Chromosome instability and tumor lethality suppression in carcinogenesis, J Cell Biochem. 105 (2008) 1327-1341. https://doi.org/10.1002/jcb.21937.

[6] J. Ferlay, M. Colombet, I. Soerjomataram, D.M. Parkin, M. Piñeros, A. Znaor, F. Bray, Cancer statistics for the year 2020: an overview, J. Cancer 149 (2021) 778-789. https://doi.org/10.1002/ijc.33588.

[7] J. Martinez-Useros, M. Martin-Galan, M. Florez-Cespedes, J. Garcia-Foncillas, Epigenetics of most aggressive solid tumors: pathways, targets, and treatments, Cancers 13 (2021) 1-28. https://doi.org/10.3390/cancers13133209.

[8] B. Chen, C. Chen, Y. Zhang, J. Xu, Recent incidence train of elderly patients with glioblastoma in the United States, 2000-2017, BMC Cancer 21 (2021) 1-10. https://doi.org/10.1186/s12885-020-07778-1.

[9] N. Pandey, P. Anastasiadis, C.P. Carney, P.P. Kanvinde, G.F. Woodworth, J.A. Winkles, A.J. Kim, Nanotherapeutic treatment of the invasive glioblastoma tumor microenvironment, Adv. Drug Deliv. Rev. 188 (2022) 1-23. https://doi.org/10.1016/j.addr.2022.114415.

[10] B. Delgado-Martín, M.A. Medina, Advances in the knowledge of the molecular biology of glioblastoma and its impact in patient diagnosis, stratification, and treatment, Adv. Sci. 7 (2020) 1-20. https://doi.org/10.1002/advs.201902971.

[11] M. Liu, J.P. Thakkar, C.R. Garcis, T.A. Dolecek, L.M. Wagner, E.V.M. Dressler, J.L. Villano, National cancer database analysis of outcomes in pediatric glioblastoma, Cancer Medicine 7 (2018) 1151-1159. https://doi.org/10.1002/cam4.1404.

[12] X.Z. Dai, L.Y. Wang, Y. Shan, J. Qian, K. Xue, J.Ye, Clinicopathological analysis of 719 pediatric and adolescents' ocular tumors and tumor-like lesions: a retrospective study from 2000 to 2018 in China, Int J Ophthalmol. 13 (2020) 1961-1967. https://doi.org/10.18240%2Fijo.2020.12.18.

[13] S. Kaliki, C.L. Shields, Uveal melanoma: relatively rare but deadly cancer, Eye 31 (2017) 241-257. https://doi.org/10.1038/eye.2016.275.

[14] K.N. Smit, M.J. Jager, A. de Klein, E. Kiliç, Uveal melanoma: towards a molecular understanding, Prog. Retin. Eye Res. 75 (2020) 1-15. https://doi.org/10.1016/j.preteyeres.2019.100800.

[15] M. Fallico, G. Raciti, A. Longo, M. Reibaldi, V. Bonfiglio, A. Russo, R. Caltabiano, G. Gatusso, L. Falzone, T. Avitabile, Current molecular and clinical insights into uveal melanoma (Review), Int. J. Oncol. 58 (2021) 1-22. https://doi.org/10.3892/ijo.2021.5190.

[16] N.J. Lamas, A. Martel, S. Nahon-Estève, S. Goffinet, A. Macocco, C. Bertolotto, S. Lassalle, P. Hofman, Prognostic biomarkers in uveal melanoma: the status quo, recent advances, and future directions, Cancer, 22 (2022) 1-44. https://doi.org/10.3390/cancers14010096.

[17] K. J. McKelvey, E.B. Wilson, S. Short, A.A. Melcher, M. Biggs, C.I. Diakos, V.M. Howell, Glycolisis and fatty acid oxidation inhibition improves survival in glioblastoma, Front. Oncol. 11 (2021) 1-18. https://doi.org/10.3389/fonc.2021.633210.

[18] E.S. Rantala, M.M. Hernberg, S. Piperno-Neumann, H.E. Grossniklaus, T.T. Kivelä, Metastatic uveal melanoma: the final frontier, Prog. Retin. Eye Res. 90 (2022) 1-53. https://doi.org/10.1016/j.preteyeres.2022.101041.

[19] Y. Zou, X. Sun, Y. Wang, C. Yan, Y. Liu, J. Li, D. Zhang, M. Zheng, R.S. Chung, B. Shi, Single siRNA nanocapsules for effective siRNA brain delivery and glioblastoma treatment, Adv. Mater. 32 (2020) 1-9. https://doi.org/10.1002/adma.202000416.

[20] J. Yang, D.K. Manson, B.P. Marr, R.D. Carvajal, Treatment of uveal melanoma: where are we now? Ther. Adv. Med. Oncol. 10 (2018) 1-17. https://doi.org/10.1177/1758834018757175.

[21] H. Zhang, R. Wang, Y. Yu, J. Liu, T. Luo, F. Fan, Glioblastoma treatment modalities besides surgery, J. Cancer 10 (2019) 4793-4806. https://doi.org./10.7150/jca.32475.

[22] J.S. Heng, B.M. Perzia, J.H. Sinard, R. Pointdujour-Lim, Local recurrence of uveal melanoma and concomitant brain metastases associated with an activating telomerase promoter mutation seven years after secondary enucleation, AM. J. Ophthalmol. Case Rep. 27 (2022) 2-4. https://doi.org/10.1016/j.ajoc.2022.101607.

[23] A. Azevedo, D. Farinha, C. Geraldes, H. Faneca, Combining gene therapy with other therapeutic strategies and imaging agents for cancer theranostics, Int. J. Pharm. 606 (2021) 1-23. https://doi.org/10.1016/j.ijpharm.2021.120905.

[24] H.S. Hamza, A.M. Elhusseiny, Choroidal melanoma resection, Middle East Afr. J. Ophthalmol. 25 (2018) 65-70. https://doi.org/10.4103%2Fmeajo.MEAJO_73_18

[25] E. Liljedahl, E. Konradsson, E. Gustafsson, K.F. Jonsson, J.K. Olofsson, C. Ceberg, H.N. Redebrandt, Long-term anti-tumor effects following both conventional radiotherapy and FLASH in fully immunocompetent animals with glioblastoma, Sci. Rep. 12 (2022) 1-12. https://doi.org/10.1038/s41598-022-16612-6.

[26] K. Bulaklak, C.A. Gersbach, The once and future gene therapy, Nat. Commun. 11 (2020) 5820. https://doi.org/10.1038/s41467-020-19505-2.

[27] L. Abballe, E. Miele, Epigenetic modulators for brain cancer stem cells: Implications for anticancer treatment, World J Stem Cells. 13 (2021) 670-684. https://doi.org/10.4252/wjsc.v13.i7.670.

[28] M.L. Santa-Armas, C.T. de Ilarduya, Strategies for cancer gene-delivery improvement by non-viral vectors, Int. J. Pharm. 596 (2021) 2-9. https://doi.org/10.1016/j.ijpharm.2021.120291.

[29] Z. Zhao, A.C. Anselmo, S. Mitragotri, Viral vector-based gene therapies in the clinic, Bioeng. Transl. Med. 7 (2021) 1-20. https://doi.org/10.1002/btm2.10258.

[30] S.A. Rosenberg, P. Aebersold, K. Cornetta, A. Kasid, R.A. Morgan, R. Moen, E.M. Karson, M.T. Lotze, J.C. Yang, S.L. Topalian, M.J. Merino, K. Culver, A.D. Miller, R.M. Blaese, W.F. Anderson, Gene transfer into humans-immunotherapy of patients with advanced melanoma, using tumor-infiltrating lymphocytes modified by retroviral gene transduction, N. Engl. J. Med. 323 (1990) 570-578. https://doi.org/10.1056/NEJM199008303230904.

[31] J.T. Bulcha, Y. Wang, H. Ma, P.W.L. Tai, G. Gao, Viral vector platforms within the gene therapy landscape, Sig. Transduct. Target. Ther. 53 (2021) 1-24. https://doi.org/10.1038/s41392-021-00487-6.

[32] S. Damke, K.A. Nilay, A review on Gene therapy, J. Pharm. Res. Int. 33 (2021) 635-645. https://doi.org/10.9734/jpri%2F2021%2Fv33i60B34662.

[33] S. Saeb, J.V. Assche, T. Loustau, O. Rohr, C. Wallet, C. Schwartz, Suicide gene therapy in cancer and HIV-1 infection: an alternative to conventional treatments, Biochem. Pharmacol. 197 (2022) 1-13. https://doi.org/10.1016/j.bcp.2021.114893.

[34] S. Xi, Y.G. Yang, J. Suo, T. Sun, Research progress on gene editing based on nano-drug delivery vectors for tumor therapy, Bioeng Biotechnol. 10 (2022) 1-16. https://doi.org/10.3389/fbioe.2022.873369

[35] N. Sayef, P. Allawadhi, A. Kharuna, V. Singh, U. Kavik, S.K. Pasumarthi, I. Khurana, A.K. Banothu, R. Weiskirchen, K.K. Bharani, Gene therapy: comprehensive overview and therapeutic applications, Life Science 294 (2022) 1-21. https://doi.org/10.1016/j.lfs.2022.120375.

[36] A.I.S. van den Berg, C.O. Yun, R.M. Schiffelers, W.E. Hennink, Polymeric delivery systems for nucleic acid therapeutics: approaching the clinic, JCR 331 (2021) 121-141. https://doi.org/10.1016/j.jconrel.2021.01.014.

[37] A.C. Silva, C.M. Lopes, J.M. Sousa Lobo, M.H. Amaral, Nucleic acids delivery systems: a challenge for pharmaceutical technologists, Curr Drug Metab. 16 (2015) 3-16. https://doi.org/10.2174/1389200216666150401110211

[38] T. Ramasamy, S. Munusamy, H.B. Ruttala, J.O. Kin, Smart nanocarriers for the delivery of nucleic acid-based therapeutics: a compressive review, Biotechnol. J. 16 (2020) 1-14. https://doi.org/10.1002/biot.201900408.

[39] M.E. Barry, D. Pinto-González, F.M. Orson, G.J. Mckenzie, G.R. Petry, M.A Barry, Role of endogenous endonucleases and tissue site in transfection and GpC-mediated immune activation after naked DNA and injection, Hum 10 (1999) 2461-2480. https://doi.org/10.1089/10430349950016816.

[40] A.S. Piotrowski-Daspit, A.C. Kauffman, L.G. Bracaglioa, W.M. Saltzman, Polymeric vehicles for nucleic acid delivery, Adv. Drug Deliv. Rev. 156 (2020) 119-132. https://doi.org/10.1016/j.addr.2020.06.014

[41] R. Prajapati, A. Somoza, Albumin nanostructures for nucleic acid delivery in cancer: current trend, emerging issues, and possible solutions, Cancers, 13 (2021) 1-16. https://doi.org/10.3390/cancers13143454.

[42] M. Schlich, R. Paloma, G. Costabile, S. Mizrahy, M. Pannuzzo, D. Peer, P. Decuzzi, Cytosolic delivery of nucleic acids: the case of ionizable lipid nanoparticles, Bioeng. Trasnl, Med. 6 (2021) 1-16. https://doi.org/10.1002/btm2.10213.

[43] L.M.P. Vermeulen, T. Brans, S.C. de Smedt, K. Remaut, K. Braeckmans, Methodologies to investigate intracellular barriers for nucleic acid delivery in non-viral gene therapy, Nanotoday 21 (2018) 74-90. https://doi.org/10.1016/j.nantod.2018.06.007.

[44] R. Ni, R. Feng, Y. Chau, Synthetic approaches for nucleic acid delivery: choosing the right carries, Life 9 (2019) 1-28. https://doi.org/10.3390/life9030059.

[45] S. Singh, A.S, Narang, R.I. Mahato, Subcellular fate and off-targeted effects of siRNA, shRNA, and miRNA, Pharm. Res. 28 (2011) 2996-3015. https://doi.org/10.1007/s11095-011-0608-1.

[46] Y. Rui, M. Varanasi, S. Mendes, H.M. Yamagata, D.R. Wilson, J.J. Green, Poly(beta-amino ester) nanoparticles enable non-viral delivery of CRISPR-Cas9 plasmids for gene knockout and gene deletion, Mol. Ther. Nucleic 20 (2020) 661-672. https://doi.org/10.1016/j.omtn.2020.04.005.

[47] L. Fang, S.S.C. Hung, J. Yek, L. El Wazan, T. Nguyen, S. Khan, S.Y. Lim, A.W. Hewitt, R.C.B. Wong, A simple cloning-free method to efficiently induce gene expression using CRISPR/Cas9, Mol. Ther. Nucleic 14 (2019) 184-191. https://doi.org/10.1016/j.omtn.2018.11.008.

[48] L. Salvioni, M.A. Rizzuto, J.A. Bertolini, L. Pandolfi, M. Colombo, D. Prosperi, Thirty years of cancer nanomedicine: success, frustration and hope, Cancers 11 (2019) 1-21. https://doi.org/10.3390/cancers11121855.

[49] M. San Anselmo, A. Postigo, A. Lancelot, J.L. Serrano, T. Sierra, S. Hernández-Ainsa, Dendron-functionalized hyperbranched bis-MPA polyesters as efficient non-viral vectors for gene therapy in different cell lines, Biomater. Sci. 10 (2022) 2706-2719. https://doi.org/10-1039/D2BM00365A

[50] J.L. Shirley, Y.P. de Jong, C. Terhorst, R.W. Herzog, Immune responses to viral gene therapy vectors, Mol. Ther. 28 (2020) 709-722. https://doi.org/10.1016/j.ymthe.2020.01.001.

[51] V.C. Vetter, E. Wagner, Targeting nucleic-acids based therapeutics to tumors: challenges and strategies for polyplexes, JCR 346 (2022) 110-135. https://doi.org/10.1016/j.jconrel.2022.04.013.

[52] S. Ren, M. Wang, C. Wang, Y. Wang, C. Sun, Z. Zeng, H. Cui, X. Zhao, Application of non-viral vectors in drug delivery and gene therapy, Polymers 13 (2021) 1-28. https://doi.org/10.3390/polym13193307.

[53] A.R. Nectow, E.J. Nestler, Viral tools for neuroscience, Nat. Rev. Neurosci. 21 (2020) 669-681. https://doi.org/10.1038/s41583-020-00382-z.

[54] J. Xiang, X. Liu, Z. Zhou, D. Zhu, Q. Zhou, Y. Piao, L. Jiang, J. Tang, X. Liu, Y. Shen, Reactive Oxygen species (ROS)-responsive charge-switchable nanocarriers for gene therapy of metastatic cancer, ACS Appl. Mater. Interfaces 10 (2018) 43352-43362. https://doi.org/10.1021/acsami.8b13291.

[55] I.M.S. Degors, C. Wang, Z.U. Rehman, I.S. Zuhorn, Carriers break barriers in drug delivery: endocytosis and endosomal escape of gene delivery vectors, ACC. Chem. Res. 52 (2019) 1750-1760. https://doi.org/10.1021/acs.accounts.9b00177.

[56] A.A. Mokhtarieh, J. Lee, S. Kim, M.K. Lee, Preparation of siRNA encapsulated nanosliposomes suitable for siRNA delivery by simply discontinuous mixing, Biochim. Biophys. Acta Biomembr. 1860 (2018) 1318-1325. https://doi.org/10.1016/j.bbamem.2018.02.027.

[57] H. Wang, S. Liu, F. Chu, Y. Zhou, Z. He, M. Guo, C. Chen, L. Xu, Nanostructured lipid carriers for microRNA delivery in tumor gene therapy, Cancer Cell Int. 18 (2018) 1-6. https://doi.org/10.1186/s12935-018-0596-x.

[58] M.S. Pou, S. Prieto-Sánchez, Y. El Yousfi, S. Boyero-Corral, A.N. Ricart, I.N. Roig, P.P. Lozano, E.G. Montoya, M.M. Carmona, J.R.T. Grau, J.M.S I Negre, C. Hernández-Munain, C. Suñé, Cholesteryl oleate-loaded cationic solid lipid nanoparticles as carriers for efficient gene-silencing therapy, Int- J. Nanomedicine, 13 (2018) 3223-3233. https://doi.org/10.2147/IJN.S158884.

[59] C. Olbrich, U. Bakowsky, C-M. Lehr, R.H. Müller, C. Kneuer, Cationic solid-lipid nanoparticles can efficiently bind and transfect plasmid DNA, JCR 77 (2001) 345-355. https://doi.org/10.1016/S0168-3659(01)00506-5.

[60] C. Horejs, From lipids to nanoparticles to mRNA vaccines, Nat. Rev. Mater. 6 (2021) 1075-1076. https://doi.org/10.1038/s41578-021-00379-9.

[61] M.J. Mulligan, K.E. Lyke, N. Kitchin, J. Absalon, A. gurtman, S. Lockhart, K. Neuzil, V. Raabe, R. bailey, K.A. Swanson, P. Li, K. Koury, W. Kalina, D. Cooper, C. Fontes-Garfias, P.Y. Shi, Ö. Türeci, K.R. Tompkins, E.E. Walsh, R. Frenck, A.R. Falsey, P.R. Dormitzer, W.C. Gruber, U. Sahin, K.U. Jansen, PhaseI/II study of COVID-19 RNA vaccine BNT162b1 in adults, Nature 586 (2020) 589-593. https://doi.org/10.1038/s41586-020-2639-4.

[62] C. Liu, Y. Xie, X. Li, X. Yao, X. Wang, M. Wang, Z. Li, F. Cao, Folic acid/peptides modified PLGA-PEI-PEG polymeric vectors as efficient gene delivery vehicles: synthesis, characterization and their biological performance, Mol. Biotechnol. 63 (2021) 63-79. https://doi.org/10.1007/s12033-020-00285-5.

[63] N. Zheng, D.K. Cudjoe, W. Song, Multicomponent polymerization cationic polymers for efficient gene delivery, Macromol. Rapid. Commun. 42 (2020) 1-7. https://doi.org/10.1002/marc.202000464.

[64] V. Chrysostomoy, H. Katifelis, M. Gazouli, K. Dimas, C. Demetzos, S. Pispas, Hydrophilic random cationic copolymers as polyplexes-formation vectors for DNA, Materials 15 (2022) 1- 26. https://doi.org/10.3390/ma15072650.

[65] Y. Wang, M. Ye, R. Xie, S. Gong, Enhancing the in vitro and in vivo stabilities of polymeric nucleic acid delivery nanosystems, Bioconjugate Chem. 30 (2019) 325-337. https://doi.org/10.1021/acs.bioconjchem.8b00749.

[66] E. Koren, V.P. Torchilin, Cell-penetrating peptides: breaking through to the other side, Trends Mol. Med. 18 (2012) 385-393. https://doi.org/10.1016/j.molmed.2012.04.012.

[67] M. Sanchez-Martos, G. Martinez-Navarrete, A. Bernabeu-Zornoza, L. Humphreys, E. Fernandez, Evaluation, and optimization of poly-D-lysine as a non-natural cationic polypeptide for gene transfer in neuroblastoma cells, J. Nanomater. 11 (2021) 1-14. https://doi.org/10.3390/nano11071756.

[68] K. Kardani, A. Milani, S.H. Shabani, A. Bolhassani, Cell penetrating peptides: The potent multi-cargo intracellular carriers, Expert Opin. Drug Deliv. (2019) 1227-1258. https://doi.org/10.1080/17425247.2019.1676720.

[69] P.R. Dash, M.L. Read, K.D. Fisher, K.A. Howard, M. Wolfert, D. Oupicky, V. Subr, J. Strohalm, K. Ulbrich, L.W. Seymour, Decreased binding to proteins and cells of polymeric gene delivery vectors surface modified with a multivalent hydrophilic polymer and retargeting through attachment of transferrin, J. Biol. Chem. 275 (2000) 3793-3802. https://doi.org/10.1074/jbc.275.6.3793.

[70] M. Morga, P. Batys, D. Kosior, P. Bonarek, Z. Adamczyk, Poly-L-Arginine molecule properties in simple electrolytes: molecular dynamic modeling and experiments, Int. J. Environ. Res. Public. Health 19 (2022) 1-17. https://doi.org/10.3390/ijerph19063588.

[71] J.M. Ageitos, J.A. Chuah, K. Numata, Chemo-enzymatic synthesis of linear and branched cationic peptides: evaluation as gene carriers, Macromol. Biosci. 15 (2015) 990-1003. https://doi.org/10.1002/mabi.201400487.

[72] S. Robla, M.J. Alonso, N. Csaba, Polyaminoacid-based nanocarriers: a review of the latest candidates for oral drug delivery, Expert Opin. Drug Deliv. 17, (2020) 1081-1092. https://doi.org/10.1080/17425247.2020.1776698.

[73] Y. Takechi, H. Tanaka, H. Kitayama, H. Yoshii, M. Tanaka, H. Saito, Comparative study on the interaction of cell-penetrating polycationic polymers with lipid membranes, Chem. Phys. Lipids 165 (2012) 51-58. https://doi.org/10.1016/j.chemphyslip.2011.11.002.

[74] Z.X. Zhao, S.Y. Gao, J.C. Wang, C.J. Chen, E.Y. Zhao, W.J. Hou, Q. Feng, L.Y. Gao, X.Y. Liu, L.R. Zhang, Q. Zhang, Self-assembly nanomicelles based on cationic mPEG-PLA-b-polyarginine (R15) triblock copolymer for siRNA delivery, Biomaterials 33 (2012) 6793-6807. https://doi.org/10.1016/j.biomaterials.2012.05.067.

[75] C. Fu, X. Sun, D. Liu, Z. Chen, Z. Lu, Na Zhang, Biodegradable tri-block copolymer poly(lactic acid)-poly(ethylene glycol)-poly(L-lysine)(PLA-PEG-PLL) as a non-viral

vector to enhanced gene transfection, Int. J. Mol. Sci. 12 (2011) 1371-1388. https://doi.org/10.3390/ijms12021371.

[76] C. Lim, T. Sim, N.H. Hoang, K.T. Oh, A stable nanoplatform for antitumor activity using PEG-PLL-PLA triblock co-polyelectrolyte, Colloids Surf. B Biointerfaces 153 (2017) 10-18. https://doi.org/10.1016/j.colsurfb.2017.01.027.

[77] H.K. Kim, E. Davaa, C.S. Myung, J.S. Park, Enhanced siRNA delivery using cationic liposomes with new polyarginine-conjugated PEG-lipid, Inter. J. Pharm. 392 (2010) 141-147. https://doi.org/10.1016/j.ijpharm.2010.03.047.

[78] H. Tian, L. Lin, Z. Jiao, Z. Guo, J. Chen, S. Gao, X. Zhu, X. Chen, Polylysine-modified polyethyleneimine inducing tumor apoptosis as an efficient gene carrier, JCR 172 (2013) 410-418. https://doi.org/10.1016/j.jconrel.2013.06.026.

[79] Y.S. Malik, M.A. Sheikh, Z. Xing, Z. Guo, X.Zhu, H. Tian, X. Chen, Polylysine-modified polyethylenimine polymer can generate genetically engineering mesenchymal stem cells for combinational suicidal gene therapy in glioblastoma, Acta Biomater. 15 (2018) 144-153. https://doi.org/10.1016/j.actbio.2018.09.015.

[80] A. Kossel, Weitere mittheilungen über die protamine, Biol. Chem. 26 (2009) 588- 592. https://doi.org/10.1515/bchm2.1899.26.6.588.

[81] Z. Zeng, C.H. Tung, Y. Zu, Aptamer-equipped protamine nanomedicine for precision lymphoma therapy, Cancers 12 (2020) 1-13. https://doi.org/10.3390/cancers12040780.

[82] H. Amos, Protamine enhancement of RNA uptake by cultured chick cells, Biochem. Biophys. Res. Commun. 5 (1961) 1-4. https://doi.org/10.1016/0006-291X(61)90069-9.

[83] J.V. González-Aramundiz, E. Presas, I. Dalmau-Mena, S. Martínez-Pulgarín, C. Alonso, J.M. Escribano, M.J. Alonso, N.S. Csaba, Rational design protamine nanocapsules as antigen delivery carriers, JCR 245 (2017) 62-69. https://doi.org/10.1016/j.jconrel.2016.11.012.

[84] M. Peleteiro, E. Presas J.V. González-Aramundiz, B. Sánches-Correa, R. Simón-Vázquez, N. Csaba, M.J. Alonso, A. González-Fernández, Polymeric nanocapsules for vaccine delivery: influence of polymeric shell on the interaction with the immune system, Front. Immunol. 9 (2018) 1-17. https://doi.org/10.3389/fimmu.2018.00791.

[85] J.V. González-Aramundiz, M. Peleteiro, A. González-Fernández M.J. Alonso, N.S. Csaba, Protamine nanocapsules for the development of thermostable adjuvanted nanovaccines, Mol. Pharmaceutics, 15 (2018) 5653-5664. https://doi.org/10.1021/acs.molpharmaceut.8b00852.

[86] J. Crecente-Campo, S. Lorenzo-Abalde, A. Mora, J. Marzoa, N. Csaba, J. Blanco, A. González-Fernández, M.J. Alonso, Bilayer polymeric nanocapsules: a formulation approach for a thermostable and adjuvanted E. coli antigen vaccine, JCR 286 (2018) 20-32. https://doi.org/10.1016/j.jconrel.2018.07.018.

[87] A. Umerska, K.J. Paluch, M.J. Santos-Martinez, O.I. Corrigan, C. Medina, L. Tajber, Freeze drying of polyelectrolyte complex nanoparticles: effect of nanoparticle composition and cryoprotectant selection, Int. J. Pharm. 552 (2018) 27-38. https://doi.org/10.1016/j.ijpharm.2018.09.035.

[88] J.V. González-Aramundiz, M.P. Olmedo, A. González-Fernández, M.J. Alonso, N.S. Csaba, Protamine-based nanoparticles as new antigen delivery system, Eur. J. Pharm. Biopharm. 97 (2015) 51-59. https://doi.org/10.1016/j.ejpb.2015.09.019.

[89] J.F. Correira-Pinto, M. Peleteiro, N. Csaba, A. González-Fernánde, J.J. Alonso, Multienveloping of particulated antigens with biopolymers and immunostimulant polynucleotides, J. Drug Deliv. Sci. Technol. 30 (2015) 424-434. https://doi.org/10.1016/j.jddst.2015.08.010.

[90] L.N. Thwala, D.P. Delgado, K. Leone, I. Marigo, F. Benetti, M. Chenlo, C.V. Alvarez, S. Tovar, C. Dieguez, N. S. Csaba, M.J. Alonso, Protamine nanocapsules as carriers for oral peptide delivery, JCR 291 (2018) 157-168. https://doi.org/10.1016/j.jconrel.2018.10.022.

[91] S. Reimondez-Troitiño, J.V González-Aramundiz, J. Ruiz-Bañobre, R. López-López, M.J. Alonso, N. Csaba, M. de la Fuente, Versatile protamine nanocapsules to restore miR-145 levels and interfere tumor growth in colorectal cancer cells, Eur. J. Pharm. Biopharm. 142 (2019) 449-459. https://doi.org/10.1016/j.ejpb.2019.07.016.

[92] H. Wang, Y. Zhao, H. Wang, J. Gong, H. He, M.C. Shin, V.C. Yang, Y. Huang, Low-molecular-weight protamine-modified PLGA nanoparticles for overcoming drug-resistant breast cancer, JCR 192 (2014) 47-56. https://doi.org/10.1016/j.jconrel.2014.06.051.

[93] M. Liu, B. Feng, Y. Shi, C. Su, H. Song, W. Chenkg, L. Zhao, Protamine nanoparticles for improving shRNA-mediated anticancer effects, Nanoscale Res. Lett. 10 (2015) 1-7. https://doi.org/10.1186/s11671-015-0845-z.

[94] C.H. Liu, G.J. Chern, F.F. Hsu, K.W. Huang, Y.C. Sung, H.C. Huang, J.T. Qiu, S.K. Wang, C.C. Lin, C.H. Wu, H.C. Wu, J.Y. Liu, Y. Chen, A multifunctional nanocarrier for efficient TRAIL-based gene therapy against hepatocellular carcinoma with desmoplasia in mice, Hepatology 67 (2017) 899-913. https://doi.org/10.1002/hep.29513.

[95] W. Alshaer, H. Hillaireau, J. Vergnaud, S. Mura, C. Deloménie, F. Sauvage, S. Idmail, E. Fattal, Aptamer-guided siRNA-loaded nanomedicines for systemic gene silencing in CD-44 expressing murine triple-negative breast cancer model, JCR 10 (2018) 98-106. https://doi.org/10.1016/j.jconrel.2017.12.022.

[96] L. Gharaibeh, W. Alshaer, S. Wehaibi, R.A. Buqain, d.A. Alqudah, A. Al-Kadash, H. Al-Azzawi, A. Awidi, Y. Bustanji, Fabrication of aptamer-guided siRNA loaded lipoplexes for gene silencing of notch 1 in MDA-mb-231 triple negative breast cancer cell line, J. Drug Deliver. Sci. Technol. 65 (2021) 1-10. https://doi.org/10.1016/j.jddst.2021.102733.

[97] S.N. He, Y.L. Li, J.J. Yan, W. Zhang, Y.Z. Du, H.Y. Yu, F.Q. Hu, H. Yuan, Ternary nanoparticles composed of cationic solid lipid nanoparticles, protamine, and DNA for gene delivery, Int. J. Nanomedicine 8 (2013) 2859-2869. https://doi: 10.2147/IJN.S47967.

[98] W.H. Hsu, N. Csaba, C. Alexander, M. Garcia-Fuentes, Polyphosphazenes for the delivery of biopharmaceuticals, J. Appl. Polym. Sci. 137 (2019) 1-11. https://doi.org/10.1002/app.48688.

[99] X. Zhou, S. Qiu, X. Mu, M. Zhou, W. Cai, L. Song, W. Xing, Y. Hu, Polyphosphazenes-based flame retardants: a review, Compos. B. Eng. 202 (2020) 1-17. https://doi.org/10.1016/j.compositesb.2020.108397.

[100] X. Jing, L. Meng, T. Yang, N. Zhang, S. Fan, Y. Chen, H. Yang, D. Wang, W. Ji, J. She, Biodegradable polyphosphazene-based nanodrug to regulate redox homeostasis for augmented chemo-photodynamic therapy, Dyes Pigm. 199 (2022) 1-9. https://doi.org/10.1016/j.dyepig.2022.110095.

[101] J.P. Quiñones, A. Iturmendi, H. Henke, C. Roschger, A. Zierer, O. Brüggemann, Polyphosphazene-based nanocarriers for the release of agrochemicals and potential anticancer drugs, J. Mater. Chem. B. 7, (2019) 7783-7794. http://doi.org./10.1039/C9TB01985E.

[102] N. Zhou, Z. Zhi, D. Liu, D. Wang, Y. Shao, K. Yan, L. Meng, D. Yu, Acid-responsive and biologically degradable polyphosphazene nanodrugs for efficient drug delivery, ACS Biomater. Sci. Eng. 6, (2020) 4285-4293. https://doi.org/10.1021/acsbiomaterials.0c00378.

[103] S.M. Örüm, Novel cyclomatrix polyphosphazene nanospheres: preparation, characterization, and dual anticancer drug release application, Polym. Bull. 79 (2022) 2851-2869. https://doi.org/10.1007/s00289-021-03654-5.

[104] Y. Yang, Z. Xu, S. Chen, Y. Gao, W. Gu, L. Chen, Y. Pei, Y. Li, Histidylated cationic polyorganophosphazene/DNA self-assembled NPs for gene delivery, Int. J. Pharm. 353 (2008) 277-282. https://doi.org/10.1016/j.ijpharm.2007.11.041.

[105] Y. Yang, Z. Zhang, L. Chen, W. Gu, Y. Li, Urocanic acid improves transfection efficiency of polyphosphazene with primary amino groups for gene delivery. Bioconjugate Chem. 21 (2010) 419-426. https://doi.org/10.1021/bc900267g.

[106] C. MA, X. Zhang, C. Du, B. Zhao, C. He, C. Li, R. Qiao, Water-soluble cationic polyphosphazenes grafted with cyclic polyamine and imidazole as an effective gene delivery vector, Bioconjugate Chem. 27 (2016) 1005-1012. https://doi.org/10.1021/acs.bioconjchem.6b00048.

[107] W.H. Hsu, P. Sánchez-Gómez, E. Gomez-Ibarlucea, D.P. Ivanov, R. Rahman, A.M. Grabowska, N. Csaba, C. Alexander, M. Garcia-Fuentes, Structure-optimized interpolymer polyphosphazenes complexes for effective gene delivery against glioblastoma, Adv. Ther. 2 (2018) 1-15. https://doi.org/10.1002/adtp.201800126.

[108] F. Chen, O.R. Teniola, K.S. Ogueri, C.T. Laurecin, Recent trends in the development of polyphosphazenes for bio-applications, Regen. Eng. Transl. Med 145 (2022) 1-22. https://doi.org/10.1007/s40883-022-00278-7.

[109] Z. Huang, C. Gao, Y. Huang, X. Deng, Q. Cai, X. Yang, Injectable polyphosphazene/gelatin hybrid hydrogel for biomedical applications, Mater. Des. 160 (2018) 1137-1147. https://doi.org/10.1016/j.matdes.2018.11.010.

[110] J. Luten, J.H. Steenis, R. van Someren, J. Kemmink, N.M.E. Schuurmans-Nieuwenbroek, G.A. Koning, D.J.A. Crommelin, C.F. van Nostrum, W.E. Hennink, Water-soluble biodegradable cationic polyphosphazenes for gene delivery, JCR 89 (2003) 483-497. https://doi.org/10.1016/S0168-3659(03)00127-5.

[111] V. Agrahari, P. Hiremanth, Challenges associated and approaches for successful translation of nanomedicines into commercial products, Nanomedicine 12 (2017) 819-823. https://doi.org/10.2217/nnm-2017-0039.

[112] Y.R. Zhang, R. Lin, H.J. Li, W.L. He, J.Z. Du, J. Wang, Strategies to improve tumor penetration of nanomedicines through nanoparticle design, Wiley Interdiscip. Rev. Nanomed. Nanobiotechnol. 11 (2018) 1-12. https://doi.org/10.1002/wnan.1519.

[113] H. Sajjad, S. Imtiaz, T. Noor, Y.H. Siddiqui, A. Sajjad, M. Zia, Cancer models in preclinical research: a chronicle review of advancement in effective cancer research, AMEM 4 (2021) 87-103. https://doi.org/10.1002/ame2.12165.

[114] S. Bekisz, L. Baudin, F. Buntinx, A. Noël, L. Geris, In vitro, in vivo and in silico models of Lymphangiogenesis in solid malignancies, Cancer 14 (2022) 1-30. https://doi.org/10.3390/cancers14061525.

[115] M. Kapalczynska, T. Kolenda, W. Przybyla, M. Zajaczkowska, A. Teresiak, V. Filas, M. Ibbs, R. Blizniak, L. Luczewski, K. Lamperska, 2D and 3D cell cultures - a comparison of different types of cancer cells cultures, Arch. Med. Sci. 14 (2016) 910-919. https://doi.org/10.5114/aoms.2016.63743.

[116] S.A. Langhans, Using 3D in vitro cell culture models in anticancer drug discovery, Expert Opin. Drug Discov. 16 (2021) 841-850. https://doi.org/10.1080/17460441.2021.1912731.

[117] K.G. Huo, E. D'Arcangelo, M.S. Tsao, Patient-derived cell line, xenograft, and organoid models in lung cancer therapy, Transl. Lung Cancer Res. 9 (2020) 2214-2232. https://doi.org/10.21037%2Ftlcr-20-154.

[118] C.E. Vasey, R.J. Cavanagh, V. Taresco, C. Moloney, S. Smith, R. Rahman, C. Alexander, Polymer pro-drug nanoparticles for sustained release of cytotoxic drugs evaluated in patient-derived glioblastoma cell lines and in situ gelling formulations, Pharmaceutics 13 (2021) 1-17. https://doi.org/10.3390/pharmaceutics13020208.

[119] R.L. Bailone, H.C.S. Fukushima, B.H.V. Fernandes, L.K. de Aguiar, T. Corrêa, H. Janke, P.G. Setti, R.O. Roça, R.C. Borra, Zebrafish as an alternative animal model in human and animal vaccination research, Lab. Anim. Res. 36 (2020) 1-10. https://doi.org/10.1186/s42826-020-00042-4.

[120] P. Cabezas-Sáinz, A. Pensado-López, B. Sáinz, L. Sánchez, Modeling cancer using zebrafish xenografts: drawbacks for mimicking the human microenvironment, Cells 9 (2020) 1-30. https://doi.org/10.3390/cells9091978.

HYPOTHESIS

HYPOTHESIS

1. The combination of biomaterials can yield nanosystems, such as nanoparticles, nanocomplexes or nanocapsules, with novel functionalities and improved capacity for the association and delivery of nucleic acids.

2. In particular, the combination of polypeptides, especially protamine, with natural or synthetic anionic macromolecules can improve gene delivery and transfection capacity.

3. The use of primary patient-derived cell lines in combination with advanced *in vitro* models, such as tumor spheroids and, the *in vivo* zebrafish model can be a powerful tool for the evaluation of potential nanomedicines for gene therapy applications in cancer.

OBJECTIVES

OBJECTIVES

Considering the established hypotheses, the general objective of the present work focuses on the development of tunable gene delivery platforms, and their optimization and evaluation using advanced *in vitro* models of cancer. This global objective is addressed in the following sections:

Sub-objective 1: Development and characterization of nanoparticles based on protamine and dextran as carriers for the intracellular delivery of nucleic acids, and their evaluation in 2D and 3D *in vitro* models of commercial and primary patient-derived glioblastoma cell lines.

The results are collected in Chapter I of this doctoral thesis.

Sub-objective 2: Development and characterization of nanocomplexes of protamine and polyethylenimine with the anionic polyphosphazene 6MHA-PPZ as nanocarriers for gene delivery, and their evaluation in glioblastoma tumor spheroid models and *in vivo* zebrafish models.

The results are collected in Chapter II of this doctoral thesis.

Sub-objective 3: Development and characterization of protamine nanocapsules with a vitamin E oily core as nanocarriers for gene transfer into uveal melanoma cells, and their evaluation in a 3D corneal model.

The results are collected in Chapter III of this doctoral thesis.

CHAPTER I

Protamine-based nanotherapeutic as a gene delivery system for the treatment of glioblastoma

Protamine-based nanotherapeutic as a gene delivery system for the treatment of glioblastoma

ABSTRACT

Brain tumors, especially glioblastoma, are one of the most aggressive cancers. According to the World Health Organization (WHO), glioblastoma is classified as grade IV of malignance. The standard treatment combines surgical resection, radiotherapy, and chemotherapy, but this combination presents severe side effects such as permanent neuronal damage, and the tumor typically reappears after some months. Nucleic acid-based therapy has recently received increasing attention as a promising strategy for the treatment of this tumor. This therapy has the capacity to modulate gene expression in malignant cells by transferring therapeutic genes. Previous studies have demonstrated the use of non-viral nanosystems as vehicles for gene delivery, due to their efficient nucleic acid encapsulation, protection, and delivery. In the present work, a new formulation composed of low molecular weight protamine (LMWP) and dextran sulfate was designed, synthesized, and evaluated for its gene delivery efficacy. The nanoparticles (NPs) were evaluated in terms of particle size, surface charge, morphology, and their capacity to condense different nucleic acids (pDNAs and miRNAs). The formation of these NPs by ionic gelation method resulted in a homogeneous population of spherical particles with low polydispersity index (PDI), size below 200 nm, and positive surface charge. The competitive displacement assay demonstrated that these NPs could condense nucleic acids without alterations in their morphology and physicochemical characteristics, even after long-term storage conditions. The efficacy of this formulation as a gene delivery system was evaluated by *in vitro* assays in different glioblastoma cell lines and three-dimensional (3D) glioblastoma spheroids. The formulation was evaluated at different concentrations by several cell-viability studies, showing the low/non-toxicity of the NPs in both two-dimensional (2D) and 3D cell cultures. Cellular uptake studies revealed the efficient internalization of the NPs, indicating their potential to deliver different nucleic acids. Finally, the NPs promoted efficient expression of a model plasmid encoding fluorescent/luminescent proteins. In conclusion, these cationic polymeric NPs could be a promising candidate as non-viral gene delivery vehicle to treat glioblastoma.

1.1. INTRODUCTION

Brain tumors are one of the most dangerous cancers [1]. Glioblastoma is the most common histologic subtype of gliomas [2] classified as grade IV of malignancy by WHO [3]. The incidence of this tumor is higher in adults between 60 and 70 years, in men (60%), and in individuals of European descent [4]. The main problem is the ineffectiveness of the conventional treatment that involves surgery, radiotherapy and temozolomide chemotherapy [5]. In addition, it is one of the most expensive cancer treatments [6], despite only affording an average survival rate of 14,6 months [7] due to frequent tumor recurrence [8]. Over the last decade, numerous novel targeted therapies, such as the immunotherapy, have entered clinical trials to improve this treatment [9]. However, the poor immunogenicity of glioblastoma [10] and the difficulty of drug or antibody delivery across the blood-brain barrier (BBB) make this a still unsolved problem, and clear clinical need [6] [11].

Nucleic acid-based therapy is considered a promising new option, but the delivery of exogenous genetic material requires overcoming numerous extra- and intracellular obstacles to reach the cellular cytoplasm or nucleus [12, 13]. To overcome these limits, non-viral delivery systems are promising candidates due to their ability to protect the genetic material promoting the intracellular delivery of genes [14]. Several different NPs have been investigated for glioma gene therapy, for example, cationic liposomes [15, 16] or gold NPs [17]. However, their high production costs, toxicity limitations, and their tendency to aggregate [18, 19] suggest the interest of researching also polymeric vectors [16]. Cationic polymers are the most common materials studied in gene delivery due to their versatility, biodegradability, easy synthesis, scalable production [14], and their capacity to interact with BBB endothelial cell membranes facilitating the endocytosis [20]. For example, poly(β-amino ester) NPs could encapsulate anti-glioblastoma genes causing inhibition of tumor growth, reduction of cancer cell migration, and tumor size in animal models [21]. Most commonly, polyethylenimine (PEI) nanocomplexes are considered the “gold standard” for nucleic acid delivery due to their high efficiency [22]. However, their high cytotoxicity requires the copolymerization with other polymers such as poly(lactic-co-glycolic acid) or poly(3-hydroxybutyrate) [23].

Considering the variety of polymers available to formulate gene delivery nanosystems, the present work is focused on the natural and safe biomaterial protamine (Pr). It is a cell penetrating peptide (CPP) with low molecular weight (Mw= 5 kDa) [24]. Protamine has high capacity to condense different nucleic acids such as DNAs, miRNAs, and small interference RNA (siRNAs) [25], and exhibits membrane translocation properties attributed to its arginine-rich sequence [26]. In addition, protamine sulfate salt forms are considered biologically safe and have been clinically approved by the Food and Drug Administration organization (FDA) [24]. Another interesting biomaterial is dextran (Dx), which is a negatively charged, non-immunogenic polysaccharide with variable molecular weight [27]. Low molecular weight dextran sulfate (Mw= 5 kDa) is considered a promising contributor for the association to other polymers in controlled release system, due to its non-toxicity, biocompatibility, and biodegradability [28].

In this work, polymeric NPs were designed and synthesized by combining protamine and dextran sulfate. To achieve similar conditions to the *in vivo* situation, this work focused on evaluating the NPs using a 3D cell culture model, specifically glioblastoma spheroids. Their architecture is suitable for closely mimicking tumor morphology under *in vitro* conditions. Indeed, the spheroids resemble solid tumors in many respects, such as structural organization, cell layer assembly, hypoxia, and nutrient gradients [29, 30]. Based on this information, the

main objective of the present work has been the development and characterization of protamine:dextran (Pr:Dx) NPs as gene delivery systems suitable for different types of nucleic acids for the treatment of glioblastoma using *in vitro* 2D and 3D cell culture models.

1.2. MATERIALS AND METHODS

1.2.1. Material

Protamine sulfate salt (Mw-5 kDa, European Pharmacopeia (EP) grade) was obtained from Yuki Gosei Kogyo. LTD. Dextran sulfate sodium salt from leuconostoc spp. (1 g), agarose (100 g), heparin sodium salt from porcine mucosa (25 KU), loading-buffer 10X, Agar (250 g), Tris-Acetate-EDTA (TAE) Buffer 10X (1 L), sodium chloride (NaCl) BioXtra ≥99.5% (AT) (1 kg), sodium dodecyl sulfate (SDS) (250 g), the fluoromount® aqueous mounting medium (25 mL), the 4% (*v/v*) paraformaldehyde, the phosphotungstic acid (sodium salt), the Luciferase Reporter Gene Detection kit (LUC1) and kanamycin (5g) were purchased in Sigma-Aldrich. Triton-100X (50 mL) and SYBR®Gold Nucleic Acid Gel Stain 50X (0.5 mL) were purchased from Scharlab S.L. Cellular membrane (Mw-3,5 kDa, 16 mm dry, I.D 35 feet, SnakeSkin™), diethyl pyrocarbonate ultrapure (DEPC) >97% (25 mL), LIVE/DEAD™ Fixable Aqua Dead Cell Stain Kit 405 nm excitation (200 assays), PrestoBlue™ Cell Viability reagent, Lipofectamine®2000 Transfection Reactive (0.75 mL) and micro-BCA Protein Assay kit were from Thermo Fisher Scientific™. The 5-carboxytetramethylrhodamine succinimidyl ester single isomer (5-TAMRA) (5 mg) and 4',6-diamino-2-phenylindole (DAPI) (10 mg) were purchased from Emp-Biotech and Biochem, respectively. CellTiter Blue® Cell Viability Assay (20 mL) was obtained from Promega. The decontamination solution RNase-free AWAY (475 mL) and UltraPure™ DNase/RNase-Free Distilled Water (500 mL) were from Molecular Bioproduct. The 7-aminoactinomicyn D (7-AAD) Viability Staining Solution (2 mL) was from Invitrogen. The Luciferase Reporter Gene Assay High Sensitivity kit was from Roche. The 10% (*v/v*) neutral buffered formalin (1 L) was obtained from Bio-Optica. Sodium bicarbonate ($NaHCO_3$) 99% (2500 mg) was purchased to Alfa Aesar, and dimethyl sulfoxide (DMSO) (1 L) and the ethanol gradient grade for liquid chromatography (≥99%) to Merck Millipore. The µ-Slide-8-well (1.5 polymer coverslip, tissue culture sterilized) was purchased from Ibidi®.

Regarding the cellular culture, Dulbecco's Modified Eagle's Medium 1X (DMEM) ([+] 4.5 g/L D-Glucose and 1g/L D-Glucose, [+]Pyruvate, [+]L-Glutamine) (500 mL), Dulbecco's Modified Eagle's Medium 1X (DMEM) ([+] 1 g/L D-Glucose, [+]Pyruvate, [-]L-Glutamine, no phenol red) (500 mL), Opti-Minimum Essential Medium I 1X Reduced Serum Medium (Opti-MEM) ([+]HEPES, [+]2.4 g/L Sodium Bicarbonate, [+]L-Glutamine) (500 mL), Fetal Bovine Serum Qualified (FBS) (500 mL), Penicillin-Streptomycin (P/S) ([+]10000 Units/mL Penicillin, [+]10000 µg/mL Streptomycin) (100 mL), L-Glutamine solution (200 mM, sterile-filtered, BioXtra) and 0.05% Trypsin 1X-EDTA (500 mL) (2212509) were purchased from Gibco (Life-Technologies). Dulbecco's Phosphate Buffered Salt Solution 10X (DPBS) with calcium chloride and magnesium chloride ions (500mL) and modified Hanks Balanced Salt Solution (HBSS) with phenol red, calcium free and magnesium free were also obtained from the latter supplier. The Phosphate Buffered Salt Solution 10X (PBS) was prepared in the laboratory.

The model plasmid pEGFP-Luc was donated by the group of Prof. Anxo Vidal (CiMUS, Universidad de Santiago de Compostela). The PureLink HiPure Expi Plasmid Gigaprep Kit was obtained from Invitrogen. The Cy5-modified siRNA was purchased from Eurofins MWG Operon. The Luria-Bertani medium (LB) was also prepared in the laboratory.

1.2.2. Formulation of protamine NPs

Pr:Dx NPs were prepared by an ionic cross-linking technique previously described by our research group [31]. Briefly, stock solutions of protamine and dextran were prepared in ultrapure laboratory grade water (Milli-Q water) at concentration of 2 mg/mL for protamine and 4 mg/mL for dextran. Based on previous results from the group, the prototype 4:1 (*w/w*) Pr:Dx was selected for the experiments. For this purpose, a volume of 0.250 mL of dextran solution was added drop by drop to 0.5 mL of protamine solution (1 mg of protamine was fixed) under magnetic stirring at 500 revolution per minute (rpm) at room temperature (RT) for 5 minutes (min). The NPs were spontaneously formed, as indicated by the presence of an opalescent suspension.

1.2.3. Morphological and physicochemical characterization of protamine NPs

The NPs were characterized with respect to their mean particle size, PDI, derived count rate (DCR) and surface charge. The size, PDI and DCR were measured by Photon Correlation Spectroscopy (PCS) and the zeta potential was measured by Laser Doppler Anemometry (LDA) at 25 ºC using a detection angle of 173º (Zetasizer Nano-ZS™, Malvern Instruments). Samples were prepared using a dilution 1:10 (*v/v*) in Milli-Q water and measurements were done in triplicate. The NP-morphology was analyzed by Scanning Transmission Electron Microscopy (STEM) (FESEM Ultra Plus, ZEISS) using a voltage of 20 kV and SE/InLens as detectors. For this purpose, a dilution of 1:100 (*v/v*) in Milli-Q water was stained with 2% (*w/v*) phosphotungstic acid and deposited on a copper grid, previously well-dried. The yield of the preparation process was determined by the isolation of the NPs by centrifugation (Centrifuge 5430R, Eppendorf) for 30 min at 15 ºC at 10,000 RCF. The supernatant was discarded, and the white pellet was freeze-dried (Freeze-dryer VirTis Genesis 25 EL, Labconco Corp) after 96 hours (h) of incubation at -80 ºC. The yield was calculated as follows:

$$Yield\ (\%) = \frac{NP-weight}{Theoretical\ weight\ (total\ solid\ mass)}\ x\ 100 \qquad (1)$$

1.2.4. Stability of blank protamine NPs

A long-time stability of blank NPs was determined at storage conditions (4 ºC) for one month. The colloidal stability of blank 4:1 (*w/w*) Pr:Dx NPs was also measured in relevant non-supplemented DMEM medium and supplemented with 10% (*v/v*) FBS and 1% (*v/v*) of P/S incubating at 37 ºC under horizontal shaking at 300 rpm at different time points: 0, 2 and 4 h. For both purposes, the size, PDI and DCR were determined using a dilution 1:10 (*v/v*) in the corresponding media by PCS. The zeta potential was determined by LDA following the protocol described in section 1.2.3.

1.2.5. Association of nucleic acids to protamine NPs

Pr:Dx NPs formulated at the ratio 4:1 (*w/w*) were loaded with different nucleic acids, pDNA and miRNA, at 8% (*w/w*) with respect to the theoretical total mass of solids. The genetic material was incorporated into the anionic solution prior to the NP-formulation. The morphology and physicochemical characteristics were also determined following the protocol described in section 1.2.3. In addition, the nucleic acid association efficiency was determined by agarose gel electrophoresis, using a concentration of agarose in TAE Buffer 1X of 1% (*w/v*) for pDNA and 2% (*w/v*) for miRNA. A maximum of 0.5 µg of nucleic acids was loaded per line. The gel was run for 45 min in a Sub-Cell GT 96/192 (Bio-Rad Laboratories Ltd.) at 90 V. A competitive displacement assay was carried out by incubating the NPs with an excess of

heparin sodium salt (25-fold with respect to the mass of nucleic acids) for 2 h at 37 ºC (Heidolph, tritamax 1000). To observe the displacement of each band, the gel-loading buffer 1X, composed by 25 mg of blue bromophenol, 3 mL of glycerol and 10 mL of Milli-Q water, was used, and the gels were imaged using Molecular Imager® Gel Doc™ XR$^+$ System (UV light 302; Bio-Rad) after staining with SYBR®Gold 1X nucleic acid stain.

1.2.6. Cell culture

The U87MG cell line was obtained from ATCC. They were cultured in high DMEM medium supplemented with 10% (*v/v*) FBS and 1% (*v/v*) of P/S at 37 ºC with 5% of CO_2 and 95% of relative humidity (Memmert INCO 2, (I.C.T, S.L.)). The three patient-derived glioblastoma cell lines (GIN-8, GIN-28, and GCE-28) were donated by the Children's Brain Tumor Research Group (Biodiscovery Institute, University of Nottingham). The GIN-8 cell line (Glioma INvasive margin cells) was isolated from medial front invasive margin (54 y female, wild-type IDH (primary GBM), intact ATRX, 0% MGMT promoter methylation, 90% resection plus Gliadel wafers, treatment 60Gy radiotherapy, concurrent and adjuvant temozolomide, patient died 5 months after surgery), the GIN-28 cell line was isolated from 5-ALA fluorescence-positive invasive margin (71 y male, wild-type IDH (primary GBM), intact ATRX, 0% MGMT promoter methylation, 99% resection, no adjuvant therapy (patient choice), patient died 3 months after surgery) and the GCE-28 cell line was isolated from the central tumor core (71 y male, wild-type IDH (primary GBM), intact ATRX, 0% MGMT promoter methylation, 99% resection, no adjuvant therapy (patient choice), patient died 3 months after surgery) [32]. These three patient-derived glioblastoma cells were cultured in low DMEM medium supplemented with 10% (*v/v*) FBS and 1% (*v/v*) P/S at 37 ºC with 5% of CO_2 and 95% of relative humidity (Cryofusion, MCO2OAIC-PE).

1.2.7. Cytotoxicity assay in 2D glioblastoma model

The *in vitro* cytotoxicity of blank 4:1 (*w/w*) Pr:Dx NPs was first evaluated in the commercial U87MG cell line, followed by studies in patient-derived glioblastoma cell lines (GIN-8, GIN-28, GCE-28). In all cases, viability was determined by using the resazurin viability assay. The amount of $5x10^3$ of cells were seeded in 96-well plates (Costar, Corning Incorporated) in a final volume of 0.100 mL of supplemented DMEM medium. After 24 h of incubation, the medium was replaced with 0.09 mL of fresh supplemented DMEM medium and 0.01 mL of: (i) sterile filtered Milli-Q water, as negative control, (ii) 1% (*v/v*) triton-X100 as positive control and (iii) increasing doses of blank 4:1 (*w/w*) Pr:Dx NPs from 50 to 160 µg/mL. The cells were incubated for 4 h at 37 ºC. The U87MG cells were washed with 0.100 mL of PBS 1X, and GIN and GCE cells were washed with 0.100 mL of DPBS 10X with calcium chloride and magnesium chloride. All of them were incubated in 0.100 mL of fresh supplemented medium for 24 h and 48 h. In the case of U87MG cell line, 0.02 mL of CellTiter-Blue® Cell Viability reagent was added, and the cells were incubated for 3 h at 37 ºC covering the plate with aluminum foil. To measure the fluorescence emitted by the reduced form of resazurin, the reaction was stopped and stabilized by the addition of 0.05 mL of SDS 3% (*w/v*) for 30 min at 37 ºC. The fluorescence signal was measured at 539 nm of excitation wavelength (λ_{Ex}) and 620 nm of emission wavelength (λ_{Em}) in a Synergy H1 microplate reader (Biotek) by Gen 5 Software with the previous placed of the cells in black 96-well plates (BrandPlates® pure Grade, Brand). In the case of GIN-8, GIN-28 and GCE-28 cell lines, a final volume of 0.100 mL of 10% (*v/v*) PrestoBlue™ Cell Viability reagent diluted in DMEM free red phenol supplemented with 10% (*v/v*) FBS and 1% (*v/v*) L-Glutamine was applied per well for 2 h at 37 ºC, also covering the plate with aluminum foil. The fluorescence signal was measured at

544/590 nm ($\lambda_{Ex}/\lambda_{Em}$) on a BMG Labtech FLUOstar Omega microplate reader (Isogen Life Science B.V.) by Omega Software with the previous placed of the cells in black 96-well plates (NUNC™ MicroWell™, ThermoFisher Scientific).

The cell viability (%) was calculated as follows:

$$Cell\ viability\ (\%) = \frac{Sample\ Fluorescence}{Control\ cells\ Fluorescence}\ x\ 100 \quad (2)$$

1.2.8. Nanoparticle uptake assay in 2D glioblastoma model

1.2.8.1. Polymer labelling

To study the NP-internalization, protamine was labelled with the fluorescent reagent 5-TAMRA. For this purpose, protamine sulfate salt was dissolved in 0.1 M $NaHCO_3$ buffer (pH= 8.58) at 10 mg/mL and 5-TAMRA was dissolved in DMSO at 10 mg/mL. After that, 0.06 mL of 5-TAMRA solution was added into 1 mL of protamine solution under mild stirring conditions (300 rpm) for 1 h at RT, resulting in complete homogenization. The magenta solution of 5-TAMRA-labelled protamine (Pr-TAMRA) was dialyzed using a cellulose membrane (Mw= 3.5 kDa, 16 mm dry, I.D 35 feet, SnakeSkin™) in 0.05 M NaCl buffer for 48 h and then in HPLC-grade water for 24 h under stirring (500 rpm, RT, in dark). Finally, the dialyzed solution was completed with HPLC-grade water until a final concentration of 5 mg/mL and was lyophilized. The lyophilized product was stored in a desiccator.

The total amount of Pr-TAMRA was calculated as follows:

$$mg\ (5-TAMRA-Protamine) = \frac{mg\ (vial+\ lyophilized\ product)}{mg\ (empty\ vial)} \quad (3)$$

1.2.8.2. Formulation of NPs using 5-TAMRA-labelled protamine

The formulation of NPs using TAMRA-labelled protamine was carried out following the protocol described in section 1.2.2. In this case, the 0.5 mL of protamine solution was composed by 0.3 mL of Pr-TAMRA at 0.8 mg/mL and 0.2 mL of protamine at 3.8 mg/mL. The physicochemical characterization of the formulation was also done by triplicate measuring the particle size, PDI, DCR and zeta potential under the same conditions mentioned in section 1.2.3.

1.2.8.3. *In vitro* uptake assay

The internalization study of fluorescently labelled-NPs in glioblastoma cells was evaluated by Confocal Scanning Laser Microscopy (CSLM) (Leica TCS SP5 X, Leica Microsystems, GmB, and Leica CTR 6500, Leica Microsystems, TSC/SPE) and the quantification was determined by flow cytometry (BD Accuri™ C6 Flow Cytometer and ImageStream X MkII Imaging Flow Cytometer-Luminex). In this case, $4.5x10^4$ U87MG, GIN-8, GIN-28, and GCE-28 cells/well were seeded in 24-well plates (Falcon, and Costar, Corning Incorporated, respectively), using 12 mm diameter glass round coverslips covered with poly-L-Lysine (Corning, BioCat™) in a final volume of 1 mL of supplemented DMEM medium, and they were incubated for 48 h at 37 ºC. The culture medium was replaced with 7 µg/cm^2 of 4:1 (*w/w*) Pr-TAMRA:Dx NPs in a final volume of 0.4 mL of fresh DMEM and was incubated for 4 h at 37 ºC. Untreated cells were used as negative control. After this time, cells were fixed using 0.350 mL of commercial 10% (*v/v*) neutral buffered formalin for 15 min under horizontal shaking (Rocker, VWR) at RT, after previous washing with PBS 1X buffer in the case of U87MG cells and DPBS 10X buffer with calcium chloride and magnesium chloride in the case

of GIN and GCE cells for 5 min at RT. A dilution 1:1000 (*v/v*) of DAPI (stock concentration: 1 mg/mL in PBS 1X) in a volume of 0.2 mL was added and incubated for 30 min under the same conditions. Finally, the excess of DAPI was removed and the glass round coverslips were placed on slides (Menzel-Gläser, Thermo Scientific) using fluoromount® aqueous mounting medium for the visualization by confocal microscopy using the LAS X Life Science Software (magnification 63x in U87MG and 40x in GIN-8, GIN-28, and GCE-28) ($\lambda_{Ex}/\lambda_{Em}$ (DAPI) = 358/461 nm and ($\lambda_{Ex}/\lambda_{Em}$ (5-TAMRA) = 543/578 nm).

Flow cytometry was carried out to quantify the internalization of Pr:Dx NPs. In this case, after the same treatment of the cells with NPs as above (7 µg/cm^2, 4 h, 37 ºC), 0.2 mL of LIVE/DEAD™ Fixable Aqua Dead Cell Stain reagent diluted in PBS 1X buffer was added, and the glioblastoma cells were incubated for 15 min in horizontal shaking at RT. After washing, cells were detached by 0.05% Trypsin 1X-EDTA (5 min, 37 ºC). Trypsin was deactivated by adding supplemented DMEM medium, and cells were transferred to eppendorf tubes (Deltalab) and centrifuged (Centrifuge 5430R, Eppendorf, and HAWK 15/05 refrigerated centrifuge, Sanyo MSE, respectively). In the case of U87MG cells, the pellet was resuspended in 0.5 mL of PBS 1X buffer supplemented with 10% FBS (*v/v*) and in the case of the patient-derived GIN and GCE cells, the pellet was resuspended in 0.05 mL of commercial 4% (*v/v*) paraformaldehyde. Finally, a maximum of 10,000 U87MG events were excited at 488 nm using filters BP 575/25 for 5-TAMRA and at 405 nm using filters BP 515/20 for Aqua viability reagent and they were analyzed by BD CSample Software (BD Biosciences). The same amount of GIN and GCE events were excited at 561 nm for 5-TAMRA and at 405 nm for Aqua viability reagent, and they were analyzed by IDEAS 6.2® Software (Luminex).

Additionally, the internalization of Pr:Dx NPs loaded with a siRNA labelled fluorescently with cyanine 5 (Cy5-modified siRNA) in U87MG cell line was also evaluated by CSLM. As mentioned in section 1.2.5., a concentration of 8% (*w/w*) of Cy5-modified siRNA was associated to the 4:1 (*w/w*) Pr:Dx NPs under RNase-free conditions. After the treatment of Cy5-modified siRNA-loaded NPs (7 µg/cm^2, 4 h, 37 ºC), the U87MG cells were visualized by confocal microscopy (magnification 63x) ($\lambda_{Ex}/\lambda_{Em}$ (DAPI) = 358/461 nm and ($\lambda_{Ex}/\lambda_{Em}$ (Cy5) = 635/670 nm) under the previously mentioned fixing conditions.

1.2.9. Transfection assay in 2D glioblastoma model

1.2.9.1. Amplification of plasmid DNA

To perform the transfection studies, the plasmid encoding the proteins: Enhanced Green Fluorescence Protein (EGFP) and Luciferase protein (Luc) (pEGFP-Luc), was selected (Figure 1.).

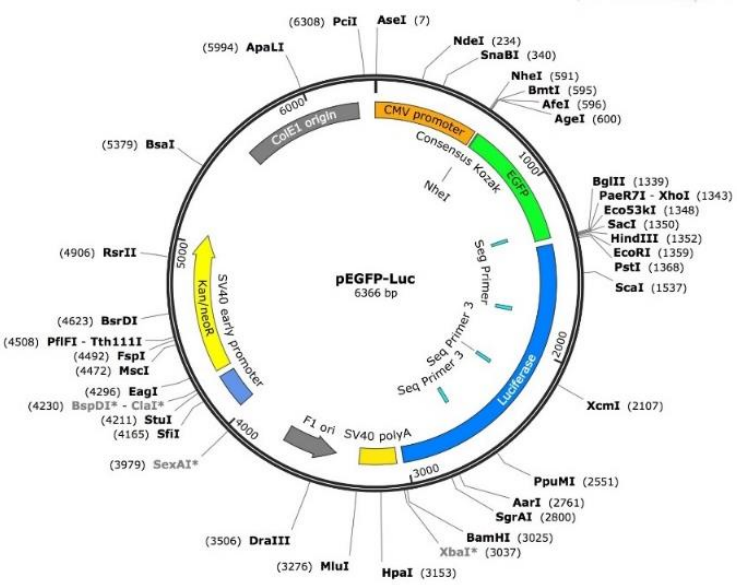

Figure 1. Plasmid map of pEGFP-Luc. Image from addgene website.

The plasmid pEGFP-Luc were amplified using competent DH5α bacteria following the standard protocol described elsewhere. The plasmid extraction was performed using the Invitrogen™ HiPure Plasmid Gigaprep Kit following the manufacturer's protocol. For this purpose, the transformed bacteria was ultra-centrifuged (Avanti® J-26 XPI Centrifuge, Beckman Coulter, rotor JA-10 (10,000 rpm), Beckman) for 15 min at 4,000 RCF. The bacteria pellet was resuspended in RNase solution and, subsequently, mixed with a lysis buffer. The removal of cell debris was carried out using a precipitation buffer and the plasmid purification using columns provided by the kit. Finally, the plasmid was eluted, precipitated and the concentration was quantified by spectral scanning UV-VIS spectrophotometry (Nanodrop, ThermoFisher). The concentration was calculated by measuring the pure plasmid solution and different dilutions. The measurements were done in triplicate.

1.2.9.2. *In vitro* 2D transfection assay

The transfection studies using 4:1 (*w/w*) Pr:Dx NPs in U87MG glioblastoma cells were carried out using the plasmid pEGFP-Luc. As mentioned in section 1.2.5., 8% (*w/w*) of pEGFP-Luc respect to the total mass of solids were associated to the NPs. For this purpose, $4.5x10^4$ glioblastoma cells/well were seeded in 24-well plates (Falcon) in a final volume of 1 mL of supplemented DMEM medium and were incubated for 24 h at 37 ºC. After that, the U87MG cells were treated with: (i) different concentrations of NPs (6.25; 12.50 and 31.25 µg/well corresponding to 0.5; 1 and 2.5 µg of pDNA/well), (ii) naked pEGFP-Luc as negative control, and (iii) Lipofectamine® 2000 reagent, prepared under the specifications of the commercial protocol, as positive control. All groups were prepared in 0.2 mL of non-supplemented Opti-MEM medium. The formulation and controls were incubated for 4 h at 37 ºC, and after their removal, the cells were washed, and 1 mL of fresh supplemented DMEM medium was added. The evaluation of the EGFP expression was carried out by direct observation by fluorescence microscopy (Olympus IX51) using the Olympus cellSens Standard Software at 24 h and 48 h.

Luciferase expression in transfected cells was also quantified after 24 h and 48 h using a specific commercial kit (Luciferase Reporter Gene Assay High Sensitivity (Roche)). In this case, after cell-washed with PBS 1X buffer, U87MG cells treated with the formulation and controls were lysed with 0.100 mL of Lysis Buffer 1X. The mucus obtained was incubated for

15 min at RT and, then centrifuged (Centrifuge 5430R, Eppendorf) for 10 min at 4 ºC at maximum speed. Immediately, 0.05 mL of the supernatant was placed on white 96-well plates (Deltalab). The Luciferase expression was measured using a Luminometer (Berthold Luminometer Mithras LB940) by adding 0.025 mL of Luciferin/well with an automatic and pre-balanced injector. The results of the measures were gathered by MicroWin2000 Software. Finally, the total protein content of each sample was determined following the instructions provided with the micro-BCA Protein Assay kit (ThermoScientific), and the results were expressed as Relative Light Units per milligram cellular protein (RLU/mg protein).

1.2.10. Generation of glioblastoma spheroids

In the case of U87MG cell line, an amount of 250 cells/well was selected to form the spheroids. For GIN and GCE cell lines, the cell density was 2,000 cells/well. Cells were seeded per well in a 96-Ultra-Low Attachment round bottom plates (ULA 96-well) (Costar, Corning Incorporated) in a final volume of 0.2 mL of supplemented DMEM medium. For U87MG cell line, the cells were centrifuged for 20-30 min at 22 ºC at 200 RCF (Centrifuge 5430R, Eppendorf) and for patient-derived cell lines, 10 min at 300 RCF (Sigma 3-16L Centrifuge, Sci-Quip). Morphological characterization of U87MG spheroids was carried out every 3-4 days by taking photos (magnification 10x) using an optical microscope (Olympus IX51). Their size was determined using the Olympus cellSens Standard Software until a value between 200-300 µm was obtained. In the case of GIN-8, GIN-28 and GCE-28 spheroids, morphological characterization was carried out after 2 days by taking photos (magnification 10x) using a plate reading widefield microscope (Nikon Intensilight C-HGFI/C-HGFIE), where their size was determined using the NIS-Elements Viewer 5.21 Software until reaching dimensions like those of U87MG spheroids.

Moreover, morphological characterization of U87MG spheroids was also analyzed by Scanning Electron Microscopy (SEM) (FESEM Ultra Plus, ZEISS). After the 4th day, the spheroids were fixed with 0.150 mL of commercial 10% (*v/v*) neutral buffered formalin and they were incubated for 15 min under horizontal shaking (Rocker, VWR) at RT, after washing with PBS 1X buffer. Following this, the spheroids were carefully washed twice with PBS 1X buffer, and once with Milli-Q water to initiate the dehydration process. Different dilutions of ethanol solution (20%, 50%, 70%, 90% and 100% (*v/v*) in Milli-Q water) were prepared, and the spheroids were transferred. Finally, the dehydrated spheroids were deposited on a copper grid, and were analyzed by SEM using a voltage of 20 kV and SE/InLens, with magnifications 1.00 KX, 3.00 KX, 5.00 KX, 10.00 KX and 30.00 KX.

1.2.11. Cytotoxicity assays in 3D glioblastoma models

The cytotoxicity assay of blank 4:1 (*w/w*) Pr:Dx NPs in glioblastoma spheroids (U87MG, GIN-8, GIN-28, and GCE-28) was carried out under the same conditions described in section 1.2.7. After spheroid formation, 0.150 mL of cell culture medium was removed, leaving the spheroid in suspension in 0.05 mL. After that, 0.140 mL of fresh supplemented DMEM medium and 0.01 mL of different concentrations of blank Pr:Dx NPs (from 5 to 40 µg/mL in U87MG spheroids and from 5 to 80 µg/mL in GIN and GCE spheroids) and controls were added and incubated for 4 h at 37 ºC. After 24 h and 48 h of NP-removal and controls, U87MG spheroids were treated adding 0.04 mL of CellTiter Blue® Cell Viability reagent and, GIN and GCE spheroids were treated with 0.2 mL of 10% (*v/v*) PrestoBlue™ Cell Viability reagent diluted in DMEM free red phenol supplemented with 10% (*v/v*) FBS and 1% (*v/v*) L-Glutamine, and they

were incubated for 4 h at 37 ºC in darkness. The fluorescence signal was measured using the same conditions described in 2D cytotoxicity assay in section 1.2.7.

Additionally, two complementary experiments were performed to achieve a complete 3D viability assay: the volume assay and evaluation of spheroid-membrane integrity.

1.2.11.1 Volume assay of glioblastoma spheroids

Simultaneously to 3D cytotoxicity assay, the volume of glioblastoma spheroids was also analyzed before and after the treatment with blank 4:1 (*w/w*) Pr:Dx NPs. Photos of U87MG spheroids (magnification 10x) were taken using an optical microscope (Olympus XI51) and analyzed by Olympus cellSens Standard Software. On the other hand, photos of patient-derived glioblastoma spheroids (magnification 10x) were taken using a plate reading widefield microscope (Nikon Intensilight C-HGFI/C-HGFIE) and analyzed by NIS-Elements Viewer 5.21 Software. The area of the spheroids was measured using Fiji Software (ImageJ) and their volume (%) compared to the control was calculated as follows:

$$Spheroid\ volume\ (\%) = \frac{Sample\ spheroid\ Volume\ *}{Control\ spheroid\ Volume}\ x\ 100 \quad (4)$$

$$*\ Spheroid\ Volume = \frac{4}{3}\ x\ \pi\ x\ r^{3**} \quad (5)$$

$$**\ Spheroid\ radius = \sqrt{\frac{Area}{4\pi}} \quad (6)$$

1.2.11.2. Membrane-integrity of U87MG spheroids

This study was carried out under the same conditions as 3D cytotoxicity assay. After 4 h, 24 h and 48 h of the NP-removal, 0.005 mL of 7-AAD viability reagent was added directly in 0.2 mL of fresh supplemented DMEM medium. The plate was gently shaken by hand for 10 s and the U87MG spheroids were incubated for 30 min at 37 ºC in the darkness. The 7-AAD expression was analyzed by fluorescence microscopy (Olympus XI51) using mCherry channel by Olympus cellSens Standard Software. In addition, the fluorescence signal of 7-AAD ($\lambda_{Ex}/\lambda_{Em}$ = 550/650 nm) was measured in a microplate reader (Synergy H1 microplate reader, Biotek) by Gen 5 Software with the previous placed of the spheroids in black 96-well plates (BrandPlates® pure Grade, Brand).

Membrane integrity (%) was calculated as follows:

$$Spheroid\ membrane\ integrity\ (\%) = \frac{Sample\ Fluorescence}{Control\ cells\ Fluorescence}\ x\ 100 \quad (7)$$

1.2.12. Nanoparticle uptake in 3D glioblastoma models

NP-internalization was evaluated in glioblastoma spheroids by SEM (FESEM Ultra Plus, ZEISS), CSLM (Leica TCS SP5 X, Leica Microsystems, GmB and Leica CTR 6500, Leica Microsystems, TSC/SPE), Light Sheet Fluorescence Microscopy (LSFM) with particle tracking microrheology (OptoRheo) [33] and by flow cytometry (BD Accuri™ C6 Flow Cytometer and ImageStream X MkII Imaging Flow Cytometer-Luminex).

After applying the same treatment of blank 4:1 (*w/w*) Pr-TAMRA:Dx NPs (7 µg/cm^2, 4 h, 37 ºC), the preparation of spheroids to analyze the NP-uptake by microscopy was the following: they were fixed in 0.150 mL of commercial 10% (*v/v*) neutral buffered formalin for 30 min

under horizontal agitation (Rocker, VWR) at RT. After washing, 0.150 mL of a dilution 1:1000 (*v/v*) of DAPI (stock concentration: 1 mg/mL in PBS 1X) was added and incubated for 30-45 min. Fixed spheroids were placed on µ-Slide-8-well chamber (1.5 polymer coverslip, tissue culture sterilized, Ibidi®) and visualized by confocal microscopy using the LAS X Life Science Software (magnification 20x-z2 in U87MG, and magnification 10x-z1.5 in GIN and GCE cell lines) ($\lambda_{Ex}/\lambda_{Em}$ (DAPI) = 358/461 nm and ($\lambda_{Ex}/\lambda_{Em}$ (5-TAMRA) = 543/578 nm). Uptake in patient-derived spheroids was also analyzed by LSFM using OptoRheo [33] in collaboration with Dr. Tania Mendonca and Dr. Amanda J. Wright, members of Optics and Photonics Research Group (University of Nottingham). In this case, the fixed spheroids were placed on a µ-Slide-4-well chamber using a glass cube to reduce the size of the well adding up the spheroid in the center and aligned with the laser incidence [34]. The fluorescence was measured at $\lambda_{Ex}/\lambda_{Em}$ (5-TAMRA) = 543/578 nm (magnification 60x), and the images were processed by Fiji Software (ImageJ). Finally, the preparation of U87MG spheroids to analyze the NP-uptake by SEM was following the same protocol previously described in section 1.2.10.

To prepare the samples (10,000 events) for the analysis by flow cytometry, 0.01 mL of LIVE/DEAD™ Fixable Aqua Dead Cell Stain reagent was added to 0.05 mL of the spheroid suspension, and incubated for 30 min at 37 ºC. After removal of the reagent, spheroids were washed and collected in a 15 mL conical falcon tube (Deltalab) for their settlement for 2 min at RT. Culture medium was replaced carefully by PBS 1X buffer in U87MG spheroids and by DPBS 10X buffer in GIN and GCE spheroids, and they were centrifuged (Centrifuge 5430R, Eppendorf, HAWK 15/05 refrigerated centrifuge, Sanyo MSE, respectively) for 1 min at 200 RCF at 22 ºC. The spheroids were de-aggregated with 0.2 mL of Trypsin 1X-EDTA for 20 min for U87MG and for 5 min for GIN and GCE cell lines at 37 ºC by manual pipetting. After trypsin deactivation, cells were centrifuged for 5 min at 200 RCF at 22 ºC. The U87MG pellet was resuspended in 0.5 mL of PBS 1X buffer supplemented with 10% FBS (*v/v*) and GIN and GCE pellets were resuspended in 0.05 mL of commercial 4% (*v/v*) paraformaldehyde. Finally, the analysis was completed using the same conditions mentioned in the 2D-uptake assay.

Internalization of Pr:Dx NPs loaded with Cy5-modified siRNA (8% (*w/w*)) was also evaluated in U87MG spheroids by confocal microscopy applying the same conditions described previously in section 1.2.8.3. (magnification 20x and 63x) ($\lambda_{Ex}/\lambda_{Em}$ (DAPI) = 358/461 nm and ($\lambda_{Ex}/\lambda_{Em}$ (Cy5) = 635/670 nm).

1.2.13. Transfection assay in 3D glioblastoma model

The transfection of blank 4:1 (*w/w*) Pr:Dx NPs were carried out in U87MG spheroids under the same conditions described for 2D transfection assay in section 1.2.9.2. The evaluation of EGFP expression was carried by fluorescence microscopy (Olympus IX51) using the Olympus cellSens Standard Software after 24 h and 48 h of NP-removal, and by LSFM (UltraMicroscope II, Miltenyi BioTec) using a dipping cap for water (DC49, WD10,9, AB6, IR:1.414-1.574, Miltenyi BioTec), selecting the amount of 2.5 µg of pDNA. For the latter purpose, the spheroids were fixed following the same protocol described in section 1.2.12. After washing with PBS 1X, 0.2-0.4 mL of 1% (*w/v*) agarose solution was added to each spheroid at 37 ºC. The agarose block embedding the spheroids was absorbed quickly with 1 mL syringe, cooled, and equilibrated in water. The fluorescence was measured at 488/525 nm ($\lambda_{Ex}/\lambda_{Em}$) to EGFP and at 405/460 nm ($\lambda_{Ex}/\lambda_{Em}$) to DAPI, using a magnification 7.2x with a zoom of 0.6x. The images were processed using the Imaris Cell Imaging Software (Oxford Instrument Imaris).

1.2.14. Statistical analysis

Differences were statistically analyzed by two-way ANOVA followed by Tukey's method, respectively if not stated otherwise. All statistical analyses were conducted using GraphPad Prism Software (version 8.0 for Windows). A *p* value<0.05 was considered to be significant (*p<0.05; **p<0.01; ***p<0.001; ****p<0.0001). Each experiment was performed independently in triplicate (n= 3), if not stated otherwise.

1.3. RESULTS AND DISCUSSION

1.3.1. Physicochemical characterization of protamine NPs

The ionic gelation method, previously developed in our research group, was used to formulate the NPs. Parameters such as the ratio of materials, the interaction mechanisms, and the process conditions play an important role to formulate optimal nanocarriers with a maximum therapeutic efficacy. The method, based on cross-linking positively charged molecules with negatively charged polyanions, presents several advantages such as the use of water-based solutions, high stability of synthetized particles, mild reaction conditions, simplicity, and cost-effectiveness [35]. Regarding the materials, protamine, a biodegradable cationic polymer, was selected due to its high capacity to condense nucleic acids and its cell membrane translocation enhancing properties [25] [26], and dextran was selected due to its negative charge and gelling capacity [28]. After previous screening studies carried out by our research group, the weight ratio 4:1 (*w/w*) Pr:Dx was considered the most suitable for the association, protection, and intracellular administration of genetic material [31] [36]. In the present work, the resulting NPs were characterized for their physicochemical characteristics such as mean particle size, PDI, and surface charge, and for their morphology. The results collected in Table 1. showed that the formulation was composed by a homogeneous population of NPs (PDI≤ 0.2) with a size below 150 nm, and positive surface charge. In addition, the reaction yield was 54±3% indicated the strong influence of the protamine.

Table 1. Mean particle size, polydispersity index (PDI) and zeta potential of blank 4:1 (*w/w*) Pr:Dx NPs and loaded with 8% (*w/w*) of pDNA and miRNA, respect to the total mass of the NPs (Mean ± SD, (n= 3)).

4:1 (*w/w*) Pr:Dx NPs	Size (nm)	PDI	Zeta potential (mV)
Unloaded	120 ± 7	0.2	+34 ± 2
pDNA	146 ± 1	0.2	+33 ± 5
miRNA	124 ± 5	0.1	+30 ± 3

Regarding the morphological characteristics, the formulation was composed by a homogeneous population of spherical NPs (Figure 2. (a)).

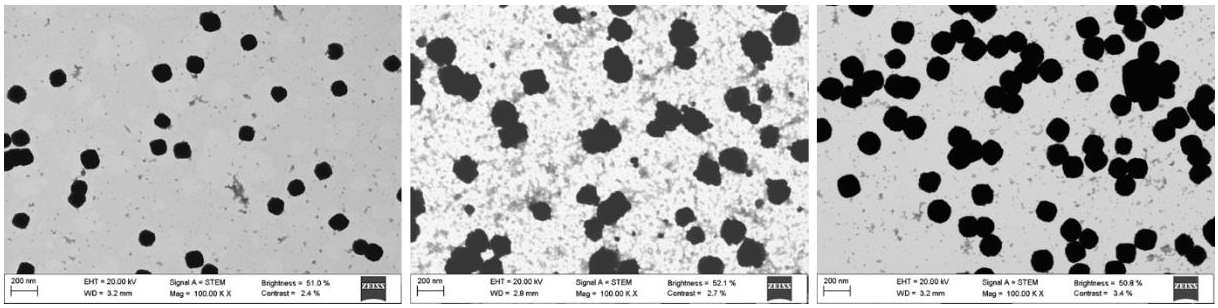

(a) (b) (c)

Figure 2. STEM images of (**a**) blank 4:1 (*w/w*) Pr:Dx NPs and associated with 8% (*w/w*) of (**b**) pDNA and (**c**) miRNA.

Different nucleic acids such as pEGFP-Luc and miRNA-145 were associated to the Pr:Dx NPs. Considering the results obtained from previous screening studies regarding the loading of genetic material in 4:1 (*w/w*) Pr:Dx NPs [36], 8% (*w/w*) payload respect to the total mass of the

NPs was selected. A slight increase was observed in the particle size of loaded NPs compared to unloaded ones, being higher in those carrying pDNA than those with miRNA (Table 1.). This difference could be related to the different molecular weight of these polynucleotides. The miRNAs are single-stranded chains composed between 21 and 25 nucleotide units, while the plasmid is composed of 6336 base pairs, and therefore could yield more complex structures. In the case of the zeta potential, a decrease was observed, probably as a consequence of the increase in negative charges present in the formulations with polynucleotides (Table 1.). On the other hand, the association of different nucleic acids did not modify the spherical morphology of the NPs, maintaining their homogeneous population as shown on the images collected in Figure 2. (b, c).

The association of these nucleic acids was further studied by agarose gel electrophoresis. To corroborate the association and reversible binding of nucleic acids to the NPs, the samples were incubated with an excess of heparin, a sulfated glycosaminoglycan with strong negative charge and high affinity to protamine, causing the competitive displacement and the release of the nucleic acids [37]. The results showed an effective binding of pDNA and miRNA when no competitor was added (lane 1), and the binding was reversible in the presence of heparin (lane 2), producing the release of intact polynucleotides (Figure 3.).

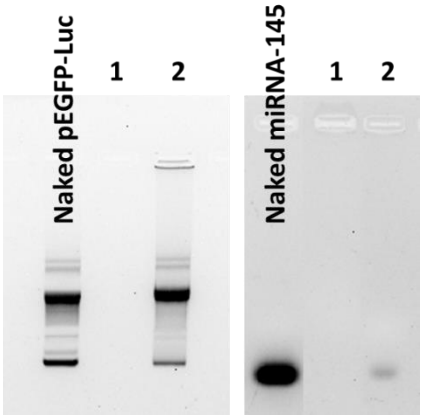

Figure 3. Agarose gel images of blank 4:1 (*w*/*w*) Pr:Dx NPs loaded with 8% (*w*/*w*) of pDNA and miRNA (lane 1). The amount of nucleic acids per lane was 0.5 μg in pDNA, and 1 μg in miRNA. The NPs were incubated with heparin for 2 h at 37 ºC using the mass ratio 1:25 (*w*/*w*) heparin:nucleic acid (lane 2).

1.3.2. Stability of blank protamine NPs

The stability of blank 4:1 (*w/w*) Pr:Dx NPs under storage conditions was determined by measuring the size, PDI, surface charge and DCR in aqueous suspension for 30 days. The optimization of the storage conditions of the NPs is highly important due to their influence on biocompatibility and their physicochemical characteristics [38]. Figure 4. (a) showed that the formulation experienced a slight increase in particle size over time, but it was constantly below 150 nm without losing homogeneity in the population. In addition, the count-rate was maintained within the same range throughout, indicating the absence of significant aggregation phenomena. Regarding the zeta potential, a positive surface charge was maintained over time (above +40 mV).

The stability of the NPs was also measured under relevant cell culture media at different time points to determinate their feasibility for *in vitro* testing. The results collected in Figure 4. (b) indicated that blank Pr:Dx NPs diluted in supplemented DMEM did not show an increase in particle size, while this phenomenon was observed after their incubation in non-

supplemented DMEM. In this case, a possible aggregation of the particles was postulated because of their stabilization mechanism, which is driven by electrostatic forces that are masked by the pH and/or the ionic strength of the cellular medium. Moreover, this process was controlled by FBS supplementation, suggesting that protein adsorption on the surface of the NPs could stabilize them. Regarding the number of the particles forming the population, a decrease in the DCR values was observed, especially, when Pr:Dx NPs were incubated in non-supplemented DMEM over the time, suggesting their aggregation. The results indicate that cell culture conditions using supplemented DMEM were favorable to carry out the next *in vitro* studies with these NPs.

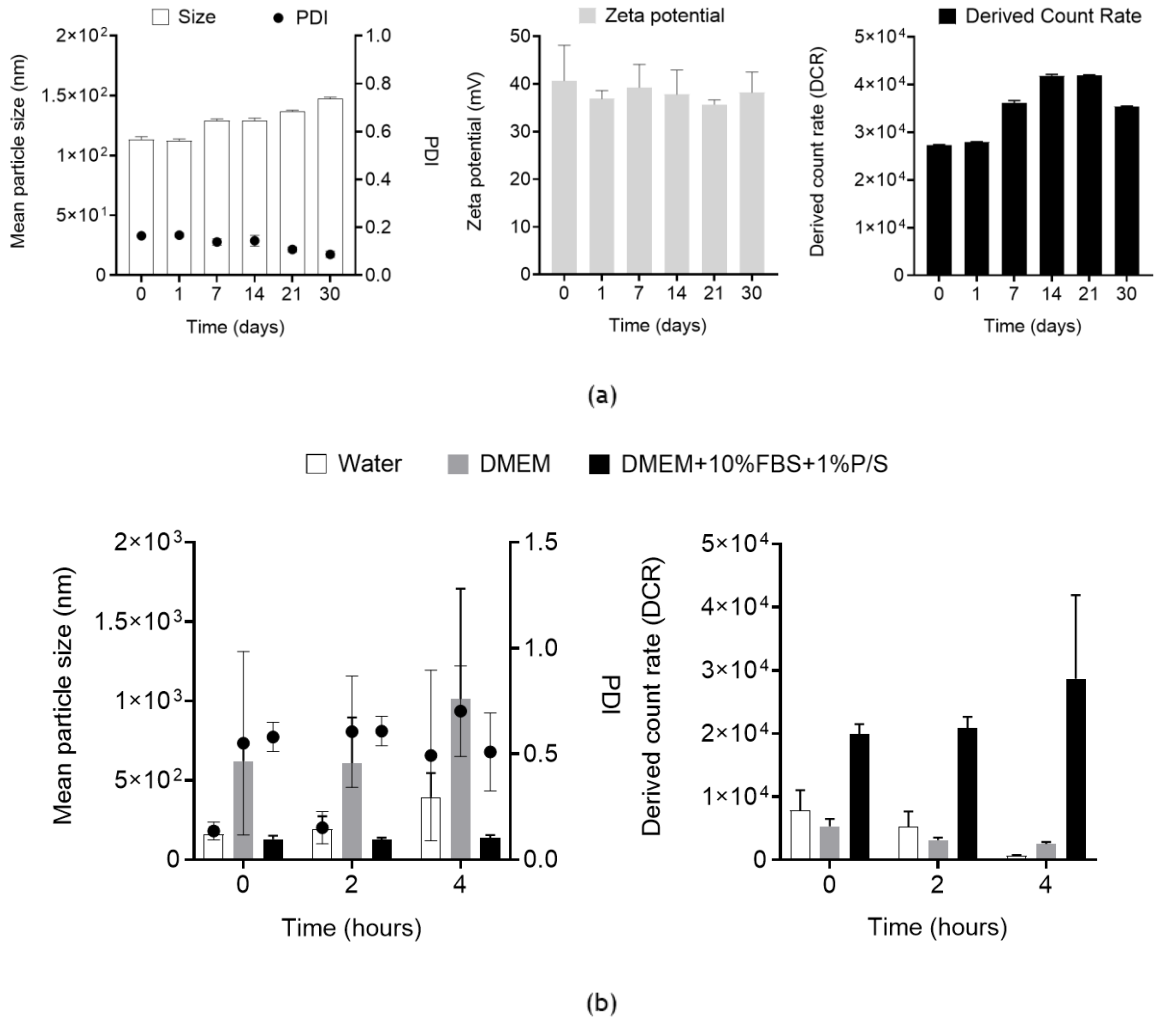

Figure 4. (**a**) Stability of aqueous suspensions of blank 4:1 (*w*/*w*) Pr:Dx NPs measuring the size, polydispersity index (PDI), zeta potential and derived count rate (DCR) at 4 ºC for 30 days (**b**) and their stability in supplemented and non-supplemented DMEM cell culture medium at time 0, 2 and 4 h at 37 ºC (Mean ± SD (n= 3)).

1.3.3. Toxicity assessment of protamine NPs in glioblastoma cells

The *in vitro* toxicity of NPs depends on their physicochemical properties. *In vitro* and *in vivo* studies have shown that when particle size is smaller, the cellular cytotoxicity tends to increase. In addition, the surface charge also plays an important role because an excess of positive makes NPs more cytotoxic [39]. In our case, we aimed to demonstrate the compatibility of Pr:Dx NPs in translationally-relevant cell lines; for that, cell viability was evaluated in a panel of primary cell lines derived from different tumor regions: the invasive margin (GIN-8

and GIN-28) and core of glioblastoma (GCE-28). These studies were based on the previous work carried out by Alexander et al. [40].

In general, blank Pr:Dx NPs showed low cytotoxicity on U87MG, GIN and GCE cell lines at 24 h and 48 h post-treatment (Figure 5.). In the case of U87MG cells, no apparent cytotoxicity was observed compared to the control. In primary glioblastoma cell lines, the results were more diverse: in GIN-8 and GIN-28, a reduction in cell viability was observed as NP-concentration increased, and in GCE-28 no significant cytotoxicity was observed under any of the conditions tested. This diversity in the results stresses the importance of applying clinically relevant models for toxicity screening as soon as possible.

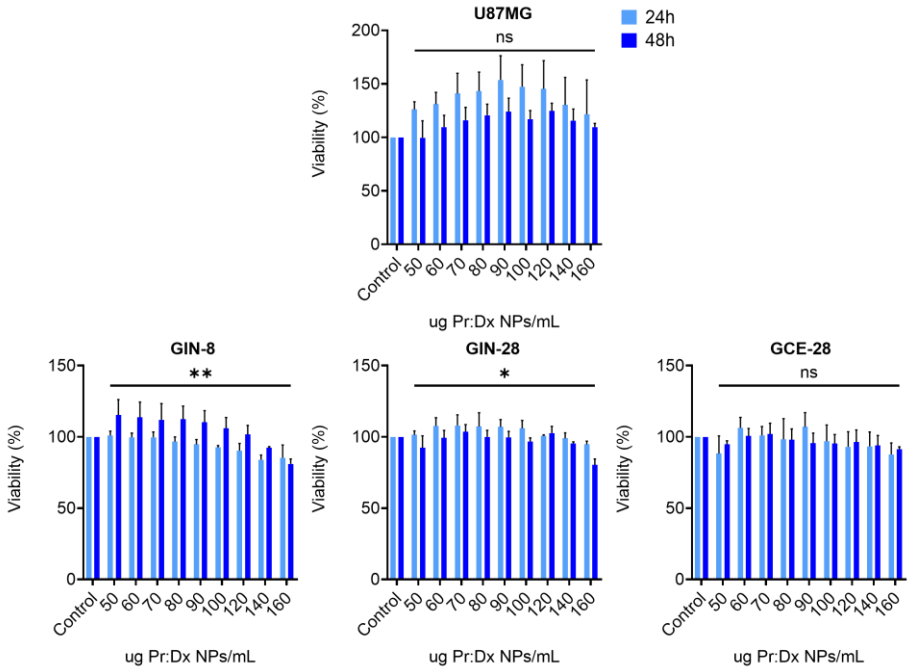

Figure 5. Cell viability assay after 24 h (light-blue bars) and 48 h (dark-blue bars) of the removal of increasing concentrations of blank 4:1 (*w*/*w*) Pr:Dx NPs from 50 to 160 µg/mL in U87MG cells and patient-derived glioblastoma cells (GIN-8, GIN-28, and GCE-28) (Mean ± SEM (n= 3)).

1.3.4. Intracellular uptake of protamine NPs in glioblastoma cells

To study the internalization of Pr:Dx NPs in glioblastoma cells, this peptide was fluorescently labelled with 5-TAMRA. The fluorophore is a succinimidyl ester that shows good reactivity and selectivity with primary and secondary aliphatic amines forming stable amides identical to natural peptide bonds [41]. Within the structure of protamine sulfate [42, 43], proline residues seem to be the most reactive for attacking this succinimidyl group [44]. After the reaction, an increase in protamine molecular weight was observed in the product reaction, because of the binding of tetramethylrhodamine.

The formulation of Pr:Dx NPs using 5-TAMRA-labelled protamine at 0.8 mg/mL of concentration was carried out using the same protocol described in section 1.2.2. The fluorescent NPs had similar physicochemical characteristics, without significant differences with the original formulation (Table 2.). Additionally, this study was also carried out with the NPs loaded with 8% (*w*/*w*) of a siRNA labelled with Cy5 (Cy5-modified siRNA) in order to also track the intracellular delivery of the associated therapeutic biomolecule (Table 2.).

Table 2. Mean particle size, polydispersity index (PDI) and zeta potential of blank 4:1 (*w*/*w*) Pr-TAMRA:Dx NPs and loaded with 8% (*w*/*w*) of Cy5-modified siRNA, respect to the total mass of the NPs (Mean ± SD (n=3)).

4:1 (*w*/*w*) Pr:Dx NPs	Size (nm)	PDI	Zeta Potential (mV)
5-TAMRA	131 ± 6	0.2	+29 ± 2
Cy5-modified siRNA	196 ± 23	0.1	+29 ± 1

After 4 h post-treatment with the fluorescent NPs, the internalization was analyzed by confocal microscopy, where the image of the maximum projection of U87MG, GIN and GCE cells showed the intracellular localization of Pr:Dx NPs (Figure 6. (a)). The image corresponding to the orthogonal section on X and Y axes further verified these findings. Moreover, this great internalization capacity of the NPs was also verified in images of the formulations loaded with the fluorescent nucleic acid (Figure 6. (b)). The efficient internalization of these NPs could be attributed to the penetration enhancing properties of protamine. In addition to its effectiveness in condensing the genetic material, this peptide can also cross cell membranes due to its arginine-rich sequence, achieving an effective delivery of proteins and genes inside the cells [45]. Previous studies found that six consecutive arginines in the protamine structure constitute a nuclear localization signal (NLS), which is why fluorescent NPs accumulated close to the cell nucleus [46, 47].

NP-uptake was also evaluated by flow cytometry. After 4 h of the treatment with fluorescently labelled-NPs, U87MG, GIN and GCE cells were treated with LIVE/DEAD™ Fixable Aqua Dead Cell Stain reagent to analyze the uptake in living cells. The flow cytometry histograms confirmed the internalization of Pr:Dx NPs in all the above glioblastoma cell lines (Figure 6. (c)). More specifically, the shift of the peak to the right side in the region marked as 5-TAMRA (+) indicated the higher expression of the marker compared to its control (unstained cells), which also indicated that almost 100% of the cells were positive for the presence of Pr:Dx NPs (Supporting Information: Table S1.). It should be noted that simultaneously there was a high cell viability indicated by the peak corresponding to the fluorescent signal of Aqua in the negative region (live region), which further confirms the low toxicity of the NPs as discussed in the previous section. In GIN and GCE cell lines, a series of images obtained by the ImageStreamer flow cytometer also indicated the presence of these fluorescent NPs inside the cells, in yellow color, compared to their corresponding controls (Supporting information: Figure S1. (b)).

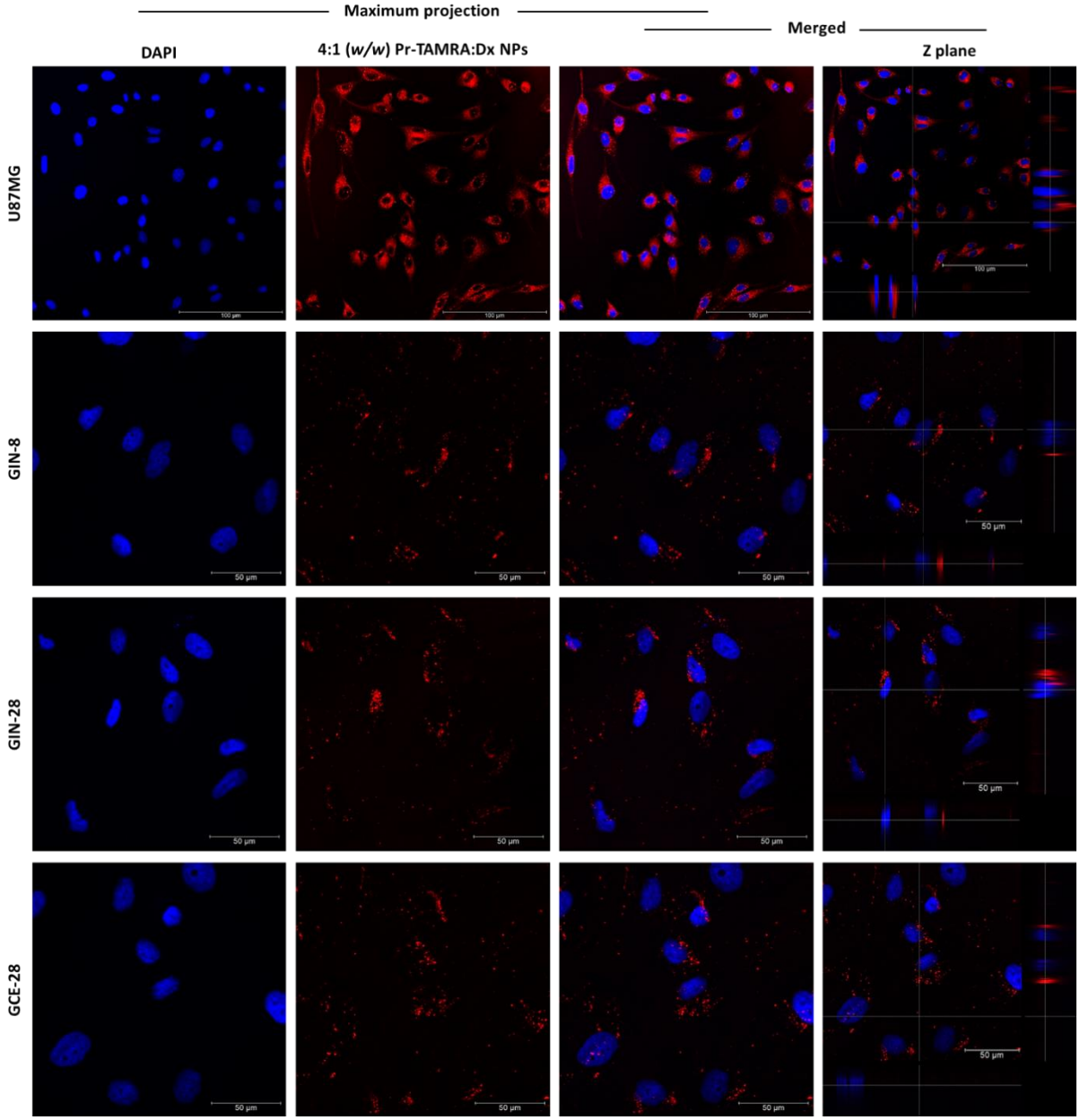

(a)

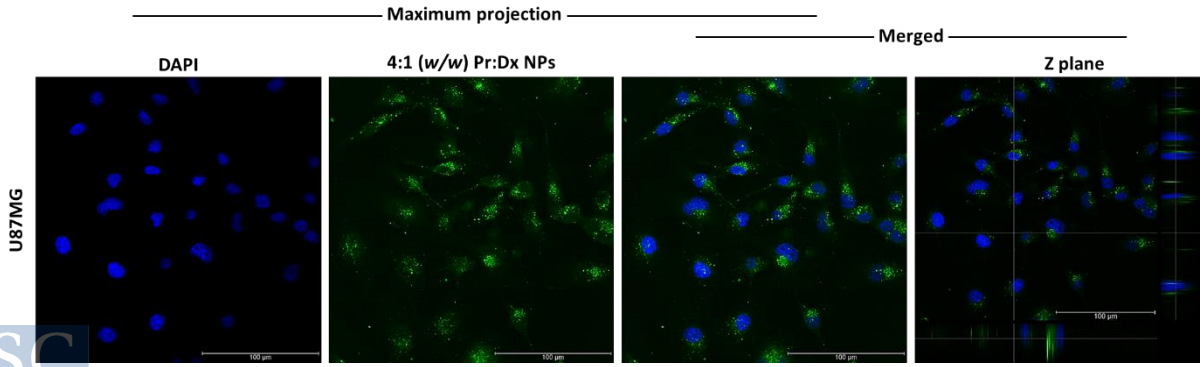

(b)

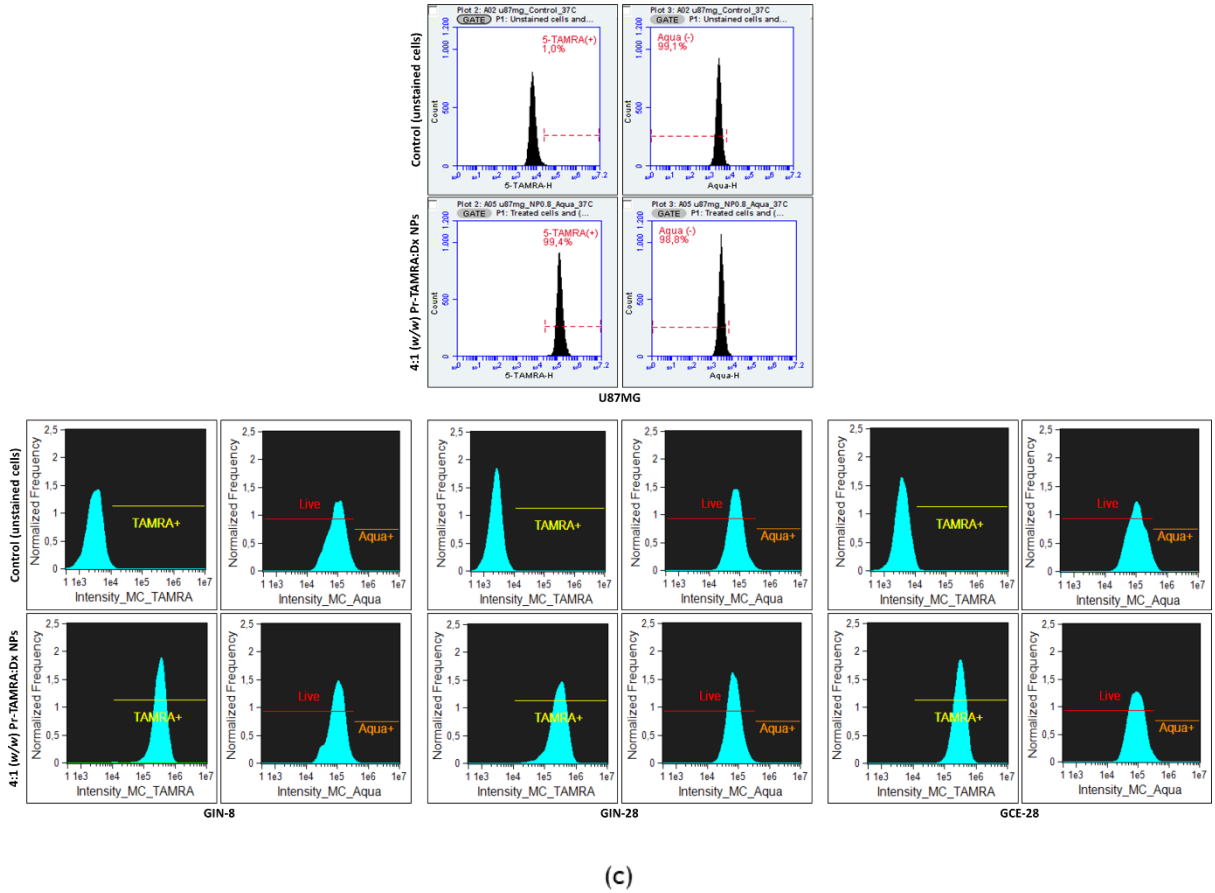

(c)

Figure 6. (**a**) Representative confocal microscopy images of NP-uptake in U87MG cells (magnification 63x, scale bar= 100 µm) and GIN-8, GIN-28, and GCE-28 (magnification 40x, scale bar= 50 µm) treated with 7 µg/cm^2 of fluorescently labelled NPs (red channel) and (**b**) treated with NPs loaded with 8% (*w*/*w*) of fluorescent Cy5-modified siRNA (green channel) incubated for 4 h at 37 ºC. Nuclei of the cells were stained with DAPI (blue channel). (**c**) Flow cytometry histograms to quantify the uptake of fluorescently Pr-TAMRA NPs (7 µg/cm^2) in U87MG, GIN-8, GIN-28, and GCE-28 after 4 h post-treatment (LIVE/DEAD™ Fixable Aqua Dead Cell Stain as a viability reagent).

1.3.5. Transfection capacity of protamine NPs in glioblastoma cells

The transfection capacity of Pr:Dx NPs was analyzed by evaluating the expression of EGFP and Luciferase at 24 h and 48 h post-treatment, in U87MG cells. EGFP expression was qualitatively analyzed by fluorescent microscopy. The images in Figure 7. (a) revealed that cells treated with naked plasmid did not show any detectable protein expression. This result was expected due to their excess negative charge limits cellular penetration, as well as, their enzymatic degradation. In the case of our NPs, the images showed a moderate expression of EGFP using 2.5 µg of pDNA.

Given these first results, the expression of Luciferase was analyzed and quantified by a Luciferase Reporter Gene commercial kit under the same conditions. This assay has higher sensitivity and a wide detection range, which is more convenient for the quantitative evaluation of gene transfection efficiency of these NPs [48]. The graphics in Figure 7. (b) showed that our NPs tended to give a better transfection after 48 h post-treatment, but lower compared with the commercial Lipofectamine® 2000.

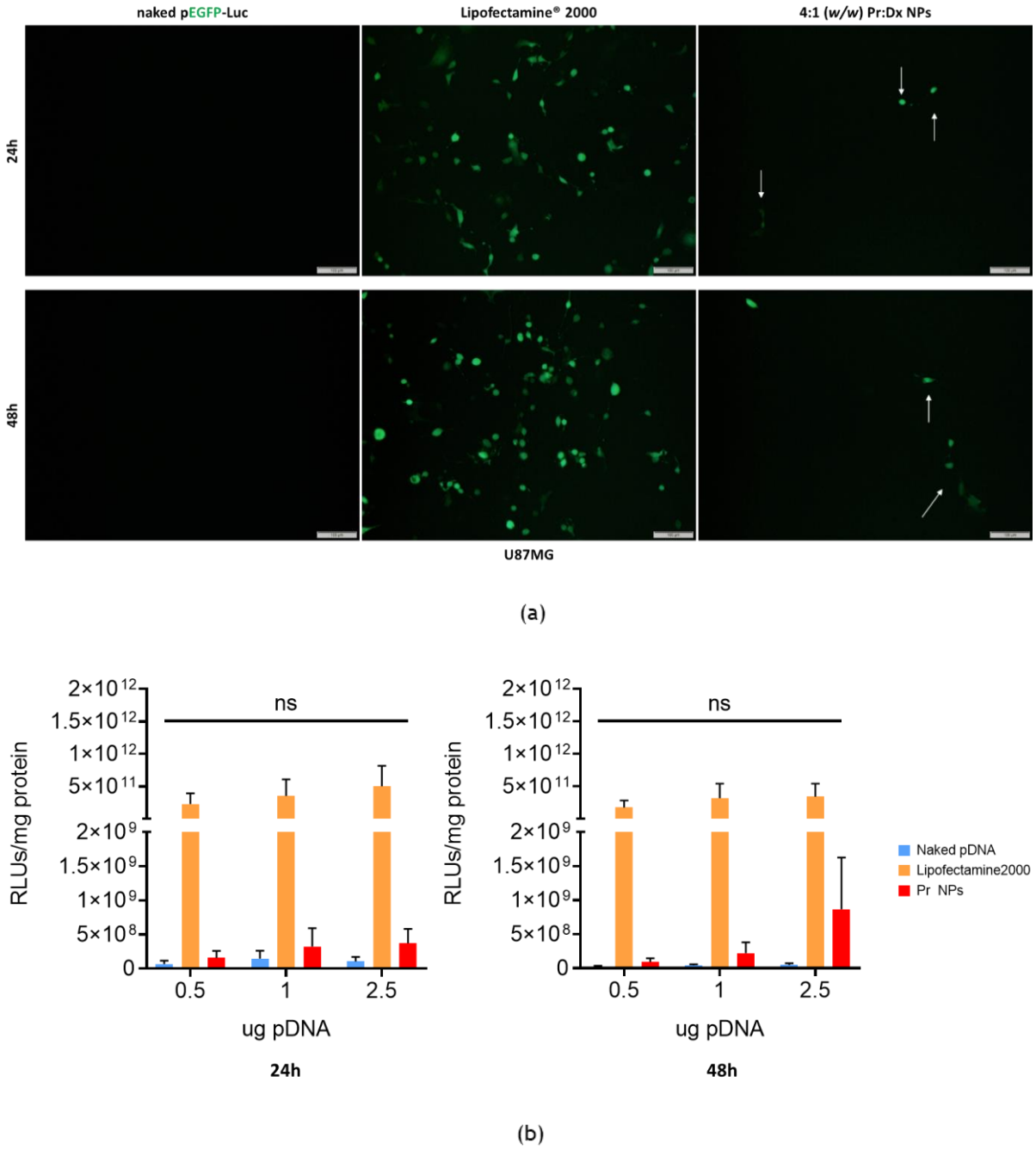

Figure 7. (**a**) Fluorescent microscopy images of EGFP expression (green channel) after 24 h and 48 h of the treatment of 4:1 (*w*/*w*) Pr:Dx NPs loaded with 8% (*w*/*w*) of pDNA at dose 2.5 µg of pDNA, incubated for 4 h at 37 ºC (scale bar= 100 µm). (**b**) Transfection efficiency of Luciferase protein expressed by RLUs/mg protein (Mean ± SEM (n= 3)).

Until now, promising results regarding the cytotoxicity and internalization of Pr:Dx NPs have been obtained. However, traditional cell culture models are unable to reproduce completely the properties of clinical tumors, as well as, their resistance to therapeutics [49]. Therefore, a step further was the evaluation of Pr:Dx NPs in 3D glioblastoma cell culture models.

1.3.6. Morphological characterization of glioblastoma tumor spheroids

The spheroids used in this study consisted of highly transformed U87MG cells (250 cells/spheroid), and patient-derived cells of GIN-8, GIN-28 and GCE-28 cell lines (2,000 cells/spheroid) previously used. The spheroids were cultured at standard conditions to obtain a size between 200-300 µm. The size is a critical parameter related to tumor biology and is determined by three factors: cell type, culture time and seeding density. In addition, tumor cells in the nucleus could be necrotic due to the hypoxic environment and lack of nutrients, creating an additional challenge for efficient gene delivery [50].

At day 4 after cell seeding, the U87MG spheroids reached the appropriate size and morphology, while the patient-derived cells formed the spheroids faster, being ready on day 2 (Figure 8. (a)). At this point, some differences between spheroid morphology could also be noticed. For example, GIN-28 and GCE-28 cells formed more compact spheroids than GIN-8 cell line. This could be explained by the fact that the first two cell lines were derived from the same patient, a 71-year-old male, and GIN-8 cells was from a 54-year-old woman [32]. Additionally, the SEM images showed the establishment of close interactions among the cells, forming extracellular matrices, and giving rise to the fully developed spheroid [51] (Figure 8. (b)). Porosity on the surface of the spheroid could be also observed (Figure 8. (b-2)), which was anticipated to be an advantage for Pr:Dx NPs entry.

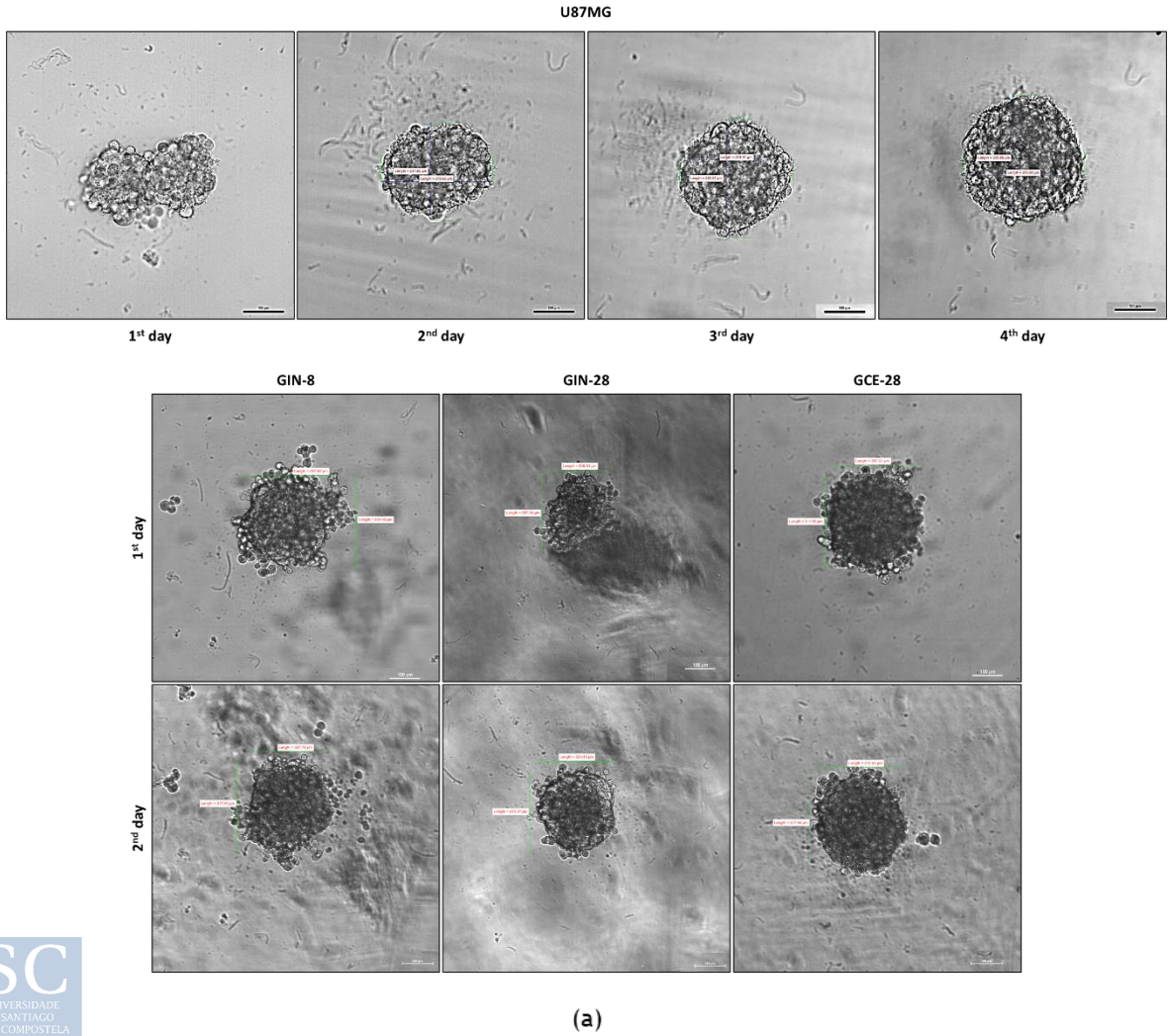

(a)

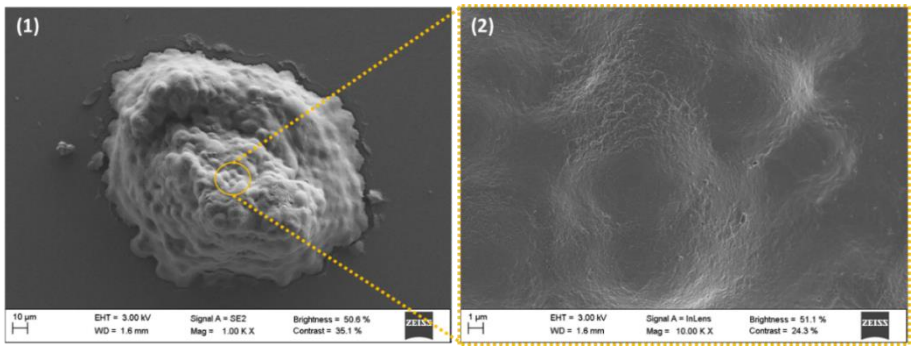

(b)

Figure 8. (**a**) Phase-contrast microscopy images of U87MG spheroid at day 1, 2, 3 and 4 (magnification 10x, scale bar= 100 µm) and GIN-8, GIN-28, and GCE-28 spheroids at day 1 and 2 (magnification 10x, scale bar= 100 µm) to get the size 250-300 µm, approximately. (**b**) SEM images of U87MG spheroid at day 4 of its formation: (**1**) the overall spherical morphology of compact spheroids, and (**2**) a closer look at the cell surface of U87MG spheroid.

1.3.7. Toxicity assessment of protamine NPs in glioblastoma spheroids

Glioblastoma spheroids were incubated with the controls and Pr:Dx NPs under the same conditions mentioned in 2D viability assays. The results shown in Figure 9. indicated low cytotoxicity at concentrations from 5 to 40 µg/mL in U87MG spheroids and from 5 to 80 µg/mL in GIN and GCE spheroids at 24 h and 48 h post-treatment. In U87MG spheroids, a slight viability increase was experienced over time, which could be due to a better recovery of the cells, and a more proliferative phenotype. Cell-cell and cell-extracellular environment interactions are responsible for cell differentiation, proliferation, viability, and other cellular functions, which in monolayer cell cultures would not be as well represented as in the 3D tumor mass [52].

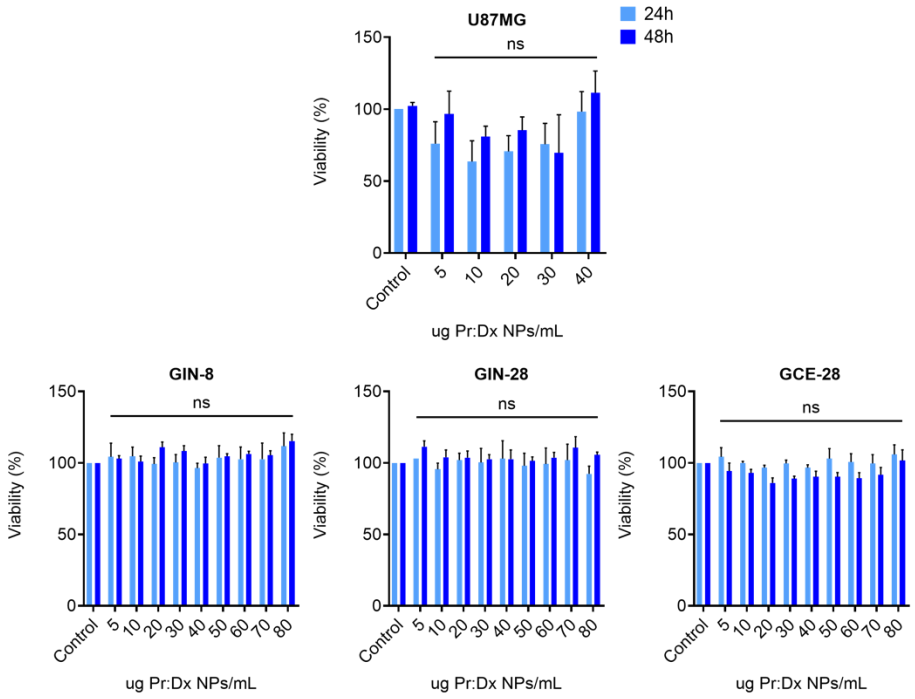

Figure 9. Cell viability assay after 24 h (light-blue bars) and 48 h (dark-blue bars) of the removal of increasing concentrations of blank 4:1 (*w*/*w*) Pr:Dx NPs from 5 to 40 µg/mL in U87MG spheroids, and from 5 to 80 µg/mL in patient-derived GIN-8, GIN-28, and GCE-28 spheroids (Mean ± SEM (n= 3)).

To perform a comprehensive viability study, the volume and morphology of the glioblastoma spheroids were also assessed. First, this parameter was qualitatively analyzed by phase contrast microscopy images (Figure 10. (a)). Apparently, negligible reduction of the volume of the spheroids was observed in all cases, as compared with the positive control (triton X-100), which caused a reduction in the spheroid size leading to its disintegration, indicating the sensitivity of the assay. In addition, the spheroids maintained their compact morphology after treatment, but cellular extensions could be seen in GIN-8 and GIN-28 spheroids, which were more pronounced with time and with higher NP-concentration. These cellular extensions could be considered as a defense mechanism against external agents, causing the loss of the spherical morphology. In addition, this cell dynamism is justified because both GIN cell lines come from the invasive region of the glioblastoma [32], which have a greater ability to migrate to other brain areas [53, 54].

Spheroid volume was further quantified from the images by measuring spheroid area. In general, the data confirmed that Pr:Dx NPs did not cause remarkable reduction in spheroid volume compared with the control (sterile filtered Milli-Q water), especially in GIN spheroids, where the spheroid volume remained constant (Figure 10. (b)). Indeed, GIN glioma cells have a more aggressive phenotype than GCE core cells, making them more resistant to therapy [53, 54]. In U87MG and GCE-28 spheroids, the volume decreased slightly at higher concentrations.

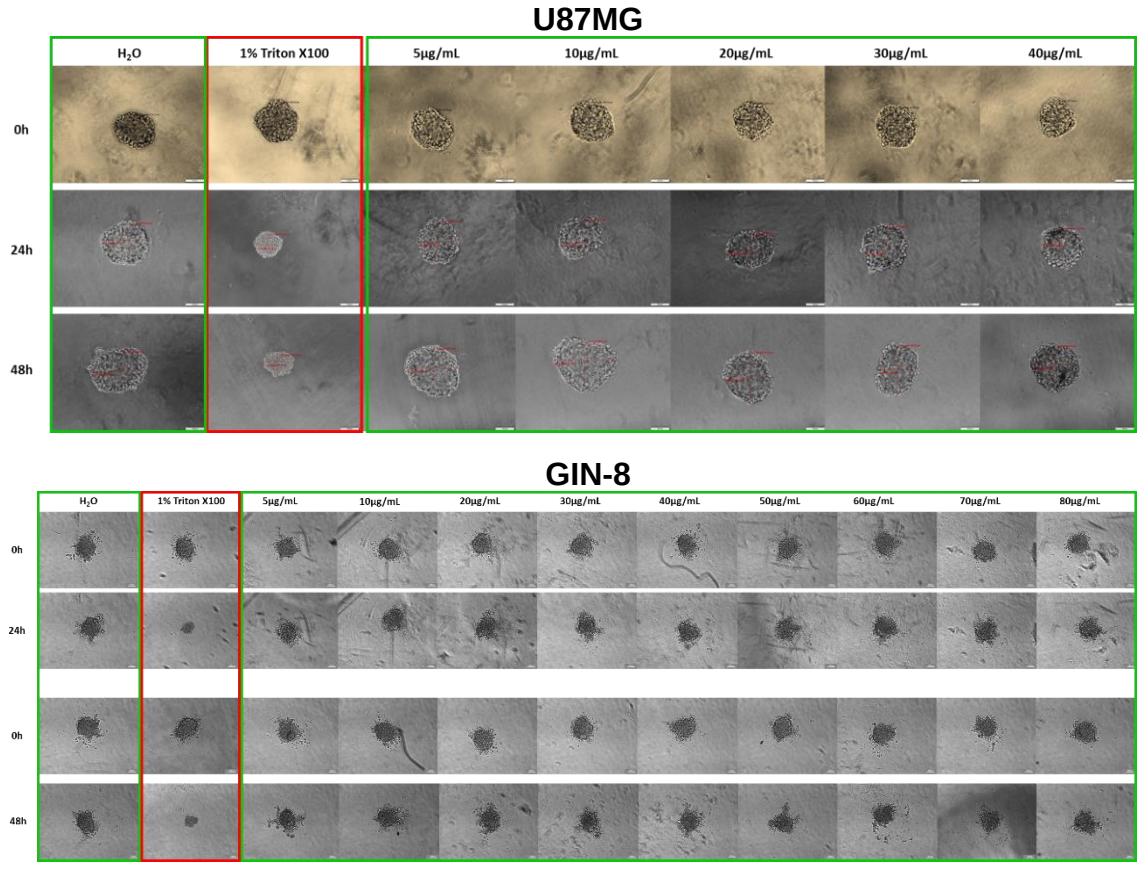

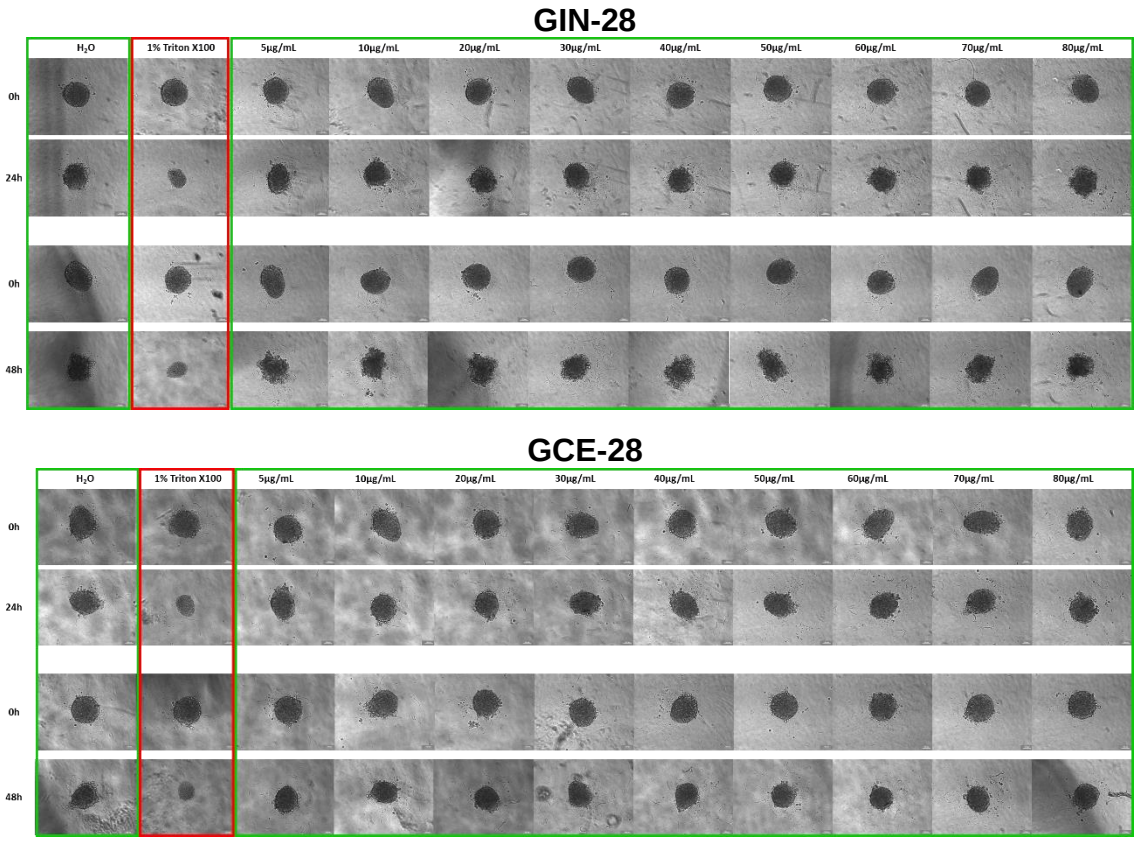

(a)

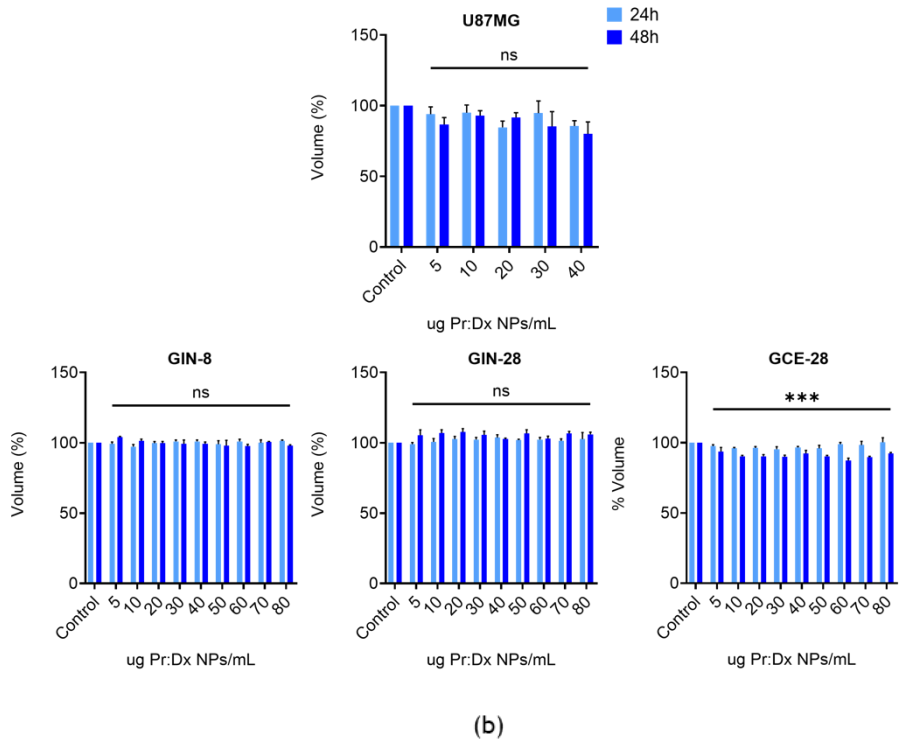

(b)

Figure 10. (**a**) Volume images and (**b**) quantification after 24 h and 48 h of the removal of increasing concentrations of blank 4:1 (*w*/*w*) Pr:Dx NPs in U87MG spheroids (from 5 to 40 µg/mL) and GIN-8, GIN-28, and GCE-28 spheroids (from 5 to 40 µg/mL) (Mean ± SEM (n= 3), scale bar= 100 µm, magnification 10x).

Another complementary viability assay was performed by analyzing the membrane integrity of cells in U87MG spheroids. For this purpose, the internalization of 7-AAD, a fluorescent apoptosis marker with strong affinity for DNA, was measured. In this assay, dead cells show red fluorescence, while living cells should not show any fluorescence signal. The results in Figure 11. (a, b) showed that spheroids treated with triton X-100 had an intense red fluorescence signal, verifying the damage done to U87MG cells. On the contrary, the lack of cytotoxicity of Pr:Dx NPs could be verified due to the absence of 7-AAD fluorescence under the experimental conditions tested.

As a conclusion, the results of these studies showed a high level of concordance and suggested a very low cytotoxicity for these NPs.

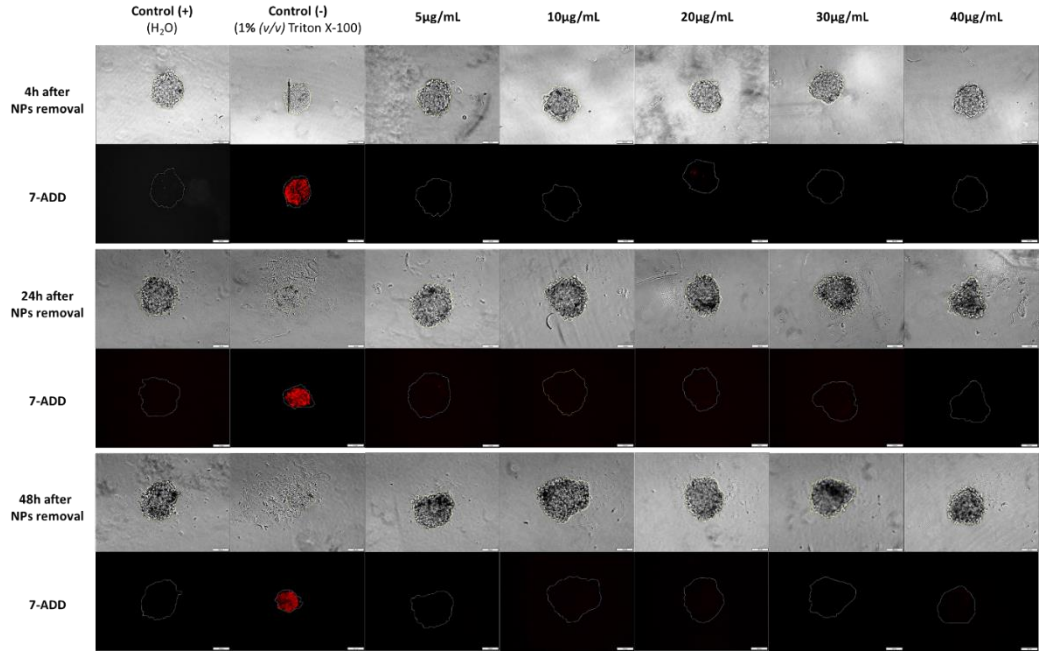

(a)

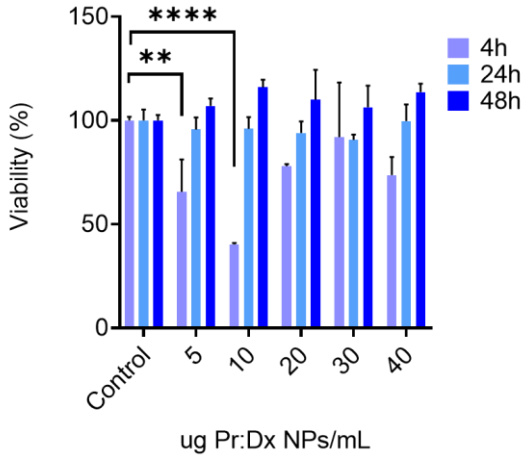

(b)

Figure 11. (**a**) 7-AAD membrane-integrity assay of U87MG spheroids after 4 h, 24 h and 48 h of the removal of different concentrations of blank 4:1 (*w*/*w*) Pr:Dx NPs analyzed by fluorescence microscopy and (**b**) quantified by fluorimetry (Mean ± SD (n= 3), scale bar= 100 µm).

1.3.8. Intracellular uptake of protamine NPs in glioblastoma spheroids

The study of the NP-uptake was also carried out in U87MG, GIN-8, GIN-28, and GCE-28 spheroids, using the same fluorescent formulation used for the 2D assays (Table 2.).

The maximum projection and the orthogonal sections of the confocal microscopy images showed the intracellular localization of Pr:Dx NPs (Figure 12. (a)). Additionally, the internalization of these NPs loaded with fluorescently-labelled siRNA was also studied, showing a greater internalization than in 2D (Figure 12. (b)).

Some differences between the spheroids composed by commercial vs patient-derived glioblastoma cells were appreciated. In U87MG spheroids, a higher intensity of fluorescence was distributed homogeneously throughout the spheroids, suggesting better internalization of the NPs in this cell line. SEM images showed how these Pr:Dx NPs were embedded by the U87MG spheroid (Figure 12. (c)). Even though all spheroids had a similar size, GIN and GCE cells were larger than commercial ones, which resulted in slightly larger spheroids, affecting the internalization of the NPs and their transport to their core. As shown by Hsu et al., NP-transport to the core can be limited for large spheroids [50]. The studies carried out with light sheet microscopy of the patient-derived GIN and GCE spheroids allowed to appreciate bright white spots indicating the presence of intense accumulations of fluorescent NPs in the proximity of the spheroid surface (Figure 12. (d)).

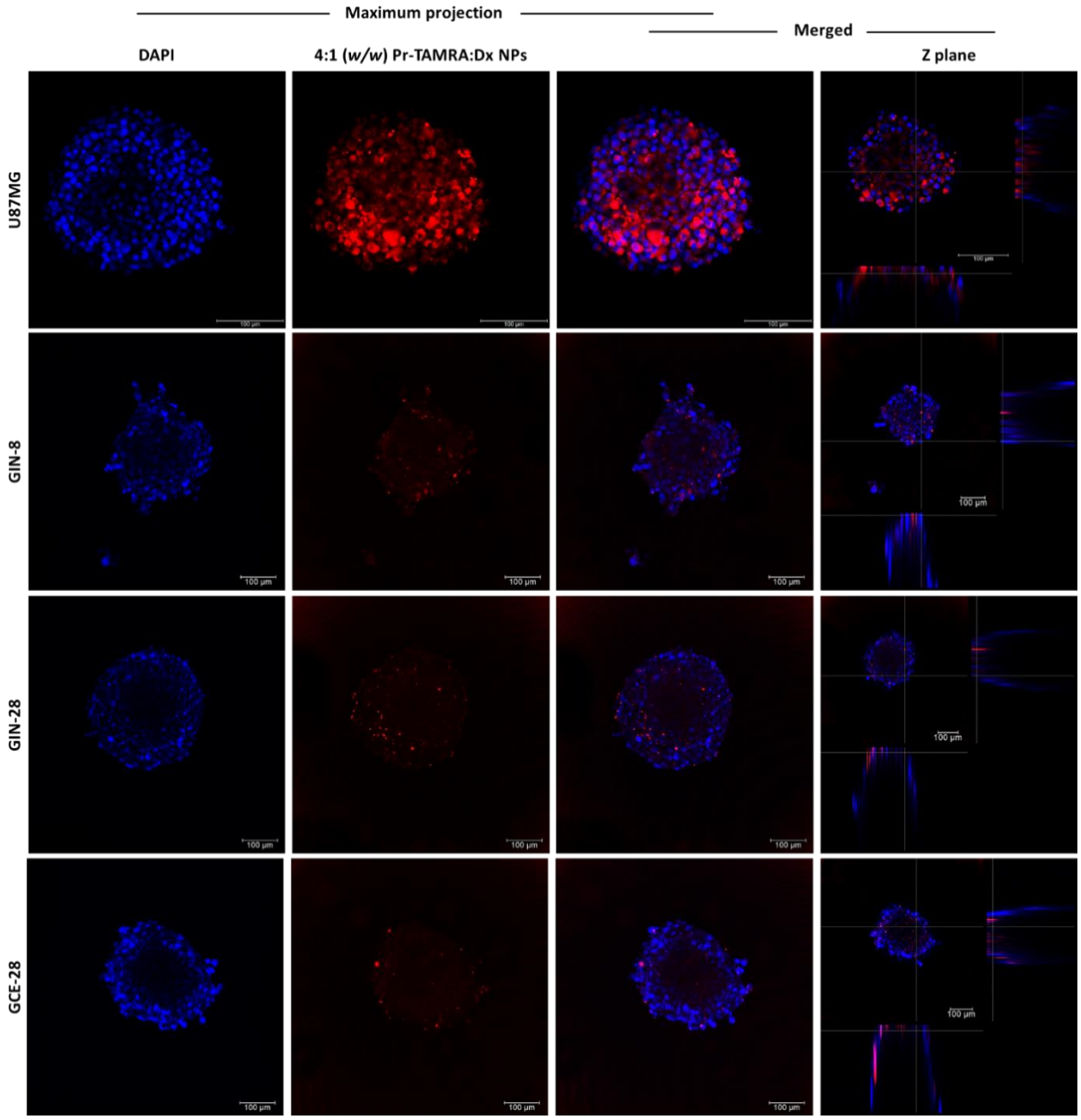

(a)

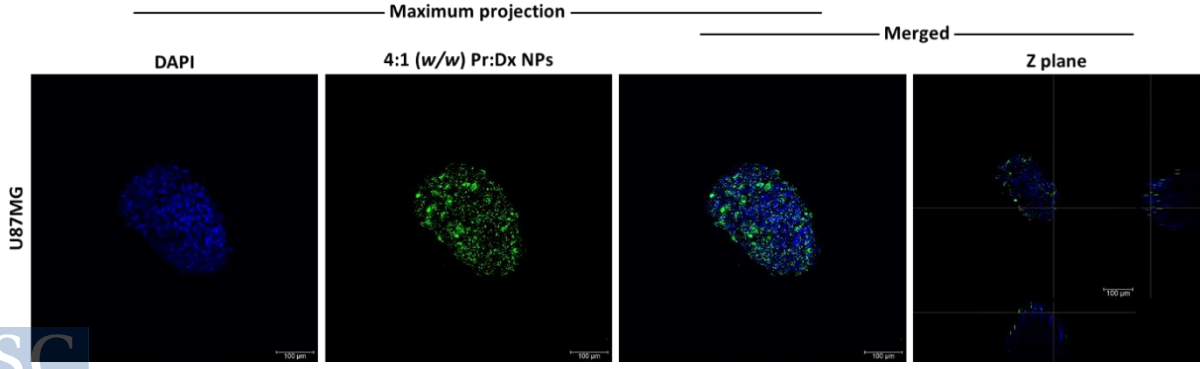

(b)

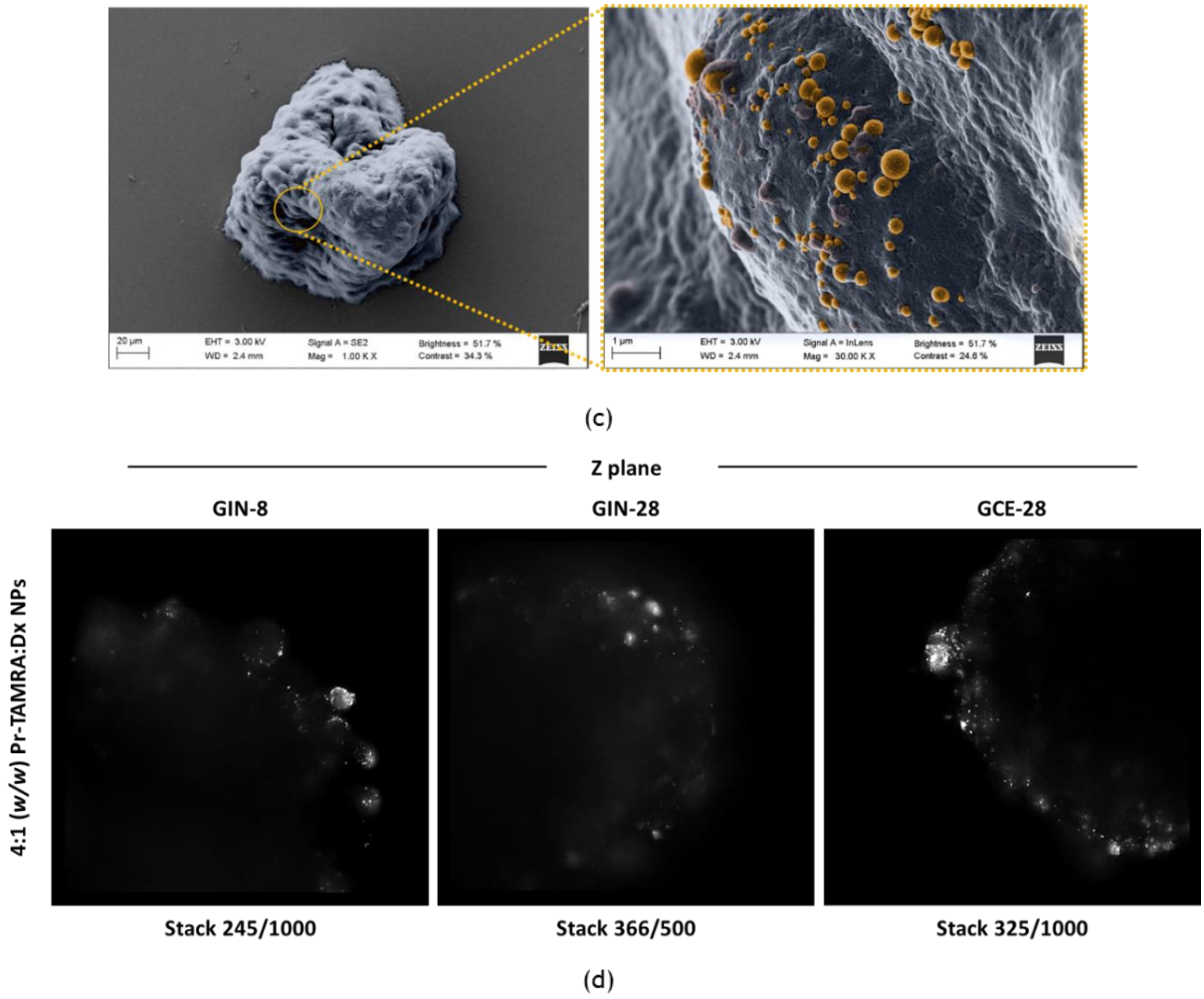

Figure 12. (**a**) Representative confocal microscopy images of NP-uptake in U87MG (magnification 20x, z2), GIN-8, GIN-28, and GCE-28 spheroids (magnification 10x, z1.50) treated with 7 μg/cm^2 of fluorescently labelled NPs (red channel) incubated for 4 h at 37 ºC (scale bar= 100 μm). (**b**) Representative confocal microscopy images of NP-uptake in U87MG spheroid (magnification 20x, z2) treated with 7 μg/cm^2 of NPs loaded with 8% (*w*/*w*) of fluorescent Cy5-modified siRNA (green channel) incubated for 4 h at 37 ºC. Nuclei of the cells were stained with DAPI (blue channel) (scale bar= 100 μm). (**c**) SEM images of U87MG spheroid with blank 4:1 (*w*/*w*) Pr:Dx NPs (colored in orange) on the surface of the spheroid (scale bar= 1 and 20 μm). (**d**) Light sheet fluorescence microscopy images (OptoRheo) of GIN-8, GIN-28, and GCE-28 spheroids (magnification 60x) treated with fluorescently labelled NPs (bright white spots) under the same conditions.

As in the 2D uptake, this parameter was also quantified by flow cytometry under the same conditions, by disaggregating the spheroids to measure single fluorescent events. As expected, the histograms in Figure 13. confirmed the NP-uptake in all the four glioblastoma spheroids models, indicating that 99.9% of cells forming the U87MG spheroid were positive for the presence of these NPs. In GIN and GCE spheroids, the values were slightly lower, where 62.9% of cells were positive in GIN-8, 58.8% of cells were positive in GIN-28 and 55.6% of cells were positive in GCE-28 (Supporting information: Table S2.). These values confirmed the conclusions from the confocal images. In addition to this, a series of flow cytometry images showed the presence of these fluorescent NPs inside the cells forming the spheroids (yellow color) compared to the images of the corresponding controls (Supporting information: Figure S2. (b)). Simultaneously, a high cell viability was maintained during these studies, as indicated by the peak corresponding to the fluorescent signal of Aqua (live region).

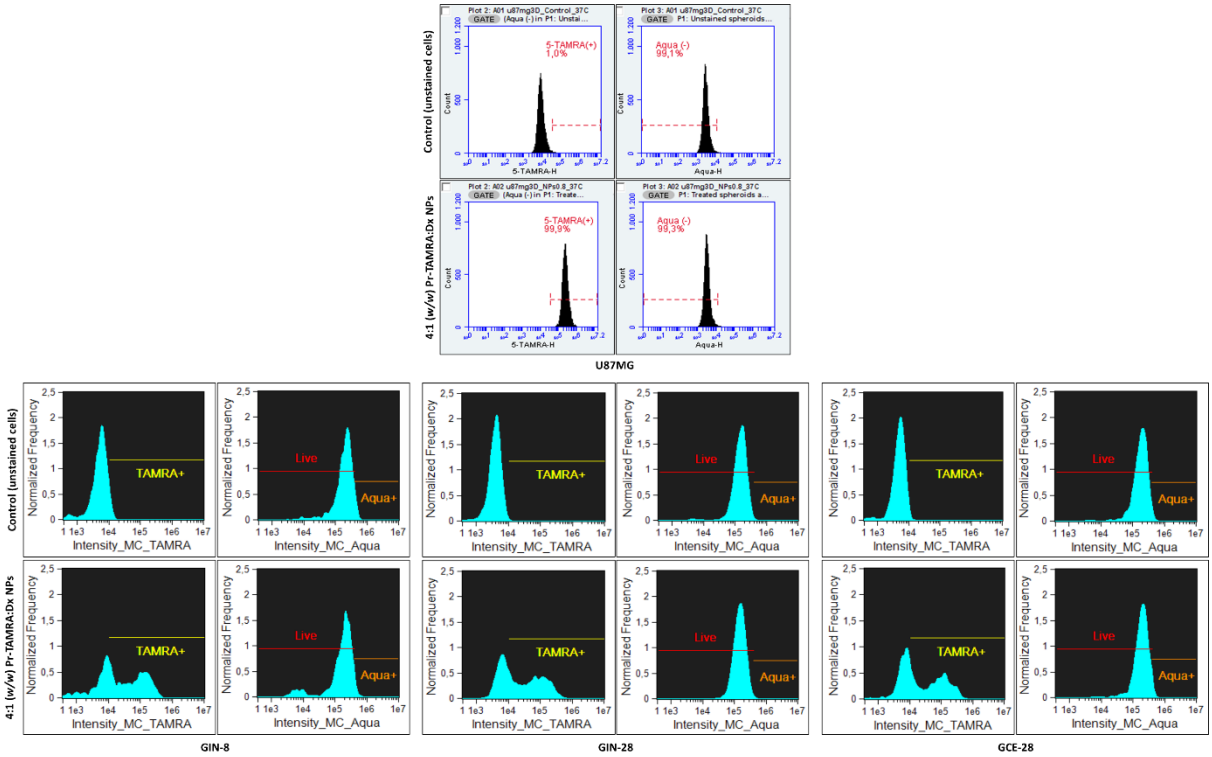

Figure 13. Flow cytometry histograms to quantify the uptake of fluorescently Pr-TAMRA NPs (7 µg/cm^2) in U87MG, GIN-8, GIN-28, and GCE-28 spheroids after 4 h post-treatment (LIVE/DEAD™ Fixable Aqua Dead Cell Stain as a viability reagent).

1.3.9. Transfection of protamine NPs into glioblastoma spheroids

The transfection capacity of the Pr:Dx NPs was also studied in U87MG spheroids, analyzing the EGFP expression by fluorescence microscopy under the same conditions used in 2D. The fluorescence images showed similar results: the naked plasmid was unable to transfect cells forming the spheroids, while those treated with Lipofectamine® 2000 showed high transfection, and treated with Pr:Dx NPs showed better transfection capacity at 24 h post-treatment at doses of 2.5 µg of pDNA (Figure 14. (a)). Studies have shown that the Green Fluorescence Protein (GFP) expression can deteriorate over time because GFP labelled cells are prone to cell death, so it could be considered as a possible reason for not observing any fluorescence signal at 48 h [55]. However, to verify this issue, the transfection capacity of the NPs was also analyzed using LSFM selecting the amount of 2.5 µg of pDNA (Figure 14. (b)). As expected, a higher intensity fluorescence signal was obtained after 24 h, and a lower signal was observed after 48 h. Compared to conventional fluorescence microscopy, LSFM is a non-destructive method that produces well-registered fluorescence signals that are suitable for 3D reconstruction of samples. In addition, this microscope offers a much higher resolution due to the fact that during the excitation process, it minimizes the bleaching of fluorophores and the phototoxic effects [56].

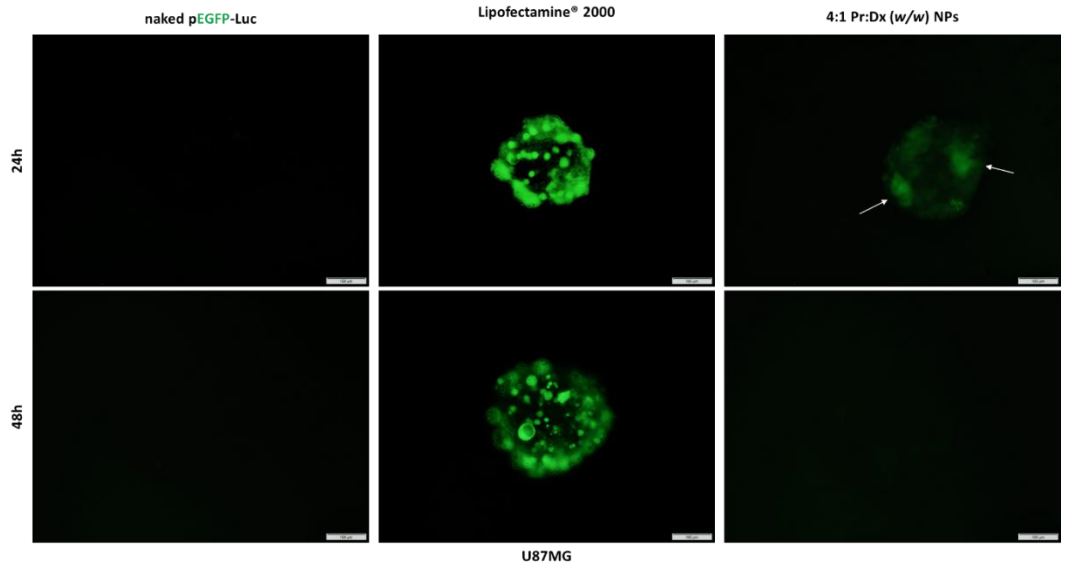

(a)

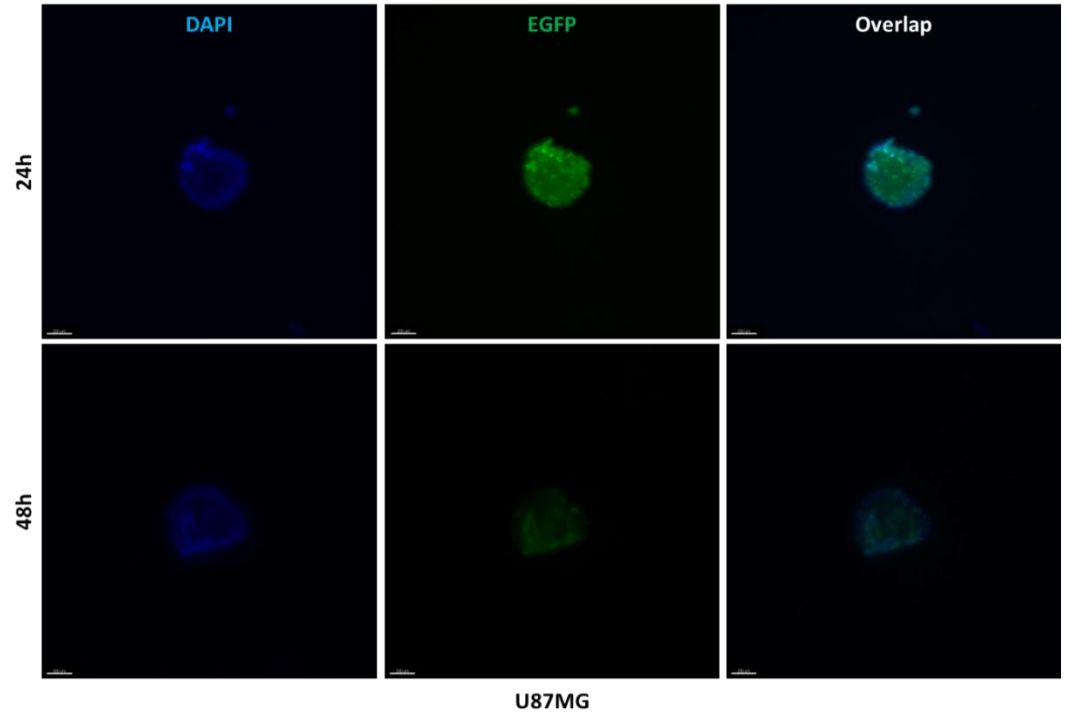

(b)

Figure 14. (**a**) Fluorescent and (**b**) light sheet fluorescence microscopy images of EGFP expression (green channel) in U87MG spheroids after 24 h and 48 h of the treatment of NPs loaded with 8% (*w*/*w*) of pDNA at dose 2.5 μg of pDNA/well, incubated for 4 h at 37 ºC (scale bar= 100 μm).

1.4. CONCLUSIONS

The combination of protamine with anionic dextran sulfate could yield matrix-structured NPs that presented characteristics useful as gene delivery nanosystems. This formulation presented several attractive features: (i) highly flexible and tunable physicochemical characteristics, (ii) effective association of different nucleic acids and (iii) stability in different biorelevant media under different conditions. In addition, these NPs showed low cytotoxicity and highly efficient internalization in 2D and 3D culture models of patient-derived cells. Further studies are needed for the optimization of their transfection capacity as a next step toward their preclinical development. Overall, these results highlight the potential interest that these nanocarriers may have for gene delivery in the treatment of glioblastoma.

REFERENCES

[1] M. Sajjad, S. Khan, K. Muhammad, W. Wu, A. Ulluah, S.W. Baik, Multi-grade brain tumor classification using deep CNN with extensive data augmentation, J. Comput. Sci. 30 (2019) 174-182. https://doi.org/10.1016/j.jocs.2018.12.003.

[2] D. Michaud, T. Batchelor, Risk factors for primary brain tumors, UpToDate (2013). http://www.uptodate.com/online/content/topic.do.

[3] H.H. Sultan, N.M. Salem, W. Al-Atabany, Multi-classification of brain tumor images using deep neural network, IEEE Access, 7 (2019) 69215-69225. https://doi.org/10.1109/ACCESS.2019.2919122.

[4] Q.T. Ostrom, M.A. Fahmideh, D.J. Cote, I.S. Muskens, Risk factors for childhood and adult primary brain tumors, Neuro-Oncol. 21 (2019) 1357-1375. https://doi.org/10.1093/neuonc/noz123.

[5] J. Gould, Breaking down the epidemiology of brain cancer, Nature 561 (2018) 40-41. https://doi.org/10.1038/d41586-018-06704-7.

[6] J. Wang, F. Shen, Y. Yao, K. Wang, Y. zhu, J. Hu, Adoptive Cell therapy: a novel and potential immunotherapy for glioblastoma, Front. Oncol. 31 (2020) 1-13. https://doi.org/10.3389/fonc.2020.00059.

[7] J. A. Hossain, M.A. Latif, L.A.R. Ystaas, S. Nainzima, K. Riecken, A. Muller, F. Azuje, J.V. Joseph, K. M. Talasila, J. Ghimire, B. Fehse, R. Bjerkivg, H. Miletic, Long-term treatment with valacyclovir improves lentiviral suicide gene therapy of glioblastoma, Neuro-Oncol. 21 (2019) 890-900. https://doi.org/10.1093/neuonc/noz060

[8] E.L. Rhun, M. Preusser, P. Roth, D.A. Reardon, M. van der Bent, P. Wen, G. Reifenberger, M. Weller, Molecular targeted therapy of glioblastoma, Caner Treat. Rev. 80 (2019) 1-13. https://doi.org/10.1016/j.ctrv.2019.101896.

[9] M. Touat, A. Idbaih, M. Sanson, K.L. Ligon, Glioblastoma targeted therapy: updated approaches form recent biological insights, Ann. Ocol. 28 (2017) 1457-1472. https://doi.org/10.1093/annonc/mdx106.

[10] B. Weenink, P.J. French, P.S. Smitt, R. Debets, M. Geurts, Immunotherapy in glioblastoma: current shortcomings and future perspectives, Cancers 12 (2020) 1-20. https://doi.org/10.3390/cancers12030751.

[11] L. Jena, E. McErlean, H. McCarthy, Delivery across the blood-brain barrier: nanomedicine for glioblastoma multiforme, Drug Deliv. and Transl. Res. 10 (2019) 304-318. https://doi.org/10.1007/s13346-019-00679-2.

[12] X. Tang, S. Zhang, R. Fu, L. Zhang, K. Huang, H. Peng, L. Dai, Q. Chen, Therapeutic prospects of mRNA-based gene therapy for glioblastoma, Front. Oncol. 9 (2019) 1-10. https://doi.org/10.3389/fonc.2019.01208.

[13] B. Caffery, J.S. Lee, A.A. Alexander-Bryant, Vectors for glioblastoma gene therapy: viral and non-viral delivery strategies, J. Nanomater. 9 (2019) 1-16. https://doi.org/10.3390/nano9010105.

[14] R. Rai, S. Alwani, I. Badea, Polymeric nanoparticles in gene therapy: new avenues of design and optimization for delivery applications, Polymers 11 (2019) 1-35. https://doi.org/10.3390/polym11040745.

[15] A. Zerrouqi, O. Rixe, A.M. Ghoumari, S.V. Yarovoi, R. Mouawad, D. Khayat, C. Soubrane. Liposomal delivery of the herpes simplex virus thymidine kinase gene in glioma: improvement of cells sensitization to ganciclovir, Cancer Gene Ther. 3 (1196) 385-392. PMID: 8988841.

[16] K. Dixit, P. Kumthekar, Gene delivery in neuro-oncology, Curr. Oncol. Rep. 19 (2017) 1-11. https://doi.org/10.1007/s11912-017-0628-z.

[17] M. Norouzi, Gold nanoparticles in glioma theranostics, Pharmacol. Res. Commun. 156 (2020) 1-17. https://doi.org/10.1016/j.phrs.2020.104753.

[18] R. di Santo, L. Digiacomo, S. Palchetti, V. Palmieri, G. Perini, D. Pozzi, M. Papi, G. Caracciolo, Microfluidic manufacturing of surface-functionalized graphene oxide nanoflakes for gene delivery, Nanoscale 11 (2019) 2733-2741. https://doi.org/10.1039/C8NR09245A.

[19] A. di Martino, O.A. Guselnikova, M.E. Trusova, P.S. Postnikov, V. Sedlarik, Organic-Inorganic hybrid nanoparticles-controlled delivery system for anticancer drugs, Int. J. Pharm. 526 (2017) 380-390. https://doi.org/10.1016/j.ijpharm.2017.04.061.

[20] N. Singh, A. Joshi, A.P. Toor, G. Verma, Chapter27-Drug delivery: advancements and challenges, MNT, (2017) 865-886. https://doi.org/10.1016/B978-0-323-46143-6.00027-0.

[21] K.L. Kozielski, A. Ruiz-Valls, S.Y. Tzeng, H. Guerrero-Cázares, Y. Ruin, Y. Li, H.J. Vaughan, M. Gionet-Gonzalez, C. Vantucci, J. Kim, P. Schiapparelli, R. Al-Kharboosh, A. Quiñones-Hinojosa, J.J. Green, Cancer-selective nanoparticles for combinatorial siRNA delivery to primary human GBM *in vitro* and *in vivo*, Biomaterials 209 (2019) 79-87. https://doi.org/10.1016/j.biomaterials.2019.04.020.

[22] M. Garcia-Fuentes, Chapter 10-Gene therapy for the treatment of chronic wounds, WOL (2020) 210-234. https://doi.org/10.1002/9781119433316.ch10.

[23] E. Memari, A. Maghsoudi, F. Yazdian, M. Yousefi, M. Mohammadi, Synthesis of PHB-co-PEI nanoparticles as gene carriers for mir-128-encoding plasmid delivery to U87 glioblastoma cells, Colloids and Sur, A Physicochem. Eng. Asp. 599 (2020) 1-9. https://doi.org/10.1016/j.colsurfa.2020.124898.

[24] Z. Zeng, C.H. Tung, Y. Zu, Aptamer-equipped protamine nanomedicine for precision lymphoma therapy, Cancers 12 (2020) 1-28. https://doi.org/10.3390/cancers12040780.

[25] S. Reimondez-Troitiño, J.V González-Aramundiz, J. Ruiz-Bañobre, R. López-López, M.J. Alonso, N. Csaba, M. de la Fuente, Versatile protamine nanocapsules to restore miR-145 levels and interfere tumor growth in colorectal cancer cells, Eur. J. Pharm. Biopharm. 142 (2019) 449-459. https://doi.org/10.1016/j.ejpb.2019.07.016.

[26] L.N. Thwala, D.P. Delgado, K. Leone, I. Marigo, F. Benetti, M. Chenlo, C.V. Alvarez, S. Tovar, C. Dieguez, N. S. Csaba, M.J. Alonso, Protamine nanocapsules as carriers for

oral peptide delivery, JCR 291 (2018) 157-168. https://doi.org/10.1016/j.jconrel.2018.10.022.

[27] W. Chen, Q. Feng, G. Zhang, Q. Yang, C. Zhang, F. Xu, The flotation separation of scheelite from calcite and fluorite using dextran sulfate sodium as depressant, Int. J. Miner. Process. 169 (2017) 53-59. https://doi.org/10.1016/j.minpro.2017.10.005.

[28] F. Wang, J. Li, X. Tang, K. Huang, L. Chen, Polyelectrolyte three-layer nanoparticles of chitosan/dextran sulfate/chitosan for dual drug delivery, Colloids Surf. B: Biointerfaces 190 (2020) 1-7. https://doi.org/10.1016/j.colsurfb.2020.110925.

[29] A.S. Nunes, A.S. Barros, E.C. Costa, A.F. Moreira, I.J. Correia, 3D tumor spheroids as in vitro models to mimic in vivo human solid tumors resistance to therapeutic drugs, Biotechnol. Bioeng. 116 (2018) 206-226. https://doi.org/10.1002/bit.26845.

[30] S. Melissaridou, E. Wiechec, M. Magan, M.V. Jain, M.K. Chung, L. Farnebo, K. Roberg, The effect of 2D and 3D cell cultures on treatment response, EMT profile and stem cell features in head and neck cancer, Cancer Cell Int. 19 (2019) 1-10. https://doi.org/10.1186/s12935-019-0733-1.

[31] J.V. González-Aramundiz, M.P. Olmedo, A. González-Fernández, M.J. Alonso, N.S. Csaba, Protamine-based nanoparticles as new antigen delivery system, Eur. J. Pharm. Biopharm. 97 (2015) 51-59. https://doi.org/10.1016/j.ejpb.2015.09.019.

[32] S.J. Smith, M. Diksin, S. Chhya, S. Sairam, M.A. Estevez-Cebrero, R. Rahman, The invasive region of glioblastoma defined by 5ALA guided surgery has an altered cancer stem cell marker profile compared to central tumor, Int. J. Mol. Sci. 18 (2017) 1-13. https://doi.org/10.3390/ijms18112452.

[33] T. Mendonca, K. Lis-Slimank, A.B. Matheson, M.G. Smith, A.B. Anane-Adjei, R. Cavanagh, L. Paterson, P.A. Dalgarno, C. Alexander, M. Tassieri, C.L.R. Merry, A.J. Wright, OptoRheo: simultaneous *in situ* micro-mechanical sensing and 3D imaging of live cells cultures, bioRxiv-the preprint server for biology (2022) 1-37. https://doi.org/10.1101/2022.04.21.489042

[34] T. Mendonca, A.B. Matheson, K. Lis-Slimak, A. Anane-Adjei, C. Alexander, C.L.R. Merry, L. Paterson, M. Tassieri, P. Dalgarno, A.J. Wright, Non-invasive micromechanical sensing and real time 3D imaging of in vitro biological systems, Proc. 11798 (2021). https://doi.org/10.1117/12.2595357.

[35] N. Csaba, M. Köping-Höggard, M.J. Alonso, Ionically crosslinked chitosan/triphosphate nanoparticles for oligonucleotide and plasmid DNA delivery, Int. J. Pharm. 382 (2009) 205-214. https://doi.org/10.1016/j.ijpharm.2009.07.028.

[36] S. Reimondez-Troitiño, Design and development of protamine based nanosystems for application in cancer and eye diseases, Doctoral Thesis, Dialnet (2017).

[37] S.M. Bromfield, E. Wilde, D.K. Smith, Heparin sensing and binding-taking supramolecular chemistry towards clinical applications, Chem. Soc. Rev. 42 (2013) 9184-9195. https://doi.org/10.1039/C3CS60278H.

[38] J. Zaloga, C. Janko, R. Agarwal, J. Nowak, R. Müller, A.R. Boccaccini, G. Lee, S. Odenbach, S. Lyer, C. Alexiou, Different storage conditions influence biocompatibility

and physicochemical properties of iron oxide nanoparticles, Int. J. Mol. Sci. 16 (2015) 9368-9384. https://doi.org/10.3390/ijms16059368.

[39] G. Badran, L. Angrand, J.D. Masson, G. Crépeaux, M.O. David, Physico-chemical properties of aluminum adjuvants in vaccines: implications for toxicological evaluation, Vaccine 40 (2022) 4881-4888. https://doi.org/10.1016/j.vaccine.2022.06.064.

[40] C.E. Vasey, R.J. Cavanagh, V. Taresco, C. Moloney, S. Smith, R. Rahman, C. Alexander, Polymer pro-drug nanoparticles for sustained release of cytotoxic drugs evaluated in patient-derived glioblastoma cell lines and in situ gelling formulations, Pharmaceutics 13 (2021) 1-17. https://doi.org/10.3390/pharmaceutics13020208.

[41] S. Kalkhof, A. Sinz, Chances, and pitfalls of chemical cross-linking with amine-reactive N-hydroxysuccinimide esters, Anal. Bioanal. Chem. 392 (2008) 305-312. https://doi.org/10.1007/s00216-008-2231-5.

[42] F.L. Sorgi, S. Bhattacharya, L. Huang, Protamine sulfate enhaces lipid-mediated gene transfer, Gene Ther. 4 (1997) 961-968. https://doi.org/10.1038/sj.gt.3300484.

[43] N.T. Jarzebska, M. Mellet, J. Frei, T.M. Künding, S. Pascolo, Protamine-based strategies for RNA transfection, Pharmaceutics 13 (2021) 1-14. https://doi.org/10.3390/pharmaceutics13060877.

[44] F. Reunolds, R. Weissleder, L. Josephson, Protamine as an Efficient membrane-translocating peptide, Bioconjugate Chem. 16 (2005) 1240-1245. https://doi.org/10.1021/bc0501451.

[45] R.S.H. Koralege, K. Sahoo, N. Flynn, J. Liu, A. Ranjan, C. Pope, J.D. Ramsey, Erythrocytes internalize nanoparticles functionalized with low molecular weight protamine, J. Nanopart. Res. 23 (2021) 1-16. https://doi.org/10.1007/s11051-021-05202-8.

[46] E. Vighi, M. Montanari, B. Ruozi, G. Tosi, A. Magli, E. Leo, Nuclear localization of cationic solid lipid nanoparticles containing protamine as transfection promoter, Eur. J. Pharm. Biopharm. 76 (2010) 384-393. https://doi.org/10.1016/j.ejpb.2010.07.012.

[47] D. Delgado, A. del Pozo-Rodríguez, M.A. Solinís, A. Rofríguez-Gascón, Understanding the mechanism of protamine in solid lipid nanoparticle-based lipofection: the importance of the entry pathway, Eur. J. Pharm, Biopharm. 79 (2011) 495-502. https://doi.org/10.1016/j.ejpb.2011.06.005.

[48] J. Song, D. Wang, J. Wang, Q. Shen, C. Xie, W. Lu, R. Wang, M. Liu, Low molecular weight polyethyleneimine modified by 2-aminoimidazole achieving excellent gene transfection efficiency, Eur. Polym. J. 140 (2020) 1-11. https://doi.org/10.1016/j.eurpolymj.2020.110017.

[49] M.A. Grimaudo, A. Herreros-Pomares, M. Alonso, S. Calabuig-Fariás, E. Jantus-Lewintre, M. de la Fuente, Chapter 3-Biofabrication of 3D tumor models in cancer research, Mater. Today (2020) 67-90. https://doi.org/10.1016/B978-0-12-818128-7.00003-4.

[50] W.H. Hsu, P. Sánchez-Gómez, E. Gomez-Ibarlucea, D.P. Ivanov, T. Rahman, An.M. Grabowska, N. Csaba, C. Alexander, M. Garcia-Fuentes, Structure-optimized

interpolymer polyphosphazene complexes for effective gene delivery against glioblastoma, Adv. Ther. 2 (2018) 1-15. https://doi.org/10.1002/adtp.201800126.

[51] K. Al-Husaini, E. Elkamel, X. Han, P. Chen, Therapeutic potential of a cell penetrating peptide (CPP, NP1) mediated siRNA delivery: evidence in 3D spheroids of colon cancer cells, Can. J. Chem. Eng. 98 (2020) 1240-1254. https://doi.org/10.1002/cjce.23743.

[52] M. Kapatczynska, T. Kolenda, W. Przybyla, M. Zajaczkowska, A. Teresiak, V. Filas, M. Ibbs, R. Blizzniak, L. Luczewski, K. Lamperska, 2D and 3D cell cultures – a comparison of different types of cancer cell cultures, Arch. Med. Sci. 14 (2018) 910-919. https://doi.org/10.5114/aoms.2016.63743.

[53] J.R. Molina, Y. Hayashi, C. Stephens, M.M. Georgescu, Invasive glioblastoma cells acquire stemness and increased Akt activation, Neoplasia 12 (2010) 453-463. https://doi.org/10.1593/neo.10126.

[54] N. Pandey, P. Anastasiadis, C.P. Carney, P.P. Kanvinde, G.F. Woodworth, J.A. Winkles, A.J. Kim, Nanotherapeutic treatment of the invasive glioblastoma tumor microenvironment, Adv. Drug Deliv. Rev. 188 (2022) 1-23. https://doi.org/10.1016/j.addr.2022.114415.

[55] A.M. Ansari, A.K. Ahmed, A.E. Masangos, F. Lay, L.J. Born, G. Marti, J.W. Harmon, Z. Sun, Cellular GFP toxicity and immunogenicity: potential confounders in in vivo cell tracking experiments, Stem Cell Rev. and Rep. 12 (2016) 553-559. https://doi.org/10.1007/s12015-016-9670-8.

[56] E.H.K. Stelzer, Light sheet fluorescence microscopy for quantitative biology, Nat. Methods 12 (2015) 23-26. https://doi.org/10.1038/nmeth.3219.

SUPPORTING INFORMATION

Table S1. Number of total positive events of control and glioblastoma cells (U87MG, GIN-8, GIN-28, and GCE-28) treated with blank 4:1 (*w*/*w*) Pr-TAMRA:Dx NPs expressing by percentage and measuring their Mean Fluorescence Intensity (MFI).

Cell line	Total (+) 5-TAMRA events		% (+) 5-TAMRA events		MFI (+) 5-TAMRA events	
	Control	Sample	Control	Sample	Control	Sample
U87MG	73	7915	1	99.4	41,725	154,580
GIN-8	10	1205	0.31	99.8	12,489	334,308
GIN-28	1	3227	0.02	100	14,561	291,450
GCE-28	24	2297	0.66	99.7	16,142	305,253

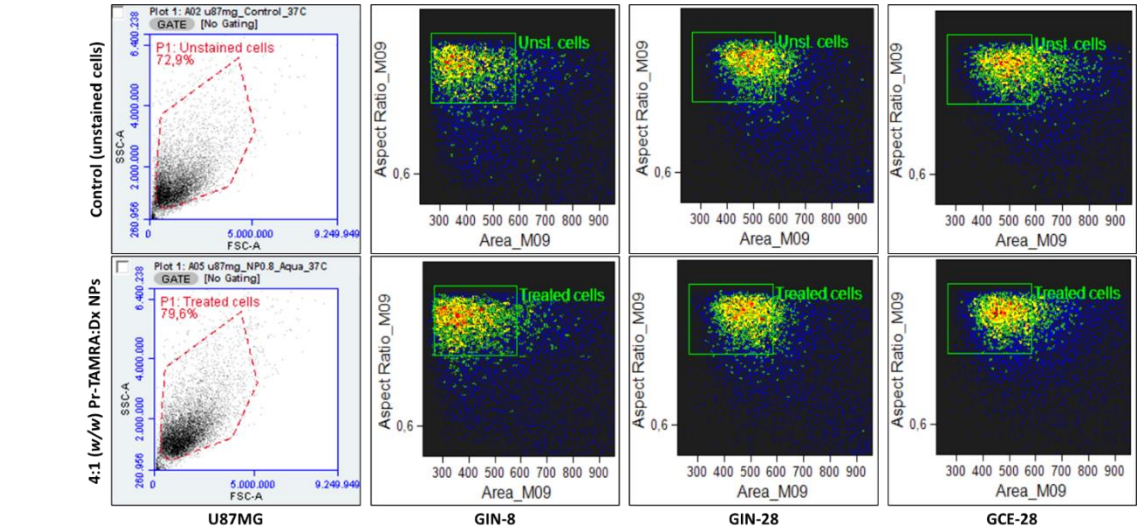

(a)

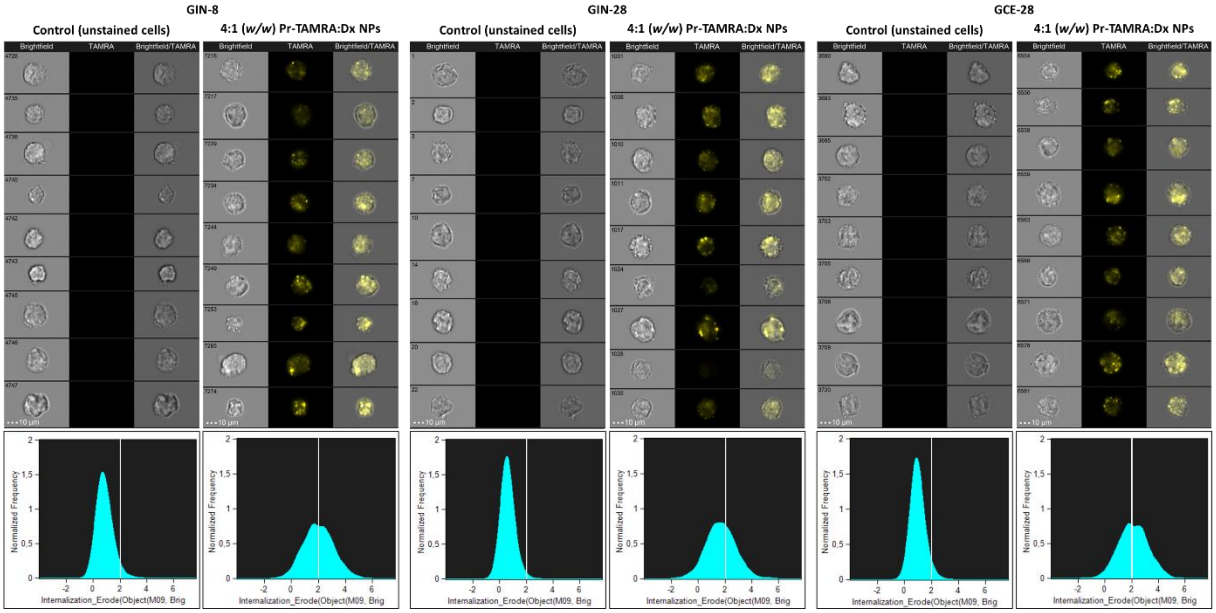

(b)

Figure S1. (**a**) Flow cytometry histograms of the total events without debris of control and glioblastoma cells (U87MG, GIN-8, GIN-28, and GCE-28) treated with blank 4:1 (*w*/*w*) Pr:Dx NPs to analyze the NP-uptake. (**b**) Flow cytometry images of positive 5-TAMRA events of control (grey) and glioblastoma cells treated with fluorescent NPs (yellow) and their corresponding internalization histogram (values ≥ 2 indicated NP-internalization).

Table S2. Number of total positive events of control and glioblastoma spheroids (U87MG, GIN-8, GIN-28, and GCE-28) treated with blank 4:1 (*w*/*w*) Pr-TAMRA:Dx NPs expressing by percentage and measuring their Mean Fluorescence Intensity (MFI).

Cell line	Total (+) 5-TAMRA events		% (+) 5-TAMRA events		MFI (+) 5-TAMRA events	
	Control	Sample	Control	Sample	Control	Sample
U87MG	74	7666	1	99.9	58,904	289,726
GIN-8	43	457	4.7	62.9	11,454	72,790
GIN-28	3	1613	0.09	58.8	10,771	66,842
GCE-28	12	744	0.75	55.6	11,269	76,936

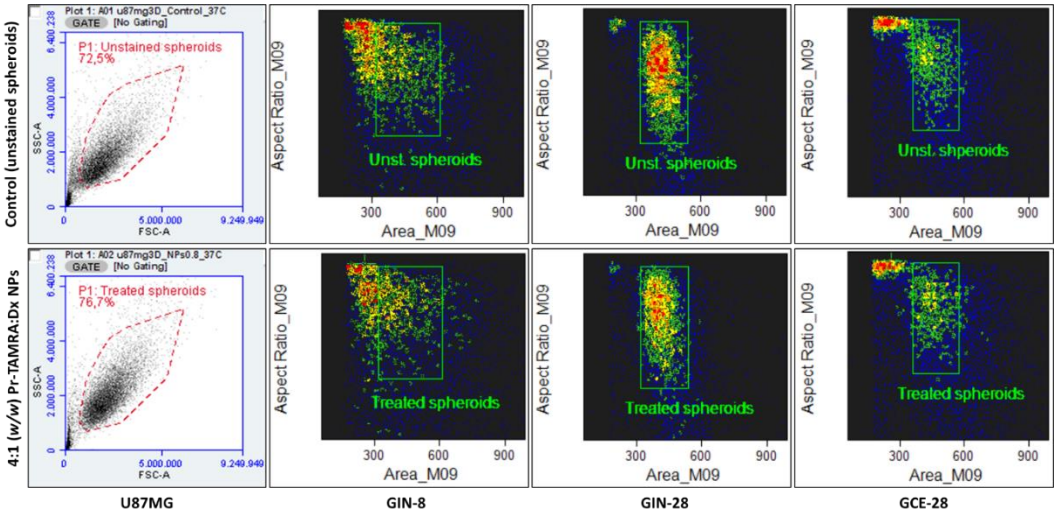

(a)

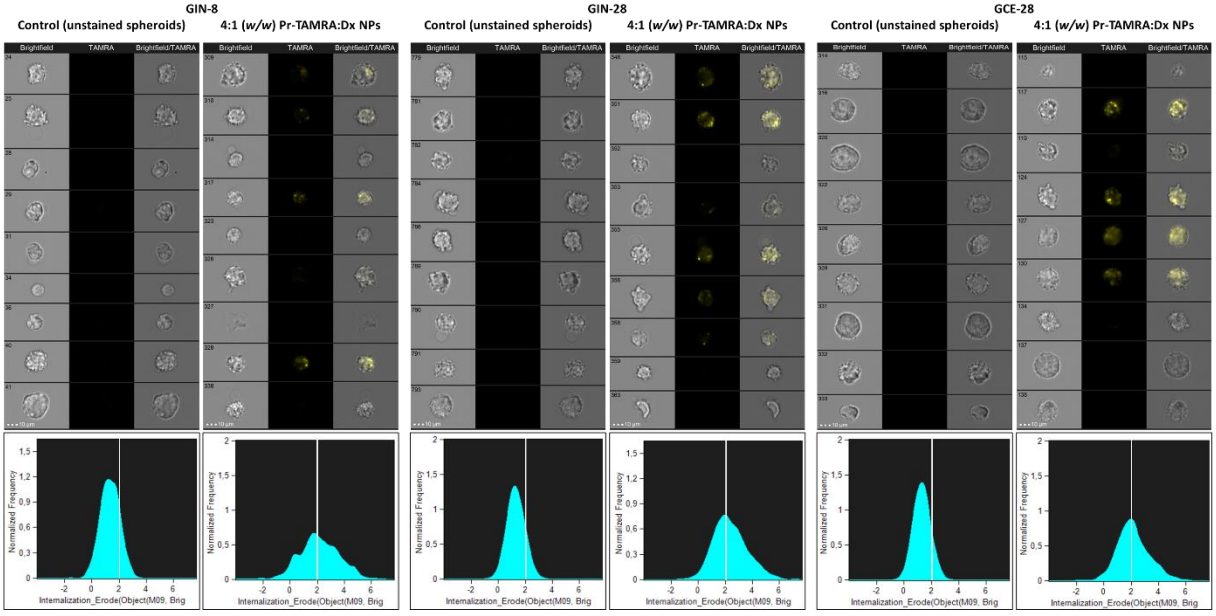

(b)

Figure S2. (**a**) Flow cytometry histograms of the total events without debris of control and glioblastoma spheroids (U87MG, GIN-8, GIN-28, and GCE-28) treated with blank 4:1 (*w*/*w*) Pr:Dx NPs to analyze the NP-uptake. (**b**) Flow cytometry images of positive 5-TAMRA events of control (grey) and glioblastoma spheroids treated with fluorescent NPs (yellow) and their corresponding internalization histogram (values ≥ 2 indicated NP-internalization).

CHAPTER II

Polymeric nanocomplexes combined with polyphosphazenes as gene delivery systems for the treatment of glioblastoma

Polymeric nanocomplexes combined with polyphosphazenes as gene delivery systems for the treatment of glioblastoma

ABSTRACT

New polymeric compositions are still needed to improve gene delivery to tumors. Previous studies showed that specifically engineered polyphosphazenes (PPZ) could have effective transfection/toxicity ratios when used as gene nanocarriers. Among them, 6MHA-PPZ polyphosphazene is a promising anionic material that, when added to cationic nanocomplexes, can improve its delivery characteristics. This has recently been demonstrated *in vitro*, using a highly transformed glioblastoma cell line (U87MG) in a traditional monolayer culture. In order to gain further insight on the potential and mechanism of action of this biomaterial, the objective of the present work has been to analyze the effect of cationic nanocomplexes of polyethylenimine (PEI) and protamine (Pr) in combination with the 6MHA-PPZ polyphosphazene in advanced preclinical models *in vitro* as spheroids and *in vivo* as zebrafish embryos. The nanocomplexes without 6MHA-PPZ were used as reference. Regarding the physicochemical characterization, the addition of this polyphosphazene did not cause significant modifications in terms of particle size and surface charge, although the yield was significantly increased in the Pr-based nanocomplexes. Stability studies at 4 ºC and colloidal stability in cell culture medium showed that the formulations maintained their properties constant for one month, and in short periods up to 4 h, respectively. However, the nanocomplexes experienced aggregation in conventional zebrafish culture media at 96 h, while in dechlorinated sterile tap water, their colloidal stability was not affected. In general, it is known that nanocomplexes composed with PEI tend to be more cytotoxic, while those formed by protamine present a lower transfection efficiency. Regarding cytotoxicity, the addition of the anionic 6MHA-PPZ showed a reduction especially in PEI nanocomplexes with similar results in 2D and 3D culture models formed by a panel of patient-derived glioblastoma cells. Regarding gene transfer, the presence of 6MHA-PPZ significantly improved transfection efficiency especially of Pr nanocomplexes, in 2D culture models and in commercial glioblastoma spheroids, almost reaching the levels induced by PEI. However, it is important to point out the disparity of these results in primary 3D glioblastoma models, concluding that the sensitivity of the nanocomplexes will depend on the preclinical model. Finally, biodistribution studies in zebrafish embryos at 48 hours post-fecundation showed an accumulation of these formulations in their yolk sac, especially for PEI nanocomplexes. A small proportion of these particles diffused to the head area at 5-day post injection. The addition of 6MHA-PPZ improved the fluorescence signal of PEI nanocomplexes confirming the capacity of this polymer to enhance the endosomal escape of cationic peptides. In conclusion, the addition of the anionic 6MHA-PPZ polyphosphazene to cationic nanocomplexes could improve their efficiency making them promising carriers for glioblastoma gene therapy.

2.1. INTRODUCTION

Nucleic acid therapies offer attractive possibilities for the precise modulation of genes involved in the progression of brain tumors such as glioblastoma [1, 2]. The delivery of polynucleotides to specific cells requires the development of vectors capable of targeting specific tissues, protecting them from degradation by nucleases, and having low immunogenicity [3]. Viral vectors became the first choice due to their high transfection efficiency, but their complex production and potential safety problems made non-viral vectors more relevant over the years. These non-viral carriers have multitransgenic capacity, lower immunogenicity, and they are easier to modulate [1] [4]. Polymeric nanoparticles (NPs) presenting positive surface charge can condense DNA molecules, and promote their cellular internalization, including an enhanced endosomal escape [5]. However, polymeric gene carriers remain inherently inefficient with respect to several design criteria, including biocompatibility and biodegradability, adequate selective biodistribution and pharmacokinetics, ability to cross extracellular and intracellular barriers [4] [6]. Because of this, there is an active search for new materials and architectures to improve nanocarrier performance.

Polyphosphazenes, a family of polymers based on a nitrogen-phosphorus skeleton, are increasingly important in biomedical applications. The first poly(organo)phosphazenes were synthesized by Harry R. Allcock in 1976, but it was Hennink's group who synthesized the first cationic polyphosphazene for gene delivery [7]. Since then, hundreds of new PPZ have been explored by varying the backbone side groups [8], including a few derivatives used in gene delivery such as amino acid esters [9-12], peptides [10] [13, 14], saccharides [15-17], arylcarboxylates [18], ethylene oxide/PEG [19-21] and other biomolecules [22, 23]. Within this field, our research group designed a medium molecular weight charged anionic polyphosphazene (6MHA-PPZ) that was capable of improving the cytotoxicity, transfection, and endosomal escape characteristics of polymeric NPs [6] [24]. It was observed that these properties were caused by the pH-sensitive behavior of the polymer as it destabilized the membrane of the endosomal compartment. Nanocomplexes formulated by adding this polymer showed transfection efficiencies like those of PEI in two-dimensional (2D) cell cultures, but it was in three-dimensional (3D) where a significant improvement in transfection was observed. Even more surprisingly, the resulting transfection was found to be homogeneously distributed in spheroids even reaching their core region. This 3D cell culture model is a representative model of the environment of a real solid tumor as cells grown in these structures maintain gene expression and genomic pattern comparable to those of clinical tumors; besides, their architecture allows to study cell-cell interactions on different tumor layers, including their hypoxic/necrotic inner core [25]. Thus, these positive results suggested that mixed polymeric compositions had enhanced tumor penetration properties and a high transfection capacity due to a combination of zwitterionic and pH-sensitive properties [6].

In a further work from our group, 6MHA-PPZ was incorporated in PEI and Pr nanocomplexes, used as gene delivery carriers. In this work, 6MHA-PPZ was also capable of enhancing the efficacy/toxicity ratio of PEI and Pr nanocomplexes. However, those results were obtained in a heavily transformed glioblastoma cell line (i.e., U87MG), and in flat cell cultures, a model of limited clinical relevance. Therefore, we consider interesting to further analyze the gene delivery properties of PEI/6MHA-PPZ and Pr/6MHA-PPZ nanocomplexes in more advanced models such as 3D spheroids, and using primary tumor-derived cell cultures. Those advanced models would allow us to grasp the expected clinical performance of these nanocomplexes.

2.2. MATERIALS AND METHODS

2.2.1. Material

Protamine sulfate (Mw-5 kDa,) European Pharmacopeia (EP) grade was purchased from Yuki Gosei Kogyo. LTD. Branched polyethylenimine (PEI) (Mw-25 kDa), HEPES (≥99.5%) (25 g), Luciferase Reporter Gene Detection kit (LUC1), 10% (*v/v*) formalin neutral solution, 4% (*v/v*) paraformaldehyde, 6-mercaptohexanoic acid, calcium chloride dihydrate ($CaCl_2 \cdot 2H_2O$), magnesium sulfate ($MgSO_4 \cdot 7H_2O$), sodium bicarbonate ($NaHCO_3$), and potassium chloride (KCl) were purchased from Sigma-Aldrich. Poly(phosphazene) polymer substituted with 6-mercaptohexanoic acid (6MHA-PPZ) was synthesized in our laboratory [6]. Triton-100X (50 mL) was purchased from Scharlab S.L. Lipofectamine®2000 transfection reagent (0.75 mL), micro-BCA protein assay kit, PrestoBlue™ Cell Viability Assay Reagent (100 mL) and 4',6-diamino-2-phenylindole (DAPI) (10 mg) were obtained from Thermo Fisher Scientific. The UltraPure™ DNase/RNase-Free Distilled Water (500 mL) were from Molecular Bioproduct. The sterile dechlorinated tap water (SDT water) was prepared in the laboratory.

Regarding the cellular culture, Dulbecco's Modified Eagle's Medium 1X (DMEM) ([+] 4.5 g/L D-Glucose and 1g/L D-Glucose, [+]Pyruvate, [+]L-Glutamine) (500 mL), Dulbecco's Modified Eagle's Medium 1X (DMEM) ([+] 1 g/L D-Glucose, [+]Pyruvate, [-]L-Glutamine, no phenol red) (500 mL), Opti-Minimum Essential Medium I 1X Reduced Serum Medium (Opti-MEM) ([+]HEPES, [+]2.4 g/L Sodium Bicarbonate, [+]L-Glutamine) (500 mL), Fetal Bovine Serum Qualified (FBS) (500 mL), Penicillin-Streptomycin (P/S) ([+]10000 Units/mL Penicillin, [+]10000 µg/mL Streptomycin) (100 mL), L-Glutamine solution (200 mM, sterile-filtered, BioXtra), and 0.05% Trypsin 1X-EDTA (500 mL) were purchased from Gibco (Life-Technologies). Dulbecco's Phosphate Buffered Salt Solution 10X (DPBS) with calcium chloride and magnesium chloride ions (500mL) and modified Hanks Balanced Salt Solution (HBSS) with phenol red, calcium and magnesium free were also obtained from the latter supplier. Kanamycin was bought from Sigma-Aldrich. The Phosphate Buffered Salt Solution 10X (PBS) was prepared in the laboratory.

The model plasmid pEGFP-Luc was donated by the group of Prof. Anxo Vidal (CiMUS, Universidad de Santiago de Compostela). The model Cy3-siRNA (MISSION® siRNA fluorescent Universal Negative Control, Cyanine 3) was purchased from Sigma-Aldrich, and the siRNA to silence the expression of Green Fluorescence Protein (siRNA-GFP) was donated by the group of Prof. M.J. Alonso (CiMUS, Universidad de Santiago de Compostela). The PureLink HiPure Expi Plasmid Gigaprep Kit was obtained from Invitrogen. The Luria-Bertani medium (LB) was prepared in the laboratory.

2.2.2. Development, synthesis, and chemical characterization of zwitterionic polymers

2.2.2.1. Synthesis of precursor poly(allylamino)phosphazene

The synthesis of the precursor poly(allylamino)phosphazene (AAPPZ) has been described previously [6]. First, in a dried round bottom flask, 5 grams (g) of hexachloro-cyclo-triphosphazene (HCP) and 0.405 g of the catalyst aluminum chloride were mixed under nitrogen atmosphere. The mixture was heated at 240-250 °C for 3 hours (h). Once the polymerization was finished, the product was cooled slowly until reaching 120 ºC, where it was immediately dissolved in 8 mL of diglyme. To eliminate the excess of aluminum chloride, a centrifugation was carried out at 7,000 RCF for 15 min at -10 ºC. The supernatant was transferred to a previously dried new flask and 50 mL of anhydrous tetrahydrofuran was added under nitrogen

atmosphere. To carry out the nucleophilic substitution of the chlorines by allylamine, 3 equivalents per chlorine atom of both triethylamine and allylamine were added, and the reaction was left on ice for 24 h, and, then at room temperature (RT). The supernatant was filtered using 0.22 µm polyethersulfone (PES) filter to remove the excess of trimethylamine hydrochloride. The polymer was precipitated using a mixture of anhydrous tetrahydrofuran and water (25 mL:25 mL), removing impurities by centrifugation at 7,000 RCF for 10 min at -4 ºC and 10 ºC, respectively. The product was filtered by vacuum, reprecipitated with 25 mL of water, and centrifuged again for 10 min at 10 °C. Finally, an extraction with chloroform and water in the same proportions was performed, and, finally, the supernatant was precipitated with 25 mL of water and centrifuged for 10 min at 0 ºC. The precipitate was dried under vacuum for 72 h and stored at -20 °C. The precursor AAPPZ was characterized by Nuclear Magnetic Resonance (NMR) of phosphorus (^{31}P) and proton (^{1}H) (Bruker DPX-400 spectrometer). For this, a small amount of the product was dissolved in 0.7 mL of deuterated water (D_2O).

2.2.2.2. Synthesis of anionic polyphosphazene

Once the precursor AAPPZ was obtained, two side chains of carboxylic acid were introduced in the polyphosphazene backbone by a thiol-ene addition reaction on the allyl groups of AAPPZ. For this purpose, 100 mg of AAPPZ were dissolved in 7.5 mL of trifluoroethanol. The precursor was added to 6MHA acid (3 equivalents per allyl group) under a nitrogen atmosphere. The thiol-ene reaction was initiated by adding the 2,2-dimethoxy-2-phenylacetophenone photoinitiator (0.5 equivalents per allyl group) under ultraviolet light ($\lambda_{excitation}$= 365 nm) and was left to proceed under stirring at RT and for 3 h. The product obtained (Mw= 7 kDa) was dialyzed in 50 mM sodium hydroxide solution for 24 h and in ultrapure water for 48 h. Finally, the anionic polyphosphazene was lyophilized and stored at -20 °C. The 6MHA-PPZ polymer was characterized by ^{1}H-NMR (Bruker DPX-400 spectrometer). For this, a small amount of polymer was dissolved in 0.7 mL of deuterated water (D_2O).

2.2.3. Formulation of nanocomplexes

The nanocomplexes were prepared by the ionic complexation method. After previous screening studies, the (N:C:P) charge ratios 8:0:1 and 8:4:1 were selected. The first charge ratio was a function of the number of primary amines of the cationic polymer branches (N) and the plasmid phosphates (P); and the second one also considered the number of carboxyl groups of 6MHA-PPZ (C) (N:C:P). The stock solutions of cationic polymers such as PEI (0.72 mg/mL) and protamine (0.4 mg/mL), and the anionic polyphosphazene (1 mg/mL) were prepared in HEPES 10 mM (pH= 5.5). For both nanocomplexes, a fixed amount of plasmid was dissolved in 0.05 mL of ultrapure water (Milli-Q water). In the case of formulation with 8:0:1 (N:C:P) charge ratio, the plasmid solution was added dropwise to a final volume of 0.450 mL of PEI and protamine solutions under magnetic stirring for 1 h at RT. In the case of formulation with 8:4:1 (N:C:P) charge ratio, 0.085 mL of the anionic phase, composed of 6MHA-PPZ and plasmid, was added drop by drop under the same conditions. The nanocomplexes were spontaneously formed indicated by the presence of a slight opalescence suspension.

2.2.4. Physicochemical characterization of nanocomplexes

All formulations were characterized with respect to their mean particle size, polydispersity index (PDI), derived count rate (DCR) and surface charge. Size, PDI and DCR were measured by Dynamic Light Scattering (DLS) or Photon Correlation Spectroscopy (PCS) and the zeta potential was measured by Laser Doppler Anemometry at 25 ºC and with a detection angle of

173º (Zetasizer Nano-ZS™, Malvern Instruments). Samples were prepared using a dilution 1:10 (*v/v*) in Milli-Q water and measurements were performed in triplicate.

2.2.5. Stability of nanocomplexes

First, the stability of PEI and Pr nanocomplexes with/out 6MHA-PPZ was analyzed at storage conditions (4 ºC) for 30 days. To perform cell culture studies, the colloidal stability of the nanocomplexes was also evaluated in DMEM, non-supplemented and supplemented with 10% (*v/v*) of FBS and 1% (*v/v*) of P/S, at 37 ºC under horizontal shaking at 300 revolution per minute (rpm) at different time points (0, 2 and 4 h). In addition, for the *in vivo* study using a zebrafish model, the colloidal stability of nanocomplexes was also analyzed in E3 media (294 mg/L $CaCl_2 \cdot 2H_2O$, 123.25 mg/L $MgSO_4 \cdot 7H_2O$, 64.75 mg/L $NaHCO_3$ and 5.75 mg/L KCl, (OECD 203 annex 2, 1992)) and in SDT water at RT under horizontal shaking at 150 rpm at different time points (0, 2, 4, 24, 48, 72 and 96 h) [26]. The particle size, PDI and DCR of three different batches of each nanocomplex were determined as described in section 2.2.4. using the dilution 1:10 (*v/v*) in the corresponding media. In the case of the stability at storage conditions, the zeta potential was also analyzed as previously mentioned.

2.2.6. Cell culture

The U87MG cell line was obtained from ATCC. These cells were cultured in high glucose DMEM medium supplemented with 10% (*v/v*) FBS and 1% (*v/v*) of P/S at 37 ºC with 5% of CO_2 and 95% of relative humidity (Memmert INCO 2, (I.C.T, S.L.)). The patient-derived glioblastoma cell lines were donated by the Children's Brain Tumor Research Group (Biodiscovery Institute, University of Nottingham). In this case, the GIN-8 cells (Glioma INvasive margin cells) were isolated from medial front invasive margin (54 y female, wild-type IDH (primary GBM), intact ATRX, 0% MGMT promoter methylation, 90% resection plus Gliadel wafers, treatment 60Gy radiotherapy, concurrent and adjuvant temozolomide, patient died 5 months after surgery), the GIN-28 cells were isolated from 5-ALA fluorescence-positive invasive margin (71 y male, wild-type IDH (primary GBM), intact ATRX, 0% MGMT promoter methylation, 99% resection, no adjuvant therapy (patient choice), patient died 3 months after surgery) and the GCE-28 cells were isolated from the central tumor core (71 y male, wild-type IDH (primary GBM), intact ATRX, 0% MGMT promoter methylation, 99% resection, no adjuvant therapy (patient choice), patient died 3 months after surgery) [27]. These three glioblastoma cell lines were cultured also in low glucose DMEM medium supplemented with 10% (*v/v*) FBS and 1% (*v/v*) P/S at 37 ºC with 5% of CO_2 and 95% of relative humidity (Cryofusion, MCO2OAIC-PE).

2.2.7. *In vitro* viability assay in 2D glioblastoma models

The *in vitro* viability of both nanocomplexes prototypes has been previously evaluated in U87MG cell line [28]. In the present work, the viability of nanocomplexes was further investigated in three patient-derived glioblastoma cell lines: GIN-8, GIN-28, and GCE-28 by the PrestoBlue™ Cell Viability assay. For this purpose, $8x10^3$ glioblastoma cells/well were seeded in 96-well plates (Costar, Corning Incorporated) in a final volume of 0.100 mL of supplemented DMEM medium. After 24 h, the medium was replaced by 0.074 mL of fresh supplemented medium and 0.026 mL of: (i) HEPES 10 mM (pH= 5.5) (positive control), (ii) 0.1% (*v/v*) triton-X100 (negative control) and (iii) different concentrations of nanocomplexes from 0.10 to 2.00 µg of pDNA/cm^2. The cells were incubated for 4 h at 37 °C. After this, the cells were washed with DPBS 10X buffer with calcium and magnesium chloride ions and incubated again in 0.100 mL of fresh supplemented DMEM medium for 48 h under the same

conditions. A final volume of 0.100 mL of 10% (*v/v*) PrestoBlue™ reagent diluted in DMEM free red phenol supplemented with 10% (*v/v*) FBS and 1% (*v/v*) of L-Glutamine was incubated with the cells for 2 h at 37 °C, covering the plate with aluminum foil. Fluorescence signal was measured at 544/590 nm ($\lambda_{Ex}/\lambda_{Em}$) in the BMG Labtech FLUOstar Omega microplate reader (Isogen Life Science B.V.) using the Omega software in black 96-well plates (NUNCTM MicroWell™, ThermoFisher Scientific).

The cell viability (%) compared with the control was calculated as following:

$$Cell\ viability\ (\%) = \frac{Sample\ Fluorescence}{Control\ cells\ Fluorescence}\ x\ 100 \quad (1)$$

2.2.8. *In vitro* transfection assay in 2D glioblastoma models

Before the transfection assay, the amplification of the plasmid encoding the Enhanced Green Fluorescent Protein (EGFP) and Luciferase protein (Luc) (pEGFP-Luc) was carried out applying the same conditions mentioned in section 1.2.9.1. of Chapter I.

In the present work, the *in vitro* transfection study was carried out in U87MG cell line, and in the three patient-derived glioblastoma cell lines (GIN-8, GIN-28, and GCE-28). For this purpose, 5.6 x10^4 U87MG cells and 4x10^4 GIN and GCE cells per well were seeded in 24-well plates (Costar, Corning Incorporated) in a final volume of 1 mL of supplemented DMEM medium and they were incubated for 24 h at 37 ºC. After that, the four cell lines were transfected using (i) 8:0:1 and 8:4:1 (N:C:P) charge ratios PEI/Pr:pEGFP-Luc:6MHA-PPZ nanocomplexes, (ii) the naked pEGFP-Luc plasmid, such as negative control, and (iii) the Lipofectamine® 2000 commercial reagent prepared under the specification of the commercial protocol, as positive control, at 0.5 µg of pDNA/cm^2 of concentration. The formulations and controls were prepared in a final volume of 0.2 mL of non-supplemented Opti-MEM medium, incubating with cells for 4 h at 37 °C. After their removal, the U87MG cells were washed with PBS 1X buffer and the GIN and GCE cells were washed with DPBS 10X buffer with calcium chloride and magnesium chloride, and 1 mL of fresh supplemented DMEM medium was added. The evaluation of Luciferase expression was quantified after 48 h using the commercial Luciferase Reporter Gene Assay High Sensitivity (Roche) in the case of U87MG cell line, and Luciferase Reporter Gene Detection Kit (LUC1) (Sigma-Aldrich) in the case of GIN and GCE cell lines. For this, after washing, the cells were lysed with 0.100 mL of the corresponding lysis buffer 1X. The mucus obtained was incubated for 15 min at RT and, then, centrifuged (Centrifuge 5430R, Eppendorf, and HAWK 15/05 refrigerated centrifuge, Sanyo MSE, respectively) for 10 min at maximum speed at 4 ºC until a pellet was observed at the bottom of the eppendorf. Immediately, 0.05 mL of the supernatant was placed in untreated white 96-well plates (Deltalab) and 0.025 mL of the luciferin reagent was added per well, previously prepared under the recommendations of the commercial kit and pre-equilibrated at 15-25 ºC. The Luciferase expression in U87MG cells was measured using a Luminometer (Berthold Luminometer Mithras LB940), and in the case of GIN-8, GIN-28, and GCE-28 cells, it was measured at 525 nm using the BMG Labtech FLUOstar Omega microplate reader (Isogen Life Science B.V.). The results were gathered by MicroWin2000 and by Omega Software, respectively. Finally, the total protein content of each sample was determined following the instructions provided with the micro-BCA Protein Assay kit (ThermoScientific), and the results were expressed as Relative Light Units per milligram cellular protein (RLU/mg protein).

2.2.9. Generation of glioblastoma spheroids

The amount of 500 cells per well were selected to form the U87MG glioblastoma spheroids, and the amount of 2,000 cells per well to form the GIN and GCE spheroids using the conditions previously mentioned in section 1.2.10. of Chapter I. Briefly, the cells were seeded in Ultra-Low Attachment round-bottom 96-well plates (ULA-96 well) in a final volume of 0.2 mL supplemented DMEM medium and then, they were centrifuged (Centrifuge 5430R, Eppendorf, and Sigma 3-16L Centrifuge, Sci-Quip). The morphological characterization of the spheroids was performed 3 days after seeding U87MG cells and 2 days after seeding patient-derived glioblastoma cells using an optical microscope (Olympus IX51) and the plate reading widefield microscope (Nikon Intensilight C-HGFI/C-HGFIE), respectively. Spheroid size was monitored using the Olympus cellSens Standard Software and the NIS-Elements Viewer 5.21 Software until reaching a diameter between 200-300 µm, approximately.

2.2.10. *In vitro* viability assay in 3D glioblastoma models

As mentioned in 2D viability assay of PEI and Pr nanocomplexes with/out the polyphosphazene, this assay was also evaluated in U87MG spheroids [28], and then, it was performed on patient-derived glioblastoma spheroids (GIN-8, GIN-28, and GCE-28), applying similar conditions. After the spheroid formation, 0.150 mL of cell culture medium was removed, leaving the spheroid in suspension in 0.05 mL. The spheroids were treated with 0.097 mL of fresh DMEM supplemented medium and 0.053 mL of: (i) HEPES 10 mM (pH= 5.5) (positive control), (ii) 0.1% (*v/v*) of triton-X100 (negative control) and (iii) different concentrations of nanocomplexes from 0.33 to 6.67 µg of pDNA/mL, incubating for 12 h at 37 ºC. After removing the formulations and the respective washes, the spheroids were incubated in fresh supplemented DMEM medium for 72 h at 37 °C. To determine the viability, the spheroids were incubated with 0.2 mL of 10% (*v/v*) PrestoBlue™ diluted in DMEM phenol red free supplemented with 10% (*v/v*) FBS and 1% (*v/v*) of L-Glutamine for 4 h at 37 °C, covering the plate with aluminum foil. Fluorescence was measured at 544/590 nm ($\lambda_{Ex}/\lambda_{Em}$) in the BMG Labtech FLUOstar Omega microplate reader (Isogen Life Science B.V.) using the Omega Software with previous placed of the spheroids in black 96-well plates (NUNCTM MicroWell™, ThermoFisher Scientific). Viability was determined using the same calculations as in the 2D viability study described in section 2.2.7.

2.2.10.1. Volume assay of patient-derived glioblastoma spheroids

In parallel to the metabolic cytotoxicity assay, the spheroid volume was also analyzed before and after treatment with nanocomplexes (from 0.33 to 6.67 µg of pDNA/mL). The GIN-8, GIN-28, and GCE-28 photos (magnification 10x) were taken using the plate reading widefield microscope (Nikon Intensilight C-HGFI/C-HGFIE) by the NIS-Elements Viewer 5.21 Software. To quantify this parameter, the area of the spheroids was measured using the Fiji Software (ImageJ) and their volume, expressed in %, was calculated compared to the control-treated spheroids as follows:

$$Spheroid\ volume\ (\%) = \frac{Sample\ spheroid\ Volume\ *}{Control\ spheroid\ Volume}\ x\ 100 \quad (2)$$

$$*\ \text{Spheroid Volume} = \frac{4}{3}\ x\ \pi\ x\ r^{3**} \quad (3)$$

$$** \text{ Spheroid radius} = \sqrt{\frac{Area}{4\pi}} \quad (4)$$

2.2.11. *In vitro* transfection assay in 3D glioblastoma models

Transfection study was also carried out in U87MG, GIN and GCE spheroids using 8:0:1 and 8:4:1 (N:C:P) charge ratios PEI/Pr:pEGFP-Luc:6MHA-PPZ and, naked pEGFP-Luc and Lipofectamine® 2000 as controls. The treatment of the spheroids was carried out under the same conditions previously mentioned in section 2.2.8, transfecting 1.5 µg of pDNA/mL in a final volume of 0.2 mL of non-supplemented Opti-MEM medium, and incubating 12 h at 37 ºC. After 72 h of their removal, the spheroids were collected and disaggregated, and, the same protocol as in 2D transfection was applied to prepare the samples using the Luciferase Reporter Gene Detection Kit (LUC1) (Sigma-Aldrich). The Luciferase expression in the four glioblastoma cell lines was measured using a Luminometer (Berthold Luminometer Mithras LB940) correcting the Relative Light Units (RLUs) by the micro-BCA Protein Assay kit (Thermo Scientific). The results were expressed in RLUs per milligram cellular protein (RLU/mg protein).

2.2.12. Zebrafish care and maintenance

Adult zebrafish (*Danio rerio*, Wild-Type (WT)) were maintained in 30 L aquaria with a ratio of one fish per liter of water, 14:10 light/night cycle and a mean temperature of 28.5 ºC according to the procedures described elsewhere [29]. Zebrafish embryos were obtained by mating the adults in controlled conditions. All procedures used in the experiments, fish care and treatment were performed in agreement with the Animal Care and Use Committee of the University of Santiago de Compostela and the standard protocols of the European Union (Directive 2012-63-UE) and Spanish Government guidelines (Real Decreto 53/2013) conducted in the animal facilities in the Veterinary School of the University of Santiago de Compostela (Campus Lugo) (AE-LU-003). At the final point of the experiments, zebrafish embryos were euthanized by tricaine overdose.

2.2.13. Evaluation of *in vivo* biodistribution in zebrafish embryos

Studies in WT zebrafish embryos were performed in collaboration with Dr. Pablo Cabezas-Sáinz and Dr. Laura Sánchez Piñón, members of ZebraBioRes Group (University of Santiago de Compostela). Prior to the biodistribution studies, toxicity assays were carried out following the test 203 (Fish, Accurate Toxicity test) of the Organization for Economic Cooperation and Development (OECD) [28].

First, PEI and Pr nanocomplexes, with/out the 6MHA-PPZ, were formulated using a model siRNA conjugated to cyanine 3 (Cy3-siRNA) and, using a siRNA to silence the GFP expression as negative fluorescence control, following the same protocol mentioned in section 2.2.3 in RNAse-free conditions. Their physicochemical characterization was also tested by triplicate measuring the particle size, PDI, and zeta potential as mentioned in section 2.2.4. For the biodistribution assay, untreated WT zebrafish embryos and treated with naked Cy3-siRNA were used as negative fluorescence controls. Microinjections of PEI and Pr nanocomplexes and controls at 25 µg of siRNA/mL per embryo were carried out in the circulatory system (Duct of Cuvier) in 48 hours post-fecundation (hpf) WT zebrafish embryos (n= 10/condition). The animals were incubated at 34 ºC in salt dechlorinate tap water (Memmert-Sfb500) and were photographed at 5-days post-injection (dpi) with a fluorescence microscope (Nikon AZ-100)

(magnification 6x, scale bar= 200 μm, $\lambda_{Ex}/\lambda_{Em}$ (Cy3) = 554/568 nm and $\lambda_{Ex}/\lambda_{Em}$ (GFP) = 488/510 nm). Image analysis of the photographed zebrafish embryos was carried out using Quantifish Software [30], yielding the integrated intensity of each image. To quantify the Cy3-fluorescence signal, the results were plotted and analyzed as Integrated Intensity by the GraphPad Prism Software (version 7.0 for Windows).

2.2.14. Statistical analysis

Differences were statistically evaluated by one-way ANOVA followed by Sidak's method, if not stated otherwise. All statistical analyses were performed with GraphPad Prism Software (version 8.0 for Windows). A value of $p<0.05$ (*$p<0.05$; **$p<0.01$; ***$p<0.001$; ****$p<0.0001$) was considered significant. Each experiment was performed independently in triplicate (n= 3), unless otherwise indicated.

2.3. RESULTS AND DISCUSSION

2.3.1. Characterization of AAPPZ precursor and 6MHA-PPZ polyphosphazene

2.3.1.1. Nuclear Magnetic Resonance

The AAPPZ precursor has been previously developed by our research group [6] by a ring-opening polymerization reaction (Figure 1. (a)), based on the method developed by Sohn et al. In brief, this is a classical chain-growth polymerization reaction, where the end of the growing polymer chain attacks the remaining cyclic monomers to form a longer polymer [31].

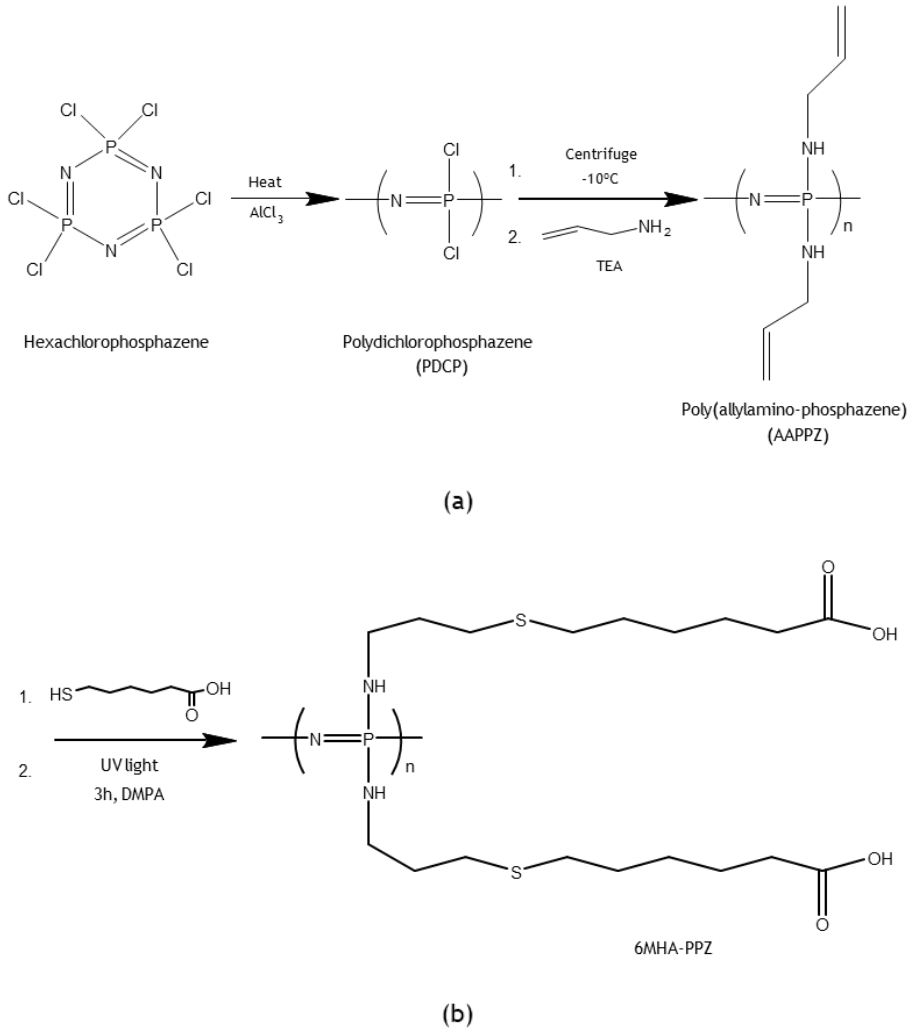

Figure 1. (**a**) Scheme of the synthesis of the precursor allylaminopolyphosphazene (AAPPZ) by the ring-opening polymerization reaction of hexa-chloro-phosphazene. (**b**) Scheme of the synthesis of the anionic polyphosphazene 6MHA-PPZ by the thiol-ene click chemistry with the introduction of the 6MHA acid.

The final AAPPZ product was characterized by ^{1}H-NMR and ^{31}P-NMR. As shown in the phosphorus spectrum in Figure 2. (a), the only peak that appears at 3.70 ppm indicated the successful substitution of allylamine on the chlorine atoms of the PDCP backbone. This spectrum agrees with those reported in the literature for the same polymer [6]. In the proton spectrum in Figure 2. (b), the correct introduction of allyl groups of the AAPPZ was observed when the two peaks at 5.09 ppm and at 5.87 ppm appeared, giving rise to a second confirmation of the successful introduction of the allyl groups in the polyphosphazene.

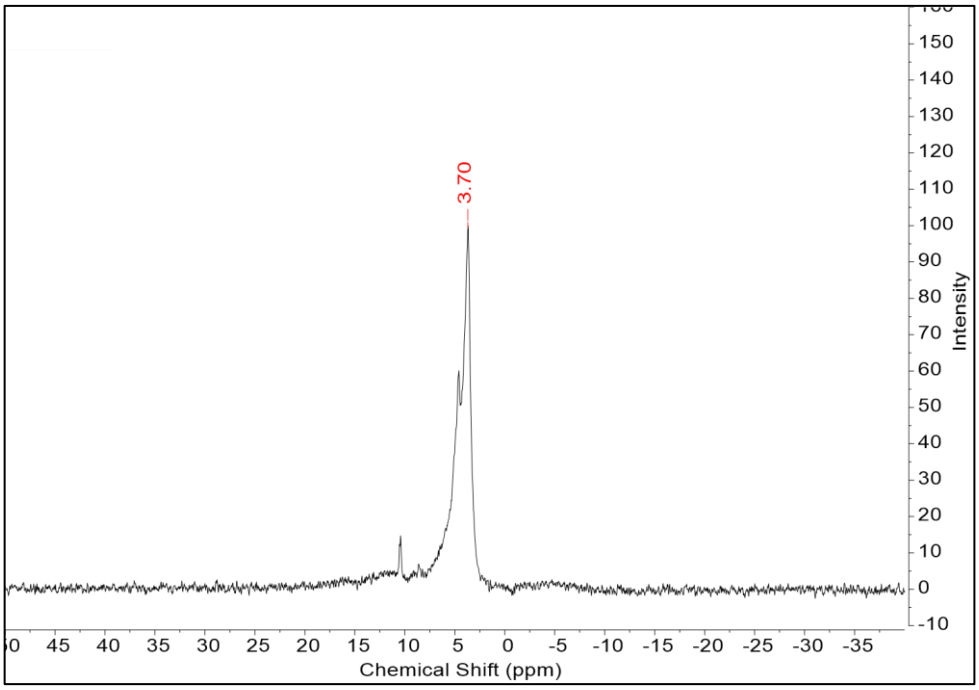

(a)

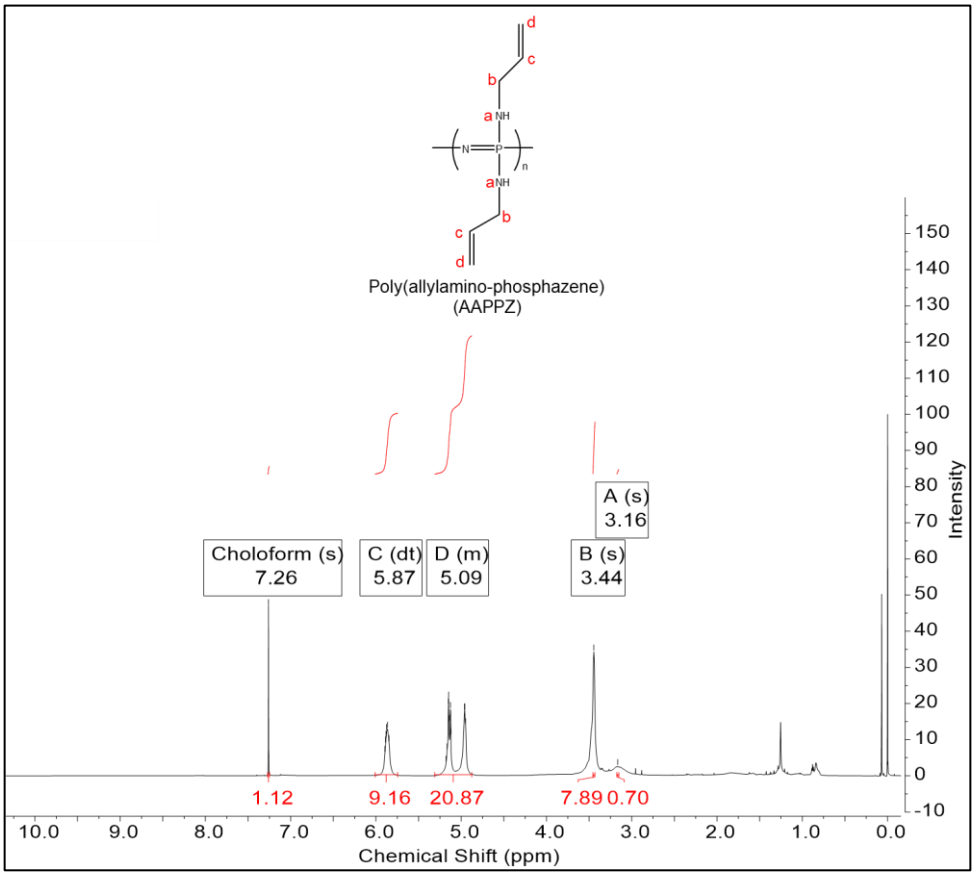

(b)

Figure 2. Spectra of allylaminopolyphosphazene (AAPPZ) by (**a**) ^{31}P-NMR and (**b**) ^{1}H-NMR.

One of the advantages of AAPPZ is its facility to thiol-ene derivatization, which allowed us to create a library of polycations and polyanions [32]. However, in the present work, AAPPZ was only used to synthesize one derivative: 6MHA-PPZ. The selection of this polymer was supported by previous studies, where its inclusion in nanocomplexes enhanced gene expression by 6-fold in glioblastoma cells, and also reduced nanocomplex cytotoxicity. These features were attributed to the pH-dependent ionization properties of 6MHA-PPZ, which improved the intracellular trafficking of the nanocomplexes [6]. The anionic side chain of 6MHA was introduced into the AAPPZ precursor backbone via thiol-ene click chemistry, using 2,2-dimethoxy-2-phenylacetophenone and ultraviolet light (UV; 365 nm) for radical initiation. The identity of the final product was confirmed by ^{1}H-NMR (Figure 3.), obtaining a spectrum identical to the one previously reported [28].

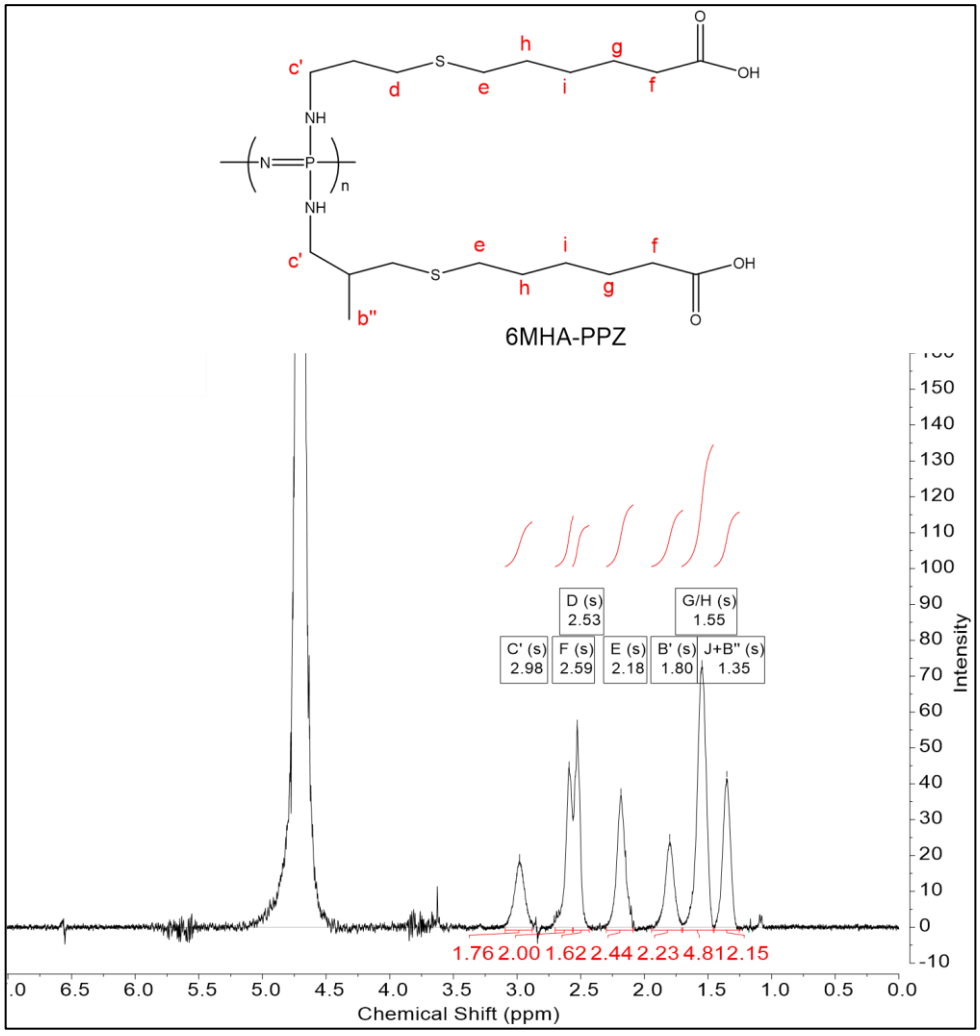

Figure 3. ^{1}H-NMR of the anionic polyphosphazene functionalized by the addition of 6-mercaptohexanoic acid (6MHA), 6MHA-PPZ, via the thiol-ene click reaction. The product was dissolved in D_2O, pH= 9-10.

2.3.2. Physicochemical characterization of nanocomplexes

The formulation of nanocomplexes was carried out by ionic complexation between the negatively charged phosphate groups of the plasmid and the protonated nitrogen atoms of selected polycations. Commercial polymers such as PEI and protamine were selected as polycations due to their efficiency as nanocarriers in gene therapy, and their use in

pharmaceutical formulations [33, 34]. In nanocomplexes with 6MHA-PPZ, this material was added together with the plasmid. The composition of the nanocomplexes is identified by the ratio between ionizing amines (N) from the cationic polymer, carboxyl groups (C) of 6MHA-PPZ, and charged phosphates (P) of DNA (i.e., the N:C:P ratio). Based on screening studies carried out by our research group, 8:0:1 and 8:4:1 (N:C:P) charge ratios had been selected as optimal ratios [28].

The selected nanocomplex compositions were characterized in terms of size, PDI, DCR, and surface charge (zeta potential). Particle size and charge are two critical parameters for gene delivery since they influence NP-transfection efficiency and cytotoxicity. A positive surface charge is crucial for the efficiency of interaction with the cell membrane, and a particle size ≤ 300 nm will facilitate their entry into the cell compartments by clathrin-mediated endocytosis [35, 36]. Table 1. showed that both 8:0:1 and 8:4:1 (N:C:P) charge ratios PEI and Pr nanocomplexes were composed by homogenous particle populations (PDI< 0.3) with a size below 150 nm, and positive zeta potential ranging between +25 and +40 mV. The addition of 6MHA-PPZ to the formulation generated a decrease in particle size that can be attributed to the formation of tighter polymer networks in the NPs [6] [36]. On the other hand, the addition of 6MHA-PPZ did not result in significant modifications in the zeta potentials, which is counterintuitive considering that this material is polyanionic. The reason could be related to the fact that 6MHA-PPZ addition increases remarkably the NP formation yield, as could be inferred from DCR measurements. Therefore, the presence of the 6MHA-PPZ induces the complexation of more polycation chains, increasing the NP formation yield, but without modifying their charge. Similar conclusions have been previously drawn in NPs having a cationic polyphosphazene and 6MHA-PPZ [6]. When comparing the present prototypes, Pr nanocomplexes have a higher formation yield than PEI nanocomplexes, and lower zeta potential. The DCR depends on the size and concentration of particles in suspension, which at the same time depends on the molecular weight of the polymer [37, 38]. Those polymers with higher molecular weight, such as PEI (Mw= 25 kDa) compared to protamine (Mw= 5 kDa), have stronger interactions with polyanions, obtaining smaller nanocomplexes and, therefore, lower DCR values.

Table 1. Mean particle size, polydispersity index (PDI), zeta potential and derived count rate (DCR) of PEI and Pr nanocomplexes with/out 6MHA-PPZ at 8:0:1 and 8:4:1 (N:C:P) charge ratios (Mean ± SD (n= 7)).

Nanocomplexes	Charge ratio (N:C:P)	Size (nm)	PDI	Zeta potential (mV)	DCR (kcps)
PEI:6MHA-PPZ:pDNA	8:0:1	114 ± 19	0.178	+27 ± 11	532 ± 251
	8:4:1	106 ± 10	0.128	+33 ± 15	1458 ± 403
PR:6MHA-PPZ:pDNA	8:0:1	128 ± 6	0.171	+26 ± 7	887 ± 129
	8:4:1	110 ± 14	0.124	+25 ± 8	2070 ± 312

2.3.3. Stability of nanocomplexes

2.3.3.1. Storage stability

Stability under storage is a critical quality for a pharmaceutical formulation, and particularly for a gene nanomedicine [39]. For this reason, the stability of both nanocomplexes was studied at 4 ºC for 30 days. The nanocomplexes, with/out the 6MHA-PPZ, maintained a stable particle size and PDI during the experimental period. In addition, both prototypes of nanocomplexes with 6MHA-PPZ preserved a smaller particle size than their corresponding

prototype without, indicating that the complexation between polyions remained (Figure 4. (a)). The zeta potential was also maintained within similar values for all prototypes during the 30 days of the experiment, although a small reduction was observed for the last data points (Figure 4. (b)). Finally, regarding the concentration, the nanocomplexes of PEI and Pr without the polyphosphazene maintained their count rates constant, even though Pr/pDNA nanocomplex experienced a non-significant increase over time. In contrast, both nanocomplexes with 6MHA-PPZ experienced a decrease in the count rates compared to the samples at t= 0 h and, with their corresponding polycation/pDNA prototype (Figure 4. (c)). In this case, the storage conditions could affect the formulations with the polyphosphazene causing aggregation, consistent with the slight increase in particle size in the final values.

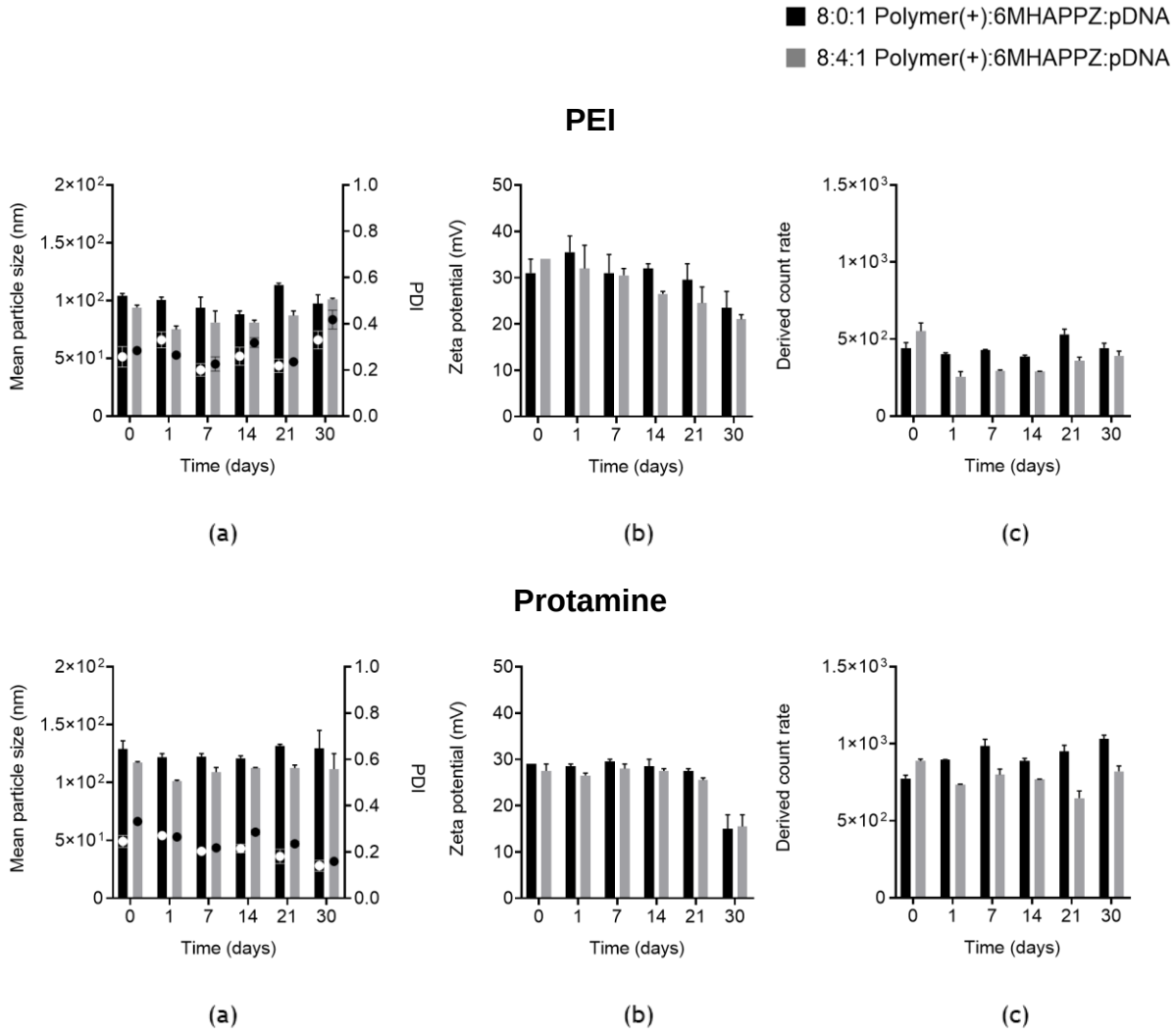

Figure 4. Stability of aqueous suspensions of 8:0:1 and 8:4:1 (N:C:P) charge ratios of PEI and Pr nanocomplexes with/out 6MHA-PPZ polyphosphazene measuring the (**a**) size (bars) and polydispersity index (PDI) (points), (**b**) zeta potential, and (**c**) derived count rate (DCR) at 4 ºC for 30 days (Mean ± SEM (n= 3)).

2.3.3.2. Stability in cell culture medium

The colloidal stability of the selected PEI and Pr nanocomplexes were studied in supplemented and non-supplemented DMEM after 2 h and 4 h of incubation at 37 ºC. Both prototypes of nanocomplexes experienced an increase in the mean particle size when they were

diluted in cell culture medium compared with the same samples diluted in Milli-Q water (Figure 5. (a)). This increase continued with incubation time, which indicated some loss of charge-induced stability in buffered media, with subsequent aggregation. However, this process was controlled with FBS supplementation, which suggested that protein adsorption on the nanocomplex surface might stabilize the formulation. The study of the DCR indicated an increase in this parameter for PEI nanocomplexes, which is consistent with larger particles that do not sediment, although these values for Pr nanocomplexes were more stable (Figure 5. (b)).

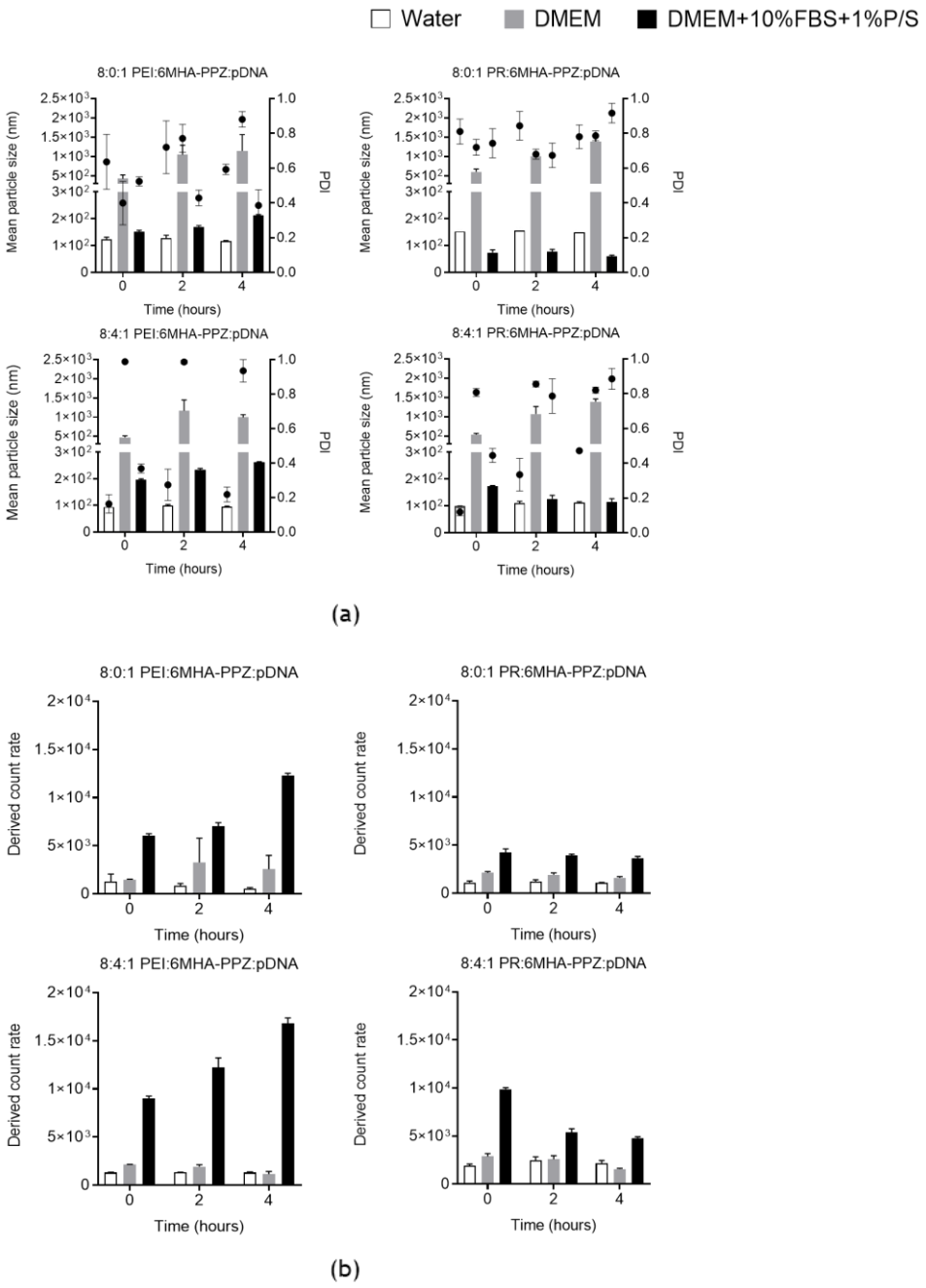

Figure 5. Stability of 8:0:1 and 8:4:1 (N:C:P) charge ratios of PEI and Pr nanocomplexes with/out 6MHA-PPZ polyphosphazene measuring the (**a**) size and polydispersity index (PDI), and (**b**) derived count rate (DCR) at 37 ºC for 0, 2 and 4 h in supplemented and non-supplemented DMEM cell culture medium (Mean ± SEM (n= 3)).

2.3.3.3. Stability in E3 culture medium

Prior to the *in vivo* studies, the physical integrity of the nanocomplexes in zebrafish embryo culture media was assessed. Both prototypes of nanocomplexes were incubated at RT, simulating the zebrafish housing conditions, for 96 h under horizontal shaking. Stability studies showed that the nanocomplexes were unstable in E3 medium, as they underwent aggregation processes reflected by size, PDI and DCR variations (Figure 6. (a, b)). On the other hand, the nanocomplexes were stable in SDT water, another medium used for zebrafish, with major variations in their particle size and PDI for the duration of the experiment. Based on these results, it was concluded that nanocomplexes could be administered in SDT water for zebrafish experiments.

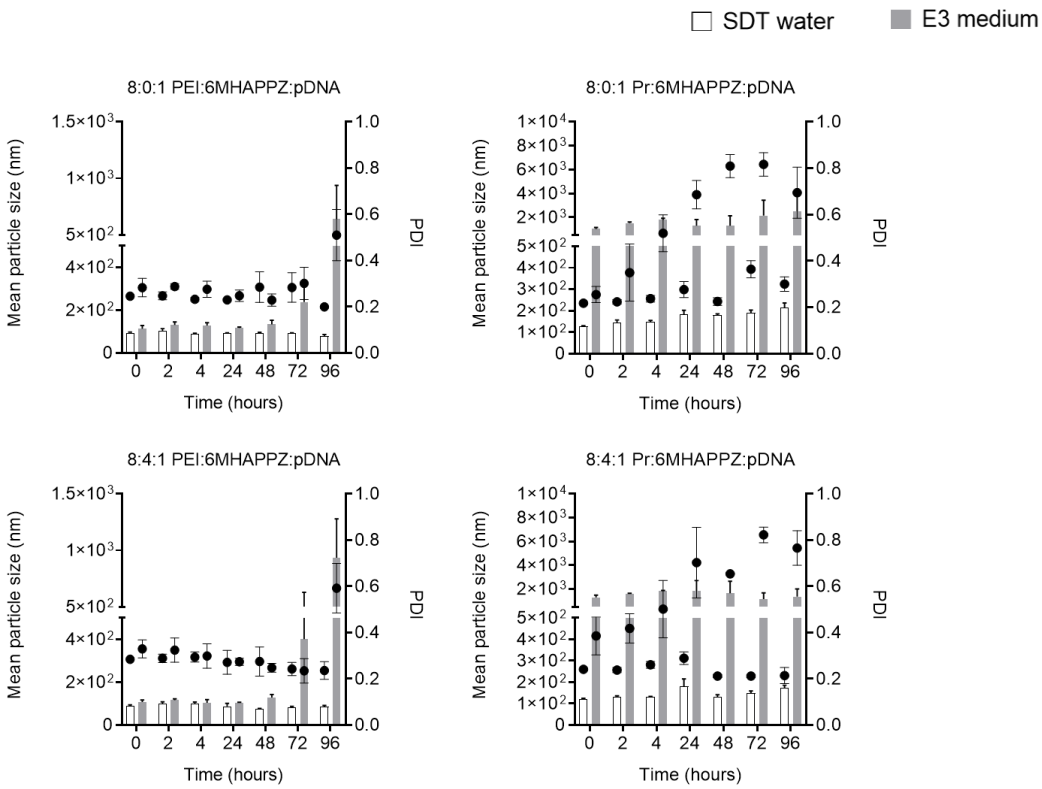

(a)

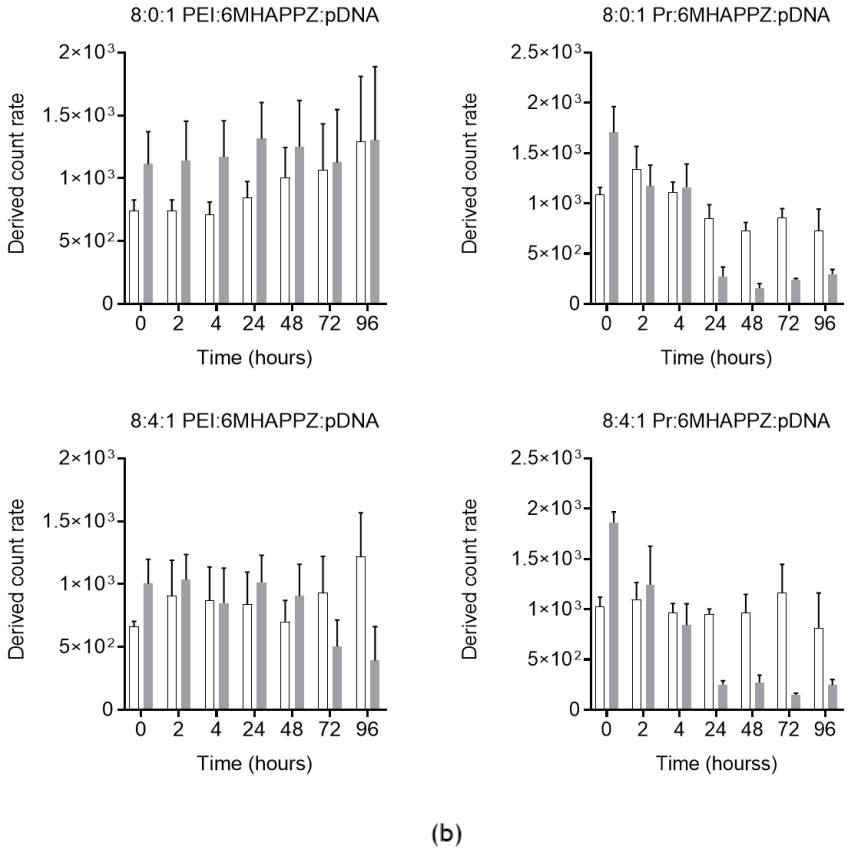

Figure 6. Stability of 8:0:1 and 8:4:1 (N:C:P) charge ratios of PEI and Pr nanocomplexes with/out 6MHA-PPZ polyphosphazene measuring the (**a**) size and polydispersity index (PDI), and (**b**) derived count rate (DCR) in E3 medium and sterile dechlorinated tap water (SDT water) (Mean ± SEM (n= 3)).

2.3.4. *In vitro* viability assay in patient-derived glioblastoma cells

It is generally regarded that positive NP-charge correlates with higher cytotoxic effects. One of the routes to solve this problem is the introduction of anionic polymers capable to reduce the charge by electrostatic interaction with the cationic ones [40]. Our previous work has indicated that the addition of 6MHA-PPZ in formulations could reduce carrier toxicity as observed in the commercial U87MG glioblastoma cell line. In this work, the objective was to validate this observation in Pr and PEI nanocomplexes using patient-derived glioblastoma cells (GIN-8, GIN-28, and GCE-28), measuring the cell viability by a resazurin reduction assay. Figure 7. showed that PEI nanocomplexes presented greater cytotoxicity compared to the nanocomplexes with Pr, and the reductions in viability started above 0.5 µg of pDNA/cm^2. On the other hand, no significant cytotoxicity was observed for Pr nanocomplexes at any of tested concentrations. In the case of GIN-28 and GCE-28 cell lines, a similar cell viability was observed due to their origin was from the same patient [27]. The GCE-28 cell line was more sensitive to PEI nanocomplex-induced toxicity.

The addition of the 6MHA-PPZ improved slightly the viability of these nanocomplexes. The capacity of 6MHA-PPZ to reduce NP-cytotoxicity agreed to previous results of pure polyphosphazene nanocomplexes [6] and those observed for similar PEI:6MHA-PPZ:pDNA and Pr:6MHA-PPZ:pDNA compositions, both in a commercial U87MG glioblastoma model. The present results indicate that these conclusions can be extrapolated to patient-derived cell lines, and thus, the rational for including the anionic polymer 6MHA-PPZ in those formulations

is further supported from a translational standpoint. Finally, the median Lethal Dose (LD_{50}) of the nanocomplexes for 50% of the glioblastoma cell population was also calculated, and this parameter verified the results discussed so far (Table 2.). Based on this data, we concluded that both nanocomplex-prototypes showed sufficient cell compatibility to support further testing in transfection studies.

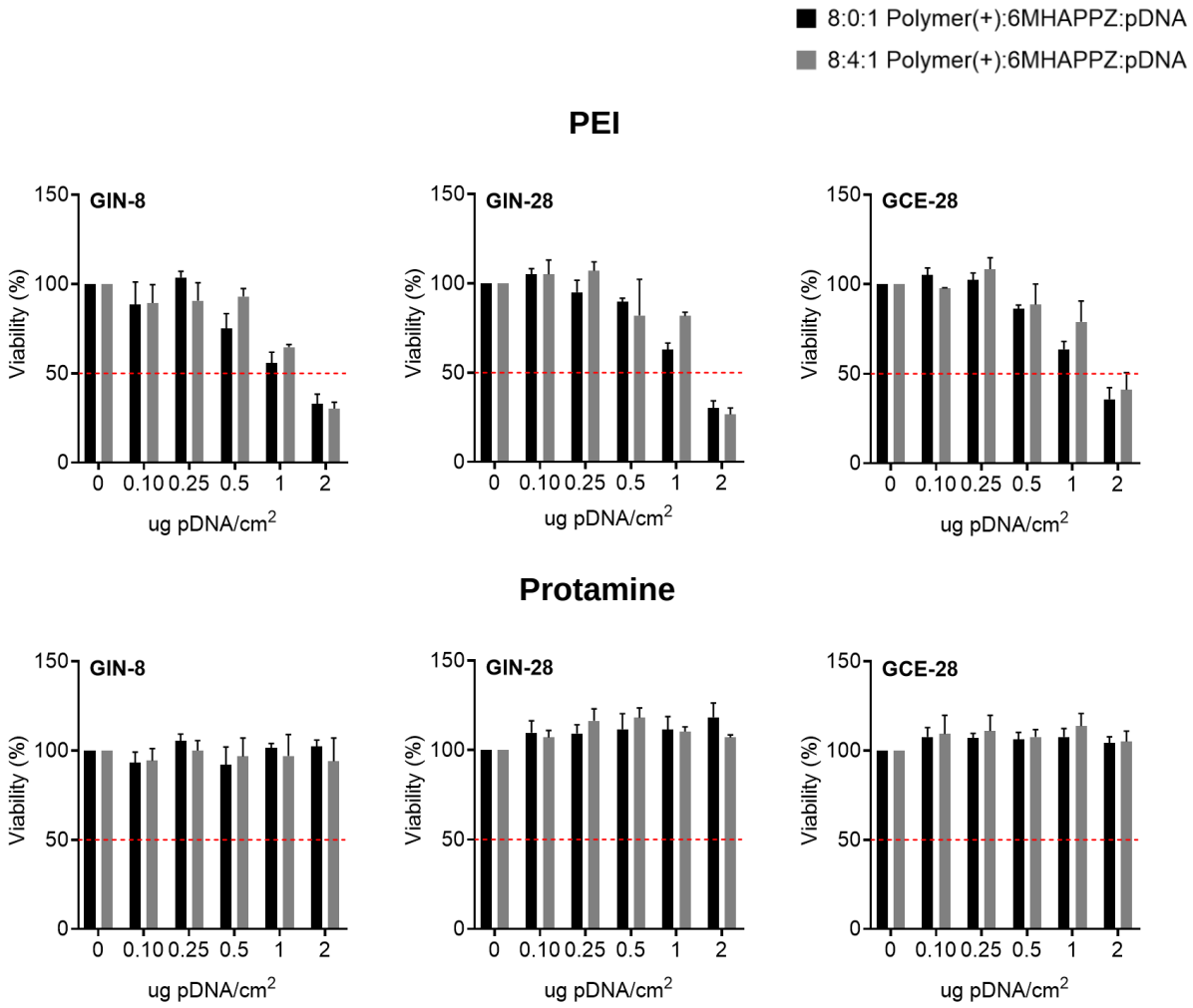

Figure 7. Cell viability assay after 48 h of the removal of increasing concentrations of 8:0:1 and 8:4:1 (N:C:P) charge ratios of PEI and Pr nanocomplexes without (black bars) and with (grey bars) the 6MHA-PPZ, respectively, from 0.10 to 2 µg of pDNA/cm^2 in patient-derived glioblastoma cell lines: GIN-8, GIN-28, and GCE-28 (Mean ± SEM (n= 3)).

Table 2. Median Lethal Dose (LD_{50}) of nanocomplexes for 50% of the glioblastoma cells (GIN-8, GIN-28, and GCE-28) after 48 h of their removal. The parameter was calculated by extrapolation after the representation of the normalized NP concentration (Mean ± SEM (n= 3)).

Nanocomplexes	Charge ratio (N:C:P)	LD_{50}		
		GIN-8	GIN-28	GCE-28
PEI:6MHA-PPZ:pDNA	8:0:1	1.201	1.321	1.410
	8:4:1	1.352	1.481	1.716
Pr:6MHA-PPZ:pDNA	8:0:1	> 2		
	8:4:1			

2.3.5. *In vitro* transfection assay in glioblastoma cells

Once the compatibility ranges of the nanocomplexes were determined, their transfection capacity was evaluated by analyzing the expression of the Luciferase protein 48 h post-treatment. The assay was optimized first in the commercial U87MG cell line, and then, translated to the three patient-derived glioblastoma cell lines.

PEI and Pr nanocomplexes, with/out the anionic polyphosphazene, presented higher transfection efficiency compared to naked pDNA (negative transfection control), and in general PEI nanocomplexes showed the highest performance (Figure 8.). Also, the addition of the anionic 6MHA-PPZ polymer had a different effect on PEI and Pr nanocomplexes. For Pr nanocomplexes, transfection efficiency was significantly improved in all glioblastoma cell lines when 6MHA-PPZ was included. In addition, an interesting result was that the presence of the anionic polyphosphazene in Pr nanocomplexes made their transfection values reach the reference model 8:0:1 (N:C:P) charge ratio PEI:6MHA-PPZ:pDNA, especially in the patient-derived glioblastoma cell lines. These results suggest this formulation as a good candidate for its evaluation in 3D cell cultures and *in vivo* zebrafish model. For PEI nanocomplexes tested in U87MG, the addition of 6MHA-PPZ provided slightly higher transfection levels than the reference 8:0:1 (N:C:P) charge ratio formulation. However, in patient-derived cell lines the transfection was lower for the PEI/pDNA nanosystem.

Previous results had indicated that 6MHA-PPZ acts as a transfection enhancer [6] due to its capacity to generate endosomal escape. As a consequence of this mechanism, it is possible that this transfection enhancing effect might be particularly effective in improving the performance of carriers with moderate endosomal escape properties. The relative performance seems also to be very sensitive to cell model, which underlines the interest of testing gene nanocarriers in clinically relevant models.

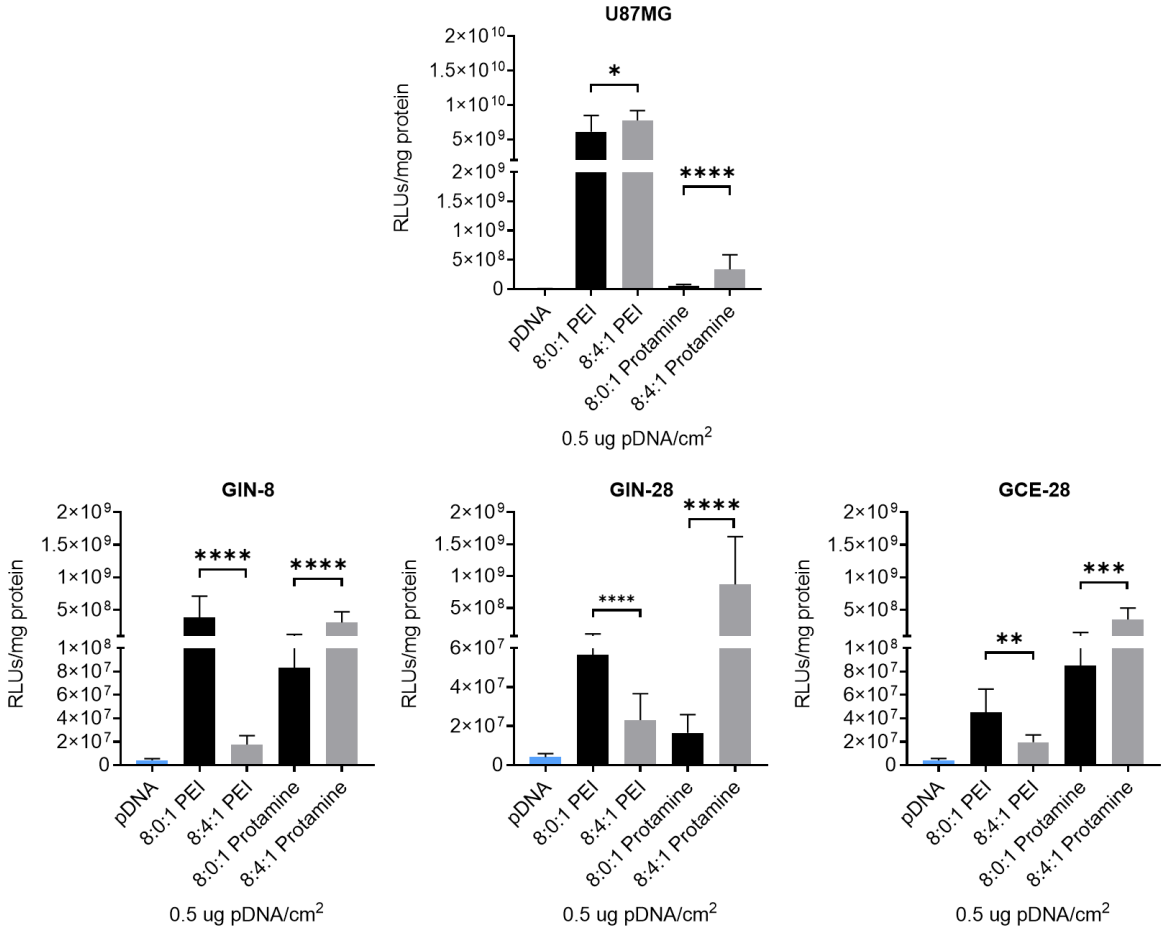

Figure 8. Transfection efficiency of 8:0:1 and 8:4:1 (N:C:P) charge ratios of PEI and Pr nanocomplexes evaluated by Luciferase expression. Study performed at 0.5 µg of pDNA/cm^2, 48 h post-treatment in U87MG, GIN-8, GIN-28, and GCE-28 cells. The results were expressed in RLUs/mg of protein (Mean ± SEM (n= 3)).

2.3.6. Morphological characterization of glioblastoma spheroids

Glioblastoma spheroids were used as a 3D cell culture model that simulates more reliably clinical tumors, by resembling more closely the microenvironment and therapeutic response [41]. As discussed in Chapter I, gene transfection depends on the diameter of the spheroids [6]. The larger spheroid, the higher the distance that the nanocomplexes will have to cross to reach the tumor core. In the present work, spheroids with a size between 200-300 µm were also used for testing.

2.3.7. *In vitro* viability assay in glioblastoma spheroids

Viability in the 3D models was tested after 72 h of the removal of the nanocomplexes and results are expressed relative to the positive control (HEPES, 10 mM (pH= 5.5)). In general, cytotoxicity data from 3D cell cultures, collected in Figure 9., led to similar conclusions than 2D cell culture assays. PEI nanocomplexes were more cytotoxic than Pr. Besides, nanocomplexes showed lower cytotoxicity when incorporating 6MHA-PPZ, an effect that was more significant for PEI-based compositions. Higher viability was observed in GIN-28 and GCE-28 cell lines as compared to GIN-8, tendency similar to that observed for the same cell lines for 2D cell cultures. Finally, the LD_{50} of the nanocomplexes for 50% of the glioblastoma

spheroids was also calculated (Table 3.), and the parameter led to similar conclusions to those previously stated.

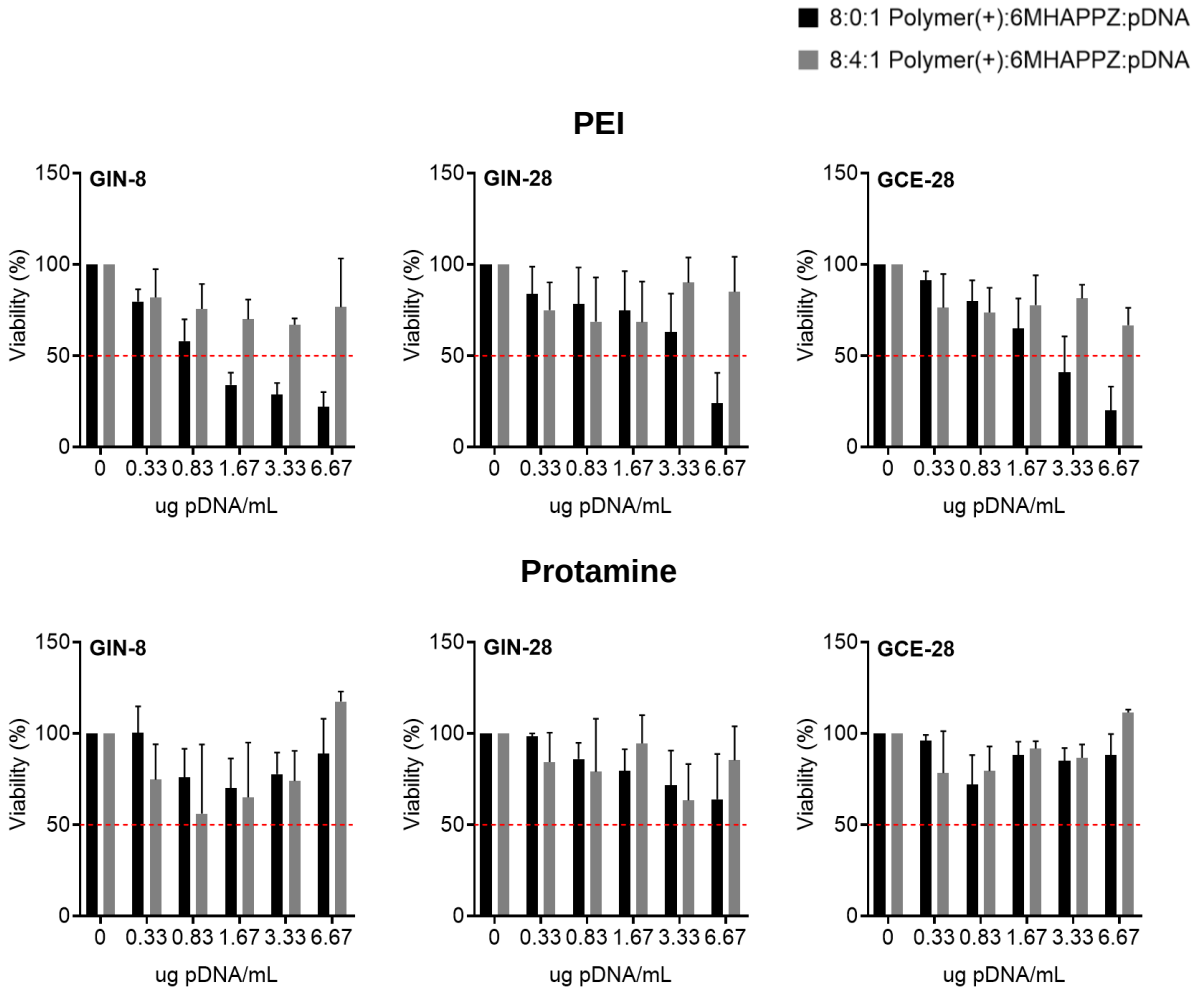

Figure 9. Cell viability assay after 72 h of the removal of increasing concentrations of 8:0:1 and 8:4:1 (N:C:P) charge ratios of PEI and Pr nanocomplexes without (black bars) and with (grey bars) the anionic 6MHA-PPZ, respectively, from 0.33 to 6.67 µg of pDNA/mL in patient-derived glioblastoma spheroids: GIN-8, GIN-28, and GCE-28 (Mean ± SEM) (n= 3)).

Table 3. Median Lethal Dose (LD_{50}) of nanocomplexes for 50% of the glioblastoma spheroids (GIN-8, GIN-28, and GCE-28) after 72 h of their removal. The parameter was calculated by extrapolation after the representation of the normalized NP concentration (Mean ± SEM (n= 3)).

Nanocomplexes	Charge ratio (N:C:P)	LD_{50}		
		GIN-8	GIN-28	GCE-28
PEI:6MHA-PPZ:pDNA	8:0:1	1.151	3.658	2.500
	8:4:1	> 6.67		
Pr:6MHA-PPZ:pDNA	8:0:1			
	8:4:1			

In addition to the metabolic cytotoxicity assay, a complementary study where the volume of the spheroids after 72 h of treatment with nanocomplexes was performed. First, spheroid volume was analyzed by phase-contrast microscopy images (Figure 10. (a)). Tumor spheroids incubated with the nanocomplexes seemed to lose their spherical morphology as cellular extensions from the main mass appeared. These cellular extensions could be considered a defense mechanism against the nanocomplexes, and they were more evident in spheroids treated with PEI nanocomplexes, especially those lacking 6MHA-PPZ. In addition, more extensions were observed in GIN-8 and GIN-28 spheroids in comparison to GCE-28. This cell dynamism observed in GIN cell lines is justified by their origin in the invasive margin of the tumor [42], where these glioma cells have the ability to migrate extensively into the brain, and their significantly more aggressive phenotype than core cells makes them more resistant to therapy [43, 44].

Tumor volume was calculated from the images using the ImageJ software (Figure 10. (b)). The data confirmed that Pr nanocomplexes did not reduce the spheroid volume at 72 h, which remained constant in the three glioblastoma cell lines. In the case of spheroids treated with PEI nanocomplexes, the results were more diverse: spheroid volume increased for GIN-28, was constant for GCE-28, and was reduced for GIN-8. The increase in spheroid volume might be the result of the cellular extensions as a signal of cell stress. In spite of these disparities, the tumor volume assay supported the conclusions drawn by the metabolic assays where PEI nanocomplexes were more toxic than Pr, and the prototypes including 6MHA-PPZ had better compatibility profile.

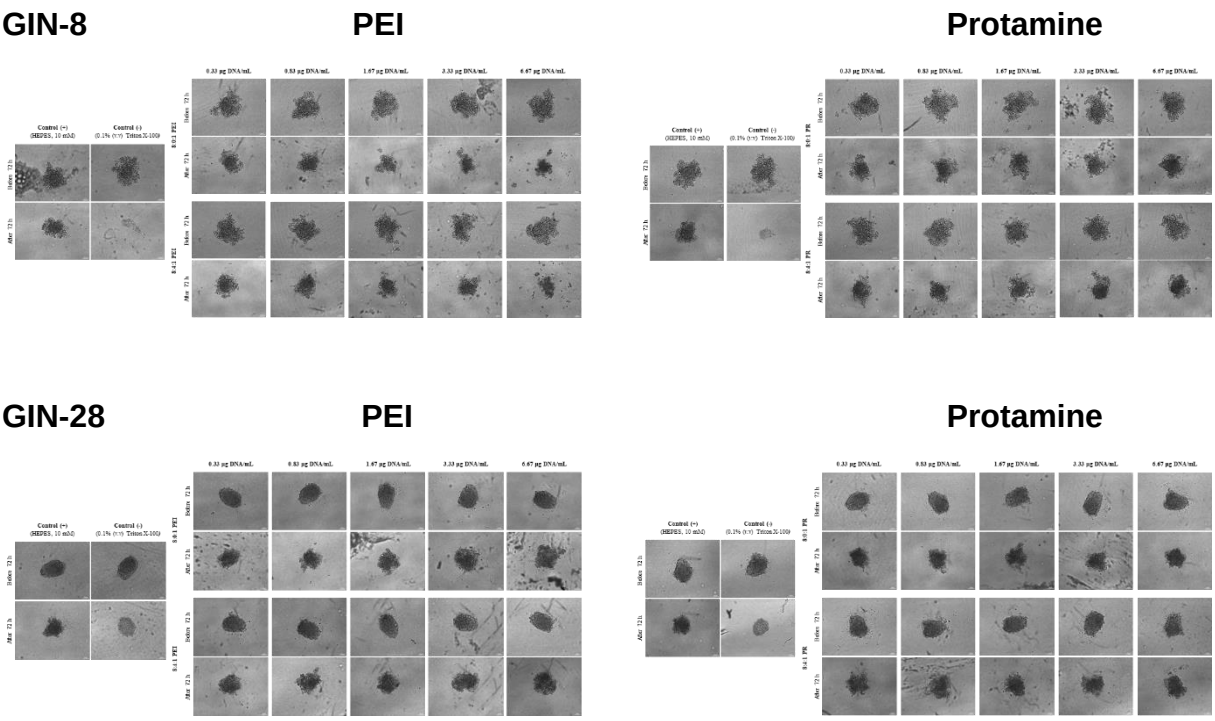

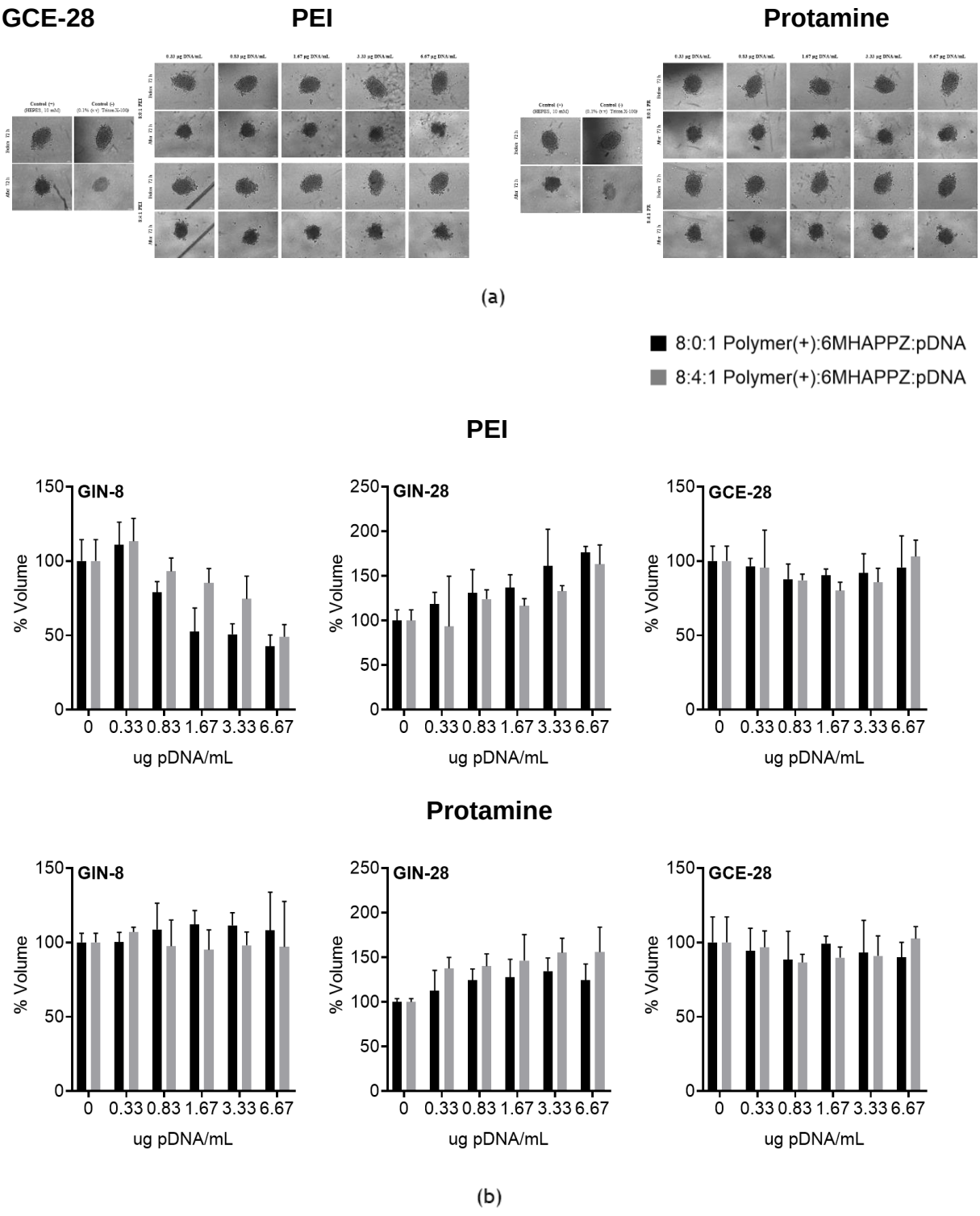

Figure 10. (**a**) Volume images and (**b**) quantification after 72 h of the removal of increasing concentrations of 8:0:1 and 8:4:1 (N:C:P) charge ratios of PEI and Pr nanocomplexes without (black bars) and with (grey bars) the anionic 6MHA-PPZ, respectively, in GIN-8, GIN-28, and GCE-28 spheroids (from 0.33 to 6.67 μg of pDNA/mL) (Mean ± SD (n= 4), scale bar= 100 μm, magnification 10x).

2.3.8. *In vitro* transfection of glioblastoma spheroids

The transfection capacity of PEI and Pr nanocomplexes with/out 6MHA-PPZ was also studied in 3D cell culture models. In this case, nanocomplexes were incubated for 12 h with U87MG, GIN-8, GIN-28, and GCE-28 spheroids, evaluating the expression of Luciferase protein after 72 h post-treatment. (Figure 11.). In the case of U87MG spheroids, transfection results were similar to those obtained in 2D, being PEI nanocomplexes the most efficient. This tendency was not reproduced in the clinical cell culture models, where PEI and Pr nanocomplexes performed more similarly. The effect of 6MHA-PPZ was unclear, which contrasted with previous studies carried out by our research group [6]. Indeed, the main conclusion of the experiment is that gene nanocomplexes performance is sensitive to the cell model used, underlining the importance of using clinically relevant models as early as possible.

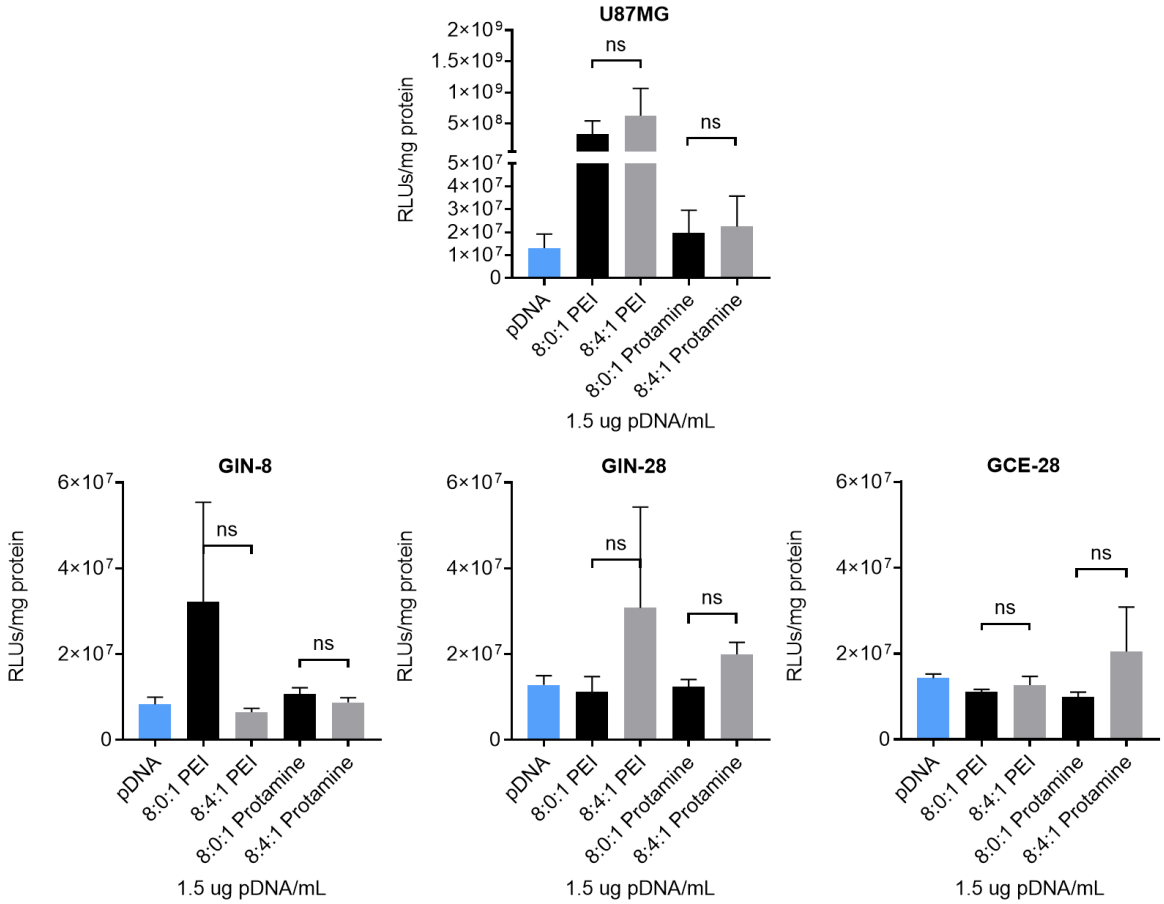

Figure 11. Transfection efficiency of 8:0:1 and 8:4:1 (N:C:P) charge ratios of PEI and Pr nanocomplexes evaluated by Luciferase expression. Study performed at 1.5 µg pDNA/mL, 72 h post-treatment in U87MG, GIN-8, GIN-28, and GCE-28 spheroids. The results were expressed in RLUs/mg of protein (Mean ± SEM (n= 3)).

2.3.9. *In vivo* biodistribution assay in a zebrafish model.

Zebrafish are used as an intermediate between *in vitro* and *in vivo* rodent models. It is a simple and reliable model whose transparency offers the possibility of studying the role of the interaction of nanocomplexes at the cellular level through biodistribution studies [45]. In the present work, we evaluated the biodistribution of fluorescently labelled PEI and Pr nanocomplexes injected intravenously into the Duct of Cuvier of 48 hpf WT zebrafish embryos (Figure 12.).

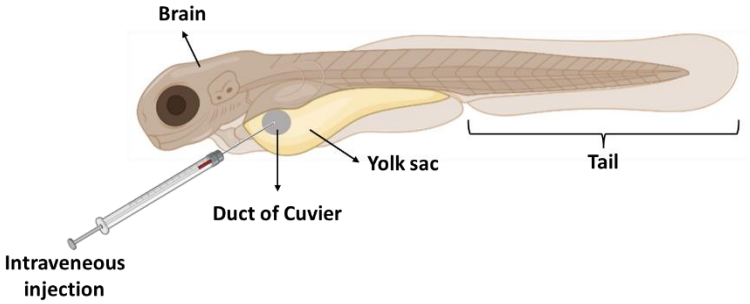

Figure 12. Representative scheme of the intravenous administration of PEI and Pr nanocomplexes into the Duct of Cuvier (grey area) and relevant anatomical regions of zebrafish embryos. Created in BioRender.com

The physicochemical characteristics of formulations labelled with Cy3-siRNA and with siRNA-GFP (Table 4.) were similar to those of the non-labelled formulations ones in terms of size, PDI and zeta potential (Table 1.). The controls were selected to verify that intrinsic zebrafish and free label fluorescence did not interfere with the signal emitted by formulations.

Table 4. Physicochemical characteristics of PEI and Pr nanocomplexes with/out 6MHA-PPZ formulated with Cy3-siRNA and siRNA-GFP at 8:0:1 and 8:4:1 (N:C:P) charge ratios by mean particle size, polydispersity index (PDI) and zeta potential (Mean ± SD (n= 3)).

Nanocomplexes	Charge ratio (N:C:P)	Size (nm)	PDI	Zeta potential (mV)
		Cy3-siRNA		
PEI:6MHA-PPZ:siRNA	8:0:1	100 ± 24	0.222	+25 ± 9
	8:4:1	82 ± 6	0.157	+29 ± 5
PR:6MHA-PPZ:siRNA	8:0:1	180 ± 18	0.115	+21 ± 5
	8:4:1	108 ± 7	0.086	+20 ± 7
		siRNA-GFP		
PEI:6MHA-PPZ:siRNA	8:0:1	146 ± 1	0.126	+22 ± 2
	8:4:1	95 ± 2	0.164	+30 ± 1
PR:6MHA-PPZ:siRNA	8:0:1	172 ± 7	0.108	+21 ± 1
	8:4:1	94 ± 2	0.206	+23 ± 1

Figure 13. (a) collects the images of WT zebrafish embryos at day 5 after intravenous injection of the nanocomplexes and controls. When observing the embryos at this time, a strong fluorescence signal was obtained mainly with PEI/pDNA and PEI/6MHA-PPZ nanocomplexes (photos: 7-8). These nanocomplexes were mostly located in the yolk sac of the zebrafish. These results were similar to previous studies, where hyaluronic acid nanocapsules and their combination with protamine, also formed as reservoir at the yolk sac. The accumulation of the formulations in this cavity could be due to the effect of its complex components, such as the yolk syncytial layer, hindering diffusion to other areas of the embryo [26]. In our case, it was possible to see how a small portion of PEI/6MHA-PPZ formulation diffusing towards the head area, and even reaching the brain. This behavior could depend on the physicochemical characteristics of the formulation, especially the particle size. In previous work, our group also evaluated the diffusion of intravenously injected nanosystems with different sizes and surface charges [46]. The studies demonstrated that the smallest prototypes reached embryo tissues such as brain and visceral organs, justifying the biodistribution obtained with these nanocomplexes. The fluorescence signal observed did not interfere with the autofluorescence

from the zebrafish embryo or from the fluorescence of naked Cy3-siRNA or polymers, as their corresponding controls did not emit any signal (photos: 1-6).

As mentioned in the previous paragraph, there was a statistically significant difference in the values of the fluorescence signal intensity between PEI and Pr nanocomplexes, and the formulation with/out the 6MHA-PPZ polyphosphazene. The graphic in Figure 13. (b) confirmed that PEI nanocomplexes emitted a much stronger fluorescence signal than Pr nanocomplexes. In addition, this signal was even higher in zebrafish embryos injected with PEI nanocomplexes containing the polyphosphazene. The signal intensity could be correlated with the capacity of the cationic polymers to complex the genetic material. The low signal of Pr nanocomplexes could be due to their strong complexation of siRNA, masking the siRNA signal and making its release difficult [47]. On the other hand, we could see how the addition of the polyphosphazene improved the efficiency of cationic polymers, facilitating the endosomal escape by breaking endosome membranes due to the presence of their carboxylic groups [48] releasing the genetic load more easily [6].

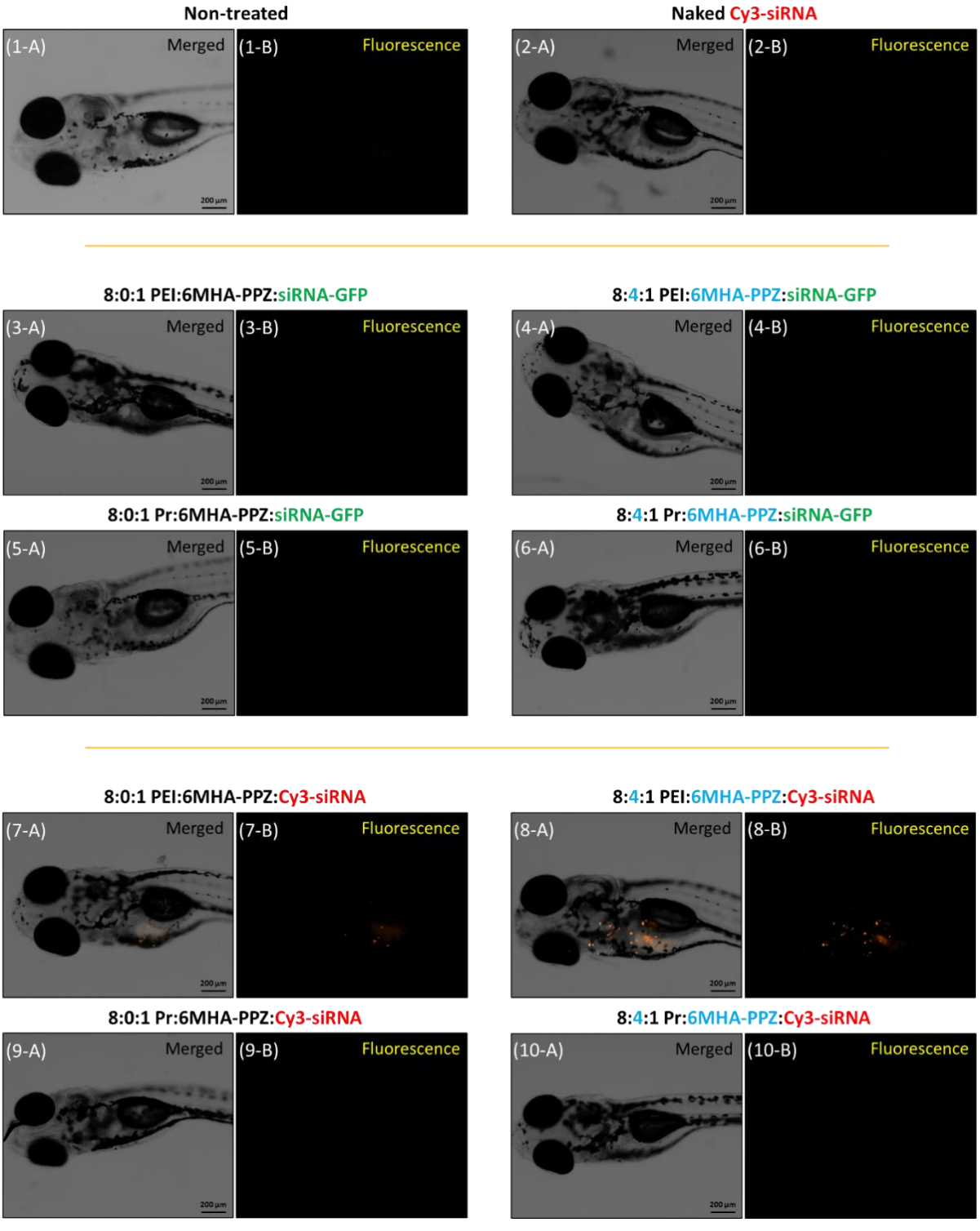
Non-treated
(1-A) Merged
(1-B) Fluorescence
Naked Cy3-siRNA
(2-A) Merged
(2-B) Fluorescence
8:0:1 PEI:6MHA-PPZ:siRNA-GFP
(3-A) Merged
(3-B) Fluorescence
8:4:1 PEI:6MHA-PPZ:siRNA-GFP
(4-A) Merged
(4-B) Fluorescence
8:0:1 Pr:6MHA-PPZ:siRNA-GFP
(5-A) Merged
(5-B) Fluorescence
8:4:1 Pr:6MHA-PPZ:siRNA-GFP
(6-A) Merged
(6-B) Fluorescence
8:0:1 PEI:6MHA-PPZ:Cy3-siRNA
(7-A) Merged
(7-B) Fluorescence
8:4:1 PEI:6MHA-PPZ:Cy3-siRNA
(8-A) Merged
(8-B) Fluorescence
8:0:1 Pr:6MHA-PPZ:Cy3-siRNA
(9-A) Merged
(9-B) Fluorescence
8:4:1 Pr:6MHA-PPZ:Cy3-siRNA
(10-A) Merged
(10-B) Fluorescence
200 µm

(a)

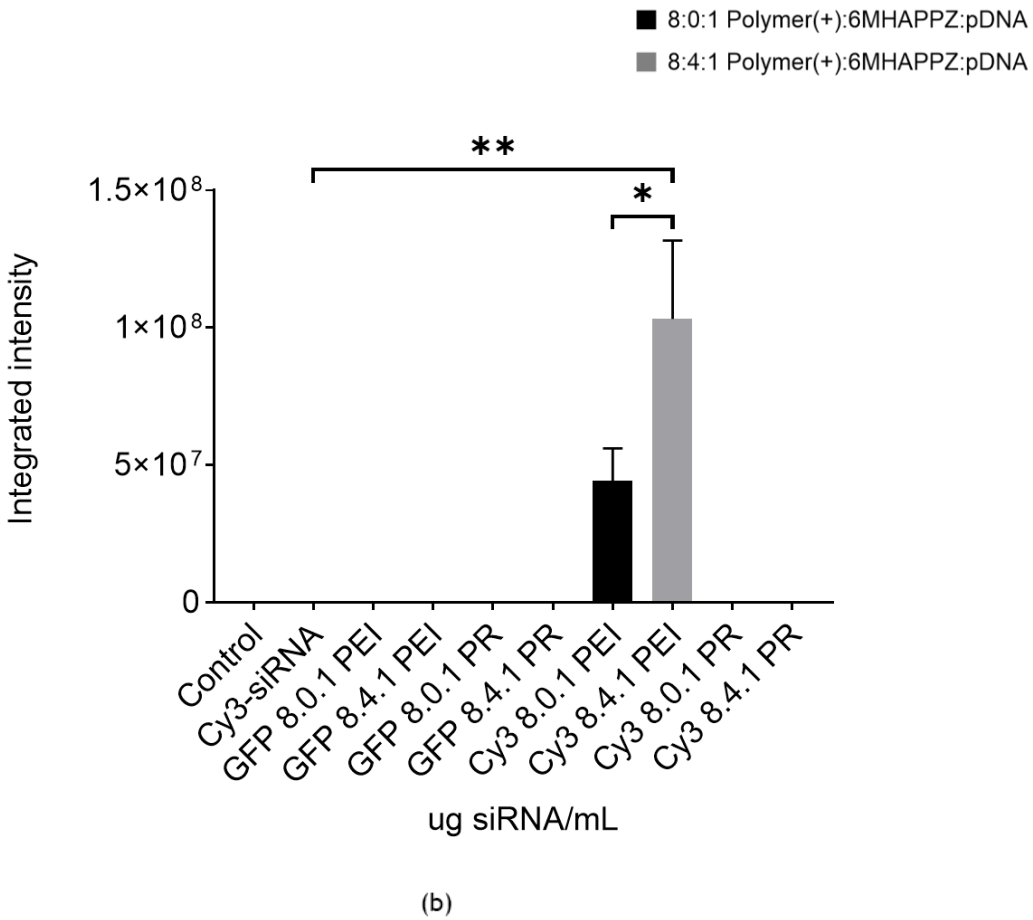

Figure 13. Biodistribution of 8:0:1 and 8:4:1 (N:C:P) charge ratios of PEI and Pr nanocomplexes in 48 hpf WT zebrafish embryos after intravenous administration through the Duct of Cuvier. (**a**) Images were taken at 5-dpi with a fluorescence microscope (scale bar= 200 μm, magnification 6x). (**b**) Quantification of fluorescence intensity from the WT zebrafish embryos treated with controls, 8:0:1 and 8:4:1 (N:C:P) charge ratios of PEI and Pr nanocomplexes at 25 μg of siRNA/mL (Mean ± SEM (n= 10/condition)).

2.4. CONCLUSIONS

6MHA-PPZ polyphosphazene is a recently developed anionic polymer with potential gene delivery properties. Its combination with representative cationic polymers in gene therapy did not cause significant modifications in their physicochemical properties, but it induced an increase in the formulation yield. In general, the stability of the polycation/pDNA nanocomplexes was not affected by the incorporation of the polyphosphazene under storage conditions nor in different biorelevant media. The presence of 6MHA-PPZ experienced a clear reduction in the cytotoxicity of the nanocomplexes, especially of PEI/pDNA nanocomplex in 2D monolayer and advanced 3D models of primary patient-derived glioblastoma cells. In general, the polymer/pDNA nanocomplexes in presence of this anionic polyphosphazene showed better transfection efficiency than the original polycation system, especially the Pr/6MHA-PPZ nanocomplex. However, a dependence of its yield as a gene nanocarrier and the cell model to be used was highlighted. Finally, the addition of the polyphosphazene improved the efficiency of the cationic polymers, especially the biodistribution of PEI nanocomplexes in *in vivo* models of zebrafish embryos with their accumulation in the yolk sac and some particles displaced towards the head area. Overall, the data indicated the advantages of associating the 6MHA-PPZ to cationic nanosystems for more effective gene delivery.

REFERENCES

[1] J. Karlsson, K.M. Luly, S.Y. Tzeng, J.J. Green, Nanoparticle designs for delivery of nucleic acid therapeutics as brain cancer therapies, Adv. Drug Deliv. Rev. 179 (2021) 1-21. https://doi.org/10.1016/j.addr.2021.113999.

[2] C. Garcia-Mazas, S. Barrios-Esteban, N. Csaba, M. Garcia-Fuentes, Chapter13-Suppression of cancer stem cells, Woodhead Publ. Ser. Biomater. (2020) 365-398. https://doi.org/10.1016/B978-0-08-102983-1.00013-2.

[3] T.A. Dick, E.D. Sone, H. Uludag, Mineralized vectors for gene therapy, Acta Biomater. 147 (2022) 1-33. https://doi.org/10.1016/j.actbio.2022.05.036.

[4] G. Wang, S. Chen, N, Qiu, B. Wu, D. Zhu, Z. Zhou, Y. Piao, J. Tang, Y. Shen, Virus-mimetic DNA-ejecting polyplexes for efficient intracellular cancer gene delivery, Nanotoday 39 (2021) 1-14. https://doi.org/10.1016/j.nantod.2021.101215.

[5] T.J. Thomas, H.A. Tajmir-Riahi, C.K.S. Pillai, Biodegradable polymers for gene delivery, Molecules 24 (2019) 1-24. https://doi.org/10.3390/molecules24203744.

[6] W.H. Hsu, P. Sánchez-Gómez, E. Gomez-Ibarlucea, D.P. Ivanov, T. Rahman, An.M. Grabowska, N. Csaba, C. Alexander, M. Garcia-Fuentes, Structure-optimized interpolymer polyphosphazene complexes for effective gene delivery against glioblastoma, Adv. Ther. 2 (2018) 1-15. https://doi.org/10.1002/adtp.201800126

[7] J. Luten, J.H. van Steenis, R. van Someren, J. Kemmink, N.M.E. Schuurmans-Nieuwenbroek, G.A. Koning, D.J.A. Crommelin, C.F. van Nostrum, W.E. Hennink, Water-soluble biodegradable cationic polyphosphazenes for gene delivery, JCR 89 (2003) 483-497. https://doi.org/10.1016/S0168-3659(03)00127-5.

[8] H.R. Allcock, Generation of structural diversity in polyphosphazenes, Appl. Organomet. Chem. 27 (2013) 620-629. https://doi.org/10.1002/aoc.2981.

[9] H.R. Allcock, N.L. Morozowich, Bioerodible polyphosphazenes and their medical potential, Polym. Chem. 3 (2012) 578-590. https://doi.org/10.1039/C1PY00468A.

[10] C.J. Chun, H.J. Lim, K.T. Hong, K.H. Park, S.C. Song, The use of injectable, thermosensitive poly(organophosphazene)-RGD conjugates for the enhancement of mesenchymal stem cell osteogenic differentiation, Biomaterials 30 (2009) 6295-6308. https://doi.org/10.1016/j.biomaterials.2009.08.011.

[11] H.R. Allcock, S.R. Pucher, Poly[(amino acid ester) phosphazenes]: synthesis, crystallinity, and hydrolytic sensitivity in solution and the solid state, Macromolecules 27 (1994) 1071-1075. https://doi.org/10.1021/ma00083a001.

[12] H. Balk, O.S. Jung, Y.K. Sung, Y.S. Sohn, Synthesis and properties of novel Pt(II)-containing polyphosphazene, Bull. Korean Chem. Soc. 16 (1995) 1074-1079. https://doi.org/10.5012/bkcs.1995.16.11.1074.

[13] S. Rothemund, T.B. Aigner, A. Iturmendi, M. Rigau, B. Husár, F. Hildner, E. Oberbauer, M. Prambauer, G. Olawale, R. Forstner, R. Liska, K.R. Schröder, O. Brüggemann, I. Teasdale, Degradable glycine-based photo-polymerizable polyphosphazenes for use as

scaffolds for tissue regeneration, Macromol. Biosci. 15 (2014) 351-363. https://doi.org/10.1002/mabi.201400390.

[14] M. Deng, S.G. Kumbar, Y. Wan, U.S. Toti, H.R: Allcock, C.T. Laurencin, Polyphosphazenepolymers for tissue engineering: an analysis of materials synthesis, characterization, and applications, Soft. Matter. 6 (2010) 3119-3132. https://doi.org/10.1039/B926402G.

[15] Y.C. Qian, X.J. Huang, C. Chen, N. Ren, X. Huang, Z.K. Xu, A versatile approach to the synthesis of polyphosphazene derivatives via the thiol-ene reaction, J. Polym. Sci., Part A: Polymer Chemistry 50 (2012) 5170-5176. https://doi.org/10.1002/pola.26361.

[16] N. Ren, X.J. Huang, X. Huang, Y.C. Qian, C. Wang, Z.K. Xu, Controllable glycosylation of polyphosphazene via radical thiol-ne click chemistry, J. Polym. Sci., Part A: Polymer Chemistry 50 (2012) 3149-3157. https://doi.org/10.1002/pola.26101.

[17] Y. Qian, Z. Xu, Synthesis of polyphosphazene derivates via thiol-ene click reactions in an aqueous medium, Macromol. Chem. Phys. 216 (2015) 671-677. https://doi.org/10.1002/macp.201400545.

[18] D.P. DeCollibus, A. Marin, A.K. Andrianov, Effect of environmental factors on hydrolytic degradation of water-soluble polyphosphazene polyelectrolyte in aqueous solutions, Biomacromolecules 11 (2010) 2033-2038. https://doi.org/10.1021/bm100395u.

[19] C. Zheng, L. Qiu, K. Zhu, Novel polymersomes based on amphiphilic graft polyphosphazenes and their encapsulation of water-soluble anticancer drug, Polymers 50 (2009) 1173-1177. https://doi.org/10.1016/j.polymer.2009.01.004.

[20] B.H. Lee, S.C. Song, Synthesis, and characterization of biodegradable thermosensitive poly(organophosphazenes) gels, Macromolecules 37 (2004) 4533-4537. https://doi.org/10.1021/ma0305838.

[21] C. Zheng, L. Qiu, X. Yao, K. Zhu, Novel micelles form graft polyphosphazenes as potential anticancer drug delivery systems: drug encapsulation and in vitro evaluation, Inter. J. Pharm. 373 (2009) 133-140. https://doi.org/10.1016/j.ijpharm.2009.01.025.

[22] N.R. Krogman, M.D. Hindenlang, L.S. Nair, C.T. Laurencin, H.R. Allcock, Synthesis of purine- and pyrimidine- containing polyphosphazenes: physical properties and hydrolytic behavior, Macromolecules 41 (2008) 8467-8472. https://doi.org/10.1021/ma8008417.

[23] N.L. Morozowich, A.L. Wikel, J.L. Nichol, C. Chen, L.S. Nair, C.T. Laurecin, H.R. Allcock, Polyphosphazenes containing vitamin substituents: synthesis, characterization, and hydrolytic sensitivity, Macromolecules 44 (2011) 1355-1364. https://doi.org/10.1021/ma1027406.

[24] W.H. Hsu, N. Csaba, C. Alexander, M. Garcia-Fuentes, Polyphosphazenes for the delivery of biopharmaceuticals, J. Appl. Polym. Sci. 137 (2019) 1-11. https://doi.org/10.1002/app.48688.

[25] M. Paolillo, S. Comincini, S. Schinelli, In vitro glioblastoma models: a journey into the third dimension, Cancers 13 (2021) 1-25. https://doi.org/10.3390/cancers13102449.

[26] C. Teijeiro-Valiño, E. Yebra-Pimentel, J. Guerra-Varela, N. Csaba, M.J. Alonso, Assessment of the permeability and toxicity of polymeric nanocapsules using the zebrafish model, Nanomedicine 12 (2017) 2069-2082. https://doi.org/10.2217/nnm-2017-0078.

[27] S.J. Smith, M. Diksin, S. Chhya, S. Sairam, M.A. Estevez-Cebrero, R. Rahman, The invasive region of glioblastoma defined by 5ALA guided surgery has an altered cancer stem cell marker profile compared to central tumor, Int. J. Mol. Sci. 18 (2017) 1-13. https://doi.org/10.3390/ijms18112452.

[28] C. Garcia-Mazas, New biomaterials for the design of nanomedicines that modulate glioblastoma stem cells, Doctoral Thesis, Minerva Repositorio Institucional da USC (2020). http://hdl.handle.net/10347/25173.

[29] M. Westerfield, The zebrafish book. A guide for the laboratory use of zebrafish (Danio rerio), 4th ed. Eugene: University of Oregon Press (2000).

[30] D.R. Stirling, O. Suleyman, E. Gil, P.M. Elks, V. Torraca, M. Noursadeghi, G.S. Tomlinson, Analysis tools to quantify dissemination of pathology in zebrafish larvae, Sci. Rep. 10 (2020) 1-10. https://doi.org/10.1038/s41598-020-59932-1.

[31] Y.S. Sohn, Y.H. Cho, H. Baek, O.S. Jung, Synthesis, and properties of low molecular weight polyphosphazenes, Macromolecules 28 (1995) 7566-7568. https://doi.org/10.1021/ma00126a039.

[32] R.A. Montague, K. Matyjaszewski, Controlled synthesis of polyphosphazenes with chain-capping agents, Molecules 26 (2021) 1-15. https://doi.org/10.3390/molecules26020322.

[33] R.K. Oskuee, M. Dabbaghi, L. Gholami, S. Taheri-Bojd, M. Balali-Mood, S.H. Mousavi, B. Malaekeh-Nikouei, Investigating the influence of polyplex size on toxicity properties of polyethylenimine mediated gene delivery, Life Sci. 197 (2018) 101-108. https://doi.org/10.1016/j.lfs.2018.02.008.

[34] H. Zarei, B. Malaekeh-Nikouei, M. Ramezani, F. Soltani, Multifunctional peptides based on low molecular weight protamine (LMWP) in the structure of polyplexes and lipoplexes: design, preparation and gene delivery characterization, Drug Deliv. Sci. Technol. 62 (2021) 1-8. https://doi.org/10.1016/j.jddst.2021.102422.

[35] J.F.A. Valente, P. Pereira, A. Sousa, J.A. Queiroz, F. Sousa, Effect of plasmid DNA size on chitosan or polyethylenemine polyplexes formulation, Polymers 13 (2021) 1-15, https://doi.org/10.3390/polym13050793.

[36] K. Kim, H.S. Hwang, M.S. Shim, Y.Y. Cho, J.Y. Lee, H.S. Lee, H.C. Kang, Controlling complexation/decomplexation and sizes of polymer-based electrostatic pDNA polyplexes in one of the key factors in effective transfection, Colloids Surf. B: Biointerfaces 184 (2019) 1-12. https://doi.org/10.1016/j.colsurfb.2019.110497.

[37] A.E. Jundi, M. Morille, N. Bettache, A. Bethry, J. Berthelot, J. Salvador, S. Hunger, Y. Bakkour, E. Belamie, B. Nottelet, Degradable double hydrophilic block copolymers and tripartite polyionic complex micelles thereof for small interfering ribonucleotide acids (siRNA) delivery, J. Colloid Interface Sci. 580 (2020) 449-459. https://doi.org/10.1016/j.jcis.2020.07.057.

[38] Y. Wang, M. Ye, R. Xie, S. Gong, Enhancing the in vitro and in vivo stabilities of polymeric nucleic acid delivery nanosystems, Bioconjugate Chem. 30 (2019) 325-337. https://doi.org/10.1021/acs.bioconjchem.8b00749.

[39] C.T. de Ilarduya, Y. Sun, N. Düzgünes, Gene delivery by lipoplexes and polyplexes, Eur. J- Pharm. Sci. 40 (2010) 159-170, https://doi.org/10.1016/j.ejps.2010.03.019.

[40] F. Richter, K. Leer, L. Martin, P. Mapfumo, J.I. Solomun, M.T. Kuchenbrod, S. Hoeppener, J.C. Brendel, A. Traeger, The impact of anionic polymers on gene delivery: how composition and assembly help evading the toxicity-efficacy dilemma, J. Nanobiotechnol. 19 (2021) 1-15. https://doi.org/10.1186/s12951-021-00994-2.

[41] Y. Bae, C. Joo, K.H. Park, S.W. Kang, K.M. Huh, J. S. Choi, Preparation and characterization of 3D human glioblastoma spheroids using a N-octanoyl glycol chitosan hydrogel, Inter. J. Biol. Macromol. 185 (2021) 87-97. https://doi.org/10.1016/j.ijbiomac.2021.06.083.

[42] C.E. Vasey, R.J. Cavanagh, V. Taresco, C. Moloney, S. Smith, R. Rahman, C. Alexander, Polymer pro-drug nanoparticles for sustained release of cytotoxic drugs evaluated in patient-derived glioblastoma cell lines and in situ gelling formulations, Pharmaceutics 13 (2021) 1-17. https://doi.org/10.3390/pharmaceutics13020208.

[43] J.R. Molina, Y. Hayashi, C. Stephens, M.M. Georgescu, Invasive glioblastoma cells acquire stemness and increased Akt activation, Neoplasia 12 (2010) 453-463. https://doi.org/10.1593/neo.10126.

[44] N. Pandey, P. Anastasiadis, C.P. Carney, P.P. Kanvinde, G.F. Woodworth, J.A. Winkles, A.J. Kim, Nanotherapeutic treatment of the invasive glioblastoma tumor microenvironment, Adv. Drug Deliv. Rev. 188 (2022) 1-23. https://doi.org/10.1016/j.addr.2022.114415.

[45] A. Pensado-López, J. Fernández-Rey, P. Reimunde, J. Crecente-Campo, L. Sánchez, F.T. Andón, Zebrafish models for the safety and therapeutic testing of nanoparticles with a focus on macrophages, Nanomaterials 11 (2017) 1-34. https://doi.org/10.3390/nano11071784.

[46] J. Crecente-Campo, J. Guerra-Varela, M. Peleteiro, C. Guitérrez-Lovera, I. Fernández-Mariño, A. Diéguez-Docampo, A. González-Fernández, L. Sánchez, M.J. Alonso, The size and composition of polymeric nanocapsules dictate their interaction with macrophages and biodistribution in zebrafish, JCR 308 (2019) 98-108. https://doi.org/10.1016/j.jconrel.2019.07.011.

[47] H. Al-Azzawi, W. Alshaer, E. Esawi, Z. Lafi, D. Abuarqoub, R. Zaza, M. Zraikat, A. Battah, A. Awidi, Multifunctional nanoparticles recruiting hyaluronic acid ligand and polyplexes containing low molecular weight protamine and ATP-sensitive DNA motif for doxorubicin delivery, J. Drug Deliv. Sci. Technol. 69 (2022) 1-11. https://doi.org/10.1016/j.jddst.2022.103169.

[48] K. Sakamoto, M. Akishiba, T. Iwata, K. Murata, S. Mizuno, K. Kawano, M. Imanishi, F. Sugiyama, S. Fuyaki, Optimizing charge switching in membrane lytic peptides for endosomal release of biomacromolecules, Angew. Chem. Int. 59 (2020) 19990-19998. https://doi.org/10.1002/anie.202005887.

CHAPTER III

Protamine nanocapsules as gene delivery carriers for the treatment of intraocular tumors

Protamine nanocapsules as gene delivery carriers for the treatment of intraocular tumors

ABSTRACT

Uveal melanoma (UM) is the most common primary intraocular tumor in adults, where it appears mainly in the choroid, the ciliary body, or the iris. The standard treatment is based on radiotherapy, chemotherapy by intravitreal injection of drugs and/or surgery, including enucleation in severe cases. Alternative treatments have been explored due to the unpleasant side effects, and frequent recurrence and metastasis observed after the standard treatment. Gene therapy is a promising choice capable of targeting specific pathways in UM cells by introducing tumor suppressor sequences that are rendered therapeutically effective by the use of gene delivery vectors. In the present work, the use of protamine nanocapsules (Pr NCs) as vehicles for the administration of genes has been studied due to their intrinsic capacity of encapsulation and protection of nucleic acids such as pDNA and miRNA, their biocompatibility, and their delivery efficacy. Pr NCs were formulated by the solvent displacement technique and consisted of spherical oily droplets surrounded by a protamine shell. The formulation was composed of particles with a size below 250 nm and positive surface charge. Previous studies showed that Pr NCs had adequate quality attributes for their use as topical ocular delivery vehicles, which is less invasive than intravitreal injections. Short-term stability of Pr NCs for up to 4 hours (h) in simulated tear fluid (37 °C, pH= 7.4) was studied. In addition, the colloidal stability was also analyzed in cell culture medium, and under storage conditions (4 ºC) for one month, obtaining satisfactory results. Furthermore, Pr NCs showed efficient association of nucleic acids as confirmed by agarose gel electrophoresis. *In vitro* assays demonstrated that Pr NCs exhibited low cytotoxicity on UM cells and an efficient internalization in the cytoplasmic compartment. The permeabilization capacity of the NCs in a 3D corneal model was evaluated by measuring the transepithelial electrical resistance (TEER). Finally, transfection studies using increasing doses of plasmid DNA revealed an efficient ability of these NCs to transfect UM cells. The results suggested that the developed NCs could be further considered for a safe and suitable treatment method of intraocular tumors by gene therapy.

3.1. INTRODUCTION

Ocular tumors are unique among vision- and life- threatening eye diseases [1]. The origin of these tumors can be either on the surface or in the internal part of the eye, and they can involve structures secondary to the metastatic spread of cancer in other parts of the body [2]. The most common malignant intraocular tumors are retinoblastoma in children and UM in adults [3]. The latter originates from the melanocytes of the uvea comprising the pigment tissues of the iris (anterior segment of the eye), the ciliary body, and the choroid [4]. Its average annual incidence depends on the ethnic groups and regions ranging from 5 to 7 cases per million in northern Europe and United States, 8 cases per million in Australia, and the lowest rates are found in Asian, Hispanic, and Black population in the last 30 years [5-7]. Therefore, the high mortality rate of this tumor justifies the urgent development of effective treatments [8]. Conventional treatment depends on the characteristics of the lesion, such as location of the tumor, magnitude, its spreading, as well as, the patient's health and age [9]. Most cases of UM originate in the choroid (90%), followed by the ciliary body (7%) and the iris (3%) [10], and are treated by a combination of selective surgery, chemotherapy and/or radiotherapy [8]. However, as a consequence of the poor response to this treatment, gene therapy also has also been studied as a new approach [11-14].

As mentioned in previous chapters, gene therapy is based on the administration and delivery of exogenous genes to cells using viral and non-viral systems, where the latter have increasingly acquired a more important role. Our research group has investigated several platforms of non-viral nanosystems [15, 16] composed mainly by natural polymers, such as chitosan and protamine [17-19], synthetic polymers such as poly(lactic-co-glycolic acid) (PLGA), polylactic acid (PLA), polyethylene glycol (PEG), poloxamines, poly(ethylene oxide) and polyphosphazenes, or the combination thereof [20-22]. Nanocarriers based on chitosan, hyaluronic acid [23-26], polyarginine and protamine [27] have stood out as promising vehicles for drug and gene delivery to the eye [28-32]. In the case of intraocular tumors, the most common administration route of nanocarriers is the intravitreal injection, as it offers good bioavailability in the retina due to its proximity. However, this route is highly invasive and carries the risk of serious side effects such as retinal hemorrhage, and/or detachment, endophthalmitis and cataracts [33]. Topical delivery is a preferred non-invasive route to treat such diseases as UM, affecting the posterior segment of the eye [34].

Currently, more than 90% of the formulations in the global ophthalmic drug market are eye drops [35], despite the adversities of the rapid and extensive precorneal loss due to the high turnover of lacrimal fluid, nasolacrimal drainage, reflex blinking, and induced tearing [34]. In addition to the physical barriers of the eye, the corneal epithelium is composed of multiple layers of tightly knit epithelial cells and it represents the main biological barrier to topical drug absorption [36]. Several types of nanocarriers have been explored as tools to enhance the efficacy of topical administration [37]. In fact, several studies based on polymeric nanoparticles (NPs) showed that they could be suitable delivery systems to enhance corneal transport, to solve problems of repeated administration, and to protect therapeutic molecules from degradation [38]. Our research group has successfully developed new formulations based on protamine and polyarginine, with promising properties for topical instillation loaded with different therapeutic molecules such as cyclosporine A or vitamin A [27].

In the present work, Pr NCs were explored as gene delivery carriers for the treatment of UM. In addition to the above-mentioned advantages of this nanosystem for ocular delivery [27], low molecular weight protamine has high translocation capacity across the cell membrane, as

well as, and high gene delivery capacity [39]. These NCs also presented a hydrophobic oily core of DL-α-tocopherol (vitamin E), chosen for its ability to protect cells from oxidative stress damage [38] [40-42], as well as, surfactants and co-surfactants to improve carrier stability and enhance interaction between the oily core and the polymer [43, 44].

3.2. MATERIALS AND METHODS

3.2.1 Material

Protamine sulfate salt (Mw-5 kDa, European Pharmacopeia (EP) grade) was obtained from Yuki Gosei Kogyo LTd. DL-α-Tocopherol was obtained from EMD Millipore Corp. Tween-80 was from Acofarma, and the cholic acid sodium salt was from Dextra Technologies. The ethanol 96% (*v/v*) for reversed phase polarity HPLC was purchased from VWR International Eurolab, S.L.U. and acetone for HPLC Isocratic Grade was from Carlo Erba Reagents S.A.S. Agarose (100 g), heparin sodium salt from porcine mucosa (25 KU), loading-buffer 10X, Agar (250 g), Tris-Acetate-EDTA (TAE) buffer 10X (1 L), sodium chloride (NaCl) BioXtra ≥99.5% (AT) (1 kg), sodium dodecyl sulfate (SDS) (250 g), phosphotungstic acid (sodium salt), potassium chloride (KCl), calcium chloride ($CaCl_2$ $2{\cdot}H_2O$) and magnesium chloride ($MgCl_2$), insulin (5 mL), hydrocortisone (10 mL), triiodothyronine (1 mg), methyl acetate 99.5% (100 mL), adenine (24 mg/mL), fluoromount® aqueous mounting medium (25 mL) and Mayer's Hematoxylin solution (1 L) were purchased in Sigma-Aldrich. Triton-100X 99% (50 mL) and SYBR®Gold Nucleic Acid Gel Stain 50X (0.5 mL) were purchased from VWR and Scharlab S.L., respectively. Cellular membrane (MW = 3.5 kDa, 16 mm dry, I.D 35 feet, SnakeSkin™), diethyl pyrocarbonate ultrapure (DEPC) >97% (25 mL), LIVE/DEAD™ Fixable Aqua Dead Cell Stain Kit 405 nm excitation (200 assays), Lipofectamine®2000 Transfection Reactive (0.75 mL) and sucrose 99% (1 kg) were from Thermo Fisher Scientific™. 5-carboxytetramethylrhodamine succinimidyl ester single isomer (5-TAMRA) (5 mg) and 4',6-diamino-2-phenylindole (DAPI) (10 mg) were purchased from Emp-Biotech and Biochem, respectively. CellTiter Blue® Cell Viability Assay (20 mL) was obtained from Promega. The decontamination solution RNase-free AWAY (475 mL) (18430457) and UltraPure™ DNase/RNase-Free Distilled Water (500 mL) were from Molecular Bioproducts. The 10% (*v/v*) neutral buffered formalin (1L) was obtained from Bio-Optica. Sodium bicarbonate ($NaHCO_3$) 99% (2500 mg) was purchased from Alfa Aesar, and dimethyl sulfoxide (DMSO) (1 L), paraformaldehyde 99% (2.5 kg) and Eosin Y were purchased to Merck. The µ-Slide-8-well (1.5 polymer coverslip, tissue culture sterilized) was purchased from Ibidi®. The Rabbit monoclonal antibody to β-catenin was from Abcam. The Alexa Fluor 594 Goat anti-rabbit secondary antibody was obtained from Molecular Probes. In Situ Cell Death Detection Kit (TMR red) was from Roche Diagnostics.

Regarding the cellular culture, Roswell Park Memorial Institute Medium 1640 1X (RPMI) ([+]L-Glutamine, [+] 25 mM HEPES) (500 mL), Dulbecco's Modified Eagle Medium:Nutrient Mixture F-12 (DMEM:F12) (500 mL), Opti-Minimum Essential Medium I 1x Reduced Serum Medium (Opti-MEM) ([+]HEPES, [+]2.4 g/L Sodium Bicarbonate, [+]L-Glutamine) (500 mL), the Fetal Bovine Serum Qualified (FBS) (500 mL), Penicillin-Streptomycin (P/S) ([+]10000 Units/mL Penicillin, [+]10000 µg/mL Streptomycin) (100 mL), L-Glutamine 2 mM (100 mL), Hank's Balanced Salt Solution (HBSS) (500 mL) and 0.05% Trypsin 1X-EDTA (500 mL) were from Gibco (Life-Technologies). The Phosphate-Buffered Saline 1X (PBS) (pH= 7.2) (500 mL) was prepared in the laboratory.

The pEGFP-Luc plasmid sequence was a kind donation by the group of Prof. Anxo Vidal (CiMUS, Universidad de Santiago de Compostela), and it was produced by the PureLink HiPure Expi Plasmid Gigaprep Kit was from Invitrogen. The Cy5-modified siRNA were purchased from Eurofins MWG Operon.

3.2.2. Formulation of protamine NCs

Pr NCs were formulated by a solvent-displacement method as described in previous works of our group [39] [45]. The stock solutions of protamine and cholic acid sodium salt were prepared in Milli-Q water at 0.5 mg/mL and 250 mg/mL, respectively. The vitamin E and tween-80 were dissolved in ethanol at 133.34 mg/mL and 21.34 mg/mL, respectively. The organic phase was prepared with 0.375 mL of vitamin E, 0.375 mL of tween-80, 0.016 mL of cholic acid sodium salt and 4.25 mL of acetone. After complete mixing, the organic phase was added to the aqueous phase composed by 10 mL of protamine, and heterogeneous phase was stirred for 10 min at room temperature (RT). The organic solvent was evaporated using a rotavapor (Rotavapor® R-300, BÜCHI) to get a final volume of 5 mL of aqueous NC suspension. The formulation was centrifuged using an ultracentrifuge Beckman Coulter (Optima™ L-90K Ultracentrifuge) for 1 h at 30,000 revolution per minute (rpm) at 15 ºC. Finally, the purified Pr NCs forming a cream were separated and resuspended in 5 mL of Milli-Q water obtaining a final concentration of 13.4 mg/mL.

3.2.3. Morphological and physicochemical characterization of protamine NCs

The NCs were characterized with respect to particle size, polydispersity index (PDI) and surface charge (zeta potential). The particle size and PDI of blank Pr NCs diluted in Milli-Q water (1:10 (*v/v*)) were characterized by Photon Correlation Spectroscopy (PCS) and the zeta potential was measured by Laser Doppler Anemometry (LDA) using the Zetasizer Nano-ZS™ (Malvern Instruments) at 25 ºC with a detection angle of 173º. All measurements were done in triplicate. Morphology was analyzed by Scanning Transmission Electron Microscopy (STEM) and Field Emission Scanning Electron Microscopy (FESEM) (FESEM Ultra Plus, ZEISS, Germany) using a voltage of 20 kV and SE/InLens as detectors. For this purpose, a dilution of the formulation (1:100 (*v/v*)) in Milli-Q water was stained with 2% (*w/v*) phosphotungstic acid and deposited on a copper grid.

3.2.4. Nucleic acid association and release

To associate different nucleic acids, such as pDNA (pEGFP-Luc) and miRNA (miRNA-145), the formulation was first diluted to a final concentration of 9 mg/mL. Then, 0.2 mL of this dilution were mixed with 0.05 mL of a nucleic acids solution at theoretical loadings (1; 1.5 and 2.5% (*w/w*) of pDNA). The mixture was incubated under stirring for 1 h at RT. The association was determined by agarose gel electrophoresis at 1% (*w/v*) for pDNA and 2% (*w/v*) for miRNA using TAE buffer 1X. A maximum of 0.135 µg of pDNA and 1 µg of miRNA labelled with SYBR® Gold were loaded per lane. In addition, the same formulations were also incubated with an excess of heparin at 1 mg/mL (25-fold with respect to the amount of pDNA/miRNA) for 2 h at 37 ºC. The gel was run for 45 min in a Sub-Cell GT 96/192 (Bio-Rad Laboratories Ltd.) at 90 V. Gels were imaged using Molecular Imager® Gel Doc™ XR$^+$ System (UV light 302; Bio-Rad). The same protocol was followed in the case of Pr NCs loaded with 1% and 2.5% (*w/w*) of pDNA, and incubated in simulated lacrimal fluid (SLF) at 37 ºC at different time points (t= 0 h, 30 min, and 4 h).

3.2.5. Stability of blank and loaded protamine NCs

First, the stability of blank and nucleic acid-loaded Pr NCs (1% and 2.5% (*w/w*) of pDNA) stored as aqueous suspension for one month at 4 ºC (dilution 1:10 (*v/v*)) was evaluated. The stability of the formulation was also evaluated in RPMI medium with/out 10% (*v/v*) FBS and 1% (*v/v*) of P/S, at 37 ºC and under horizontal shaking at 300 rpm, for a total time of

4 h. In addition, the NCs loaded with 1% and 2.5% (*w/w*) of pDNA were also analyzed in SLF at pH= 7.4 (0.18% KCl, 0.63% NaCl, 0,006% $CaCl_2$ $2{\cdot}H_2O$ and 0,01% $MgCl_2$) as relevant biological medium, also for 4 h. The size, PDI, zeta potential and derived count rate (DCR) were determined as described in the section 3.2.3. The measurements were done in triplicate.

3.2.6. Cell culture

The bi-dimensional (2D) *in vitro* assays were performed in a UM cell line donated by the Nano-Oncology and Translational Therapeutics Group and Obesidomics Group (Fundación Instituto de Instituto de Investigación Sanitaria de Santiago de Compostela (IDIS), Hospital Clínico Universitario de Santiago (CHUS)). The cells were cultured in RPMI medium supplemented with 10% (*v/v*) of FBS and 1% (*v/v*) of P/S at 37 ºC with 5% of CO_2 and 95% of relative humidity (Memmert INCO 2, (I.C.T, S.L.)).

The three-dimensional (3D) *in vitro* assays were performed in collaboration with the Laboratory of Cellular Biology and Innervation of the Ocular Surface (Fundación de Investigación Oftalmológica (FIO), Instituto Universitario Fernández-Vega, University of Oviedo) in a 3D Reconstructed human Corneal Epithelium (RhCE, described in section 3.2.6.1.). All cell strains used for the 3D model were derived from corneal donor rims specimens obtained after isolation of the central corneal button for transplantation. They were grown in QN medium composed by DMEM:F12, 10% (*v/v*) FBS, 5 mg/mL of insulin, 0.4 mg/mL of hydrocortisone, 1.3 ng/mL of triiodothyronine, 24 mg/mL of adenine, L-Glutamine 2 mM, and 1% (*v/v*) antibiotic mix, and cultured at 37 ºC with 5% of CO_2 and 95% of relative humidity (Thermo Scientific). All cells were screened for bacteria, yeast, and fungi. All tissue donors were also tested negative for HIV and hepatitis B and C. Cells from different donors were not pooled together.

3.2.6.1. Generation of 3D corneal model

The QobuR-RhCE model is constituted by human corneal epithelial cells that form a stratified squamous cellular superstructure resembling a healthy human corneal epithelium [46, 47]. Briefly, $5x10^4$ corneal-limbal primary epithelial cells/cm^2 were seeded in polycarbonate 12-well transwell inserts (Corning) and placed in 12-well cultures plates (Sarstedt). The cells were cultured in absence of feeder cells using the QN medium optimized for the expansion of the epithelial cells without 10% (*v/v*) FBS. To promote 3D differentiation, the models were cultured at the air-liquid interface for 7-10 days until TEER values were between 750-2,500 Ωcm^2 based on historical data on model production [48].

3.2.7. *In vitro* cytotoxicity studies

In order to study the effect of blank Pr NCs on cell viability, the CellTiter-Blue® Cell Viability Assay was performed using resazurin as a viability reagent. A total amount of $3x10^3$ of UM cells/well were seeded in 96-well plates (Costar, Corning Incorporated) in a final volume of 0.100 mL of supplemented RPMI cell culture medium incubating them during 72 h at 37 ºC. At this point, seven concentrations of blank Pr NCs (1.34, 0.67, 0.34, 0.17, 0.09, 0.05 and 0.03 mg/mL) were tested using a dilution of 1:10 (*v/v*) in supplemented RPMI medium. Sterile filtered Milli-Q water was used as positive control and 1% (*v/v*) triton-X100 was used as negative control. The incubation with NCs and controls was for 4 h at 37 ºC. After that time, the cells were washed with 0.100 mL of PBS 1X and incubated in fresh supplemented medium for 24 h and 48 h and then, 0.02 mL of CellTiter-Blue® Cell Viability was added incubating the cells for 3 h at 37 ºC covering the plate with aluminum foil. The conversion of resazurin to

resorufin was stopped by adding 0.05 mL of SDS 3% (*w/v*) incubating for 30 min at 37 ºC. Fluorescence signal was measured at 539 nm of excitation wavelength (λ_{Ex}) and 620 nm of emission wavelength (λ_{Em}) in a Synergy H1 microplate reader (Biotek) by Gen 5 Software in black 96-well plates (BrandPlates® pure Grade, Brand). The percentage of viability was calculated as follows:

$$Cell\ viability\ (\%) = \frac{Sample\ Fluorescence}{Control\ cells\ Fluorescence}\ x\ 100 \qquad (1)$$

3.2.8. Cellular uptake

To study the NC-internalization, protamine was labelled with the fluorescent reagent 5-TAMRA following the same protocol described in section 1.2.8.1. of Chapter I, and fluorescent protamine was used at 1 mg/mL of concentration. The uptake study of this nanosystem in UM cells was qualitatively analyzed by CSLM (Leica TCS SP5 X, Leica Microsystems, GmB) and quantitatively by flow cytometry (BD Accuri™ C6 Flow Cytometer).

For confocal microscopy, $4.5x10^4$ UM cells/well were seeded in 24-well plates (Falcon), using 12 mm diameter glass round Poly-L-Lysine coated coverslips (Corning, BioCat™) in a final volume of 1 mL of supplemented RPMI medium. The cells were incubated for 24 h at 37 ºC before the experiment. The culture medium was replaced with 54 µg/cm^2 of Pr-TAMRA NCs in a final volume of 0.4 mL of fresh supplemented cell culture medium incubating for 4 h at 37 ºC. Untreated cells were used as negative control. After this, cells were fixed using commercial 10% (*v/v*) neutral buffered formalin (0.350 mL) incubating for 15 min under horizontal agitation (Rocker, VWR) at RT. Then, a dilution 1:1000 (*v/v*) of DAPI (stock concentration: 1 mg/mL in PBS 1X) was added and incubated for 30 min, and, finally, the coverslips were placed on slides (Menzel-Gläser, Thermo Scientific) using fluoromount® aqueous mounting medium to their visualization in confocal microscope (magnification 20x, z1.25) ($\lambda_{Ex}/\lambda_{Em}$ (DAPI) = 358/461 nm and ($\lambda_{Ex}/\lambda_{Em}$ (5-TAMRA) = 543/578 nm) by the LAS X Life Science Software.

For flow cytometry, cells incubated with Pr-TAMRA NCs were treated with 0.2 mL of LIVE/DEAD™ Fixable Aqua Dead Cell Stain reagent diluted in PBS 1X buffer. Cells were incubated with this reagent for 15 min under horizontal agitation at RT. After washing, the cells were detached using 0.05% Trypsin 1X-EDTA for 5 min at 37 ºC and were centrifuged (Centrifuge 5430R, Eppendorf) for 5 min at 200 RCF at 22 ºC obtaining a pellet which was resuspended in 0.5 mL of PBS 1X buffer supplemented with 10% FBS (*v/v*). Finally, a maximum of 10,000 events were excited at 488 nm using filters BP 575/25 for 5-TAMRA, and at 405 nm using filters BP 515/20 for Aqua. Results were analyzed by BD CSample Software (BD Biosciences, CA).

3.2.9. Transfection assay in uveal melanoma cells

The plasmid encoding the Enhanced Green Fluorescent Protein (EGFP) and Luciferase protein (Luc) (pEGFP-Luc) was used for transfection studies. In this case, 2.5% of pDNA, with respect to the total mass of NCs was selected for the transfection studies.

A total amount of $4.5x10^4$ UM cells/well were seeded in 24-well plates (Falcon) in a final volume of 1 mL of supplemented RPMI medium. After 24 h, the cells were treated with: (i) 0.5, 1 and 2.5 µg of pDNA/well, (ii) naked pEGFP-Luc (negative control), and (iii) Lipofectamine® 2000 reagent prepared under the specifications of the commercial protocol (positive control) in a final volume of 0.2 mL of non-supplemented Opti-MEM, incubating for

4 h at 37 ºC. After removal of the NCs and the corresponding washes, 1 mL of fresh supplemented RPMI medium was added and the cells were incubated again for 24 h and 48 h. EGFP expression was observed by fluorescence microscopy using the Thunder microscope (Leica Microsystems, GmB) and the LAS X Life Science Software. For flow cytometry, the cells were detached using 0.120 mL of 0.05% Trypsin 1X-EDTA for 5 min at 37 ºC and then, the enzyme was deactivated using 0.280 mL of supplemented cell culture medium. Finally, the cells were centrifuged (Centrifuge 5430R, Eppendorf) for 5 min at 200 RCF at 22 ºC obtaining a pellet, which was resuspended in 0.5 mL of PBS 1X buffer supplemented with 10% FBS (*v/v*). A maximum of 10,000 events were excited at 488 nm using the filter BP 525/50 for EGFP and they were analyzed by BD CSample Software (BD Biosciences, CA).

3.2.10. Permeability assay in 3D inserts

TEER was measured using a pair of Ag/AgCl chopstick electrodes connected to a Millicell ERS-2 epithelial volt-ohm meter (Millipore). For this purpose, the inserts containing day-10 QobuR-RhCE models were washed with HBSS medium, and the TEER was measured before adding samples to obtain initial basal resistance. Three TEER registers were obtained for each measurement. Then, the QobuR-RhCE inserts were treated with 0.3 mL of (i) sterile distilled water (H_2Od) as negative control of barrier disruption, (ii) methyl acetate as positive control of barrier disruption, (iii) Pr-TAMRA NCs (13.4 mg/mL) and, (iv) Pr NCs associated with 2.5% (*w/w*) of pDNA (2.5 µg of pDNA/insert). The controls and samples were incubated for 4 h at 37 ºC. After this time, the QobuR-RhCE models were washed with HBSS medium, and the TEER of each sample was again measured to obtain final resistance. Measurements were corrected against the values obtained for the empty control wells. The percentage of the TEER was calculated as follows:

$$Permeability - TEER\ (\%) = \frac{post - treatment\ TEER}{pre - treatment\ TEER}\ x\ 100 \qquad (2)$$

3.2.10.1. Histological and immunohistochemical analysis

A complementary assay to analyze the morphology and integrity of the epithelial barrier in the QobuR-RhCE models with respect to the permeability of Pr-TAMRA NCs and Pr NCs associated with 2.5% (*w/w*) of pDNA was carried out by immunofluorescence detection.

For this purpose, after 4 h, the insert membranes carrying the QobuR-RhCE with samples and controls were fixed by immersion in 4% (*w/v*) buffered paraformaldehyde for 1 h at RT, cryoprotected in 30% (*w/v*) sucrose, embedded in Optimum Cutting Temperature compound (OCT) (Tissue-Teck®) and snap frozen in liquid nitrogen. Transversal sections of 5 µm were obtained with the help of a cryostat microtome (Microm HM550 cryostat, Microm International GmbH) and they were collected in microscope slides (Thermo Scientific). The fluorescence technique was carried out as follows: these sections of 5 µm were stained with Mayer's Hematoxylin solution and Eosin Y for general histology evaluation. After that, equivalent samples were incubated overnight with a dilution 1:200 (*v/v*) of Rabbit monoclonal antibody to β-catenin, and revealed with a complementary Alexa Fluor 594 Goat anti-rabbit secondary antibody (dilution 1:200 (*v/v*)). Cell nuclei were counterstained with a solution of DAPI at 2 µg/mL. The terminal deoxynucleotidyl transferase (TUNEL) histochemical assay was performed according to the manufacturer's instructions to visualize cells undergoing apoptosis (In Situ Cell Death Detection Kit, Tetramethylrhodamine, Roche Diagnostics GmbH). Finally, the sections were examined under Leica DM 6000 fluorescence microscope by the LAS X Life

Science Software (Leica Microsystems GmbH) ($\lambda_{Ex}/\lambda_{Em}$ (DAPI) = 358/463 nm using excitation filter 360 nm, ($\lambda_{Ex}/\lambda_{Em}$ (Alexa Fluor 594) = 590/617 nm using excitation filter 560 nm, $\lambda_{Ex}/\lambda_{Em}$ (tetramethylrhodamine) = 540/580 nm using excitation filter 560 nm, magnification 40x). If the samples were not observed at the time, they were stored at -20ºC.

3.2.11. Statistical analysis

Results were statistically evaluated by two-way ANOVA followed by Tukey's method, if not stated otherwise. All statistical analyses were conducted using GraphPad Prism Software (version 8.0 for windows). A *p* value < 0.05 was considered to be significant (* p< 0.05; ** p< 0.01; *** p< 0.001; **** p< 0.0001). Each experiment was performed independently three times in triplicate, if not stated otherwise.

3.3. RESULTS AND DISCUSSION

3.3.1. Physicochemical characterization of protamine NCs

Pr NCs were prepared using a solvent-displacement method optimized by our research group [16] [39] [44] [49, 50]. The addition of the oily phase to the aqueous phase under stirring precipitates the lipid components as the polar solvent diffuses into the aqueous phase. The cationic polymer interacts electrostatically with the oil nanodroplet forming a polymeric shell surrounding them [51]. In this work, the NCs were composed by a hydrophobic oily core of vitamin E, which is reported to present beneficial effects on corneal wound healing [27]. Protamine was selected for its cell penetrating properties [39]. Tween-80 was selected as non-ionic surfactant to disperse the oil in the external aqueous phase, and to prevent the particle aggregation [43]. Cholic acid sodium salt was selected as co-surfactant due to their penetration enhancing properties [44]. The formulation was composed of a homogeneous population of blank particles with a size below 250 nm, low PDI, and positive surface charge (Table 1.). Regarding their morphological characteristics, STEM images showed a formulation composed by individual particles with spherical shape (Figure 1.).

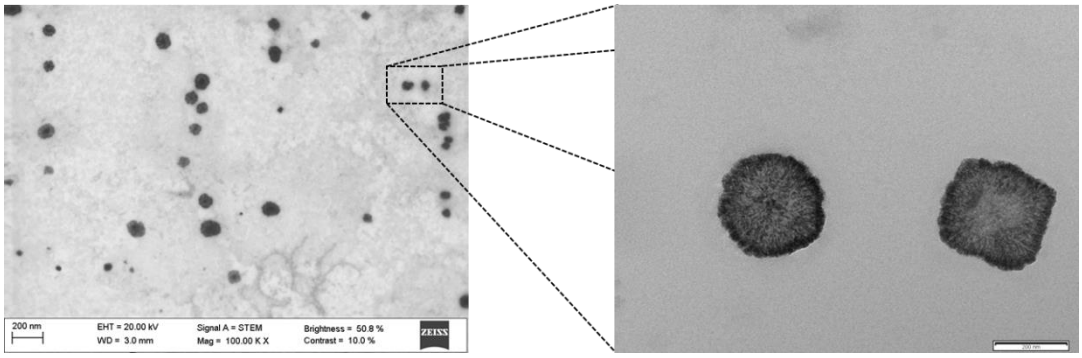

Figure 1. STEM images of blank Pr NCs formulated with tween-80 as surfactant (scale bar= 200 nm).

pEGFP-Luc and miRNA-145 were associated to Pr NCs, selecting 1% and 2.5% (*w/w*) of pDNA payload, and 1.5% (*w/w*) of miRNA payload, with respect to the total mass of the NCs. The results collected in Table 1. showed a slight increase in the size of loaded NCs compared to blank. This could be explained by a rearrangement of the polymeric protamine shell upon the incorporation of the nucleic acids. For the same reason, important changes in the surface charge of formulation were observed. The NCs loaded with both pDNA, and miRNA acquired negative zeta potential, indicating the surface association of both nucleic acids. In the case of plasmid DNA, the surface charge became increasingly negative as more pDNA was associated: -31 mV with 1% of pDNA and -42 mV with 2.5% (*w/w*) of pDNA.

Table 1. Mean particle size, polydispersity index (PDI) and zeta potential of blank Pr NCs, and loaded with 1% and 2.5% (*w/w*) of pDNA and 1.5% (*w/w*) of miRNA, respect to the total mass of the NCs (Mean ± SEM (n= 3)).

Pr NCs	Size (nm)	PDI	Zeta potential (mV)
Unloaded	242 ± 40	0.121	+33 ± 11
1% (*w/w*) of pDNA	345 ± 39	0.260	-31 ± 4
2.5% (*w/w*) of pDNA	337 ± 31	0.227	-42 ± 3
1.5% (*w/w*) of miRNA	274 ± 48	0.097	-15 ± 3

The STEM and FESEM images of pDNA-loaded NCs also showed a homogenous population of spherical particles (Figure 2.).

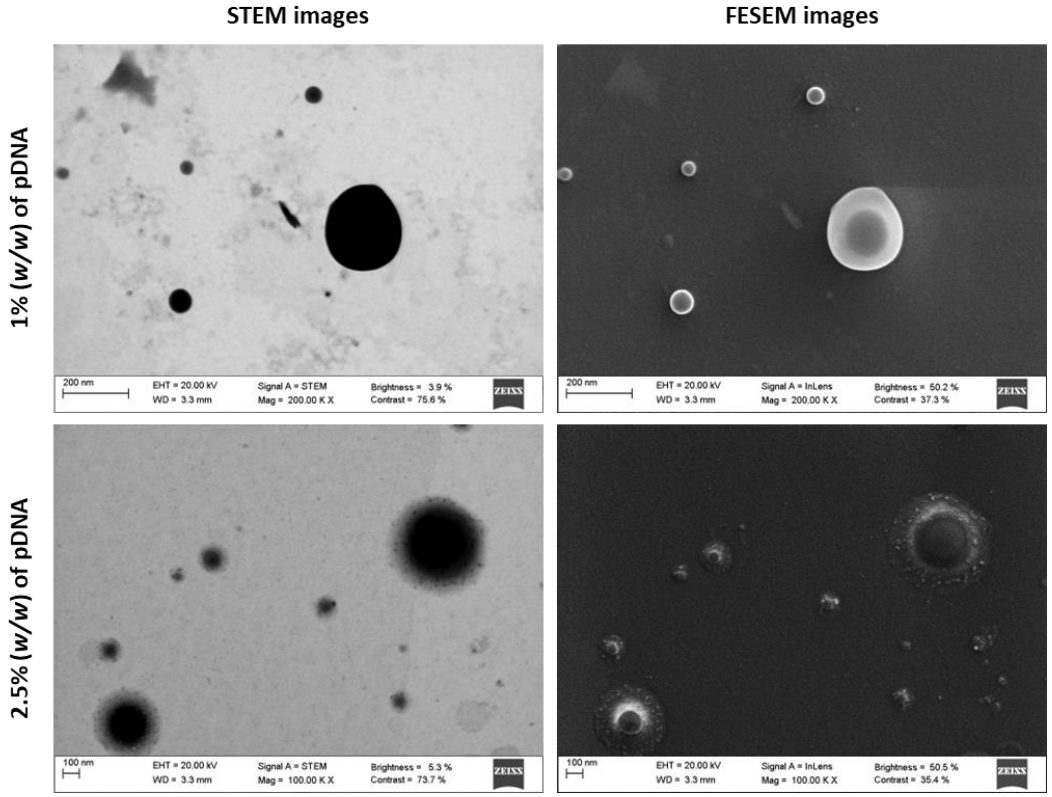

Figure 2. STEM and FESEM images of Pr NCs associated with 1% and 2.5% (*w*/*w*) of pDNA, respect to the total mass of the NCs (scale bar= 100 and 200 nm).

The nucleic acid association was analyzed by agarose gel electrophoresis in the presence/absence of heparin. As mentioned in section 1.3.1. of Chapter I, heparin is a sulfated glycosaminoglycan with strong negative charge and high affinity for protamine, and was used here as a competitor to displace the polynucleotides from their binding with the NCs [52]. After 2 h of incubation at 37 ºC, a band for pDNA could be observed for NCs with the two loadings (Figure 3.). This band was more marked when heparin was incubated with the NCs (lane 2), suggesting partial association of pDNA to the NCs, and the release of the encapsulated polynucleotide in the presence of a competitor. Comparing the association between both types of nucleic acids, a greater efficiency was observed for miRNA than for pDNA. miRNAs are short-stranded RNA, approximately 22 nucleotides in length, much shorter than plasmids [53], which allowed a larger number of them establish stronger interactions with the outer polymeric shell and part of them could encapsulate between the polymer and the oily core.

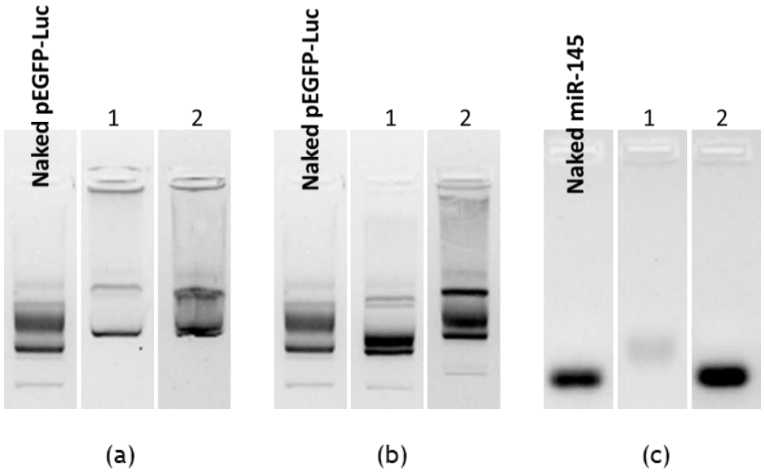

Figure 3. Agarose gel images of blank Pr NCs loaded with (**a**) 1% (*w*/*w*) and (**b**) 2.5% (*w*/*w*) of pDNA, and (**c**) 1.5% (*w*/*w*) of miRNA, respect to the total mass of the NCs (lane 1). The amount of nucleic acids per lane was 0.135 µg in pDNA and 1 µg in miRNA. The Pr NCs were incubated with heparin 2 h at 37 ºC using the mass ratio 1:25 (*w*/*w*) heparin:nucleic acid (lane 2).

3.3.2. Stability of protamine NCs

3.3.2.1. Stability at storage conditions

In the present work, the stability of blank and nucleic acid-loaded Pr NCs was analyzed for 30 days at 4 ºC. Figure 4. showed that size and PDI, the surface charge, and the count-rate of the blank formulation remained constant under these conditions. In the NCs associated with 1% and 2.5% (*w/w*) of pDNA, similar results were observed.

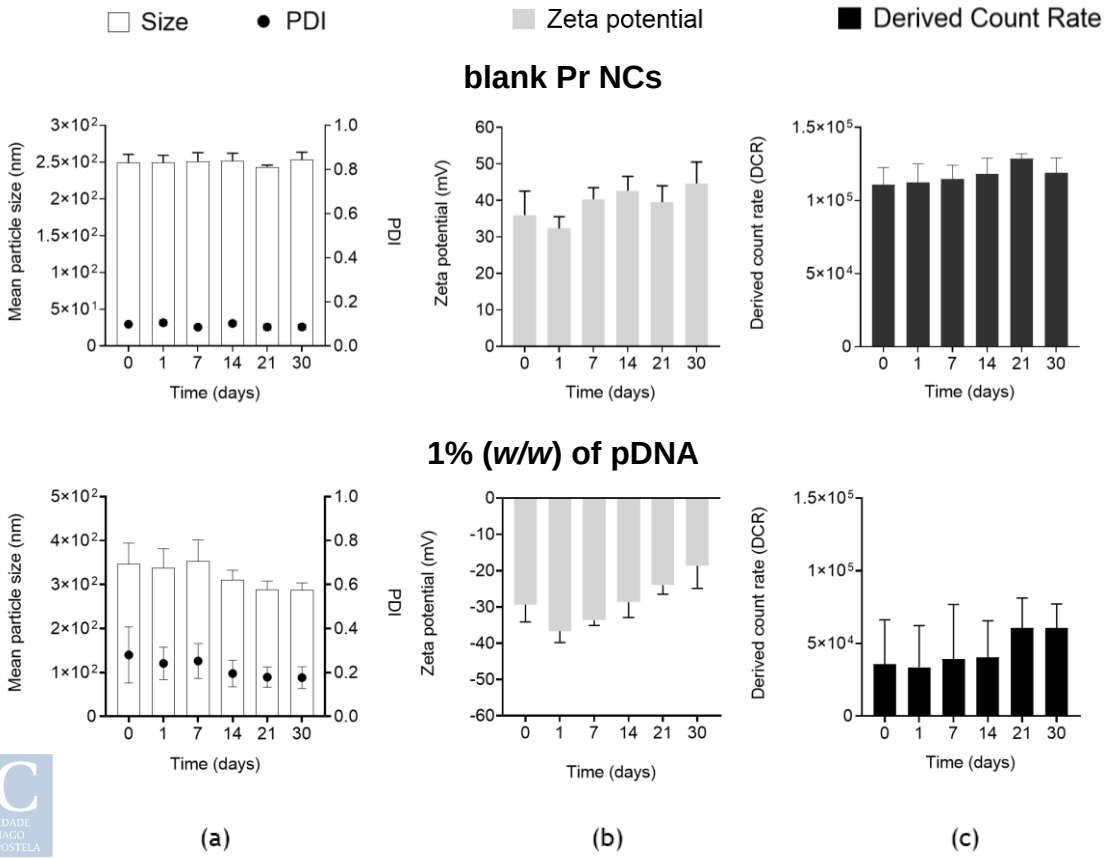

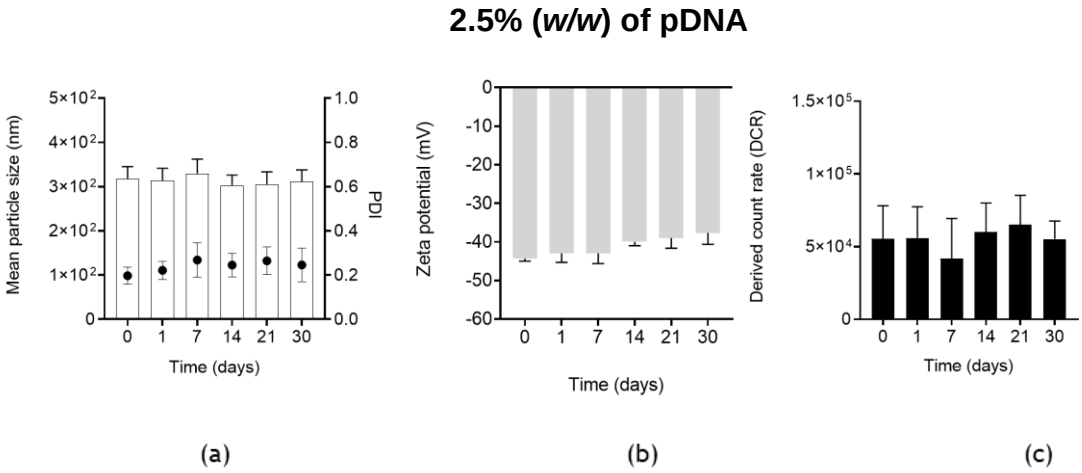

Figure 4. Stability of aqueous suspensions of blank Pr NCs and loaded with 1% and 2.5% (*w*/*w*) of pDNA, respect to the total mass of NCs, measuring the (**a**) particle size and polydispersity index (PDI), (**b**) zeta potential, and (**c**) derived count rate (DCR) at storage conditions for 30 days (Mean ± SEM (n= 3)).

3.3.2.2. Stability in cell culture medium

To determine the feasibility of the formulations for *in vitro* testing, the stability of Pr NCs was studied in cell culture medium. Blank Pr NCs experienced a slight increase in the size due to the loss of charge-induced stability in buffered media, causing the aggregation of the particles (Figure 5. (a)). However, the presence of FBS helped to control this aggregation process, probably thanks to the adsorption of proteins on the surface of the NCs that would render the surface of the nanocarrier more stable. When NPs aggregate not only their size increases, but the number of particles in suspension is reduced. As expected, a decrease in the DCR values was observed in culture media confirming the aggregation and possible precipitation of these particles (Figure 5. (b)). Regarding the stability of nucleic acid-loaded NCs, the results were similar to blank Pr NCs, but better colloidal stability was observed for Pr NCs loaded with 2.5% (*w*/*w*) of pDNA.

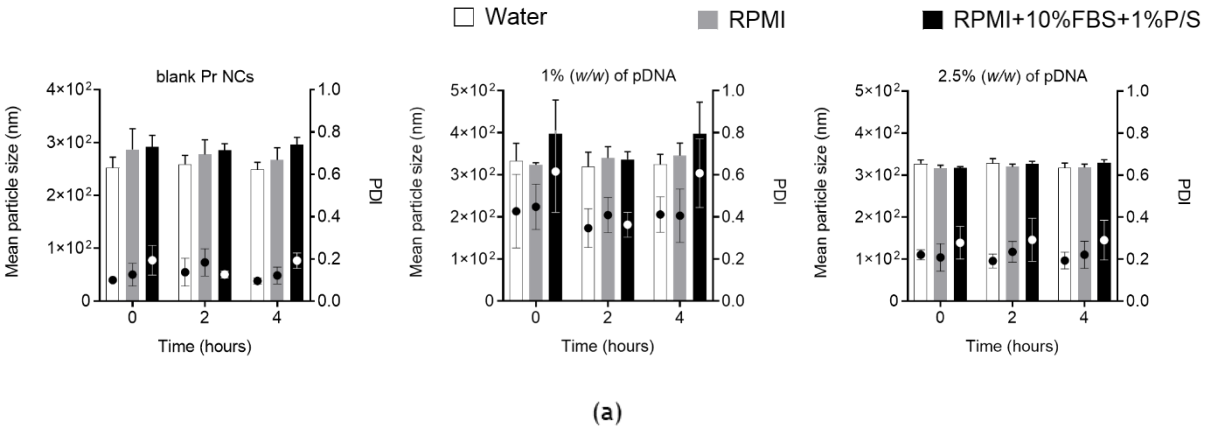

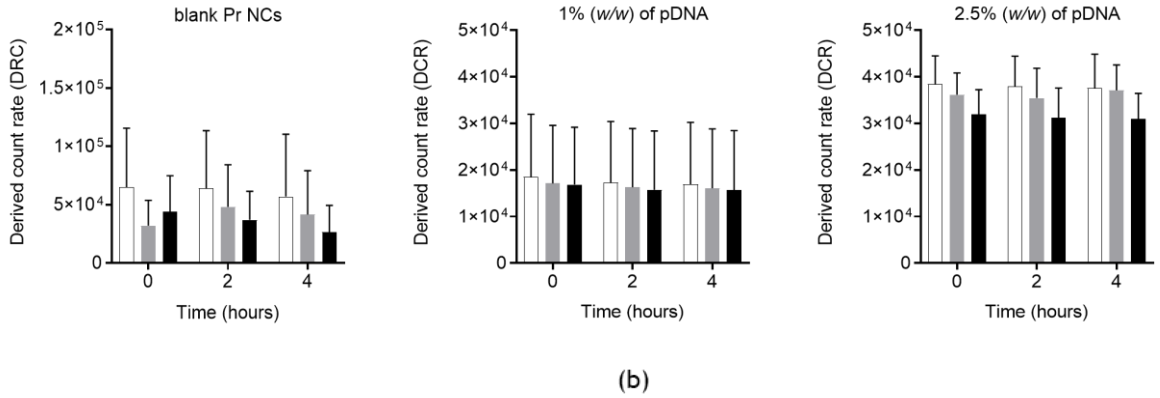

Figure 5. Stability of blank and loaded Pr NCs with 1% and 2.5% (*w*/*w*) of pDNA, respect to the total mass of NCs, measuring the (**a**) particle size (bars) and polydispersity index (PDI) (dots) and (**b**) derived count rate (DCR) at 37 ºC for 0, 2 and 4 h in supplemented and non-supplemented RPMI cell culture medium (Mean ± SEM (n= 3)).

3.3.2.3. Stability in simulated lacrimal fluid

Considering the envisaged administration route, the stability of Pr NCs associated with different percentages of plasmid was studied in SLF at different time points (0 h, 30 min, and 4 h) at 37 ºC [54]. Figure 6. (a) showed that the size of Pr NCs associated with pDNA experienced a slight increase in this medium, and this was most noticeable with 1% (*w/w*) of pDNA. As previously mentioned in section 3.3.2.2., this effect together with the decrease in the DCR (Supporting information: Figure S2.) indicated a mild aggregation process. However, we consider that *in vivo* contact times will be much shorter than the 4 hours investigated herein.

Regarding the plasmid association and release, Figure 6. (b) showed an effective and reversible binding of the genetic material (lane 1), releasing pDNA in intact form (lane 2) [55]. Association was most effective in the 1% (*w/w*) of pDNA formulation. We also observed that, in the 2.5% (*w/w*) of pDNA formulation, bands were less intense at 4 h than at the other time points. This could be due to pDNA not being completely associated with the NCs, which could result in partial degradation over time. pDNA that was associated remained intact during this time.

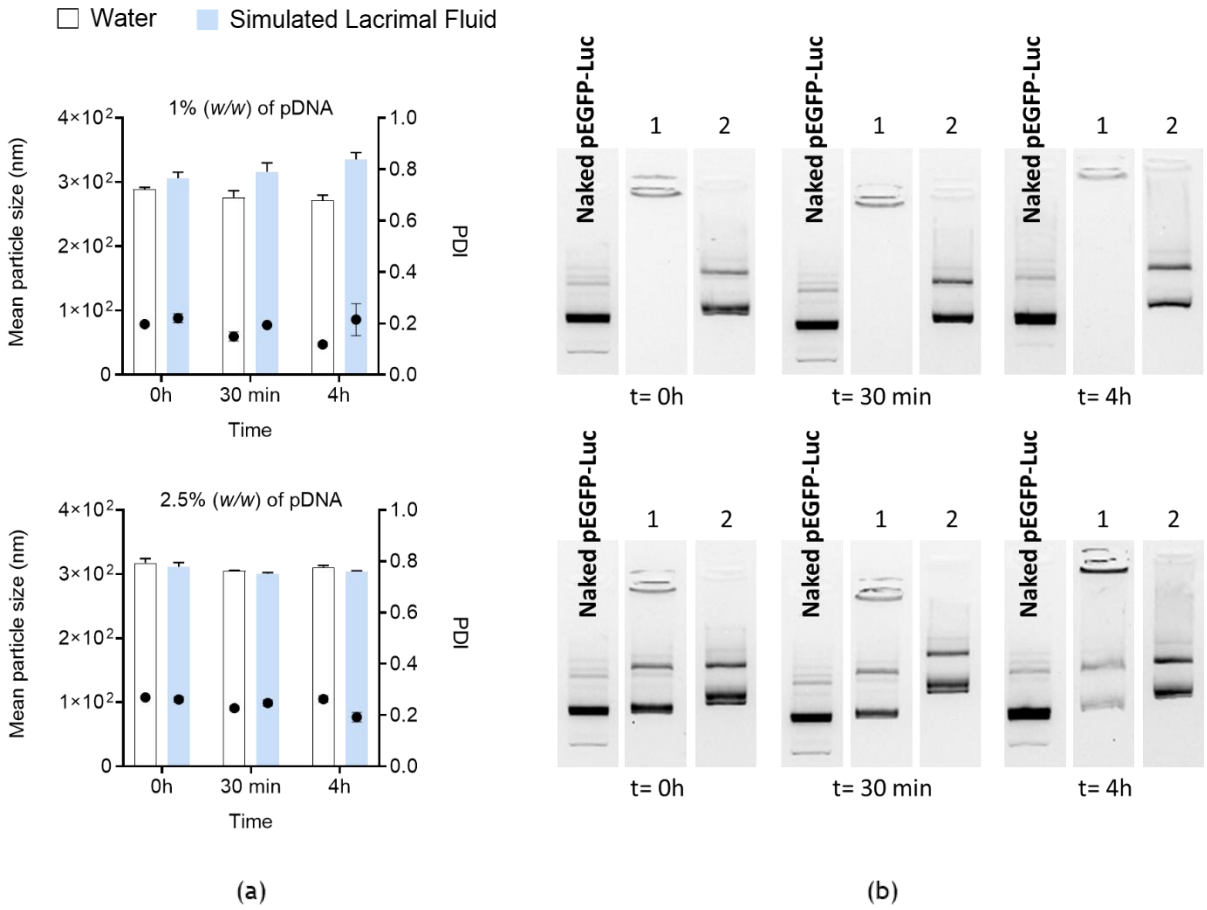

Figure 6. (**a**) Stability of loaded Pr NCs with 1% and 2.5% (*w*/*w*) of pDNA, respect to the total mass of NCs, measuring the particle size (bars) and polydispersity (PDI) (dots) at 37 ºC for 0 h, 30 min and 4 h in SLF (Mean ± SEM (n= 3)). (**b**) pDNA association evaluated by gel electrophoresis of Pr NCs loaded with 1% and 2.5% (*w*/*w*) of pDNA, respect to the total mass of the NCs, after incubation at 37 ºC for 0 h, 30 min and 4 h in SLF (lane 1). The amount of nucleic acids per lane was 0.135 μg in pDNA. The Pr NCs were incubated with heparin for 2 h at 37 ºC using the mass ratio 1:25 (*w*/*w*) heparin:nucleic acid (lane 2).

Overall, due to the results of NC stability, and those of the nucleic acid association, the formulation with 2.5% (*w*/*w*) of pDNA loading was selected for transfection assays.

3.3.3. Cell viability in uveal melanoma cells

As mentioned in previous chapters, cytotoxicity of nanocarriers is one of the most important factors limiting their medical application [56]. The physicochemical characteristics of the NCs such as size and surface charge, their hydrophobicity, and their supramolecular structure are parameters that define their biocompatibility and cellular interactions [57]. In the present work, the biocompatibility of Pr NCs was evaluated in UM cancer cells by a metabolic assay. Pr NCs did not compromise the cell viability neither at 24 h and 48 h post-incubation (Figure 7.). Indeed, metabolic activity values experienced a slight increase at 48 h, which might be as a consequence of cell growth.

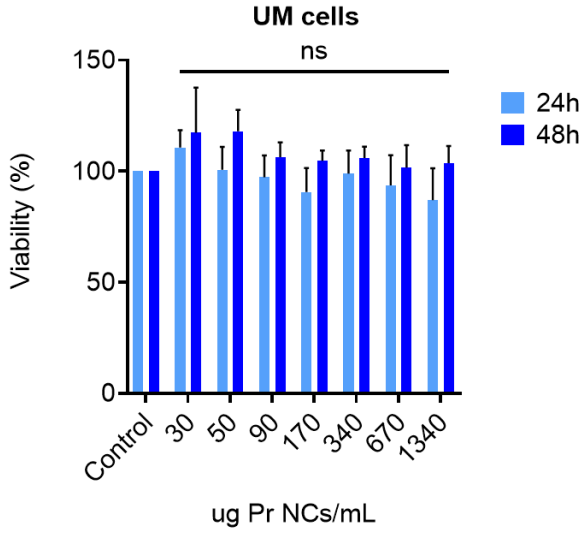

Figure 7. Cell viability assay after 24 h (light-blue bars) and 48 h (dark-blue bars) of the removal of increasing concentrations of blank Pr NCs from 30 to 1340 µg/mL in UM cancer cells (Mean ± SEM (n= 3)).

3.3.4. Uptake of protamine NCs in uveal melanoma cells

NCs were labelled with the fluorochrome 5-TAMRA to study their cellular internalization in UM cells (labelling method in Chapter I). The labelled NCs formulation presented similar physicochemical properties than the non-labelled one (Table 2.).

Table 2. Mean particle size, polydispersity index (PDI) and zeta potential of the original formulation of Pr NCs and labelled with 5-TAMRA (Mean ± SD (n= 3)).

Pr NCs	Size (nm)	PDI	Zeta Potential (mV)
Original	240 ± 40	0.121	+33 ± 11
5-TAMRA	230 ± 1	0.170	+26 ± 1

Cellular uptake was evaluated by confocal microscopy after 4 h. The maximum projection showed the intracellular localization of these Pr NCs in UM cells, a finding that could be verified by orthogonal sections on X and Y axes (Figure 8. (a)). As mentioned in previous chapters, physicochemical properties such as size, shape, and the surface charge have an important role in cellular uptake [58]. Depending on the particle size, nanocarriers can be internalized into cells following one of these six pathways: passive diffusion, phagocytosis, macropinocytosis, clathrin- or caveolin-mediated endocytosis, and clathrin- and caveolin-independent endocytosis [59]. In particles between 250 nm and 3 µm, the predominant intracellular route is the macropinocytosis, which could be the one followed by Pr NCs [60, 61]. In addition, positively charged NCs have greater internalization compared to neutral and negatively charged ones, although studies have shown that they have a greater tendency to alter the integrity of the cell membrane and, therefore, to present cytotoxicity [58]. The efficient internalization of Pr NCs might also be related to the penetration enhancing properties of protamine [62]. As mentioned previously, this peptide presents high content of arginine residues, where six of them constitute the nuclear localization signal (NLS) [63, 64]. This means that protamine has a crucial role in the process of cellular internalization [65], and in the translocation of molecules from the cytoplasm to nucleus. In addition, positively charged

proteins, such as protamine, may enter cells through multiple pathways including macropinocytosis [66].

To provide a quantitative evaluation, the uptake of the NCs was also analyzed by flow cytometry in living cell using the LIVE/DEAD™ Fixable Aqua Dead Cell Stain reagent. After cell incubation with the Pr-TAMRA NCs, the histograms corresponding to the fluorescence signal of 5-TAMRA showed a shift towards the 5-TAMRA (+) region compared to the control (unstained cells) (Figure 8. (b) and Supporting information: Figure S2.). This indicated that almost 36% of UM cells were positive for the presence of these NCs (Supporting information: Table S1.). In addition, there was high cell viability, as indicated by the peak corresponding to the fluorescence signal of Aqua mostly in the live region.

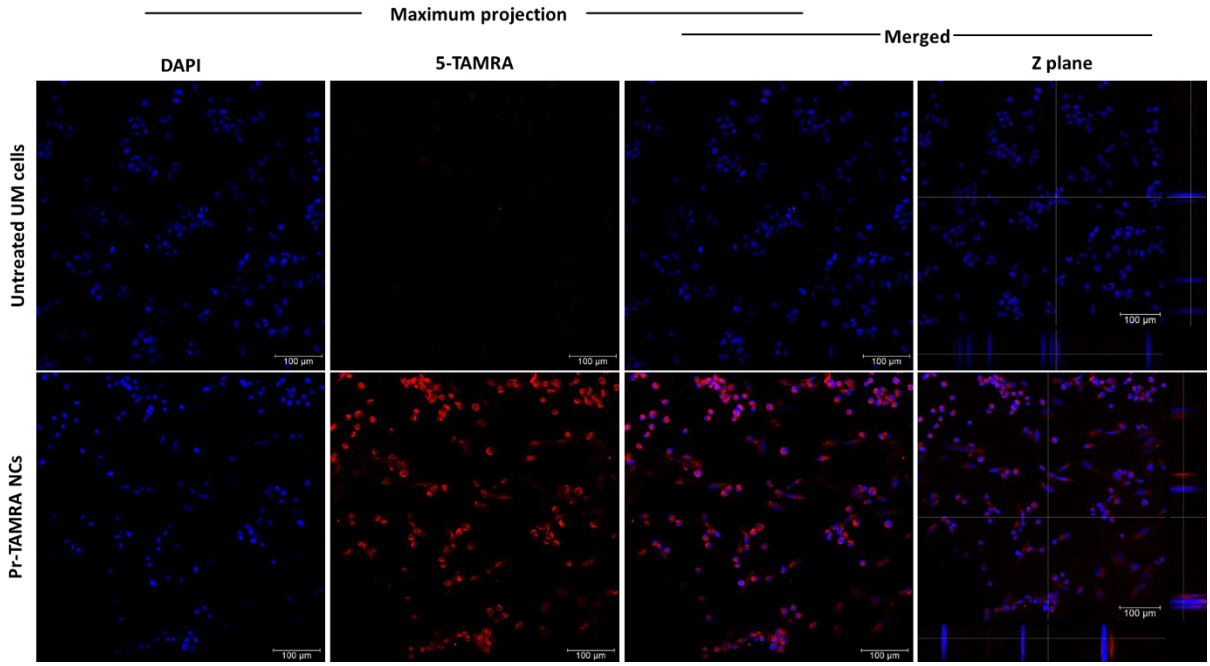

(a)

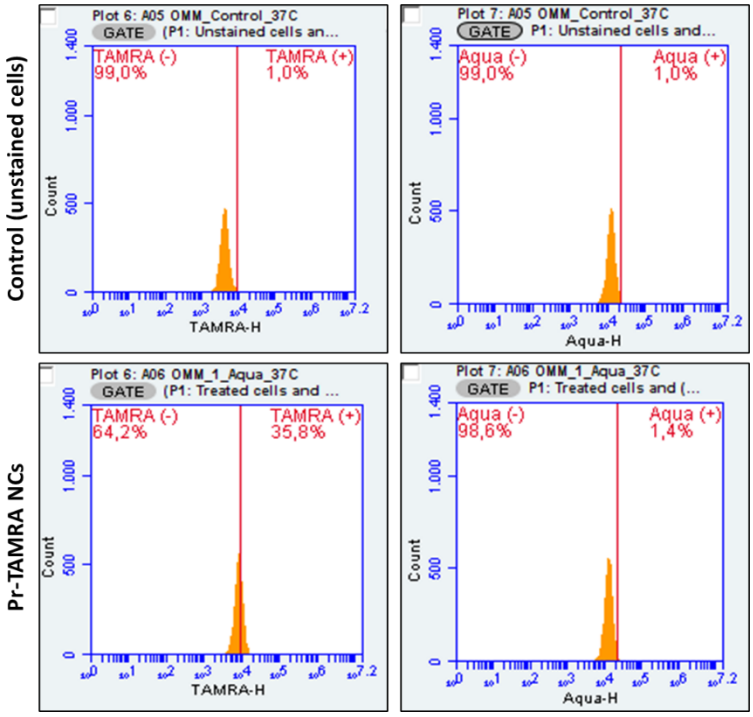

(b)

Figure 8. (**a**) Representative confocal microscopy images of NC-uptake in UM cells (magnification 20x, z1.25, scale bar= 100 µm) treated with 54 µg/cm^2 of fluorescently labelled NCs (red channel) incubated for 4 h at 37 ºC. Nuclei of the cells were stained with DAPI (blue channel). (**b**) Flow cytometry histograms to quantify the uptake of fluorescently Pr-TAMRA NCs (54 µg/cm^2) in UM cells after 4 h post-treatment (LIVE/DEAD™ Fixable Aqua Dead Cell Stain as a viability reagent).

3.3.5. Transfection studies of protamine NCs

The plasmid encoding the EGFP was also used to analyze the transfection capacity of Pr NCs in the UM cell line. The expression of this protein was qualitatively analyzed by fluorescence microscopy after 48 h of the removal of the Pr NCs, where the images showed small green bright spots in the cytoplasm, close to the cell nucleus (Figure 9.).

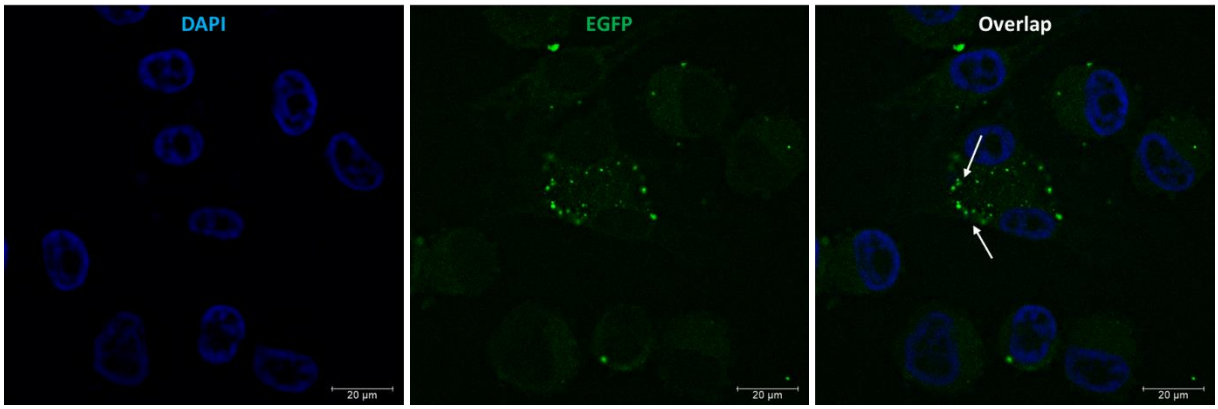

Figure 9. Fluorescent microscopy images of EGFP expression (green channel) after 48 h of the treatment of Pr NCs loaded with 1.5% (*w*/*w*) of pDNA at dose 2.5 µg of pDNA incubated for 4 h at 37 ºC (scale bar= 20 µm).

Additionally, EGFP expression was quantitatively analyzed by flow cytometry measuring the fluorescence-positive events corresponding to cells treated with Pr NCs associated with

2.5% (*w/w*) of pDNA in comparison with those treated with naked plasmid and non-treated (unstained cells). The graphics collected in Figure 10., corresponding to the percentage of EGFP-positive cells, showed the transfection capacity of Pr NCs. At 48 h after exposure to the transfection vehicles, Pr NCs showed higher expression than the naked plasmid. However, the percentages were still low compared to those obtained with the commercial reagent Lipofectamine® 2000. To conclude, further studies will be necessary to optimize the transfection of these nanocarriers.

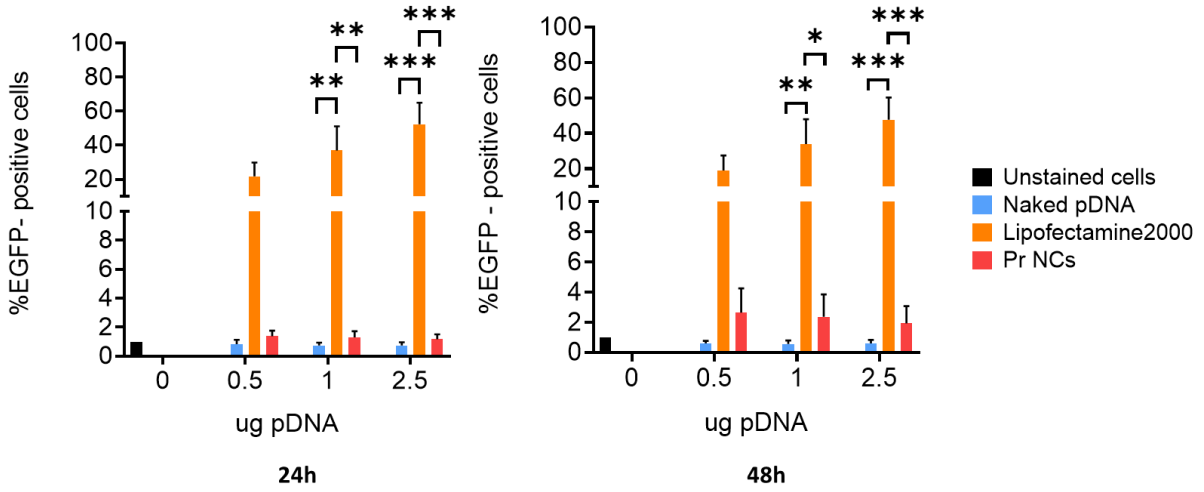

Figure 10. Quantification of EGFP expression by flow cytometry measuring the percentage of UM positive cells for the presence of this protein after 24 h and 48 h (Mean ± SEM (n= 3)).

3.3.6. Permeability assay in 3D corneal model

3.3.6.1. Transepithelial Electrical Resistance measurements

TEER measurement is the most widely used method to study the corneal permeability and the integrity of cell barriers [48]. Modifications in the membrane permeability are usually associated with a reduction in TEER values, which indicates an alteration of the ocular barrier due to the opening of tight junctions [67].

In the present work, TEER was measured in the QobuR-RhCE model before (blue bars) and after (green bars) the treatment with fluorescently labelled and plasmid-loaded Pr NCs. The graphic in Figure 11. (a-1) showed that Pr-TAMRA NCs produced a significant reduction in TEER at 4 h post-treatment. The reduction of approximately 53% in the TEER caused by the Pr-TAMRA NCs indicated the opening of tight junctions and the increased permeability of the NCs through the 3D corneal model, but not an irreversible alteration of the ocular barrier. However, the 3D corneal models treated with methyl acetate, the reduction in TEER was higher, approximately 89%, compared to the fluorescently labelled NCs. This drastic reduction in TEER was associated with the loss of the epithelial integrity in corneal models. Studies of Becker et al., described that TEER values of human corneas in the range of 500 Ωcm^2 could be due to alterations in the corneal epithelium [46] (Figure 11. (a-1, b-1)). Comparable results were obtained when QobuR-RhCE models were treated with pDNA-loaded Pr NCs (Figure 11.(b-1)), where the formulation also caused a reversible reduction in post-treatment TEER value (56%), which also indicated no alterations in the corneal epithelium as those treated with methyl acetate (93%) (Figure 11. (b-2)). Based on these results, both formulations could pass through the corneal barrier maintaining the cell integrity of the 3D corneal models.

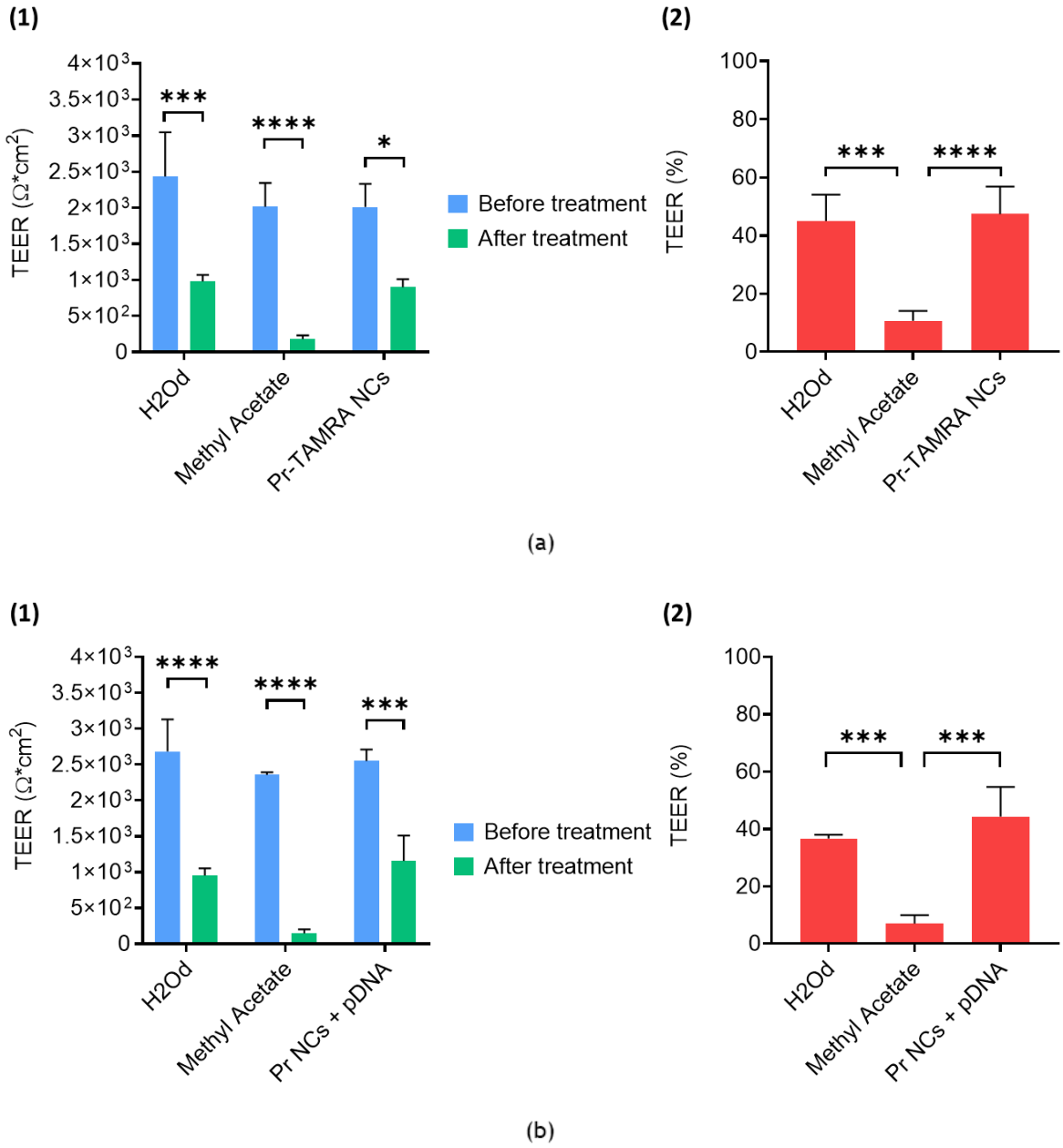

Figure 11. (**a**) Transepithelial electric resistance (TEER) of QobuR-RhCE models composed by normal human corneal epithelial cells exposed to 0.3 mL of Pr-TAMRA NCs (C= 13.4 mg/mL), and (**b**) Pr NCs associated with 2.5% (*w*/*w*) of pDNA, before and after 4 h of incubation at 37 ºC (Mean ± SEM (n= 3)). Graphics a-2 and b-2: differences were statistically evaluated by one-way ANOVA followed by Sidak's method.

3.3.6.2. Histology and immunohistochemistry

To further explore the interaction of Pr NCs with the epithelial barrier, a histology and immunohistochemical analysis of sections from QobuR-RhCE models were also carried out.

Figure 12. shows the images of the histological evaluation of QobuR-RhCE models after 4 h of treatment with controls and both formulations. The image (1), corresponding to the corneal model treated with H_2Od (negative control), showed a structure that faithfully represented a normal epithelium, with a basal layer formed by cells with cubic and/or cylindrical morphology, two or three layers of elongated cells (wing layer), and, in the upper zone, one or two layers of

flat and scaly cells (apical layer) [47]. The images corresponding to the 3D corneal models treated with Pr-TAMRA NCs (3) and Pr NCs associated with 2.5% (*w/w*) of pDNA (4), showed very similar general histological appearance to the negative control. Therefore, both formulations were capable of passing through the corneal model maintaining almost intact the integrity and morphology of the epithelial barrier, contrary to those treated with methyl acetate (positive control). In this case, the thickness of the epithelium was significantly reduced, formed by few layers of nuclei and a basal layer of flattened nuclei (2).

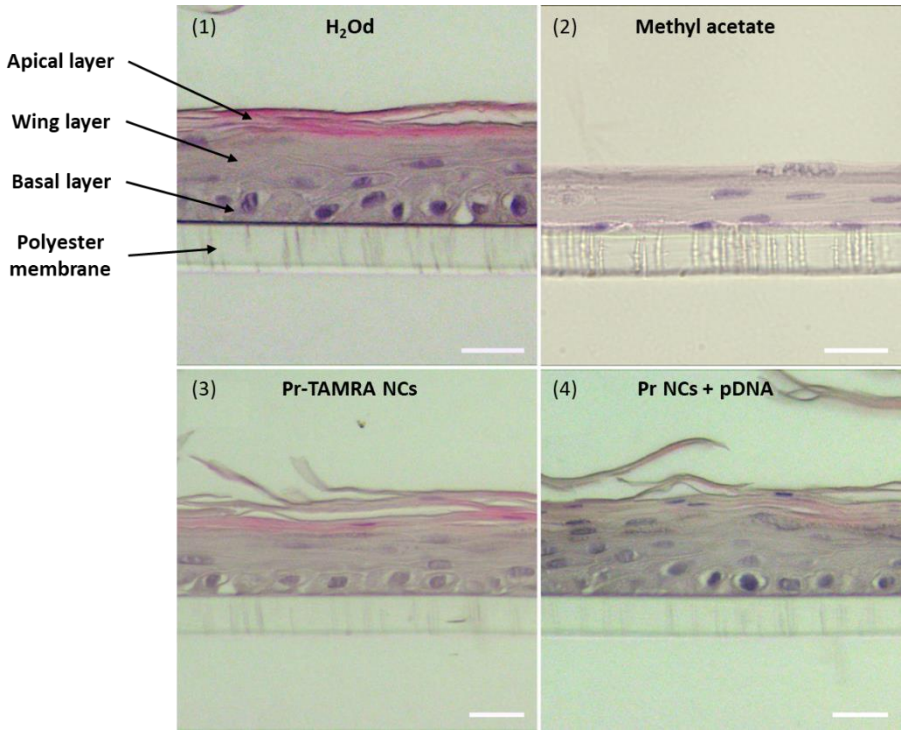

Figure 12. Representative Hematoxylin and Eosin stained histological images of the cross-section of QobuR-RhCE models after 4 h of the treatment with 0.3 mL of (1) H_2Od (negative control), (2) methyl acetate (positive control), (3) fluorescently labelled Pr NCs at 13.4 mg/mL, and (4) Pr NCs associated with 2.5% (*w/w*) of pDNA (2.5 μg of pDNA/insert) (magnification 40x, scale bar= 20 μm).

Previous studies have shown that representative markers of protein families, such as β-catenin, are expressed in QobuR human corneal epithelial models prepared with primary cultures of human limbal epithelial cells. The β-catenin is an adherent junction protein highly expressed in all epithelial layers, which is responsible for regulating actin organization and providing strong mechanical binding [46] [68]. In addition to the histological evaluation, a comparison of the immunofluorescence for β-catenin was performed, evaluating the barrier damage caused through cell junctions and the morphology of the cell membrane (Figure 13. (a)). In addition to this, cell death was studied by evaluating apoptotic cells following a TUNEL staining assay (Figure 13. (b)).

The corneal models exposed to H_2Od for 4 h showed no apparent damage to their structure. The epithelial cells were found stacked, forming at least 5 layers, constituting the three-dimensional epithelium with an intense expression of β-catenin in the periphery of the cells, outlining their contour (Figure 13. (a-1)). In addition, normal viability conditions were observed since TUNEL positive cells were only seen in the outer layers of the epithelium, where it is normal to find apoptotic figures due to the epithelial renewal process. On the contrary, in the

corneal models treated with methyl acetate, its effect on cell viability was clearly observed with practically all cells in apoptosis, including the basal layer (Figure 13. (b-2)). In addition to the reduction in the thickness of the epithelium, a delocalized expression of β-catenin from the membrane indicated inappropriate binding processes and loss in epithelial barrier morphology (Figure 13. (a-2)). In the case of both formulations, the thickness of the epithelium was very similar to the negative control, formed by 5-6 cell layers. The β-catenin labelling was located in the cell membrane and the cells had an elongated appearance typical of the intermediate zones of a mature epithelium (Figure 13. (a-3 and a-4)). Finally, only TUNEL positive cells were observed on the surface of the epithelium such as in the negative control of barrier disruption (Figure 13. (b-3 and b-4)).

In conclusion, these results, in agreement with TEER data, demonstrated the permeabilization capacity of both formulations through 3D corneal models without causing permanent damage to the endothelial barrier. Furthermore, these data agreed with previous *in vivo* studies of protamine and polyarginine NCs in healthy mice. In this case, it was observed that the topical instillation of both formulations did not cause any ocular irritation or epithelial alterations. In addition to this, it was also observed that the integrity of the membrane remained intact by not observing any positive reaction to the staining test performed [27].

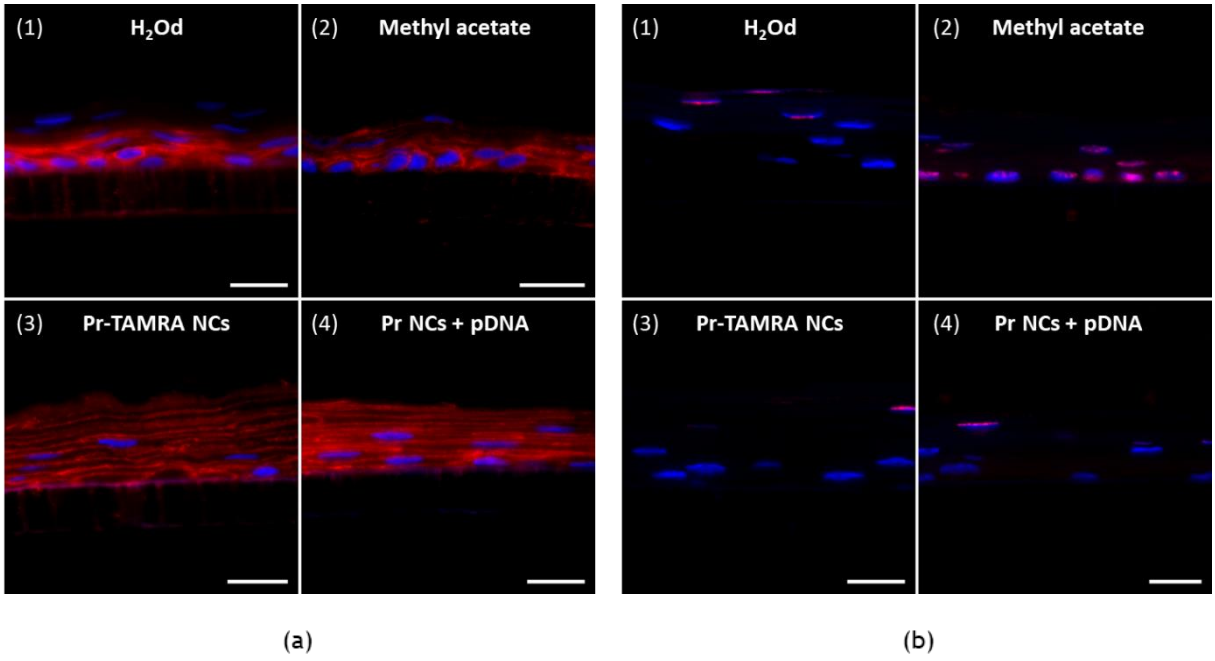

Figure 13. (**a**) Immunohistochemical images of cell junctions and cell membrane morphology by ß-catenin labelling (red channel), and (**b**) localization of TUNEL positive cells (red channel) on cross-section of QobuR-RhCE models after 4 h of treatment with 0.3 mL of (1) H_2Od (negative control), (2) methyl acetate (positive control), (3) fluorescently labelled NCs (C= 13.4 mg/mL), and (4) Pr NCs associated with 2.5% (*w*/*w*) of pDNA (2.5 µg of pDNA/insert). Cell nuclei were stained with DAPI (blue channel), (magnification 40x, scale bar= 20 µm).

3.4. CONCLUSIONS

A reservoir-type nanosystem consisting of an oily core of vitamin E surrounded by a layer of protamine was optimized for gene delivery to the eye. The formulation presented good physicochemical properties for ophthalmic administration, satisfactory short- and long-term stability in different biorelevant media, and efficient association of different nucleic acids such as pDNA and miRNA. The *in vitro* studies demonstrated that these NCs exhibited low cell cytotoxicity and efficient internalization in UM cells. The NCs also generated a permeabilization effect, without causing permanent alterations in a 3D human corneal epithelial cell model. In general, this formulation showed a promising profile for its exploration as a gene carrier by topical administration in the treatment of intraocular tumors. However, transfection efficiency should be further optimized in order to achieve therapeutic gene expression at the target tissue.

REFERENCES

[1] A. Maheshwari, P-T Finger, Cancers of the eye, Cancer Metastasis Rev. 37 (2018) 677-690. https://doi.org/10.1007/s10555-018-9762-9.

[2] B.K. William, M. di Nicola, Ocular oncology-primary and metastatic malignances, Med. Clin. 105 (2021) 531-550. https://doi.org/10.1016/j.mcna.2021.02.005.

[3] P. Chévez-Barrios, L.A.C. Espinosa, Selective pathology of intraocular tumors, Springer (2020) 461-469. https://doi.org/10.1007/978-3-319-96681-6_4.

[4] M.J. Jager, C.L. Shields, C.M. Cebulla, M.H. Abdel-Rahman, H.E. Grossniklaus, M.H. Stern, R.D. Carvajal, R.N. Belfort, R. Jia, J.A. Shields, B.E. Damato, Uveal melanoma, Nat. Rev. Dis. Primers 24 (2020) 1-25. https://doi.org/10.1038/s41572-020-0158-0.

[5] S. Kastelan, D.M. Zimak, I. Markovic, A.G. Antunica, Liver metastasis in uveal melanoma-treatment options and clinical outcome, Front. Biosci. 27 (2022) 1-16. https://doi.org/10.31083/j.fbl2702072.

[6] M.S. Nowak, B. Romanowska-Dixon, I. Grabska-Liberek, M. Zurek, Incidence, and survival of ocular melanoma in national cancer registry of Poland in 2010-2017, Adv. Clin. Exp. Med. (2022) 1-7. https://doi.org/10.17219/acem/146581.

[7] M. Fallico, G. Raciti, A. Longo, M. ribald, V. Bonfiglio, A. Russo, R. Caltabiano, G. Gattuso, L. Falzone, Current molecular and clinical insights into uveal melanoma, Int. J. Oncol. 58 (2021) 1-22. https://doi.org/10.3892/ijo.2021.5190.

[8] Z. Tang, X. Fan, Y. Chen, P. Gu, Ocular nanomedicine, Adv. Sci. 9 (2022) 1-36. https://doi.org/10.1002/advs.202003699.

[9] G. Giannaccare, F. Bernabei, M. Angi, M. Pellegrini, A. Maestri, V. Romano, V. Scorcia, P.R. Rothschild, Iatrogenic ocular surface diseases occurring during and/or after different treatments for ocular tumours, Cancers 13 (2021) 1-17. https://doi.org/10.3390/cancers13081933.

[10] S. Valasapalli, A.K. Guddati, Nation-wide trends in incidence-based mortality of patients with ocular melanoma in USA: 200 to 2018, Int. J. Gen. Med. 14 (2021) 4171-4176. https://doi.org/10.2147/IJGM.S299144.

[11] M. Andrawiss, A. Maron, W. Beltran, P. Opolon, E. Connault, F. Griscelli, P. Yeh, M. Perricaudet, P. Devauchelle, Adenovirus-mediated gene transfer in canine eyes: a preclinical study of gene therapy of human uveal melanoma, J. Gene Med. 3 (2001) 1-12. https://doi.org/10.1002/1521-2254(200105/06)3:3<228::AID-JGM186>3.0.CO;2-A.

[12] Y. Wang, L. Mo, W. Wein, X. Shi, Efficacy, and safety of dendrimer nanoparticles with coexpression of tumor necrosis factor-α and herpes simplex virus thymidine kinase in gene radiotherapy of the human uveal melanoma OCM-1 cell line, Int. J. Nanomedicine 8 (2013) 3805-3816. https://doi.org/10.2147/IJN.S48950.

[13] L. Xie, Y. Yang, J. Shen, Effect inhibition of uveal melanoma via ternary siRNA complexes, Int. J. Pharm. 573 (2020) 1-11. https://doi.org/10.1016/j.ijpharm.2019.118894.

[14] C. Yang, R. Wang, P. Hardy, Potential of miRNA-based nanotherapeutics for uveal melanoma, Cancers 13 (2021) 1-17. https://doi.org/10.3390/cancers13205192.

[15] E. Fernández-Paz, L. Feijoo-Siota, M.M. Gaspar, N. Csaba, C. Remuñán-López, Microencapsulated chitosan-based nanocapsules: a new platform for pulmonary gene delivery, Pharmaceutics 13 (2021) 1-24. https://doi.org/10.3390/pharmaceutics13091377.

[16] E. Fernández-Paz, C. Fernández-Paz, S. Barrios-Esteban, I. Santalices, N. Csaba, C. Remuñán-López, Dry powders containing chitosan-based nanocapsules for pulmonary administration: Adjustment of spray-drying process and in vitro evaluation in A549 cells, Powder Technol. 399 (2022) 1-19. https://doi.org/10.1016/j.powtec.2022.117149.

[17] N. Csaba, A. Sanchez, E. Fernandez-Megia, R. Novoa-Carballal, M.J. Alonso, Chitosan nanoparticles for the delivery of plasmid DNA: preparation and characterisation, Eur. J. Pharm. Sci. 23 (2004). Conference: 8th European Congress of Pharmaceutical Sciences.

[18] N. Csaba, M. Köping-Höggard, M.J. Alonso, Ionically crosslinked chitosan/tripolyphosphate nanoparticles for oligonucleotide and plasmid DNA delivery, Int. J. Pharm. 382 (2009) 205- 214. https://doi.org/10.1016/j.ijpharm.2009.07.028.

[19] N. Csaba, M. Köping-Höggard, E. Fernandez-Megia, R. Novoa-Carballal, R. Riguera, M.J. Alonso, Ionically crosslinked chitosan nanoparticles as gene delivery systems: effect of PEGylation degree on in vitro and in vivo gene transfer, J. Biomed. Nanotech. 5 (2009) 162-171. https://doi.org/10.1166/jbn.2009.1017.

[20] N. Csaba, P. Caamaño, A. Sánchez, F. Domínguez, M.J. Alonso, PLGA:poloxamer and PLGA:poloxamine blend nanoparticles: new carriers for gene delivery, Biomacromolecules 6 (2005) 271-278. https://doi.org/10.1021/bm049577p.

[21] N. Csaba, A. Sánchez, M.J. Alonso, PLGA:poloxamer and PLGA:poloxamine blend nanostructures as carriers for nasal gene delivery, JCR 113 (2006) 164-172. https://doi.org/10.1016/j.jconrel.2006.03.017.

[22] N.S. Csaba, A. Sánchez, M.J. Alonso, Preparation of poly(lactic acid) (PLA) and poly(ethylene oxide) (PEO) nanoparticles as carriers for gene delivery, Cold Spring Harbor Protoc. (2010) 1-5. https://doi.org/10.1101/pdb.prot5468.

[23] Y. Diebold, A.E. de Salamanca, M. Calongue, A. vila, E.L.S. Carvalho, M. de la Fuente, B. Seijo, M.J. Alonso, Ocular surface in vivo tolerance to new nanoparticle polymer systems designed for drug delivery, Invest. Ophthalmol. Vis. Sci. 46 (2005).

[24] Y. Diebold, A.E. de Salamanca, M. Orea, V. Sáez, C. García-Vázquez, M. de la Fuente, B. Seijo, M.J. Alonso, M. Calonge, In vivo uptake of nanoparticulate drug delivery systems by ocular surface structures, Invest. Ophthalmol. Vis. Sci. 47 (2006).

[25] L. Contreras, A. López-García, M. Calonge, M. de la Fuente, D. Seijo, M.J. Alonso, Hyaluronic receptor-mediated uptake of hyaluronic acid-chitosan nanoparticles in ocular epithelial cells, Invest. Ophthalmol. Vis. Sci. 49 (2008).

[26] L. Contreras-Ruiz, M. de la Fuente, C. García-Vázquez, V. Sáez, B. Seijo, M.J. Alonso, M. Calonge, Y. Diebold, Ocular tolerance to a topical formulation of hyaluronic acid and

chitosan-based nanoparticles, Cornea 29 (2010) 550-558. https://doi.org/10.1097/ICO.0b013e3181bd9eee.

[27] S. Reimondez-Troitiño, I. Alcalde, N. Csaba, A. Íñigo-Portugués, M. de la Fuente, F. Bech, A.C. Riestra, J. Merayo-Lloves, M.J. Alonso, Polymeric nanocapsules: a potential new therapy for corneal wound healing, Drug Deliv. and Transl. Res. 6 (2016) 708-721. https://doi.org/10.1007/s13346-016-0312-0.

[28] M. de la Fuente, M.J. Alonso, Bioadhesive hyaluronic-chitosan nanoparticles can transport genes across the ocular mucosa and transfect ocular tissue, Gene Ther. 15 (2008) 668-676. https://doi.org/10.1038/gt.2008.16.

[29] Y. Diebold, L. Contreras-Ruiz, A. López-García, M. Calonge, M. de la Fuente, B. Seijo, M.J. Alonso, Intracellular trafficking of hyaluronic acid-chitosan nanoparticles in ocular epithelial cells, Invest. Ophthalmol. Vis. Sci. 49 (2008).

[30] M de la Fuente, B. Seijo, M.J. Alonso, Novel hyaluronic acid-chitosan nanoparticles for ocular gene therapy, Physiol. Pharmacol. 49 (2008) 2016-2024. https://doi.org/10.1167/iovs.07-1077.

[31] M. Hornof, M. de la Fuente, M. Hallikainen, R.H. Tammi, A. Urtti, Low molecular weight hyaluronan shielding of DNA/PEI polyplexes facilitates CD44 receptor mediated uptake in human corneal epithelial cells, J. Gene Med. 10 (2007) 70-80. https://doi.org/10.1002/jgm.1125.

[32] L. Contreras-Ruiz, M. de la Fuente, J.E. Párraga, A. López-García, I. Fernández, B. Seijo, A. Sánchez, M. Calonge, Y. Diebold, Intracellular trafficking of hyaluronic acid-chitosan oligomer-based nanoparticles in cultured human ocular surface, Mol. Vis. 17 (2011) 279-290. PMC3030601.

[33] S. Swetledge, J.P. Jung, R. Carter, C. Sabliov, Distribution of polymeric nanoparticles in the eye: implications in ocular disease therapy, J. Nanobiotechnol. 19 (2021) 1-19. https://doi.org/10.1186/s12951-020-00745-9.

[34] S. Johannsdottir, P. Jansook, E. Stefansson, I.M. Kristinsdottir, Z. Fulop, G.M. Asgrimsdottir, M. Thorsteindsottir, F.F. Eiriksson, T. Loftsson, Topical drug delivery to the posterior segment of the eye: dexamethasone concentrations in various eye tissues after topical administration for up 15 days to rabbits, J. Drug Deliv. Sci. Technol. 45 (2018) 449-454. https://doi.org/10.1016/j.jddst.2018.04.007.

[35] C. Jumelle, S. Gholizadeh, N. Annabi, R. Dana, Advances and limitations of drug delivery systems formulated as eye drops, JCR 321 (2020) 1-22. https://doi.org/10.1016/j.jconrel.2020.01.057.

[36] R. Suri, S. Beg, K. Kohli, Targeting strategies for drug delivery bypassing ocular barriers, J. Drug Deliv. Sci. Technol. 55 (2020) 1-17. https://doi.org/10.1016/j.jddst.2019.101389.

[37] C.H. Tsai, P.Y. Wang, I.C. Lin, H. Huang, G.S. Liu, C.L. Tseng, Ocular drug delivery: role of degradable polymeric nanocarriers for ophthalmic application, Int. J. Mol. Sci. 19 (2018) 1-20. https://doi.org/10.3390/ijms19092830.

[38] B.S. Winkler, M.E. Boulton, J.D. Gottsch, P. Sternberg, Oxidative damage and age-related macular degeneration, Mol. Vis. 32 (1999) 1-27. PMC1773059.

[39] S. Reimondez-Troitiño, J.V González-Aramundiz, J. Ruiz-Bañobre, R. López-López, M.J. Alonso, N. Csaba, M. de la Fuente, Versatile protamine nanocapsules to restore miR-145 levels and interfere tumor growth in colorectal cancer cells, Eur. J. Pharm. Biopharm. 142 (2019) 449-459. https://doi.org/10.1016/j.ejpb.2019.07.016.

[40] M.J. Fyer, Evidence for the photoprotective effects of vitamin E, Photochem. Photobiol. 58 (1993) 304-312. https://doi.org/10.1111/j.1751-1097.1993.tb09566.x.

[41] R.K. Seth, S. Kharb, Protective function of alpha-tocopherol against the process of cataractogenesis in humans, Ann. Nutr. Metab. 43 (1999) 286-289. https://doi.org/10.1159/000012796.

[42] J. Xin, J. Tang, M. Bu, Y. Sun, X. Wang, L. Wu, H. Liu, A novel eye drop of alpha tocopherol to prevent ocular oxidant damage: improve the stability and ocular efficacy, Drug Deliv. Ind. Pharm. 42 (2016) 1-11. https://doi.org/10.3109/03639045.2015.1082582.

[43] Y. Singh, J.G. Meher, K. RAval, F.A. Khan, M. Chaurasia, N.K. Jain, M.K. Chourasia, Nanoemulsion: concepts, development, and applications in drug delivery, JCR 252 (2017) 28-49. https://doi.org/10.1016/j.jconrel.2017.03.008.

[44] L.N. Thwala, D.P. Delgado, K. Leone, I. Marigo, F. Benetti, M. Chenlo, C.V. Alvarez, S. Tovar, C. Dieguez, N. S. Csaba, M.J. Alonso, Protamine nanocapsules as carriers for oral peptide delivery, JCR 291 (2018) 157-168. https://doi.org/10.1016/j.jconrel.2018.10.022.

[45] P. Calvo, A. Sánchez, J. Martínez, M.I. López, M. Calonge, J.C. Pastor, M.J. Alonso, Polyester nanocapsules as new topical ocular delivery systems for cyclosporin A, Pharm. Res. 13 (1996) 311-315. https://doi.org/10.1023/A:1016015803611.

[46] M. Chacón, N. Vázquez, S. Berisa, M. Persinal, M. Sánchez, B. Baamonde, J.F. Alfonso, L. Fernández-Vega Cueto, J. Merayo-Lloves, A. Meana, QobuR-a new in vitro human corneal epithelial model for preclinical drug screening, Eur. J. Pharm. Biopharm. 136 (2019) 164-173. https://doi.org/10.1016/j.ejpb.2019.01.023.

[47] M. Chacón, N. Vázquez, M. Persinal-Medina, S. Alonso-Alonso, I. Alcalde, J. Merayo-Lloves, A. Meana, In-house performance assessment of 3D QobuR-reconstructed human cornea-like epithelium (RhCE) for the evaluation of eye hazard, Toxicol. In Vitro 82 (2022) 1-7. https://doi.org/10.1016/j.tiv.2022.105390.

[48] M. Chacón, M. Sánchez, N. Vázquez, M. Persinal-Medina, S- Alonso-Alonso, B. Baamonde, J.F. Alfonso, L. Fernández-Vega-Cueto, J. Merayo-Lloves, A. Meana, Impedance-based non-invasive assay for ocular damage prediction on in vitro 3D reconstructed human corneal epithelium, Bioelectrochemistry 146 (2022) 1-7. https://doi.org/10.1016/j.bioelechem.2022.108129.

[49] M. Peleteiro, E. Presas, J.V. González-Aramundiz, B. Sánchez-Correa, R. Simón-Vázquez, N. Csaba, M.J. Alonso, A. González-Fernández, Polymeric nanocapsules for vaccine delivery: influence of the polymeric shell on the interaction with the immune system, Front. Immunol. 19 (2018) 1-17. https://doi.org/10.3389/fimmu.2018.00791.

[50] S. Robla, M. Prasanna, R. Varela-Calviño, C. Grandjean, N. Csaba, A chitosan-based nanosystems as pneumococcal vaccine delivery platform, Drug Deliv. and Transl. Res. 11 (2021) 581-597. https://doi.org/10.1007/s13346-021-00928-3.

[51] J.V. González-Aramundiz, E. Presas, I. Dalmau-Mena, S. Martínez-Pulgarín, C. Alonso, J.M. Escribano, M.J. Alonso, N.S. Csaba, Rational design of protamine nanocapsules as antigen delivery carriers, JCR 245 (2017) 62-69. https://doi.org/10.1016/j.jconrel.2016.11.012.

[52] S.M. Bromfield, E. Wilde, D.K. Smith, Heparin sensing and binding-taking supramolecular chemistry towards clinical applications, Chem. Soc. Rev. 42 (2013) 9184-9195. https://doi.org/10.1039/C3CS60278H.

[53] M. Radanova, M. Levkova, G. Mihaylova, R. Manev, M. Maneva, R. Hadgiev, N. Conev, I. Donev, Single nucleotide polymorphisms in microRNA genes and colorectal cancer risk and prognosis, Biomedicines 10 (2022) 1-24. https://doi.org/10.3390/biomedicines10010156.

[54] Z. Chen, M. Yang, Q. Wang, J. Bai, C. McAlinden, E. Skiadaresi, J. Zhang, L. Pan, C. Mei, Z. Zeng, J. Yu, Y. Feng, Z. Jiang, W. Xu, H. Xu, X. Ye, H. He, Q. Wang, J. Deng, J. Huang, Hydrogel eye drops as a non-invasive drug carrier for topical enhanced adalimumab permeation and highly efficient uveitis treatment, Carbohydr. Polym. 253 (2021) 1-10. https://doi.org/10.1016/j.carbpol.2020.117216.

[55] S.M. Bromfield, E. Wilde, D.K. Smith, Heparin sensing and binding-taking supramolecular chemistry towards clinical applications, Chem. Soc. Rev. 42 (2013) 9184-9195. https://doi.org/10.1039/C3CS60278H.

[56] A. Karabasz, K. Szczepanowicz, A. Cierniak, J. Bereta, M. Bzowska, In vitro toxicity studies of biodegradable, polyelectrolyte nanocapsules, Int. J. Nanomedicine 13 (2018) 5159-5172. https://doi.org/10.2147/IJN.S169120.

[57] M.P. Pereira, M.G. de Gomes, J.C. Izoton, K.A. Nakama, R.B. dos Santos, A.S.P. Savall, J.B. Ramalho, S.S. Roman, C. Luchese, F.W. Cibin, S. Pinton, S.E. Haas, Cationic and anionic unloaded polymeric nanocapsules: toxicological evaluation in rats shows low toxicity, Biomed. Pharmacother. 116 (2019) 1-8. https://doi.org/10.1016/j.biopha.2019.109014.

[58] P. Foroozandeh, A.A. Aziz, Insight into cellular uptake and intracellular trafficking of nanoparticles, Nanoscale Res. Lett. 13 (2018) 1-12. https://doi.org/10.1186/s11671-018-2728-6.

[59] B. Lu, A.J. Hendriks, T.M. Nolte, A genetic model based on the properties of nanoparticles and cells for predicting cellular uptake, Colloids Surf. B Biointerfaces 209 (2022) 1-9. https://doi.org/10.1016/j.colsurfb.2021.112155.

[60] S. Mazumdar, D. Chitkara, A. Mittal, Exploration and insight into cellular internalization and intracellular fate of amphiphilic polymeric nanocarriers, Acta Pharm. Sin. B 11 (2021) 903-924. https://doi.org/10.1016/j.apsb.2021.02.019.

[61] D. Manzanares, V. Ceña, Endocytosis: the nanoparticle and submicron nanocompounds gateway into the cell, Pharmaceutics 12 (2020) 1-22. https://doi.org/10.3390/pharmaceutics12040371.

[62] M.C. Shin, J. Zhang, K.A. Min, K. Lee, Y. Byun, A.E. David, H. He, V.C. Yang, Cell-penetrating peptides: achievements and challenges in application for cancer treatment, J. Biomed. Mater. Res. A 102 (2013) 575-587. https://doi.org/10.1002/jbm.a.34859.

[63] E. Vighi, M. Montanari, B. Ruozi, G. Tosi, A. Magli, E. Leo, Nuclear localization of cationic solid lipid nanoparticles containing protamine as transfection promoter, Eur. J. Pharm. Biopharm. 76 (2010) 384-393. https://doi.org/10.1016/j.ejpb.2010.07.012.

[64] D. Delgado, A. del Pozo-Rodríguez, M.A. Solinís, A. Rofríguez-Gascón, Understanding the mechanism of protamine in solid lipid nanoparticle-based lipofection: the importance of the entry pathway, Eur. J. Pharm, Biopharm. 79 (2011) 495-502. https://doi.org/10.1016/j.ejpb.2011.06.005.

[65] K.Y. Lu, R. Li, C.H. Hsu, C.W. Lin, S.C. Chou, M.L. Tsai, F.L. Mi, Development of a new type of multifunctional fucoidan-based nanoparticles for anticancer drug delivery, Carbohydr. Polym. 165 (2017) 410-420. https://doi.org/10.1016/j.carbpol.2017.02.065.

[66] D.B. Thompson, R. Villaseñor, B.M. Dorr, M. Zerial, D.R. Liu, Cellular uptake mechanisms and endosomal trafficking of supercharged proteins, Chem. Biol. 19 (2012) 831-843. https://doi.org/10.1016/j.chembiol.2012.06.014.

[67] D. Hernandez-Patlan, B. Solis-Cruz, M.A. Cano-Vega, E. Beyssac, G. Garrait, X. Hernandez-Velasco, R. Lopez-Arenallo, G. Tellez, G.R. Rivera-Rodriguez, Development of chitosan and alginate nanocapsules to increase the solubility, permeability, and stability of curcumin, J. Pharm. Innov. 14 (2019) 132-140. https://doi.org/10.1007/s12247-018-9341-1

[68] L. Li, R. Hartley, B. Reiss, Y. Sun, J. Pu, D. Wu, F. Lin, T. Hoang, S. Yamada, J. Jiang, M. Zhao, E-cadherin plays an essential role in collective directional migration of large epithelial sheets, Cell. Mol. Life Sci. 69 (2012) 2779-2789. https://doi.org/10.1007/s00018-012-0951-3

SUPPORTING INFORMATION

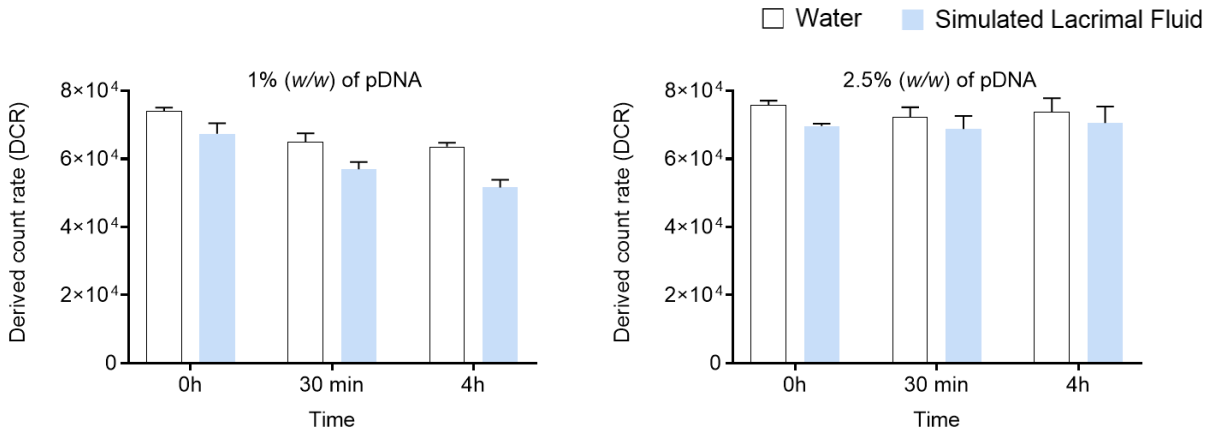

Figure S1. Stability of loaded Pr NCs with 1% and 2.5% (*w*/*w*) of pDNA respect to the total mass of NCs, measuring the derived count rate (DCR) at 37 ºC for 0 h, 30 min and 4 h in SLF (Mean ± SEM (n= 3)).

Table S1. Number of total positive events of control and UM treated with blank Pr-TAMRA NCs expressing by percentage and measuring their Mean Fluorescence Intensity (MFI).

Cell line	Total (+) 5-TAMRA events		% (+) 5-TAMRA events		MFI (+) 5-TAMRA events	
	Control	Sample	Control	Sample	Control	Sample
UM	32	1302	1	35.8	4,486	8,789

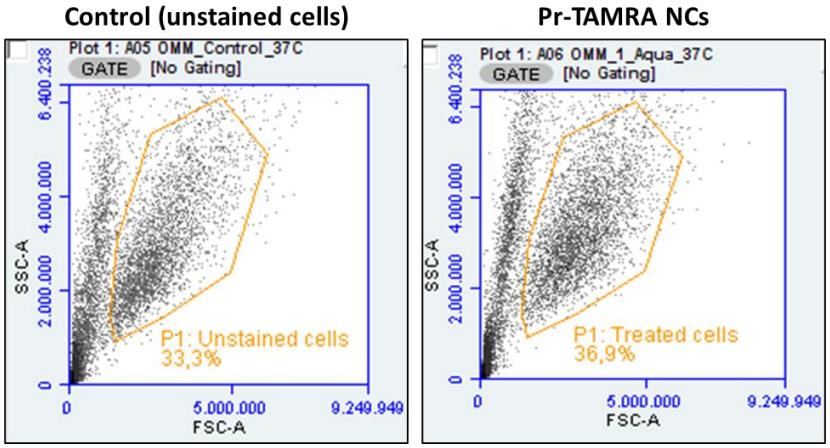

Figure S2. Flow cytometry histograms of the total events without debris of control and UM cells treated with blank Pr-TAMRA NCs to analyze the NP-uptake.

OVERALL DISCUSSION

OVERALL DISCUSSION

Current basis for the classical treatment for any aggressive tumor consists of three fundamental pillars: surgical resection, radiotherapy, and chemotherapy. Regarding the latter, most treatments rely on small molecular weight drugs to achieve a better therapeutic efficacy with effective inhibition of tumor growth [1]. However, the use of radiotherapy and chemotherapy have significant limitations, including severe side effects. The main mechanism of radiotherapy to kill tumor cells is based on generating DNA damage, where such effects can also occur in healthy cells triggering antitumor responses far from the irradiated zone [2]. In the case of chemotherapeutic agents, they lack tumor-targeting and can damage both cancer and surrounding healthy cells and tissues, resulting in suboptimal efficacy and high toxicity [3]. These complications have fueled research on more specific strategies for effective drug delivery.

Polynucleotide-based therapies are gaining increasing attention due to their ability to provide safe and effective treatment for diseases such as cancer [4]. However, the efficacy of gene therapy is hindered by several biological barriers, which requires the use of efficient nanocarriers to facilitate the intracellular entry and release of genetic material in target tumor cells [5]. Engineered viruses are dominant vectors in current clinical gene therapy, but they still have drawbacks related to host immune response, safety, and their complex manufacturing. Non-viral vectors have become a promising alternative to overcome gene delivery limitations. Despite their great progress, many facets of non-viral vectors require further investigation to enhance transfection efficiency towards their transition to the clinical field [6, 7]. Considering this information, the present work focused on investigating different polymeric compositions structured as nanocarriers for antitumoral gene medicines. The polymers selected have several characteristics in common, such as biodegradability and biocompatibility, in addition to positive charge that allows them to complex polynucleotides. The cationic nature of protamine (Pr) helps the nanosystems to interact with the cell membrane, achieving easy and rapid penetration. In addition, protamine assembles with DNA, protecting this polynucleotide against degradation, which ultimately results in improved gene expression [8, 9]. On the other hand, polyethylenimine (PEI) has been considered a gold-standard in this area due to its high efficacy in gene delivery [10, 11].

Protamine was combined with dextran (Dx) using the mass ratio 4:1 (*w/w*), after an exhaustive screening. The electrostatic interactions between the anionic groups of dextran [12], and the cationic groups of protamine led to the formation of spherical nanoparticles (NPs) (Figure 1. (a)). This ionic cross-linking method [13, 14] was also used to obtain protamine and PEI nanocomplexes combined with plasmid DNA and the anionic polyphosphazene 6MHA-PPZ, selecting the optimal charge ratios of 8:0:1 and 8:4:1 (N:C:P) (see Chapter II, section 2.2.3.) [15]. Protamine nanocapsules (Pr NCs) were obtained by a previously developed solvent

displacement method [16] [17-21], where the cationic protamine formed a polymeric shell around oily nanodroplets of vitamin E, selected for its antioxidant properties that could protect cells from oxidative stress [22]. To prevent the aggregation of particles and provide greater stability to the oily core, tween-80 and sodium cholate were added as surfactants [23]. Moreover, tween-80, which is short-chain polyethylene glycol (PEG) surfactant with a branched structure, is less prone to interfere with the association of polypeptides to NCs, and improves the uptake of the particles favoring the endosomal escape [20]. The combination of all these compounds gave rise to a reservoir-type formulation composed of spherical particles (Figure 1. (b)).

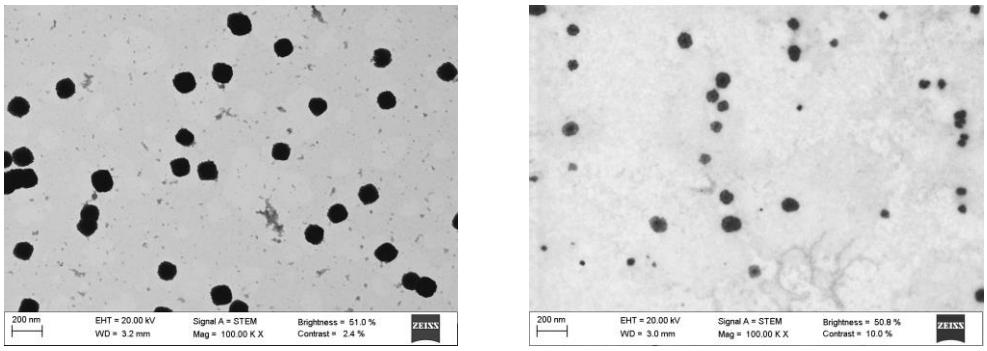

Figure 1. STEM images of blank (**a**) 4:1 (*w*/*w*) Pr:Dx NPs and (**b**) Pr NCs. Scale bar= 200 nm.

The bioavailability of therapeutic agents after systemic or local administration depends on the physicochemical properties of the delivery system. In this work, the nanocarriers presented similar properties, with a particle size less than 250 nm, polydispersity index less than 0.3, and a positive surface charge around +30 mV (Table 1.). The size and charge of these nanosystems allow good cell uptake and internalization, as well as, good biodistribution [24].

Table 1. Physicochemical characterization of a panel of cationic polymeric nanosystems, by measuring the particle size (nm), polydispersity index (PDI) and zeta potential (mV) (Mean ± SD).

Formulation	Size (nm)	PDI	Zeta Potential (mV)
4:1 (*w/w*) Pr:Dx NPs	120 ± 7	0.2	+34 ± 2
8:0:1 PEI/pDNA nanocomplex	114 ± 19	0.2	+27 ± 11
8:0:1 Pr/pDNA nanocomplex	106 ± 10	0.1	+33 ± 15
8:4:1 PEI/6MHA-PPZ nanocomplex	128 ± 6	0.2	+26 ± 7
8:4:1 Pr/6MHA-PPZ nanocomplex	110 ± 14	0.1	+25 ± 8
Pr NCs	242 ± 40	0.1	+33 ± 11

The ability of nanosystems to bind, associate and release nucleic acids is an important characteristic for the design of gene nanocarriers. This parameter depends on the amount and disposition of the cationic amines of polymers in the nanocarriers because they establish the interactions with negatively charged groups of the nucleic acids [25]. pDNA and miRNA molecules can be embedded in the polymeric matrix of 4:1 (*w/w*) Pr:Dx NPs, associating up to 8% (*w/w*), corresponding to a maximum concentration of 133 µg of pDNA/mL. In Pr NCs, the

nucleic acids are bound to the external polymeric shell of preformed nanosystems. In this case, 1% and 2.5% (*w/w*) of pDNA could be associated corresponding to a maximum concentration of 72 µg of pDNA/mL and 180 µg of pDNA/mL, respectively, and up to 1.5% (*w/w*) of miRNA corresponding to a maximum concentration of 108 µg of miRNA/mL. The nucleic acid binding can be markedly different for shorter therapeutic nucleic acids such as siRNAs and miRNAs versus plasmid DNA. In this case, agarose gel electrophoresis showed better association efficiency with short-chain nucleic acids, especially for Pr NCs, due to stronger interactions with the cationic peptide in comparison with their incubation with an excess of heparin as anionic competitor. In general, for all nanosystems, their spherical morphology and their particle size were not significantly altered by the association of the genetic material, but the surface charge of Pr NCs was reduced with higher concentration of polynucleotides (Table 2.). On the other hand, it should be noticed that the addition of 6MHA-PPZ to the PEI and Pr formulations did not alter their particle size and zeta potential (Table 1.).

Table 2. Physicochemical characterization of a panel of cationic polymeric nanosystems loaded with different percentages of different nucleic acids, by measuring the particle size (nm), polydispersity index (PDI) and zeta potential (mV) (Mean ± SD).

Formulation	Nucleic acid	Size (nm)	PDI	Zeta Potential (mV)
4:1 (*w/w*) Pr:Dx NPs	8% (*w/w*) of pDNA	146 ± 1	0.2	+33 ± 5
	8% (*w/w*) of miRNA	124 ± 5	0.1	+30 ± 3
Pr NCs	1% (*w/w*) of pDNA	345 ± 39	0.3	-31 ± 4
	2.5% (*w/w*) of pDNA	337 ± 31	0.2	-42 ± 3
	1.5% (*w/w*) of miRNA	274 ± 48	0.1	-15 ± 3

The stability of the formulation characteristics is crucial to their successful biomedical application [26]. The applicability of polymeric nanocarriers may be limited over time due to particle aggregation in injection and physiological media, chemical degradation, and premature release of active agents [27]. An exhaustive study was carried out regarding the stability of these nanosystems under storage conditions, and in different biorelevant media, prior to any cell culture and *in vivo* experiment. Regarding the stability of the formulations under storage conditions, their properties in terms of size, surface charge and yield remained constant for at least 30 days (Figure 2. (a)). In the case of NP-stability in biological media, the matrix-type formulations such as 4:1 (*w/w*) Pr:Dx NPs and, PEI and Pr nanocomplexes with/out the 6MHA-PPZ, they experienced an increase in their size when diluted in cell culture media due to a possible aggregation of the particles (Figure 2. (b)). However, this process was controlled over time when proteins on their surface allowed a better stabilization of the nanosystems. In the case of the Pr NCs, this instability was less pronounced. In addition, formulations with a nanocapsular structure have been studied for more than two decades with respect to their utility for ocular administration [28-33], and recently, Pr NCs have been explored for the same purpose [34]. The colloidal stability of this formulation was also analyzed in simulated lacrimal fluid, where Pr NCs associated with 2.5% (*w/w*) of pDNA were found more stable and released less plasmid over time than those associated with 1% (*w/w*) of pDNA. Finally, PEI and Pr nanocomplexes were analyzed in zebrafish culture media, where these nanocomplexes aggregated in conventional media, but they were stable in dechlorinated tap water.

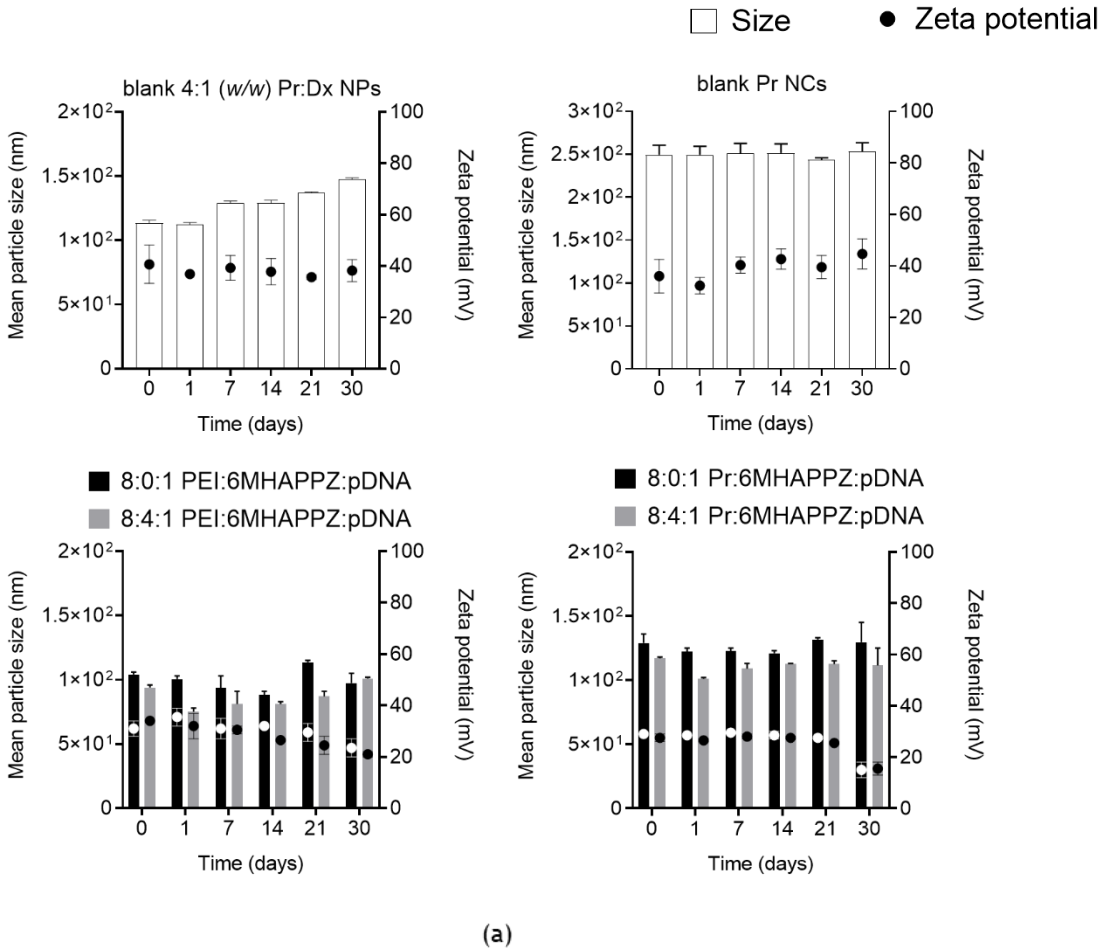

(a)

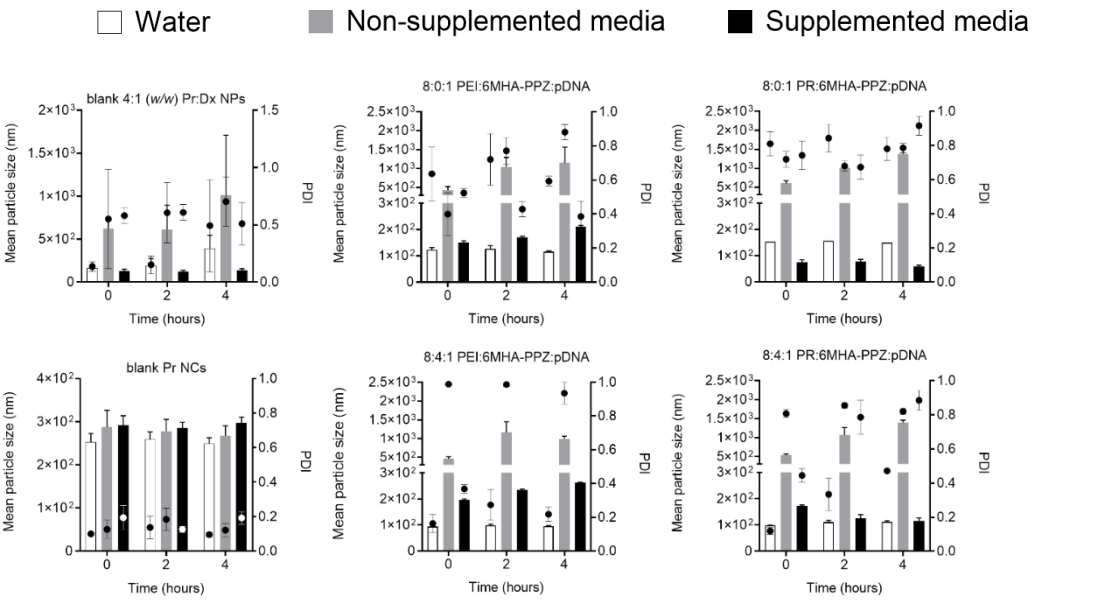

(b)

Figure 2. Stability of blank 4:1 (*w*/*w*) Pr:Dx NPs, 8:0:1 and 8:4:1 (N:C:P) charge ratios of PEI and Pr nanocomplexes with/out 6MHA-PPZ and blank Pr NCs, by measuring the particle size and zeta potential (**a**) under storage conditions for 30 days, and (**b**) in cell culture media at time 0, 2 and 4 h at 37 ºC (Mean ± SEM (n= 3)).

Once these nanosystems had been characterized, their potential for gene delivery was evaluated in the conventional cell culture models, three-dimensional (3D) tumor models and in an *in vivo* zebrafish model. Spheroid models were formed using transformed glioblastoma cells (U87MG) and a panel of primary patient-derived glioblastoma cells with different tumor origin: GIN-8 and GIN-28 cell lines had been harvested from the invasive marginal area of the tumor whereas GCE-28 cell line were harvested from the tumor core. Spherical cell aggregates are being implanted in drug screening platforms in the field of oncology prior to *in vivo* experiments because they closely resemble the tumor microenvironment, and exhibit the ability to form proliferative gradients, hypoxia, and necrotic tumor areas [35, 36]. Furthermore, their ability to offer more realistic results has allowed us to reduce the number of animals in the *in vivo* experimentation, which use, for both ethical and economic reasons, is increasingly complicated and restricted [37]. The size in tumor biology is a limiting factor due to gene transfection depends on the diameter of the spheroids. The larger the spheroid, the higher the distance that the nanosystems will have to cross to reach the tumor core. In addition to this, tumor cells in the nucleus could be necrotic due to the hypoxic environment and lack of nutrients, creating an additional challenge for efficient gene delivery [38]. The size above 250 µm was confirmed by phase-contrast microscopy images and the spherical morphology and cell compactness by Scanning Electron Microscopy (SEM) (Figure 3.). In addition, for the ocular delivery project, the 3D model (QobuR-RhCE) composed of normal human corneal epithelial cells was used. These cells have the ability to form a stratified squamous epithelium resembling a normal human corneal epithelium [39-41].

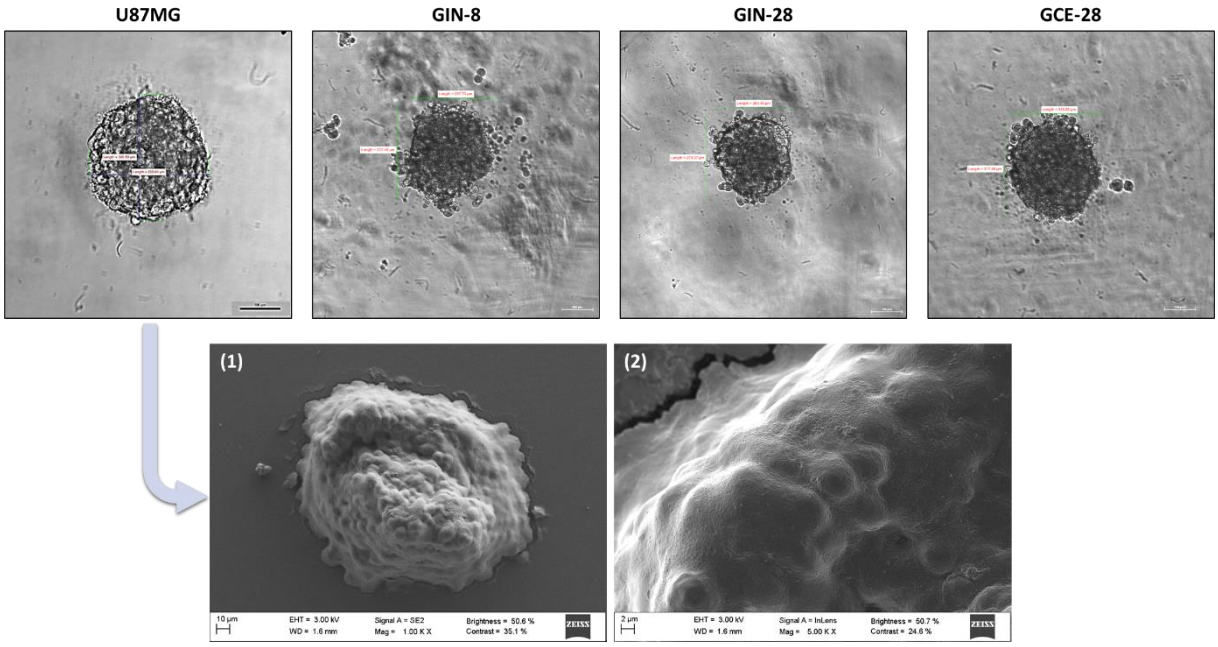

Figure 3. Phase-contrast microscopy images of U87MG spheroid (magnification 10x, scale bar= 100 µm) and GIN-8, GIN-28, and GCE-28 spheroids (magnification 10x, scale bar= 100 µm) with size between 250-300 µm, approximately. SEM images of U87MG spheroid showing: (**1**) the overall spherical morphology of compact spheroids, and (**2**) a closer look at the cell surface of the spheroid.

The nanosystems formulated with protamine showed low cytotoxicity in transformed and primary glioblastoma cells and tumor spheroids, as well as, in uveal melanoma cells. Furthermore, Pr NCs had the ability to permeabilize cell layers in the 3D corneal model without causing permanent alteration of the epithelia. The reduction in TEER values demonstrated the permeabilization capacity of this nanosystem through the QobuR-RhCE model, which together

the histological images (Figure 4. (a-3, 4)), demonstrated how the structure of the epithelial barrier remained almost undistinguishable from undamaged epithelium [40]. In addition, the intense, well-localized expression of β-catenin in the cell membrane indicated strong mechanical binding between the epithelial layers in the 3D corneal models after contact with the formulations (Figure 4. (b-3,4)), verifying their passage through the epithelial barrier maintaining the cell integrity and morphology. Despite the fact that PEI is one of the most studied polymers for gene therapy due to its effective endosomal escape and high transfection [42], this polymer turned out to be more toxic at high concentrations. However, the addition of the anionic polyphosphazene 6MHA-PPZ reduced the cytotoxicity of these cationic PEI nanocomplexes, as previously observed in highly transformed glioblastoma cultures [15] [38].

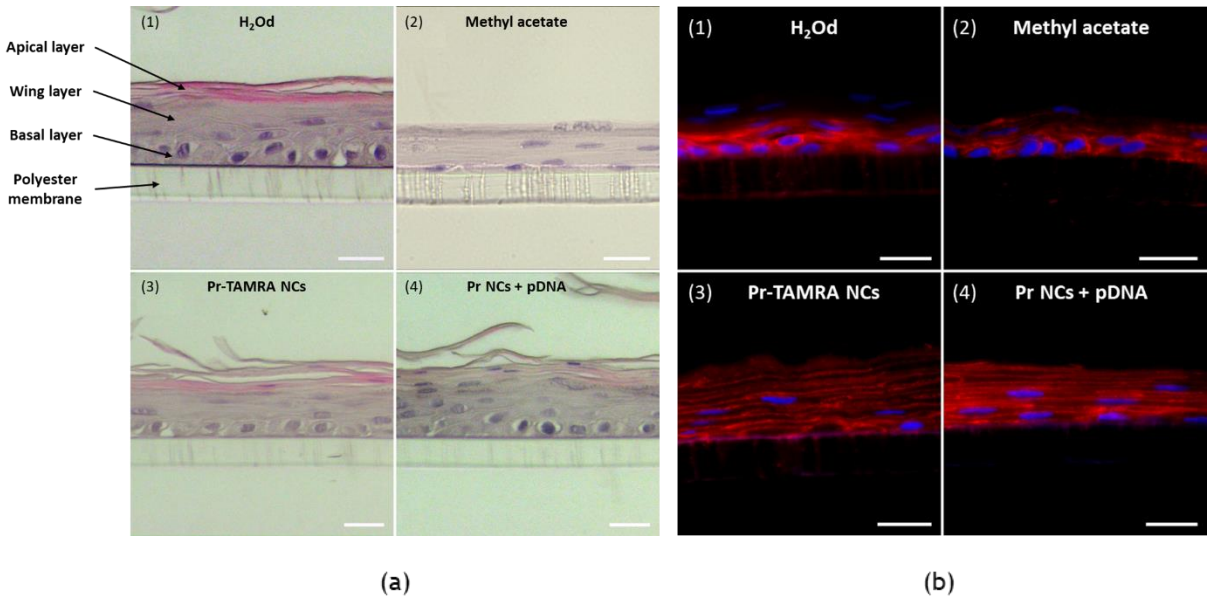

Figure 4. (**a**) Hematoxylin and Eosin stained histological images and (**b**) immunohistochemical images of cell junctions and cell membrane morphology by ß-catenin labelling (red channel) of the cross-section of QobuR-RhCE models after 4 h of the treatment with (1) H_2Od (negative control), (2) methyl acetate (positive control), (3) fluorescently labelled Pr NCs, and (4) Pr NCs associated with 2.5% (*w*/*w*) of pDNA (2.5 µg of pDNA/insert). Cell nuclei were stained with DAPI (blue channel) (magnification 40x, scale bar= 20 µm).

To visualize the internalization of 4:1 (*w/w*) Pr:Dx NPs and Pr NCs by confocal and light sheet fluorescence microscopy (LSFM), it was necessary label the polymer with a fluorescent label (5-TAMRA). This labelling did not affect the physicochemical characteristics of the nanosystems. In parallel, their internalization was also evaluated by detecting a fluorescent siRNA model. Monolayer cultures showed an efficient cell uptake in all cancer cell lines (Figure 5. (a)), reaching values of 36% for Pr-TAMRA NCs and almost 100% for 4:1 (*w/w*) Pr-TAMRA:Dx NPs. The size and shape of the particles and their surface charge have an important role in cellular uptake [43]. For example, in particles larger than 250 nm such as Pr NCs, the macropinocytosis tends to be the most prominent route [44]. Despite having different routes of entry into cells, it was observed that both nanosystems were highly localized close to the cell nucleus. This targeting of protamine formulations to the nucleus has been studied in detail in previous works, that postulated that six consecutive arginines in the structure of this polypeptide constitute a nuclear localization signal (NLS), which can translocate molecules from the cytoplasm to nucleus [45, 46]. The evaluation of the cellular uptake of the 4:1 (*w/w*) Pr-TAMRA:Dx NPs in glioblastoma spheroids revealed less internalization of this formulation compared with 2D cell culture model (Figure 5. (a)), especially in those spheroids formed by

primary glioblastoma cells (≃50%). A greater accumulation of these NPs was seen on the surface of the spheroids, where the LSFM and SEM images showed how these particles internalized inside the spheroid (Figure 5. (a: photos 7-9), b)).

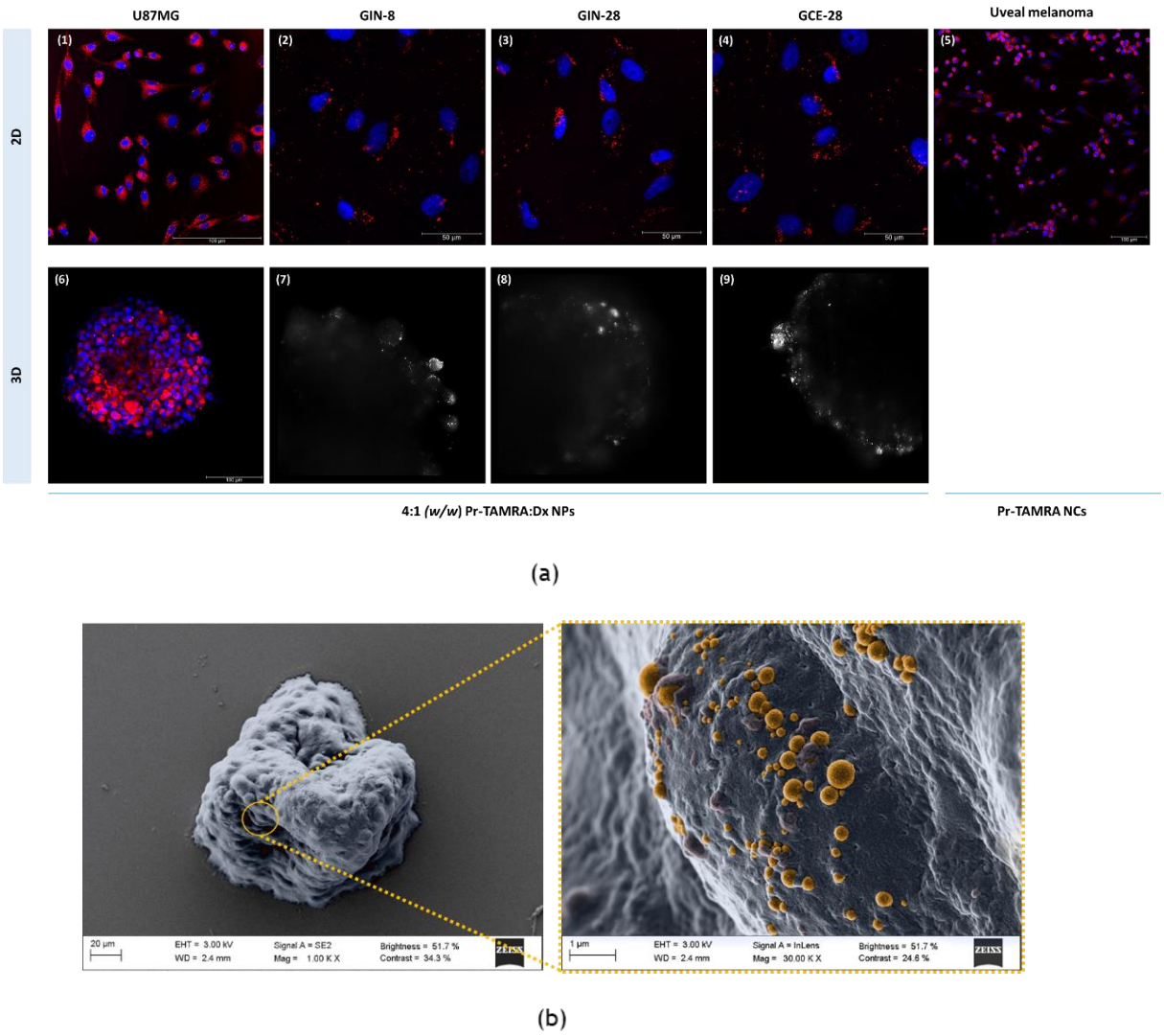

Figure 5. (**a**) Maximum projection of confocal microscopy images (photos: **1-6**) of glioblastoma cells (photos: **1-4**) and spheroids (photo: **6**), and uveal melanoma cells (photo: **5**) treated with Pr labelled nanosystems (red channel) (magnification 10x, scale bar= 50 and 100 µm). Cell nuclei stained with DAPI (blue channel). Maximum projection of light sheet fluorescence microcopy images (photos: **7-8**) of patient-derived glioblastoma spheroids treated with Pr-TAMRA nanosystems (bright white spots). (**b**) SEM images of U87MG spheroid treated with blank 4:1 (*w*/*w*) Pr:Dx NPs (colored in orange) on the surface of the spheroid.

As a final step, an *in vivo* biodistribution study in zebrafish embryos at 48 hours post-fecundation (hpf) was also performed. This zebrafish model has gained popularity because it shows many similarities with the behavior of tumors in mammalian models such as mice. In addition to this, the biodistribution of NPs can be easily monitored due to the transparency of the zebrafish embryo models [47]. The results from this biodistribution study made clear the localization of the nanocomplexes in the yolk sac of the zebrafish embryos at 5-day post-injection (dpi). Better results were obtained with PEI nanocomplexes, and especially, with the addition of 6MHA-PPZ. These findings were consistent with those obtained in previous biodistribution studies, concluding that the accumulation of formulations in this cavity could

be due to the hindering effect of the components forming the yolk sac, such as the yolk syncytial layer [48]. However, in our case, it was observed that a small proportion of the PEI/6MHA-PPZ nanocomplexes diffused towards the head area. This could be due to the smaller size of these formulations, allowing their diffusion to other tissues of zebrafish embryos [49].

Regarding the fluorescence signal, the low signal corresponding to the fluorescence intensity of Pr nanocomplexes could be a consequence of their ability to strongly complex the genetic material [8], while the addition of 6MHA-PPZ improved the efficacy of PEI nanocomplexes due to its capacity to improve the endosomal escape [33] releasing the nucleic acid easily (Figure 6.).

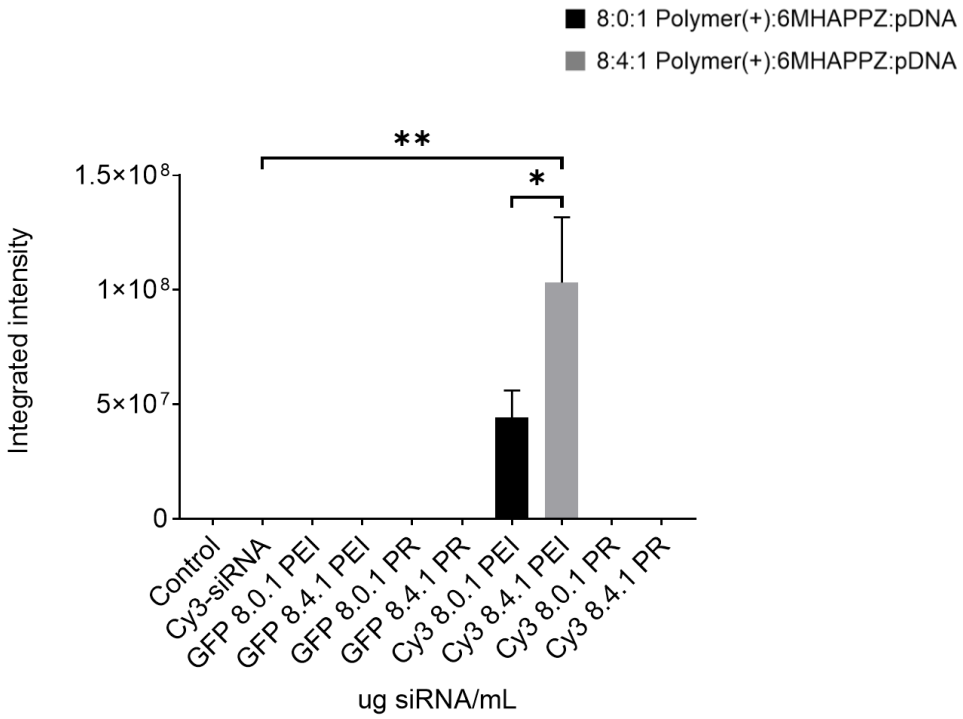

Figure 6. Quantification of fluorescence intensity from the 48 hpf WT zebrafish embryos treated with controls and 8:0:1 and 8:4:1 (N:C:P) charge ratios of PEI and Pr nanocomplexes at 25 μg of siRNA/mL at 5-day post-injection (Mean ± SEM (n= 10/condition).

Transfection efficiency was confirmed by delivering a plasmid encoding the Enhanced Green Fluorescent (EGFP) and Luciferase proteins (Luc). In the experiments, Lipofectamine®2000 was used as positive control and reference. The necessity to use a delivery system for the administration of genetic material was confirmed by the low levels of expression achieved with the naked pDNA. In general, the results obtained in transfection assays showed that the nanocarriers investigated were efficient as gene transfer agents, in particular, PEI and Pr nanocomplexes. In conventional monolayer cultures, 4:1 (*w/w*) Pr:Dx NPs and Pr NCs were effective from concentrations of 1 μg of pDNA, similar levels to those reported with other nanosystems based on protamine [20] [50]. Their transfection capacity was prolonged for at least 48 h, but it should be further optimized to achieve therapeutic gene expression in the target cancer tissue (Figure 7.). With PEI and Pr nanocomplexes, the association of the anionic polyphosphazene 6MHA-PPZ improved their transfection levels [38]. Noteworthy, the Pr nanocomplexes even reached transfection values similar to the PEI/pDNA nanocomplex in primary glioblastoma cell lines. This result was important, since this polymer had better

biocompatibility and biodegradability, and therefore, this mixture could become an interesting prototype for *in vivo* translation.

In 3D glioblastoma models, an efficient transfection of 4:1 (*w/w*) Pr:Dx NPs was also observed with a homogeneous distribution mainly on the spheroid surface (Figure 7. (a)). For PEI and Pr nanocomplexes, an improvement in transfection levels was also observed with those nanocomplexes containing 6MHA-PPZ in highly transformed glioblastoma spheroids. With primary glioblastoma spheroids, there was a variation in performance for the different models, a result that underlines the importance of considering patient-to-patient variability for nanocarrier design.

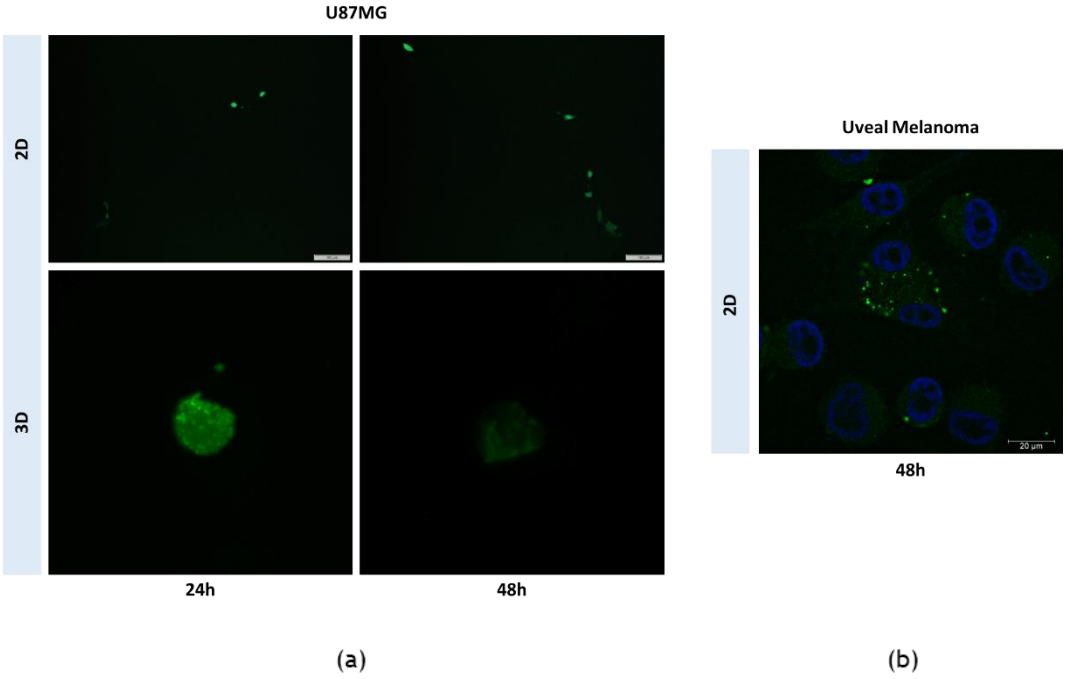

Figure 7. Fluorescence microscopy images showing the expression of EGFP protein (green channel) using (**a**) 4:1 (*w*/*w*) Pr:Dx NPs in glioblastoma cells and spheroids and (**b**) Pr NCs in uveal melanoma cells after 24 h and 48 h of their removal (scale bar= 20 and 100 μm). Cell nuclei stained with DAPI (blue channel).

In summary, a variety of nanosystems based on biodegradable and biocompatible cationic polymers have been optimized for their application in cancer gene therapy. Their evaluation in different *in vitro* preclinical cancer models and *in vivo* zebrafish model showed promising results in terms of intracellular delivery and gene transfer, making them potential carriers for future application in gene medicine.

REFERENCES

[1] T.I. Lui, Y.C. Yang, W.H. Chiang, C.K. Hung, Y.C. Sai, C.S. Chiand, C. Liang, H.C. Chiu, Radiotherapy-controllable chemotherapy from reactive oxygen species-responsive polymeric nanoparticles for effective local dual modality treatment of malignant tumors, Biomacromolecules 19 (2018) 3825-3839. https://doi.org/10.1021/acs.biomac.8b00942.

[2] W.D. Yu, G. Sun, J. Li, J. Xu, X. Wang, Mechanisms, and therapeutic potentials of cancer immunotherapy in combination with radiotherapy and/or chemotherapy, Cancer Lett. 452 (2019) 66-70. https://doi.org/10.1016/j.canlet.2019.02.048.

[3] I.I. Lungu, A.M. Grumezescu, A. Volveanov, E. Andronescu, Nanobiomaterials used in cancer therapy: an up-to-date overview, Molecules 24 (2019) 1-21. https://doi.org/10.3390/molecules24193547.

[4] Y. Nademi, T. Tang, H. Uludag, Steered molecular dynamics simulations reveal self-protecting configuration of nanoparticles during membrane penetration, Nanoscale 10 (2018) 17671-17682. https://doi.org/10.1039/C8NR04287J.

[5] E. Fernádez-Paz, L. Feijoo-Siota, M.M. Gaspar, N. Csaba, C. Remuñán-López, Microencapsulation chitosan-based nanocapsules: a new platform for pulmonary gene delivery, Pharmaceutics 13 (2021) 1-24. https://doi.org/10.3390/pharmaceutics13091377.

[6] M. San Anselmo, A. Postigo, A. Lancelot, J.L. Serrano, T. Sierra, S. Hernández-Ainsa, Dendron-functionalized hyperbranched bis-MPA polyesters as efficient non-viral vectors for gene therapy in different cell lines, Biomater. Sci. 10 (2022) 2706-2719. https://doi.org/10.1039/D2BM00365A.

[7] M. Karam, D. Fahs, B. Maatouk, B. Safi, A.A. Jaffa, R. Mahnna, Polymeric nanoparticles in the diagnosis and treatment of myocardial infarction: challenges and future prospects, Mater. Today Bio 14 (2022) 1-30. https://doi.org/10.1016/j.mtbio.2022.100249.

[8] H. Al-Azzawi, W. Alshaer, E. Esawi, Z. Lafi, D. Abuarquob, R. Zaza, M. Zraikat, A. Battah, A. Awidi, Multifunctional nanoparticles recruiting hyaluronic acid ligand and polyplexes containing low molecular weight protamine and ATP-sensitive DNA motif for doxorubicin delivery, Drug Deliv. Sci. Technol. 69 (2022) 1-11. https://doi.org/10.1016/j.jddst.2022.103169.

[9] I. Ahmad, M.F.A. Khan, A. Rahdar, S. Hussain, F.K. Tareen, M.W. Salim, N. Ajalli, M. I. Amirzada, A. Khan, Design, and evaluation of pH sensitive PEG-protamine nanocomplex of doxorubicin for treatment of breast cancer, Polymers, 14 (2022) 1-13. https://doi.org/10.3390/polym14122403.

[10] H. Rilo-Alvarez, A.M. Ledo, A. Vidal, M. Garcia-Fuentes, Delivery of transcription factors as modulators of cell differentiation, Drug Deliv. Transl. Res. 11 (2021) 426-444. https://doi.org/10.1007/s13346-021-00931-8.

[11] M. Garcia-Fuentes, Chapter-10 Gene therapy for treatment of chronic wounds, WOL (2020) 210-234. https://doi.org/10.1002/9781119433316.ch10.

[12] A. Delvart, C. Moreau, B. Cathala, Dextrans and dextran derivates as polyelectrolytes in layer-by-layer processing materials-a review, Carbohydr. Polym. 293 (2022) 1-17. https://doi.org/10.1016/j.carbpol.2022.119700.

[13] N. Csaba, M. Köping-Höggard, M.J. Alonso, Ionically crosslinked chitosan/triphosphate nanoparticles for oligonucleotides and plasmid DNA delivery, Int. J. Pharma. 382 (2009) 205-214. https://doi.org/10.1016/j.ijpharm.2009.07.028.

[14] N. Csaba, M. Köping-Höggard, E. Fernandez-Megia, R. Novoa-Carballal, R. Riguera, M.J. Alonso, Ionically crosslinked chitosan nanoparticles as gene delivery systems: effect of PEGylation degree on in vitro and in vivo gene transfer, J. Biomed. Nanotech. 5 (2009) 162-171. https://doi.org/10.1166/jbn.2009.1017.

[15] C. Garcia-Mazas, New biomaterials for the design of nanomedicines that modulate glioblastoma stem cells, Doctoral Thesis, Minerva Repositorio Institucional da USC (2020). http://hdl.handle.net/10347/25173.

[16] M. Peleteiro, E. Presas, J.V. González-Aramundiz, B. Sánchez-Correa, R. Simón-Vázquez, N. Csaba, M.J. Alonso, A. González-Fernández, Polymeric nanocapsules for vaccine delivery: influence of the polymeric shell on the interaction with the immune system, Front. Immunol. 19 (2018) 1-17. https://doi.org/10.3389/fimmu.2018.00791.

[17] J. Crecente-Campo, S. Lorenzo-Abalde, A. Mora, J. Marzoa, N. Csaba, J. Blanco, A. González-Fernández, M.J. Alonso, Bilayer polymeric nanocapsules: a formulation approach for a thermostable and adjuvanted E. coli antigen vaccine, JCR 286 (2018) 20-32. https://doi.org/10.1016/j.jconrel.2018.07.018.

[18] J.V. González-Aramundiz, M. Peleteiro, A. González-Fernández M.J. Alonso, N.S. Csaba, Protamine nanocapsules for the development of thermostable adjuvanted nanovaccines, Mol. Pharmaceutics, 15 (2018) 5653-5664. https://doi.org/10.1021/acs.molpharmaceut.8b00852.

[19] L.N. Thwala, D.P. Delgado, K. Leone, I. Marigo, F. Benetti, M. Chenlo, C.V. Alvarez, S. Tovar, C. Dieguez, N. S. Csaba, M.J. Alonso, Protamine nanocapsules as carriers for oral peptide delivery, JCR 291 (2018) 157-168. https://doi.org/10.1016/j.jconrel.2018.10.022.

[20] S. Reimondez-Troitiño, J.V González-Aramundiz, J. Ruiz-Bañobre, R. López-López, M.J. Alonso, N. Csaba, M. de la Fuente, Versatile protamine nanocapsules to restore miR-145 levels and interfere tumor growth in colorectal cancer cells, Eur. J. Pharm. Biopharm. 142 (2019) 449-459. https://doi.org/10.1016/j.ejpb.2019.07.016.

[21] E. Fernández-Paz, C. Fernández-Paz, S. Barrios-Esteban, I. Santalices, N. Csaba, C. Remuñán-López, Dry powders containing chitosan-based nanocapsules for pulmonary administration: adjustment of spray-drying process and in vitro evaluation in A549 cells, Powder Technol. 399 (2022) 1-19. https://doi.org/10.1016/j.powtec.2022.117149.

[22] A. Mirzaei-Mohkam, F. Garavand, D. Dehnad, J. Keramat, A. Nasirpour, Optimization, antioxidant attributes, stability, and release behavior of carboxymethyl cellulose films incorporated with nanoencapsulated vitamin E, Prog. Org, Coat. 134 (2019) 333-341. https://doi.org/10.1016/j.porgcoat.2019.05.026.

[23] S. Robla, M. Prasanna, R. Varela-Calviño, C. Grandjean, N. Csaba, A chitosan-based nanosystems as pneumococcal vaccine delivery platform, Drug Deliv. and Transl. Res. 11 (2021) 581-597. https://doi.org/10.1007/s13346-021-00928-3.

[24] J.D. Hyun, K.J. Hyoung, L.T. Geol, K.J. Hun, Size, surface charge and shape determine therapeutic effects of nanoparticles on brain and retinal diseases, Nanomed.: Nanotechnol. Biol. Med. 11 (2015) 1603-1611. https://doi.org/10.1016/j.nano.2015.04.015.

[25] C.J. Bishop, K.L. Kozielski, J.J. Green, Exploring the role of polymer structure on intracellular nucleic acid delivery via polymeric nanoparticles, JCR 219 (2015) 488-499. https://doi.org/10.1016/j.jconrel.2015.09.046.

[26] V.M. Samsonov, I.V. Talyzin, A.Y. Kartoshkin, S.A. Vasilyev, M.I. Alymov, On the problem of stability/instability of bimetallic core-shell nanostructures: molecular dynamics and thermodynamic simulations, Comput. Mater. Sci. 199 (2021) 1-11. https://doi.org/10.1016/j.commatsci.2021.110710.

[27] A. Zielinska, F. Carreiró, A.M. Oliveira, A. Neves, B. Pires, D.N. Venkatesh, A. Durazzo, M. Lucarini, P. Eder, A.M. Silva, A. Santini, E.B. Souto, Polymeric nanoparticles: production, characterization, toxicology, and ecotoxicology, 25 (2020) 1-20, https://doi.org/10.3390/molecules25163731.

[28] C. Losa, L. Marchal-Heussler, F. Orallo, J.L.V. Jato, M.J. Alonso, Design of new formulations for topical ocular administration: polymeric nanocapsules containing metipranolol, Pharm. Res. 10 (1993) 80-87. https://doi.org/10.1023/A:1018977130559.

[29] P. Calvo, C. Thomas, M.J. Alonso, J.L. Vila-Jato, J.R. Robinson, Study of mechanism of interaction of poly(ϵ-caprolactone) nanocapsules with the corneal by confocal laser scanning microscopy, Inter. J. Pharm. 103 (1994) 283-291. https://doi.org/10.1016/0378-5173(94)90179-1.

[30] P. Calvo, M.J. Alonso, J.L. Vila-Jato, J.R. Robinson, Improved ocular bioavailability of indomethacin novel ocular drug carriers, J. Phram. Pharmacol. 48 (1996) 1147-1152. https://doi.org/10.1111/j.2042-7158.1996.tb03911.x.

[31] P. Calvo, A. Sánchez, J. Martínez, M.I. López, M. Calonge, J.C. Pastor, M.J. Alonso, Polyester nanocapsules as a new topical ocular delivery system for cyclosporin A, Pharm. Res. 13 (1996) 311-315. https://doi.org/10.1023/A:1016015803611.

[32] P. Calvo, J.L. Vila-Jato, M.J. Alonso, Evaluation of cationic polymer-coated nanocapsules as ocular drug carriers, Inter. J. Pharm. 153 (1997) 41-50. https://doi.org/10.1016/S0378-5173(97)00083-5.

[33] A.M. de Campos, A. Sánchez, R. Gref, P. Calvo, M.J. Alonso, The effect of a PEG versus a chitosan coating on the interaction of drug colloidal carriers with the ocular mucosa, Eur. J. Pharm. Sci. 20 (2003) 73-81. https://doi.org/10.1016/S0928-0987(03)00178-7.

[34] S.M. Saraiva, Polymeric nanocapsules for the ocular delivery siRNA, Doctoral Thesis, Minerva Respositorio Institucional da USC (2020). https://hdl.handele.net/10347//20532.

[35] A. Tcchoryk, V. Taresco, R.H. Argent, M. Ashford, P.R. Gellert, S. Stolnik, A. Grabowska, M.C. Garnett, Penetration, and uptake of nanoparticles in 3D tumor spheroids, Bioconjugate Chem. 30 (2019) 1371-1384. https://doi.org/10.1021/acs.bioconjchem.9b00136.

[36] M. Ugrinic, D. Decanini, N. Bidan, G. Lazzari, A. Harouri, G. Hwang, A.M. Haghiri-Gosnet, S. Mura, Fabrication of high aspect ratio microfluidic devices for long term in vitro

culture 3D tumor models, Microelectron. Eng. 267-268 (2023) 1-9. https://doi.org/10.1016/j.mee.2022.111898.

[37] D. Antoni, H. Buerckel, E. Josset, G. Noel, Three-dimensional cell culture: a breakthrough in vivo, Int. J. Mol. Sci. 16 (2015) 5517-5527. https://doi.org/10.3390/ijms16035517.

[38] W.H. Hsu, P. Sánchez-Gómez, E. Gomez-Ibarlucea, D.P. Ivanov, R. Rahman, A.M. Grabowska, N. Csaba, C. Alexander, M. Garcia-Fuentes, Structure-optimized interpolymer polyphosphazenes complexes for effective gene delivery against glioblastoma, Adv. Ther. 2 (2018) 1-15. https://doi.org/10.1002/adtp.201800126.

[39] M. Chacón, N. Vázquez. M. Persinal-Medina, S. Alonso-Alonso, I. Alcalde, M. Sánchez, L. Fernandez-Vega-Cueto, J. Merayo-Lloves, A. Meana, Evaluation of ocular irritancy based on cell membrane capacitance on a cruelty-free in vitro corneal model, IVOS 62 (2021).

[40] M. Chacón, N. Vázquez, M. Persinal-Medina, S. Alonso-Alonso, I. Alcalde, J. Merayo-Lloves, A. Meana, In-house performance assessment of 3D QobuR-reconstructed human cornea-like epithelium (RhCE) for the evaluation of eye hazard, Toxicol. In Vitro 82 (2022) 1-7. https://doi.org/10.1016/j.tiv.2022.105390.

[41] M. Chacón, N. Vázquez, S. Berisa, M. Persinal, M. Sánchez, B. Baamonde, J.F. Alfonso, L. Fernández-Vega Cueto, J. Merayo-Lloves, A. Meana, QobuR-a new in vitro human corneal epithelial model for preclinical drug screening, Eur. J. Pharm. Biopharm. 136 (2019) 164-173. https://doi.org/10.1016/j.ejpb.2019.01.023.

[42] C. Garcia-Mazas, S. Barrios-Esteban, N. Csaba, M. Garcia-Fuentes, Chapter13-Suppression of cancer stem cells, Woodhead Publ. Ser. Biomater. (2020) 365-398. https://doi.org/10.1016/B978-0-08-102983-1.00013-2.

[43] S. Salatin. S.M. Dizaj, A.Y. Khosroushahi, Effect of the surface modification, size, and shape on cellular uptake of nanoparticles, Cell Biol. Int. 39 (2015) 881-890. https://doi.org/10.1002/cbin.10459.

[44] D. Manzanares, V. Ceña, Endocytosis: the nanoparticle and submicron nano-compounds gateway into the cell, Pharmaceutics 12 (2020) 1-22. https://doi.org/10.3390/pharmaceutics12040371.

[45] E. Vighi, M. Montanari, B. Ruozi, G. Tosi, A. Magli, E. Leo, Nuclear localization of cationic solid lipid nanoparticles containing protamine as transfection promoter, Eur. J. Pharm. Biopharm. 76 (2010) 384-393. https://doi.org/10.1016/j.ejpb.2010.07.012.

[46] D. Delgado, A. del Pozo-Rodríguez, M.A. Solinís, A. Rofríguez-Gascón, Understanding the mechanism of protamine in solid lipid nanoparticle-based lipofection: the importance of the entry pathway, Eur. J. Pharm, Biopharm. 79 (2011) 495-502. https://doi.org/10.1016/j.ejpb.2011.06.005.

[47] L. Evensen, P.L. Johansen, G. Koster, K. Zhu, L. Herfindal, M. Speth, F. Fenaroli, J. Hildahl, S. Bagherifam, C. Tulotta, L. Prasmickaite, G.M. Maelandsmo, E. Snaar-Jagalska, G. Griffiths, Zebrafish as a model system for characterization of nanoparticles against cancer, Nanoscale 8 (2016) 862-877. https://doi.org/10.1039/C5NR07289A.

[48] C. Teijeiro-Valiño, E. Yebra-Pimentel, J. Guerra-Varela, N. Csaba, M.J. Alonso, Assessment of the permeability and toxicity of polymeric nanocapsules using the zebrafish model, Nanomedicine 12 (2017) 2069-2082. https://doi.org/10.2217/nnm-2017-0078.

[49] J. Crecente-Campo, J. Guerra-Varela, M. Peleteiro, C. Guitérrez-Lovera, I. Fernández-Mariño, A. Diéguez-Docampo, A. González-Fernández, L. Sánchez, M.J. Alonso, The size and composition of polymeric nanocapsules dictate their interaction with macrophages and biodistribution in zebrafish, JCR 308 (2019) 98-108. https://doi.org/10.1016/j.jconrel.2019.07.011.

[50] H. Zarei, B. Malaekeh-Nikouei, M. Ramezani, F. Soltani, Multifunctional peptides based on low molecular weight protamine (LMWP) in the structure of polyplexes and lipoplexes: design, preparation and gene delivery characterization, Drug Deliv. Sci. Technol. 62 (2021) 1-8. https://doi.org/10.1016/j.jddst.2021.102422.

CONCLUSIONS

CONCLUSIONS

In this thesis, the capacity of different nanometric platforms based on cationic polymers for the association of different nucleic acid molecules and their evaluation in different advanced preclinical models with application in cancer gene therapy have been described.

Results obtained from the experimental work led us to draw the following conclusions:

CHAPTER I:

1. Protamine:Dextran nanoparticles (Pr:Dx NPs) with a 4:1 (*w/w*) polymer ratio, present flexible and adjustable physicochemical characteristics with successful association of different nucleic acids providing protection against degradation, and adequate stability in different relevant biological fluids under different conditions.

2. Pr:Dx NPs show low cytotoxicity, and efficient intracellular internalization in conventional and 3D patient-derived glioblastoma models. Additional experiments for transfection optimization should be performed for future preclinical development.

CHAPTER II:

3. The addition of the house-made 6MHA-PPZ polyphosphazene preserves the physicochemical characteristics of cationic PEI/pDNA and Pr/pDNA nanocomplexes, achieving an increase in the reaction yield, and without affecting their stability in different biorelevant media under different conditions.

4. The incorporation of this anionic polymer to polycation/pDNA formulations reduces their cytotoxicity, especially for PEI/pDNA nanocomplexes, and this polymer also acts as a transfection enhancer, especially for Pr/pDNA nanocomplexes, in preclinical 2D and 3D patient-derived glioblastoma models, with clear evidence of dependence on the cell model.

5. The results obtained in the *in vivo* preclinical model of zebrafish embryos reveal the extraordinary accumulation of PEI/6MHA-PPZ nanocomplexes in their yolk sac with the diffusion of some particles towards the head area.

CHAPTER III:

6. Nanocapsules with an oily core of vitamin E surrounded by a protamine shell present adequate physicochemical properties for topical ocular administration, with satisfactory short- and long-term stability in different biological media, and an efficient ability to associate, retain and release different nucleic acids.

7. *In vitro* evaluation of protamine nanocapsules shows their low intrinsic toxicity and their capacity to interact and penetrate in 2D uveal melanoma and 3D human corneal epithelial models, respectively.

ABBREVIATIONS

ABBREVIATIONS

µg	Micrograms
µm	Microns
^{1}H-NMR	Proton nuclear magnetic resonance
2D	Two-dimensional
^{31}P-NMR	Phosphorus nuclear magnetic resonance
3D	Three-dimensional
5-TAMRA	5-Carboxytetramethylrhodamine
6MHA	6-mercaptohexanoic acid
6MHA-PPZ	6-mercaptohexanoic acid substituted polyphosphazene
7-AAD	7-Aminoactinomycin D
AAPPZ	Allylamine substituted polyphosphazene
ARRIVE	Animal Research: Reporting of In Vivo Experiments
ATCC	American Type Culture Collection
BBB	Blood-brain barrier
cDNA	Complementary DNA
cm^2	Square centimeters
CPP	Cell penetrating peptide
CRISP-Cas9	Clustered regularly interspaced short palindromic repeats
CS	Chitosan
CSCs	Cancer stems cells
CSLM	Confocal scanning laser microscopy
Cy3	Cyanine-3
Cy5	Cyanine-5
DAPI	4’6-diamidino-2-phenylindole

DCR	Derived count rate
DEPC	Diethylpyrocarbonate
DLin-DMA	4-[dimethylamine]-butanoic acid
DMAE	2-Dimethylaminoethanol
DMAEA	2-Dimethylaminoethylamine
DMPA	2,2-Dimethoxy-2-phenylacetophenone
DMRIE	1,2-dimyristyloxypropyl-3-dimethyl-hydroxyethylammonium bromide
DMSO	Dimethyl sulfoxide
DNA	Deoxyribonucleic acid
DODAP	1,2-Dioleoyl-3-dimethylammonium propane
DODMA	1,2-Dioleoyl-3-dimethylaminopropane
DOGS	2,5-Bis[3-aminopropylamino]-N-[2-[di[heptadecyl]amino]-2-oxoethyl]pentanamide lipid
DOPE	1,2-Dioleoyl-phosphatidyl-ethanolamine
DOTAP	N-[1-[2,3-dioleoyloxy]propyl]-N,N,N-trimethylammonium chloride
DOTMA	N-[1-[2,3-dioleyloxy]propyl]-N,N,N-trimethylammonium
DPBS	Dulbecco's phosphate-buffered saline
dpi	Days post-injection
DPSC	1,2-Distearoyl-sn-glycero-3-phosphorylcholine
Dx	Dextran
EGFP	Enhanced green fluorescence protein
EMA	European Medicines Agency
EP	European Pharmacopeia
FBS	Fetal bovine serum
FDA	Food and Drug Administration
FESEM	Field emission scanning electron microscopy
g	Grams
GCE	Glioblastoma central tumor core cell line
GFP	Green fluorescence protein

GIN	Glioblastoma invasive margin cell line
h	hours
HBSS	Hank's balanced salt solution
HCP	Hexachlorocyclotriphosphazene
HEPES	N-(2-Hydroxyethyl)piperazine-N'-(2-ethanesulfonic acid)
HIV	Human immunodeficiency virus
hpf	Hours post-fecundation
HPLC	High performance liquid chromatography
IARC	International Agency for Research on Cancer
kDa	Kilodalton
kV	Kilovolts
LB	Luria-Bertani
LD50	Lethal dose for the 50% of the cell population
LDA	Laser Doppler Anemometry
LMWP	Low molecular weight protamine
LSFM	Light sheet fluorescence microscopy
Luc	Luciferase
M	Molar
MFI	Mean Fluorescence Intensity
mg	Milligrams
min	Minutes
miRNA	Micro-RNA
mL	Milliliters
mm	Millimeters
mM	Millimolar
mRNA	Messenger RNA
Mw	Molecular weight
N/P ratio	Nitrogen/Phosphorus ratio
NCDB	National Cancer Database
NCs	Nanocapsules
ng	Nanograms

NLC	Nanostructured lipid nanocarriers
NLS	Nuclear localization signal
nm	Nanometers
NPC	Nuclear pore complexes
NPs	Nanoparticles
OCT	Optimum cutting temperature medium
OECD	Organization for Economic Cooperation and Development
OMS	Organización Mundial de la Salud
Opti-MEM	Opti-Minimum Essential Medium I 1X Reduced Serum Medium
P/S	Penicillin/streptomycin
PAMAM	Polyamidoamine
P-Arg	Poly-L-arginine
PBS	Phosphate buffered salt
PCS	Photon correlation spectroscopy
PDCP	Polydichlorophosphazene
PDI	Polydispersity index
pDNA	Plasmid DNA
PEG	Polyethylene glycol
PEI	Polyethylenimine
PES	Polyethersulfone
PGA	Polyglutamic acid
PLA	Polylactic acid
PLGA	Poly(lactic-co-glycolic acid)
PLL	Poly-L-lysine
ppm	Parts per million
PPZ	Polyphosphazenes
Pr	Protamine
PVI	Poly(vinyl imidazole)
RCF	Relative centrifugal force
RhCE	Reconstructed human corneal epithelium
RLUs	Relative luminiscence units

RNA	Ribonucleic acid
RNase	Ribonuclease
rpm	Revolutions per minute
RPMI	Roswell Park Memorial Institute
RT	Room temperature
s	Seconds
SD	Standard deviation
SDS	Sodium dodecyl sulfate
SDT	Sterile dechlorinated tap
SEM	Scanning electron microscopy
SEM	Standard error of the mean
shRNA	Short hairpin RNA
siRNA	Small interfering RNA
SLF	Simulated lacrimal fluid
SLN	Solid lipid nanoparticles
STEM	Scanning transmission electron microscopy
TAE	Tris-acetate-EDTA
TEA	Triethylamine
TEER	Transepithelial Electrical Resistance
TUNEL	Terminal deoxynucleotidyl transferase
ULA	Ultra-low attachment
UM	Uveal melanoma
UV	Ultraviolet
UV-VIS	Ultraviolet-Visible
w/w	Weight/weight
WHO	World Health Organization
WT	Wild Type
z	Zoom
Ω	Ohms

AGRADECIMIENTOS

La tesis ha sido como una montaña rusa que me ha hecho vivir muy buenos momentos para recordar, pero también, otros no tan buenos de los que he podido sacar su lado positivo. Haciendo memoria de estos últimos 5 años, me gustaría agradecer de corazón a todas las personas que han hecho posible que este largo camino fuera mucho más llevadero.

Gracias…

A mis directores de tesis Noémi Csaba y Marcos García Fuentes por darme la oportunidad de formar parte del mundo de la investigación, siendo una más en su grupo, y de poder desarrollar esta tesis doctoral.

A la financiación recibida por todas las entidades, pero en especial a la BritishSpanish Society y a la Diputación de A Coruña, ya que no habría sido posible el desarrollo de estos proyectos sin su aportación.

A la Universidad de Santiago de Compostela, al CIMUs y su gran equipo, por proporcionarme la ayuda necesaria para poder desarrollar cada proyecto. En especial me gustaría agradecer a Carmen y Ruth, a Lucía Alvariño, a Pilar y a Montse, sin olvidarme del equipo de asuntos económicos y los conserjes. Al equipo del departamento de Farmacología, Farmacia y Tecnología Farmacéutica por compartir sus grandes vivencias y consejos.

A todos aquellos con los que he tenido el placer de colaborar, haciendo este trabajo más multidisciplinar: Dr. María de la Fuente junto con Dr. María Pardo, Dr. Pablo Sáinz junto con Dr. Laura Elena Sánchez Piñón, y Dr. Ignacio Alcalde. Especially, I would like to thank Dr. Cameron Alexander and Dr. Ruman Rahman for letting me be part of their group with whom I shared experiences that enriched me personally and professionally. I would like to especially thank Nurcan, Karolina and Pratik for helping me inside and outside the laboratory, but without forgetting Eduardo, Rob, Michaela, Thais, Ahamed and, Rebeca: una gallega en tierras inglesas que me hizo sentir como en casa.

A colegas y amigos del P2L6: Héctor: por tu bendita paciencia, Rocío: la frase “malo será” se ha convertido en una de mis favoritas, Lorena: mucha suerte y ánimo en tu nueva etapa, y Sara: siempre fiel a tus conjuros. En especial quiero agradecer a Sandra: por tus ánimos de tirar pa’lante; espero de corazón que en el 2023 (en adelante) sigamos dando mucha guerra juntas porque…¡es nuestro año!, Chema: por tus sabios consejos, y por tu disponibilidad a dar siempre enormes abrazos, Carla: sí, finalmente conquistamos el laboratorio, Diego: pocas palabras, pero las perfectas para no rendirme, to Saeedeh and Maruthi: thank you for your contagious positivity, and finally, to Paul and Howl: because you included me into the group as one more.

A toda la gente de Nanochachos, y de los laboratorios P5 y P6: por los cafés compartidos, las grandes cenas, los carnavales, los secret Santa, y mucho más. En especial a Iago y Sergio: por vuestros consejos que hicieron mis agobios menos agobios. Gracias a todos por formar parte de esta experiencia de la que me llevo muchas anécdotas para recordar.

A mis visitantes favoritos a nuestro laboratorio: Lucía: por las conversaciones/cotilleos en la sala de cultivos, pero, sobre todo, gracias por hacerme ver las cosas desde otro punto de vista, y David (o David-Cientisol) mi comercial favorito y más eficaz. A la gente del P2L5 y P2L7:

por vuestro buen rollo a la hora de trabajar. A Alberto, Estefanía y Cristina, y en especial a Clara, mi primera pupila, de la que también aprendí mucho.

A mis amigas invisibles: por nuestros planes planeados y no tan planeados que fueron necesarios para parar y respirar. Porque vuestras palabras de ánimo y admiración me ayudaron a no rendirme. A Víctor: por tus interesantes preguntas sobre los experimentos que me ayudaron a tener otra perspectiva.

A Noemi y Lorena: por estar ahí desde que me embarqué en esta aventura. Por vuestros ánimos, pero en especial gracias por nuestras salidas memorables de desconexión de tesis (y de no tesis).

Al baile: por ser mi vía de escape, y ayudarme a recargar las pilas cuando más lo necesitaba. Gracias por hacerme coincidir con personas maravillosas. En especial a Susana ("tú mini yo"), Vicky, Inma, Jose, Miguel-profe, Ana y Cristóbal, Bárbara y mi otro-Miguel: gracias por acogerme como una galleguiña más desde el primer momento, y por hacer la parte dura de la tesis mucho más llevadera, siempre bailando. A Adrián (emoticono puño): por ser el amigo salsero más fiel, por tus ánimos, y, sobre todo, por tu insistencia para no dejar que el "sintrón" me hiciera perder muchos momentos bailongos.

A mi grupo "Sargentín": por ser únicas y, simplemente, las mejores. Gracias, chicas, porque habéis estado y estáis pendiente de mí en las distancias largas y cortas, y porque sé que siempre estaréis ahí.

A Bea (la Tata) y familia: por entenderme cuando hablaba de las "cosas de tesis" y, sobre todo, por los sabios consejos cuando, a veces, me encontraba desorientada. Gracias por todo vuestro apoyo y ánimo.

A Alberto: la palabra *gracias* se me queda corta. Gracias por tu divina paciencia y por ver siempre el lado positivo de los problemas. Gracias de corazón por ayudarme en esos momentos duros que te hace vivir una tesis, pero, sobre todo, gracias por ser el primero en formar parte de los buenos. Gracias por estar ahí en todo momento; simplemente gracias por ser mi mitad.

A mi familia: porque, aunque a veces os lieis con mi mundo de "bichos", siempre habéis estado pendiente de mí, en especial, mi tía Candelas. Y, gracias a ti, Rubén, que, junto con el abuelo, sé que me habéis mandado toda la fuerza para disfrutar de esta experiencia al máximo.

A mis padres: no tengo suficientes palabras para agradeceros todo lo que habéis hecho, estáis haciendo y sé que haréis por mí. Gracias con todo mi corazón por ayudarme y por formar parte de esta etapa de mi vida que ha sido importante para mí. Soy el motor tu vuestra vida, pero vosotros sois los engranajes de la mía; sin vosotros, nada funciona.

A ti, abuela: simplemente, por ser mi modelo a seguir.

ETHICAL ISSUES

ETHICAL ISSUES

IMAGES AND FIGURES

All the images presented in this thesis have been produced by myself, with the exception of zebrafish images which were obtained in collaboration with Dr. Pablo Cabezas-Sáinz (ZebraBioRes Group at the University of Santiago de Compostela) and histological and immunohistochemical images of 3D corneal models which were obtained in collaboration with Dr. Ignacio Alcalde (Laboratory of Cellular Biology and Innervation of the Ocular Surface, Fundación de Investigación Oftalmológica (FIO) at the University of Oviedo).

In addition, the Scanning Electron Microscope image of the U87MG glioblastoma spheroid, the nanoparticles were colored in orange by a kind contribution of Dr. Jose Manuel Ageitos (BioNanoTools Group at the University of Santiago de Compostela).

The figures in the present thesis were created in BioRender.com (https://biorender.com) and Servier Medical Art (http://smart.servier.com). The chemical structure images of polymers and lipids were from PubChem 2023 update (https://pubchem.ncbi.nlm.nih.gov) and the plasmid DNA map was from Addgene.com (https://www.addgene.org)

HUMAN CELL CULTURE

The primary glioblastoma patient-derived cell lines: GIN-8, GN-28 and GC-28 were kindly donated by Dr. Ruman Rahman (Children's Brain Tumor Research Group at the University of Nottingham). The project was approved by the National Research Ethics Committee East Midlands with Reference Number: 11/EM/0076.

The human corneal epithelial cells to form the QobuR-RhCE model was collected from corneal donor rims specimens after isolation of the central corneal button for transplantation by the collaboration of Dr. Ignacio Alcalde (Laboratory of Cellular Biology and Innervation of the Ocular Surface, Fundación de Investigación Oftalmológica (FIO) at the University of Oviedo). The project with number 2020.050 was approved by the Ethics Committee for Drug Research of the Principado de Asturias.

All cell lines were cultured in the conditions recommended by the manufacturers and collaborators, and only used for research purposes specifically described in this thesis.

ANIMAL STUDIES

The animal handling and the experimental procedures, care, and treatment were performed in agreement with the Animal Care and Use Committee of the University of Santiago de Compostela (project reference: 01/20/LU-003). Procedures followed by the European Union (Directive 2012-63-UE) and Spanish Government guidelines (Real Decreto 53/2013), conducted in the animal facilities in the Veterinary School of the University of Santiago de Compostela (Campus Lugo) (AE-LU-003)

ANNEXES

ANNEX I

Suppression of cancer stem cells

Carla Garcia-Mazas[*], **Sheila Barrios-Esteban**[*], Noemi Csaba and Marcos Garcia-Fuentes

[*]These authors contributed equally.

SUPPRESSION OF CANCER STEM CELLS

Carla Garcia-Mazas, **Sheila Barrios-Esteban**[*], Noemi Csaba and Marcos Garcia-Fuentes

[*]These authors contributed equally.

Biomaterials for Cancer Therapeutics (Second Edition) in Woodhead Publishing Series in Biomaterials. Chapter 13. pp. 365-398. ISBN 9780081029831

DOI: https://doi.org/10.1016/B978-0-08-102983-1.00013-2

Department of Pharmacology, Pharmacy and Pharmaceutical Technology, Center for Research in Molecular Medicine, and Chronic Diseases (CiMUS), University of Santiago de Compostela, Santiago de Compostela, Spain.

ABSTRACT

Current evidence confirms that tumor initiation and recurrence is generally governed by a subpopulation of tumor cells with stem-like signatures: cancer stem cells (CSCs). This population needs to be considered a pivotal target for tumor treatment, since it combines drug resistance and the capacity to restore tumors even from a few cells. Several drugs and biopharmaceuticals are being tested for their capacity to suppress CSCs based on their capacity to interfere with key-signaling pathways required to maintain this privileged and aggressive phenotype. However, these molecules have often poor biopharmaceutical properties, significant side effects, difficulties to reach their target site, and short half-lives. These limitations have motivated the integration of these therapeutic molecules in advanced drug delivery systems for improved stability, intratumoral penetration, and efficacy. We envisage that such delivery technologies will have important roles in new promising strategies based on combined drug therapies for disrupting the CSC niche and achieving cancer remission.

Keywords: Cancer stem cells, controlled release, drug delivery, nanomedicine, tumor initiating cells.

Suppression of cancer stem cells

13

Carla Garcia-Mazas, Sheila Barrios-Esteban*, Noemi Csaba and Marcos Garcia-Fuentes*
Department of Pharmacology, Pharmacy and Pharmaceutical Technology, Centre for Research in Molecular Medicine and Chronic Diseases (CiMUS), University of Santiago de Compostela, Santiago de Compostela, Spain

13.1 Introduction

13.1.1 Models of cancer origin

In the late 1990s Dick's group documented and characterized the existence of specific cancer cells subpopulations responsible of initiating malignant hematopoietic tumors [1]. These studies substantiated the cancer stem cell (CSC) model (Fig. 13.1) that postulates that a subset of neoplastic cells, that is, CSCs, is responsible for sustaining tumorigenesis and establishing tumor heterogeneity through self-renewal and differentiation [2]. From this point the CSC model has been extended to most solid tumors, where sizable evidence of the presence of this cancer cell subpopulation has been found [3].

Still, controversies persist about the concept of CSCs due to the lack of functional reference tests, variable cell surface markers, inconsistencies in terminology, and plasticity between cell types. The necessity to consider this evidence has put forward a new model of CSCs, proposing a bidirectional conversion equilibrium between CSCs and non-CSCs (Fig. 13.1). By this model, both the accumulation of genetic/epigenetic alterations and transformation between "stem-like" and "differentiated" cancer cells are responsible of tumor cell heterogeneity [4,5] (Chapter 21: The future of drug delivery in cancer treatment). This cancer cell plasticity has been linked to the epithelial-to-mesenchymal transition (EMT) program [6], a cellular process by which adherent epithelial cells lose their cell-to-cell adherence and become individual mesenchymal cells with the ability to migrate and invade adjacent tissues. Indeed, cancer cells that have gone through the EMT program present many of the characteristics of CSCs [7]. Besides, several studies have indicated that interactions between the CSC niche (see Section 13.1.3) and differentiated tumor cells might suffice to induce the transformation of these cells to CSCs [8].

* These authors contributed equally.

Biomaterials for Cancer Therapeutics. DOI: https://doi.org/10.1016/B978-0-08-102983-1.00013-2

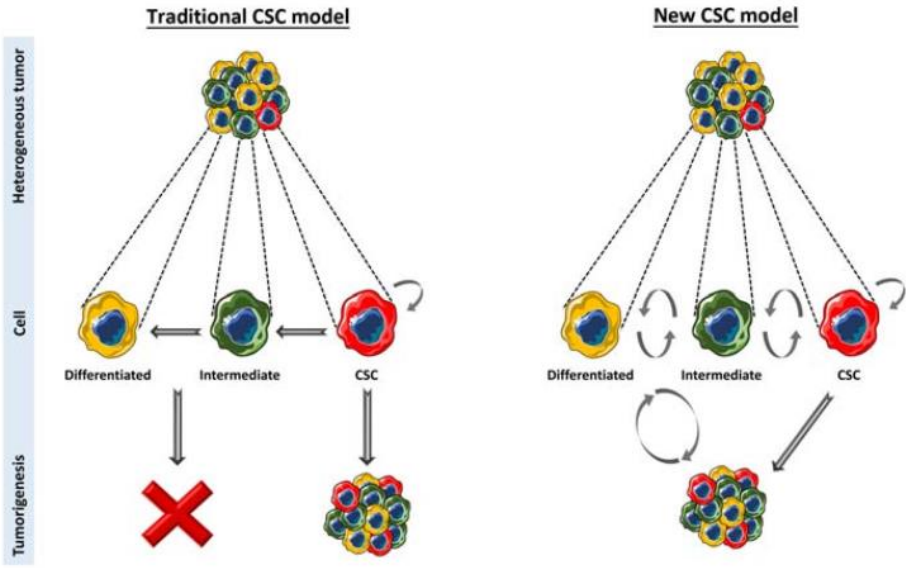

Figure 13.1 The evolution of the CSC model and its relationship with tumor heterogeneity and tumorigenesis. The traditional CSC model postulates that a small population of stem cells is responsible for the development of heterogeneous tumors and that tumor cells follow a rigid hierarchy created by unidirectional differentiation processes. The new CSC model acknowledges higher plasticity, with bidirectional conversion equilibria between CSC and non-CSCs. *CSCs*, Cancer stem cells.

13.1.2 Characteristics of cancer stem cells

Functional characteristics define CSCs compared to other tumor cells: (1) they have a high tumorigenic potential when transplanted in immunodeficient mice, (2) they can be isolated prospectively from other cancer cells according to their cell surface markers, and (3) they can be serially transplanted through generations [9,10]. Typically, CSCs represent a small fraction of the total tumor cells, but some reports indicate several exceptions to this rule [11].

From a phenotypic perspective, CSCs are enriched in the following surface markers: CD34, CD44, CD117, CD123, CD133, and ABCG2 [12]. CSCs are also enriched in some intracellular markers that promote their specific phenotype: Oct4, Sox2, Nanog, and aldehyde dehydrogenase (ALDH) [13,14]. ALDH is the most studied CSC marker. The human genome contains 19 putatively functional genes of ALDH. ALDH1 is a marker of stem cells from normal tissue and CSCs, where it participates in renewal, differentiation and self-protection. It presents three main isotypes: ALDH1A1, ALDH1A2, and ALDH1A3. In cancer therapy, ALDH1A1 provides a useful therapeutic target of CSCs in organs that do not normally express high levels of ALDH1A1, including breast, lung, esophagus, colon, and stomach tissue [15].

13.1.3 The cancer stem cell niche

CSCs reside in special microenvironments with other cells that nurture and protect them by inhibiting the activation of T lymphocytes and natural killer cells [16]. Moreover, factors secreted by CSCs induce angiogenesis and the activation of cancer associated fibroblasts [17] that can protect CSCs (Chapter 2: Phenotypic evolution of cancer cells: structural requirements for survival) and mediate immunosuppression [18]. Each tumor type can have specialized CSC niches, but two general structures have been described: the perivascular niche [19] and the hypoxic niche [20]. These are not mutually exclusive since hypoxic/necrotic regions can arise even at perivascular sites by the failure of vasculature to efficiently exchange oxygen [21].

In the CSC niche, paracrine signaling from immune and perivascular cells, including effectors of the Wnt, Hedgehog (Hh), and Notch pathways [22], and the activation of hypoxia-inducible factors (HIF) maintain the critical signaling networks that support the CSC phenotype [23]. These also protect the cells from the effect of many drugs. For instance, the hypoxic niche is known to protect glioblastoma CSCs from bone morphogenic protein (BMP)−induced CSC differentiation [24]. Besides cellular signaling considerations, CSC targeting requires the therapeutics to reach the niche at hardly accessible necrotic/hypoxic locations. This is a major delivery problem as pointed out by recent works, indicating the intrinsic difficulties of chemotherapy for achieving tumor penetration [25]. Although still an unresolved issue, transporting therapies to the CSC niche might benefit from the use of tissue penetrating nanoparticles with small particle size [26], slightly negative or neutral particle surface charges [27], and high stability in biological media [28].

13.1.4 Cancer stem cell drug resistance

An important characteristic of CSCs is their higher resistance to radiotherapy and chemotherapy as compared to bulk tumor cells, which, combined with their tumor reinitiating capacity, indicates their major role in treatment failure and tumor recurrence (Chapter 2: Phenotypic evolution of cancer cells: structural requirements for survival). Indeed, preclinical and clinical studies have confirmed the repopulation of recurrent tumors by CSCs after cytotoxic radio- and chemotherapy [29−31]. Other potent antiangiogenic drugs have also failed to provide significant survival benefits in clinical trials [32] due to CSC enrichment and the subsequent recurrence of the disease with resistant tumors [33].

A major mechanism behind CSCs drug resistance is the upregulation of efflux pumps. Efflux pumps are characteristic of many nonpathogenic and cancer cells but are upregulated in CSCs [34,35]. The principal multifunctional efflux pumps refer to adenosine triphosphate (ATP)−binding cassette (ABC) transporters [36]. For many years, researchers have focused on investigating different members of the ABC superfamily. A breakthrough occurred in 1976, when drug resistance was connected with the overexpression of a protein encoded by the ATP gene binding cassette, subfamily B, member 1: ABCB1 (MDR1 or P-glycoprotein). Some years later, ABCC1 (MRP1) and ABCG2 (BCRP or MXR) were also identified [37].

ABCG2 is a 72 kDa transport protein first found in a breast cancer cell line resistant to doxorubicin and then associated with tumor resistance to many other drugs such as mitoxantrone, camptothecin, anthracycline, flavopiridol, and antifolates [38]. Currently, ABCG2 is identified in most tumor types and is considered the major efflux pump inducing CSC resistance, being also upregulated under hypoxia [39]. ABCB1 and ABCC1 are unique polypeptides larger than 170−190 kDa, the former being a product of the MDR1 gene and acting as an ATP-dependent pump for a variety of hydrophobic compounds including anticancer and antimicrobial drugs. Its overexpression has been found in more than 50% of all drug-resistant tumors [34] (Chapter 5: Polymer therapeutics).

Another characteristic of CSCs that limit drug efficacy is quiescence (Chapter 21: The future of drug delivery in cancer treatment). It has been described that CSCs can stay for long periods in the G0 (resting) phase of the cell cycle [40,41], reducing the effect of many anticancer drugs that were designed to take advantage of the quick replication of the bulk tumor cells [42,43]. Besides, some drugs and gene therapies use the nuclear membrane disruption during mitosis to reach their target site in the nucleus, and, thus, these therapies are also blocked by quiescence [44]. Besides cell cycle effects, it should be noted that most signaling networks implicated in maintaining the CSC phenotype inhibit apoptosis and senescence, and by this mechanism, the pharmacological actions of many drugs on CSCs are also reduced.

13.2 Pharmacological strategies for suppressing cancer stem cells

In current protocols, CSCs are treated together with the other tumor cells using conventional cytotoxic drugs (e.g., doxorubicin and taxanes). This often results in low efficacy due to the inherent resistance of CSCs, which ultimately leads to tumor recurrence. This does not imply that CSCs are insensitive to chemotherapy; in fact, these cells present dysregulated signaling pathways necessary to maintain their phenotypic signatures. These signaling pathways open new opportunities for pharmacological treatments of CSCs, and CSC drugs might be applied either as a monotherapy or in combination with cytotoxic drugs that eliminate differentiated tumor cells (Fig. 13.2). Most CSC-specific drugs interact with one or multiple signaling networks and have broad cellular effects. Major signaling networks that can be altered are Hh, Notch, Wnt/β-catenin, transforming growth factor (TGF-β), phosphatidylinositol 3-kinase (PI3K)/Akt/mTOR, and NF-κB pathways. These signaling networks can also be manipulated by oligonucleotides [e.g., small interfering RNA (siRNA)] targeting pathway mediators or by shifting the balance of micro-RNAs (miRs) in the cells. Based on the type of applied therapies, in the following sections, we have divided the pharmacological strategies between those amenable to manipulation by conventional drugs (“druggable targets”) and those that can be manipulated with gene therapy.

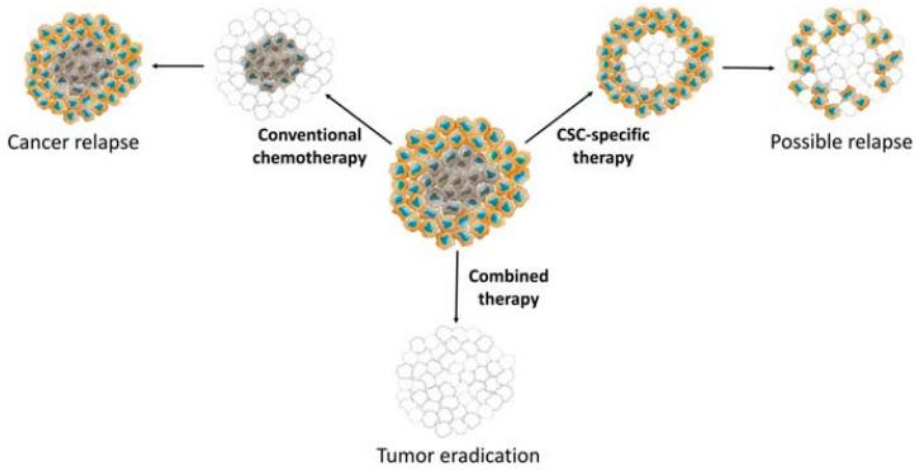

Figure 13.2 Overview of therapeutic strategies in cancer treatment. Conventional chemotherapy only destroys differentiated tumor cells (orange cells), without affecting CSCs population (gray cells), resulting in a high probability of relapse. CSC-specific therapies produce tumor degeneration through the elimination of CSCs, but relapses can occur due to de novo tumor cell dedifferentiation. The combination of both therapies is suggested to be the most efficient strategy for tumor eradication. *CSCs*, Cancer stem cells.

13.2.1 Druggable pharmacological strategies

13.2.1.1 Inhibitors of the Hedgehog pathway

This pathway is regulated through an extracellular and intracellular molecule known as Hh, which binds and inhibits the transmembrane protein Ptch1. Ptch1 itself is an inhibitor of the expression and activity of another group of membrane proteins called Smoothened (Smo). Therefore in CSCs, Hh overexpression leads to Smo activation that results in the activation of the Gli transcription factor and its accumulation in the cytoplasm (Fig. 13.3). Gli promotes many biological effects related to cell proliferation, survival, and stemness [45,46]. The Hh pathway can be inhibited by cyclopamine, a natural steroid alkaloid from corn lily that stabilizes Smo in its inactive form [45,47]. It can also be modulated by Gli-inhibitors such as JK184 and HPI-1 (Hh Pathway Inhibitor-1) [48,49]. In 2018, FDA approved the oral Hh inhibitor glasdegib for the treatment of acute myeloid leukemia [50].

13.2.1.2 Inhibitors of the Notch pathway

The Notch receptor is located in the cell membrane where it presents intracellular and extracellular domains. When its physiological ligand (delta-like ligands, DLLs) interacts with the external part, a proteolytic cleavage of the internal domain is produced by γ-secretase. This fragment migrates to the nucleus where it acts as a transcription factor [45] (Fig. 13.3). This transcription factor segment activates cellular programs involved in the maintenance of the CSC phenotype through the regulation of proliferation, differentiation, and apoptosis.

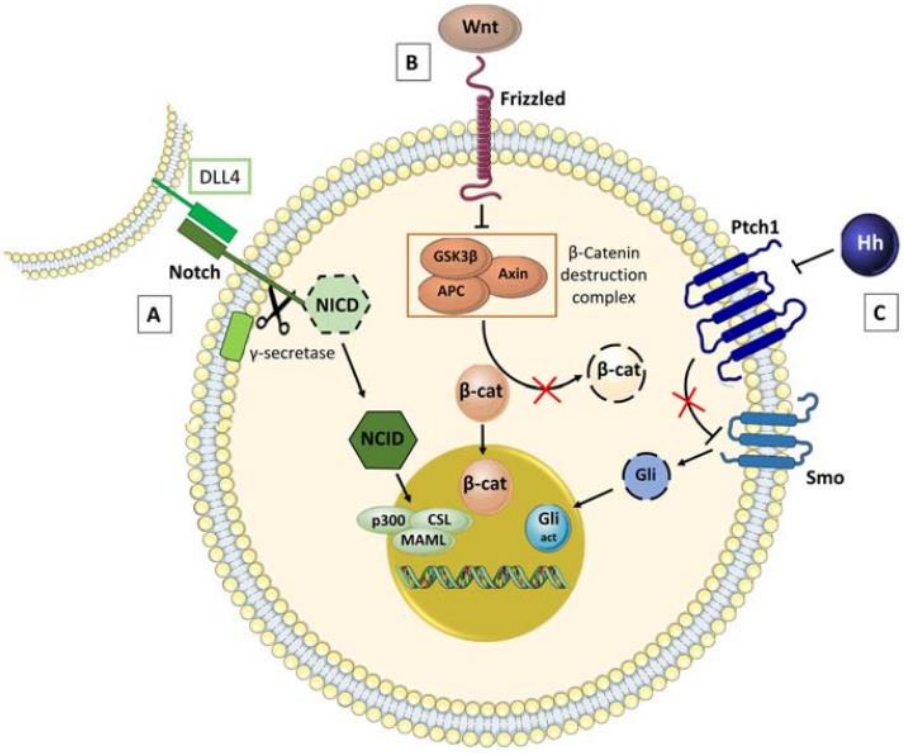

Figure 13.3 CSCs signaling pathways. The figure represents three major signaling pathways overexpressed in CSCs. (A) Notch pathway: the interaction of ligand DLL4 with the Notch receptor produces the cleavage of its intracellular domain, which migrates to the nucleus and acts as a transcription factor. (B) Wnt/β-catenin pathway: the interaction of Wnt factor with the Fz receptor blocks the β-catenin destruction complex, and this leads to the cytoplasmic accumulation of β-catenin and its migration to the nucleus, where it acts as transcription factor. (C) Hh pathway: the Hh molecule binds the transmembrane protein Patched-1 (Ptch1) that unblocks another membrane protein (Smo) activating the Gli factor, which migrates to the nucleus and activates gene transcription. All these pathways result in the transcription of genes involved in maintaining the CSC phenotype. *CSCs*, Cancer stem cells; *Fz*, frizzled; *Hh*, Hedgehog; *Smo*, smoothened.

Some inhibitors of the Notch pathway already tested on CSCs are semagacestat, DAPT, and DLL4 antibodies. The first two are inhibitors of γ-secretase: semagacestat is a repurposed small molecule in clinical trials for Alzheimer's disease [45] and DAPT is a modified dipeptide [51]. Antibodies against the Notch ligand DLL4 have also shown the capacity to inactivate the pathway and act upon CSCs by generating disorganized angiogenesis and EMT inhibition [52,53].

13.2.1.3 Inhibitors of Wnt/β-catenin

In this pathway the Wnt factor binds to the transmembrane receptor, Frizzled, which disrupts the formation of the multiprotein destruction complex (axin-APC-

GSK3β) that degrades β-catenin. This allows β-catenin to be translocated to the nucleus where it acts as a transcription [45,54] (Fig. 13.3), with effects on apoptosis, differentiation, migration, and proliferation.

The most important Wnt inhibitor is all-*trans*-retinoic acid (ATRA), an analog of vitamin A. ATRA has already been used as a differentiation therapy for acute promyelocytic leukemia [55], although the molecular mechanism of this activity is not yet completely elucidated. ATRA is part of the current first-line treatment for this disease together with arsenic trioxide. This combination has completely turned a fatal disease in one of the most treatable cancers, with remission in more than 90% of the patients [56]. Other Wnt inhibitors under investigation are repurposed dietary molecules such as quercetin [57], resveratrol [58], and curcumin. Curcumin, in fact, is not only a Wnt/β-catenin inhibitor, but it can also act on the Notch, Hh, and NF-κB pathways [59,60].

13.2.1.4 Modulators of the TGF-β pathway

This signaling pathway is involved in proliferation, invasion, metastasis, angiogenesis, and differentiation of CSCs and modification of the tumor niche. Some of the factors included in the TGF family are activin, nodal, BMPs, and growth and differentiation factors. These factors play an important role in stem cell differentiation and organogenesis [61,62]. TGF-β is an oncogenic cytokine when it is linked to a membrane complex formed by two receptors (TbRI and TbRII). This complex produces the phosphorylation of Smad transcription factors, which migrate to the nucleus to regulate transcription. The TGF-β pathway regulates the expression of DNA binding protein inhibitors (Id proteins), interfering with transcription factors and preventing differentiation of cells. In CSCs, these proteins are overexpressed and block cell differentiation [63].

BMPs also regulate cell differentiation, proliferation, and survival and can have paradoxical effects on CSCs, either promoting or suppressing tumor progression depending on BMP type. BMPs bind to both type I and II TGF-receptors, forming a complex that also transduces through Smad phosphorylation. In addition, they also participate in the regulation of other signaling pathways such as Notch, Hh, or Wnt [64]. BMP-2 promotes the proliferation and invasion of CSCs, while BMP-4 and BMP-7 have the opposite effect, reducing self-renewal and chemotherapy-resistance, enhancing differentiation and apoptosis [65,66]. Sustained levels of BMPs delivered by microspheres can suppress glioblastoma stem cells and result in reduced tumor growth and a more benign tumor phenotype [67,68].

13.2.1.5 Inhibitors of phosphatidylinositol 3-kinase/Akt/mTOR pathway

Upon the interaction of growth factors with their membrane receptor, PI3K converts phosphatidylinositol (4,5)-bisphosphate to phosphatidylinositol (3,4,5)-trisphosphate. This product activates Akt, which in turn regulates the phosphorylation of

different downstream targets in the NF-κB, GSK3β, mTOR pathways [69,70]. The effect over these molecular networks results in suppressed apoptosis, enhanced angiogenesis, and shifted metabolism.

Important molecules that have shown inhibition of this pathway in CSC models are rapamycin and perifosine. Rapamycin is a microbial drug with antibiotic, immunosuppressive, and antitumoral activity. It has potent inhibitory capacity on mTOR [69,71], resulting in specific effects over CSCs [72]. Perifosine is an alkylphospholipid that can also suppress CSCs by preventing Akt translocation to the plasma membrane [73]. Other drugs that can also act as PI3K antagonist are quercetin [74] and curcumin [75].

13.2.1.6 Inhibitors of NF-κB

This molecular network is involved in the maintenance, expansion, proliferation, and survival of CSCs. NF-κB signaling can be divided in two distinct pathways: canonical (inflammation and rapid immune response) and noncanonical (cell development) [76]. The canonical pathway is activated by the binding of cytokines or danger molecular patterns. This activates a kinase complex (IκB kinase, IKK) that degrades the IκB complex, releasing the transcription factors p50 and p65 to the nucleus where they induce proliferation, metastasis, antiapoptotic activity, angiogenesis, and stemness [77]. In contrast, the noncanonical NF- κB pathway is activated by lymphotoxin β, CD40 ligand, B-cell activating factor, and receptor activators of NF-κB ligand. The activation of this pathway requires the synthesis of NIK protein (NF-κB interacting kinase), which phosphorylates the IKKα that degrades p100, releasing p52. p52 is implicated in lymphoid organogenesis and B-cell function, and it is also a tumor-promoting transcription factor [78,79]. NF-κB can be inactivated by curcumin, as previously described, and by celastrol, a natural triterpenoid with the capacity to induce CSC apoptosis through IKK inhibition [76,80].

13.2.2 Gene therapies for cancer stem cells

Gene therapies have a huge potential against CSCs because of their capacity to act upon specific signaling pathways or even to modulate entire transcriptional networks. Because of their potency, oligonucleotides for RNA interference (RNAi), and mostly siRNA and micro-RNA (miR) have been the most explored nucleic acid therapeutics. The use of siRNA as CSC treatment is based on its selective inhibitory effect on key genes modulating their phenotype, many implicated in the pathways previously described. miRs are endogenous RNA sequences that regulate transcriptional networks. It is known that in CSCs, miRs are dysregulated with lower expression of onco-suppressive miRs and higher expression of the oncogenic ones. Pharmacologically, this imbalance can be shifted by miR supplementation or by the delivery of anti-miRs [81] (Chapter 7: Nucleic acid anticancer agents).

13.2.2.1 Small interfering RNAs for cancer stem cells therapy

siRNAs can be applied as therapy against CSCs by using inhibitory sequences against membrane receptors that participate in phenotype acquisition. For example, tumors treated with CD44-siRNA, [82], EpCAM-siRNA [83], GLUT3-siRNA [84], and CD95/Fas-siRNA [85] show growth inhibition, sensitization to chemotherapy, and reduced tumor initiating properties. The delivery of DRYRK1A-siRNA modulated epidermal growth factor receptor (EGFR) recycling, induced apoptosis, and reduced invasion/proliferation in CSCs [86]. Other regulators of CSC signaling pathways have also been silenced, including important regulators Bmi-1, Gli, and Notch1. Inhibition of these targets have shown reductions in tumor volume, cell proliferation, and cell invasiveness [87–89].

13.2.2.2 Micro-RNAs for cancer stem cells therapy

Several endogenous miRs with onco-suppressive activity are downregulated in CSCs, as observed in different tumors. The most important ones are miR-7, miR-34a (Chapter 7: Nucleic acid anticancer agents), miR-145, and miR-200. While each one of these miRs will act upon their specific transcriptional targets, the most important pathways implicated are Bcl-2, mTOR, Notch, Wnt, CD44, and TGF-β [90–93]. Some other targets of interest are EGFR, regulated by miR-7 [94]; HIF-2α and Oct4, regulated by miR-145 [95,96]; and platelet-derived growth factor D, regulated by miR-200 [97]. These miRs produce a common set of biological actions characterized by the inhibition of CSC traits: dedifferentiation/EMT, proliferation, invasiveness, and drug resistance [93]. The supplementation of these miRs inhibits CSCs and makes them more sensitive to conventional therapies.

On the other hand, some miRs have demonstrated to be upregulated in CSCs and have oncogenic properties. The most important oncogenic miRs are miR-21 and miR-155. The effect of miR-21 is mediated by Wnt-β/catenin, Notch, and mTOR/PI3K/Akt pathways and by the enhanced expression of Bcl-2 and HIF-1α [90,98–100]. On the other hand, miR-155 promotes TGF-β pathway and the expression of CSCs markers ABCG2, CD44, and CD90. It also inhibits the expression of TP53INP1, a nuclear protein with cancer suppressor properties [92,101,102]. These miRs mediate many CSC properties: tumor proliferation, invasiveness and metastasis, drug resistance, and dedifferentiation [93]. Since these miRs are upregulated and contribute to the CSC phenotype, their inhibition by anti-miRs is a logical therapeutic strategy to suppress CSCs. Indeed, the use of an antisense miR-21 oligonucleotide has led to a decline in tumor growth in vivo and in vitro [90].

13.3 Nanomedicines for cancer stem cell therapy

13.3.1 Delivery of small drugs to cancer stem cells

Most drugs used for CSC suppression have low solubility (e.g., HPI-1), low cellular uptake (curcumin), low oral absorption (e.g., cyclopamine), low bioavailability

(e.g., resveratrol), low stability (e.g., quercetin), or high toxicity (e.g., ATRA). Inclusion of drugs in suitable delivery systems improves their physicochemical properties, such as water solubility, and imparts the final formulations with better efficacy/toxicity ratios (Chapter 3: Immunoactive drug carriers in cancer therapy and Chapter 21: The future of drug delivery in cancer treatment). Besides, these strategies allow the codelivery of drugs in the same vehicle, creating a synergistic effect against CSCs or combinations that target simultaneously CSCs and other relevant cell types.

13.3.1.1 Polymer nanoparticles and micelles

Considering the hydrophobicity of most CSC-specific drugs, many groups have opted to design nanoformulations based on polyethylene glycol (PEG)-polyester block copolymers that form core−shell nanoparticles and micelles. The most used copolymers were poly(lactic acid)-PEG (PLA-PEG) [103], poly(lactic-*co*-glycolic acid)−PEG (PLGA-PEG) [49,104] (Chapter 6: pH-sensitive biomaterials for cancer therapy and diagnosis) and polycaprolactone-PEG (PCL-PEG) [105,106]. The hydrophobic core of these formulations provides an environment with high affinity for the drugs. For instance, ATRA, cyclopamine and resveratrol showed encapsulation efficacies higher than 70% [107−109]. Besides, the degradation profile of the composing polymers can provide sustained release of the drugs, from a few hours [109] to more than 2 weeks [107], depending on the drug, nanoparticle composition, and drug loading.

On the other hand, the PEG shell is known to provide these formulations with long-circulating properties and often with better biodistribution pattern that results in higher tumor accumulation. For instance, the concentration of drugs in the tumor 24-hour postinjection can increase more than fourfold with the PEGylated nanoparticles compared to the free drugs, as it has been seen for bortezomib and ATRA/doxorubicin [103,110]. Moreover, the plasma concentration of nanoencapsulated drugs such as docetaxel can increase more than fourfold in relation with the free drug and twofold when compared with non-PEGylated PLGA particles [111]. This can be important to counteract some of the important side effects of drugs such as ATRA, rapamycin, bortezomib, or cyclopamine [103,110,112,113].

The combination of the above characteristics has resulted in several successful examples of anticancer effect. Core−shell nanosystems have been used for the delivery of ATRA [107] and ATRA/doxorubicin [103] in glioblastoma models, resveratrol and cyclopamine/paclitaxel in prostate cancer models [109,114], and bortezomib and rapamycin/paclitaxel in breast cancer models [110,112]. The encapsulation of the drug in the nanocarrier increased the activity of these drugs in vitro [103,109,114]. Interestingly, a few studies have also confirmed specific effects over the CSCs or the malignancy of the tumor. For instance, coencapsulation ATRA and doxorubicin in a nanoparticle reduces the CSC population by almost half compared to the combined free drugs [103]. Likewise, the delivery of cyclopamine/paclitaxel in polymer micelles resulted in an increase in tumor-suppressive miRs in an orthotopic prostate tumor [114]. Several other studies have confirmed

that nanoencapsulation provides efficacy benefits as compared to the free drugs in vivo, both by providing a further reductions in tumor volume and in CSC frequency [103,110,114].

Considering the physiological role of albumin as drug transporter, this material is a logical choice for designing anticancer drug nanocarriers. Albumin formulations have indeed resulted in the first marketed nanoparticle formulation (Abraxane) for the delivery of anticancer drugs, FDA-approved already in 2005. Albumin nanoparticles have also been tested with CSC-specific drugs. Human serum albumin (HSA) nanoparticles loaded with resveratrol were tested in vivo in an ovarian carcinoma model, and they showed increased drug concentrations in the tumor and further reductions in tumor volume as compared to the free drug. The nanoparticle formulation also produced an overall increase in apoptosis markers [115]. HSA nanoparticles loaded with rapamycin and perifosine have also shown higher tumor accumulation [116] and higher antitumoral efficacy in a mouse myeloma model [117]. HSA nanoparticles with rapamycin are being tested in eight phases 1 and 2 clinical trials for a large range of tumors (https://clinicaltrials.gov: NCT03660930; NCT02646319; NCT02975882; NCT03817515; NCT03670030; NCT00934895; NCT03463265; NCT02009332).

An important strategy when dealing with CSCs is combination therapy. Such strategy can further benefit from nanomedicines where several drugs can be codelivered in the same carrier, therefore, potentially acting on the same cells. Polyester-PEG carriers have been investigated in detail for these codelivery strategies. For instance, PLA-PEG has been loaded with chloroquine and coencapsulated with doxorubicin or docetaxel. This combined therapy increased the efficacy of doxorubicin and docetaxel in vitro by the inhibitory effect of chloroquine in autophagy, which resulted in decreased "stemness" of the tumor cells. When tested in an orthotopic breast tumor model, those nanoparticles having the chloroquine/docetaxel or chloroquine/doxorubicin cotherapy showed higher growth inhibition and CSCs elimination than a mixture of nanoparticles delivering separately the two drugs [118]. PLA-PEG nanoparticles have also been investigated for delivering ATRA and doxorubicin in an orthotopic breast cancer model. This combination benefited from the capacity of ATRA to induce differentiation, sensitizing cells to the action of doxorubicin, and the combination therapy decreased tumor volume without enrichment of CSCs population [103]. PLGA-PEG nanoparticles have also been loaded with HPI-1 and gemcitabine. These nanoparticles inhibited tumor growth in vivo in murine medulloblastoma allografts, orthotopic pancreatic xenografts, and hepatocellular cancer xenografts. Besides these reductions in tumor volume, these nanoparticles also depleted the $CD133^+$ CSC population, and this activity was higher than that of the drugs given separately [119,120].

The examples of improved delivery of combination therapies extend to several other core−shell systems and cancer models. Indeed, significant antitumoral effects have been obtained: in ovarian xenografts treated with PCL-PEG micelles encapsulating cyclopamine, paclitaxel, and gossypol [105], in multiple myeloma models treated with HSA nanoparticles encapsulating rapamycin and perifosine [117], in multiresistant breast cancer models treated with PEGylated-rapamycin nanoparticles encapsulating paclitaxel [113] and in chemoresistant orthotopic prostate tumor

models treated with PEG-poly(2-methyl-2-carboxyl-prolylene carbonate) nanoparticles conjugated with paclitaxel and cyclopamine [114]. All these data in several types of cancer support the interest of investigating optimized nano-delivered drug combinations as new anticancer treatments.

13.3.1.2 Liposomes

Because of their extensive research in anticancer drug delivery, including the experience accumulated with FDA-approved formulations such as Doxil, PEGylated liposomes have become some of the most studied carriers for the delivery to CSCs. The rationale of their use is based on the affinity of most hydrophobic molecules for their lipid bilayer, while taking advantage of the biodistribution and long-circulating properties provided by the PEG shell [121,122]. Most of these liposomes are prepared from cholesterol, natural phospholipids, and PEG-modified phospholipids. Similar to nanoparticles, a major advantage of liposomes is the possibility of encapsulating more than one drug for combined CSC therapies (Chapter 3: Immunoactive drug carriers in cancer therapy).

Liposomes typically show good encapsulation properties for most of the previously mentioned drugs, with more than 90% encapsulation efficiency in the case of quercetin and ATRA [106,123], and 75% for rapamycin [124]. In general, drug release from liposomes is often pH-dependent and can last for 24 hours [125]. On the other hand, liposomes with optimized PEG coatings are known for their long-circulating properties and capacity to alter drug biodistribution [126] (Chapter 21: The future of drug delivery in cancer treatment). Indeed, most liposome formulations can prolong drug plasma half-life, and shift drug biodistribution to increase tumor accumulation as compared to the free drugs [127–129]. An added benefit of liposome delivery is that encapsulation often improves drug penetration in the cells. The delivery benefits of PEG-liposomes were seen in a prototype encapsulating ATRA and vinorelbine. This formulation showed enhanced cellular uptake and reduced opsonization in vitro [106].

Drug-loaded liposomes have shown efficacy in a variety of CSC-specific models. For instance, quercetin-loaded PEG-liposomes downregulated NF-κB and upregulated caspase-3 in breast and esophageal cancer models [123,130]. Moreover, the association of these liposomes with a CD133 antiserum exhibited additional apoptotic effect in an esophageal carcinoma model in vitro, where the treatment also showed the depletion of the $CD133^+$ CSC population [130]. PEG-liposomes functionalized with trastuzumab and loaded with resveratrol and curcumin have been tested in vitro in breast cancer cell lines where they showed enhanced drug activity as compared to the free drugs [131]. The same functionalized PEG-liposomes were loaded with paclitaxel and rapamycin and evaluated in breast cancer animal models. The PEG-liposome treatment provided tumor volume reductions and an increased survival rate without relevant side effects [132]. Liposomes loaded with disulfiram have also been tested for breast cancer therapy. In vitro, the liposomes resulted in the inhibition of the NF-κB pathway, increased reactive oxygen species activity, higher ALDH expression, and higher cytotoxicity. In vivo, they generated a strong anticancer effect without causing liver toxicity [133].

13.3.2 Gene delivery to cancer stem cells

Most gene therapies directed to CSCs have relied on the concept of RNAi, either by deploying siRNA, miR, or anti-miRs. The biological actions of these molecules against CSC have been described before (Section 13.2.2.), but their interest is also related to their manufacturing and delivery advantages that make them easier for pharmaceutical development than viral vectors and plasmid DNA. To begin with, RNAi molecules are easier to manufacture by industry [93,134]. Besides, they are potent, amenable to some chemical modifications, and have a cytosolic target site [135]. This makes their intracellular trafficking simpler than gene therapies aiming for the nucleus, particularly in slow-cycling cells [136]. Despite these delivery advantages, RNAi therapy is still limited by its inefficient delivery and transient effect. The inefficient transfer of RNAi oligonucleotides at the cellular level is caused by their poor membrane penetration capacity and by their degradation at the endo-lysosomal pathway [137,138]. In vivo, it is likely that extracellular mechanisms related to poor epithelial permeability and fast enzymatic degradation already eliminate the large majority of the oligonucleotides before even reaching the target cells [137]. Improvements in oligonucleotide delivery and stability can be achieved by chemical modification of the oligonucleotides, as reviewed recently [139], and by their association to optimized nanocarriers as summarized in the following paragraphs with specific focus on CSC therapies (Fig. 13.4).

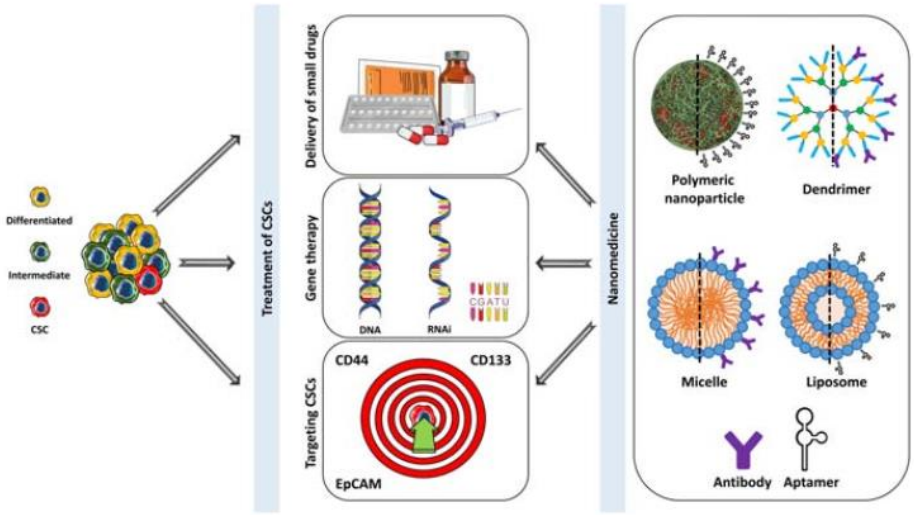

Figure 13.4 Scheme of the main strategies for CSC treatment where nanomedicine can provide added value. The most investigated nanocarriers for small drugs are core−shell polymeric micelles and PEGylated liposomes. The most investigated nanocarriers for gene therapy are polyplexes and lipoplexes. Targeting based on ligand-receptor interaction has been mostly based on specific coating polymers such as hyaluronic acid, or by conjugation of antibodies and aptamers. *CSCs*, Cancer stem cells.

13.3.2.1 Polymeric systems

The most used polymeric systems are based on cationic materials that condense the oligonucleotides and form nanocomplexes by electrostatic interaction [140]. Typical condensing polymers are chitosan [141], polyethyleneimine (PEI), polylysine (PLL), and poly(β-amino esters) [142] (Chapter 3: Immunoactive drug carriers in cancer therapy). Also, dendrimers based on poly(amido amine)s (PAMAM) have been frequently tested [143,144]. These nanoparticles provide the oligonucleotides with protection against RNAases and with a more efficient intracellular trafficking [145]. Indeed, the most studied polymers are materials with endosomal escape properties like PEI, which can enhance the intracellular delivery of oligonucleotides by several orders of magnitude. Another advantage of polymer nanoparticles is their tunable properties that can make them responsive to external stimuli (e.g., temperature, pH) facilitating gene delivery and triggered release [139,146].

Chitosan nanoparticles have been used as efficient vectors for the transport of RNAi oligonucleotides such as miR-34a in the treatment of prostate, colon, and laryngeal cancers. The encapsulation of nucleic acids in the nanocarrier increased the activity of these oligonucleotides in vitro and achieved significant reductions in tumor volume in vivo compared to blank controls [147–149]. Other in vitro studies have shown that PEI nanoparticles are effective carriers for siRNA delivery and can achieve significant reductions in neurosphere formation in glioblastoma models when combined with low doses of temozolomide [150]. When grafted to polyurethane, PEI showed great efficacy both in vitro and in vivo: PEI nanoparticles loaded with miR-145 or siRNA against critical CSC receptors inhibited CSC proliferation and reduced tumor volume in glioblastoma [151], lung adenocarcinoma [152], colon [153], leukemia [154], and breast cancer [155].

Several studies have also investigated PAMAM dendrimers as gene nanotransporters (Chapter 6: pH-sensitive biomaterials for cancer therapy and diagnosis) in CSC therapies. PAMAM sixth generation dendrimers loaded with siRNA against $p70S^{6K}$ were able to reduce the tumorogenicity and metastatic properties of CSCs of ovarian cancer [144]. This gene therapy also inhibited the growth of xenograft tumors from CSCs. In contrast, third generation PAMAM dendrimers loaded with siRNA against TWIST were only effective in vitro against ovarian carcinoma CSCs, but not in vivo [156]. The transfection capacity of PAMAM was also used to design a codelivery nanocarrier where the dendrimers with anti-miR-21 and doxorubicin were associated to hollow gold nanoparticles for sequential release of both active compounds. This combined therapy produced a synergistic effect and superior anticancer efficacy [157].

An emerging idea for gene delivery in cancer is the exploration of polymer libraries to select materials with the best delivery properties [158]. The process of polymer library synthesis can be streamlined by the use of polymers with "click" handles that are modified by postpolymerization reactions. Such approach has recently been used for the generation of gene delivery systems against CSCs based on cationic and anionic polyphosphazenes [146]. The optimized nanoparticles, which included a cationic and a pH-sensitive anionic polyphosphazene counterpart,

showed better transfection/toxicity ratios than PEI in 3D spheroid models. Polyphosphazene nanoparticles loaded with a siRNA against DYRK1A reduced glioblastoma CSC tumorigenesis in vitro and produced significant tumor volume reduction in vivo when used as an adjuvant to temozolomide [146].

Other interesting nanocarriers for CSC gene therapy are core−shell structures where hydrophobic polymers (e.g., PLA, PLGA, and PCL) are coated with cationic groups that promote oligonucleotide condensation [159,160]. Typical cationic shell-forming blocks comprise PEI, poly(dimethylaminoethyl methacrylate) and poly(2-aminoethylethylene phosphate) (PAEEP). This core−shell disposition allows the formation of micelle-type structures that are very useful for the combined delivery of drugs and oligonucleotides [160]. In these cationic micelles, small drugs encapsulated in their core can benefit from the same solubilization and controlled release properties as described previously (13.3.1), while oligonucleotides benefit from the intracellular delivery characteristics imparted by the polymeric shell.

Based on this strategy, polymeric micelles based on PEGylated multiblock polymers having pendent cationic groups and sites for drug conjugation have been explored for CSC-targeted therapies. Polymer conjugates of gemcitabine efficiently complexed miR-205, and this therapy was able to reduce the chemoresistance and invasiveness of gemcitabine-resistant pancreatic CSCs. In vivo studies performed in pancreatic cancer xenografts showed significant inhibition of tumor growth, reduced cell proliferation, and increased apoptosis [161]. Other PEGylated micelles based on PLL derivatives have been used for the codelivery of siRNA and doxorubicin and showed significant tumor inhibition in nonsmall cell lung cancer as compared to the same nanoparticles loaded either with the siRNA or the drug [162]. A core−shell system prepared by mixing diblock copolymers of PCL-b-PEG and PCL-b-PAEEP was used to deliver siRNA against Notch1 in combination with platinum (IV) drugs in hepatocellular carcinoma. The nanoparticles achieved increased therapeutic efficacy in comparison to the drug monotherapy and the free drug through a direct effect on CSCs [163].

13.3.2.2 Lipid systems

Liposomes and lipidic nanosystems based on cationic lipids are among the most effective synthetic carriers for oligonucleotide delivery [139] due to their biocompatibility, capacity to stabilize the nucleic acids, and ability to promote their internalization [164,165]. Typical lipid formulations for gene delivery are based on *N*-[1-(2,3-dioleyloxy) propyl]-*N*,*N*,*N*-trimethylammonium chloride or 1,2-bis (oleoyloxy)-3-(trimethylammonio) propane [166] and are usually mixed with an "endosomal escape helper" lipid such as dioleoylphosphatidylethanolamine [167]. Other lipids present in most gene delivery formulations are cholesterol, used for improving membrane stability [168] and PEG-modified lipids, for enhancing circulation time [169]. Similar to the case of polymeric micelles, the presence of the hydrophobic membrane and the cationic shell of the liposomes make them very versatile for integrating combination therapies of small drugs and oligonucleotides [139].

Lipid nanoparticles based on these lipids have been used to treat breast CSCs by encapsulating a combination of camptothecin and siRNAs against clustein, another protein implicated in chemoresistance. The study showed that this delivery system provided more effective gene delivery than the standard transfecting agent lipofectamine and the combination therapy also improved antitumoral effects as compared to the drugs delivered separately [170]. Improvements on the treatment of breast CSCs could also be obtained with the same lipid particles with paclitaxel/miR-200c combinations [171]. Lipid nanoparticles delivering cisplatin and siRNA against Bmi-1 also showed significant efficacy for combination therapy in CSCs of hepatocellular carcinoma and this translated to higher antitumoral activity in tumor xenografts [172].

Other lipid nanoparticle compositions have also achieved interesting results recently. For instance, nanoparticles combining 1,2-diolyl-3-dimethylammonium-propane, a PEGylated sphingosine derivative, and disteroylphosphatidylcholine were used to deliver miR-199b-5p. The formulation showed high antitumoral efficacy with shifts in CSCs markers observed in different cancer types: colon, breast, prostate, and brain [173]. An anionic lipid nanoparticle conjugated to anti-miR-126 has also been used to treat acute myeloid leukemia, resulting in CSC depletion and increased survival in secondary tumor cell transplantation experiments [174]. We have identified at least 10 gene therapies related to CSCs and delivered in lipid nanocarriers that are currently in clinical trials. The studies cover a variety of cancers and are all in clinical phases 1 and 2 (https://clinicaltrials.gov: NCT03323398; NCT01437007; NCT02716012; NCT02110563; NCT02314052; NCT03323398; NCT01437007; NCT02716012; NCT02110563; NCT02314052).

13.3.3 Targeting to cancer stem cells

Considering the key role of CSCs in cancer relapse and metastasis, several groups have pursued strategies to target therapeutic molecules to this cell population. While there is some heterogeneity on the phenotypic markers of CSCs, most works have focused on targeting three receptors: CD44, CD133, and EpCAM [175,176]. All of them are membrane glycoproteins and have biological activities linked to the maintenance of the CSC phenotype [177–181]. Targeting these receptors can be achieved by antibodies and aptamers. Out of these, antibody ligands represent most broadly used strategy for CSC targeting [182–184]. Aptamer ligands have also been used for all the three receptors [185,186] but have been extensively explored for EpCAM [104,187,188]. Besides the previous strategies, CD44 targeting has been mostly addressed by coating nanocarriers with its endogenous receptor ligand hyaluronic acid [46,189–191] (Chapter 3: Immunoactive drug carriers in cancer therapy).

In vitro, several of these systems have shown the capacity to selectively bind to CSC receptors [185] and be preferentially internalized by CSCs in the presence of other cell populations [192]. In vivo, a few articles have reported higher tumor accumulation of CSC-targeted nanoparticles as compared to the same nonfunctionalized carriers [193]. Besides, several observations have indicated that targeted

nanoparticles also accumulate preferentially in the CSC population in vivo [194,195]. Still, these observations need to be seen with caution since the general concept of targeting is currently under debate. Indeed, a systematic review concluded that only around 0.7% of nanoparticles are distributed to the tumors and that targeting has little effect on this result [196]. Besides, even with targeted systems, the percentage of nanoparticles that reach cancer cells has been calculated to be around 0.0014% of the injected dose [197]. These results indicate that the assumed targeting is not really occurring in vivo, and this is understandable because targeting can occur only after the delivery systems reach the target. Delivering more drugs to targets in vivo is the single most important problem in making all formulations effective in clinical trials.

Despite these open questions, several in vitro and in vivo studies have shown indications that nanocarriers targeted to CSCs by specific ligands could outperform nontargeted ones for anticancer efficacy. CD44-targeted carriers have shown significantly higher antitumoral effect than nontargeted systems [46,190,192,198,199], together with the capacity to reduce the CSC population in breast and pancreatic cancer as well as in hepatocellular carcinoma [46,185,191,199,200]. Drug-loaded nanoparticles and liposomes functionalized with anti-CD133 antibodies have also shown improved efficacy against CSCs, with higher tumor reduction and lower tumor recurrence in breast cancer, colorectal cancer, and glioblastoma [183,201–204]. Drug-loaded nanoparticles targeted against EpCAM have also led to higher efficacy in breast adenocarcinoma [104], lung [187], colon [104], and ovarian cancer [188] as compared to the free drug and the nontargeted carrier. Immunoliposomes targeted to EpCAM and loaded with doxorubicin and siRNA were significantly more cytotoxic to CSCs than the same nontargeted formulation. They were also able to generate tumor regression even at very low concentrations when tested in breast cancer, small cell lung carcinoma [184], and in epithelial in vivo cancer models [205]. While is still unclear whether this improved anticancer efficacy observed for some nanocarriers with specific receptor binding will translate to human patients, several ongoing clinical trials might soon shed some light on the issue (https://clinicaltrials.gov: NCT03774680, NCT02979392, NCT01702129, NCT02766699).

13.4 Concluding remarks

The existence of CSCs and their implication in tumorigenesis and recurrence is now broadly accepted for most tumors. However, in contrast with the initial CSC hypothesis, this phenotype does not seem to be fully restricted to a defined set of cells at the top of a rigid hierarchy but rather results from cell plasticity. This new concept of cell plasticity makes the treatment of CSCs more complex since all cells that are—or could become—part of this population need to be eliminated to suppress tumor recurrence.

Stimulated by the success of ATRA in acute promyelocytic leukemia, many clinical trials have been launched to investigate molecules that suppress CSCs [206], and this has resulted in two recent FDA approvals (glasdegib and venetoclax), both for acute myeloid leukemia. Still, the arsenal against CSCs is restricted to a few active molecules, mostly with low solubility and important side effects, and to oligonucleotides with inherent difficulties to overcome cellular barriers. These limitations on drug toxicity and poor delivery are being tackled by encapsulating the drugs in optimized nanocarriers, an idea that has already been translated to a few clinical trials. As relevant examples, albumin nanoparticles with rapamycin are being tested in a variety of tumor types, and several lipid nanocarriers are being explored for gene therapy approaches. Nanocarriers are also ideally suited for the development of combined therapies since they can deliver several drugs simultaneously to the same target region [207].

A critical challenge for new therapies acting on CSCs is to reach all their target cells. This is a complex problem since many CSCs are hidden in tumor regions with poor accessibility and a protective niche environment. Delivery improvements can be achieved by the coadministration of degradative enzymes (e.g., hyaluronidases and collagenases) to digest the extracellular matrix, but this idea is restricted to intratumoral administration modalities [208,209]. There is now higher awareness regarding the relevance of drug carriers to promote intratumoral transport, and some recent studies have identified some physicochemical properties required for efficient tumor penetration [210]. Another promising strategy is based on the use of tumor-penetrating peptides [211]. Still, the process of drug and carrier transport through the tumors seems to be highly inefficient, and further studies will be required to clarify the main bottlenecks and design technologies that could overcome them.

Since CSCs require support from their niche to maintain their phenotype, therapies directed toward its disruption are highly promising. Many of the drugs covered in this chapter are, in essence, capable of disrupting the niche temporally by their effect on key-signaling pathways (Notch, Wnt, Hh, etc.). However, once the drug is eliminated, the niche will restore its functionality. The next generation of controlled delivery systems may bring great value in this context, since these technologies could achieve continuous disruption of the niche, both eliminating CSCs and preventing the restoration of this population from newly dedifferentiated tumor cells. For instance, this idea has been applied to generate microspheres that provide continuous delivery of BMP-7 for more than 2 months, and this technology has been used to suppress glioblastoma CSCs [67,68]. We envisage that this strategy will translate into important clinical benefits, mostly in combination with classical cytotoxic drugs to eliminate the bulk tumor.

Acknowledgments

This work was supported by Ministerio de Economía y Competitividad (MAT2017-84361-R, FEDER Funds) and Xunta de Galicia (Grupos de Referencia Competitiva, FEDER Funds). CGM is funded by predoctoral grant from Ministerio de Educación, Cultura y Deporte (FPU16/03836).

Abbreviations

ABC	Adenosine triphosphate−binding cassette
ALDH	aldehyde dehydrogenase
ATP	adenosine triphosphate
ATRA	all-trans-retinoic acid
BMPs	bone morphogenic proteins
CSCs	cancer stem cells
DLLs	delta-like ligands
EGFR	epidermal growth factor receptor
EMT	epithelial-to-mesenchymal transition
Fz	frizzled
Hh	Hedgehog
HIF	hypoxia-inducible factors
HPI-1	Hedgehog pathway inhibitor-1
HSA	human serum albumin
miRNA or miR	micro-RNA
PAEEP	poly(2-aminoethylethylene phosphate)
PAMAM	poly(amido amine)s
PCL-PEG	polycaprolactone-poly(ethylene glycol)
PEG	polyethylene glycol
PEI	polyethyleneimine
PI3K	phosphatidylinositol 3-kinases
PLA-PEG	poly(lactic acid)-poly(ethylene glycol)
PLGA-PEG	poly(lactic-co-glycolic acid)-poly(ethylene glycol)
PLL	polylysine
RNAi	RNA interference
siRNA	small interfering RNA
Smo	smoothened
TGF	transforming growth factor

References

[1] T. Lapidot, C. Sirard, J. Vormoor, B. Murdoch, T. Hoang, J. Caceres-Cortes, et al., A cell initiating human acute myeloid leukaemia after transplantation into SCID mice, Nature 367 (1994) 645−648. Available from: https://doi.org/10.1038/367645a0.

[2] J.E. Visvader, G.J. Lindeman, Cancer stem cells: current status and evolving complexities, Cell Stem Cell 10 (2012) 717−728. Available from: https://doi.org/10.1016/j.stem.2012.05.007.

[3] A. Kreso, J.E. Dick, Evolution of the cancer stem cell model, Cell Stem Cell 14 (2014) 275−291. Available from: https://doi.org/10.1016/j.stem.2014.02.006.

[4] A.K. Singh, R.K. Arya, S. Maheshwari, A. Singh, S. Meena, P. Pandey, et al., Tumor heterogeneity and cancer stem cell paradigm: updates in concept, controversies and clinical relevance, Int. J. Cancer 136 (2015) 1991−2000. Available from: https://doi.org/10.1002/ijc.28804.

[5] E. Batlle, H. Clevers, Cancer stem cells revisited, Nat. Med. 23 (2017) 1124−1134. Available from: https://doi.org/10.1038/nm.4409.

[6] C. Scheel, R.A. Weinberg, Phenotypic plasticity and epithelial-mesenchymal transitions in cancer and normal stem cells? Int. J. Cancer 129 (2011) 2310–2314. Available from: https://doi.org/10.1002/ijc.26311.
[7] M. Luo, M. Brooks, M. Wicha, Epithelial-mesenchymal plasticity of breast cancer stem cells: implications for metastasis and therapeutic resistance, Curr. Pharm. Des. 21 (2015) 1301–1310. Available from: https://doi.org/10.2174/1381612821666141211120604.
[8] T. Sato, J.H. van Es, H.J. Snippert, D.E. Stange, R.G. Vries, M. van den Born, et al., Paneth cells constitute the niche for Lgr5 stem cells in intestinal crypts, Nature 469 (2011) 415–418. Available from: https://doi.org/10.1038/nature09637.
[9] P.B. Gupta, C.L. Chaffer, R.A. Weinberg, Cancer stem cells: mirage or reality? Nat. Med. 15 (2009) 1010–1012. Available from: https://doi.org/10.1038/nm0909-1010.
[10] L. Ricci-Vitiani, D.G. Lombardi, E. Pilozzi, M. Biffoni, M. Todaro, C. Peschle, et al., Identification and expansion of human colon-cancer-initiating cells, Nature 445 (2007) 111–115. Available from: https://doi.org/10.1038/nature05384.
[11] E. Quintana, M. Shackleton, M.S. Sabel, D.R. Fullen, T.M. Johnson, S.J. Morrison, Efficient tumour formation by single human melanoma cells, Nature 456 (2008) 593–598. Available from: https://doi.org/10.1038/nature07567.
[12] M. Cojoc, K. Mäbert, M.H. Muders, A. Dubrovska, A role for cancer stem cells in therapy resistance: cellular and molecular mechanisms, Semin. Cancer Biol. 31 (2015) 16–27. Available from: https://doi.org/10.1016/j.semcancer.2014.06.004.
[13] T. Itinteang, J.C. Dunne, A.M. Chibnall, H.D. Brasch, P.F. Davis, S.T. Tan, Cancer stem cells in moderately differentiated oral tongue squamous cell carcinoma express components of the renin–angiotensin system, J. Clin. Pathol. 69 (2016) 942–945. Available from: https://doi.org/10.1136/jclinpath-2016-203736.
[14] M.-Q. Gao, Y.-P. Choi, S. Kang, J.H. Youn, N.-H. Cho, CD24 + cells from hierarchically organized ovarian cancer are enriched in cancer stem cells, Oncogene 29 (2010) 2672–2680. Available from: https://doi.org/10.1038/onc.2010.35.
[15] H. Tomita, K. Tanaka, T. Tanaka, A. Hara, Aldehyde dehydrogenase 1A1 in stem cells and cancer, Oncotarget 7 (2016) 11018–11032. Available from: https://doi.org/10.18632/oncotarget.6920.
[16] J.M. Pitt, A. Marabelle, A. Eggermont, J. Soria, G. Kroemer, Targeting the tumor microenvironment: removing obstruction to anticancer immune responses and immunotherapy, Ann. Oncol. 27 (2016) 1482–1492. Available from: https://doi.org/10.1093/annonc/mdw168.
[17] Z. Castaño, C.M. Fillmore, C.F. Kim, S.S. McAllister, The bed and the bugs: Interactions between the tumor microenvironment and cancer stem cells, Semin. Cancer Biol. 22 (2012) 462–470. Available from: https://doi.org/10.1016/j.semcancer.2012.04.006.
[18] J. Wei, J. Barr, L. Kong, Y. Wang, A. Wu, A.K. Sharma, et al., Glioblastoma cancer-initiating cells inhibit T-cell proliferation and effector responses by the signal transducers and activators of transcription 3 pathway, Mol. Cancer Ther. 9 (2010) 67–78. Available from: https://doi.org/10.1158/1535-7163.MCT-09-0734.
[19] C. Calabrese, H. Poppleton, M. Kocak, T.L. Hogg, C. Fuller, B. Hamner, et al., A Perivascular niche for brain tumor stem cells, Cancer Cell 11 (2007) 69–82. Available from: https://doi.org/10.1016/j.ccr.2006.11.020.
[20] F.E. Lock, P.C. McDonald, Y. Lou, I. Serrano, S.C. Chafe, C. Ostlund, et al., Targeting carbonic anhydrase IX depletes breast cancer stem cells within the hypoxic niche, Oncogene 32 (2013) 5210–5219. Available from: https://doi.org/10.1038/onc.2012.550.

[21] Y. Rong, D.L. Durden, E.G. Van Meir, D.J. Brat, 'Pseudopalisading' necrosis in glioblastoma: a familiar morphologic feature that links vascular pathology, hypoxia, and angiogenesis, J. Neuropathol. Exp. Neurol. 65 (2006) 529–539. Available from: https://doi.org/10.1097/00005072-200606000-00001.

[22] V. Plaks, N. Kong, Z. Werb, The cancer stem cell niche: how essential is the niche in regulating stemness of tumor cells? Cell Stem Cell 16 (2015) 225–238. Available from: https://doi.org/10.1016/j.stem.2015.02.015.

[23] T. Borovski, F. De Sousa, E. Melo, L. Vermeulen, J.P. Medema, Cancer stem cell niche: the place to be, Cancer Res. 71 (2011) 634–639. Available from: https://doi.org/10.1158/0008-5472.CAN-10-3220.

[24] F. Pistollato, E. Rampazzo, S. Abbadi, A. Della Puppa, R. Scienza, D. D'Avella, et al., Molecular mechanisms of HIF-1α modulation induced by oxygen tension and BMP2 in glioblastoma derived cells, PLoS One 4 (2009) e6206. Available from: https://doi.org/10.1371/journal.pone.0006206.

[25] M. Prieto-Vila, R. Takahashi, W. Usuba, I. Kohama, T. Ochiya, Drug resistance driven by cancer stem cells and their niche, Int. J. Mol. Sci. 18 (2017) 2574. Available from: https://doi.org/10.3390/ijms18122574.

[26] J. Choi, Q. Zhang, V. Reipa, N.S. Wang, M.E. Stratmeyer, V.M. Hitchins, et al., Comparison of cytotoxic and inflammatory responses of photoluminescent silicon nanoparticles with silicon micron-sized particles in RAW 264.7 macrophages, J. Appl. Toxicol. 29 (2009) 52–60. Available from: https://doi.org/10.1002/jat.1382.

[27] J. Panyam, M.M. Dali, S.K. Sahoo, W. Ma, S.S. Chakravarthi, G.L. Amidon, et al., Polymer degradation and in vitro release of a model protein from poly(D,L-lactide-*co*-glycolide) nano- and microparticles, J. Control. Release 92 (2003) 173–187. Available from: https://doi.org/10.1016/S0168-3659(03)00328-6.

[28] F.M. Goycoolea, F. Brunel, N.E. El Gueddari, A. Coggiola, G. Lollo, B.M. Moerschbacher, et al., Physical properties and stability of soft gelled chitosan-based nanoparticles, Macromol. Biosci. 16 (2016) 1873–1882. Available from: https://doi.org/10.1002/mabi.201600298.

[29] K. Rycaj, D.G. Tang, Cancer stem cells and radioresistance, Int. J. Radiat. Biol. 90 (2014) 615–621. Available from: https://doi.org/10.3109/09553002.2014.892227.

[30] M. Diehn, M.F. Clarke, Cancer stem cells and radiotherapy: new insights into tumor radioresistance, JNCI J. Natl. Cancer Inst. 98 (2006) 1755–1757. Available from: https://doi.org/10.1093/jnci/djj505.

[31] L. Wang, X. Liu, Y. Ren, J. Zhang, J. Chen, W. Zhou, et al., Cisplatin-enriching cancer stem cells confer multidrug resistance in non-small cell lung cancer via enhancing TRIB1/HDAC activity, Cell Death Dis. 8 (2017) e2746. Available from: https://doi.org/10.1038/cddis.2016.409.

[32] G. Bergers, D. Hanahan, Modes of resistance to anti-angiogenic therapy, Nat. Rev. Cancer 8 (2008) 592–603. Available from: https://doi.org/10.1038/nrc2442.

[33] S.J. Conley, E. Gheordunescu, P. Kakarala, B. Newman, H. Korkaya, A.N. Heath, et al., Antiangiogenic agents increase breast cancer stem cells via the generation of tumor hypoxia, Proc. Natl. Acad. Sci. U.S.A. 109 (2012) 2784–2789. Available from: https://doi.org/10.1073/pnas.1018866109.

[34] K. Moitra, Overcoming multidrug resistance in cancer stem cells, Biomed. Res. Int. 2015 (2015) 1–8. Available from: https://doi.org/10.1155/2015/635745.

[35] R. Rosa, V. D'Amato, S. De Placido, R. Bianco, Approaches for targeting cancer stem cells drug resistance, Expert Opin. Drug Discov. 11 (2016) 1201–1212. Available from: https://doi.org/10.1080/17460441.2016.1243525.

[36] K. Moitra, H. Lou, M. Dean, Multidrug efflux pumps and cancer stem cells: insights into multidrug resistance and therapeutic development, Clin. Pharmacol. Ther. 89 (2011) 491–502. Available from: https://doi.org/10.1038/clpt.2011.14.
[37] J.I. Fletcher, M. Haber, M.J. Henderson, M.D. Norris, ABC transporters in cancer: more than just drug efflux pumps, Nat. Rev. Cancer 10 (2010) 147–156. Available from: https://doi.org/10.1038/nrc2789.
[38] L. Austin Doyle, D.D. Ross, Multidrug resistance mediated by the breast cancer resistance protein BCRP (ABCG2), Oncogene 22 (2003) 7340–7358. Available from: https://doi.org/10.1038/sj.onc.1206938.
[39] Y. An, W.M. Ongkeko, ABCG2: the key to chemoresistance in cancer stem cells? Expert Opin. Drug Metab. Toxicol. 5 (2009) 1529–1542. Available from: https://doi.org/10.1517/17425250903228834.
[40] O. Govaere, J. Wouters, M. Petz, Y.-P. Vandewynckel, K. Van den Eynde, A. Van den broeck, et al., Laminin-332 sustains chemoresistance and quiescence as part of the human hepatic cancer stem cell niche, J. Hepatol. 64 (2016) 609–617. Available from: https://doi.org/10.1016/j.jhep.2015.11.011.
[41] Y. Kamohara, N. Haraguchi, K. Mimori, F. Tanaka, H. Inoue, M. Mori, et al., The search for cancer stem cells in hepatocellular carcinoma, Surgery 144 (2008) 119–124. Available from: https://doi.org/10.1016/j.surg.2008.04.008.
[42] H.R. Mellor, D.J.P. Ferguson, R. Callaghan, A model of quiescent tumour microregions for evaluating multicellular resistance to chemotherapeutic drugs, Br. J. Cancer 93 (2005) 302–309. Available from: https://doi.org/10.1038/sj.bjc.6602710.
[43] M. Ookura, T. Fujii, H. Yagi, T. Ogawa, S. Kishi, N. Hosono, et al., YM155 exerts potent cytotoxic activity against quiescent (G_0/G_1) multiple myeloma and bortezomib resistant cells *via* inhibition of survivin and Mcl-1, Oncotarget 8 (2017) 111535–111550. Available from: https://doi.org/10.18632/oncotarget.22871.
[44] N.L. Komarova, D. Wodarz, Stochastic modeling of cellular colonies with quiescence: an application to drug resistance in cancer, Theor. Popul. Biol. 72 (2007) 523–538. Available from: https://doi.org/10.1016/j.tpb.2007.08.003.
[45] N. Takebe, P.J. Harris, R.Q. Warren, S.P. Ivy, Targeting cancer stem cells by inhibiting Wnt, Notch, and Hedgehog pathways, Nat. Rev. Clin. Oncol. 8 (2011) 97–106. Available from: https://doi.org/10.1038/nrclinonc.2010.196.
[46] Z. Yang, N. Sun, R. Cheng, C. Zhao, J. Liu, Z. Tian, Hybrid nanoparticles coated with hyaluronic acid lipoid for targeted co-delivery of paclitaxel and curcumin to synergistically eliminate breast cancer stem cells, J. Mater. Chem., B. 5 (2017) 6762–6775. Available from: https://doi.org/10.1039/c7tb01510k.
[47] C. Zhao, A. Chen, C.H. Jamieson, M. Fereshteh, A. Abrahamsson, J. Blum, et al., Hedgehog signalling is essential for maintenance of cancer stem cells in myeloid leukaemia, Nature 458 (2009) 776–779. Available from: https://doi.org/10.1038/nature07737.
[48] N. Zhang, S. Liu, N. Wang, S. Deng, L. Song, Q. Wu, et al., Biodegradable polymeric micelles encapsulated JK184 suppress tumor growth through inhibiting hedgehog signaling pathway, Nanoscale 7 (2015) 2609–2624. Available from: https://doi.org/10.1039/C4NR06300G.
[49] V. Chenna, C. Hu, D. Pramanik, B.T. Aftab, C. Karikari, N.R. Campbell, et al., A polymeric nanoparticle encapsulated small-molecule inhibitor of hedgehog signaling (NanoHHI) bypasses secondary mutational resistance to smoothened antagonists, Mol. Cancer Ther. 11 (2012) 165–173. Available from: https://doi.org/10.1158/1535-7163.MCT-11-0341.

[50] S.M. Hoy, Glasdegib: first global approval, Drugs 79 (2019) 207–213. Available from: https://doi.org/10.1007/s40265-018-1047-7.
[51] D.B. Henley, P.C. May, R.A. Dean, E.R. Siemers, Development of semagacestat (LY450139), a functional γ-secretase inhibitor, for the treatment of Alzheimer's disease, Expert Opin. Pharmacother. 10 (2009) 1657–1664. Available from: https://doi.org/10.1517/14656560903044982.
[52] B.-B.S. Zhou, H. Zhang, M. Damelin, K.G. Geles, J.C. Grindley, P.B. Dirks, Tumour-initiating cells: challenges and opportunities for anticancer drug discovery, Nat. Rev. Drug Discov. 8 (2009) 806–823. Available from: https://doi.org/10.1038/nrd2137.
[53] L.-C. Li, Y. Peng, Y.-M. Liu, L.-L. Wang, X.-L. Wu, Gastric cancer cell growth and epithelial-mesenchymal transition are inhibited by γ-secretase inhibitor DAPT, Oncol. Lett. 7 (2014) 2160–2164. Available from: https://doi.org/10.3892/ol.2014.1980.
[54] M. Kahn, Can we safely target the WNT pathway? Nat. Rev. Drug Discov. 13 (2014) 513–532. Available from: https://doi.org/10.1038/nrd4233.
[55] H. Meng-er, Y. Yu-Chen, C. Shu-rong, C. Jin-ren, L. Jia-xiang, Z. Lin, et al., Use of all-trans retinoic acid in the treatment of acute promyelocytic leukemia, Blood 72 (1988) 567–572.
[56] F. Lo-Coco, G. Avvisati, M. Vignetti, C. Thiede, S.M. Orlando, S. Iacobelli, et al., Retinoic acid and arsenic trioxide for acute promyelocytic leukemia, N. Engl. J. Med. 369 (2013) 111–121. Available from: https://doi.org/10.1056/NEJMoa1300874.
[57] C.H. Park, J.Y. Chang, E.R. Hahm, S. Park, H.-K. Kim, C.H. Yang, Quercetin, a potent inhibitor against β-catenin/Tcf signaling in SW480 colon cancer cells, Biochem. Biophys. Res. Commun. 328 (2005) 227–234. Available from: https://doi.org/10.1016/j.bbrc.2004.12.151.
[58] Y. Fu, H. Chang, X. Peng, Q. Bai, L. Yi, Y. Zhou, et al., Resveratrol inhibits breast cancer stem-like cells and induces autophagy via suppressing Wnt/β-catenin signaling pathway, PLoS One 9 (2014) e102535. Available from: https://doi.org/10.1371/journal.pone.0102535.
[59] S.S. Chung, J.V. Vadgama, Curcumin and epigallocatechin gallate inhibit the cancer stem cell phenotype via down-regulation of STAT3-NFκB signaling, Anticancer Res. 35 (2015) 39–46. Available from: http://www.ncbi.nlm.nih.gov/pubmed/25550533.
[60] Y. Li, T. Zhang, Targeting cancer stem cells by curcumin and clinical applications, Cancer Lett. 346 (2014) 197–205. Available from: https://doi.org/10.1016/j.canlet.2014.01.012.
[61] J. Seoane, The TGFß pathway as a therapeutic target in cancer, Clin. Transl. Oncol. 10 (2008) 14–19. Available from: https://doi.org/10.1007/s12094-008-0148-2.
[62] J. Massagué, TGFβ in cancer, Cell 134 (2008) 215–230. Available from: https://doi.org/10.1016/j.cell.2008.07.001.
[63] J. Anido, A. Sáez-Borderías, A. Gonzàlez-Juncà, L. Rodón, G. Folch, M.A. Carmona, et al., TGF-β receptor inhibitors target the CD44high/Id1high glioma-initiating cell population in human glioblastoma, Cancer Cell 18 (2010) 655–668. Available from: https://doi.org/10.1016/j.ccr.2010.10.023.
[64] L. Zhang, Y. Ye, X. Long, P. Xiao, X. Ren, J. Yu, BMP signaling and its paradoxical effects in tumorigenesis and dissemination, Oncotarget 7 (2016) 78206–78218. Available from: https://doi.org/10.18632/oncotarget.12151.
[65] S.G.M. Piccirillo, Ba Reynolds, N. Zanetti, G. Lamorte, E. Binda, G. Broggi, et al., Bone morphogenetic proteins inhibit the tumorigenic potential of human brain tumour-initiating cells, Nature 444 (2006) 761–765. Available from: https://doi.org/10.1038/nature05349.

[66] P. González-Gómez, N.P. Anselmo, H. Mira, BMPs as therapeutic targets and biomarkers in astrocytic glioma, Biomed. Res. Int. 2014 (2014) 1–8. Available from: https://doi.org/10.1155/2014/549742.

[67] E. Reguera-Nuñez, C. Roca, E. Hardy, M. de la Fuente, N. Csaba, M. Garcia-Fuentes, Implantable controlled release devices for BMP-7 delivery and suppression of glioblastoma initiating cells, Biomaterials 35 (2014) 2859–2867. Available from: https://doi.org/10.1016/j.biomaterials.2013.12.001.

[68] P. González-Gómez, J. Crecente-Campo, C. Zahonero, M. de la Fuente, A. Hernández-Laín, H. Mira, et al., Controlled release microspheres loaded with BMP7 suppress primary tumors from human glioblastoma, Oncotarget 6 (2015) 10950–10963. Available from: https://doi.org/10.18632/oncotarget.3459.

[69] P. Xia, X.Y. Xu, PI3K/Akt/mTOR signaling pathway in cancer stem cells: from basic research to clinical application, Am. J. Cancer Res. 5 (2015) 1602–1609. Available from: https://doi.org/2156-6976/ajcr0007096.

[70] B.T. Hennessy, D.L. Smith, P.T. Ram, Y. Lu, G.B. Mills, Exploiting the PI3K/Akt pathway for cancer drug discovery, Nat. Rev. Drug Discov. 4 (2005) 988–1004. Available from: https://doi.org/10.1038/nrd1902.

[71] D. Benjamin, M. Colombi, C. Moroni, M.N. Hall, Rapamycin passes the torch: a new generation of mTOR inhibitors, Nat. Rev. Drug Discov. 10 (2011) 868–880. Available from: https://doi.org/10.1038/nrd3531.

[72] A.M. Martelli, P.L. Tazzari, C. Evangelisti, F. Chiarini, W.L. Blalock, A.M. Billi, et al., Targeting the phosphatidylinositol 3-kinase/Akt/mammalian target of rapamycin module for acute myelogenous leukemia therapy: from bench to bedside, Curr. Med. Chem. 14 (2007) 2009–2023. Available from: https://doi.org/10.2174/092986707781368423.

[73] J.J. Gills, P.A. Dennis, Perifosine: update on a novel Akt inhibitor, Curr. Oncol. Rep. 11 (2009) 102–110. Available from: https://doi.org/10.1007/s11912-009-0016-4.

[74] M. Russo, A. Milito, C. Spagnuolo, V. Carbone, A. Rosén, P. Minasi, et al., CK2 and PI_3K are direct molecular targets of quercetin in chronic lymphocytic leukaemia, Oncotarget 8 (2017) 42571–42587. Available from: https://doi.org/10.18632/oncotarget.17246.

[75] E. Zendehdel, E. Abdollahi, A.A. Momtazi-Borojeni, M. Korani, S.H. Alavizadeh, A. Sahebkar, The molecular mechanisms of curcumin's inhibitory effects on cancer stem cells, J. Cell. Biochem. 120 (2019) 4739–4747. Available from: https://doi.org/10.1002/jcb.27757.

[76] K. Vazquez-Santillan, J. Melendez-Zajgla, L. Jimenez-Hernandez, G. Martínez-Ruiz, V. Maldonado, NF-κB signaling in cancer stem cells: a promising therapeutic target? Cell. Oncol. 38 (2015) 327–339. Available from: https://doi.org/10.1007/s13402-015-0236-6.

[77] V.F.-S. Shih, R. Tsui, A. Caldwell, A. Hoffmann, A single NFκB system for both canonical and non-canonical signaling, Cell Res. 21 (2011) 86–102. Available from: https://doi.org/10.1038/cr.2010.161.

[78] N.D. Perkins, Oncogenes, tumor suppressors and p52 NF-κB, Oncogene 22 (2003) 7553–7556. Available from: https://doi.org/10.1038/sj.onc.1207139.

[79] G. Qing, Z. Qu, G. Xiao, Stabilization of basally translated NF-κB-inducing kinase (NIK) protein functions as a molecular switch of processing of NF-κB2 p100, J. Biol. Chem. 280 (2005) 40578–40582. Available from: https://doi.org/10.1074/jbc.M508776200.

[80] H. Moreira, A. Szyjka, K. Gąsiorowski, Chemopreventive activity of celastrol in drug-resistant human colon carcinoma cell cultures, Oncotarget 9 (2018) 21211–21223. Available from: https://doi.org/10.18632/oncotarget.25014.
[81] C. Chakraborty, K.-Y. Chin, S. Das, miRNA-regulated cancer stem cells: understanding the property and the role of miRNA in carcinogenesis, Tumor Biol. 37 (2016) 13039–13048. Available from: https://doi.org/10.1007/s13277-016-5156-1.
[82] P. Van Phuc, P.L. Chinh Nhan, T.H. Nhung, N.T. Tam, N.M. Hoang, V.G. Tue, et al., Downregulation of CD44 reduces doxorubicin resistance of CD44 + CD24- breast cancer cells, Onco Targets Ther. 4 (2011) 71–78. Available from: https://doi.org/10.2147/OTT.S21431.
[83] A. Gilboa-Geffen, P. Hamar, M.T.N. Le, L.A. Wheeler, R. Trifonova, F. Petrocca, et al., Gene knockdown by EpCAM aptamer-siRNA chimeras suppresses epithelial breast cancers and their tumor-initiating cells, Mol. Cancer Ther. 14 (2015) 2279–2291. Available from: https://doi.org/10.1158/1535-7163.MCT-15-0201-T.
[84] H.-L. Zhang, M.-D. Wang, X. Zhou, C.-J. Qin, G.-B. Fu, L. Tang, et al., Blocking preferential glucose uptake sensitizes liver tumor-initiating cells to glucose restriction and sorafenib treatment, Cancer Lett. 388 (2017) 1–11. Available from: https://doi.org/10.1016/j.canlet.2016.11.023.
[85] A.E. Murmann, K.M. McMahon, A. Haluck-Kangas, N. Ravindran, M. Patel, C.Y. Law, et al., Induction of DISE in ovarian cancer cells *in vivo*, Oncotarget 8 (2017) 84643–84658. Available from: https://doi.org/10.18632/oncotarget.21471.
[86] A. Radhakrishnan, V. Nanjappa, R. Raja, G. Sathe, V.N. Puttamallesh, A.P. Jain, et al., A dual specificity kinase, DYRK1A, as a potential therapeutic target for head and neck squamous cell carcinoma, Sci. Rep. 7 (2017) 46864. Available from: https://doi.org/10.1038/srep46864.
[87] H. Cui, B. Hu, T. Li, J. Ma, G. Alam, W.T. Gunning, et al., Bmi-1 is essential for the tumorigenicity of neuroblastoma cells, Am. J. Pathol. 170 (2007) 1370–1378. Available from: https://doi.org/10.2353/ajpath.2007.060754.
[88] G. Bosco-Clément, F. Zhang, Z. Chen, H.-M. Zhou, H. Li, I. Mikami, et al., Targeting Gli transcription activation by small molecule suppresses tumor growth, Oncogene 33 (2014) 2087–2097. Available from: https://doi.org/10.1038/onc.2013.164.
[89] J. Wang, C. Wang, Q. Meng, S. Li, X. Sun, Y. Bo, et al., siRNA targeting Notch-1 decreases glioma stem cell proliferation and tumor growth, Mol. Biol. Rep. 39 (2012) 2497–2503. Available from: https://doi.org/10.1007/s11033-011-1001-1.
[90] B. Xiong, Y. Cheng, L. Ma, C. Zhang, MiR-21 regulates biological behavior through the PTEN/PI-3 K/Akt signaling pathway in human colorectal cancer cells, Int. J. Oncol. 42 (2013) 219–228. Available from: https://doi.org/10.3892/ijo.2012.1707.
[91] G. Yu, H. Li, J. Wang, K. Gumireddy, A. Li, W. Yao, et al., miRNA-34a suppresses cell proliferation and metastasis by targeting CD44 in human renal carcinoma cells, J. Urol. 192 (2014) 1229–1237. Available from: https://doi.org/10.1016/j.juro.2014.05.094.
[92] F. Liu, X. Kong, L. Lv, J. Gao, TGF-β1 acts through miR-155 to down-regulate TP53INP1 in promoting epithelial–mesenchymal transition and cancer stem cell phenotypes, Cancer Lett. 359 (2015) 288–298. Available from: https://doi.org/10.1016/j.canlet.2015.01.030.
[93] Z. Asadzadeh, B. Mansoori, A. Mohammadi, M. Aghajani, K. Haji-Asgarzadeh, E. Safarzadeh, et al., microRNAs in cancer stem cells: biology, pathways, and therapeutic opportunities, J. Cell. Physiol. (2018) 1–16. Available from: https://doi.org/10.1002/jcp.27885.

[94] F.C. Kalinowski, R.A.M. Brown, C. Ganda, K.M. Giles, M.R. Epis, J. Horsham, et al., microRNA-7: a tumor suppressor miRNA with therapeutic potential, Int. J. Biochem. Cell Biol. 54 (2014) 312–317. Available from: https://doi.org/10.1016/j.biocel.2014.05.040.

[95] J. Hu, L. Xu, J. Wang, M. Qiu, F. Jiang, X. Yang, et al., MiR-145 regulates cancer stem-like properties and epithelial-to-mesenchymal transition in lung adenocarcinoma-initiating cells, Tumor Biol. 35 (2014) 8953–8961. Available from: https://doi.org/10.1007/s13277-014-2158-8.

[96] D. Ren, M. Wang, W. Guo, S. Huang, Z. Wang, X. Zhao, et al., Double-negative feedback loop between ZEB2 and miR-145 regulates epithelial-mesenchymal transition and stem cell properties in prostate cancer cells, Cell Tissue Res. 358 (2014) 763–778. Available from: https://doi.org/10.1007/s00441-014-2001-y.

[97] D. Kong, Y. Li, Z. Wang, S. Banerjee, A. Ahmad, H.-R.C. Kim, et al., miR-200 regulates PDGF-D-mediated epithelial-mesenchymal transition, adhesion, and invasion of prostate cancer cells, Stem Cells 27 (2009) 1712–1721. Available from: https://doi.org/10.1002/stem.101.

[98] M. Han, Y. Wang, M. Liu, X. Bi, J. Bao, N. Zeng, et al., MiR-21 regulates epithelial-mesenchymal transition phenotype and hypoxia-inducible factor-1α expression in third-sphere forming breast cancer stem cell-like cells, Cancer Sci. 103 (2012) 1058–1064. Available from: https://doi.org/10.1111/j.1349-7006.2012.02281.x.

[99] Y. Yu, F.H. Sarkar, A.P.N. Majumdar, Down-regulation of miR-21 induces differentiation of chemoresistant colon cancer cells and enhances susceptibility to therapeutic regimens, Transl. Oncol. 6 (2013) 180–186. Available from: https://doi.org/10.1593/tlo.12397.

[100] J. Ma, J. Xia, L. Miele, F.H. Sarkar, Z. Wang, Notch signaling pathway in pancreatic cancer progression, Pancreat. Disord. Ther. 3 (2013) 1000114. Available from: https://doi.org/10.4172/2165-7092.1000114.

[101] A. Singh, J. Settleman, EMT, cancer stem cells and drug resistance: an emerging axis of evil in the war on cancer, Oncogene 29 (2010) 4741–4751. Available from: https://doi.org/10.1038/onc.2010.215.

[102] J. Zuo, Y. Yu, M. Zhu, W. Jing, M. Yu, H. Chai, et al., Inhibition of miR-155, a therapeutic target for breast cancer, prevented in cancer stem cell formation, Cancer Biomarkers 21 (2018) 383–392. Available from: https://doi.org/10.3233/CBM-170642.

[103] R. Sun, Y. Liu, S.-Y. Li, S. Shen, X.-J. Du, C.-F. Xu, et al., Co-delivery of all-trans-retinoic acid and doxorubicin for cancer therapy with synergistic inhibition of cancer stem cells, Biomaterials 37 (2015) 405–414. Available from: https://doi.org/10.1016/j.biomaterials.2014.10.018.

[104] M. Alibolandi, M. Ramezani, F. Sadeghi, K. Abnous, F. Hadizadeh, Epithelial cell adhesion molecule aptamer conjugated PEG–PLGA nanopolymersomes for targeted delivery of doxorubicin to human breast adenocarcinoma cell line in vitro, Int. J. Pharm. 479 (2015) 241–251. Available from: https://doi.org/10.1016/j.ijpharm.2014.12.035.

[105] H. Cho, T.C. Lai, G.S. Kwon, Poly(ethylene glycol)-block-poly(ε-caprolactone) micelles for combination drug delivery: evaluation of paclitaxel, cyclopamine and gossypol in intraperitoneal xenograft models of ovarian cancer, J. Control. Release 166 (2013) 1–9. Available from: https://doi.org/10.1016/j.jconrel.2012.12.005.

[106] R.-J. Li, X. Ying, Y. Zhang, R.-J. Ju, X.-X. Wang, H.-J. Yao, et al., All-trans retinoic acid stealth liposomes prevent the relapse of breast cancer arising from the cancer stem cells, J. Control. Release 149 (2011) 281–291. Available from: https://doi.org/10.1016/j.jconrel.2010.10.019.

[107] Y.-I. Jeong, M.-K. Kang, H.-S. Sun, S.-S. Kang, H.-W. Kim, K.-S. Moon, et al., All-trans-retinoic acid release from core-shell type nanoparticles of poly(ε-caprolactone)/poly(ethylene glycol) diblock copolymer, Int. J. Pharm. 273 (2004) 95–107. Available from: https://doi.org/10.1016/j.ijpharm.2003.12.012.

[108] S. shantanu, A.K.D. Chandratre, Multifunctional nanoparticles for prostate cancer therapy, AAPS PharmSciTech 16 (2015) 98–107. Available from: https://doi.org/10.1208/s12249-014-0202-z.

[109] V. Sanna, I.A. Siddiqui, M. Sechi, H. Mukhtar, Resveratrol-loaded nanoparticles based on poly(epsilon-caprolactone) and poly(D,L-lactic-*co*-glycolic acid)–poly(ethylene glycol) blend for prostate cancer treatment, Mol. Pharm. 10 (2013) 3871–3881. Available from: https://doi.org/10.1021/mp400342f.

[110] S. Shen, X.-J. Du, J. Liu, R. Sun, Y.-H. Zhu, J. Wang, Delivery of bortezomib with nanoparticles for basal-like triple-negative breast cancer therapy, J. Control. Release 208 (2015) 14–24. Available from: https://doi.org/10.1016/j.jconrel.2014.12.043.

[111] P. Rafiei, A. Haddadi, Docetaxel-loaded PLGA and PLGA-PEG nanoparticles for intravenous application: pharmacokinetics and biodistribution profile, Int. J. Nanomedicine. 12 (2017) 935–947. Available from: https://doi.org/10.2147/IJN.S121881.

[112] E. Blanco, T. Sangai, S. Wu, A. Hsiao, G.U. Ruiz-Esparza, C.A. Gonzalez-Delgado, et al., Colocalized delivery of rapamycin and paclitaxel to tumors enhances synergistic targeting of the PI3K/Akt/mTOR pathway, Mol. Ther. 22 (2014) 1310–1319. Available from: https://doi.org/10.1038/mt.2014.27.

[113] W. Tian, J. Liu, Y. Guo, Y. Shen, D. Zhou, S. Guo, Self-assembled micelles of amphiphilic PEGylated rapamycin for loading paclitaxel and resisting multidrug resistant cancer cells, J. Mater. Chem., B. 3 (2015) 1204–1207. Available from: https://doi.org/10.1039/C4TB01633E.

[114] R. Yang, G. Mondal, D. Wen, R.I. Mahato, Combination therapy of paclitaxel and cyclopamine polymer-drug conjugates to treat advanced prostate cancer, Nanomed. Nanotechnol., Biol. Med. 13 (2017) 391–401. Available from: https://doi.org/10.1016/j.nano.2016.07.017.

[115] L. Guo, Y. Peng, J. Yao, L. Sui, A. Gu, J. Wang, Anticancer activity and molecular mechanism of resveratrol–bovine serum albumin nanoparticles on subcutaneously implanted human primary ovarian carcinoma cells in nude mice, Cancer Biother. Radiopharm. 25 (2010) 471–477. Available from: https://doi.org/10.1089/cbr.2009.0724.

[116] F. Wang, K. Yang, Z. Wang, Y. Ma, J.S. Gutkind, N. Hida, et al., Combined image guided monitoring the pharmacokinetics of rapamycin loaded human serum albumin nanoparticles with a split luciferase reporter, Nanoscale 8 (2016) 3991–4000. Available from: https://doi.org/10.1039/C5NR07308A.

[117] D. Cirstea, T. Hideshima, S. Rodig, L. Santo, S. Pozzi, S. Vallet, et al., Dual inhibition of Akt/mammalian target of rapamycin pathway by nanoparticle albumin-bound rapamycin and perifosine induces antitumor activity in multiple myeloma, Mol. Cancer Ther. 9 (2010) 963–975. Available from: https://doi.org/10.1158/1535-7163.MCT-09-0763.

[118] R. Sun, S. Shen, Y.-J. Zhang, C.-F. Xu, Z.-T. Cao, L.-P. Wen, et al., Nanoparticle-facilitated autophagy inhibition promotes the efficacy of chemotherapeutics against breast cancer stem cells, Biomaterials 103 (2016) 44–55. Available from: https://doi.org/10.1016/j.biomaterials.2016.06.038.

[119] Y. Xu, V. Chenna, C. Hu, H.X. Sun, M. Khan, H. Bai, et al., Polymeric nanoparticle-encapsulated hedgehog pathway inhibitor HPI-1 (NanoHHI) inhibits systemic metastases in an orthotopic model of human hepatocellular carcinoma, Clin. Cancer Res. 18 (2012) 1291–1302. Available from: https://doi.org/10.1158/1078-0432.CCR-11-0950.

[120] V. Chenna, C. Hu, D. Pramanik, B.T. Aftab, C. Karikari, N.R. Campbell, et al., A polymeric nanoparticle encapsulated small-molecule inhibitor of hedgehog signaling (NanoHHI) bypasses secondary mutational resistance to smoothened antagonists, Mol. Cancer Ther. 11 (2011) 165–173. Available from: https://doi.org/10.1158/1535-7163.mct-11-0341.

[121] G.J.R. Charrois, T.M. Allen, Drug release rate influences the pharmacokinetics, biodistribution, therapeutic activity, and toxicity of pegylated liposomal doxorubicin formulations in murine breast cancer, Biochim. Biophys. Acta – Biomembr. 1663 (2004) 167–177. Available from: https://doi.org/10.1016/j.bbamem.2004.03.006.

[122] S.P. David, N.V. Murthy, E.A. Rabiner, M.R. Munafó, E.C. Johnstone, R. Jacob, et al., PEGylated PRINT nanoparticles: the impact of PEG density on protein binding, macrophage association, biodistribution, and pharmacokinetics, Nano Lett. 25 (2012) 2586–2590. Available from: https://doi.org/10.1038/nature09421.Oxidative.

[123] M. Sun, S. Nie, X. Pan, R. Zhang, Z. Fan, S. Wang, Quercetin-nanostructured lipid carriers: characteristics and anti-breast cancer activities in vitro, Colloids Surf., B: Biointerfaces 113 (2014) 15–24. Available from: https://doi.org/10.1016/j.colsurfb.2013.08.032.

[124] M.A. Rouf, I. Vural, J.M. Renoir, A.A. Hincal, Development and characterization of liposomal formulations for rapamycin delivery and investigation of their antiproliferative effect on MCF7 cells, J. Liposome Res. 19 (2009) 322–331. Available from: https://doi.org/10.3109/08982100902963043.

[125] Y.-C. Chen, C.-L. Lo, Y.-F. Lin, G.-H. Hsiue, Rapamycin encapsulated in dual-responsive micelles for cancer therapy, Biomaterials 34 (2013) 1115–1127. Available from: https://doi.org/10.1016/j.biomaterials.2012.10.034.

[126] A. Gabizon, H. Shmeeda, Y. Barenholz, Pharmacokinetics of pegylated liposomal doxorubicin: review of animal and human studies, Clin. Pharmacokinet. 42 (2003) 419–436. Available from: https://doi.org/10.2165/00003088-200342050-00002.

[127] A. Gabizon, M. Chemla, D. Tzemach, A.T. Horowitz, D. Goren, Liposome longevity and stability in circulation: effects on the in vivo delivery to tumors and therapeutic efficacy of encapsulated anthracyclines, J. Drug Target 3 (1996) 391–398. Available from: https://doi.org/10.3109/10611869608996830.

[128] V.D. Awasthi, D. Garcia, B.A. Goins, W.T. Phillips, Circulation and biodistribution profiles of long-circulating PEG-liposomes of various sizes in rabbits, Int. J. Pharm. 253 (2003) 121–132. Available from: https://doi.org/10.1016/S0378-5173(02)00703-2.

[129] P. Milla, F. Dosio, L. Cattel, PEGylation of proteins and liposomes: a powerful and flexible strategy to improve the drug delivery, Curr. Drug Metab. 13 (2012) 105–119. Available from: https://doi.org/10.2174/138920012798356934.

[130] N.-G. Zheng, S.-J. Mo, J.-P. Li, J.-L. Wu, Anti-CSC Effects in human esophageal squamous cell carcinomas and Eca109/9706 cells induced by nanoliposomal quercetin alone or combined with CD 133 antiserum, Asian Pac. J. Cancer Prev. 15 (2014) 8679–8684. Available from: https://doi.org/10.7314/APJCP.2014.15.20.8679.

[131] A. Catania, E. Barrajón-Catalán, S. Nicolosi, F. Cicirata, V. Micol, Immunoliposome encapsulation increases cytotoxic activity and selectivity of curcumin and resveratrol against HER2 overexpressing human breast cancer cells, Breast Cancer Res. Treat. 141 (2013) 55–65. Available from: https://doi.org/10.1007/s10549-013-2667-y.

[132] J.O. Eloy, R. Petrilli, J.F. Topan, H.M.R. Antonio, J.P.A. Barcellos, D.L. Chesca, et al., Co-loaded paclitaxel/rapamycin liposomes: development, characterization and in vitro and in vivo evaluation for breast cancer therapy, Colloids Surf., B: Biointerfaces 141 (2016) 74–82. Available from: https://doi.org/10.1016/j.colsurfb.2016.01.032.

[133] P. Liu, Z. Wang, S. Brown, V. Kannappan, P.E. Tawari, W. Jiang, et al., Liposome encapsulated Disulfiram inhibits NF-κB pathway and targets breast cancer stem cells *in vitro* and *in vivo*, Oncotarget 5 (2014) 7471–7485. Available from: https://doi.org/10.18632/oncotarget.2166.

[134] S.L. Ginn, A.K. Amaya, I.E. Alexander, M. Edelstein, M.R. Abedi, Gene therapy clinical trials worldwide to 2017: an update, J. Gene Med. 20 (2018) e3015. Available from: https://doi.org/10.1002/jgm.3015.

[135] A.L. Zimmerman, S. Wu, MicroRNAs, cancer and cancer stem cells, Cancer Lett. 300 (2011) 10–19. Available from: https://doi.org/10.1016/j.canlet.2010.09.019.

[136] J. Gilleron, W. Querbes, A. Zeigerer, A. Borodovsky, G. Marsico, U. Schubert, et al., Image-based analysis of lipid nanoparticle–mediated siRNA delivery, intracellular trafficking and endosomal escape, Nat. Biotechnol. 31 (2013) 638–646. Available from: https://doi.org/10.1038/nbt.2612.

[137] M.S. Al-Dosari, X. Gao, Nonviral gene delivery: principle, limitations, and recent progress, AAPS J. 11 (2009) 671–681. Available from: https://doi.org/10.1208/s12248-009-9143-y.

[138] R.L. Juliano, K. Carver, Cellular uptake and intracellular trafficking of oligonucleotides, Adv. Drug Deliv. Rev. 87 (2015) 35–45. Available from: https://doi.org/10.1016/j.addr.2015.04.005.

[139] K. Wang, F.M. Kievit, M. Zhang, Nanoparticles for cancer gene therapy: recent advances, challenges, and strategies, Pharmacol. Res. 114 (2016) 56–66. Available from: https://doi.org/10.1016/j.phrs.2016.10.016.

[140] A.R. Kirtane, J. Panyam, Weighing up gene delivery, Nat. Nanotechnol. 8 (2013) 805–806. Available from: https://doi.org/10.1038/nnano.2013.234.

[141] K. Wang, F.M. Kievit, A.E. Erickson, J.R. Silber, R.G. Ellenbogen, M. Zhang, Culture on 3D chitosan-hyaluronic acid scaffolds enhances stem cell marker expression and drug resistance in human glioblastoma cancer stem cells, Adv. Healthcare Mater. 5 (2016) 3173–3181. Available from: https://doi.org/10.1002/adhm.201600684.

[142] H. Lopez-Bertoni, K.L. Kozielski, Y. Rui, B. Lal, H. Vaughan, D.R. Wilson, et al., Bioreducible polymeric nanoparticles containing multiplexed cancer stem cell regulating miRNAs inhibit glioblastoma growth and prolong survival, Nano Lett. 18 (2018) 4086–4094. Available from: https://doi.org/10.1021/acs.nanolett.8b00390.

[143] S. Ayatollahi, M. Hashemi, R. Kazemi Oskuee, Z. Salmasi, A. Mokhtarzadeh, M. Alibolandi, et al., Synthesis of efficient gene delivery systems by grafting pegylated alkylcarboxylate chains to PAMAM dendrimers: evaluation of transfection efficiency and cytotoxicity in cancerous and mesenchymal stem cells, J. Biomater. Appl. 30 (2015) 632–648. Available from: https://doi.org/10.1177/0885328215599667.

[144] J. Ma, S. Kala, S. Yung, T.M. Chan, Y. Cao, Y. Jiang, et al., Blocking stemness and metastatic properties of ovarian cancer cells by targeting p70S6K with dendrimer nanovector-based siRNA delivery, Mol. Ther. 26 (2018) 70–83. Available from: https://doi.org/10.1016/j.ymthe.2017.11.006.

[145] C.E. Wang, P.S. Stayton, S.H. Pun, A.J. Convertine, Polymer nanostructures synthesized by controlled living polymerization for tumor-targeted drug delivery, J. Control. Release 219 (2015) 345–354. Available from: https://doi.org/10.1016/j.jconrel.2015.08.054.

[146] W.-H. Hsu, P. Sánchez-Gómez, E. Gomez-Ibarlucea, D.P. Ivanov, R. Rahman, A.M. Grabowska, et al., Structure-optimized interpolymer polyphosphazene complexes for effective gene delivery against glioblastoma, Adv. Ther. 2 (2019) 1800126. Available from: https://doi.org/10.1002/adtp.201800126.

[147] H. Wang, P. Agarwal, S. Zhao, J. Yu, X. Lu, X. He, et al., "Nanobomb" for breaking the barriers to microRNA delivery, Adv. Mater. 28 (2016) 1723. Available from: https://doi.org/10.1002/adma.201600213.

[148] J.R. Kanwar, G. Mahidhara, K. Roy, S. Sasidharan, S. Krishnakumar, N. Prasad, et al., Fe-bLf nanoformulation targets survivin to kill colon cancer stem cells and maintains absorption of iron, calcium and zinc, Nanomedicine 10 (2015) 35–55. Available from: https://doi.org/10.2217/nnm.14.132.

[149] X. Wei, J. He, J. Wang, W. Wang, MPEG-CS/Bmi-1RNAi nanoparticles synthesis and its targeted inhibition effect on CD133 + laryngeal stem cells, J. Nanosci. Nanotechnol. 18 (2018) 1577–1584. Available from: https://doi.org/10.1166/jnn.2018.14303.

[150] J.R. Melamed, S.A. Ioele, A.J. Hannum, V.M. Ullman, E.S. Day, Polyethylenimine–spherical nucleic acid nanoparticles against Gli1 reduce the chemoresistance and stemness of glioblastoma cells, Mol. Pharm. 15 (2018) 5135–5145. Available from: https://doi.org/10.1021/acs.molpharmaceut.8b00707.

[151] Y.-P. Yang, Y. Chien, G.-Y. Chiou, J.-Y. Cherng, M.-L. Wang, W.-L. Lo, et al., Inhibition of cancer stem cell-like properties and reduced chemoradioresistance of glioblastoma using microRNA145 with cationic polyurethane-short branch PEI, Biomaterials 33 (2012) 1462–1476. Available from: https://doi.org/10.1016/j.biomaterials.2011.10.071.

[152] G.-Y. Chiou, J.-Y. Cherng, H.-S. Hsu, M.-L. Wang, C.-M. Tsai, K.-H. Lu, et al., Cationic polyurethanes-short branch PEI-mediated delivery of Mir145 inhibited epithelial–mesenchymal transdifferentiation and cancer stem-like properties and in lung adenocarcinoma, J. Control. Release 159 (2012) 240–250. Available from: https://doi.org/10.1016/j.jconrel.2012.01.014.

[153] V. Subramaniam, I.R. Vincent, M. Gilakjan, S. Jothy, Suppression of human colon cancer tumors in nude mice by siRNA CD44 gene therapy, Exp. Mol. Pathol. 83 (2007) 332–340. Available from: https://doi.org/10.1016/j.yexmp.2007.08.013.

[154] H. Gul-Uludağ, J. Valencia-Serna, C. Kucharski, L.A. Marquez-Curtis, X. Jiang, L. Larratt, et al., Polymeric nanoparticle-mediated silencing of CD44 receptor in CD34 + acute myeloid leukemia cells, Leuk. Res. 38 (2014) 1299–1308. Available from: https://doi.org/10.1016/j.leukres.2014.08.008.

[155] N. Subramanian, J.R. Kanwar, P. Athalya, N. Janakiraman, V. Khetan, R.K. Kanwar, et al., EpCAM aptamer mediated cancer cell specific delivery of EpCAM siRNA using polymeric nanocomplex, J. Biomed. Sci. 22 (2015) 1–10. Available from: https://doi.org/10.1186/s12929-014-0108-9.

[156] C.M. Roberts, S.A. Shahin, W. Wen, J.B. Finlay, J. Dong, R. Wang, et al., Nanoparticle delivery of siRNA against TWIST to reduce drug resistance and tumor growth in ovarian cancer models, Nanomed. Nanotechnol., Biol. Med. 13 (2017) 965–976. Available from: https://doi.org/10.1016/j.nano.2016.11.010.

[157] Y. Ren, R. Wang, L. Gao, K. Li, X. Zhou, H. Guo, et al., Sequential co-delivery of miR-21 inhibitor followed by burst release doxorubicin using NIR-responsive hollow gold nanoparticle to enhance anticancer efficacy, J. Control. Release 228 (2016) 74–86. Available from: https://doi.org/10.1016/j.jconrel.2016.03.008.

[158] M. Goldberg, K. Mahon, D. Anderson, Combinatorial and rational approaches to polymer synthesis for medicine, Adv. Drug Deliv. Rev. 60 (2008) 971–978. Available from: https://doi.org/10.1016/j.addr.2008.02.005.

[159] J. Zhou, T.R. Patel, M. Fu, J.P. Bertram, W.M. Saltzman, Octa-functional PLGA nanoparticles for targeted and efficient siRNA delivery to tumors, Biomaterials 33 (2012) 583–591. Available from: https://doi.org/10.1016/j.biomaterials.2011.09.061.

[160] W. Huang, L. Chen, L. Kang, M. Jin, P. Sun, X. Xin, et al., Nanomedicine-based combination anticancer therapy between nucleic acids and small-molecular drugs, Adv. Drug Deliv. Rev. 115 (2017) 82–97. Available from: https://doi.org/10.1016/j.addr.2017.06.004.

[161] A. Mittal, D. Chitkara, S.W. Behrman, R.I. Mahato, Efficacy of gemcitabine conjugated and miRNA-205 complexed micelles for treatment of advanced pancreatic cancer, Biomaterials 35 (2014) 7077–7087. Available from: https://doi.org/10.1016/j.biomaterials.2014.04.053.

[162] S. Fang, L. Wu, M. Li, H. Yi, G. Gao, Z. Sheng, et al., ZEB1 knockdown mediated using polypeptide cationic micelles inhibits metastasis and effects sensitization to a chemotherapeutic drug for cancer therapy, Nanoscale 6 (2014) 10084–10094. Available from: https://doi.org/10.1039/C4NR01518E.

[163] S. Shen, C.-Y. Sun, X.-J. Du, H.-J. Li, Y. Liu, J.-X. Xia, et al., Co-delivery of platinum drug and siNotch1 with micelleplex for enhanced hepatocellular carcinoma therapy, Biomaterials 70 (2015) 71–83. Available from: https://doi.org/10.1016/j.biomaterials.2015.08.026.

[164] G. Cevc, Rational design of new product candidates: the next generation of highly deformable bilayer vesicles for noninvasive, targeted therapy, J. Control. Rel. 160 (2012) 135–146. Available from: https://doi.org/10.1016/j.jconrel.2012.01.005.

[165] V.P. Torchilin, Targeted pharmaceutical nanocarriers for cancer therapy and imaging, AAPS J. 9 (2007) E128–E147. Available from: https://doi.org/10.1208/aapsj0902015.

[166] A. Schroeder, C.G. Levins, C. Cortez, R. Langer, D.G. Anderson, Lipid-based nanotherapeutics for siRNA delivery, J. Intern. Med. 267 (2010) 9–21. Available from: https://doi.org/10.1111/j.1365-2796.2009.02189.x.

[167] Y. Zhang, H. Li, J. Sun, J. Gao, W. Liu, B. Li, et al., DC-Chol/DOPE cationic liposomes: a comparative study of the influence factors on plasmid pDNA and siRNA gene delivery, Int. J. Pharm. 390 (2010) 198–207. Available from: https://doi.org/10.1016/j.ijpharm.2010.01.035.

[168] H. Kim, M. Choi, S. Jon, S. Kang, J.-I. Kim, Y. Lee, et al., Mono-arginine cholesterol-based small lipid nanoparticles as a systemic siRNA delivery platform for effective cancer therapy, Theranostics 6 (2015) 192–203. Available from: https://doi.org/10.7150/thno.13657.

[169] M.D. Joshi, V. Patravale, R. Prabhu, Polymeric nanoparticles for targeted treatment in oncology: current insights, Int. J. Nanomed. 10 (2015) 1001. Available from: https://doi.org/10.2147/IJN.S56932.

[170] A.A.S. Samson, S. Park, S.-Y. Kim, D.-H. Min, N.L. Jeon, J.M. Song, Liposomal co-delivery-based quantitative evaluation of chemosensitivity enhancement in breast cancer stem cells by knockdown of GRP78/CLU, J. Liposome Res. 29 (2019) 44–52. Available from: https://doi.org/10.1080/08982104.2017.1420081.

[171] J. Liu, T. Meng, Y. Ming, L. Wen, B. Cheng, N. Liu, et al., MicroRNA-200c delivered by solid lipid nanoparticles enhances the effect of paclitaxel on breast cancer stem cell, Int. J. Nanomed. 11 (2016) 6713–6725. Available from: https://doi.org/10.2147/IJN.S111647.

[172] T. Yang, Y. Chen, P. Zhao, H. Xue, J. You, B. Li, et al., Enhancing the therapeutic effect via elimination of hepatocellular carcinoma stem cells using Bmi1 siRNA delivered by cationic cisplatin nanocapsules, Nanomed. Nanotechnol., Biol. Med. 14 (2018) 2009–2021. Available from: https://doi.org/10.1016/j.nano.2018.05.012.

[173] P. de Antonellis, L. Liguori, A. Falanga, M. Carotenuto, V. Ferrucci, I. Andolfo, et al., MicroRNA 199b-5p delivery through stable nucleic acid lipid particles (SNALPs) in tumorigenic cell lines, Naunyn-Schmiedeberg's Arch. Pharmacol. 386 (2013) 287–302. Available from: https://doi.org/10.1007/s00210-013-0837-4.

[174] A.M. Dorrance, P. Neviani, G.J. Ferenchak, X. Huang, D. Nicolet, K.S. Maharry, et al., Targeting leukemia stem cells in vivo with antagomiR-126 nanoparticles in acute myeloid leukemia, Leukemia 29 (2015) 2143–2153. Available from: https://doi.org/10.1038/leu.2015.139.

[175] T.M. Allen, I. Ahmad, D.E.L. de Menezes, E.H. Moase, Immunoliposome-mediated targeting of anti-cancer drugs in vivo, Biochem. Soc. Trans. 23 (1995) 1073–1079. Available from: https://doi.org/10.1042/bst0231073.

[176] E. Mastrobattista, G.A. Koning, G. Storm, Immunoliposomes for the targeted delivery of antitumor drugs, Adv. Drug Deliv. Rev. 40 (1999) 103–127. Available from: https://doi.org/10.1016/S0169-409X(99)00043-5.

[177] L. Arabi, A. Badiee, F. Mosaffa, M.R. Jaafari, Targeting CD44 expressing cancer cells with anti-CD44 monoclonal antibody improves cellular uptake and antitumor efficacy of liposomal doxorubicin, J. Control. Release 220 (2015) 275–286. Available from: https://doi.org/10.1016/j.jconrel.2015.10.044.

[178] X.-P. Li, X.-W. Zhang, L.-Z. Zheng, W.-J. Guo, Expression of CD44 in pancreatic cancer and its significance, Int. J. Clin. Exp. Pathol. 8 (2015) 6724–6731. Available from: https://doi.org/10.3969/j.issn.1674-8115.2015.09.022.

[179] Z. Li, CD133: a stem cell biomarker and beyond, Exp. Hematol. Oncol. 2 (2013) 17. Available from: https://doi.org/10.1186/2162-3619-2-17.

[180] P.M. Glumac, A.M. LeBeau, The role of CD133 in cancer: a concise review, Clin. Transl. Med. 7 (2018) 1–14. Available from: https://doi.org/10.1186/s40169-018-0198-1.

[181] W. Alshaer, N. Ababneh, M. Hatmal, H. Izmirli, M. Choukeife, A. Shraim, et al., Selection and targeting of EpCAM protein by ssDNA aptamer, PLoS One 12 (2017) e0189558. Available from: https://doi.org/10.1371/journal.pone.0189558.

[182] I. Verel, K.-H. Heider, M. Siegmund, E. Ostermann, E. Patzelt, M. Sproll, et al., Tumor targeting properties of monoclonal antibodies with different affinity for target antigen CD44V6 in nude mice bearing head-and-neck cancer xenografts, Int. J. Cancer 99 (2002) 396–402. Available from: https://doi.org/10.1002/ijc.10369.

[183] S.-T. Ning, S.-Y. Lee, M.-F. Wei, C.-L. Peng, S.Y.-F. Lin, M.-H. Tsai, et al., Targeting colorectal cancer stem-like cells with anti-CD133 antibody-conjugated SN-38 nanoparticles, ACS Appl. Mater. Interfaces 8 (2016) 17793–17804. Available from: https://doi.org/10.1021/acsami.6b04403.

[184] S. Hussain, A. Pluckthun, T.M. Allen, U. Zangemeister-Wittke, Antitumor activity of an epithelial cell adhesion molecule targeted nanovesicular drug delivery system, Mol. Cancer Ther. 6 (2007) 3019–3027. Available from: https://doi.org/10.1158/1535-7163.MCT-07-0615.

[185] W. Alshaer, H. Hillaireau, J. Vergnaud, S. Ismail, E. Fattal, Functionalizing liposomes with anti-CD44 aptamer for selective targeting of cancer cells, Bioconjug. Chem. 26 (2015) 1307−1313. Available from: https://doi.org/10.1021/bc5004313.

[186] Z. Yu, M. Ni, M. Xiong, X. Zhang, G. Cai, H. Chen, et al., Poly(lactic-co-glycolic acid) nanoparticles conjugated with CD133 aptamers for targeted salinomycin delivery to CD133 + osteosarcoma cancer stem cells, Int. J. Nanomed. 10 (2015) 2537−2554. Available from: https://doi.org/10.2147/IJN.S78498.

[187] M. Alibolandi, M. Ramezani, K. Abnous, F. Sadeghi, F. Atyabi, M. Asouri, et al., In vitro and in vivo evaluation of therapy targeting epithelial-cell adhesion-molecule aptamers for non-small cell lung cancer, J. Control. Release 209 (2015) 88−100. Available from: https://doi.org/10.1016/j.jconrel.2015.04.026.

[188] M. Das, W. Duan, S.K. Sahoo, Multifunctional nanoparticle−EpCAM aptamer bioconjugates: a paradigm for targeted drug delivery and imaging in cancer therapy, Nanomed. Nanotechnol., Biol. Med. 11 (2015) 379−389. Available from: https://doi.org/10.1016/j.nano.2014.09.002.

[189] A. Tirella, K. Kloc-Muniak, L. Good, J. Ridden, M. Ashford, S. Puri, et al., CD44 targeted delivery of siRNA by using HA-decorated nanotechnologies for KRAS silencing in cancer treatment, Int. J. Pharm. 561 (2019) 114−123. Available from: https://doi.org/10.1016/j.ijpharm.2019.02.032.

[190] N.K. Han, D.H. Shin, J.S.J.S. Kim, K.Y. Weon, C.Y. Jang, J.S.J.S. Kim, Hyaluronan-conjugated liposomes encapsulating gemcitabine for breast cancer stem cells, Int. J. Nanomed. 11 (2016) 1413−1425. Available from: https://doi.org/10.2147/IJN.S95850.

[191] A. Marengo, S. Forciniti, I. Dando, E. Dalla Pozza, B. Stella, N. Tsapis, et al., Pancreatic cancer stem cell proliferation is strongly inhibited by diethyldithiocarbamate-copper complex loaded into hyaluronic acid decorated liposomes, Biochim. Biophys. Acta − Gen. Subj. 1863 (2019) 61−72. Available from: https://doi.org/10.1016/j.bbagen.2018.09.018.

[192] S. Qiao, Y. Zhao, S. Geng, Y. Li, X. Hou, Y. Liu, et al., A novel double-targeted non-drug delivery system for targeting cancer stem cells, Int. J. Nanomed. 11 (2016) 6667−6678. Available from: https://doi.org/10.2147/IJN.S116230.

[193] J.M. Wickens, H.O. Alsaab, P. Kesharwani, K. Bhise, M.C.I.M. Amin, R.K. Tekade, et al., Recent advances in hyaluronic acid-decorated nanocarriers for targeted cancer therapy, Drug Discov. Today 22 (2017) 665−680. Available from: https://doi.org/10.1016/j.drudis.2016.12.009.

[194] Y. Zhong, K. Goltsche, L. Cheng, F. Xie, F. Meng, C. Deng, et al., Hyaluronic acid-shelled acid-activatable paclitaxel prodrug micelles effectively target and treat CD44-overexpressing human breast tumor xenografts in vivo, Biomaterials 84 (2016) 250−261. Available from: https://doi.org/10.1016/j.biomaterials.2016.01.049.

[195] R.G. Thomas, M. Moon, S. Lee, Y.Y. Jeong, Paclitaxel loaded hyaluronic acid nanoparticles for targeted cancer therapy: in vitro and in vivo analysis, Int. J. Biol. Macromol. 72 (2015) 510−518. Available from: https://doi.org/10.1016/j.ijbiomac.2014.08.054.

[196] S. Wilhelm, A.J. Tavares, Q. Dai, S. Ohta, J. Audet, H.F. Dvorak, et al., Analysis of nanoparticle delivery to tumours, Nat. Rev. Mater. 1 (2016) 16014. Available from: https://doi.org/10.1038/natrevmats.2016.14.

[197] Q. Dai, S. Wilhelm, D. Ding, A.M. Syed, S. Sindhwani, Y. Zhang, et al., Quantifying the ligand-coated nanoparticle delivery to cancer cells in solid tumors, ACS Nano 12 (2018) 8423−8435. Available from: https://doi.org/10.1021/acsnano.8b03900.

[198] L. Wang, W. Su, Z. Liu, M. Zhou, S. Chen, Y. Chen, et al., CD44 antibody-targeted liposomal nanoparticles for molecular imaging and therapy of hepatocellular carcinoma, Biomaterials 33 (2012) 5107–5114. Available from: https://doi.org/10.1016/j.biomaterials.2012.03.067.

[199] Y. Li, S. Shi, Y. Ming, L. Wang, C. Li, M. Luo, et al., Specific cancer stem cell-therapy by albumin nanoparticles functionalized with CD44-mediated targeting, J. Nanobiotechnol. 16 (2018) 99. Available from: https://doi.org/10.1186/s12951-018-0424-4.

[200] E. Muntimadugu, R. Kumar, S. Saladi, T.A. Rafeeqi, W. Khan, CD44 targeted chemotherapy for co-eradication of breast cancer stem cells and cancer cells using polymeric nanoparticles of salinomycin and paclitaxel, Colloids Surf., B: Biointerfaces 143 (2016) 532–546. Available from: https://doi.org/10.1016/j.colsurfb.2016.03.075.

[201] S.K. Swaminathan, E. Roger, U. Toti, L. Niu, J.R. Ohlfest, J. Panyam, CD133-targeted paclitaxel delivery inhibits local tumor recurrence in a mouse model of breast cancer, J. Control. Release 171 (2013) 280–287. Available from: https://doi.org/10.1016/j.jconrel.2013.07.014.

[202] D.H. Shin, S. Xuan, W.-Y. Kim, G.-U. Bae, J.-S. Kim, CD133 antibody-conjugated immunoliposomes encapsulating gemcitabine for targeting glioblastoma stem cells, J. Mater. Chem., B. 2 (2014) 3771–3781. Available from: https://doi.org/10.1039/c4tb00185k.

[203] D.H. Shin, S.-J. Lee, J.S. Kim, J.-H. Ryu, J.-S. Kim, Synergistic effect of immunoliposomal gemcitabine and bevacizumab in glioblastoma stem cell-targeted therapy, J. Biomed. Nanotechnol. 11 (2015) 1989–2002. Available from: https://doi.org/10.1166/jbn.2015.2146.

[204] J.S. Kim, D.H. Shin, J.-S. Kim, Dual-targeting immunoliposomes using angiopep-2 and CD133 antibody for glioblastoma stem cells, J. Control. Release 269 (2018) 245–257. Available from: https://doi.org/10.1016/j.jconrel.2017.11.026.

[205] D. Bhavsar, K. Subramanian, S. Sethuraman, U.M. Krishnan, EpCAM-targeted liposomal si-RNA delivery for treatment of epithelial cancer, Drug Deliv. 23 (2014) 1–14. Available from: https://doi.org/10.3109/10717544.2014.973082.

[206] C. Garcia-Mazas, N. Csaba, M. Garcia-Fuentes, Biomaterials to suppress cancer stem cells and disrupt their tumoral niche, Int. J. Pharm. 523 (2017) 490–505. Available from: https://doi.org/10.1016/j.ijpharm.2016.12.013.

[207] S. Shen, M. Liu, T. Li, S. Lin, R. Mo, Recent progress in nanomedicine-based combination cancer therapy using a site-specific co-delivery strategy, Biomater. Sci. 5 (2017) 1367–1381. Available from: https://doi.org/10.1039/C7BM00297A.

[208] A.R. Kirtane, S.M. Kalscheuer, J. Panyam, Exploiting nanotechnology to overcome tumor drug resistance: challenges and opportunities, Adv. Drug Deliv. Rev. 65 (2013) 1731–1747. Available from: https://doi.org/10.1016/j.addr.2013.09.001.

[209] E. Muntimadugu, N. Kommineni, W. Khan, Exploring the potential of nanotherapeutics in targeting tumor microenvironment for cancer therapy, Pharmacol. Res. 126 (2017) 109–122. Available from: https://doi.org/10.1016/j.phrs.2017.05.010.

[210] Q. Sun, T. Ojha, F. Kiessling, T. Lammers, Y. Shi, Enhancing tumor penetration of nanomedicines, Biomacromolecules 18 (2017) 1449–1459. Available from: https://doi.org/10.1021/acs.biomac.7b00068.

[211] E. Ruoslahti, Tumor penetrating peptides for improved drug delivery, Adv. Drug Deliv. Rev. 110–111 (2017) 3–12. Available from: https://doi.org/10.1016/j.addr.2016.03.008.

ANNEX II

Microencapsulated Isoniazid-Loaded Metal-Organic Frameworks for Pulmonary Administration of Antituberculosis Drugs

Cristina Fernández-Paz, Estefanía Fernández-Paz, Pablo Salcedo-Abraira, Sara Rojas, **Sheila Barrios-Esteban**, Noemi Csaba, Patricia Horcajada, Carmen Remuñán-López.

MICROENCAPSULATED ISONIAZID-LOADED METAL-ORGANIC FRAMEWORKS FOR PULMONARY ADMINISTRATION OF ANTITUBERCULOSIS DRUGS

Cristina Fernández-Paz[1], Estefanía Fernández-Paz[1], Pablo Salcedo-Abraira[2], Sara Rojas[2], **Sheila Barrios-Esteban**[3], Noemi Csaba[3], Patricia Horcajada[2], Carmen Remuñán-López[1].

[1]Faculty of Pharmacy, University of Santiago de Compostela, Campus Vida, 15782 Santiago de Compostela, Galicia, Spain; cristina.fernandez.paz@rai.usc.es (C.F.-P.); estefania.fernandez.paz@rai.usc.es (E.F.-P.)
[2]Advanced Porous Materials Unit (APMU), IMDEA Energy Institute, Av. Ramón de la Sagra, 3, 28035 Móstoles, Madrid, Spain; pablo.salcedo@imdea.org (P.S.-A.); srojas@ugr.es (S.R.); patricia.horcajada@imdea.org (P.H.)
[3]Nanobiofar Group-Natural Polymers and Biomimetics (NPNB) Group, Center of Research in Molecular Medicine, and Chronic Diseases (CiMUS), University of Santiago de Compostela, Campus Vida, 15706 Santiago de Compostela, Galicia, Spain; sheila.barrios@rai.usc.es (S.B.-E.); noemi.csaba@usc.es (N.C.)
*Correspondence: mdelcarmen.remunan@usc.es; Tel.: +34-881815045

Molecules 2021, 26 (21), 6408, 1-27.

DOI: https://doi.org/10.3390/molecules26216408

molecules

MDPI

Article

Microencapsulated Isoniazid-Loaded Metal–Organic Frameworks for Pulmonary Administration of Antituberculosis Drugs

Cristina Fernández-Paz [1], Estefanía Fernández-Paz [1], Pablo Salcedo-Abraira [2], Sara Rojas [2], Sheila Barrios-Esteban [3], Noemi Csaba [3], Patricia Horcajada [2] and Carmen Remuñán-López [1,*]

[1] Nanobiofar Group, Department of Pharmacology, Pharmacy & Pharmaceutical Technology, Faculty of Pharmacy, University of Santiago de Compostela, Campus Vida, 15782 Santiago de Compostela, Galicia, Spain; cristina.fernandez.paz@rai.usc.es (C.F.-P.); estefania.fernandez.paz@rai.usc.es (E.F.-P.)
[2] Advanced Porous Materials Unit (APMU), IMDEA Energy Institute, Av. Ramón de la Sagra, 3, 28035 Móstoles, Madrid, Spain; pablo.salcedo@imdea.org (P.S.-A.); srojas@ugr.es (S.R.); patricia.horcajada@imdea.org (P.H.)
[3] Nanobiofar Group-Natural Polymers and Biomimetics (NPNB) Group, Center of Research in Molecular Medicine and Chronic Diseases (CiMUS), University of Santiago de Compostela, Campus Vida, 15706 Santiago de Compostela, Galicia, Spain; sheila.barrios@rai.usc.es (S.B.-E.); noemi.csaba@usc.es (N.C.)
* Correspondence: mdelcarmen.remunan@usc.es; Tel.: +34-881815045

check for updates

Citation: Fernández-Paz, C.; Fernández-Paz, E.; Salcedo-Abraira, P.; Rojas, S.; Barrios-Esteban, S.; Csaba, N.; Horcajada, P.; Remuñán-López, C. Microencapsulated Isoniazid-Loaded Metal–Organic Frameworks for Pulmonary Administration of Antituberculosis Drugs. *Molecules* **2021**, *26*, 6408. https://doi.org/10.3390/molecules26216408

Academic Editors: Carlos A. García-González, Ana Leite Oliveira, Pasquale Del Gaudio and Ricardo Starbird

Received: 9 September 2021
Accepted: 13 October 2021
Published: 23 October 2021

Publisher's Note: MDPI stays neutral with regard to jurisdictional claims in published maps and institutional affiliations.

Abstract: Tuberculosis (TB) is an infectious disease that causes a great number of deaths in the world (1.5 million people per year). This disease is currently treated by administering high doses of various oral anti-TB drugs for prolonged periods (up to 2 years). While this regimen is normally effective when taken as prescribed, many people with TB experience difficulties in complying with their medication schedule. Furthermore, the oral administration of standard anti-TB drugs causes severe side effects and widespread resistances. Recently, we proposed an original platform for pulmonary TB treatment consisting of mannitol microspheres (Ma MS) containing iron (III) trimesate metal–organic framework (MOF) MIL-100 nanoparticles (NPs). In the present work, we loaded this system with the first-line anti-TB drug isoniazid (INH) and evaluated both the viability and safety of the drug vehicle components, as well as the cell internalization of the formulation in alveolar A549 cells. Results show that INH-loaded MOF (INH@MIL-100) NPs were efficiently microencapsulated in Ma MS, which displayed suitable aerodynamic characteristics for pulmonary administration and non-toxicity. MIL-100 and INH@MIL-100 NPs were efficiently internalized by A549 cells, mainly localized in the cytoplasm. In conclusion, the proposed micro-nanosystem is a good candidate for the pulmonary administration of anti-TB drugs.

Keywords: A549 cells; isoniazid; mannitol; metal–organic frameworks; microencapsulation; pulmonary administration; tuberculosis

1. Introduction

Currently, TB continues to be one of the principal 10 causes of death worldwide [1,2], and is the second leading cause of death (1.5 million people in the world per year [3]) due to an infectious disease, behind SARS-CoV-2 (>1.9 million deaths in 2020 [4]). TB is mainly caused by the bacteria *Mycobacterium tuberculosis* [5] and principally affects the lungs but also can be spread to other organs (e.g., productive cough, fatigue, fever, malaise, night sweats, and weight loss) [6].

Once in the body, alveolar macrophages are a growth niche in which the bacilli reside and multiply. The conventional TB therapy recommended by the World Health Organization (WHO) consists of a difficult daily oral multidrug regimen that is prolonged in time (often lasts up to 2 years), in which the treatment during the first two months is with INH, rifampicin, ethambutol, and pyrazinamide (first-line anti-TB drugs), and

the following four months with INH and rifampicin [7]. Although the treatment efficacy was estimated to be of 85% [8], there are several factors that can negatively affect the success rate, such as: (i) the inappropriate use of anti-TB drugs (e.g., employed medicines of deficient quality or bad storage); (ii) low stability and poor oral absorption of anti-TB drugs; (iii) important first-pass metabolism of anti-TB drugs, making difficult to reach the granulomas and penetrate into the bacteria; and (iv) a too-long treatment duration (often lasts up to 2 years) that is generally associated with important undesirable side effects (e.g., depression, psychosis, kidney impairment, or resistances [8]). Therefore, a controlled and targeted release of anti-TB drugs should be able to overcome these drawbacks and achieve a more effective treatment of TB.

The pulmonary route is suitable to administrate either small or large molecules for local or systemic treatments [9–11] by using aerosols [12]. In this regard, it has attracted great interest due to its advantages for the local delivery of anti-TB drugs [12], such as: (i) its non-invasive and pain-free way of administration that favors the comfort and dosing compliance of the patient [13]; (ii) direct administration at the site of action, reducing the administered dose and potential side effects; (iii) low enzymatic activity in comparison with other mucosal surfaces, avoiding, for example, the gastrointestinal degradation inherent to oral administration; and (iv) absence of the hepatic first-pass effect [14]. The pulmonary route is especially attractive for TB treatment in comparison with the traditional oral and parenteral routes, as it increases the local drug concentration, thus improving the pharmacological action and decreasing the drug systemic dosage, which are associated to side effects and to the risk of resistant-strain development [15–17].

Nano and microsystems arouse great interest for the delivery of active ingredients (AIs) directly to the lung to treat pulmonary diseases such as cystic fibrosis or TB, and also for gene therapy, as they can help to overcome the difficulties associated with their pulmonary administration. Additionally, the direct administration of AIs to the lung makes it possible to optimize their therapeutic effect in comparison with traditional treatments administered orally. Different types of nanosystems (NPs, solid lipid NPs (SLN), nanocapsules (NCs), nanoemulsions, liposomes, and micelles) and microsystems (microparticles and MS) [18–23] were investigated; among them, the MOFs stood out. They are crystalline hybrid materials of high porosity, which are formed by the association of inorganic subunits (cations, clusters, chains, etc.) and polydentate organic ligands (carboxylates, azolates, etc.) [24]. It is worthy to note that the presence of metals in the structure of some MOFs have antibacterial activity and a synergistic effect with antibacterial drugs; therefore, these MOFs have great potential for anti-TB therapy. This is the case of MOFs containing silver and gold [25]. MOFs (unlike other rigid NPs) are tunable, can be functionalized, have an adjustable porosity and high drug loads, and are thermo-resistant. Particularly, nanoscaled MOFs (nanoMOFs) have proven to be excellent platforms for the delivery of drugs through different routes such as the intravenous or cutaneous route [26]. The active compounds can be adsorbed or entrapped inside the pores or can be a constituent of the MOF itself as a biologically active building block. MOFs can transport large quantities of different AIs (drugs, nucleic acids, enzymes, etc.) and release them in a controlled manner [24]. Mainly mesoporous iron (III) trimesate, named MIL-100(Fe) (MIL = Material of Institute Lavoisier) [19], is a promising candidate as a drug delivery vehicle since: (i) it can be synthetized at difference sizes (from 80 nm to some microns) [24]; (ii) is highly porous (Brunauer, Emmett, and Teller (BET) surface area ~2000 $m^2 \cdot g^{-1}$, Vp = 1.2 $cm^3 \cdot g^{-1}$; with mesoporous voids of 2.5 and 2.9 nm accessible through microporous windows ca. 4.8–5.8 and 8.6 Å, respectively), which allows for the encapsulation of important drug doses; and (iii) is biodegradable and non-toxic, as it has not shown signs of toxicity after pulmonary [19] or intravenous [27] administration to rats. To prepare an optimal pulmonary formulation it is important to know where the drug must be deposited. In this sense, to achieve the deep lung, the aerodynamic diameter should be between 1 and 5 μm [14,28]. However, good distributions into the deep lung are achieved with particles lower in size and presenting hollow structure [29,30]. Regarding to the nature of inhaled formulations,

dry powders are generally preferred over their liquid counterparts since: (i) they present a higher stability [31] and drug bioavailability [32]; (ii) are easily stored; and (iii) are easy to handle since, for example, the nebulization systems require special equipment [13,33]. Taking into account the fact that the MIL-100(Fe) NPs present a size of around 150 nm, it is not enough to reach the deep lung. In this regard, one efficient strategy can be the microencapsulation of MIL-100 NPs in MS with suitable aerodynamic properties to achieve the deep lung. The most common excipients used for the preparation of MS are the saccharides, as they are biocompatible, biodegradable, easily functionalizable, and cheap [34].

In this work, we microencapsulated INH@MIL-100 NPs by spray-drying in order to improve their stability [35] and their aerosolization pattern [36–38] to achieve a deposition and delivery in the lower respiratory tract [39,40]. Different biocompatible polysaccharides were initially spray-dried (obtaining control MS) to select the best excipient for the microencapsulation. The encapsulation of the INH first-line anti-TB drug was carried out in the nanoscaled MIL-100 MOFs, fully characterizing the resulting drug-loaded nanosystem (INH@MIL-100). Then, INH@MIL-100 NPs were microencapsulated in the MS of the selected excipient. The resulting micro-nanoMOFs were investigated to guarantee their biocompatibility with the pulmonary epithelium and the cell internalization of NPs in adenocarcinoma human alveolar basal epithelial cells (A549 cells) was examined. The developed Ma-INH@MIL-100 MS exhibited suitable aerodynamic properties for pulmonary administration. In addition, MIL-100 and INH@MIL-100 NPs, as well as the Ma excipient, were non-toxic for A549 cells, as the NPs were efficiently captured by these cells and the nanocarriers were found mainly in the cytoplasm.

It is important to bear in mind that in certain cases where TB is advanced, pulmonary fibrosis can occur. If the lung tissue is fibrotic [41], the normal lung function is impaired. This modified functionality causes the diminishing of the iron uptake of the macrophages [42] and causes a low amount of phagocytosed iron to be less metabolized. Therefore, greater amounts of iron accumulate in the lung. This excess iron levels increases the activity of prolyl hydroxylase, an important enzyme involved in the synthesis [43] and maturation [44] of collagen, and, in consequence, worsens the fibrotic disease. The elevated iron levels can also increase the proliferation of pro-inflammatory cytokines. Hence, we did not rule out that in these circumstances, the pulmonary fibrosis may develop further after administration of MOFs containing iron. Therefore, Ma-INH@MIL-100 MS are more interesting for the early treatment of TB. We have recently reported the preparation of Ma MS containing MIL-100(Fe) MOFs, which have adequate aerodynamic properties to reach the deep lung after intratracheal administration to rats and are susceptible to being phagocytosed by alveolar macrophages. Therefore, Ma-INH@MIL-100 MS emerge as promising candidates to combat certain infectious diseases, such as TB, by the pulmonary route.

2. Results and Discussion

2.1. INH Encapsulation

The previously reported outstanding results in the efficient in vivo release of MIL-100 NPs uniformly along the lungs, reaching the bronchioles and alveoli [19], prompted us to explore the incorporation and posterior release of the first-line anti-TB drug INH ($7.3 \times 4.6 \times 3.0$ Å^3) in detail. INH was successfully encapsulated into the porosity of the MIL-100 NPs with a two-step impregnation method of the porous material in an aqueous solution of INH, reaching a drug loading of 29.5 ± 2.21 wt%. Powder X-ray diffraction (PXRD) patterns evidenced that the drug-encapsulation process did not alter the crystalline structure of the porous material (Figure 1a). The absence of Bragg peaks corresponding to free INH rules out the presence of free recrystallized drugs outside the pores of MIL-100. The drug content was estimated by combining high-performance liquid chromatography (HPLC) and thermogravimetric analysis (TGA; Figure 1b). This INH loading is excellent in comparison with that obtained for MIL-101-NH_2(Fe) (12 wt%) in other anterior studies [45] and remains in the range of previously incorporated drugs in MIL-100 MOF (e.g., 25 wt% of acetylsalicylic acid [46] and 31 wt% of ibuprofen [47]).

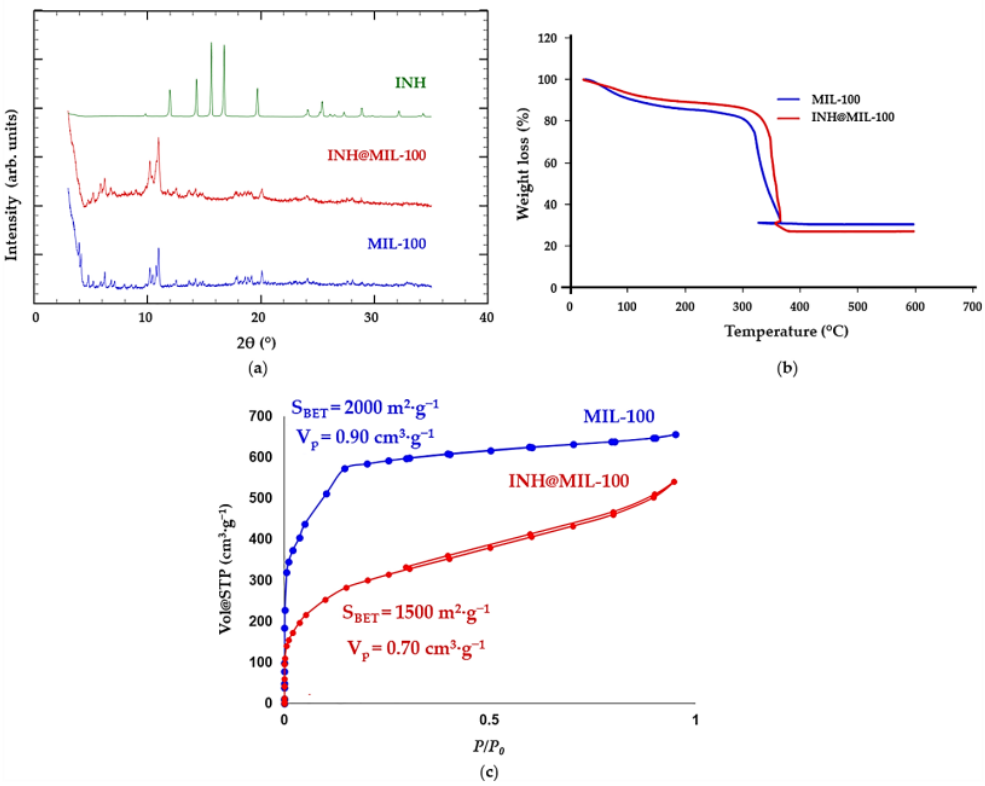

Figure 1. (**a**) PXRD patterns; (**b**) TGA; and (**c**) N_2 sorption isotherms at 77 K of MIL-100 and INH@MIL-100 nanomaterials. PXRD pattern of the free INH has been included for comparison in Figure 1a. Close and open symbols in Figure 1c indicate adsorption and desorption branches, respectively.

Furthermore, the incorporation of the anti-TB drug within the cavities of MIL-100 NPs was demonstrated by the dramatic reduction of the N_2 sorption capacity of both the MOF and pore size (Figure 1c). In the INH@MIL-100 NPs, there was still some residual porosity after the drug encapsulation process (SBET = 1500 $m^2 \cdot g^{-1}$, pore volume-Vp = 0.70 $cm^3 \cdot g^{-1}$). To shed some light on the influence of porosity on drug adsorption, we estimated the volume occupied by each INH molecule inside the MOF by considering the variation of the MOF pore volume after the drug encapsulation and the total amount of loaded drug using a previously reported procedure described by Rojas et al. [47]. The higher INH occupancy volume in MIL-100 compared to the INH-free MIL-100 volume (435 vs. 105 $Å^3$, as estimated under vacuum by ChemDraw) is related to the partial pores' occupancy, as confirmed by the important remaining porosity after INH insertion. This suggests that the maximum drug loading is not reached in MIL-100 or that some cages are not accessible to the drug but only to N_2. In fact, the adsorption of the INH might preferentially occur in the larger cages of MIL-100 (accessible via hexagonal windows of ~8.6 Å). In contrast, the dimensions of INH might prevent its crossing through the pentagonal windows (ca. 4.8–5.8 Å; note that van der Waals radii have been considered), in agreement with the selective location of other drugs in MIL-100 (e.g., ibuprofen) [48]. Finally, if one excludes the drug location within the smaller pores, a more realistic volume of the MIL-100 occupied by INH (44%)

is estimated, corresponding to an INH occupancy volume of 191.4 Å^3 (much closer to the free molecule 105 Å^3).

Fourier transform infrared (FTIR) spectra of INH@MIL-100 confirmed the presence of INH in the MOF NPs through the presence of some bands corresponding to the drug (Figure 2). It can be seen, for instance, the ν(ring C-C-H) asymmetric and symmetric bending 1217, 1195 cm^{-1}, and 843 cm^{-1}, respectively; and ν(C-C=O) 689 cm^{-1} [49]. Furthermore, the FTIR spectrum of INH@MIL-100 NPs showed a shift in the wavelengths in comparison with the empty MIL-100 characteristic bands: ν(C-O) band of carboxylate groups (from 1630 to 1624 cm^{-1}) and both the asymmetric and symmetric vibrational band characteristics of the -O-C-O- group (from 1449 to 1443 cm^{-1} and from 1378 to 1371 cm^{-1}) [50]. These results suggest the formation of interactions between the drug and the hybrid framework.

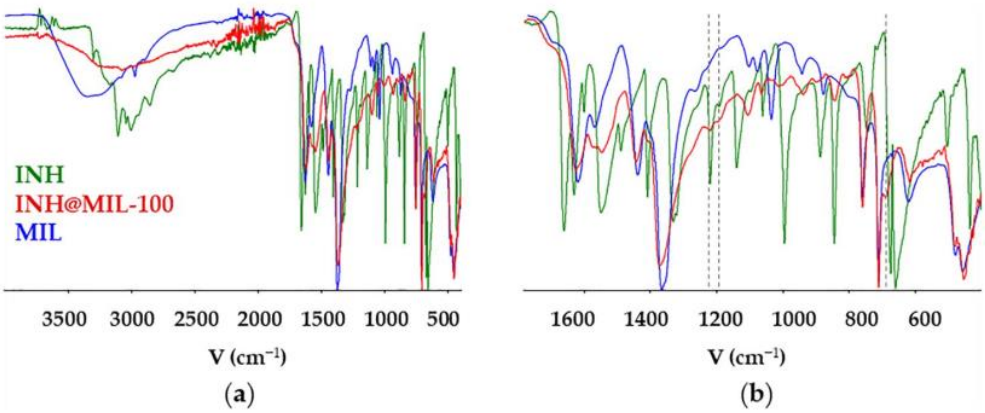

Figure 2. FTIR spectra of INH, INH@MIL-100, and MIL-100 materials with a (**a**) wider spectrum range, approximately from 4000 to 400 υ(cm^{-1}). (**b**) A part of these spectra are around 1800 to 400 υ(cm^{-1}).

2.2. *Preparation and Characterization of MS*

A preliminary spray-drying screening study of the preparation of control MS (without NPs) was initially performed, employing the aqueous solutions of seven excipients: D-mannitol (Ma), α-cyclodextrin (α-CD), dextran (Dex), D-(+)-mannose (Man), D-(+)-trehalose dihydrate (Tre), D-sorbitol (Sor), and D-(−)-fructose (Fru). The resulting powders were characterized, with special attention provided to the process yield (PY), morphology, and apparent density (Table 1). In this regard, high PY was obtained for α-CD and Ma (74.0 ± 3.0 and 58.5 ± 3.5 wt%, respectively), in contrast to the low PY found for Tre and Dex (27.0 ± 1.0 and 10.5 ± 1.5 wt%, respectively). Sor, Man, and Fru did not allow for the recovery of measurable powder amounts; therefore, they were discarded. Conversely, SEM images (Figure 3) showed that the MS morphology was highly dependent on the used excipient. Ma MS were well-defined non-aggregated spherical particles with a continuous smooth surface (Figure 3a), whereas α-CD MS and Dex MS were more irregular and with a heterogeneous surface (Figures 3b and 3c, respectively). In contrast, the resulting Tre structures did not present qualities for pulmonary administration because they resulted in agglomerates. One could expect that regular spherical Ma MS, with fewer contact points between particles and less friction between them [51], will present improved flow properties, facilitating their pulmonary administration.

Table 1. Process yield (wt, percentage) as well as morphology and apparent density (g·cm^{-3}) of control MS (dry powders) prepared with different excipients (mean ± S.D.; n = 3).

Control MS	Process Yield (wt, %)	Morphology	Apparent Density (g·cm^{-3})
Ma MS	58.5 ± 3.5	Spherical	0.43 ± 0.01
α-CD MS	74.0 ± 3.0	Less spherical	0.36 ± 0.01
Dex MS	10.5 ± 1.5	Less spherical	–[1]
Tre MS	27.0 ± 1.0	Agglomerate	–[1]

[1] Not enough samples to perform this calculation.

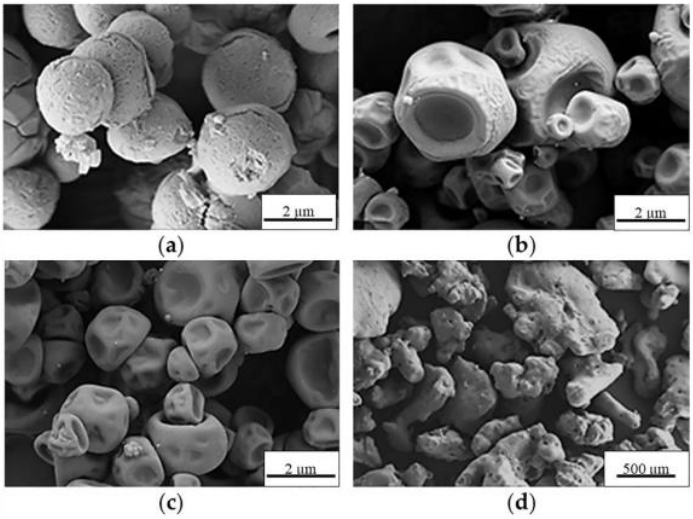

Figure 3. SEM microphotographs of the control MS of (**a**) Ma, (**b**) α-CD, (**c**) Dex, and (**d**) Tre.

The higher apparent density obtained for Ma MS (0.43 ± 0.01 g·cm^{-3}) compared to the α-CD MS (0.36 ± 0.01 g·cm^{-3}; Table 1) can be explained by their different surface morphologies. In fact, the apparent density of α-CD MS was very similar to that of locust bean gum MS (around 0.37 g·cm^{-3}), which present analogous surface morphology [52]. The apparent densities of Dex MS and Tre MS could not be determined due to their low PY (9–28%). Ma was the only excipient that resulted in control MS with good handling properties, probably because Ma allows for obtaining powders with low humidity content [53], which would also facilitate the in vivo aerosolization. Considering the advantages of Ma MS dry powder, such as elevated spray-drying PY as well as regular spherical particles with a priori improved flow properties and better handling (drier powder), Ma was selected as the excipient for INH@MIL-100 NPs microencapsulation. Ma has been extensively used in aerosolization [54]. It is accepted by regulatory authorities for its use in inhalation pharmaceutical products; it has suitable characteristics for spray-drying, allowing for the easy adaptation of the morphology and size of the particles [55]; and it improves the handling of the powder formulation as compared to other excipients, such as lactose [56]. In addition, Ma dry-powder facilitates the mucocilliary clearance and the cough in people with asthma and mucocilliary dysfunction [57] due to its osmotic effect, which improves the hydration of the mucus.

Once Ma was selected as the best excipient, the preparation of Ma-INH@MIL-100 MS was performed in consideration of various parameters, such as the shear and temperature in the nozzle that can affect to the drug stability and adsorption effect at the air–liquid interface upon the drying of droplets [58]. First, the physicochemical properties of INH@MIL-

100 NPs dispersed in the Ma solution were evaluated to verify their colloidal stability. The INH@MIL-100 NPs in Ma solution maintained their size in the nanometric range (127 ± 27 nm) as well as their ζ-potential in negative values (−22 ± 4 mV). The INH@MIL-100:Ma ratio was chosen after some preliminary spray-drying proofs of MIL-100 NPs in Ma solution. For that, three distinct MIL-100:Ma ratios (1:5, 1:10, 1:100) were assayed and the spray-drying process was carried out as described in our previous work [19], except the inlet temperature (T_{inlet}: 170 ± 2 °C) was higher than that used previously (T_{inlet}: 160 ± 2 °C). The results showed that the MS had a rounded and hollow shape, and presented characteristic porosity (see Figure 4).

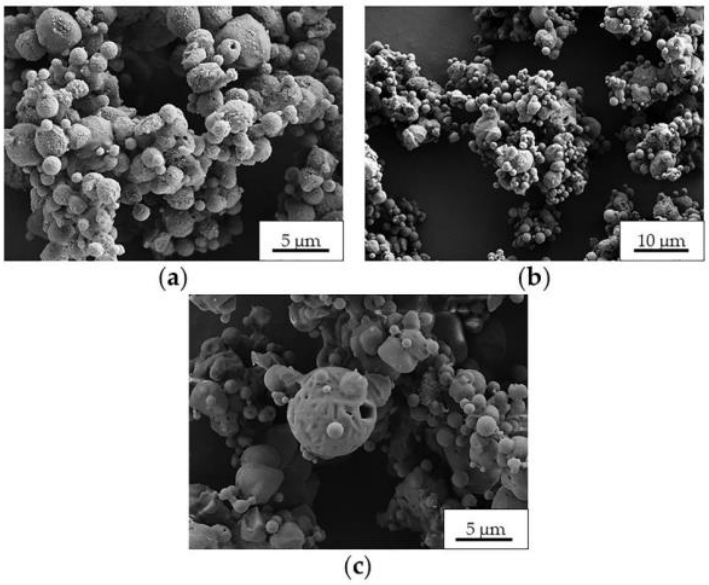

Figure 4. SEM microphotographs of Ma-MIL-100 MS prepared with (**a**) 1:5, (**b**) 1:10, and (**c**) 1:100 MIL-100:Ma ratios.

As can be seen in Figure 4, the MS porosity appearance decreased as the Ma content increased. All the obtained powder samples presented a similar size in the range of 1.8–2.2 µm. Initially, the MS with the 1:5 ratio were discarded since that MS were more agglomerated compared to the other powders (Figure 4). Finally, we chose the sample with the 1:10 ratio because it had a higher NPs load and a more homogeneous appearance than MS with the 1:100 ratio.

For caution, the T_{inlet} of the INH@MIL-100 microencapsulation process was adjusted to 160 °C due to the INH presence in the vehicle (INH melting temperature: 173 °C). Control Ma MS were prepared at 160 °C as well. The surface morphologies of the Ma MS prepared at both T_{inlets} (170 and 160 °C) are different (see Figure 5): Ma MS prepared at 170 °C have a more porous structure (Figure 5a) than those obtained at 160 °C (Figure 5b). This could be explained by the different T_{inlet} used in the spray-drying process. At 170 °C, the water evaporation during the MS preparation was more abrupt and effective, generating pores in greater quantity and larger sizes, meanwhile the Ma stood more dry and compact compared with the sample obtained at 160 °C.

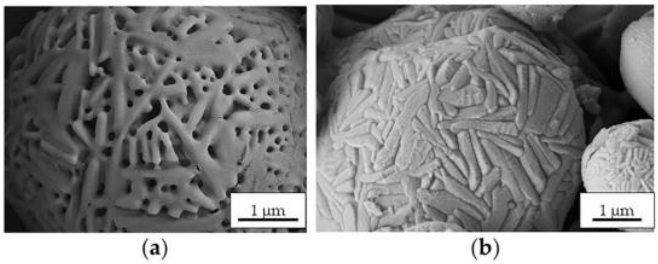

Figure 5. SEM microphotographs of Ma MS prepared at (**a**) 170 °C and (**b**) 160 °C.

Therefore, the INH@MIL-100 NPs were spray-dried using Ma as the excipient and by employing the conditions that are indicated in Section 3.3. The resulting process yield was high (74.5 ± 3.5 wt%) and the Ma-INH@MIL-100 MS were non-aggregated, exhibiting a well-defined and spherical shape, as well as smooth surface (Figure 6).

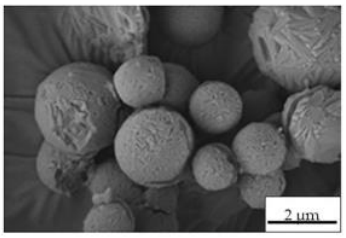

Figure 6. SEM microphotograph of Ma-INH@MIL-100 MS.

The crystalline structure of the MIL-100 material was kept on the MS formulation, as evidenced by the presence of the characteristic Bragg peaks of the MIL-100 structure (Figure 7). In addition, the typical diffraction peaks of Ma were present in the MS.

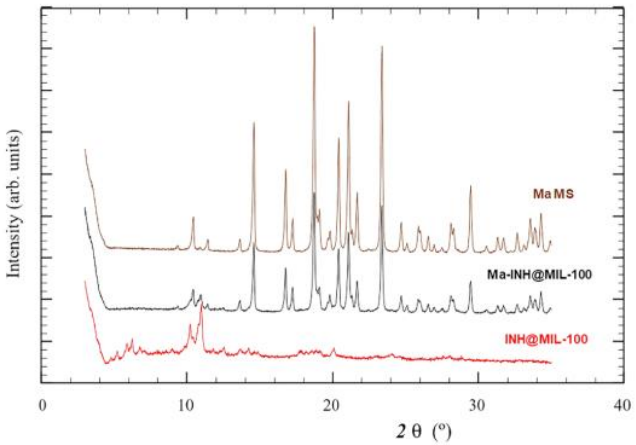

Figure 7. PXRD patterns of INH@MIL-100, Ma-INH@MIL-100 MS, and Ma MS (control formulation included for comparison purposes).

The compositional analyses of the different MS were carried out by means of elemental analysis (Table 2), determining the content of INH, MIL-100, and Ma by measuring the nitrogen, iron, and carbon, respectively. Additionally, it is important that their comparison with the theoretical values of these characteristic elements was employed to prepare the powder samples. Experimental values agreed with the theoretical values, confirming that the final composition of the prepared formulations maintained the amounts of the estimated elements.

Table 2. Elemental composition (weight percentage) of Ma MS, Ma-MIL-100 MS, and Ma-INH@MIL-100 MS.

Samples	Theoretical Values				Experimental Values			
	%C	%H	%N	%Fe	%C	%H	%N	%Fe
Ma MS	39.50	7.68	-	-	39.72 ± 0.24	7.50 ± 0.01	-	-
Ma-MIL-100 MS	38.89	7.08	-	2.50	39.79 ± 0.06	6.75 ± 0.07	-	2.68 ± 0.13
Ma-INH@MIL-100 MS	39.40	7.32	0.55	1.60	39.98 ± 0.09	7.24 ± 0.06	0.56 ± 0.07	1.25 ± 0.06

To evaluate the potential interest of Ma-INH@MIL-100 MS for pulmonary administration, their aerodynamic and physical properties were characterized (Table 3). Traditionally, diameters between 1 and 5 µm are associated with deep lung deposition; however, the geometric and aerodynamic diameters of our formulation (1.4 ± 0.4 and 0.422 ± 0.007 µm, respectively) could be considered suitable for pulmonary administration since other formulations with similar characteristics reached the deep lung in previous in vivo studies [56,59], for instance, as it was demonstrated by our research group for the Ma-MIL-100 MS in Wistar–Kyoto rats [19]. It should be noted that the low aerodynamic diameter (0.422 ± 0.007 µm, Table 3) was related with the hollow nature (ca. 70–90%) of the MS. As expected, the apparent density of Ma-INH@MIL-100 MS (0.52 ± 0.01 g·cm^{-3}) was higher than that of Ma MS (0.43 ± 0.01 g·cm^{-3}) considering the INH@MIL-100 cargo (Table 3). The estimated low apparent density, jointed to the small diameters for the Ma-INH@MIL-100 MS (0.52 ± 0.01 g·cm^{-3}) was related to a good behavior of the aerodynamic flow, as previously demonstrated for other formulations [19,60,61]. The real density and aerodynamic diameter values of Ma-INH@MIL-100 MS were in the same range as previously obtained for Ma-MIL-100 MS [19] and other types of hollow particles that demonstrated to be acceptable for pulmonary administration [29,30].

Table 3. Aerodynamic and physical properties of Ma MS, Ma-MIL-100 MS, and Ma-INH@MIL-100 MS (mean ± S.D., n = 3).

Sample	Geometric Diameter (µm)	Real Density (g·cm^{-3})	Apparent Density (g·cm^{-3})	Aerodynamic Diameter (µm)
Ma MS	2.3 ± 1.0	0.0666 ± 0.0001	0.43 ± 0.01	0.594 ± 0.010
Ma-MIL-100 MS	1.8 ± 0.7	0.0550 ± 0.0001	0.44 ± 0.02	0.422 ± 0.007
Ma-INH@MIL-100 MS	1.4 ± 0.4	0.0907 ± 0.0003	0.52 ± 0.01	0.422 ± 0.007

Overall, Ma-INH@MIL-100 MS presented suitable characteristics for drug delivery to the deep lung. The selection of Ma between different excipients resulted in good results, as has been previously seen for other types of NPs, i.e., solid lipid nanoparticles (SLN) and chitosan NPs (CS NPs) [59,62].

2.3. Ma-INH@MIL-100 MS: Colloidal and Chemical Stability, and INH Release

Excipients can protect the nanosystems from spray-drying conditions, in particular from the heating process and intra-formulation interactions that could cause aggregation, hindering their deposition in the deep lung [56,63]. Both the release of INH@MIL-100 NPs from the MS and their colloidal stability during the release process were evaluated by monitoring the evolution of the particle size and ζ-potential of the released NPs in three simulated physiological conditions (MilliQ water; phosphate buffered saline (PBS), pH = 7.4; and simulated lung fluid (SLF) at 37 °C) for 24 h (Figures 8 and 9).

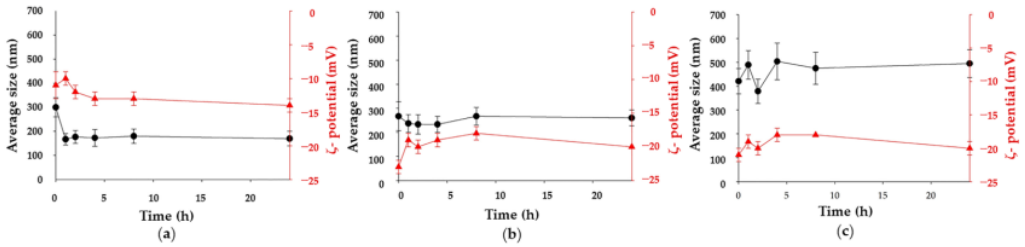

Figure 8. Colloidal stability of INH@MIL-100 NPs following their release from Ma MS in (**a**) water, (**b**) PBS, and (**c**) SLF, showing NPs' size (black, left) and surface charge (red, right) vs. time (h; mean ± S.D.; *n* = 3).

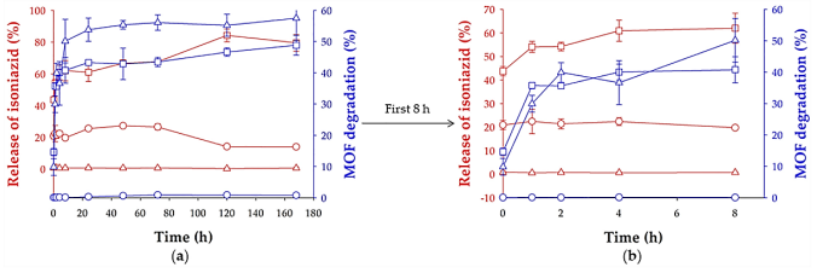

Figure 9. Release of INH (percentage, red) from INH@MIL-100 NPs and MOF degradation (percentage, blue) in water (circle), PBS (pH = 7.4; square), and SLF (triangle) vs. time during (**a**) 168 h and (**b**) 8 h (mean ± S.D.; *n* = 3).

Concerning the INH release (Figure 9), there was a rapid initial (t = 0 h) drug release of INH in MilliQ water and PBS of 21% and 44%, respectively. Then, a constant release was observed during 1 week, reaching a maximum release of 27% and 84%, at 48 h and 120 h, respectively. The incomplete release of INH could be explained by the important interactions with the MOF. Note that released INH could not be detected in SLF probably because of the formation of interactions between the drug and phospholipids of the medium, hindering its quantification by HPLC. The difference of release kinetics between MilliQ water and PBS could be related to a much faster degradation of MIL-100 NPs in PBS (1% (t = 72 h) and 49% (t = 168 h) maximum degradation, respectively; Figure 9) since phosphates from the medium can compete with carboxylates from the MIL-100 structure by the iron coordination. In SLF, the chemical stability of these NPs was similar than in PBS, although after 6 h, the MOF degradation was higher than in PBS. The difference of degradation in each medium was verified by TEM (Figure 10), where it was noticed that the INH@MIL-100 NPs maintained their initial shape in water (Figure 10a) but not in PBS with a not-defined morphology because of their higher degradation (Figure 10b). Conversely, when NPs were released in SLF, a substantial amount of particles was recovered, showing a fairly well-faceted aspect (see Figure 10c) when compared to those suspended in PBS.

In the three tested media, the Ma excipient was quickly solubilized, releasing the INH@MIL-100 NPs from the MS. In the first hour, the NPs decreased their size in water and PBS (from 300 to 167 nm and from 267 to 237 nm, respectively), but slightly increased in the SLF (from 421 to 489 nm). In later times (up to 24 h), the MOFs were colloidally stable in water and PBS (167–180 nm and 233–267 nm, respectively), as well as in SLF where, despite their initial aggregation, the particles kept their size almost constant (over 500 nm). The ζ-potential values of released INH@MIL-100 NPs were negative and stable independently of the media: from −10 to −14 mV in MilliQ water; from −18 to −23 mV in PBS; and from −18 to −21 mV in SLF. This could be seen as an advantage because negatively charged NPs often generate lower inflammatory responses than positive NPs [64]. The increase of size (from 194.5 ± 51.9 to 460.5 ± 49.6 nm) and the reduction of the ζ-potential (from

−12.2 ± 1.5 to −19.3 ± 1.2 mV) of INH@MIL-100 NPs in SLF compared to the NPs in MilliQ water could be explained by the creation of a corona constituted by proteins and lipids derived from the SLF.

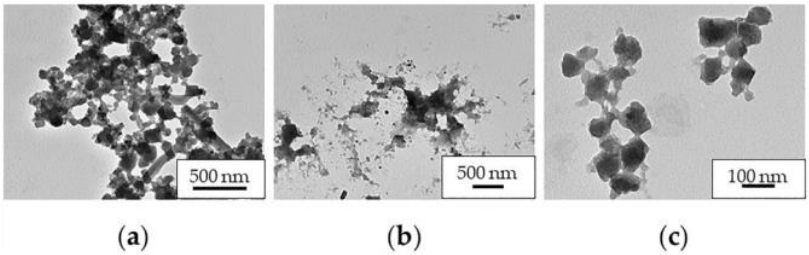

Figure 10. TEM microphotographs of released INH@MIL-100 NPs from Ma MS in (**a**) MilliQ water, (**b**) PBS, and (**c**) SLF.

These results were concordance with those demonstrated in our recent previous publication [19], in which empty MIL-100 NPs were easily released from Ma MS, maintaining their colloidal stability in the different simulated media for 24 h. In addition, the particle size evolution of INH@MIL-100 NPs was quite similar to that found for empty MIL-100 NPs, reducing their dimensions from 267 to 133 nm and from 253 to 145 nm after 1 h in MilliQ water and PBS, respectively. Similarly, in SLF, the INH@MIL-100 NPs behaved similar to their empty analogue; the MIL-100 NPs released as aggregates of around 500 nm and maintain their size for 24 h. Moreover, the surface charge of INH@MIL-100 NPs was less negative than the non-loaded MIL-100 NPs in all the media, with values of −8.0 vs. −12.2 mV (in MilliQ water); −19.5 vs. −19.8 mV (in PBS); and −18.2 vs. −19.3 mV (in SLF) for INH-loaded vs. non-loaded NPs. It is probably a consequence of the drug located both in the inner porous surface and on the outer NP surface.

The crystallinity of released INH@MIL-100 NPs was also analyzed by PXRD. In this case, the INH@MIL-100 NPs released from Ma MS in SLF (at different release times: 0, 1, 8, 24, and 72 h) were compared with the Ma-INH@MIL-100 MS (Figure 11).

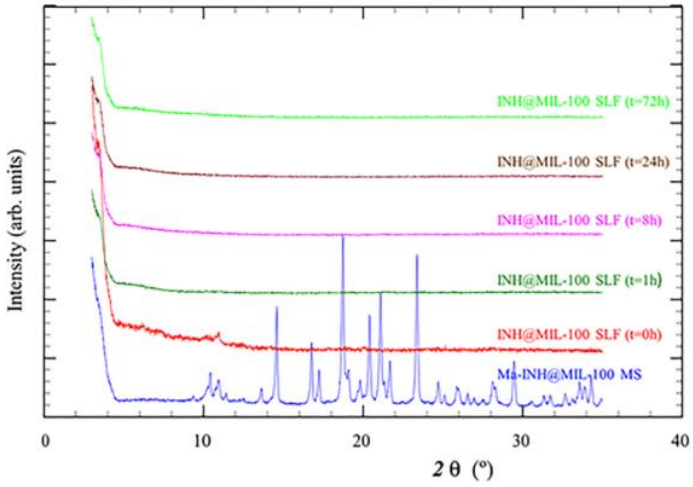

Figure 11. PXRD patterns of released INH@MIL-100 NPs in SLF and Ma-INH@MIL-100 MS.

In the diffractogram, Ma diffraction peaks of the MS were observed (over 20 2 θ (°) in the blue line), showing the crystallinity of these macro-vehicles. At different release times,

the Ma diffraction peaks were not appreciated because the excipient was dissolved in SLF, while the NPs were already released. As the release time progressed, the characteristic peaks of the INH@MIL-100 (over 10 2 θ (°)) were less pronounced due to the degradation of the NPs in SLF. This study confirms the crystallinity of Ma and NPs before the release, alongside the Ma solubilization and the MOFs degradation during the process, which facilitate the INH release. However, it is supposed that INH@MIL-100 NPs will be released from Ma MS in a slower manner in the alveolar fluid due to its small liquid volume (vs. experimental conditions of 4 $mg \cdot mL^{-1}$ of powder in release medium) [62]. Either way, it is expected that the release of INH@MIL-100 NPs from Ma MS would be good.

2.4. Characterization of Test Formulations for Cell Studies

To ensure the MIL-100 and INH@MIL-100 quality for their use in cell studies, their size and ζ-potential were anteriorly determined in MilliQ water. NPs exhibited sizes in the nanometric range (101 ± 19 and 137 ± 51 nm) and negative ζ-potentials (−10 ± 11 and −18 ± 8 mV), being theoretically suitable for cell studies, as demonstrated in our previous in vivo study [19].

2.5. Cell Viability Studies

The A549 cell line was extensively studied in vitro to evaluate the efficacy and safety of diverse drug delivery systems [65]. For this reason, it was also employed in the present viability study. Specifically, it was determined using different concentrations of MIL-100, INH@MIL-100 NPs, and Ma (see Section 3.10 for experimental details). After 24 h post-incubation, cell viability was not affected by the lower concentrations (<0.01 $mg \cdot mL^{-1}$) of both MIL-100 and INH@MIL-100 NPs (Figure 12). From 0.02 $mg \cdot mL^{-1}$, the cell viability slightly decreased with increasing NP concentration. Similar results were obtained at 48 h post-treatment. In conclusion, the cytotoxicity study shows the low toxicity of both nanosystems, indicating also that the presence of INH did not negatively affect the cell viability of the A549 cells. The results obtained here are in agreement with previous studies, in which MIL-100 NP did not induce in vitro toxicity in A549 cells (measured as cell survival/death, cell impedance, DNA damage, and ROS generation) [66]. When compared with other common nanocarriers, the viability of our systems is higher than that obtained with, for example, solid lipid NPs (SLN) of glyceryl dibehenate or glyceryl tristearate with/without rifabutin (RFB) [67], as well as with cells were treated with chitosan/tripolyphosphate (CS/TPP) NPs [65]. Finally, after 24 and 48 h post-incubation with Ma, it was confirmed that Ma was totally biocompatible with the cells (100% viability; Figure 12).

A complementary cell viability assay was carried out using Luna II, where the above results were visually corroborated by the automatic counting of live cells. As shown in Figure 13, the viability of the cells incubated with MIL-100 NPs was 90.8 ± 2.6%, while the viability when employing INH@MIL-100 NPs was 80.4 ± 7.4%.

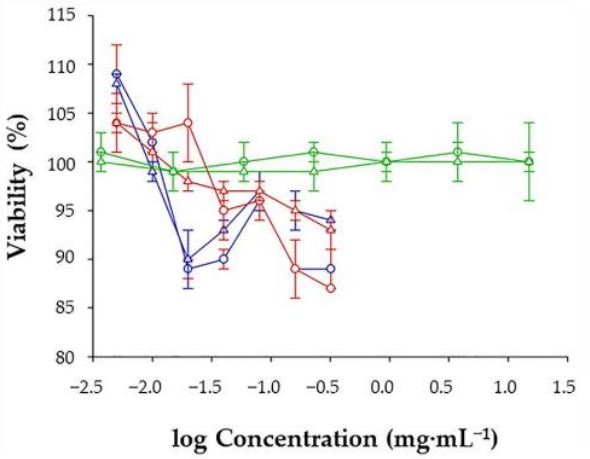

Figure 12. Cell viability assay 24 (circle) and 48 h (triangle) after the removal of MIL-100 (blue), INH@MIL-100 (red), and Ma (green) from A549 cells, measured by the fluorescence of CellTiter-Blue® (mean ± S.D., $n = 4$).

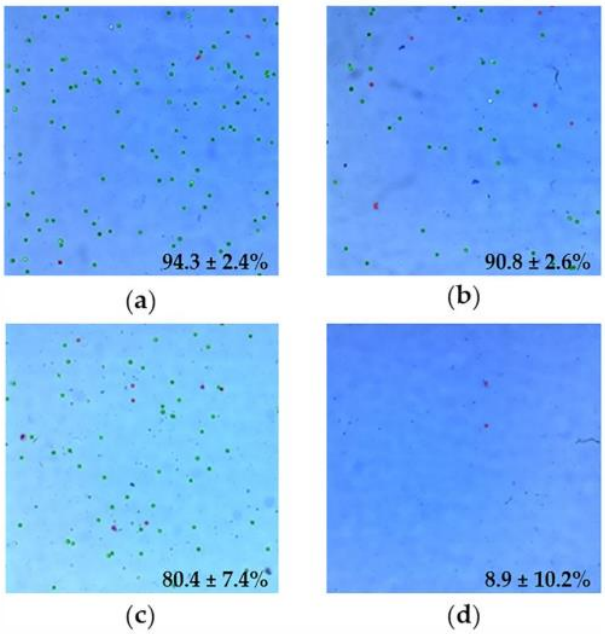

Figure 13. Luna II images of: (**a**) A549 cells (positive control of viability); (**b**) A549 cells treated with MIL-100 NPs; (**c**) A549 cells incubated with INH@MIL-100 NPs; and (**d**) A549 treated with Triton (negative control of viability). Living and dead cells were marked by a green or red circle, respectively. The percentages indicate the amount of living cells in each sample (mean ± S.D., $n = 3$).

2.6. Intracellular Uptake and Distribution

Intracellular uptake of MIL-100 and INH@MIL-100 NPs was evaluated in A549 cells by Fe self-reflection with confocal microscopy. The images of the cells (Figure 14), using 4′,6-diamino-2-phenylindole (DAPI) for nuclear staining, verified the cytoplasmic localization of MIL-100 and INH@MIL-100 NPs. It should be emphasized that the Fe self-reflection signal belonging to MIL-100 NPs (Figure 14d–f) was higher than those of INH@MIL-100 NPs (Figure 14g–i). This fact was due to a possible screening effect produced by the INH. However, the signal gain of INH@MIL-100 NPs was corrected by increasing the (i) dispersion volume of these nanosystems (20, 30, 40, and 50 µL); (ii) laser power; and (iii) number of accumulations per plane (see Figure 14j–l and Supporting Information, Figure S1).

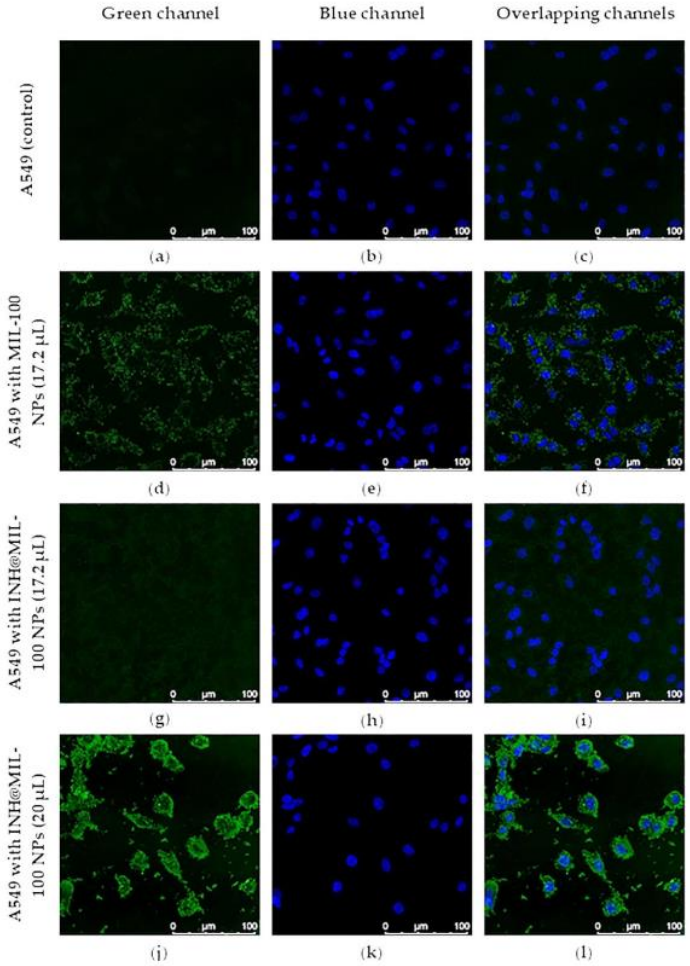

Figure 14. Confocal microscopy images of A549 cells: (**a–c**) without NPs (control); (**d–f**) with MIL-100 NPs (17.2 µL); (**g–i**) with INH@MIL-100 NPs (17.2 µL); and (**j–l**) with INH@MIL-100 NPs (20 µL; Fe self-reflection, green channel). Cell nuclei (DAPI, blue channel). Scale bar = 100 nm.

When the added dispersion volume of INH@MIL-100 NPs was progressively increased (maintaining the concentration at 3.2 mg·mL^{-1}), it was detected that gradually there were more NPs outside the cells and the cells' morphology was affected for volumes higher than 40 µL. However, these elevated volumes were only used to detect the INH@MIL-100 NPs presence inside the cells. If the results obtained from MIL-100 NPs are compared with those from INH@MIL-100 NPs using volumes of 17.2 µL and 20 µL, it could be concluded that in both cases, the nanoMOFs were perfectly internalized within the A549 cells, mainly located in the cytoplasm (Figure 15).

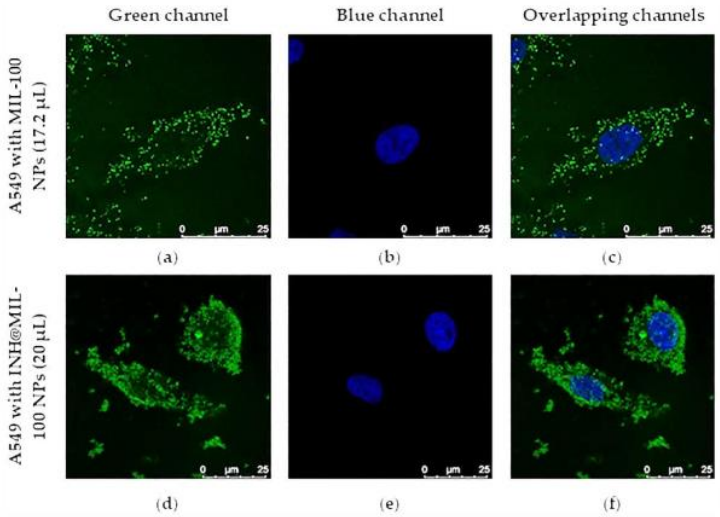

Figure 15. Confocal microscopy images of A549 cells (**a–c**) with MIL-100 NPs (17.2 µL) a d (**d–f**) with INH@MIL-100 NPs (20 µL; Fe self-reflection, green channel). Cell nuclei (DAPI, blue channel). Scale bar = 25 nm.

2.7. Quantification of A549 Cells Internalized with NPs: Flow Cytometry

Once the internalization was visually confirmed, the quantification of that cells that had taken up NPs was carried out by flow cytometry (FCM). The study was based on a complexity analysis comparing over 10,000 events before and after the uptake of NPs. In this case, cells containing INH@MIL-100 NPs were more complex than cells containing MIL-100 NPs and these are more complex than the control (cells without NPs). In Figure 16, the first column of the FCM scatter plots represents the total population of the analyzed events. The second column of the FCM scatter plots, where the debris (apoptotic cells, membrane fragments, etc.) are excluded, corresponds with those events that present positive cellular complexity. The third column of the FCM histograms represents the mean of the fluorescence intensity (MFI) of the Aqua viability reagent to verify the viability of those selected events with positive complexity.

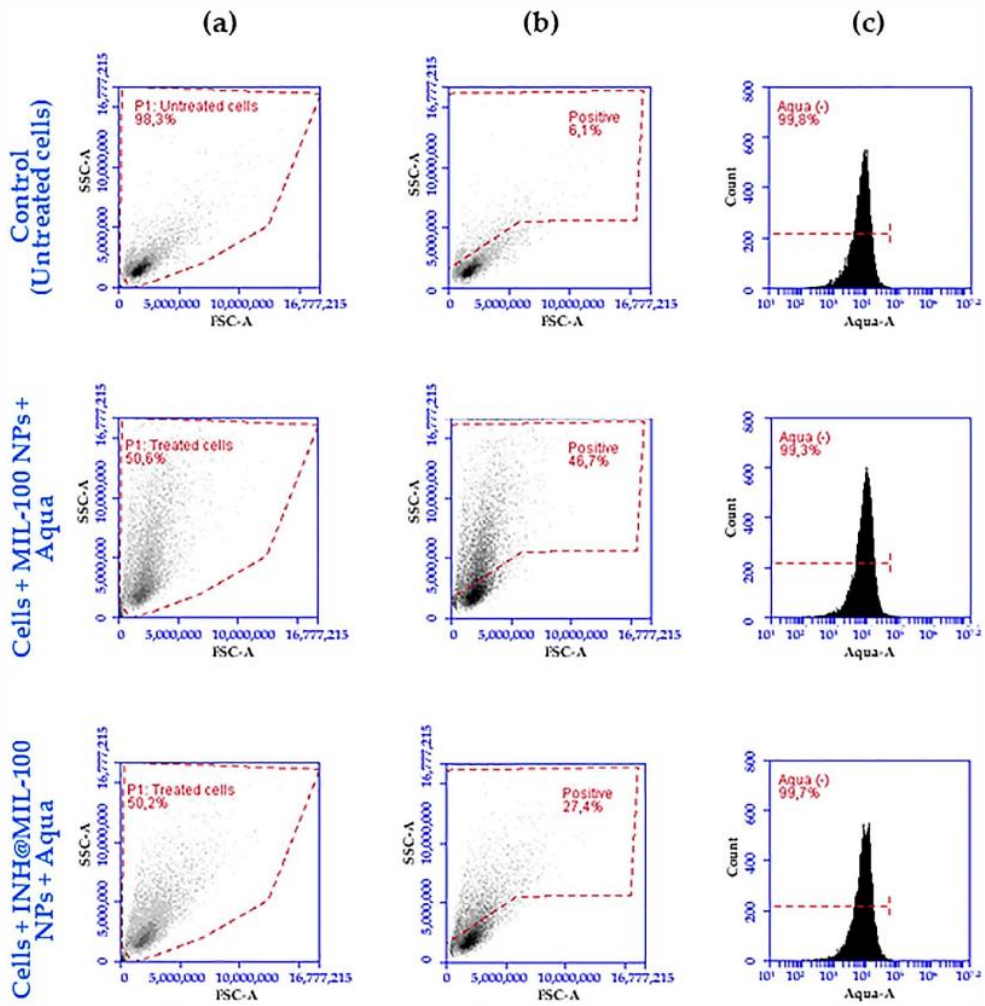

Figure 16. Analysis of the first replicate of MIL-100 and INH@MIL-100 NP-loaded cells by FCM: (**a**) FCM scatter plots of the total event population; (**b**) FCM scatter plots of the selected positive complexity area (the vertical axis is referred to as side scattering (SSC) and the horizontal axis is referred to as forward scattering (FSC)); and (**c**) FCM histograms of the mean fluorescence intensity of the Aqua viability reagent.

For the replicates of control (untreated cells) FCM scatter plots, almost 100% of the total events were analyzed (93.5 ± 4.5%) and compared to those of the cells treated with MIL-100 NPs (68.8 ± 15.9%) and INH@MIL-100 NPs (50.0 ± 3.4%; see Figure 16a and Supporting Information, Figures S2a and S3a). The decrease of this percentage was due to the exposure of A549 cells to the MIL-100 and INH@MIL-100 NPs, leading to a number of events belonging to the debris which had to be excluded for the analysis of the cellular complexity. In the FCM scatter plot, where the area of cellular complexity is determined, the control showed low values of complexity, as expected (7.4 ± 1.3%; see Figure 16b and Supporting Information, Figures S2b and S3b), verifying that the analyzed cells were found without NPs. However, in the FCM scatter plots of the treated A549 cells, they

showed a higher percentage of cellular complexity compared to the control. In the case of treatment with MIL-100 NPs, positive complexity values (43.8 ± 5.0%) were obtained (see Figure 16b and Supporting Information, Figures S2b and S3b). Hence, we could assume that this cell's percentage was positive for the presence of this nanosystem. In the case of cells treated with INH@MIL-100 NPs, positive complexity values (25.5 ± 1.8%) were also obtained but they were lower than those relative to the previous nanosystem (see Figure 16b and Supporting Information, Figures S2b and S3b). Therefore, these cells' percentage was positive for the presence of INH@MIL-100 NPs. Although the detector was not sensitive enough to determine the difference in the complexity between control cells and NP-internalized cells due to the small size of the nanosystems, logical results were obtained. Then, it was thought that these experimental values underestimate NPs' uptake, especially in the case of the INH-loaded nanosystem (probably as a consequence of a drug interference in the analysis method). In fact, a good uptake of both systems was confirmed anteriorly by confocal study, corroborated by Wyszogrodzka-Gaweł's study [45], in which the authors also demonstrated that the INH-loaded Fe-MIL-101-NH_2 were captured in greater quantities compared to the non-loaded NPs.

Finally, it is worth highlighting the lack of cytotoxicity in the all cases, as seen in the FCM histograms (Aqua (−); see Figure 16c and Supporting Information, Figures S2c and S3c). In addition, an important viability of A549 cells was confirmed with both MIL-100 and INH@MIL-100 NPs, as can also be seen in the FCM histograms (99.4 ± 0.2% and 99.6 ± 0.2%, respectively), in comparison with the control (99.7 ± 0.1%; see Figure 16c and Supporting Information, Figures S2c and S3c), which was higher for the INH-loaded NPs than for the non-loaded nanosystems.

3. Materials and Methods

3.1. Materials

Trimesic acid (H_3BTC, 95%, Molecular Weight-MW: 210.14 g·mol^{-1}), iron(III) chloride hexahydrate ($FeCl_3 \cdot 6H_2O$ ≥99%, MW: 162.20 g·mol^{-1}), isoniazid (INH, ≥99%, MW: 137.14 g·mol^{-1}), D-mannitol (Ma, ≥98%, MW: 182.17 g·mol^{-1}), α-cyclodextrin (α-CD, ≥99%, MW: 972.84 g·mol^{-1}), dextran (Dex, ≥99%, MW = 72,200 g·mol^{-1}), D-(+)-mannose (Man, ≥99%, MW: 180.16 g·mol^{-1}), D-(+)-trehalose dihydrate (Tre, ≥99%, MW: 378.33 g·mol^{-1}), D-sorbitol (Sor, ≥98%, MW: 182.17 g·mol^{-1}), D-(−)-fructose (Fru, ≥99%, MW: 180.16 g·mol^{-1}), L-glutamine, sodium dodecyl sulphate (SDS), and phosphate-buffered saline tablet (PBS, pH = 7.4) were acquired from Sigma Aldrich (Madrid, Spain). The A549 cell line was obtained from ATCC (Manassas, VA, USA). Dulbecco's Modified Eagle Medium (DMEM), fetal bovine serum (FBS), trypsin-EDTA (0.05%), and Fluoromount® were purchased to Gibco™ (ThermoFisher Scientific, Madrid, Spain). Potassium fluoride (KF, 99%, MW: 58.09 g·mol^{-1}) was obtained from Acros Organics™ (Madrid, Spain). Triton® X-100 (molecular biology grade) was acquired from Scharlab S.L. Laboratories (Barcelona, Spain). CellTiter-Blue (AlamarBlue®) was obtained from Promega (Fitchburg, MA, USA). The LIVE/DEAD™ Fixable Aqua Dead Cell Stain Kit was acquired from Invitrogen™ (Waltham, MA, USA). 4′,6-diamino-2phenylindole (DAPI) was obtained from Emp-Biotech (Berlin, Germany). Trypan Blue was obtained from Logos Biosystems (Sainghin-en-Mélantois, France). Neutral buffered formalin (10% *v/v*) was purchased from Bio-Optica (Milan, Italy). MilliQ water was obtained by filtration (filters 0.2 µm, Millex®-GN, Millipore Iberica, Madrid, Spain). Ethanol (96%) was purchased from Labkem (Murcia, Spain). Curosurf® (pig lung surfactant, 80 mg·mL^{-1} of pulmonary phospholipids) was facilitated by Professor Almeida (of the University of Lisbon, Portugal) who obtained it from Angelini Pharmacêutica, Lda. (Lisbon, Portugal).

All materials were commercially obtained and used without further purification.

3.2. Synthesis of MIL-100(Fe) and INH Encapsulation

MIL-100(Fe) NPs were synthesized following a previously described protocol [26]. Briefly, 6.0 mmol of $FeCl_3 \cdot 6H_2O$ and 4.0 mmol of H_3BTC were dissolved in 30 mL of

distilled water. The reaction was carried out by the microwave-assisted synthesis Mars-5 instrument, CEM (Midland, ON, Canada), with 130 °C over 30 s; then maintained at this temperature for 5 min and 30 s; and cooled down to room temperature (RT). The obtained NPs were centrifuged at 10,500 rpm for 25 min and then purified with both 20 mL of water (6-fold) and ethanol (1-fold) in a Thermo Scientific Heraeus Megafuge 16R Centrifuge (Loughborough, UK). After, the NPs were stored in ethanol [19].

For the INH encapsulation in MIL-100(Fe) NPs, a 0.15 M INH solution in water was firstly prepared. A MIL-100(Fe) NPs suspension (0.029 mmol dried powder in 500 µL of MilliQ water) was mixed with 0.6 mL of INH solution under stirring for 4 h. The obtained INH@MIL-100 solid was recovered by centrifugation (14,500 rpm for 10 min) and re-suspended in a new solution of INH, repeating the same procedure. The amount of INH incorporated in MIL-100(Fe) NPs was determined by high performance liquid chromatography (HPLC) and thermogravimetric analysis (TGA). The HPLC conditions were as follows: mobile phase was a 98:2 solution (*v*/*v*) of PBS (0.02 M, pH = 6.8) and methanol (MeOH). The volume of injection was set at 30 µL, the flow rate was of 1 mL·min^{-1}, and the column temperature was fixed at 25 °C. The curve of the standard calibration exhibited a good correlation coefficient ($\geq$0.99). The standard solution's chromatogram presented a retention time of 8.77 min, identified as INH (λ_{max} at 266 nm). TGA were performed in an SDT Q-600 thermobalance (TA Instruments, New Castle, DE, USA) using a general heating profile (from 30 to 600 °C), with a heating rate of 5 °C·min^{-1}, under air employing a flux of 100 mL·min^{-1}.

3.3. Preparation of MS

Seven saccharides (Ma, α-CD, Dex, Man, Tre, Sor, and Fru) were chosen as spray-drying excipients. They belong to the World Health Organization (WHO) Model List of Essential Medicines [68] and/or to the Inactive Ingredient Search for Approved Drug Products of the Food and Drug Administration (FDA) [69], and are employed in medical applications, healthcare, and in the food and beverage industry [70]. Solutions of these excipients were spray-dried by a simple technique using a Buchi® Mini Spray Dryer B-290 (Flawil, Switzerland). The total solids content (t.s.c.) was set at 3.7 wt%; the spray-drying conditions were of the inlet temperature (T_{inlet}) 102 and 160 °C; aspirator: 70%; nozzle cleaner: 5 (diameter of 0.7 mm); feed rate: 2 mL·min^{-1}; air flow rate: 400 Nl·h^{-1}; and the resulting outlet temperature (T_{outlet}) was 61–94 °C. The obtained dried powders, consisting of MS, were collected and stored at RT in a desiccator until use.

Once the Ma was selected as the best spray-drying excipient, 190 mg of INH@MIL-100 NPs was dispersed in 55.48 mL (34.1 mg·mL^{-1}) of an Ma aqueous solution, employing an ultrasound tip (Ultrasonic Processor UP400 S—Hielscher 700 W Digital Sonifer, Teltow, Germany, at 10% amplitude and 30 s of time, in addition to two more pulses of 1 s using a water-ice bath) and an ultrasonic bath Branson 1210 (North Hampton, NH, USA) over the course of 15 min. Particle size and ζ-potential were determined by Dynamic Light Scattering (DLS) and Laser Doppler Anemometry (LDA) using a Zetasizer (Nano-ZS Nano-Series, Malvern Instruments, Malvern, UK) fixed at 25 °C. The physicochemical properties of these INH@MIL-100 NPs were examined in triplicates (n = 3). Afterwards, the dispersion was spray-dried by a simple technique using a Buchi® Mini Spray Dryer B-290 (Flawil, Switzerland) to obtain Ma-INH@MIL-100 MS. The employed parameters to obtain the MS were of the 1:10 (*w*/*w*) INH@MIL-100:Ma ratio; t.s.c.: 3.7 wt%; T_{inlet}: 160 ± 2 °C; aspirator: 70%; nozzle cleaner: 5 (diameter of 0.7 mm); feed rate: 2 mL·min^{-1}; air flow rate: 400 Nl·h^{-1} [19]; and the resulting T_{outlet} of 92–94 °C. The powders were collected and stored at RT in a desiccator until use.

The spray-drying process yield (PY) was calculated by employing the following formula:

$$PY\ (\%) = \frac{MS\ weight}{t.s.c.\ weight} \times 100 \quad (1)$$

3.4. Characterization of MS

The morphology of the MS was characterized by Scanning Electron Microscopy (SEM) using an ULTRA PLUS microscope (Zeiss, FESEM Ultra-Plus, Germany) at 3 KV. Samples were located over stubs using a double-sided adhesive graphite disc and coated with a layer of 10 nm of iridium using an Emitechk 550 Sputter Coater (London, UK). This process was also employed to obtain their Feret diameters (spaces between two tangents on opposite sides of a MS), which were obtained by measuring over the MS SEM images using the program z-SmartTiff (n = 50). Then, the geometric diameters were calculated as the averages of the obtained Feret diameters (µm). Apparent densities were calculated after submitting a powder to mechanical tapping with the device Tecnociencia (A Coruña, Spain). For that, a powder sample of known weight was introduced in a test tube of 10 mL into this apparatus, which was previously calibrated at 30 tap·min^{-1}, and was submitted to simultaneous rotating and vertical movement. The volume of the powder was checked every 5 min until it became constant (n = 3). As the process was carried out by triplicates, the average of the three values was used to obtain the apparent densities. To obtain the theoretical aerodynamic diameter, the following formula was used:

$$D_{aer} = D_g \sqrt{\frac{\rho_{real}}{\rho_0 \lambda}} \quad (2)$$

where ρ_0 is 1 g·cm^{-3}, D_g is the geometric diameter (result of the average of the Feret diameters (µm)), ρ_{real} is the real density of the MS (g·cm^{-3}), and λ is the dynamic shape factor of the MS, with its value of 1 in spherical MS or 2 in irregular MS [71–73].

3.5. Study of Composition and Structural Integrity of Ma-INH@MIL-100 MS

Once the INH@MIL-100 NPs were incorporated inside the Ma MS, the Ma-INH@MIL-100 MS were analyzed with respect to their composition and structural integrity. Powder X-ray diffraction (PXRD) patterns of samples were collected in an Empyream Panalytical diffractometer equipped with a PIXcel3D detector and copper radiation source (Cu Kα, λ = 1.5406 Å), operating at 45 kV and 40 mA. Profiles were generally collected in the 3° < 2θ < 35° range with a typical step size of 0.013° and 40 s of acquisition. N_2 sorption isotherms were obtained at 77 K using an AutosorbQ2 (Quantachrome Instruments, Boynton Beach, FL, USA). Before to the measurement, samples were evacuated at 130 °C for 3 h. Specific surface areas were determined by applying Brunauer, Emmett, and Teller equation (BET) in the relative pressure interval of p/p_0 = 0.01–0.3 (wherein p_0 is the saturation pressure). Thermogravimetric analyses (TGA) were carried out in an SDT Q-600 thermobalance (TA Instruments, New Castle, DE, USA), with a general heating profile from 30 to 600 °C and a heating rate of 5 °C·min^{-1} under air, using a flux of 100 mL·min^{-1}. Elemental analyses (EA) were determined using FLASH 2000 (Thermoscientific, Waltham, MA, USA). Inductively coupled plasma atomic emission spectroscopy (ICP-OES) analyses were performed in a Perkin Elmer Optima 7300 DV (Madrid, Spain).

3.6. Ma-INH@MIL-100 MS: Colloidal and Chemical Stability, and INH Release

A quantity of 4 mg of Ma-INH@MIL-100 MS was incubated in 1 mL of different media (MilliQ water, phosphate-buffered solution (PBS, pH = 7.4), and SLF) under bidimensional stirring at 37 °C to examine the physicochemical characteristics of the released INH@MIL-100 NPs (particle size, surface charge, and colloidal stability), as well as the drug release profiles. At different times (0, 1, 2, 4, 8, and 24 h), an aliquot of 50 µL of the released INH@MIL-100 was suspended in 950 µL of its respective medium and their physicochemical properties were characterized. Particle size and ζ-potential were determined by Dynamic Light Scattering (DLS) and Laser Doppler Anemometry (LDA) using a Zetasizer (Nano-ZS Nano-Series, Malvern Instruments, Malvern, UK) fixed at 37 °C. The remaining sample was centrifuged with a Beckman Coulter™ Microfuge® 22R Centrifuge at 14,500 rpm for 10 min (Hyland Scientific, Stanwood, WA, USA). The recovered solid was

measured by XRPD and, in order to quantify the H_3BTC and INH, the supernatant was analyzed by HPLC using a reversed phase HPLC system Jasco LC-4000 series equipped with a PDA detector MD-4015 and a multisampler AS-4150 controlled by ChromNav software (Jasco Inc, Madrid, Spain). A Purple ODS reverse-phase column (5 µm, 4.6 × 150 mm, Análisis Vínicos, Tomelloso, Spain) was employed. For the H_3BTC, the mobile phase used consisted of 50:50 solution (*v/v*) of PBS (0.02 M, pH = 2.5) and MeOH. For the INH, the mobile phase consisted of 98:2 solution (*v/v*) of PBS (0.02 M, pH = 6.8) and MeOH. The injection volume was set at 30 µL (with a flow rate of 1 $mL \cdot min^{-1}$) and the column temperature was fixed at 25 °C. The standard calibration curve showed a good correlation coefficient of ≥0.99. The chromatogram of the standard solutions showed a retention time of 3.51 min (identified as H_3BTC, λ_{max} at 225 nm) and 8.77 min (identified as INH, λ_{max} at 266 nm). The studies were performed in triplicates (n = 3).

The morphological examination of the released INH@MIL-100 NPs was performed by Transmission Electron Microscopy (TEM; Jem-2010 Electron Microscope, Peabody, MA, USA) at 120 KV. For this purpose, an aliquot of 10 µL of the released sample was deposited on a copper grid (with carbon film) and the NPs were stained with 2% (*w/v*) phosphotungstic acid over the course of 2 min.

3.7. A549 Cell Line

A cell line of alveolar adenocarcinoma (human alveolar adenocarcinoma basal epithelial cells, A549) [74] was used as a model to evaluate the toxicity of MIL-100 NPs, INH@MIL-100 NPs, and the Ma excipient (viability study); the intracellular uptake and intracellular distribution of NPs (confocal fluorescence microscopy study (CLSM)); and the quantification of internalized A549 cells (cytometry study). The A549 cells were grown in DMEM supplemented with 200 mM of L-Glutamine (antibiotic) and 10% (*v/v*) FBS. Cells were incubated at 37 °C with a humidified atmosphere of 5% CO_2 and 95% air. The A549 cells were employed between passages 12 and 32.

3.8. Preparation and Characterization of Test Formulations for Cell Studies

MIL-100 and INH@MIL-100 NPs were dispersed in MilliQ water (3.2 $mg \cdot mL^{-1}$) by vortex and an ultrasound tip (Ultrasonic Processor UP400 S–Hielscher 700 W Digital Sonifer, Germany) at 10% amplitude and 30 s of time, in addition to two more pulses of 1 s using a water-ice bath. MIL-100 NPs were previously washed twice with MilliQ water to remove the ethanol, employing a Beckman Coulter™ Microfuge® 22R Centrifuge (Hyland Scientific, Stanwood, WA, USA).

The physicochemical properties of MIL-100 and INH@MIL-100 NPs were characterized. Particle size and ζ-potential were determined by Dynamic Light Scattering (DLS) and Laser Doppler Anemometry (LDA) using a Zetasizer (Nano-ZS Nano-Series, Malvern Instruments, Malvern, UK) fixed at 25 °C. The physicochemical properties were analyzed in triplicates (n = 3).

3.9. Preparation of Test-Ma Solutions for the Viability Study

A Ma solution at 15% (*w/v*) was directly prepared by dissolving the Ma excipient in supplemented DMEM under sterile conditions. Then, a serial dilution to the fourth part was made using supplemented DMEM to test the cell viability at different concentrations of the Ma solution.

3.10. Cell Viability Studies

The viability studies of A549 cells treated with MIL-100 and INH@MIL-100 NPs aqueous dispersions, as well as the Ma solution, were evaluated using CellTiter-Blue® as a viability reagent. Two plates of 96 wells were seeded with 100 µL of A549 cells and DMEM (9000 cells/well), and they were incubated at 37 °C for 48 h, employing a humidified atmosphere of 5% CO_2 and 95% air, to facilitate the growing and development of the cells until they were confluents. The media were replaced with 100 µL of a mixture of: (i) 1:10

(*v*/*v*) MilliQ water:DMEM (positive control); (ii) 1:10 (*v*/*v*) MIL-100:DMEM; (iii) 1:10 (*v*/*v*) INH@MIL-100:DMEM; (iv) 1:10 (*v*/*v*) Triton (1% (*v*/*v*)):DMEM (negative control); and (v) Ma:DMEM. Different concentrations of nanoMOFs (MIL-100 NPs and INH@MIL-100 NPs) and Ma in DMEM were tested (see Table 4).

Table 4. Tested concentrations of nanoMOF suspensions and Ma solutions in DMEM tested in A549 cells.

NanoMOFs (mg·mL^{-1})	Ma (mg·mL^{-1})
0.32	15.00
0.16	3.75
0.08	0.94
0.04	0.23
0.02	0.059
0.01	0.015
0.005	0.0037

After 4 h of incubation at 37 °C, the controls and samples were removed and the cells were washed with PBS (pH = 7.4). Then, 100 µL of fresh DMEM was added to each well. Cells were incubated for 24 and 48 h. Next, 20 µL of CellTiter-Blue® was added to every well in darkness to label cell nuclei and the metabolic capacity of live cells was measured according to the manufacturer's instructions after lysis with 3% (*w*/*v*) SDS. Briefly, lysates were placed into a black 96-well plate and fluorescence was measured in a microplate reader (SYNERGY H1M BioTek®) at 539 nm of excitation wavelength and 620 nm of emission wavelength by Gen5 Software (Image Sofware BioTek®).

Cell viability (percentage) compared with the control cells was calculated as follows:

$$Cell\ viability\ (\%) = \frac{Sample\ fluorescence}{Positive\ control\ fluorescence} \times 100 \quad (3)$$

The study was carried out in quadruplicates (n = 4).

Moreover, a complementary assay to test the cell viability was performed using the Luna II instrument (Luna II™ Automated Cell Counter, Logos Biosystems, Annandale, VA, USA). For this purpose, plates of 24 wells were seeded with 400 µL of A549 cells and DMEM (60,000 cells/well), and then they were incubated at 37 °C for 48 h, employing a humidified atmosphere of 5% CO_2 and 95% air, to facilitate the growth and development of the cells until their confluence. The media were replaced with 400 µL of a mixture of: (i) 1:10 (*v*/*v*) MilliQ water:DMEM (positive control); (ii) 1:23 (*v*/*v*) MIL-100:DMEM; (iii) 1:20 (*v*/*v*) INH@MIL-100:DMEM; and (iv) 1:10 (*v*/*v*) Triton:DMEM (negative control). Originally, both nanoMOF dispersions in MilliQ water presented a concentration of 3.2 mg·mL^{-1} and posteriorly with DMEM presented a concentration of 0.14 and 0.16 mg·mL^{-1}/well for MIL-100 and INH@MIL-100 NPs, respectively. Plates were incubated at 37 °C for 4 h and then cells were washed 3 times with PBS (pH = 7.4, 5 min at RT in rocking-stirring, with a 15° inclination, using VWR Rocking platform shaker 230V, Lutterworth, UK). Cells were detached by 120 µL of trypsin (5 min, 37 °C). To deactivate the trypsin, 280 µL of DMEM was added. Cells were centrifuged at 1477 rpm (Eppendorf 5415R Refrigerated Centrifuge, North Hampton, NH, USA) for 5 min, obtaining a pellet that was resuspended in 500 µL of PBS (pH = 7.4), supplemented with 10% (*v*/*v*) FBS. In total, 10 µL of each sample was mixed by vortex with 10 µL of 0.4% (*w*/*v*) Trypan Blue stain and was observed in a cell count camera to obtain the viability values by automatic image counting. The study was carried out in triplicates (n = 3).

3.11. Intracellular Uptake and Distribution

Plates of 24 wells were seeded with 400 µL of A549 cells in DMEM (60,000 cells/well) using polylysine-treated coverslips. As it was previously indicated, the cells were incubated at 37 °C for 48 h, employing a humidified atmosphere of 5% CO_2 and 95% air, to facilitate

the growth and development of the cells until their confluence. The media were replaced with 400 µL of (i) DMEM (control) and with a mixture of (ii) 1:23 (*v/v*) MIL-100:DMEM and (iii) 1:20 (*v/v*) INH@MIL-100:DMEM. Originally, both nanoMOF dispersions in MilliQ water presented a concentration of 3.2 mg·mL^{-1} and posteriorly with DMEM presented a concentration of 0.14 mg·mL^{-1}/well. In the case of the drug-loaded NPs, to verify their better visualization in confocal microscopy, different volumes of 3.2 mg·mL^{-1} INH@MIL-100 NPs aqueous dispersion (20, 30, 40, and 50 µL) were employed. Cells were incubated at 37 °C for 4 h and then washed 3 times with PBS (pH = 7.4, 5 min at RT in rocking-stirring with a 15° inclination). Cells were fixed by adding 350 µL of 10% (*v/v*) neutral-buffered formalin (15 min at RT in rocking-stirring with a 15° inclination). Then, another 3 washes were carried out as previously described and the nuclei of the cells were labelled with 200 µL of a dilution 1:1000 (*v/v*) of DAPI in PBS (1 mg·mL^{-1}). The excess of DAPI was removed by washing 3 times as previously mentioned. The glass coverslips were placed on glass slides employing Fluoromount® aqueous mounting medium for their visualization by CLSM (confocal microscope Leica TCS SP5 X, Wetzlar, Germany), employing an objective HCX PL APO CS 63.0 x 1.30 GLYC 21 °C UV (at 63X) and a white laser. To visualize the samples, a drop of immersion oil was added (oil immersion lens HCX PL Fluotar).

The visualization of the MIL-100 and INH@MIL-100 NPs was obtained by Fe self-reflection ($\lambda_{Ex/Em:}$ 488/485–490 nm). The green color was manually set for MIL-100 and INH@MIL-100 NPs by employing the LAS AF (Leica Application Suite Advanced Fluorescence) software. To visualize the nuclei of the cells labelled with DAPI, the software was employed on other channels ($\lambda_{Ex/Em:}$ 405/414–440 nm) and the color blue was fixed. Therefore, both two signals were collected using separate channels. The conditions tested by confocal microscopy are summarized in Table 5.

Table 5. Conditions employed in the study of the intracellular uptake and distribution of MIL-100 NPs and INH@MIL-100 NPs (3.2 mg·mL^{-1} in MilliQ water) in A549 cells.

Sample	Volume of NP Dispersions (µL)	Number of Accumulations Per Plane
Without NPs	-	2
MIL-100	17.2	2
INH@MIL-100	17.2	2
INH@MIL-100	20.0	16
INH@MIL-100	30.0	16
INH@MIL-100	40.0	16
INH@MIL-100	50.0	16

3.12. Quantification of A549 Cells Internalized with NPs: Flow Cytometry

To quantify the A549 cells internalized with nanoMOFs, a study based on flow cytometry (FCM) was carried out. Plates of 24 wells were seeded with 400 µL of A549 cells and DMEM (60,000 cells/well). As it was previously indicated, the cells were incubated at 37 °C for 48 h, employing a humidified atmosphere of 5% CO_2 and 95% air, to facilitate the growing and development of the cells until they were confluents. The media were replaced with 400 µL of (i) DMEM (control) and a mixture of (ii) 1:23 (*v/v*) MIL-100:DMEM and (iii) 1:20 (*v/v*) INH@MIL-100:DMEM. Originally, both nanoMOF dispersions in MilliQ water presented a concentration of 3.2 mg·mL^{-1} and posteriorly with DMEM presented a concentration of 0.14 and 0.16 mg·mL^{-1}/well for MIL-100 and INH@MIL-100 NPs, respectively. Cells were incubated at 37 °C for 4 h and then washed 3 times with PBS (pH = 7.4, 5 min at RT in rocking-stirring with a 15° inclination). Then, except for the control, cells were treated with 200 µL of the LIVE/DEAD™ Fixable Aqua Dead Cell Stain Kit diluted in PBS (1 µL of Aqua in 2 mL of PBS (*v/v*); 15 min at RT in rocking-stirring with a 15° inclination). The A549 cells were washed with PBS as mentioned previously and then were detached by 120 µL of trypsin (5 min, 37 °C). To deactivate the trypsin, 280 µL of DMEM was added. Cells were centrifuged at 1477 rpm (Eppendorf 5415R Refrigerated Centrifuge, North Hampton, NH, USA) for 5 min, obtaining a pellet that was resuspended in 500 µL of

PBS (pH = 7.4), supplemented with 10% (*v*/*v*) FBS. Finally, a total of approximately 10,000 events were automatically counted by employing a cytometer model Accuri Becton Dickinson (BD Accuri™, Ann Arbor, MI, USA) and were analyzed by BD sample software (BD Biosciences, San Jose, CA, USA). The quantification of cells internalized with MIL-100 and INH@MIL-100 NPs was performed by complexity, with the detector side scatter employed (SSC-A). In addition, to verify the viability of the internalized cells, the filter BP 515/20 (Waltham, MA, USA) for the Aqua viability reagent was used. The study was carried out in triplicates (n = 3).

4. Conclusions

In this work, the first line anti-TB drug INH was efficiently loaded in highly porous and biocompatible MIL-100 NPs, and was further effectively microencapsulated in Ma MS by a simple spray-drying technique, with the aim of producing a suitable pulmonary formulation and to offer a better vehicle to improve the traditional anti-TB treatment. The MS obtained in the form of dry powders present suitable characteristics for deep lung delivery, such as regarding their morphology and aerodynamic properties. Additionally, Ma-INH@MIL-100 MS are able to carry high-drug loadings, as well as can release the NPs and INH in different aqueous media. MIL-100 NPs, INH@MIL-100 NPs, and Ma demonstrated, by in vitro studies, low toxicity for the human alveolar adenocarcinoma basal epithelial cells (A549) and were efficiently internalized by them, with the main location in the cytoplasmic zone. These systems, due to their biosafety and adapted pulmonary formulation, are promising candidates for the local pulmonary treatment of infectious diseases and thus they interesting for TB.

Supplementary Materials: The following materials are available online. Figure S1: Confocal microscopy images of A549 cells: (**a–c**) with INH@MIL-100 NPs (30 µL); (**d–f**) with INH@MIL-100 NPs (40 µL); (**g–i**) with INH@MIL-100 NPs (50 µL) (Fe self-reflection, green channel). Cell nuclei (DAPI, blue channel). Scale bar = 100 nm. Figure S2: Analysis of the second replicate of MIL-100 and INH@MIL-100 NPs-loaded cells by FCM: (**A**) FCM scatter plots of total event population; (**B**) FCM scatter plots of the selected positive complexity area (the vertical axis is referred to as side scattering (SSC) and the horizontal axis is referred to as forward scattering (FSC)); (**C**) FCM histograms of the mean fluorescence intensity of the Aqua viability reagent. Figure S3: Analysis of the third replicate of MIL-100 and INH@MIL-100 NPs-loaded cells by FCM: (**A**) FCM scatter plots of total event population; (**B**) FCM scatter plots of the selected positive complexity area (the vertical axis is referred to as side scattering (SSC) and the horizontal axis is referred to as forward scattering (FSC)); (**C**) FCM histograms of the mean fluorescence intensity of the Aqua viability reagent.

Author Contributions: Conceptualization, C.F.-P., N.C., P.H. and C.R.-L.; methodology, C.F.-P., E.F.-P., P.S.-A., S.R., S.B.-E., N.C., P.H. and C.R.-L.; software, C.F.-P., E.F.-P. and S.B.-E.; validation, C.F.-P., E.F.-P., P.S.-A. and S.R.; formal analysis, C.F.-P. and E.F.-P.; investigation, C.F.-P., P.S.-A. and S.R.; resources, C.F.-P., N.C., P.H. and C.R.-L.; data curation, C.F.-P.; writing—original draft preparation, C.F.-P.; writing—review and editing, E.F.-P., P.S.-A., S.R., S.B.-E., N.C., P.H. and C.R.-L.; visualization, C.F.-P., E.F.-P., S.B.-E. and C.R.-L.; supervision, C.R.-L.; project administration, C.R.-L.; funding acquisition, N.C., P.H. and C.R.-L. All authors have read and agreed to the published version of the manuscript.

Funding: This research publication is part of the I+D+I Grant PID2019-107500RB-I00, funded by MCIN/AEI/10.13039/501100011033; by Instituto de Salud Carlos III of Spain (Strategic Health Action, Grants FIS PS09/00816 and FIS PSI14/00059); by Xunta de Galicia (Competitive Reference Groups, ED431C 2021/17-FEDER); by Regional Madrid funding (Talento 2017 Modality 2, 2017-T2/IND-5149); by the Multifunctional Metallodrugs in Diagnosis and Therapy Network (MICIU, RED2018-102471-T); and by the H + MOF Ramón Areces project and the Spanish Ramón y Cajal Programme (grant agreement 2014-16823). The publication was financed with the first prize received by C.F.-P. for the Best Collaborative Poster Contribution at the International Conference on Aerogels for Biomedical and Environmental Applications (Santiago de Compostela, Spain; February 2020).

Institutional Review Board Statement: Not applicable.

Informed Consent Statement: Not applicable.

Data Availability Statement: Data did not present in this study are available in supplementary material.

Acknowledgments: The authors are very grateful to Raquel Antón Segurado (for the preparation of SEM microphotographs), María José Pazos Guldrís (for the realization of TEM microphotographs), Lucía Alvariño Sanjurjo (for her technical assistance in the cell studies), and Montserrat García Lavandeira (for the preparation of CLSM microphotographs).

Conflicts of Interest: The authors declare no conflict of interest.

Sample Availability: Not available.

References

1. Smulan, L.J.; Martinez, N.; Kiritsy, M.C.; Kativhu, C.; Cavallo, K.; Sassetti, C.M.; Singhal, A.; Remold, H.G.; Kornfeld, H. Sirtuin 3 downregulation in mycobacterium tuberculosis-infected macrophages reprograms mitochondrial metabolism and promotes cell death. *mBio* **2021**, *12*, e03140-20. [CrossRef] [PubMed]
2. Mello, F.C.D.Q.; Silva, D.R.; Dalcolmo, M.P. Tuberculosis: Where are we? *J. Bras. Pneumol.* **2018**, *44*, 82. [CrossRef] [PubMed]
3. World Health Organization. Tuberculosis. Available online: https://www.who.int/health-topics/tuberculosis#tab=tab_1 (accessed on 4 September 2021).
4. World Health Organization. WHO Coronavirus (COVID-19) Dashboard. Available online: https://covid19.who.int/ (accessed on 4 September 2021).
5. Fogel, N. Tuberculosis: A disease without boundaries. *Tuberculosis* **2015**, *95*, 527–531. [CrossRef]
6. Vishwa, B.; Moin, A.; Gowda, D.V.; Rizvi, S.M.D.; Hegazy, W.A.H.; Abu Lila, A.S.; Khafagy, E.-S.; Allam, A.N. Pulmonary targeting of inhalable moxifloxacin microspheres for effective management of tuberculosis. *Pharmaceutics* **2021**, *13*, 79. [CrossRef] [PubMed]
7. World Health Organization. Guidelines for treatment of tuberculosis. Available online: https://www.who.int/tb/publications/2010/9789241547833/en/ (accessed on 4 September 2021).
8. World Health Organization. *Global Tuberculosis Report*; World Health Organization: Geneva, Switzerland, 2020. Available online: https://apps.who.int/iris/bitstream/handle/10665/336069/9789240013131-eng.pdf (accessed on 4 September 2021).
9. Lee, S.L.; Adams, W.P.; Li, B.V.; Conner, D.P.; Chowdhury, B.A.; Yu, L.X. In vitro considerations to support bioequivalence of locally acting drugs in dry powder inhalers for lung diseases. *AAPS J.* **2009**, *11*, 414–423. [CrossRef]
10. Miranda, M.; Rodrigues, M.; Domingues, R.; Torrado, E.; Reis, R.L.; Pedrosa, J.; Gomes, M.E. Exploring inhalable polymeric dry powders for anti-tuberculosis drug delivery. *Mater. Sci. Eng. C* **2018**, *93*, 1090–1103. [CrossRef]
11. Grenha, A.; Carrión-Recio, D.; Teijeiro-Osorio, D.; Seijo, B.; Remuñán-López, C. Nano and micro-particulate carriers for pulmonary drug delivery. In *Handbook of Particulate Drug Delivery*, 1st ed.; Kumar, M.N.V., Ed.; American Scientific Publishers: Valencia, CA, USA, 2008; Volume 2, pp. 165–192.
12. Brain, J.D. Inhalation, deposition, and fate of insulin and other therapeutic proteins. *Diabetes Technol. Ther.* **2007**, *9*, S4–S15. [CrossRef]
13. Ogienko, A.; Bogdanova, E.; Trofimov, N.; Myz, S.; Kolesov, B.; Yunoshev, A.; Zubikov, N.; Manakov, A.; Boldyrev, V.; Boldyreva, E. Large porous particles for respiratory drug delivery. Glycine-based formulations. *Eur. J. Pharm. Sci.* **2017**, *110*, 148–156. [CrossRef] [PubMed]
14. Sharma, R.; Saxena, D.; Dwivedi, A.K.; Misra, A. Inhalable microparticles containing drug combinations to target alveolar macrophages for treatment of pulmonary tuberculosis. *Pharm. Res.* **2001**, *18*, 1405–1410. [CrossRef]
15. D'Angelo, I.; Perfetto, B.; Costabile, G.; Ambrosini, V.; Caputo, P.; Miro, A.; Bianca, R.D.D.V.; Sorrentino, R.; Donnarumma, G.; Quaglia, F.; et al. Large porous particles for sustained release of a decoy oligonucelotide and poly(ethylenimine): Potential for combined therapy of chronic pseudomonas aeruginosa lung infections. *Biomacromolecules* **2016**, *17*, 1561–1571. [CrossRef]
16. Muttil, P.; Kaur, J.; Kumar, K.; Yadav, A.; Sharma, R.; Misra, A. Inhalable microparticles containing large payload of anti-tuberculosis drugs. *Eur. J. Pharm. Sci.* **2007**, *32*, 140–150. [CrossRef] [PubMed]
17. Parikh, R.; Patel, L.; Dalwadi, S. Microparticles of rifampicin: Comparison of pulmonary route with oral route for drug uptake by alveolar macrophages, phagocytosis activity and toxicity study in albino rats. *Drug Deliv.* **2013**, *21*, 406–411. [CrossRef]
18. Mohamed, A.; Kunda, N.K.; Ross, K.; Hutcheon, G.A.; Saleem, I.Y. Polymeric nanoparticles for the delivery of miRNA to treat Chronic Obstructive Pulmonary Disease (COPD). *Eur. J. Pharm. Biopharm.* **2019**, *136*, 1–8. [CrossRef] [PubMed]
19. Fernández, P.S.; Rojas, S.; Salcedo-Abraira, P.; Simón-Yarza, T.; Remuñán-López, C.; Horcajada, P. Metal-organic framework microsphere formulation for pulmonary administration. *ACS Appl. Mater. Interfaces* **2020**, *12*, 25676–25682. [CrossRef] [PubMed]
20. Fernández-Paz, E.; Feijoo-Siota, L.; Gaspar, M.M.; Csaba, N.; Remuñán-López, C. Microencapsulated chitosan-based nanocapsules: A new platform for pulmonary gene delivery. *Pharmaceutics* **2021**, *13*, 1377. [CrossRef]
21. Shah, K.; Chan, L.W.; Wong, T.W. Critical physicochemical and biological attributes of nanoemulsions for pulmonary delivery of rifampicin by nebulization technique in tuberculosis treatment. *Drug Deliv.* **2017**, *24*, 1631–1647. [CrossRef] [PubMed]

22. Haque, S.; Feeney, O.; Meeusen, E.; Boyd, B.J.; McIntosh, M.P.; Pouton, C.W.; Whittaker, M.; Kaminskas, L.M. Local inflammation alters the lung disposition of a drug loaded pegylated liposome after pulmonary dosing to rats. *J. Control. Release* **2019**, *307*, 32–43. [CrossRef]
23. Grotz, E.; Tateosian, N.L.; Salgueiro, J.; Bernabeu, E.; Gonzalez, L.; Manca, M.L.; Amiano, N.; Valenti, D.; Manconi, M.; García, V.; et al. Pulmonary delivery of rifampicin-loaded soluplus micelles against Mycobacterium tuberculosis. *J. Drug Deliv. Sci. Technol.* **2019**, *53*, 101170. [CrossRef]
24. Baati, T.; Njim, L.; Neffati, F.; Kerkeni, A.; Bouttemi, M.; Gref, R.; Najjar, M.F.; Zakhama, A.; Couvreur, P.; Serre, C.; et al. In depth analysis of the in vivo toxicity of nanoparticles of porous iron(III) metal-organic frameworks. *Chem. Sci.* **2013**, *4*, 1597–1607. [CrossRef]
25. Nabi, B.; Rehman, S.; Aggarwal, S.; Baboota, S.; Ali, J. Nano-based anti-tubercular drug delivery: An emerging paradigm for improved therapeutic intervention. *Drug Deliv. Transl. Res.* **2020**, *10*, 1111–1121. [CrossRef] [PubMed]
26. García-Márquez, A.; Demessence, A.; Platero-Prats, A.E.; Heurtaux, D.; Horcajada, P.; Serre, C.; Chang, J.-S.; Férey, G.; de la Peña-O'Shea, V.A.; Boissière, C.; et al. Green microwave synthesis of MIL-100(Al, Cr, Fe) nanoparticles for thin-film elaboration. *Eur. J. Inorg. Chem.* **2012**, *100*, 5165–5174. [CrossRef]
27. Horcajada, P.; Chalati, T.; Serre, C.; Gillet, B.; Sebrie, C.; Baati, T.; Eubank, J.F.; Heurtaux, D.; Clayette, P.; Kreuz, C.; et al. Porous metal-organic-framework nanoscale carriers as a potential platform for drug delivery and imaging. *Nat. Mater.* **2010**, *9*, 172–178. [CrossRef]
28. Bosquillon, C.; Lombry, C.; Préat, V.; Vanbever, R. Influence of formulation excipients and physical characteristics of inhalation dry powders on their aerosolization performance. *J. Control. Release* **2001**, *70*, 329–339. [CrossRef]
29. Weers, J.; Tarara, T. The PulmoSphere ™ platform for pulmonary drug delivery. *Ther. Deliv.* **2014**, *5*, 277–295. [CrossRef]
30. Gharse, S.; Fiegel, J. Large porous hollow particles: Lightweight champions of pulmonary drug delivery. *Curr. Pharm. Des.* **2016**, *22*, 2463–2469. [CrossRef]
31. Bi, R.; Shao, W.; Wang, Q.; Zhang, N. Solid lipid nanoparticles as insulin inhalation carriers for enhanced pulmonary delivery. *J. Biomed. Nanotechnol.* **2009**, *5*, 84–92. [CrossRef] [PubMed]
32. Al-Qadi, S.; Grenha, A.; Remuñán-López, C. Microspheres loaded with polysaccharide nanoparticles for pulmonary delivery: Preparation, structure and surface analysis. *Carbohydr. Polym.* **2011**, *86*, 25–34. [CrossRef]
33. Das, S.; Tucker, I.; Stewart, P. Inhaled dry powder formulations for treating tuberculosis. *Curr. Drug Deliv.* **2015**, *12*, 26–39. [CrossRef]
34. Malafaya, P.B.; Silva, G.A.; Reis, R.L. Natural-origin polymers as carriers and scaffolds for biomolecules and cell delivery in tissue engineering applications. *Adv. Drug Deliv. Rev.* **2007**, *59*, 207–233. [CrossRef] [PubMed]
35. Peltonen, L.; Valo, H.; Kolakovic, R.; Laaksonen, T.; Hirvonen, J. Electrospraying, spray drying and related techniques for production and formulation of drug nanoparticles. *Expert Opin. Drug Deliv.* **2010**, *7*, 705–719. [CrossRef]
36. Sham, J.O.-H.; Zhang, Y.; Finlay, W.H.; Roa, W.H.; Löbenberg, R. Formulation and characterization of spray-dried powders containing nanoparticles for aerosol delivery to the lung. *Int. J. Pharm.* **2004**, *269*, 457–467. [CrossRef] [PubMed]
37. Azarmi, S.; Tao, X.; Chen, H.; Wang, Z.; Finlay, W.H.; Löbenberg, R.; Roa, W.H. Formulation and cytotoxicity of doxorubicin nanoparticles carried by dry powder aerosol particles. *Int. J. Pharm.* **2006**, *319*, 155–161. [CrossRef]
38. Guterres, S.S.; Beck, R.C.R.; Pohlmann, A.R. Spray-drying technique to prepare innovative nanoparticulated formulations for drug administration: A brief overview. *Braz. J. Physics* **2009**, *39*, 205–209. [CrossRef]
39. Pilcer, G.; Amighi, K. Formulation strategy and use of excipients in pulmonary drug delivery. *Int. J. Pharm.* **2010**, *392*, 1–19. [CrossRef]
40. Chow, A.H.; Tong, H.H.; Chattopadhyay, P.; Shekunov, B.Y. Particle engineering for pulmonary drug delivery. *Pharm. Res.* **2007**, *24*, 411–437. [CrossRef] [PubMed]
41. Ali, M.K.; Kim, R.Y.; Brown, A.C.; Donovan, C.; Vanka, K.S.; Mayall, J.R.; Liu, G.; Pillar, A.L.; Bernadette, J.-F.; Xenaki, D.; et al. Critical role for iron accumulation in the pathogenesis of fibrotic lung disease. *J. Pathol.* **2020**, *251*, 49–62. [CrossRef]
42. Allden, S.J.; Ogger, P.P.; Ghai, P.; McErlean, P.; Hewitt, R.; Toshner, R.; Walker, S.A.; Saunders, P.; Kingston, S.; Molyneaux, P.L.; et al. The transferrin receptor CD71 delineates functionally distinct airway macrophage subsets during idiopathic pulmonary fibrosis. *Am. J. Respir. Crit. Care Med.* **2019**, *200*, 209–219. [CrossRef]
43. Pietrangelo, A.; Gualdi, R.; Casalgrandi, G.; Montosi, G.; Ventura, E. Molecular and cellular aspects of iron-induced hepatic cirrhosis in rodents. *J. Clin. Invest.* **1995**, *95*, 1824–1831. [CrossRef]
44. Tuderman, L.; Myllyla, R.; Kivirikko, K.I. Mechanism of the prolyl hydroxylase reaction 1. Role of co-substrates. *JBIC Eur. J. Biochem.* **1977**, *80*, 341–348. [CrossRef]
45. Wyszogrodzka-Gaweł, G.; Dorożyński, P.; Giovagnoli, S.; Strzempek, W.; Pesta, E.; Węglarz, W.P.; Gil, B.; Menaszek, E.; Kulinowski, P. An inhalable theranostic system for local tuberculosis treatment containing an isoniazid loaded metal organic framework Fe-MIL-101-NH2-from raw MOF to drug delivery system. *Pharmaceutics* **2019**, *11*, 687. [CrossRef]
46. Singco, B.; Liu, L.-H.; Chen, Y.-T.; Shih, Y.-H.; Huang, H.-Y.; Lin, C.-H. Approaches to drug delivery: Confinement of aspirin in MIL-100(Fe) and aspirin in the de novo synthesis of metal-organic frameworks. *Microporous Mesoporous Mater.* **2016**, *223*, 254–260. [CrossRef]

47. Rojas, S.; Colinet, I.; Cunha, D.; Hidalgo, T.; Salles, F.; Serre, C.; Guillou, N.; Horcajada, P. Toward understanding drug incorporation and delivery from biocompatible metal-organic frameworks in view of cutaneous administration. *ACS Omega* **2018**, *3*, 2994–3003. [CrossRef]
48. Horcajada, P.; Serre, C.; Vallet-Regi, M.; Sebban, M.; Taulelle, F.; Ferey, G. Metal-organic frameworks as efficient materials for drug delivery. *Angew. Chem.* **2006**, *45*, 5974–5978. [CrossRef]
49. Gunasekaran, S.; Sailatha, E.; Seshadri, S.; Kumaresan, S. FTIR, FT Raman spectra and molecular structural confirmation of isoniazid. *Indian J. Pure Appl. Phys.* **2009**, *47*, 12–18.
50. Leclerc, H.; Vimont, A.; Lavalley, J.-C.; Daturi, M.; Wiersum, A.D.; Llwellyn, P.L.; Horcajada, P.; Ferey, G.; Serre, C. Infrared study of the influence of reducible iron(iii) metal sites on the adsorption of CO, CO_2, propane, propene and propyne in the mesoporous metal-organic framework MIL-100. *Phys. Chem. Chem. Phys.* **2011**, *13*, 11748–11756. [CrossRef]
51. Grenha, A.; Seijo, B.; Serra, C.; Remuñán-López, C. Chitosan nanoparticle-loaded mannitol microspheres: Structure and surface characterization. *Biomacromolecules* **2007**, *8*, 2072–2079. [CrossRef] [PubMed]
52. Alves, A.D.; Cavaco, J.S.; Guerreiro, F.; Lourenço, J.P.; da Costa, A.M.R.; Grenha, A. Inhalable antitubercular therapy mediated by locust bean gum microparticles. *Molecules* **2016**, *21*, 702. [CrossRef]
53. Jensen, D.M.K.; Cun, D.; Maltesen, M.J.; Frokjaer, S.; Nielsen, H.M.; Foged, C. Spray drying of siRNA-containing PLGA nanoparticles intended for inhalation. *J. Control. Release* **2010**, *142*, 138–145. [CrossRef]
54. Ohrem, H.L.; Schornick, E.; Kalivoda, A.; Ognibene, R. Why is mannitol becoming more and more popular as a pharmaceutical excipient in solid dosage forms? *Pharm. Dev. Technol.* **2014**, *19*, 257–262. [CrossRef]
55. Maas, S.G.; Schaldach, G.; Littringer, E.M.; Mescher, A.; Griesser, U.J.; Braun, D.E.; Walzel, P.E.; Urbanetz, N.A. The impact of spray drying outlet temperature on the particle morphology of mannitol. *Powder Technol.* **2011**, *213*, 27–35. [CrossRef]
56. Grenha, A.; Seijo, B.; Remuñán-López, C. Microencapsulated chitosan nanoparticles for lung protein delivery. *Eur. J. Pharm. Sci.* **2005**, *25*, 427–437. [CrossRef]
57. Daviskas, E.; Anderson, S.D.; Eberl, S.; Young, I.H. Beneficial effect of inhaled mannitol and cough in asthmatics with mucociliary dysfunction. *Respir. Med.* **2010**, *104*, 1645–1653. [CrossRef]
58. Elversson, J.; Millqvist-Fureby, A. In situ coating—An approach for particle modification and encapsulation of proteins during spray-drying. *Int. J. Pharm.* **2006**, *323*, 52–63. [CrossRef]
59. Gaspar, D.P.; Gaspar, M.M.; Eleutério, C.V.; Grenha, A.; Blanco, M.; Gonçalves, L.M.D.; Taboada, P.; Almeida, A.J.; Remuñán-López, C. Microencapsulated solid lipid nanoparticles as a hybrid platform for pulmonary antibiotic delivery. *Mol. Pharm.* **2017**, *14*, 2977–2990. [CrossRef] [PubMed]
60. Bailey, M.M.; Gorman, E.M.; Munson, E.J.; Berkland, C. Pure insulin nanoparticle agglomerates for pulmonary delivery. *Langmuir* **2008**, *24*, 13614–13620. [CrossRef]
61. Sinsuebpol, C.; Chatchawalsaisin, J.; Kulvanich, P. Preparation and in vivo absorption evaluation of spray dried powders containing salmon calcitonin loaded chitosan nanoparticles for pulmonary delivery. *Drug Design Dev. Ther.* **2013**, *7*, 861–873. [CrossRef]
62. Al-Qadi, S.; Grenha, A.; Carrión-Recio, D.; Seijo, B.; Remuñán-López, C. Microencapsulated chitosan nanoparticles for pulmonary protein delivery: In vivo evaluation of insulin-loaded formulations. *J. Control. Release* **2012**, *157*, 383–390. [CrossRef] [PubMed]
63. Tewa-Tagne, P.; Briançon, S.; Fessi, H. Preparation of redispersible dry nanocapsules by means of spray-drying: Development and characterization. *Eur. J. Pharm. Sci.* **2007**, *30*, 124–135. [CrossRef]
64. Elsabahy, M.; Wooley, K.L. Design of polymeric nanoparticles for biomedical delivery applications. *Chem. Soc. Rev.* **2012**, *41*, 2545–2561. [CrossRef]
65. Grenha, A.; Grainger, C.I.; Dailey, L.A.; Seijo, B.; Martin, G.P.; Remuñán-López, C.; Forbes, B. Chitosan nanoparticles are compatible with respiratory epithelial cells in vitro. *Eur. J. Pharm. Sci.* **2007**, *31*, 73–84. [CrossRef]
66. Grall, R.; Hidalgo, T.; Delic, J.; Garcia-Marquez, A.; Chevillard, S.; Horcajada, P. In vitro biocompatibility of mesoporous metal (III; Fe, Al, Cr) trimesate MOF nanocarriers. *J. Mater. Chem. B* **2015**, *3*, 8279–8292. [CrossRef]
67. Gaspar, D.P.; Faria, V.; Gonçalves, L.M.D.; Taboada, P.; Remuñán-López, C.; Almeida, A.J. Rifabutin-loaded solid lipid nanoparticles for inhaled antitubercular therapy: Physicochemical and in vitro studies. *Int. J. Pharm.* **2016**, *497*, 199–209. [CrossRef] [PubMed]
68. World Health Organization. WHO Model Lists of Essential Medicines. Available online: https://www.who.int/medicines/publications/essentialmedicines/en/ (accessed on 4 September 2021).
69. U.S. Food & Drug Administration. Inactive Ingredient Search for Approved Drug Products. Available online: https://www.accessdata.fda.gov/scripts/cder/iig/index.cfm (accessed on 4 September 2021).
70. Porru, D.; Parmigiani, A.; Tinelli, C.; Barletta, D.; Choussos, D.; di Franco, C.; Rovereto, B. Oral D-mannose in recurrent urinary tract infections in women: A pilot study. *J. Clin. Urol.* **2014**, *7*, 208–213. [CrossRef]
71. Palazzo, F.; Giovagnoli, S.; Schoubben, A.; Blasi, P.; Rossi, C.; Ricci, M. Development of a spray-drying method for the formulation of respirable microparticles containing ofloxacin-palladium complex. *Int. J. Pharm.* **2013**, *440*, 273–282. [CrossRef] [PubMed]
72. Gupta, A.; Pant, G.; Mitra, K.; Madan, J.; Chourasia, M.K.; Misra, A. Inhalable particles containing rapamycin for induction of autophagy in macrophages infected with Mycobacterium tuberculosis. *Mol. Pharm.* **2014**, *11*, 1201–1207. [CrossRef] [PubMed]

73. Bosquillon, C.; Préat, V.; Vanbever, R. Pulmonary delivery of growth hormone using dry powders and visualization of its local fate in rats. *J. Control. Release* **2004**, *96*, 233–244. [CrossRef]
74. Rodrigues, S.; Cordeiro, C.; Seijo, B.; Remuñán-López, C.; Grenha, A. Hybrid nanosystems based on natural polymers as protein carriers for respiratory delivery: Stability and toxicological evaluation. *Carbohydr. Polym.* **2015**, *123*, 369–380. [CrossRef]

ANNEX III

Dry powders containing chitosan-based nanocapsules for pulmonary administration: Adjustment of spray-drying process and *in vitro* evaluation in A549 cells

Estefanía Fernández-Paz, Cristina Fernández-Paz, **Sheila Barrios-Esteban**, Irene Santalices, Noemi Csaba, Carmen Remuñán-López.

DRY POWDERS CONTAINING CHITOSAN-BASED NANOCAPSULES FOR PULMONARY ADMINISTRATION: ADJUSTMENT OF SPRAY-DRYING PROCESS AND *IN VITRO* EVALUATION IN A549 CELLS

Estefanía Fernández-Paz[a], Cristina Fernández-Paz[a], **Sheila Barrios-Esteban**[b], Irene Santalices[a,b], Noemi Csaba[b], Carmen Remuñán-López[a*].

[a]Nanobiofar Group, Department of Pharmacology, Pharmacy & Pharmaceutical Technology, Faculty of Pharmacy, University of Santiago de Compostela, Campus Vida, 15782, Santiago de Compostela, Spain.

[b]Center of Research in Molecular Medicine and Chronic Diseases (CiMUS), University of Santiago de Compostela, Campus Vida, 15706, Santiago de Compostela, Spain.

Powder Technology 2022, 399 (2022), 117149, 1-19.

DOI: https://doi.org/10.1016/j.powtec.2022.117149

Powder Technology 399 (2022) 117149

Contents lists available at ScienceDirect

Powder Technology

journal homepage: www.elsevier.com/locate/powtec

Dry powders containing chitosan-based nanocapsules for pulmonary administration: Adjustment of spray-drying process and *in vitro* evaluation in A549 cells

Estefanía Fernández-Paz [a], Cristina Fernández-Paz [a], Sheila Barrios-Esteban [b], Irene Santalices [a,b], Noemi Csaba [b], Carmen Remuñán-López [a,*]

[a] Nanobiofar Group, Department of Pharmacology, Pharmacy & Pharmaceutical Technology, Faculty of Pharmacy, University of Santiago de Compostela, Campus Vida, 15782, Santiago de Compostela, Spain
[b] Center of Research in Molecular Medicine and Chronic Diseases (CiMUS), University of Santiago de Compostela, Campus Vida, 15706, Santiago de Compostela, Spain

ARTICLE INFO

Article history:
Received 6 November 2021
Received in revised form 14 January 2022
Accepted 18 January 2022
Available online 3 February 2022

Keywords:
A549 cells
Chitosan nanocapsules
Dry powders
Microencapsulation
Pulmonary administration
Spray-drying

ABSTRACT

In this work, it is described a novel micro-nanoplatform for pulmonary administration of active ingredients (AIs), including chitosan (CS)-based nanocapsules (NCs) with/without hyaluronic acid (HA), to treat lung diseases. Specifically, CS NCs and HA/CS NCs were microencapsulated in mannitol microspheres (Ma MS) by a simple spray-drying technique that gave as result dry powders of suitable characteristics for inhalation. Ma MS showed spherical morphology and sizes between 1 and 5 μm, with homogeneous distribution of NCs inside them. In aqueous media, the powders released rapidly the NCs, maintaining approximately their physicochemical characteristics. *In vitro* studies in A549 cells showed high cell viabilities after contact with both NCs (>90%) and Ma (≥99%); being, approximately, a 100% of cells internalized with NCs. For first time, it is exhaustively described the adjustment of the spray-drying process of NCs, resulting in a suitable and safe micro-nanoplatform of great potential for pulmonary administration.

1. Introduction

At present great efforts are directed towards the administration of AIs by the pulmonary route to achieve either local or systemic effects [1]. It is known that the AIs doses can be reduced compared to those administered by other routes like the oral, resulting in a decrease of the side effects [2,3]. Moreover, the direct AIs delivery to the lungs offers a valuable interest for local treatments, as in the cases of lung cancer, acute respiratory distress syndrome (ARDS), cystic fibrosis, α_1-antitrypsin deficiency, infections and inflammations diseases [4–7]. Nowadays, the development of new and innovative micro- and nanoplatforms is receiving growing interest, highlighting the use of nanostructures for lung delivery of peptides, proteins and genes [1]. Specifically, NCs have a versatile structure that can support high drug loadings of AIs of different molecular weight and nature, even simultaneously; for example, hydrophilic molecules (such as genetic material) on the shell and lipophilic adjuvant molecules (like capsaicin) into the core [8]. Our group developed, using a solvent displacement method, NCs consisting of a CS polymeric coating, an interface of lecithin and a Miglyol® nucleus [9–12]; and explored their application by different routes (*i.e.* ocular, nasal and oral) [11]. Recently, we have proposed them for pulmonary gene therapy [13]. The CS polysaccharide stands out in the development of nanocarriers. It is biocompatible, biodegradable (by mammalian enzymes, such as lysozyme or α-amylase) [14–16], mucoadhesive [17,18] and improves the macromolecules permeation through mucosae [19]. HA is an endogenous glycosaminoglycan that is present in human fluids and tissues [20,21], and it is also mucoadhesive and biodegradable [22,23]. It has the ability to improve absorption of drugs [24] and increase the drug circulation time in the bloodstream [25,26]. HA was also used to prepare nanocarriers that were administered by different routes [22,27–31] and has a great potential for gene therapy [32–36]. Both polysaccharides are interesting to form efficient nanocarriers for the pulmonary administration of AIs, being biosecure and biodegradable in the body. In fact, CS NCs were proposed to treat cystic fibrosis and were evaluated *in vitro*, employing the cell line CFBE41o- [8] and in A549 lung cancer cells [37].

In order to achieve a successful administration of AIs by the pulmonary route, it is necessary to overcome a number of barriers and lung defense mechanisms, such as the own anatomy of the airways, the mucociliary clearance and the uptake by the alveoli macrophages

* Corresponding author.
E-mail address: mdelcarmen.remunan@usc.es (C. Remuñán-López).

https://doi.org/10.1016/j.powtec.2022.117149
0032-5910/

[38,39]. Furthermore, in the case of nanosized carriers, there are some important inherent limitations. First, their small size and low inertia hamper their delivery in the lung deep areas [40,41]. Second, their low stability when are administered in suspension form [40]. This can be improved by transforming them into powders by lyophilization. However, their subsequent resuspension and recovery in liquid medium can be compromised. Consequently, it is essential to design suitable dry powder carriers to facilitate the successful arrival of the AIs-loaded nanocarriers in the deep lung [42]. In this respect, it is accepted that the aerodynamic diameter (D_{aer}) plays an important role in the systems deposition, among other factors. It is assumed that the particles with a D_{aer} between 1 and 5 μm will deposit mainly in the alveoli, while the largest will remain in the upper respiratory regions [43]. With this in mind, our group has already showed the efficient microencapsulation of different types of nanoparticles (NPs) (CS NPs, solid lipid NPs (SLN), MOFs MIL-100(Fe) NPs) in Ma MS, resulting in dry powders efficiently aerosolized to the deep lung giving high bioavailability of the associated AI [44–47]. Furthermore, as mentioned above, we have recently demonstrated the great potential of HA/CS-based NCs loaded with a model plasmid (pCMV-βGal) and microencapsulated in Ma MS for pulmonary gene therapy [13].

Considering the aforementioned comments, in this work a micro-nanoplatform for the pulmonary delivery of AIs with potential application in lung diseases is proposed. We report the preparation and characterization of dry powders containing CS-based NCs using Ma as excipient. This carbohydrate, a non-reducing sugar widely used in pharmaceuticals [48,49], was selected as spray-drying excipient due to its attractive characteristics. It favors the dispersibility, flowability and stability of the obtained MS [50,51], and allows to modulate their size and morphology [52]. Furthermore, it has a thermoprotective effect on AIs [46,50] and improves the passage through the lung mucus thanks to its osmotic and mucolytic effects [53]. Microencapsulated CS NCs were prepared using a spray-drying technique, which was specifically adjusted. The resulting CS-based NCs-loaded Ma MS were characterized in terms of spray-drying process yield, morphology and size, NCs distribution, and aerodynamic properties. In addition, the release of the NCs from Ma MS was investigated and *in vitro* studies were carried out on the A549 cell line (adenocarcinoma human alveolar basal epithelial cells) [54]. In this regard, it was critical to ensure that the NCs, as well as the excipient employed to prepare the micro-nanocarriers were biocompatible with the lung epithelium to guarantee their safety. Furthermore, it was important to investigate if the systems were internalized by the cells. Taking into account the obtained knowledge about the CS-based NCs benefits by other administration routes and the previously developed dry powders [13], we conjectured that MS will reach and deposit in the deep lung, where the carbohydrate carrier will dissolve, releasing the NCs and, then, the associated AIs.

2. Materials and methods

2.1. Materials

Protasan® UP CL 113 (ultrapure chitosan, hydrochloride salt, CS, deacetylation degree: 75–90%, Mw < 150 KDa) was acquired from Pronova Biopolymer, A.S. (Drammen, Norway); Epikuron® 145 V (soybean lecithin) was purchased to Cargill (Madrid, Spain); Miglyol® 812 N was a gift from Cremer Oleo Division (Hamburg, Germany); hyaluronic acid (HA, Mw ~ 166 kDa) was donated from Bioiberica (Barcelona, Spain); Curosurf® (pulmonary surfactant: 80 mg/mL of pig lung phospholipids) was generously provided by Professor Almeida (University of Lisbon, Portugal) who acquired it to Angelini Pharmacêutica, Lda. (Lisbon, Portugal); A549 cell line was obtained of ATCC (Manassas, USA); Dulbecco's Modified Eagle Medium (DMEM), Fetal Bovine Serum (FBS), Trypsin-EDTA (0.05%), and Fluoromount® were obtained from Gibco™ (ThermoFisher Scientific, Madrid, Spain); Bodipy® 630/650-X was got from Molecular Probes (Eugene, USA); Coumarin 6 (Cu^6, >99%), D-mannitol (Ma, ≥98%, Mw: 182.17 g/mol), phosphate buffered saline tablet (PBS, pH: 7.4), L-Glutamine and sodium dodecyl sulfate (SDS) were acquired to Sigma Aldrich (Madrid, Spain); AlamarBlue® (CellTiter-Blue) was obtained from Promega (Fitchburg, USA); Triton® X-100 (molecular biology grade) was purchased to Scharlab S.L. Laboratories (Barcelona, Spain); 4′,6-diamino-2-phenylindole (DAPI) was acquired from Emp-Biotech (Berlin, Germany), LIVE/DEAD™ Fixable Aqua Dead Cell Stain Kit was acquired to Invitrogen™ (Waltham, USA); Trypan Blue was obtained of Logos Biosystems (Sainghin-en-Mélantois, France); Neutral Buffered Formalin (10% *v/v*) was bought to Bio-Optica (Milan, Italy); acetone and ethanol were grade HPLC; MilliQ water (ultrapure filtered water, using filters of 0.2 μm, Millex®-GN, Millipore Iberica, Madrid, Spain). The other chemical products were reagent grade.

2.2. Preparation of CS-based NCs

CS NCs were prepared by a solvent displacement method previously development by our research group [9,11,12]. Briefly, the oil phase (mixture of 10 mg of lecithin dissolved in 250 μL of ethanol, 31.2 μL of Miglyol®, and 4.75 mL of acetone) was immediately poured into the aqueous CS phase (10 mL of CS solution (0.25 mg/mL)), under magnetic stirring (2000 rpm) (CIMAREC i Multipoint, Fisher Scientific, Spain), turning immediately in a milky mixture due to the instantaneous formation of the NCs. After 10 min mixing, solvents were evaporated under vacuum and NCs were concentrated up to 5 mL. HA/CS NCs were prepared in the same way that CS NCs but, after the 10 min of the phases mixing, 5 mL of hyaluronic acid (0.5 mg/mL) were added drop by drop (addition speed: 1 mL/min) and mixed for 10 more minutes. Then, the solvents were evaporated under vacuum until obtaining 5 mL of final volume.

NCs production yield (P.Y.) was calculated by gravimetry using the formula below. CS-based NCs were centrifuged (Ultracentrifuge Beckman Coulter: Optima™ TLX Ultracentrifuge, Rotor: TLA_100.3, California, USA) at 6000 rpm and 15 °C during 1 h. Then, the cream supernatant consisting of NCs was collected and freeze-dried (freeze dryer Telstar LyoQuest −85, Spain) during 24 h (from −80 °C to 20 °C by gradually increasing of the temperature) ($n = 3$).

$$\text{P.Y.}(\%) = \frac{\text{NCs weight}}{\text{Total solids [CS + Lecithin + Miglyol (+HA)] weight}} \times 100 \quad (1)$$

2.3. Characterization of the NCs

NCs size, polydispersity index (PdI) and ζ-potential were determined by Dynamic Light Scattering (DLS) and Laser Doppler Anemometry (LDA) using a Zetasizer® Nano-ZS (Malvern Instruments, Malvern, UK) at 25 °C. Each sample was characterized in triplicate ($n = 3$).

NCs morphology was viewed by Transmission Electron Microscopy (TEM) (Jem-2010 Electron Microscope, at 120 KV). For that, 10 μL of NCs were deposited on carbon films of copper grids and stained with 2% (*w/v*) phosphotungstic acid during 2 min, washed with MilliQ water and allowed to dry.

2.4. NCs thermal stability analysis: Heating-cooling ramps

It is very important to bear in mind that the structural stability of the NCs is conditioned by the temperature. Taking into account that the NCs will be microencapsulated in Ma MS by a spray-dry process, these nanostructures will be exposed for a certain time to a temperature (T_{Outlet}), which depends on the prefixed temperature (T_{Inlet}), among other factors. Therefore, the stability of the NCs could be compromised by the T_{Outlet}. For that, it is crucial to perform a thermal stability analysis to determine the critical temperature at which each nanosystem

(CS NCs and HA/CS NCs) could destabilize. It must be ensured that during the spray-drying process, the T_{Outlet} remains below the destabilization temperature to ensure structural integrity and, hence, the quality of the microencapsulated NCs. The structural destabilization is detected by a strong increase of NCs PdI (>0.7), which will produce large standard deviations.

To investigate the structural stability of the NCs at different temperatures, suspensions of CS NCs and HA/CS NCs were exposed to heating-cooling ramps from 25 to 90 °C (large range of possible $T_{Outlets}$) and *vice versa* (with a rate of 0.5 °C/min), into quartz cuvette covered to prevent evaporation. The NCs sizes and PdI were measured each 0.5 °C by Dynamic Light Scattering (DLS) using the Zetasizer® Nano-ZS (Malvern Instruments, Malvern, UK) with an Attenuator fixed at 7. The study was done in triplicate ($n = 3$).

2.5. Stability of NCs in the spray-drying excipient solution

Before the NCs microencapsulation in Ma MS, their physicochemical stability in Ma solution was checked. For that purpose, 5 mL of NCs suspension was mixed with 5 mL of a concentrated solution of Ma (16%, *w/v*). The mixture was incubated at room temperature under magnetic stirring (300 rpm) (CIMAREC i Multipoint, Fisher Scientific, Spain). The NCs physicochemical characteristics (size and ζ-potential) were analyzed in triplicate ($n = 3$) at different times (0, 0.5, 1, 2 and 4 h), by the methods previously described.

2.6. Microencapsulation of the NCs

NCs microencapsulation was carried out using a co-current Büchi spray-dryer (Büchi® Mini Spray Dryer B-290, Flawil, Switzerland) with two fluids 0.7 mm nozzle. Volume of drying chamber was 9.3 L, with a residence time of the particles of 55.8 s. This was calculated as follows [55]:

$$t_r = \frac{V_c}{\text{Air flow rate}} \quad (2)$$

Where: t_r: residence time of the particles; V_c: volume of drying chamber: 9.3 L; air flow rate: 600 NL/h.

To microencapsulate NCs correctly, it was necessary to adjust some parameters of the spray-dry process: total solids content (t.s.c.) (*w/w*, %), air flow rate (NL/h), NCs:Ma ratio, Outlet temperature (T_{Outlet}, mainly determined by the Inlet temperature (T_{Inlet})) (°C), aspirator (%), and flow rate (F.R.) (mL/min). For this study, the CS NCs formulation was used and each variable of the process was modified step by step, while the other variables were kept constant. In the step 1, t.s.c. was tested, being the investigated values of 2.5, 5, 10, 11, and 12%, fixing the parameters air flow rate = 400, NCs:Ma = 1:10, T_{Inlet} = 170 °C, Aspirator = 75% and Flow Rate = 2 mL/min. In the step 2, the Air flow rate was checked, for which two high values were chosen for the greatest dispersion of the suspension droplets: 400 and 600 NL/h. In the step 3, the NCs:Ma ratio was verified by testing two ratios in which there was a high proportion of Ma. This is because in previous studies (data not shown) it was observed that a more similar ratio between the NCs and the excipient, does not lead to the preparation of MS, but rather agglomerates with a "flake" shape. Therefore, the 1:10 and 1:15 ratios were tested. In step 4, the effect of the T_{Outlet} was studied, considering two opposing values: 105 and 170 °C, associated with $T_{Outlets}$ around 58 and 90 °C, respectively. In this way, we want to check whether a low temperature (slightly more humid powder, but ensuring the stability of the NCs) or a high temperature (drier powder, but with risk of stability of the NCs) is better. In any case, the Aspirator was directly set at 100% in this step to decrease the T_{Outlet} and minimize the risk of instability of the NCs spray-dried at 170 °C. In addition, a F.R. of 8.8 mL/min was punctually used with the intention that the temperature had less influence on the samples, especially considering the one that was spray-dried at 170 °C. In the step 5, it was determined which F.R. was the most appropriated, keeping the Aspirator at 100% to lower the T_{Outlet}. The compared values were: 5, 7, 8.8 and 10 mL, being higher than 2 mL/min in all cases because it was observed that low F.R. values lead to too small MS. We observed the powders in terms of morphology, sphericity and aggregation of the MS. The optimum spray-dry conditions were subsequently used to microencapsulate the HA/CS NCs.

2.7. Characterization of dry powders

2.7.1. Spray-drying process yield

Process yield (P.Y.) was calculated by gravimetry by comparing the final amount of dry powder obtained by spray-drying (MS weight) with the theoretical (t.s.c. (NCs + Ma) weight), as following ($n = 3$):

$$\text{P.Y.}(\%) = \frac{\text{MS weight}}{\text{t.s.c.(NCs + Ma) weight}} \times 100 \quad (3)$$

2.7.2. Morphology and size

The MS morphology and size were characterized by Scanning Electron Microscopy (SEM) (FESEM Ultra-Plus, Zeiss, Germany). For that purpose, thin films of powders were fixed in graphite discs on stubs. The samples were metalized with a film of iridium (10 nm) by an Emitechk 550 Sputter Coater (London, England). The MS size was determined by measuring the space between two tangents of opposed margins (Feret's diameter) by the z-SmartTiff program (Zeiss, Germany). The geometric diameter (D_g) was calculated as the mean of the Feret's diameters, being employed in this study 50 MS measures for each powder ($n = 50$).

2.7.3. Distribution of NCs in Ma MS: confocal laser scanning microscopy (CLSM)

For this study, Coumarin 6 (Cu^6) was used to label the NCs, obtaining Cu^6-CS NCs and Cu^6-HA/CS NCs. Specifically, 4.5 μL of Cu^6 (10 mg Cu^6/mL of dichloromethane) was mixed homogeneously in the oil phase during the NCs preparation. Cu^6-labelled NCs were characterized for size, PdI and ζ-potential, as described above (Section 2.3.). To remove possible non-encapsulated Cu^6 residues, the labelled NCs were dialyzed (Spectra/Por® 3 MWCO Dialysis Membrane Standard RC Tube: 3.5 kD) overnight, before their microencapsulation. After dialysis, the Cu^6-labelled NCs were characterized newly. Then, both pre-dialyzed and dialyzed labelled NCs were compared by Confocal Laser Scanning Microscopy (CLSM) to confirm that the Cu^6 was perfectly encapsulated and not released. The CLSM microphotographs were taken using a Leica TCS-SP5X-AOBS microscope with a white laser (470–670 nm) and a UV laser (Leica), using LAS AF software (Leica Application Suite Advanced Fluorescence) and a 63× objective (PL oil APO63x /NA1.4–0.6 CS). The data were obtained using a green channel ($\lambda(Cu^6)$ = 455/461 nm ($\lambda_{exc/em}$)). Furthermore, Ma excipient was labelled with Bodipy® (λ(Bodipy®) = 558/568–651 nm, ($\lambda_{exc/em}$)) (Ma^B) (1 mg/mL of Bodipy® in DMSO) by addition of the fluorophore to the Ma solution (0.32 μg Bodipy®/1 mg Ma) under mild magnetic stirring for 2 h at room temperature. Then, the Cu^6-NCs were added to the Ma^B solution and were mixed for 1 h, before their atomization.

The powders samples were visualized by CLSM (Leica TCS-SP5X-AOBS microscope with LAS AF Leica Application Suite Advanced Fluorescence software, using an objective HCX PL APO CS 63.0 × 1.30 GLYC 21 °C UV). Images were captured using separate channels. The grayscale images were colored with green for Cu^6 and red for Bodipy® and were overlapped to get a multicolor image.

2.7.4. Aerodynamic properties of the dry powders

The tap density or apparent density (g/cm^3) of a powder, which is the mass located in 1 cm^3, was determined using a tap density tester

(Tecnociencia, Spain). Briefly, a volume of powder (corresponding to 1.0–1.6 g) was measured in 10 mL test-tube, prior to mechanical tap. The test-tube was tapped (30 tap/min) until the powder reached a constant volume [56] ($n = 3$).

The real density (g/cm^3) was obtained using a helium pycnometer (Quantachrome MPY-2, Syosset, NY, USA) (n = 3). The aerodynamic diameter (D_{aer}), which is defined as the diameter of a sphere of unit density that has the same terminal settlement velocity as the particle under consideration, was theoretically calculated using the following equation [57]:

$$D_{aer} = D_g \sqrt{\frac{\rho_{real}}{\rho_0 \lambda}} \quad (4)$$

Where: D_g: geometric diameter (average of Feret's diameters of MS, μm), ρ_{real}: real density of MS (g/cm^3), $\rho_0 = 1$ g/cm^3, and λ: dynamic shape factor of the MS (spherical MS: $\lambda = 1$; irregular MS: $\lambda = 2$) [58–60].

2.8. Release of NCs from Ma MS

400 mg of powder were incubated in 6 mL of either MilliQ water or simulated pulmonary medium (0.2 mL of 0.1% Curosurf® into 199.8 mL of 10 mM PBS (pH: 7.4) (*v/v*)) under mild magnetic stirring (300 rpm) at room temperature and 37 °C, respectively. At different times (0, 0.5, 1, 2 and 4 h), samples were characterized using a Zetasizer® Nano-ZS (Malvern Instruments, Malvern, UK) to check the physicochemical characteristics (size and ζ-potential) of the released NCs and to demonstrate their release. In addition, TEM microphotographs of CS-based NCs released at 1 h in MilliQ water were obtained to compare them with TEM microphotographs of fresh NCs (in MilliQ water) to determine visually if the spray-drying process affected the NCs physicochemical characteristics. The study was carried out in triplicate ($n = 3$).

2.9. Stability of NCs in cell growth medium

The stability of CS NCs and HA/CS NCs was checked in MilliQ water (control), in Dulbecco's Modified Eagle Medium (DMEM) without supplementation and in DMEM supplemented with 200 mM L-Glutamine and 10% (*v/v*) Fetal Bovine Serum (FBS). For that purpose, the suspensions of CS NCs and HA/CS NCs (2.74 mg/mL) were diluted in the different media (1:10 (*v/v*)) and mixed under gentle magnetic stirring (300 rpm) (CIMAREC i Multipoint, Fisher Scientific, Spain) at 37 °C. At different times (0, 2 and 4 h), an aliquot of each sample was characterized in terms of particle size and standard deviation, fixing the temperature at 37 °C and the attenuator at 7. The NCs are considered stable if their sizes remain in the nanometric range. The study was carried out in triplicate ($n = 3$).

2.10. Studies in A549 cells

A549 cell line was used in the cell passes from 12 to 32. Cells were grown in 10 mL plates (with TC treated surface), in a humidified incubator (inCu saFe Cooper Alloy Stainless) with 5% CO_2/95% atmospheric air at 37 °C, using DMEM supplemented with 200 mM L-Glutamine and 10% (*v/v*) FBS. *In vitro* cell studies have been carried out using CS-based NCs and Ma separately and not in form of micro-nanostructured platform. This is because *in vivo* the Ma dissolves very rapidly, releasing the NCs that are the ones that, together with the dissolved Ma, really interact with the pulmonary cells.

2.10.1. Viability study

CS NCs and HA/CS NCs were dialyzed overnight (Spectra/Por® 3 Dialysis Membrane Standard RC Tubing MWCO: 3.5 kD) to remove possible residues.

To evaluate the initial viability of the A549 cells after incubation with the nanosystems, a preliminary study with Luna II (Luna II™ Automated Cell Counter, Logos Biosystems, USA) was carried out, following the protocol specified by Fernández-Paz et al. [44]. In in the present study, 60,000 A549 cells/well were seeded in 24-well plates (Falcon®, USA) with supplemented cell culture medium, and were incubated in the humidified until confluence (48 h). Then, the cells were treated as follows: (i) 40 μL of sterile filtered MilliQ water with 360 μL of supplemented DMEM (1:10) (positive control), (ii) 55.2 μg/well of CS NCs or HA/CS NCs until a final volume of 400 μL of supplemented DMEM and (iii) a mixture of 40 μL of 1% (*v/v*) Triton with 360 μL of supplemented DMEM (1:10) (negative control). After 4 h incubation, cells were washed three times with 1× PBS (pH: 7.4) and detached with Trypsin. Then, supplemented DMEM was added to each well and cells were collected and centrifuged for 5 min at 1477 rpm (Eppendorf 5415R Refrigerated Centrifuge, Germany). The pellets were resuspended in 500 μL of 1× PBS (pH: 7.4) (supplemented with 10% (*v/v*) FBS). 10 μL of each sample were mixed homogeneously with 10 μL of (0.4%, *w/v*) Trypan Blue Stain. Finally, 10 μL of each mixture was loaded in a counting chamber to obtain images of the living and dead cells. The viability percentages of the cells incubated with the systems were obtained by automated counting in each image, taking into account the images of the positive and negative controls ($n = 3$). Percentages of viability higher than 90% are considered good results [44].

Subsequently, another cell viability study was performed to check the cells recovery at 24 and 48 h after 4 h of incubation with CS NCs, HA/CS NCs and Ma excipient. This study was carried out following also the protocol specified in the work published by Fernández-Paz et al. [44]. In the present study, 9000 A549 cells/well were seeded in 96-well plates (Corning Incorporated costar®, USA) with supplemented cell culture medium, and were incubated until confluence (48 h). Then, the medium of each well was replaced with 90 μL of fresh supplemented cell culture medium and 10 μL of: (i) sterile filtered MilliQ water (positive control), (ii) 1% (*v/v*) Triton (negative control), and (iii) suspensions of NCs (CS or HA/CS) to obtain the following concentrations: 2.74, 0.69, 0.18, 0.05, 0.02, 0.005, 0.001 mg/mL ($n = 4$). In the case of the excipient, a 15% (*w/v*) Ma solution was directly prepared in supplemented DMEM, being the analyzed final concentrations of: 15, 3.75, 0.94, 0.23, 0.059, 0.015, 0.0037 mg/mL. The cells were incubated during 4 h and washed three times with 1× PBS (pH: 7.4). After, supplemented DMEM was added. The A549 cells were incubated for 24 and 48 h in the humidified incubator. Later, 20 μL of CellTiter-Blue® was added to each well in dark conditions. The cells were incubated in the same conditions during 3 h. Finally, 50 μL of 3% (*w/v*) sodium dodecyl sulfate (SDS) was added to each well (30 min) and the lysed samples were transferred to a dark-bottom 96-well plate to measure the fluorescence. The fluorescence signal was measured at $\lambda_{Ex/Em}$: 539/620 nm using a microplate reader (SYNERGY H1M BioTek®) with the Gen5 (Image Software BioTek®) program. The percentage of cell viability (%) was calculated as follows ($n = 4$):

$$\text{Cell viability (\%)} = \frac{\text{Sample fluorescence}}{\text{Positive control fluorescence}} \times 100 \quad (5)$$

Percentages of viability higher than 90% are considered good results [44].

2.10.2. Study of intracellular uptake

For the cell internalization study, it was followed the protocol specified in the work published by Fernández-Paz et al. [44]. Briefly, to 60,000 A549 cells/well were seeded with supplemented DMEM in 24-well plates (Falcon®, USA), on polylysine-treated coverslips (Poly-L-Lysine Cellware 12 mm round Coverslips, Corning® BioCoat™), and were incubated until confluence. Then, the culture medium was substituted by: (i) 400 μL of supplemented DMEM (control) and (ii) 55.2 μg/well of Cu^6-CS NCs or Cu^6-HA/CS NCs until a final volume of

400 μL of supplemented DMEM. Cells were incubated for 4 h. Afterwards, cells were washed three times with 1× PBS (pH: 7.4). Cells were fixed by 10% (*v/v*) neutral buffered formalin for 15 min. Then, the washing process was repeated three times. Cell nuclei were labelled by adding 200 μL of a dilution 1:1000 (*v/v*) of DAPI (1 mg/mL in 1× PBS) for 30 min. The cells were washed three times again. The covers were placed on slides, using Fluoromount® (Thermo Fisher Scientific, Spain). Samples were observed by confocal laser scanning microscopy (CLSM) (Leica TCS SP5 X, Germany) using an objective HCX PL APO CS 63.0 × 1.30 GLYC 21 °C UV and a white light laser. The fluorescent emissions from Cu^6 ($\lambda_{Ex/Em}$ = 455/461 nm) and DAPI ($\lambda_{Ex/Em}$ = 405/414–440 nm) were captured and the images were colored with green for Cu^6 and blue for DAPI, and overlapped to get a multicolor image, using the LAS X Life Science Software. It is expected that the NCs are visibly inside the cells.

2.10.3. Quantification of A549 cells containing NCs

To quantify the A549 cells that have internalized CS NCs and HA/CS NCs, the Fluorescence-Activated Cells Sorting technique (FACS) was employed using dialyzed Cu^6-CS-based NCs, following the protocol specified by Fernández-Paz [44].

A number of 60,000 A549 cells were seeded per well in 24-well plates (Falcon®, USA), and incubated in a humidified incubator until confluence. The culture medium was replaced by: (i) 400 μL of supplemented DMEM (control) and (ii) 55.2 μg/well of CS NCs or HA/CS NCs until a final volume of 400 μL of supplemented DMEM (n = 3). Cells were incubated for 4 h at the same conditions. Afterwards, cells were washed three times with 1× PBS (pH: 7.4). Then, 200 μL of LIVE/DEAD™ fixable Aqua (dead cell stain reagent diluted in 1× PBS (1 μL of Aqua in 2 mL of the PBS, *v/v*)) were added for 15 min. The cells were washed three times and detached by incubation with 120 μL of Trypsin for 5 min. The cells were isolated by centrifugation for 5 min at 1477 rpm (Eppendorf 5415R Refrigerated Centrifuge, Germany). The supernatant was removed and the pellet was resuspended in 500 μL of 1× PBS (pH: 7.4) (supplemented with 10% (*v/v*) FBS). A minimum of 10,000 events were excited at 488 nm using filters BP 525/50 for Cu^6 and BP 515/20 for Aqua viability reagent. It was employed the detector forward scatter (FSC-A) by Accuri Becton Dickinson cytometer (BD Accuri™), using a BD sample software (BD Biosciences, CA). To avoid false positives due to Cu^6 signal overlapping with the Aqua signal, "colour compensation" was applied (data not shown), being the corrections of: 17.62%, 18.25% and 18.05% for the first, second, and third replicates, respectively, of the cells treated with Cu^6-labelled NCs. Good results are considered if the percentages of cells that have internalized NCs are above of the 90% [44].

3. Results and discussion

3.1. Characterization and production yield of CS-based NCs

CS NCs presented sizes over 160 nm and positive ζ-potentials (around +56 mV) (Table 1). HA/CS NCs were smaller in size (over 154 nm) and had a lower ζ-potential (about +35 mV) than their equivalent without HA (Table 1). This decrease in size and ζ-potential can be explained by the strong crosslinking effect between HA (negatively charged) and CS (positively charged) on the NCs surface. It has been previously observed for CS/HA/TPP NPs in that, maintaining constant the amounts of TPP and increasing those of HA in relation to CS, decreased the size as well as the ζ-potential [61,62]. Cu^6-CS-based NCs pre- and dialyzed maintained a similar size with respect to the unlabeled CS-based NCs. However, although the ζ-potential of the pre-dialyzed Cu^6-CS-based NCs was practically identical to the unlabeled CS-based NCs, when the Cu^6-CS-based NCs were dialyzed, they showed a decrease in the ζ-potential (Table 1). This diminution in the ζ-potential was produced by the elimination of NCs preparation components, especially of CS polymers (positively charged).

Table 1
Physicochemical properties of CS-based NCs (mean ± S.D.; n = 3).

Formulation	Size range (nm)	PdI	ζ-Potential range (mV)	Production Yield (%)
CS NCs	160 ± 3	0.19	+56 ± 1.4	83 ± 4
Pre-dialyzed Cu^6-CS NCs	161 ± 2	0.21	+57 ± 0.6	-
Dialyzed Cu^6-CS NCs	162 ± 1	0.20	+40 ± 0.1	-
HA/CS NCs	154 ± 2	0.15	+35 ± 0.8	67 ± 7
Pre-dialyzed Cu^6-HA/CS NCs	155 ± 1	0.16	+37 ± 0.4	-
Dialyzed Cu^6-HA/CS NCs	156 ± 2	0.15	+26 ± 0.1	-

The production yields were around 83% and 67% for the CS NCs and the HA/CS NCs, respectively (Table 1). The lower yield corresponding to the formulation prepared with HA can be explained because it was found experimentally that the HA/CS NCs cream is more difficult to isolate. This was also observed for the CS/HA/TPP NPs in which, as the proportion of HA increased, the yield decreased [61].

As shown in representative TEM images (Fig. 1), both types of NCs presented spherical morphology and core-shell structure. Moreover, when HA was added to the CS NCs surface, there was a change on the appearance of their surface, where the HA filaments could be observed projected outwards.

3.2. NCs thermal stability analysis: heating-cooling ramps

As explained in section 2.4., it is crucial to perform a thermal stability analysis to find out the temperature from which it is produced the structural destabilization of the NCs. The effect of the temperature on the NCs physicochemical characteristics (size and PdI) was analyzed by DLS (Fig. 2). This study was carried out because the NCs will be subsequently subjected to possible elevated $T_{Outlets}$ during the spray-drying process and it is crucial to know their destabilization temperatures to maintain the $T_{Outlets}$ with suitable values to ensure the NCs stability.

The initial mean sizes of the CS NCs and HA/CS NCs were of 165 ± 4 nm and 147 ± 10 nm, respectively. In both cases, the heating ramp at 90 °C induced a decrease in size of 48 nm and 16 nm for CS NCs and HA/CS NCs, correspondingly. In addition, the heating ramp of CS NCs showed a destabilization of the NCs structure after 80.5 °C, shown by a PdI greater than 0.7. In the case of HA/CS NCs, they were destabilized from a temperature above of 72 °C, revealed by a PdI of 1. When the temperature returned to 25 °C, the size of CS NCs decreased, staying 17 nm below the original size, while the size of HA/CS NCs increased to remain about 7 nm above their original size. In other words, during the gradual cooling ramp, the NCs returned approximately to their original sizes. This phenomenon was already reported for SLNs [63,64] in which, after the heating-cooling process, the SLNs could withstand the harsh conditions of temperature change. Surely, in the cooling process, the NCs constituent materials were relocated in function of their charges in the aqueous medium, in such a way that the Miglyol "took refuge" within the CS structure thanks to the Lecithin interface, adopting the more stable structuring again.

3.3. Stability of NCs in the spray-drying excipient solution

Ma was used as spray-drying excipient in previous microencapsulation studies of different NPs, such as: i) CS NPs, ii) SLN, and iii) mesoporous iron (III) trimesate (MIL-100(Fe) MOF), intended for pulmonary administration [44–47]. Encouraged by the good results, Ma has been selected in this work to microencapsulate NCs by spray-drying.

Initially, the size of the CS-based NCs increased about 60 nm and 30 nm for CS NCs and HA/CS NCs (see Table 1), respectively, when they were incubated in the Ma solution (see Fig. 3). Later, the CS NCs sizes remained practically constant as the incubation time progressed, while the HA/CS NCs sizes decreased slightly, remaining in both cases

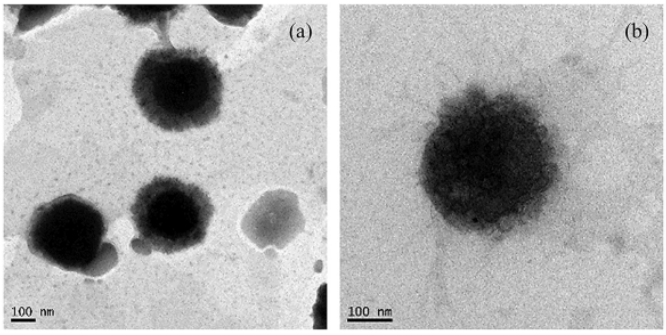

Fig. 1. TEM microphotographs of: (a) CS NCs and (b) HA/CS NC.

above their original values during all the incubation process (Table 1). In addition, the standard deviations of the CS-based NCs sizes were larger from the beginning until approximately 2 h, being less at 4 h. This suggests that the NCs sizes slightly stabilized over time. On the other hand, ζ-potentials of both types of NCs were somewhat lower than those of their corresponding fresh forms, being a decrease of around 10 mV and 4 mV for the CS NCs and HA/CS NCs, respectively. CS-based NCs kept their ζ-potentials practically constant at time 0 h and at 4 h and their standard deviations were very low (almost negligible in Fig. 3). The increase in size, as well as the decrease in the ζ-potential, were probably produced by a certain interaction of the Ma excipient (of slight negative charge) with the CS polymeric shells (of positive charge) of the two NCs formulations [44].

3.4. Microencapsulation of the NCs

Spray-drying is a fast and simple technique of enormous value for the development of AIs-loaded dry powders for pulmonary administration. Depending on the excipient and the different parameters of the spray-dry process, the physical and structural characteristics of the powders can be modulated, improving the aerosolization properties and the *in vivo* performance [65]. Therefore, for the suitable NCs microencapsulation and to obtain quality powders, it is crucial to adjust the variables of their spray-dry process.

Table 2 shows the variable investigated (second column) at each stage (from 1 to 5, first column) of the NCs microencapsulation process. In each step, the values of the studied variable appear on italic, being the selected value in bold. The other parameters remained unchanged.

In the step 1, the optimal t.s.c. (%) was determined. For that, mixtures of CS NCs suspensions in Ma solutions were prepared with t.s.c. of 2.5%, 5%, 10%, 11% and 12% (*w*/*w*), and were spray-dried fixing the rest of parameters as described in the step 1 of the Table 2, being selected a t.s.c. of 11%. Next, the optimal air flow rate was identified by comparison between 400 and 600 NL/h, maintaining the rest of the parameters stablished as showed in step 2 of the Table 2, obtaining the best results at an air flow rate of 600 NL/h. The CS NCs:Ma ratio was studied by fixing of the other parameters as showed in the step 3 of the Table 2, being compared the ratios of 1:10 (*w*/*w*, %) and 1:15 (*w*/*w*, %), getting better MS with a ratio of 1:15. To maintain a better stability of the NCs, it was important to increase the aspirator to 100% to produce a low T_{Outlet} and the F.R. was punctually selected at 8.8 mL/min, so that the temperature had less influence on the samples, especially with that spray-dried at 170 °C. The selected T_{Inlets} were 105 °C (low) and 170 °C (high), keeping the other parameters as

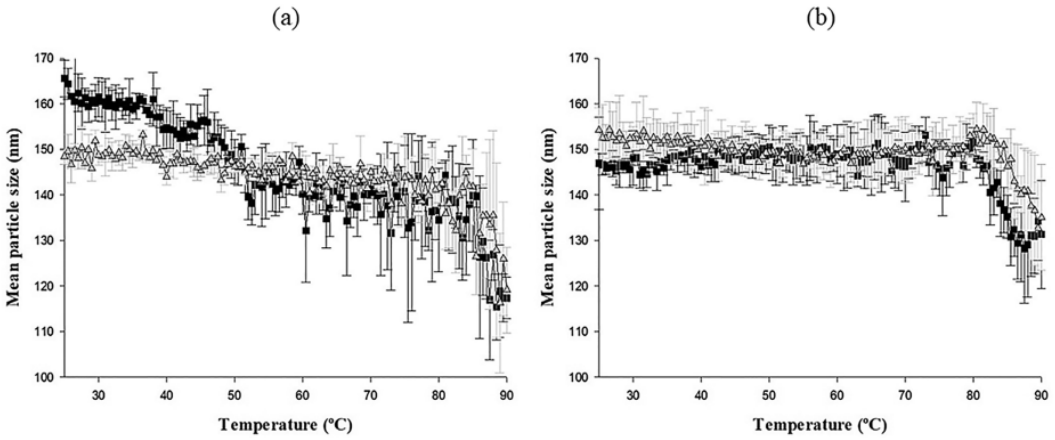

Fig. 2. DLS thermograms of: (a) CS NCs and (b) HA/CS NCs, (■) from 25 °C to 90 °C and (△) from 90 °C to 25 °C (mean ± S.D., $n = 3$).

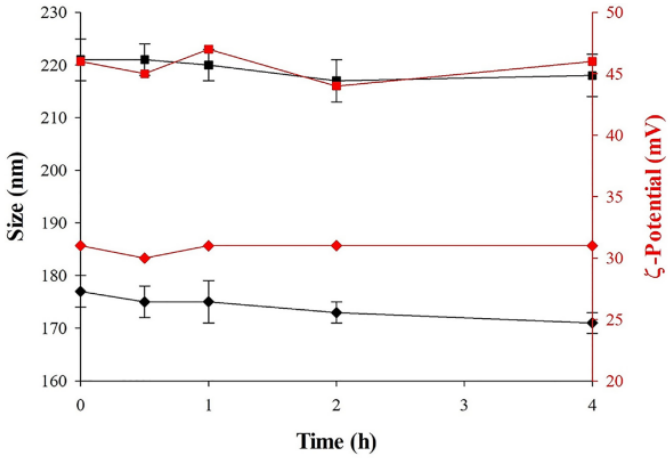

Fig. 3. Evolution of sizes (nm) (black) and ζ-potentials (mV) (red) of: CS NCs (square) and HA/CS NCs (diamond) incubated in Ma solution (16% (*w/v*) over time (h) (mean ± S.D., $n = 3$).

indicated in the step 4 of the Table 2, achieving MS of best quality with a T_{Inlet} of 105 °C. The optimal F.R. was determined testing equal or higher values than 5 mL/min (5, 7, 8.8 and 10 mL/min), maintaining the other parameters as specified in step 5 of the Table 2. Finally, the best F.R. was of 5 mL/min. The complete optimal spray-drying conditions are shown in the bottom row of the Table 2.

In this study, it was observed that the sizes of the MS were not importantly affected by the changes of the investigated variables, being all the sizes comprised between 2.0 and 3.7 μm. For this reason, as mentioned above, only the characteristics of morphology, sphericity and aggregation of the MS were observed in order to select the most appropriate parameters values.

3.4.1. Determination of the optimal total solids content (t.s.c.) (%)

Suspensions of CS NCs in Ma solutions were spray-dried with different theoretical total solids content (t.s.c.) in order to identify the most appropriate one from a morphological and size point of view. As can be seen in the Fig. 4, as the t.s.c. increased, the MS adopted a more spherical and defined morphology, with less aggregation, reaching the best characteristics when the t.s.c. was of 11% (*w/w*). Above this value, MS were less spherical, more aggregated and heterogeneous. This is the reason why t.s.c. of 11% (*w/w*) was selected as the optimum one for the CS NCs microencapsulation process. This t.s.c. is high compared to those required in other studies intended to the microencapsulation of CS NPs, in which the c.s.t. was of 2.1% - 3% [46,66], surely due to the high influence of the lipidic nature of the nanosystems.

3.4.2. Selection of the air flow rate (NL/h)

The spray-drying was carried out at different pressures (400 NL/h and 600 NL/h) in order to find the most suitable one. According to the microphotographs depicted in Fig. 5, the highest pressure produced MS more spherical and isolated. This could be explained by the better dispersion of the droplets during the spray-drying. Therefore, the pressure of 600 NL/h was selected for further studies, being higher than the used for CS-based NPs (400 NL/h) [46,66]. Perhaps, it is due to the lipidic nature of the NCs, which produces certain differences with respect to polymeric NPs (without oily core).

3.4.3. Election of the NCs:Ma ratio (w/w)

Previous studies of NPs microencapsulation [46,66] employed a NPs:Ma ratio of 1:4 (*w/w*). However, when this ratio was used in preliminary studies of this work (data not shown), the MS were not formed. In fact, it is was an insufficient amount of Ma to constitute the MS, so only formed aggregates in form of "scales". Therefore, two ratios with higher proportion of Ma (1:10 and 1:15, (*w/w*)) were selected to improve homogeneity and spherical shape of MS. According to SEM images in the

Table 2
Investigated variables to adjust the NCs spray-drying process (Nozzle diameter: 0.7 mm, Nozzle cleaner: 5).

Step	Tested variable	Total solids content (*w/w*, %)	Air flow rate (NL/h)	NCs:Ma ratio (*w/w*, %)	T_{Inlet} (°C)	Aspirator (%)	Flow rate (mL/min)
1	t.s.c.	*2.5, 5, 10,* ***11****, 12*	400	1:10	170	75	2
2	Air flow rate	11	*400,* ***600***	1:10	170	75	2
3	NCs:Ma ratio	11	600	*1:10,* ***1:15***	170	75	2
4	T_{Inlet} (T_{Outlet})	11	600	1:15	***105****(~58)* *170 (~90)*	**100**[a]	8.8[b]
5	F.R.	11	600	1:15	105	100	***5****, 7, 8.8, 10*[c]
Optimal variables		**11**	**600**	**1:15**	**105**	**100**	**5**

T_{Inlet}: Inlet temperature (°C).
[a] Aspirator was increased to 100% to decrease the T_{Outlet}.
[b] F.R. was set at 8.8 mL/min for that the temperature did not affect the samples as much as possible.
[c] F.R. equal or higher than 5 mL/min were tested because lower F.R. lead to too small MS.

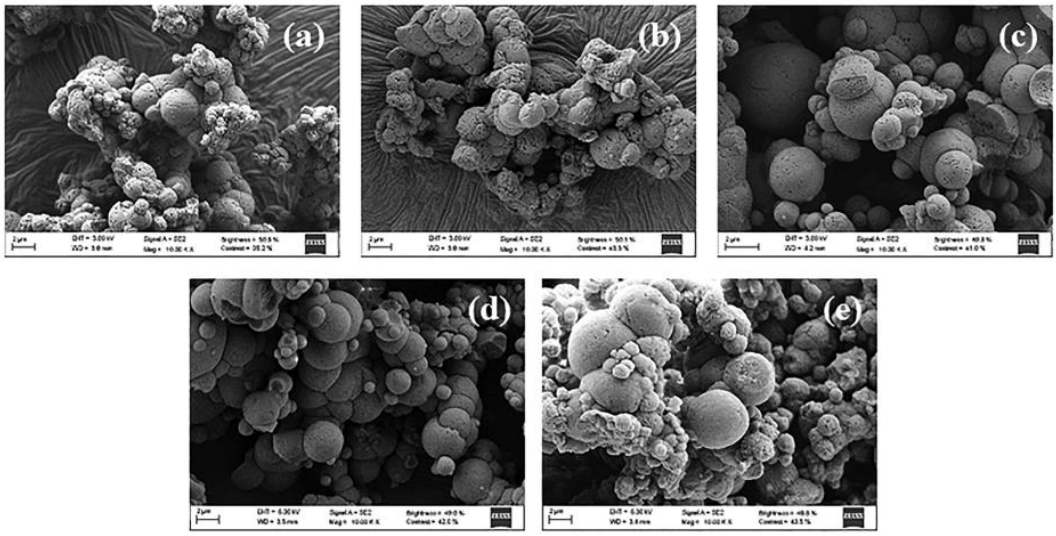

Fig. 4. SEM microphotographs of CS NCs-loaded Ma MS with a total solid content of: (a) 2.5% (*w/w*), (b) 5% (*w/w*), (c) 10% (*w/w*), (d) 11% (*w/w*), and (e) 12% (*w/w*), respectively.

Fig. 6, the MS with the 1:15 (*w/w*) ratio had a better and homogeneous appearance than those prepared with the 1:10 (*w/w*) ratio. As conclusion, the 1:15 (*w/w*) ratio was selected as the most suitable for the microencapsulation of CS NCs.

3.4.4. Determination of the suitable T_{Inlet} (°C) and aspirator (%)

In this study, CS NCs were spray-dried at two different temperatures: 105 °C and 170 °C and the Aspirator was directly adjusted to 100% in both cases to favor the decrease of the T_{Outlet}. The Fig. 7a shows that the MS prepared at the lowest temperature had more spherical morphology and were less aggregated compared with the MS obtained at the highest temperature (Fig. 7b). It could be due to the heat treatment that NCs received during the spray-drying process. When the T_{Inlet} was of 170 °C, the T_{Outlet} was high (~90 °C) and, as demonstrated by the thermal stability analysis (Fig. 2), the NCs stability could be compromised, at least in part, contributing to the worst appearance of the MS (Fig. 7b). On the contrary, when the NCs were spray-dried at 105 °C, a low T_{Outlet} was ensured (~58 °C) and the NCs remained stable, allowing an adequate microencapsulation. The T_{Inlet} selected in the present work (105 °C) was in agreement with the low T_{Inlet} employed for the microencapsulation of SLN (103 °C) and lipid – polymer hybrid NPs (LPNs) (100 °C) already reported [45,67], being these temperatures high enough to evaporate the water from the atomization suspension, generating a T_{Outlet} low enough (~58 °C) to avoid the systems destabilization.

3.4.5. Selection of the optimal flow rate (F.R.) (mL/min)

Different F.R. were tested: 5, 7, 8.8 and 10 mL/min. The MS obtained at low F.R. (2 mL/min) were small (Figs. 4 to 6), as it was expected according to the results of previous studies. Fig. 8a shows that the MS prepared at F.R. of 5 mL/min are spherical, not aggregated, and have homogeneous size and morphology. As can be appreciated in Fig. 8, as the F.R. increased, the MS were less defined, more aggregated and heterogeneous. At a F.R. of 8.8 mL/min, the powder was more humid, being affected the powder quality at a F.R. of 10 mL/min. Considering the results, F.R. of 5 mL/min was selected as the optimal for the

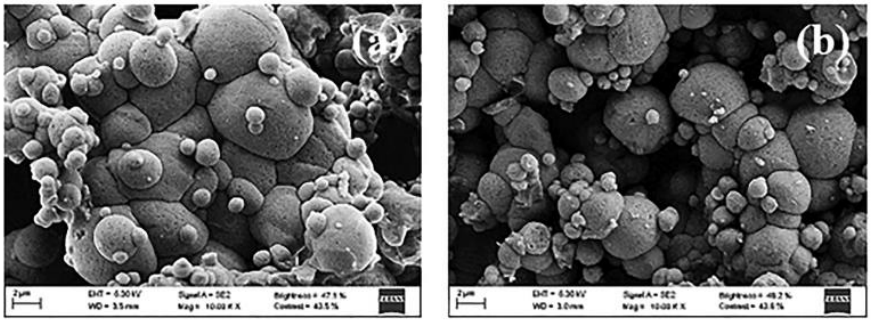

Fig. 5. SEM microphotographs of CS NCs-loaded Ma MS spray-dried with a pressure of: (a) 400 NL/h and (b) 600 NL/h.

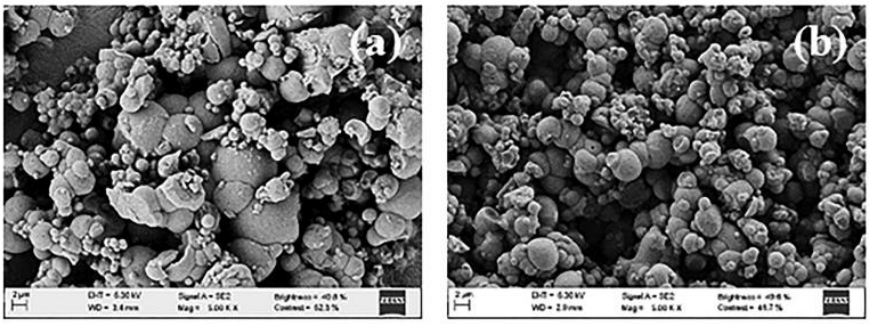

Fig. 6. SEM microphotographs of CS NCs-loaded Ma MS with a NCs:Ma ratio of: (a) 1:10 (*w/w*) and (b) 1:15 (*w/w*).

microencapsulation of NCs. This F.R. was twice as faster (5 mL/min) that the used for the microencapsulation of CS-based NPs (2.5 mL/min) [46,66], resulting in a shorter exposure time to the T_{Outlet} than CS NPs .

3.5. Characterization of dry powders

According to previous studies, the selected conditions for the microencapsulation of NCs in Ma MS were: t.s.c. = 11% (*w/w*), air flow rate = 600 NL/h, NCs:Ma ratio = 1:15 (*w/w*), T_{Inlet} = 105 °C, aspirator = 100%, and F.R. = 5 mL/min. CS NCs and HA/CS NCs were microencapsulated using the optimal conditions and the obtained dry powders were characterized according to their morphology, size, process yield, and location of the NCs in the Ma MS. In addition, Ma MS (control) were prepared at the same optimal conditions.

3.5.1. Spray-drying process yield

Yields of spray-drying process were higher than 60% (Table 3), which are similar to the obtained for the microencapsulation of non-lipid CS-based NPs [46,50,61,68], like CS/TPP NPs, CS/TPP/INS NPs, CS/HA/TPP NPs, insulin (INS)-loaded CS/HA/TPP NPs, and CS/carboxymethyl-β-cyclodextrin NPs (CS/CMCD NPs), which varied between 65 and 73% [46,50,61,68]. However, the yields were lower (≈50%) when lipid/CS NP complexes (L/CS-NP) were microencapsulated [69]. In addition, the yields obtained after the microencapsulation of glyceryl dibehenate SLN and glyceryl tristearate SLN were of 60% and 47%, respectively [45]. Consequently, the results of the present study were better than those previously reported for lipidic nanosystems. In fact, the yields of the NCs spray-drying processes were high, considering that they are lipid and non-solid systems (Table 3). The efficiency of the process in terms of capsule closure corresponds to that 10 mg of powder microencapsulated about 0.7 mg of NCs, maintaining approximately the NCs:Ma ratio of 1:15 [13].

Additionally, T_{Outlet} obtained after the microencapsulation processes were lower than 60 °C, with temperature losses of around 47 °C (Table 3), preserving the integrity and stability of the microencapsulated NCs.

3.5.2. Morphology and size

The powders of Ma MS (control), CS NCs-loaded Ma MS, and HA/CS NCs-loaded Ma MS were characterized by SEM and the microphotographs are depicted in Fig. 9. NCs-loaded Ma MS (Fig. 9b and c) were spherical, with defined edges, more homogeneous in size and less aggregated compared to the control MS (Fig. 9a).

The mean of Feret's diameters (geometric diameter) of the MS were: Ma MS = 3.7 ± 1.6 μm, CS NCs-loaded Ma MS = 2.1 ± 0.9 μm, and HA/CS NCs-loaded Ma MS = 2.8 ± 1.3 μm. Ma MS loaded with: CS/TPP NPs present geometric diameters between 1.9 ± 1.0 μm and 4.0 ± 1.8 μm [47], CS/HA/TPP NPs show values comprised among 2.2 ± 0.4 μm and 2.7 ± 1.3 μm [61], CS/CMCD/TPP (hybrid NPs prepared with carboxymethyl-β-cyclodextrin (CMCD)) exhibit a range of 2.6 ± 0.3 μm and 3.2 ± 0.6 μm [68], and glyceryl dibehenate SLN and glyceryl tristearate SLN have geometric diameters of 4.87 ± 1.61 μm and 5.54 ± 1.79 μm, respectively [45]. The MS obtained in the present study presented geometric diameters that are in agree with those one previously mentioned.

In addition, all types of MS were generally solid. However, some of the largest obtained were hollow, as the SEM microphotographs showed in the Fig. 10. This is consistent with some of the bigger CS

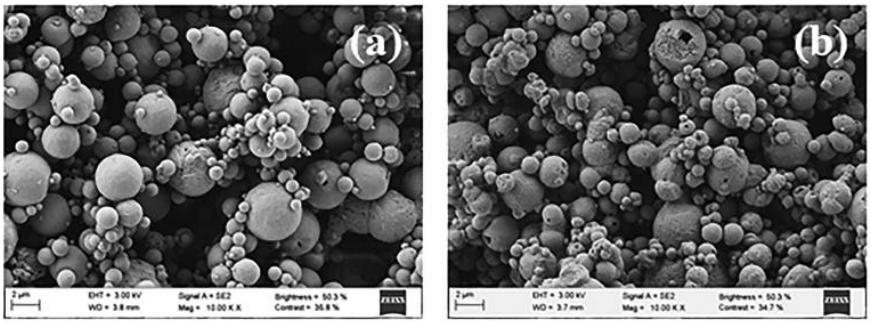

Fig. 7. SEM microphotographs of CS NCs-loaded Ma MS spray-dried with a T_{Inlet} of: (a) 105 °C (T_{Outlet} ~ 58 °C) and (b) 170 °C (T_{Outlet} ~ 90 °C).

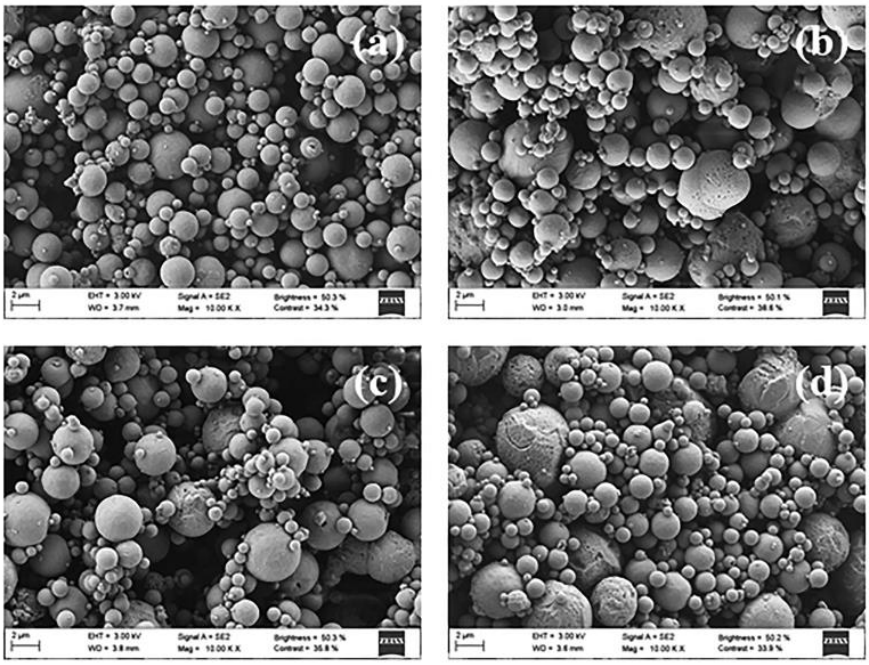

Fig. 8. SEM microphotographs of CS NCs-loaded Ma MS spray-dried with a F.R. of: (a) 5 mL/min, (b) 7 mL/min, (c) 8.8 mL/min, and (d) 10 mL/min.

NPs-loaded Ma MS, whose hollowness of some broken MS also could be seen [47]. The appearance of some large MS is a random process. Their large holes could be explained by the distribution adopted by the Ma when it is in higher proportion with respect to the nanosystems. At this point, the Ma generates MS of big structure, whose NCs charge is distributed in the Ma shell, but totally lacking of the internal framework of Ma carrying the nanosystems.

3.5.3. Distribution of NCs in Ma MS: confocal laser scanning microscopy (CLSM)

A CLSM study was carried out to determine the presence and localization of the NCs in the Ma MS. As previously explained (section 2.7.3.2.), different fluorescent labels were used in order to visualize clearly each component: CS NCs were labelled with Coumarin 6 (Cu^6) (fluorescent green) and Ma was labelled with Bodipy® (fluorescent red).

To eliminate possible non-encapsulated Cu^6 residues and avoid false signals, the Cu^6-labelled NCs were dialyzed as explained in the Methodology section. In Fig. 11, Cu^6-labelled NCs pre- (Fig. 11a) and dialyzed (Fig. 11b) can be compared. In the first case (Fig. 11a), the pre-dialyzed labelled NCs were observed, as well as the fluorescent green signal from the non-encapsulated Cu^6. In the second case (Fig. 11b), the dialyzed labelled NCs were observed, but the non-encapsulated Cu^6 signal was non-existent. These microphotographs show that, during the Cu^6-labelled NCs dialysis process, the excess of Cu^6 was successfully eliminated and the encapsulated Cu^6 was not released from the dialyzed labelled-NCs. This can be explained by the Cu^6 non-polar nature that allows it to stay inside the NC oil core. Furthermore, the pre-dialyzed labelled NCs have a more dispersed distribution (Fig. 11a), probably due to the presence of Cu^6 between the nanostructures, whose non-polar character repels them and makes them move away from each other. In contrast, dialyzed labelled NCs showed certain trend to approximate between them in form of groups; however, their physicochemical properties were normal (see Table 1). This tendency of the NCs to approach each other is surely due to the distribution acquired between the slide and the cover.

According to the CLSM images, Ma was extended throughout the MS forming a matrix (red channel) (Fig. 12a), where the Cu^6-NCs were homogeneously distributed in the Ma MS (green channel) (Fig. 12b). The confluence of both components can be observed in the overlapping of channels (Fig. 12c). This type of micro-nanostructure is different to those seen for microencapsulated CS NPs [61,66,68], where the CS NPs were distributed inside the MS, but covered by an outer layer of Ma. However, this study is agreement with a study of SLN of glyceryl dibehenate and glyceryl tristearate microencapsulated in Ma MS, in that the outer layer of Ma was not present and the nanosystems were distributed up to the edge of the MS [45]. There are two hypotheses that explain the presence of this Ma outer cover in the nanosystems-loaded Ma MS. The first one is based on the T_{Inlet} employed in the spray-drying process. For the CS NPs microencapsulation [61,66,68], the T_{Inlets} were of 160 °C and 170 °C, while in the present work was of 105 °C, similar to that used for the SLN microencapsulation, of 103 °C

Table 3
$T_{Outlets}$, temperature losses and spray-drying processes yields (mean ± S.D.; n = 3; NCs: Ma = 1:15, *w/w*).

Type of powder	T_{Outlet} (°C)	Temperature Loss (°C)	Process Yield (%)
Ma MS	57	48	64 ± 4
CS NCs-loaded Ma MS	59	46	67 ± 5
HA/CS NCs-loaded Ma MS	58	47	67 ± 6

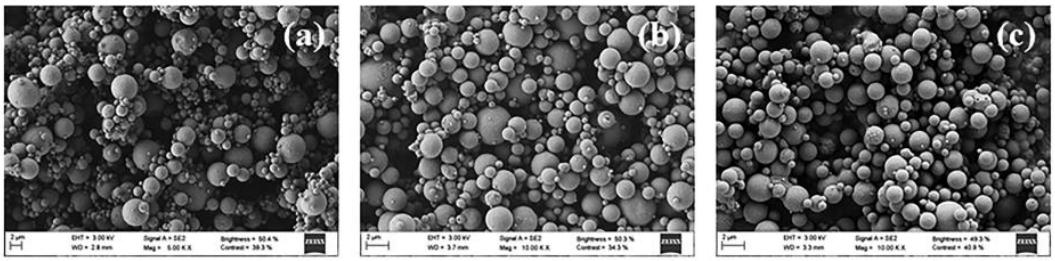

Fig. 9. SEM microphotographs of MS obtained using the adjusted spray-drying conditions: (a) Ma MS (control), (b) CS NCs-loaded Ma MS, and (c) HA/CS NCs-loaded Ma MS.

[45]. At high temperature, there is an increased drying of Ma in the outer layer of the MS compared to the lowest temperatures. The second hypothesis is focused on the concentration of the excipient used during the spray-drying process. In fact, a higher Ma concentration, which was used for CS NCs and SLN [45] compared to the CS NPs [61,66,68], is associated to a higher viscosity of the Ma solution. This fact hinders the water and excipient molecules diffusion during the drying process, thus preventing the possible formation of a Ma outer cover.

3.5.4. Aerodynamic properties of the dry powders

The combination of particle size and density are two important factors that determine the dispersion and sedimentation of the dry powders in the lung [70,71] and, hence, their success [72]. The MS were characterized in terms of physical and aerodynamic properties (geometric diameter, real density, apparent density, and theoretical aerodynamic diameter).

For a proper administration to the lung, the aerodynamic diameter of the particles should be between 1 and 5 μm, approximately [70,73–76]. Particles with aerodynamic diameters less than 1 μm will be expelled with exhaled air, and particles larger than 5 μm will be deposited in the upper respiratory tract [47,74]. Table 4 collect the physical and aerodynamic properties of dry powders obtained by spray-drying. The values of theoretical aerodynamic diameters (2–4 μm, approximately) agree with the obtained for the microencapsulated SLN and CS/TPP NPs, and were in the optimal range of particle size (1–5 μm) for their adequate administration to the deep lung [45,47,61,66,68]. The geometric diameter of Ma MS was higher and more heterogeneous than those of CS-based NCs-loaded Ma MS, probably due to a more porous and less compact structure. In addition, all cases exhibited low apparent densities, which are usually associated with proper aerodynamic flow behaviors, as were previously demonstrated for different inhalation powders with low apparent densities that also were analyzed by cascade impactor and in *in vivo* studies [44,45,47,56,65,75]. The present results fit within the range for the microencapsulated SLN and CS/TPP NPs (0.3–0.6 g/cm^3) [45,47,61,66,68]. Despite the apparent density of the Ma MS was higher than for NCs-loaded Ma MS, the real density was lower, according with their higher porosity and largest aerodynamic diameter. Conversely, the CS-based NCs-loaded Ma MS presented smaller geometric diameter compared to Ma MS due to their more compact and less porous structure, which is verified with a higher real density. Furthermore, both types of NCs-loaded Ma MS exhibited similar densities (real and apparent), while the geometric and theoretical aerodynamic diameters were slightly higher in the case of HA/CS NCs-loaded Ma MS, probably due to the additional presence of HA in the structure. In all cases, the real densities were similar with those obtained for the microencapsulated SLN and CS/TPP NPs in Ma MS [45,47,61,66,68] (1.3–1.5 g/cm^3). Therefore, taking into account their physical and aerodynamic properties, it was concluded that the powders obtained in the present study were theoretically suitable [77] for their correct administration to the deep lung regions (bronchioles and alveoli).

3.6. Release of NCs from Ma MS

Ma MS act as carriers to facilitate the NCs delivery to the lungs. In this study it was demonstrated the ability of the Ma MS to rapidly release the CS-based NCs in MilliQ water at room temperature and in simulated pulmonary medium at 37 °C (similar to physiological conditions). The latter was a mixture of PBS-Curosurf®, with a pH similar to the lung fluid, interstitial fluid, and plasma (pH: 7.4) [78]. When the powders came into contact with both media, the NCs were immediately released. The Fig. 13 shows the TEM microphotographs of CS NCs (Fig. 13a) and HA/CS NC (Fig. 13b) released in MilliQ water after 1 h, where both types of NCs were very similar to their corresponding fresh NCs (compare microphotographs depicted in Figs. 1 and 13).

The values of sizes and ζ-potentials of the released CS-based NCs at the different release times up to 4 h are depicted in Fig. 14. At time 0 h, the NCs showed increased sizes in both media with respect to the

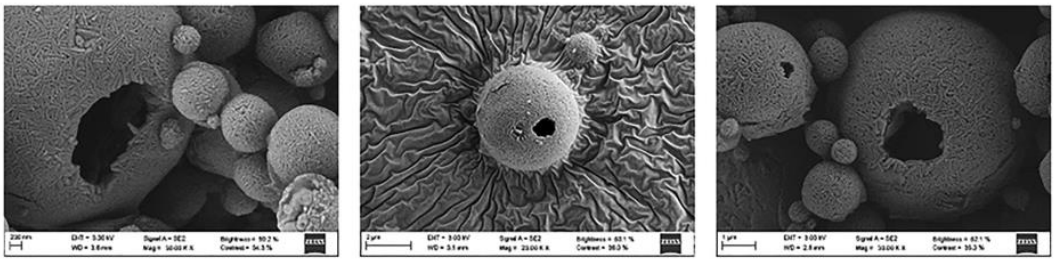

Fig. 10. SEM microphotographs of hollow CS NCs-loaded Ma MS.

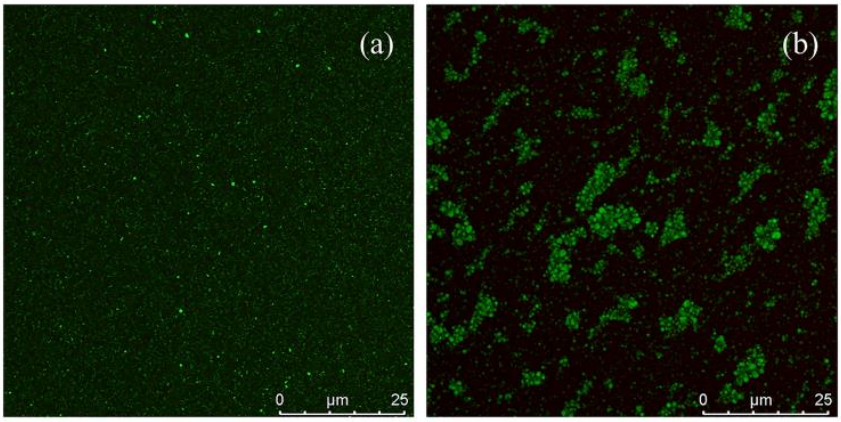

Fig. 11. CLSM microphotographs of: (a) pre-dialyzed Cu^6-CS NCs and (b) dialyzed Cu^6-CS NCs.

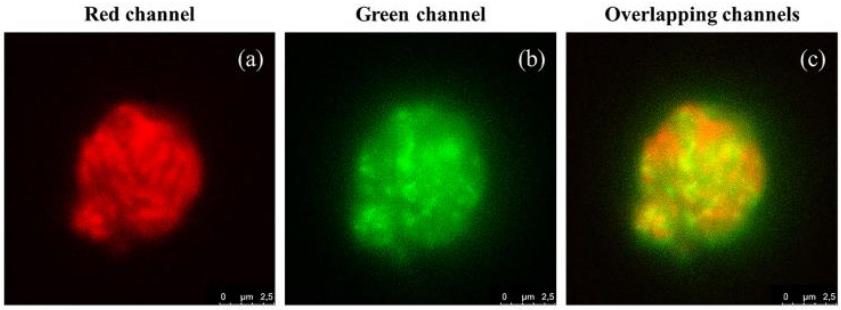

Fig. 12. CLSM microphotographs of Cu^6-CS NCs-loaded Ma^B MS: (a) red channel, (b) green channel, and (c) overlapping channels.

Table 4
Physical and aerodynamic properties of dry powders obtained by spray-drying (mean ± S.D.; n = 3).

Dry powders	Theoretical aerodynamic diameter (µm)	Geometric diameter (µm)	Apparent density (g/cm^3)	Real density (g/cm^3)
Ma MS	4.21 ± 0.01	3.75 ± 1.56	0.50 ± 0.01	1.29 ± 0.01
CS NCs-loaded Ma MS	2.51 ± 0.02	2.10 ± 0.86	0.44 ± 0.02	1.43 ± 0.01
HA/CS NCs-loaded Ma MS	3.35 ± 0.02	2.77 ± 1.35	0.42 ± 0.02	1.43 ± 0.02

original values (see Table 1), probably due to the presence of Ma, acting as an excipient bridge. This increase was higher in the case of the NCs released in simulated pulmonary medium, surely due to electrostatic interaction between the negative molecules of the medium and the positive surface of the NCs. An increase in size has been observed in previous works when the CS NPs [47] and SLN [45] were released from Ma MS in aqueous medium, which confirms this phenomenon. From 0.5 h onwards, the sizes of released CS NCs and HA/CS NCs decreased until reaching values higher than those that had fresh NCs, before spray-drying (Fig. 14). Regarding the ζ-potentials of both types of released NCs, Fig. 14 showed that this parameter decreased slightly in MilliQ water remaining positive; while it was considerably reduced to negative values in simulated pulmonary medium. In the latter case, it is supposed that it was due to the electrostatic union of negative molecules (proteins of the Curosurf® lung surfactant) to the positive surface of the NCs. In addition, Ma MS have efficiently released NCs because have not been detected micrometer sizes and ζ-potentials of around −8 mV in MilliQ water, characteristic of the Ma MS. Therefore, we could conclude that the CS-based NCs were released and maintained their physicochemical characteristics with suitable values for the purpose of this study.

3.7. Stability of NCs in cell growth medium

The stability of CS NCs and HA/CS NCs in supplemented DMEM and in DMEM without supplementation while mimicking physiological conditions (37 °C, pH: 7.4) was determined at different times (0, 2 and 4 h), being also checked in MilliQ water as control. Specifically, we considered to examine the NCs size and their standard deviations, being desirable that the sizes remain in the nanometric range. Sizes of CS NCs and HA/CS NCs in the different media are shown in Fig. 15. Both types of NCs remained practically constant in MilliQ water with time, as expected. However, an increase of size with time was observed when CS-based

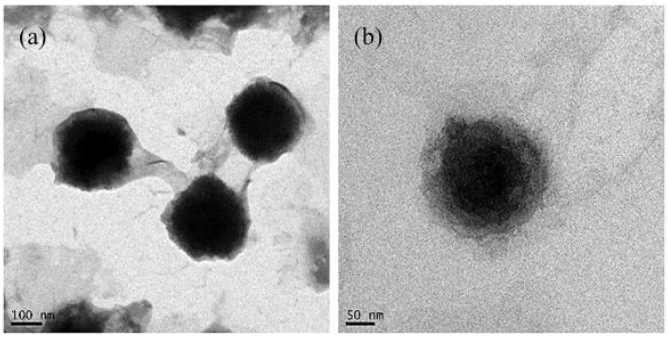

Fig. 13. TEM microphotographs of released: (a) CS NCs and (b) HA/CS NC in MilliQ water at 1 h.

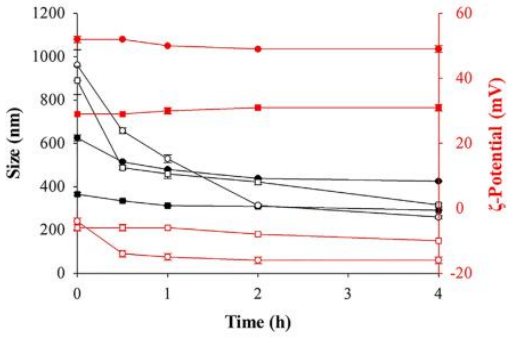

Fig. 14. Physicochemical characterization of CS-based NCs released from Ma MS in MilliQ water at room temperature and in simulated pulmonary medium at 37 °C, at different times (0, 0.5, 1, 2 and 4 h) (mean ± S.D., $n = 3$). Legend: ● Sizes of CS NCs released in MilliQ water at room temperature, ■ Sizes of HA/CS NCs released in MilliQ water at room temperature, ○ Sizes of CS NCs released in simulated pulmonary medium at 37 °C, □ Sizes of HA/CS NCs released in simulated pulmonary medium at 37 °C, ● ζ-Potentials of CS NCs released in MilliQ water at room temperature, ■ ζ-Potentials of HA/CS NCs released in MilliQ water at room temperature, ○ ζ-Potentials of CS NCs released in simulated pulmonary medium at 37 °C, □ ζ-Potentials of HA/CS NCs released in simulated pulmonary medium at 37 °C.

NCs were incubated in supplemented DMEM, achieving the 500 nm for the CS NCs at 4 h, and being practically constant below the 250 nm for the HA/CS NCs. When NCs were incubated in DMEM without supplementation, the sizes also increased with time, achieving more than 500 nm the CS NCs, and over the 400 nm the HA/CS NCs at 4 h. In addition, the standard deviations were more ample for the CS NCs (around 14–31 nm) than HA/CS NCs (about 3–7 nm), independently of the employed medium. It is remarkable that both sizes and standard deviations were notably higher for the CS NCs than for the HA/CS NCs. The higher stability of the HA/CS NCs can be explained by the presence of HA on their structure, which produces a lower superficial ζ-potential with respect to the CS NCs, so HA/CS NCs interacted less with the media negative components. In this sense, it could be a certain adhesion of the media negative molecules on the NCs positive surface, increasing their sizes; but also it is reasonable that the negative charges that surround the NCs "stretch" the CS strands by electrostatic interactions, making them larger. Consequently, HA/CS NCs seem to be more stable than CS NCs in both media. However, both formulations were suitable for the purpose of the *"in vitro"* cell studies.

3.8. Studies in A549 cells

3.8.1. Viability study

A preliminary cell viability assay was carried out using Luna II under the conditions mentioned in section 2.10.1. Mean viability values (mean

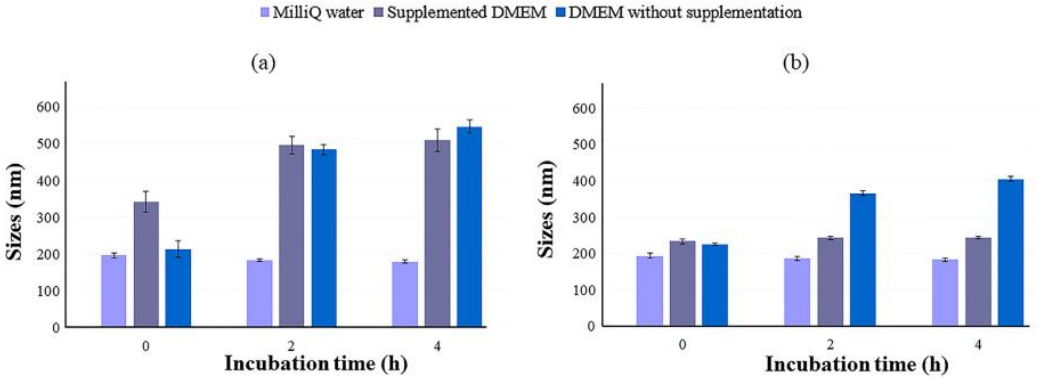

Fig. 15. Size (nm) *vs.* incubation time (h) of: (a) CS NCs and (b) HA/CS NCs in MilliQ water, in supplemented DMEM, and in DMEM without supplementation after 0, 2, and 4 h of incubation at 37 °C (mean ± S.D., $n = 3$).

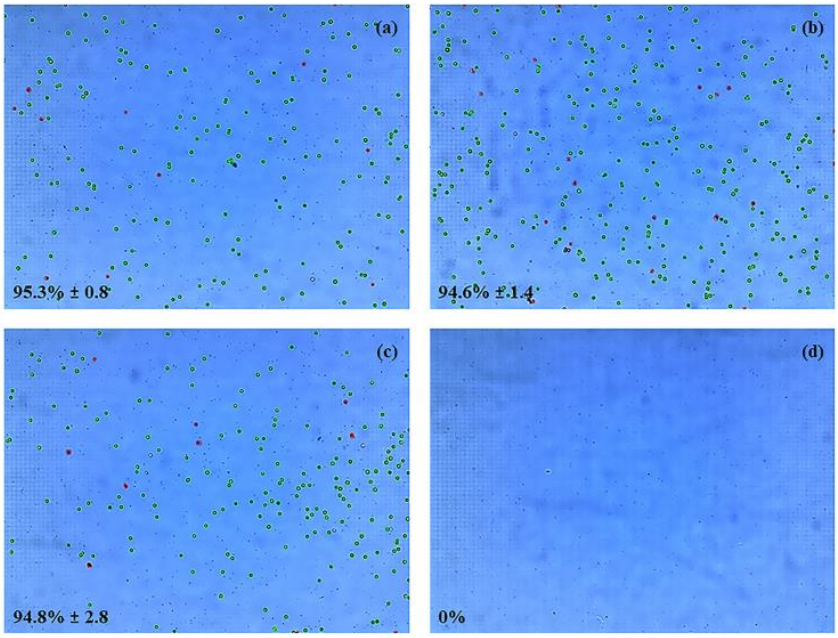

Fig. 16. Luna II images of A549 cells incubated in supplemented DMEM with: (a) nothing (positive control), (b) CS NCs, (c) HA/CS NCs, and (d) 1% (*v/v*) Triton (negative control), for 4 h at 37 °C (% average viability ± S.D.).

± SD; n = 3) were calculated and expressed as percentage of live cells (%). Fig. 16 shows living cells with a green circle and the dead cells with a red circle. Luna II device is an automated cell counter, so the obtained images had not scale. The positive control presented a maximum of viability slightly higher than 95% (Fig. 16a), whereas the negative control showed a 0% of viability (Fig. 16d), as expected. When the cells were incubated with CS NCs and HA/CS NCs presented a viability around 95% in both cases (Fig. 16b and c). In view of the good results obtained in this preliminary experiment, another viability study was next carried out to assess specifically the metabolic activity of the cells.

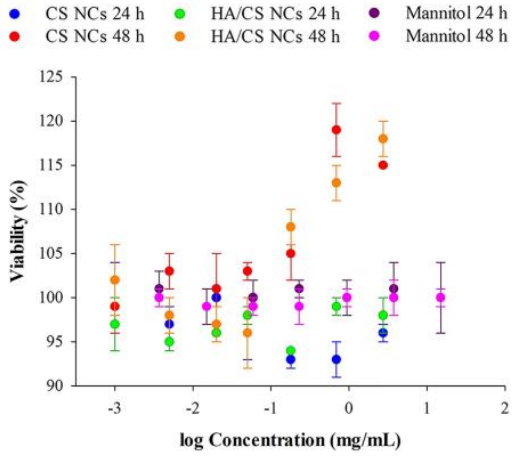

Fig. 17. Cell viability after 24 and 48 h of recovery after removal of CS NCs, HA/CS NCs and Ma excipient of the A549 cells, measuring the fluorescence signal of CellTiter-Blue® (mean ± S.D., *n* = 4).

Cell viability of A549 cells was studied using CellTiter-Blue® (AlamarBlue®). The cells were treated with increasing concentrations of CS-based NCs and Ma excipient and incubated for 4 h at 37 °C. The results are shown in Fig. 17, where the viability was expressed as percentage of living cells compared to positive control. After 24 h of the removal of CS NCs the cell viability was comprised between, approximately, 93 and 102% in all the tested concentrations; while in the case of HA/CS NCs, the viability was between 94 and 99%, being similar for both nanosystems. These viability results at 24 h were in agreement with those previously reported for A549 cells treated with CS/TPP NPs, whose values ranged from approximately 90 to 100% [54,79]. Furthermore, the viabilities were higher than those of SLN (both glyceryl dibehenate and glyceryl tristearate empty or with rifabutin) (80%) [63]. After 48 h of removal CS NCs, the viabilities were between 99 and 119%. In the case of HA/CS NCs the viabilities were of 96 to 118% for all the tested concentrations, being similar for both nanosystems. Taking into account that at 24 h the viabilities were close to 100% for both NCs, it is possible that at 48 h there were so high viabilities due to the recovery of the cells. The opposite occurred with the CS/TPP NPs that, at the lowest concentration, presented a viability of 120% but, as the concentrations increased, the viability decreased to a value of around 90% [54]. This discrepancy could be due to a better recovery of the cell division cycle when the cells were treated with the CS-based NCs compared to the CS/TPP NPs. In addition, constant high viability values around 100% were obtained at 24 and 48 h post-treatment in presence of Ma

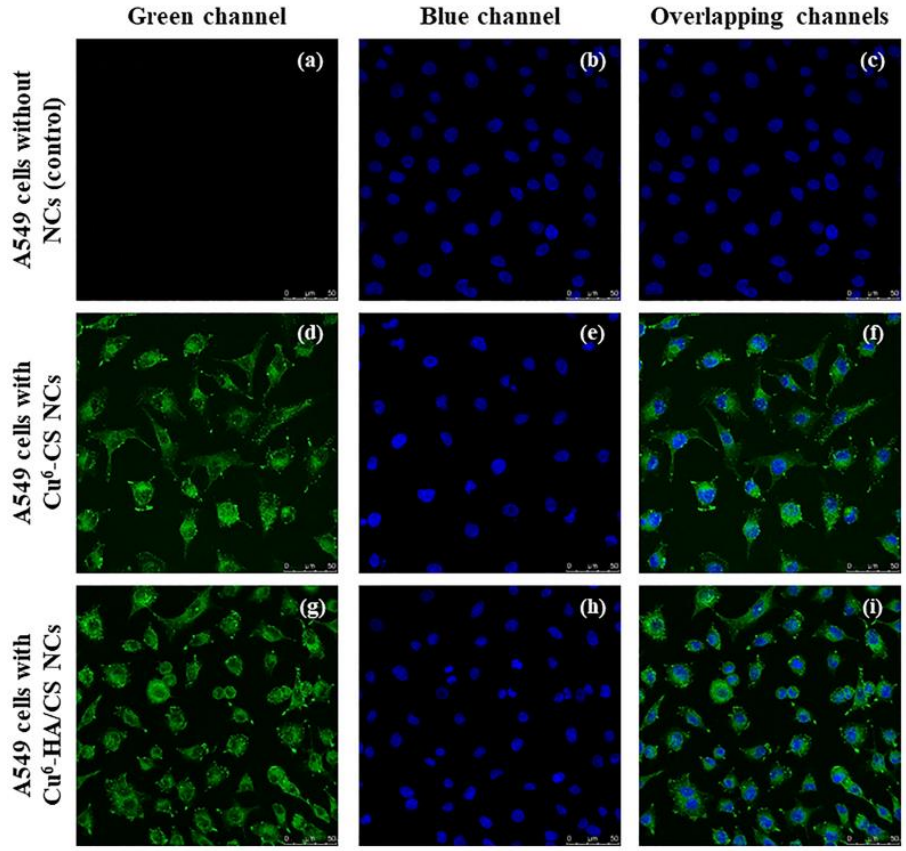

Fig. 18. Confocal microscopy images of A549 cells: control (without CS-based NCs) (a-c), treated with 55.2 μg/well of Cu^6-CS NCs (d-f), and treated with 55.2 μg/well of Cu^6-HA/CS NCs (g-i) (green channel). Cell nuclei were stained with DAPI (blue channel). Scale bar = 50 μm.

excipient. These values were higher than those obtained in the work of Grenha et al. [54], showing that Ma, has good *in vitro* biocompatibility. In summary, the results of this study indicated that CS-based NCs and Ma excipient led to high viabilities in the A549 cell line. Therefore, these micro-nanosystems are expected to be suitable for lung delivery.

3.8.2. Study of intracellular uptake

CS promotes the transcellular and paracellular permeability of macromolecules-loaded nanosystems due to its mucoadhesive and permeability properties [11,19]. Therefore, CS NCs and HA/CS NCs were expected to penetrate A549 cells. The internalization was observed by CLSM using DAPI (blue channel) to label the cell nuclei and Coumarin 6 (Cu^6) (green channel) to label the NCs, as previously described in 2.10.2. section. Fig. 18 shows the confocal images of control cells (A549 cells without treatment) (a-c), cells incubated with Cu^6-CS NCs (d-f), and cells treated with Cu^6-HA/CS NCs (g-i).

These images verified the internalization of the nanosystems inside cells in comparison with the images of the control cells. The excess of Cu^6-NCs was previously eliminated in the washing processes, so that the Cu^6-NCs observed in the images are within the cells. These results agree with those obtained in previous studies. Specifically, CS/TPP NPs were also internalized in high quantities in A549 cells [54].

Table 5
Number of events (Count) and percentage of alive cells (%) of control cells (first column), cells incubated with Cu^6-CS NCs (second column), and cells treated with Cu^6-HA/CS NCs (third column) (mean ± S.D.; n = 3).

Control cells		Cells with Cu^6-CS NCs		Cells with Cu^6-HA/CS NCs	
Count	Alive cells (%)	Count	Alive cells (%)	Count	Alive cells (%)
10,919.0 ± 153.7	80.6 ± 0.5	10,646.0 ± 41.2	85.7 ± 0.8	10,711.0 ± 299.5	83.3 ± 6.3

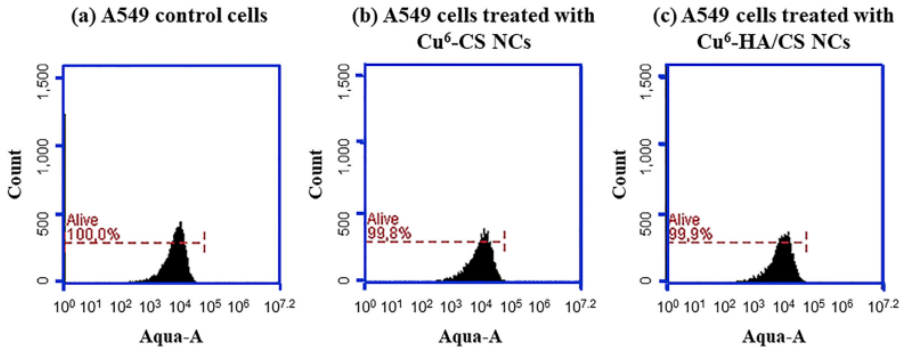

Fig. 19. FACS histograms of A549 cells: (a) control (without treatment), (b) treated with 55.2 μg/well of Cu^6-CS NCs, and (c) treated with 55.2 μg/well of Cu^6-HA/CS NCs to evaluate the cell viability.

Furthermore, Fig. S1 (zoom of Fig. 18, included in Supporting Information) shows more clearly how cells maintained their integrity, as well as a more intense fluorescence signal coming from Cu^6-HA/CS NCs than that from the Cu^6-CS NCs. This is probably due to the penetration-enhancing effect of the HA [34,80]. In any case, both nanosystems were efficiently uptaked by the A549 cell line.

3.8.3. Quantification of A549 cells containing NCs

To quantify the A549 cells that have internalized CS NCs and HA/CS NCs, the FACS technique was carried out by the analysis of a minimum of 10,000 events per sample. Table 5 shows the data of number of events (Count) and the percentage of alive cells (%) selected of their corresponding Dot Plot.

The histograms of the control cells were considered the basal signal to correct the signal obtained from the cells treated with Cu^6-NCs. The histogram of the control cells (Fig. 19a) confirmed a positive viability of 100%, as expected. When the cells were treated with Cu^6-CS NCs and Cu^6-HA/CS NCs, their respective histograms (previously corrected by "colour compensation") (Fig. 19b and c, correspondingly) showed that the cells were negative to Aqua, indicating also a high viability (99.83% and 99.93% on average for Cu^6-CS NCs and Cu^6-HA/CS NCs, respectively) (see complete information in Supporting Information, Fig. S2).

To determine the percentage of cells internalized with NCs (see complete information in Supporting Information, Fig. S3), the histogram of control cells (Fig. 20a) was compared with those obtained for the cells treated with Cu^6-CS NCs (Fig. 20b) and Cu^6-HA/CS NCs (Fig. 20c). As expected, control cells (Fig. 20a) were negative to the signal of Cu^6. When cells were treated with Cu^6-CS NCs and Cu^6-HA/CS NCs, they were positive to the signal of Cu^6, showing that the nanosystems were internalized, corresponding to 100% of the cells. Therefore, both types of nanosystems were uptaked by the total of the A549 cells.

Similar results were obtained in numerous studies of CS-based nanosystems investigated for the encapsulation of antitumoral drugs [81–83]. On the contrary, it was found that CS/TPP NPs [54] did not penetrate in A549 and Calu-3 cell lines; but they remained attached to the surface of the cells. Unlike that study, the NCs remained incubated with the cells for 4 h, while the NPs were only 2 h. Therefore, and taking into account the good results of this study and of previous ones based on CS nanosystems, it is very probable that CS/TPP NPs also internalize the cells with a more adequate incubation time. In addition, the results of this study were congruent with those obtained by CLSM (section 3.8.2.) because we could verify the cellular internalization of the nanosystems, but also quantifying the % of A549 cells internalized with the NCs. It can be concluded that both confocal images and flow cytometry studies showed an efficient internalization of CS-based NCs in the A549 cell line. Furthermore, it was revealed that the internalization of the

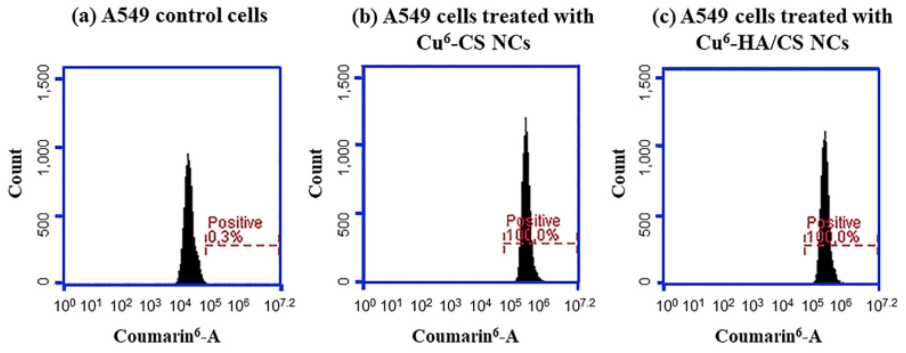

Fig. 20. FACS histograms of A549 cells: (a) control (without treatment), (b) treated with 55.2 μg/well Cu^6-CS NCs, and (c) treated with 55.2 μg/well of Cu^6-HA/CS NCs to evaluate the cell internalization.

nanosystems did not affect to the cell viability (see Fig. 19), which was consistent with the results of previous studies (section 3.8.1). Therefore, the microencapsulated CS-based NCs seem to be safe and suitable for their administration by the pulmonary route.

4. Conclusion

This work describes for the first time the adjust of the NCs microencapsulation process (CS NCs and HA/CS NCs) in Ma MS by the spray-drying technique, aimed to provide dry powders of suitable characteristics for inhalation and administration to the deep lung. CSLM study confirm the presence and homogeneous distribution of the NCs in Ma MS. NCs are rapidly released in aqueous media, being not altered by the spray-drying process, demonstrating that Ma MS act as inert carriers for the pulmonary administration of NCs. *In vitro* cell studies revealed high viability of A549 cells in presence of the nanosystems, as well as of the Ma atomization excipient. Moreover, there was a high cellular uptake of the nanosystems, maintaining the cell integrity. Taking into account all these results, this work demonstrates the safe application of a novel and versatile micro-nanoplatform for pulmonary delivery, which opens a wide field of investigation to carry out a more complete, effective and successful treatment of pulmonary diseases.

Author contributions statement

All authors have read and agreed to the published version of the manuscript.

Credit authorship contribution statement

Estefanía Fernández-Paz: Conceptualization, Data curation, Formal analysis, Investigation, Methodology, Project administration, Resources, Validation, Visualization, Writing – original draft. **Cristina Fernández-Paz:** Formal analysis, Investigation, Methodology, Resources, Writing – review & editing. **Sheila Barrios-Esteban:** Formal analysis, Methodology, Writing – review & editing. **Irene Santalices:** Investigation, Writing – review & editing. **Noemi Csaba:** Conceptualization, Methodology, Resources, Writing – review & editing. **Carmen Remuñán-López:** Conceptualization, Funding acquisition, Methodology, Project administration, Resources, Supervision, Writing – review & editing.

Declaration of Competing Interest

The authors declare that they have no known competing financial interests or personal relationships that could have appeared to influence the work reported in this paper.

Acknowledgments

This research publication is part of the I+D+I Grant PID2019-107500RB-I00, funded by MCIN/AEI/10.13039/501100011033; by Instituto de Salud Carlos III of Spain (Strategic Health Action, Grants FIS PS09/00816 and FIS PSI14/00059); by Xunta de Galicia (Competitive Reference Groups, ED431C 2021/17-FEDER); *In vitro* cell studies were carried out in collaboration with the Natural Polymers and Biomimetics Group (NPnB group, CiMUS). The authors want to thank to María José Pazos Guldrís, for the TEM microphotographs; to Raquel Antón Segurado, for the SEM microphotographs; to Montserrat García Lavandeira, for the CLSM microphotographs; and Lucía Alvariño Sanjurjo, for her technical assistance in the *in vitro* cell studies.

Appendix A. Supplementary data

Supplementary data to this article can be found online at https://doi.org/10.1016/j.powtec.2022.117149.

References

[1] S. Bhattacharyya, B.S. Sogali, Inhalation therapy – approaches and challenges, Asian J. Pharm. Clin. Res. 11 (2018) 9–16, https://doi.org/10.22159/ajpcr.2018.v11i4.24117.
[2] S.P. Newman, Delivering drugs to the lungs: the history of repurposing in the treatment of respiratory diseases, Adv. Drug Deliv. Rev. 133 (2018) 5–18, https://doi.org/10.1016/j.addr.2018.04.010.
[3] S. Azarmi, W.H. Roa, R. Löbenberg, Targeted delivery of nanoparticles for the treatment of lung diseases, Adv. Drug Deliv. Rev. 60 (2008) 863–875, https://doi.org/10.1016/j.addr.2007.11.006.
[4] J. Geiger, M.K. Aneja, C. Rudolph, Vectors for pulmonary gene therapy, Int. J. Pharm. 390 (2010) 84–88, https://doi.org/10.1016/j.ijpharm.2009.10.010.
[5] X.-P. Zhang, W.-T. Zhang, Y. Qiu, M.-J. Ju, G.-W. Tu, Z. Luo, Understanding gene therapy in acute respiratory distress syndrome, Curr. Gene Ther. 19 (2019) 93–99, https://doi.org/10.2174/1566523219666190702154817.
[6] I. Villate-Beitia, J. Zarate, G. Puras, J.L. Pedraz, Gene delivery to the lungs: pulmonary gene therapy for cystic fibrosis, Drug Dev. Ind. Pharm. 47 (2017) 1071–1081, https://doi.org/10.1080/03639045.2017.1298122.
[7] A.J. Simpson, J.A. King, P.H. Thorpe, G. McLachlan, J.-M. Sallenave, Towards gene therapy for inflammatory and infective pulmonary diseases, Curr. Genom. 5 (2004) 365–383, https://doi.org/10.2174/1389202043349264.
[8] A.K. Kolonko, J. Efing, Y. González-Espinosa, N. Bangel-Ruland, W. van Driessche, F.M. Goycoolea, W.-M. Weber, Capsaicin-loaded chitosan nanocapsules for wtCFTR-mRNA delivery to a cystic fibrosis cell line, Biomed. 8 (2020) 364, https://doi.org/10.3390/biomedicines8090364.
[9] P. Hervella, G. Lollo, F. Oyarzún-Ampuero, G. Rivera, D. Torres, M.J. Alonso, Nanocapsules as carriers for the transport and targeted delivery of bioactive molecules, in: A.L. Daniel da Silva (Ed.), Nanocomposite Particles for Bio-Applications: Materials and Bio-Interfaces, Pan Stanford Publishing, Singapore, Ana Luisa Da Silva and Tito Trindade 2011, pp. 45–67.
[10] C. Prego, D. Torres, M.J. Alonso, The potential of chitosan for the oral administration of peptides, Expert Opin. Drug Deliv. 2 (2005) 843–854, https://doi.org/10.1517/17425247.2.5.843.
[11] P. Calvo, C. Remuñán-López, J.L. Vila-Jato, M.J. Alonso, Development of positively charged colloidal drug carriers: chitosan-coated polyester nanocapsules and submicron-emulsions, Colloid Polym. Sci. 275 (1997) 46–53, https://doi.org/10.1007/s003960050050.
[12] I. Santalices, D. Torres, M.V. Lozano, M.M. Arroyo-Jiménez, M.J. Alonso, M.J. Santander-Ortega, Influence of the surface properties of nanocapsules on their interaction with intestinal barriers, Eur. J. Pharm. Biopharm. 133 (2018) 203–213, https://doi.org/10.1016/j.ejpb.2018.09.023.
[13] E. Fernández-Paz, L. Feijoo-Siota, M.M. Gaspar, N. Csaba, C. Remuñán-López, Microencapsulated chitosan-based nanocapsules: a new platform for pulmonary gene delivery, Pharm. 13 (2021) 1377, https://doi.org/10.3390/pharmaceutics13091377.
[14] A.S. Halim, L.C. Keong, I. Zainol, R. Abdul, H. Ahmad, Biocompatibility and biodegradation of chitosan and derivatives, J.W. Wiley & Sons (Ed.), Chitosan-Based Systems for Biopharmaceuticals: Delivery, Targeting and Polymer Therapeutics, Bruno Sarmento and José das Neves, New York 2012, pp. 57–73.
[15] R. Parhi, Drug delivery applications of chitin and chitosan: a review, Environ. Chem. Lett. 18 (2020) 577–594, https://doi.org/10.1007/s10311-020-00963-5.
[16] L.V. Barros-Lima, M.E.F.A.G. Oliveira, R.V.S. Amorim, Design and evaluation of chitosan-based microparticles as models of protein delivery systems, Int. J. Pharm. Sci. Res. 9 (2018) 466–474, https://doi.org/10.13040/ijpsr.0975-8232.9(2).466-74.
[17] T.M.M. Ways, W.M. Lau, V.V. Khutoryanskiy, Chitosan and its derivatives for application in mucoadhesive drug delivery systems, Polym. 10 (2018)https://doi.org/10.3390/polym10030267 267/1-267/37.
[18] G. Sandri, S. Rossi, M.C. Bonferoni, F. Ferrari, M. Mori, C. Caramella, The role of chitosan as a mucoadhesive agent in mucosal drug delivery, J. Drug Deliv. Sci. Technol. 22 (2012) 275–284, https://doi.org/10.1016/S1773-2247(12)50046-8.
[19] A. Bernkop-Schnürch, C.E. Kast, D. Guggi, Permeation enhancing polymers in oral delivery of hydrophilic macromolecules: Thiomer/GSH systems, J. Control. Release 93 (2003) 95–103, https://doi.org/10.1016/j.jconrel.2003.05.001.
[20] N. Volpi, J. Schiller, R. Stern, L. Soltés, Role, metabolism, chemical modifications and applications of hyaluronan, Curr. Med. Chem. 16 (2009) 1718–1745, https://doi.org/10.2174/092986709788186138.
[21] E.R. Bastow, S. Byers, S.B. Goluba, C.E. Clarkinc, A.A. Pitsillides, A.J. Fosang, Hyaluronan synthesis and degradation in cartilage and bone, Cell. Mol. Life Sci. 65 (2008) 395–413, https://doi.org/10.1007/s00018-007-7360-z.
[22] S. Vasvani, P. Kulkarni, D. Rawtani, Hyaluronic acid: a review on its biology, aspects of drug delivery, route of administrations and a special emphasis on its approved marketed products and recent clinical studies, Int. J. Biol. Macromol. 151 (2020) 1012–1029, https://doi.org/10.1016/j.ijbiomac.2019.11.066.
[23] E. Ahmadian, S.M. Dizaj, A. Eftekhari, E. Dalir, P. Vahedi, A. Hasanzadeh, M. Samiei, The potential applications of hyaluronic acid hydrogels in biomedicine, Drug Res. 70 (2020) 6–11, https://doi.org/10.1055/a-0991-7585.
[24] S. Chono, S.-D. Li, C.C. Conwell, L. Huang, An efficient and low immunostimulatory nanoparticle formulation for systemic siRNA delivery to the tumor, J. Control. Release 131 (2008) 64–69, https://doi.org/10.1016/j.jconrel.2008.07.006.
[25] G. Jiang, K. Park, J. Kim, K.S. Kim, E.J. Oh, H. Kang, S.-E. Han, Y.-K. Oh, T.G. Park, S.K. Hahn, Hyaluronic acid–polyethyleneimine conjugate for target specific hyaluronic intracellular delivery of siRNA, Biopolym. 89 (2008) 635–642, https://doi.org/10.1002/bip.20978.
[26] D. Peer, R. Margalit, Loading mitomycin C inside long circulating hyaluronan targeted nano-liposomes increases antitumor its activity in three mice tumor models, Int. J. Cancer 108 (2004) 780–789, https://doi.org/10.1002/ijc.11615.

[27] S.M. Hwang, D. Kim, S.J. Chung, C.K. Shim, Delivery of ofloxacin to the lung and alveolar macrophages via hyaluronan microspheres for the treatment of tuberculosis, J. Control. Release 129 (2008) 100–106, https://doi.org/10.1016/j.jconrel.2008.04.009.

[28] M.B. Brown, S.A. Jones, Hyaluronic acid: a unique topical vehicle for the localized delivery of drugs to the skin, J. Eur. Acad. Dermatol. Venereol. 19 (2005) 308–318, https://doi.org/10.1111/j.1468-3083.2004.01180.x.

[29] J.J. Rouse, T.L. Whateley, M. Thomas, G.M. Eccleston, Controlled drug delivery to the lung: influence of hyaluronic acid solution conformation on its adsorption to hydrophobic drug particles, Int. J. Pharm. 330 (2007) 175–182, https://doi.org/10.1016/j.ijpharm.2006.11.066.

[30] K. Surendrakumar, G.P. Martyn, E.C.M. Hodgers, M. Jansen, J.A. Blair, Sustained release of insulin from sodium hyaluronate based dry powder formulations after pulmonary delivery to beagle dogs, J. Control. Release 91 (2003) 385–394, https://doi.org/10.1016/s0168-3659(03)00263-3.

[31] M. de la Fuente, B. Seijo, M.J. Alonso, Novel hyaluronan-based nanocarriers for transmucosal delivery of macromolecules, Macromol. Biosci. 8 (2008) 441–450, https://doi.org/10.1002/mabi.200700190.

[32] I. Serrano-Sevilla, A. Artiga, S.G. Mitchell, L. de Matteis, J.M. de la Fuente, Natural polysaccharides for siRNA delivery: nanocarriers based on chitosan, hyaluronic acid, and their derivatives, Molecules. 24 (2019) 2570, https://doi.org/10.3390/molecules24142570.

[33] K. Shah, S. Chawla, A. Gadeval, G. Reddy, R. Maheshwari, K. Kalia, R.K. Tekade, Nanostructured hyaluronic acid-based materials for the delivery of siRNA, Curr. Pharm. Des. 24 (2018) 2678–2691, https://doi.org/10.2174/1381612824666180807123705.

[34] S. Al-Qadi, M. Alatorre-Meda, E.M. Zaghloul, P. Taboada, C. Remunán-López, Chitosan–hyaluronic acid nanoparticles for gene silencing: the role of hyaluronic acid on the nanoparticles' formation and activity, Colloids Surf. B: Biointerfaces 103 (2013) 615–623, https://doi.org/10.1016/j.colsurfb.2012.11.009.

[35] M. de La Fuente, M. Raviña, P. Paolicelli, A. Sanchez, B. Seijo, M.J. Alonso, Chitosan-based nanostructures: a delivery platform for ocular therapeutics, Adv. Drug Deliv. Rev. 62 (2010) 100–117, https://doi.org/10.1016/j.addr.2009.11.026.

[36] M. de la Fuente, B. Seijo, M.J. Alonso, Novel hyaluronic acid-chitosan nanoparticles for ocular gene therapy, Invest. Ophthalmol. Vis. Sci. 49 (2008) 2016–2024, https://doi.org/10.1167/iovs.07-1077.

[37] A. Cadete, A. Olivera, M. Besev, P.K. Dhal, L. Gonçalves, A.J. Almeida, G. Bastiat, J.-P. Benoit, M. de la Fuente, M. García-Fuentes, M.J. Alonso, D. Torres, Self-assembled hyaluronan nanocapsules for the intracellular delivery of anticancer drugs, Sci. Rep. 9 (2019) 1–11, https://doi.org/10.1038/s41598-019-47995-8.

[38] R.U. Agu, M.I. Ugwoke, M. Armand, R. Kinget, N. Verbeke, The lung as a route for systemic delivery of therapeutic proteins and peptides, Respir. Res. 2 (2001) 198–209, https://doi.org/10.1186/rr58.

[39] R.H. Hastings, H.G. Folkesson, M.A. Matthay, Mechanism of alveolar protein clearance in the intact lung, Am. J. Physiol. Lung Cell Mol. Physiol. 286 (2004) 679–689, https://doi.org/10.1152/ajplung.00205.2003.

[40] W. Yang, J.I. Peters, R.O. Williams III, Inhaled nanoparticles – a current review, Int. J. Pharm. 356 (2008) 239–247, https://doi.org/10.1016/j.ijpharm.2008.02.011.

[41] J. Sung, B. Pulliam, D. Edwards, Nanoparticles for drug delivery to the lungs, Trends Biotechnol. 25 (2007) 563–570, https://doi.org/10.1016/j.tibtech.2007.09.005.

[42] S.P. Newman, Drug delivery to the lungs: challenges and opportunities, Ther. Deliv. 8 (2017) 647–661, https://doi.org/10.4155/tde-2017-0037.

[43] H. Chrystyn, Is total particle dose more important than particle distribution? Respir. Med 91 (Supplement A) (1997) 17–19, https://doi.org/10.1016/s0954-6111(97)90100-1.

[44] C. Fernández-Paz, S. Rojas, P. Salcedo-Abraira, T. Simón-Yarza, C. Remuñán-López, P. Horcajada, Metal-organic framework microsphere formulation for pulmonary administration, ACS Appl. Mater. Interfaces 12 (2020) 25676–25682, https://doi.org/10.1021/acsami.0c07356.

[45] D.P. Gaspar, M.M. Gaspar, C.V. Eleutério, A. Grenha, M. Blanco, L.M.D. Gonçalves, P. Taboada, A.J. Almeida, C. Remuñán-López, Microencapsulated solid lipid nanoparticles as a hybrid platform for pulmonary antibiotic delivery, Mol. Pharm. 14 (2017) 2977–2990, https://doi.org/10.1021/acs.molpharmaceut.7b00169.

[46] S. Al-Qadi, A. Grenha, D. Carrión-Recio, B. Seijo, C. Remuñán-López, Microencapsulated chitosan nanoparticles for pulmonary protein delivery: in vivo evaluation of insulin-loaded formulations, J. Control. Release 157 (2012) 383–390, https://doi.org/10.1016/j.jconrel.2011.08.008.

[47] A. Grenha, B. Seijo, C. Remuñán-López, Microencapsulated chitosan nanoparticles for lung protein delivery, Eur. J. Pharm. Sci. 25 (2005) 427–437, https://doi.org/10.1016/j.ejps.2005.04.009.

[48] H.L. Ohrem, E. Schornick, A. Kalivoda, R. Ognibene, Why is mannitol becoming more and more popular as a pharmaceutical excipient in solid dosage forms? Pharm. Dev. Technol. 19 (2013) 257–262, https://doi.org/10.3109/10837450.2013.775154.

[49] U.S. Food & Drug Administration, Inactive Ingredient Search for Approved Drug Products, https://www.accessdata.fda.gov/scripts/cder/iig/index.cfm (accessed 11 May 2021).

[50] S. Al-Qadi, P. Taboada, C. Remuñán-López, Micro/nanostructured inhalable formulation based on polysaccharides: effect of a thermoprotectant on powder properties and protein integrity, Int. J. Pharm. 551 (2018) 23–33, https://doi.org/10.1016/j.ijpharm.2018.08.049.

[51] X. Li, F.G. Vogt, D. Jr, H.M. Mansour Hayes, Design, characterization, and aerosol dispersion performance modeling of advanced spray-dried microparticulate/nanoparticulate mannitol powders for targeted pulmonary delivery as dry powder inhalers, J. aerosol med. Pulm, Drug Deliv. 27 (2014) 81–93, https://doi.org/10.1089/jamp.2013.1078.

[52] S.G. Maas, G. Schaldach, E.M. Littringer, A. Mescher, U.J. Griesser, D.E. Braun, P.E. Walzel, N.A. Urbanetz, The impact of spray drying outlet temperature on the particle morphology of mannitol, Powder Technol. 213 (2011) 27–35, https://doi.org/10.1016/j.powtec.2011.06.024.

[53] A. Teper, A. Jaques, B. Charlton, Inhaled mannitol in patients with cystic fibrosis: a randomised open-label dose response trial, J. Cyst. Fibros. 10 (2011) 1–8, https://doi.org/10.1016/j.jcf.2010.08.020.

[54] A. Grenha, C.I. Grainger, L.A. Dailey, B. Seijo, G.P. Martin, C. Remuñán-López, B. Forbes, Chitosan nanoparticles are compatible with respiratory epithelial cells in vitro, Eur. J. Pharm. Sci. 31 (2007) 73–84, https://doi.org/10.1016/j.ejps.2007.02.008.

[55] A. Ousset, J. Meeus, F. Robin, M.A. Schubert, P. Somville, K. Dodou, Comparison of a novel miniaturized screening device with Büchi B290 Mini spray-dryer for the development of spray-dried solid dispersions (SDSDs), Processes. 6 (2018) 129, https://doi.org/10.3390/pr6080129.

[56] I. El-Gibaly, Development and in vitro evaluation of novel floating chitosan microcapsules for oral use: comparison with non-floating chitosan microspheres, Int. J. Pharm. 294 (2002) 7–21, https://doi.org/10.1016/S0378-5173(02)00396-4.

[57] A.D. Alves, J.S. Cavaco, F. Guerreiro, J.P. Lourenço, A.M.R. da Costa, A. Grenha, Inhalable antitubercular therapy mediated by locust bean gum microparticles, Molecules. 21 (2016)https://doi.org/10.3390/molecules21060702 702/1-702/22.

[58] A. Gupta, G. Pant, K. Mitra, J. Madan, M.K. Chourasia, A. Misra, Inhalable particles containing rapamycin for induction of autophagy in macrophages infected with mycobacterium tuberculosis, Mol. Pharm. 11 (2014) 1201–1207, https://doi.org/10.1021/mp4006563.

[59] F. Palazzo, S. Giovagnoli, A. Schoubben, P. Blasi, C. Rossi, M. Ricci, Development of a spray-drying method for the formulation of respirable microparticles containing ofloxacin–palladium complex, Int. J. Pharm. 440 (2013) 273–282, https://doi.org/10.1016/j.ijpharm.2012.05.045.

[60] C. Bosquillon, V. Préat, R. Vanbever, Pulmonary delivery of growth hormone using dry powders and visualization of its local fate in rats, J. Control. Release 96 (2004) 233–244, https://doi.org/10.1016/j.jconrel.2004.01.027.

[61] S. Al-Qadi, A. Grenha, C. Remuñán-López, Microspheres loaded with polysaccharide nanoparticles for pulmonary delivery: preparation, structure and surface analysis, Carbohydr. Polym. 86 (2011) 25–34, https://doi.org/10.1016/j.carbpol.2011.03.022.

[62] M. De la Fuente, B. Seijo, M.J. Alonso, Design of novel polysaccharidic nanostructures for gene delivery, Nanotechnol. 19 (2008), 075105https://doi.org/10.1088/0957-4484/19/7/075105.

[63] D.P. Gaspar, V. Faria, L.M.D. Gonçalves, P. Taboada, C. Remuñán-López, A.J. Almeida, Rifabutin-loaded solid lipid nanoparticles for inhaled antitubercular therapy: physicochemical and in vitro studies, Int. J. Pharm. 497 (2016) 199–209, https://doi.org/10.1016/j.ijpharm.2015.11.050.

[64] H. Rouco, P. Diaz-Rodriguez, D.P. Gaspar, L.M.D. Gonçalves, M. Cuerva, C. Remuñán-López, A.J. Almeida, M. Landin, Rifabutin-loaded nanostructured lipid carriers as a tool in oral anti-mycobacterial treatment of Crohn's disease, Nanomater. 10 (2020) 2138, https://doi.org/10.3390/nano10112138.

[65] G. Pilcer, K. Amighi, Formulation strategy and use of excipients in pulmonary drug delivery, Int. J. Pharm. 392 (2010) 1–19, https://doi.org/10.1016/j.ijpharm.2010.03.017.

[66] A. Grenha, B. Seijo, C. Serra, C. Remuñán-López, Chitosan nanoparticle-loaded mannitol microspheres: structure and surface characterization, Biomacromol. 8 (2007) 2072–2079, https://doi.org/10.1021/bm061131g.

[67] A. Bhardwaj, S. Mehta, S. Yadav, S.K. Singh, A. Grobler, A.K. Goyal, A. Mehta, Pulmonary delivery of antitubercular drugs using spray-dried lipid – polymer hybrid nanoparticles, Artif. Cell. Nanomed. Biotechnol. 44 (2015) 1544–1555, https://doi.org/10.3109/21691401.2015.1062389.

[68] S. Al-Qadi, C. Remuñán-López, A micro- and nano-structured drug carrier based on biocompatible, hybrid polymeric nanoparticles for potential application in dry powder inhalation therapy, Polym. 55 (2014) 4012–4021, https://doi.org/10.1016/j.polymer.2014.06.046.

[69] A. Grenha, C. Remuñán-López, E.L.S. Carvalho, B. Seijo, Microspheres containing lipid/chitosan nanoparticles complexes for pulmonary delivery of therapeutic proteins, Eur. J. Pharm. Biopharm. 69 (2008) 83–93, https://doi.org/10.1016/j.ejpb.2007.10.017.

[70] I. Khan, M. Apostolou, R. Bnyan, C. Houacine, A. Elhissi, S.S. Yousaf, Paclitaxel-loaded micro or nano transfersome formulation into novel tablets for pulmonary drug delivery via nebulization, Int. J. Pharm. 575 (2020), 118919https://doi.org/10.1016/j.ijpharm.2019.118919.

[71] A.M. Hillery, A.W. Lloyd, J. Swarbrick, Drug Delivery and Targeting: For Pharmacists and Pharmaceutical Scientists, Taylor & Francis, New York, 2001.

[72] H.M. Courrier, N. Butz, T.F. Vandamme, Pulmonary drug delivery systems: recent developments and prospects, Crit. Rev. Ther. Drug Carr. Syst. 19 (2002) 425–498, https://doi.org/10.1615/critrevtherdrugcarriersyst.v19.i45.40.

[73] A. Grenha, D. Carrión-Recio, D. Teijeiro-Osorio, B. Seijo, C. Remuñán-López, Nano- and microparticulate carriers for pulmonary drug delivery, in: M.N.V. Kumar (Ed.), Handbook of Particulate Drug Delivery, American Scientific Publishers, Stevenson Ranch, Valencia (Calif) 2008, pp. 165–192.

[74] C. Bosquillon, C. Lombry, V. Préat, R. Vanbever, Influence of formulation excipients and physical characteristics of inhalation dry powders on their aerosolization performance, J. Control. Release 70 (2001) 329–339, https://doi.org/10.1016/s0168-3659(00)00362-x.

[75] J.C. Mejias, K. Roy, In-vitro and in-vivo characterization of a multi-stage enzyme-responsive nanoparticle-in-microgel pulmonary drug delivery system, J. Control. Release 316 (2019) 393–403, https://doi.org/10.1016/j.jconrel.2019.09.012.

[76] C. Sinsuebpol, J. Chatchawalsaisin, P. Kulvanich, Preparation and in vivo absorption evaluation of spray dried powders containing salmon calcitonin loaded chitosan

nanoparticles for pulmonary delivery, Drug Des. Dev. Ther. 7 (2013) 861–873, https://doi.org/10.2147/DDDT.S47681.
[77] M. Paranjpe, C. Müller-Goymann, Nanoparticle-mediated pulmonary drug delivery: a review, Int. J. Mol. Sci. 15 (2014) 5852–5873, https://doi.org/10.3390/ijms15045852.
[78] A.R. Berkebile, P.B. McCray, Effects of airway surface liquid pH on host defense in cystic fibrosis, Int. J. Biochem. Cell Biol. 52 (2014) 124–129, https://doi.org/10.1016/j.biocel.2014.02.009.
[79] N. Changsan, N.C. Sinsuebpol, Dry powder inhalation formulation of chitosan nanoparticles for co-administration of isoniazid and pyrazinamide, Pharm. Dev. Technol. 26 (2020) 181–192, https://doi.org/10.1080/10837450.2020.1852570.
[80] H. Mok, J.W. Park, T.G. Park, Antisense oligodeoxynucleotide-conjugated hyaluronic acid/protamine nanocomplexes for intracellular gene inhibition, Bioconjug. Chem. 18 (2007) 1483–1489, https://doi.org/10.1021/bc070111o.
[81] Y. Tao, J. Han, H. Dou, Paclitaxel-loaded tocopheryl succinate-conjugated chitosan oligosaccharide nanoparticles for synergistic chemotherapy, J. Mater. Chem. 22 (2012) 8930–8937, https://doi.org/10.1039/c2jm30290j.
[82] E. Yan, Y. Fu, X. Wang, Y. Ding, H. Qian, C.-H. Wang, Y. Hu, X. Jiang, Hollow chitosan-silica nanospheres for doxorubicin delivery to cancer cells with enhanced antitumor effect in vivo, J. Mater. Chem. 21 (2011) 3147–3155, https://doi.org/10.1039/c0jm03234d.
[83] A. Portero, C. Remuñán-López, H.M. Nielsen, The potential of chitosan in enhancing peptide and protein absorption across the TR146 cell culture model-an in vitro model of the buccal epithelium, Pharm. Res. 19 (2002) 169–174, https://doi.org/10.1023/a:1014220832384.

Estefanía Fernández-Paz is a PhD student in the last stage of her PhD, under the supervision of Prof. Carmen Remuñán-López, at the University of Santiago de Compostela (USC), Spain (NanoBiofar Group, Nanotechnologies Applied to the Design of Drug Delivery Systems). Her expertise fields are in the development of nanocarriers based in the polysaccharides chitosan and hyaluronic acid, and in pulmonary gene delivery. She is author of two research publications "Microencapsulated chitosan-based nanocapsules: a new platform for pulmonary gene delivery", first author; "Microencapsulated isoniazid-loaded metal-organic frameworks for pulmonary administration of antituberculosis drugs", second author, with three more manuscripts pending publication.

Cristina Fernández-Paz (NanoBiofar Group) is a PhD student, who will soon defend her doctoral thesis, directed by Prof. Carmen Remuñán-López (USC) and Dr. Patricia Horcajada (Institute IMDEA). Her research interest is in metal-organic frameworks (MOFs), microencapsulation, pulmonary drug delivery, and preparation and characterization of dry powders. She has two publications as first author: "Metal-organic framework microsphere formulation for pulmonary administration" and "Microencapsulated isoniazid-loaded metal-organic frameworks for pulmonary administration of antituberculosis drugs", with three more manuscripts pending of publication. She received the award at the Best Collaborative Poster Contribution at the International Conference on Aerogels for Biomedical and Environmental Applications.

Sheila Barrios-Esteban is a 4th year PhD student under the supervision of Professors Noemi Csaba and Marcos García-Fuentes (Natural and Biomimetic Polymers Unit; CIMUS) at the USC. Her research interest is in cancer (brain and ocular cancer), synthesis of inorganic/organic polymers and in development of polymeric nanocarriers (polyplexes, nanoparticles and nanocapsules) as gene delivery systems for the treatment of glioblastoma and melanoma uveal. Currently, she has published a book chapter titled "Suppression of cancer stem cells", a conference paper titled "Protamine-based nanoparticles: an attractive gene delivery system for 2D and 3D glioblastoma models" and has a manuscript pending publication.

Dr. Irene Santalices has defended her PhD at the USC in 2018, directed by Prof. María J. Alonso and Dolores Torres (NanoBiofar Group, CIMUS), under the TRANSINT Project (New Oral Nanomedicines: Transporting Therapeutic Macromolecules across the Intestinal barrier, FP7/2007–2013). Experienced in rational design and development of nanosystems to overcome biological barriers. Competent in a variety of techniques aimed to establish appropriate *in vitro – in vivo* correlations. She is an expert in translational research for drug delivery (nano-immunotherapy for oncology) obtained as formulation scientist within the IGNICIA "ONCOMETA" Project (2003-A1AP-64,100). Currently, she is working at CZ Vaccines as Project Manager/Technical Services.

Dr. Noemi Csaba [ORCID: 0000–0002–6187–7717] is Associate Professor in the Department of Pharmacology, Pharmacy and Pharmaceutical Technology of the USC (Faculty of Pharmacy). She is leader of the Natural and Biomimetic Polymers Unit, at CIMUS at the same University. From 2005 to 2007 she made a post-doctoral research stay at the Institute of Pharmaceutical Sciences, in the ETH Zurich. She has more 75 scientific publications and 6 patents. Moreover, she is advisor in national and international funding agencies. Her research interests are nanomedicine, biomaterials, controlled release, drug delivery, vaccines and immune responses.

Prof. Carmen Remuñán-López [ORCID:0000–0002–3460–7121] belongs to the Department of Pharmaceutical Technology, Faculty of Pharmacy, USC. She defended her PhD in 1991 and initiated a two-years post-doctoral stay at the UT (Austin, USA). She is PI of Nanobiofar Group since its creation; belongs to the Editorial Board of scientific journals and to national and international funding advisory agencies; has numerous research publications and six patents. She is expertise in nanomedicine/nanotechnologies, biomaterials, mucosal drug and gene delivery, being involved in the design/development of novel delivery platforms such as chitosan nanostructures and microencapsulated nanocarriers for pulmonary administration of protein, anti-tuberculosis drugs and genes.

PERMISSIONS

ELSEVIER LICENSE TERMS AND CONDITIONS

Jan 31, 2023

This Agreement between SHEILA BARRIOS ESTEBAN ("You") and Elsevier ("Elsevier") consists of your license details and the terms and conditions provided by Elsevier and Copyright Clearance Center.

The publisher has provided special terms related to this request that can be found at the end of the Publisher's Terms and Conditions.

License Number	5472970465072
License date	Jan 20, 2023
Licensed Content Publisher	Elsevier
Licensed Content Publication	Elsevier Books
Licensed Content Title	Biomaterials for Cancer Therapeutics
Licensed Content Author	Carla Garcia-Mazas,Sheila Barrios-Esteban,Noemi Csaba,Marcos Garcia-Fuentes
Licensed Content Date	Jan 1, 2020
Licensed Content Pages	34
Start Page	365
End Page	398
Type of Use	reuse in a thesis/dissertation
I am an academic or government institution with a full-text subscription to this journal and the audience of the material consists of students and/or employees of this institute?	No
Portion	full chapter
Circulation	34
Format	both print and electronic
Are you the author of this Elsevier chapter?	Yes
How many pages did you author in this Elsevier book?	34
Will you be translating?	No
Title	Polypeptide and polyphosphazene based nanosystems for anticancer gene therapy
Institution name	University of Santiago de Compostela
Expected presentation date	Jan 2023
Requestor Location	SHEILA BARRIOS ESTEBAN Rua García Prieto, 66, 1ºB Santiago de Compostela, A Coruña 15706 Spain Attn: SHEILA BARRIOS ESTEBAN
Publisher Tax ID	GB 494 6272 12
Billing Type	Invoice
Billing Address	SHEILA BARRIOS ESTEBAN Rua García Prieto, 66, 1ºB Santiago de Compostela, Spain 15706 Attn: SHEILA BARRIOS ESTEBAN
Total	**0.00 EUR**

Terms and Conditions

INTRODUCTION

1. The publisher for this copyrighted material is Elsevier. By clicking "accept" in connection with completing this licensing transaction, you agree that the following terms and conditions apply to this transaction (along with the Billing and Payment terms and conditions established by Copyright Clearance Center, Inc. ("CCC"), at the time that you opened your Rightslink account and that are available at any time at http://myaccount.copyright.com).

GENERAL TERMS

2. Elsevier hereby grants you permission to reproduce the aforementioned material subject to the terms and conditions indicated.
3. Acknowledgement: If any part of the material to be used (for example, figures) has appeared in our publication with credit or acknowledgement to another source, permission must also be sought from that source. If such permission is not obtained then that material may not be included in your publication/copies. Suitable acknowledgement to the source must be made, either as a footnote or in a reference list at the end of your publication, as follows:
"Reprinted from Publication title, Vol /edition number, Author(s), Title of article / title of chapter, Pages No., Copyright (Year), with permission from Elsevier [OR APPLICABLE SOCIETY COPYRIGHT OWNER]." Also Lancet special credit - "Reprinted from The Lancet, Vol. number, Author(s), Title of article, Pages No., Copyright (Year), with permission from Elsevier."
4. Reproduction of this material is confined to the purpose and/or media for which permission is hereby given.
5. Altering/Modifying Material: Not Permitted. However figures and illustrations may be altered/adapted minimally to serve your work. Any other abbreviations, additions, deletions and/or any other alterations shall be made only with prior written authorization of Elsevier Ltd. (Please contact Elsevier's permissions helpdesk here). No modifications can be made to any Lancet figures/tables and they must be reproduced in full.
6. If the permission fee for the requested use of our material is waived in this instance, please be advised that your future requests for Elsevier materials may attract a fee.
7. Reservation of Rights: Publisher reserves all rights not specifically granted in the combination of (i) the license details provided by you and accepted in the course of this licensing transaction, (ii) these terms and conditions and (iii) CCC's Billing and Payment terms and conditions.
8. License Contingent Upon Payment: While you may exercise the rights licensed immediately upon issuance of the license at the end of the licensing process for the transaction, provided that you have disclosed complete and accurate details of your proposed use, no license is finally effective unless and until full payment is received from you (either by publisher or by CCC) as provided in CCC's Billing and Payment terms and conditions. If full payment is not received on a timely basis, then any license preliminarily granted shall be deemed automatically revoked and shall be void as if never granted. Further, in the event that you breach any of these terms and conditions or any of CCC's Billing and Payment terms and conditions, the license is automatically revoked and shall be void as if never granted. Use of materials as described in a revoked license, as well as any use of the materials beyond the scope of an unrevoked license, may constitute copyright infringement and publisher reserves the right to take any and all action to protect its copyright in the materials.
9. Warranties: Publisher makes no representations or warranties with respect to the licensed material.
10. Indemnity: You hereby indemnify and agree to hold harmless publisher and CCC, and their respective officers, directors, employees and agents, from and against any and all claims arising out of your use of the licensed material other than as specifically authorized pursuant to this license.
11. No Transfer of License: This license is personal to you and may not be sublicensed, assigned, or transferred by you to any other person without publisher's written permission.
12. No Amendment Except in Writing: This license may not be amended except in a writing signed by both parties (or, in the case of publisher, by CCC on publisher's behalf).
13. Objection to Contrary Terms: Publisher hereby objects to any terms contained in any purchase order, acknowledgment, check endorsement or other writing prepared by you, which terms are inconsistent with these terms and conditions or CCC's Billing and Payment terms and conditions. These terms and conditions, together with CCC's Billing and Payment terms and conditions (which are incorporated herein), comprise the entire agreement between you and publisher (and CCC) concerning this licensing transaction. In the event of any conflict between your obligations established by these terms and conditions and those established by CCC's Billing and Payment terms and conditions, these terms and conditions shall control.
14. Revocation: Elsevier or Copyright Clearance Center may deny the permissions described in this License at their sole discretion, for any reason or no reason, with a full refund payable to you. Notice of such denial will be made using the contact information provided by you. Failure to receive such notice will not alter or invalidate the denial. In no event will Elsevier or Copyright Clearance Center be responsible or liable for any costs, expenses or damage incurred by you as a result of a denial of your permission request, other than a refund of the amount(s) paid by you to Elsevier and/or Copyright Clearance Center for denied permissions.

LIMITED LICENSE

The following terms and conditions apply only to specific license types:
15. **Translation**: This permission is granted for non-exclusive world **English** rights only unless your license was granted for translation rights. If you licensed translation rights you may only translate this content into the languages you requested. A professional translator must perform all translations and reproduce the content word for word preserving the integrity of the article.
16. **Posting licensed content on any Website**: The following terms and conditions apply as follows: Licensing material from an Elsevier journal: All content posted to the web site must maintain the copyright information line on the bottom of each image; A hyper-text must be included to the Homepage of the journal from which you are licensing at http://www.sciencedirect.com/science/journal/xxxxx or the Elsevier homepage for books at http://www.elsevier.com; Central

Storage: This license does not include permission for a scanned version of the material to be stored in a central repository such as that provided by Heron/XanEdu.
Licensing material from an Elsevier book: A hyper-text link must be included to the Elsevier homepage at http://www.elsevier.com . All content posted to the web site must maintain the copyright information line on the bottom of each image.

Posting licensed content on Electronic reserve: In addition to the above the following clauses are applicable: The web site must be password-protected and made available only to bona fide students registered on a relevant course. This permission is granted for 1 year only. You may obtain a new license for future website posting.
17. **For journal authors:** the following clauses are applicable in addition to the above:
Preprints:
A preprint is an author's own write-up of research results and analysis, it has not been peer-reviewed, nor has it had any other value added to it by a publisher (such as formatting, copyright, technical enhancement etc.).
Authors can share their preprints anywhere at any time. Preprints should not be added to or enhanced in any way in order to appear more like, or to substitute for, the final versions of articles however authors can update their preprints on arXiv or RePEc with their Accepted Author Manuscript (see below).
If accepted for publication, we encourage authors to link from the preprint to their formal publication via its DOI. Millions of researchers have access to the formal publications on ScienceDirect, and so links will help users to find, access, cite and use the best available version. Please note that Cell Press, The Lancet and some society-owned have different preprint policies. Information on these policies is available on the journal homepage.
Accepted Author Manuscripts: An accepted author manuscript is the manuscript of an article that has been accepted for publication and which typically includes author-incorporated changes suggested during submission, peer review and editor-author communications.
Authors can share their accepted author manuscript:

- immediately
  - via their non-commercial person homepage or blog
  - by updating a preprint in arXiv or RePEc with the accepted manuscript
  - via their research institute or institutional repository for internal institutional uses or as part of an invitation-only research collaboration work-group
  - directly by providing copies to their students or to research collaborators for their personal use
  - for private scholarly sharing as part of an invitation-only work group on commercial sites with which Elsevier has an agreement
- After the embargo period
  - via non-commercial hosting platforms such as their institutional repository
  - via commercial sites with which Elsevier has an agreement

In all cases accepted manuscripts should:

- link to the formal publication via its DOI
- bear a CC-BY-NC-ND license - this is easy to do
- if aggregated with other manuscripts, for example in a repository or other site, be shared in alignment with our hosting policy not be added to or enhanced in any way to appear more like, or to substitute for, the published journal article.

Published journal article (JPA): A published journal article (PJA) is the definitive final record of published research that appears or will appear in the journal and embodies all value-adding publishing activities including peer review co-ordination, copy-editing, formatting, (if relevant) pagination and online enrichment.
Policies for sharing publishing journal articles differ for subscription and gold open access articles:
Subscription Articles: If you are an author, please share a link to your article rather than the full-text. Millions of researchers have access to the formal publications on ScienceDirect, and so links will help your users to find, access, cite, and use the best available version.
Theses and dissertations which contain embedded PJAs as part of the formal submission can be posted publicly by the awarding institution with DOI links back to the formal publications on ScienceDirect.
If you are affiliated with a library that subscribes to ScienceDirect you have additional private sharing rights for others' research accessed under that agreement. This includes use for classroom teaching and internal training at the institution (including use in course packs and courseware programs), and inclusion of the article for grant funding purposes.
Gold Open Access Articles: May be shared according to the author-selected end-user license and should contain a CrossMark logo, the end user license, and a DOI link to the formal publication on ScienceDirect.
Please refer to Elsevier's posting policy for further information.
18. **For book authors** the following clauses are applicable in addition to the above: Authors are permitted to place a brief summary of their work online only. You are not allowed to download and post the published electronic version of your chapter, nor may you scan the printed edition to create an electronic version. **Posting to a repository:** Authors are permitted to post a summary of their chapter only in their institution's repository.
19. **Thesis/Dissertation**: If your license is for use in a thesis/dissertation your thesis may be submitted to your institution in either print or electronic form. Should your thesis be published commercially, please reapply for permission. These requirements include permission for the Library and Archives of Canada to supply single copies, on demand, of the complete thesis and

include permission for Proquest/UMI to supply single copies, on demand, of the complete thesis. Should your thesis be published commercially, please reapply for permission. Theses and dissertations which contain embedded PJAs as part of the formal submission can be posted publicly by the awarding institution with DOI links back to the formal publications on ScienceDirect.

Elsevier Open Access Terms and Conditions

You can publish open access with Elsevier in hundreds of open access journals or in nearly 2000 established subscription journals that support open access publishing. Permitted third party re-use of these open access articles is defined by the author's choice of Creative Commons user license. See our open access license policy for more information.

Terms & Conditions applicable to all Open Access articles published with Elsevier:

Any reuse of the article must not represent the author as endorsing the adaptation of the article nor should the article be modified in such a way as to damage the author's honour or reputation. If any changes have been made, such changes must be clearly indicated.

The author(s) must be appropriately credited and we ask that you include the end user license and a DOI link to the formal publication on ScienceDirect.

If any part of the material to be used (for example, figures) has appeared in our publication with credit or acknowledgement to another source it is the responsibility of the user to ensure their reuse complies with the terms and conditions determined by the rights holder.

Additional Terms & Conditions applicable to each Creative Commons user license:

CC BY: The CC-BY license allows users to copy, to create extracts, abstracts and new works from the Article, to alter and revise the Article and to make commercial use of the Article (including reuse and/or resale of the Article by commercial entities), provided the user gives appropriate credit (with a link to the formal publication through the relevant DOI), provides a link to the license, indicates if changes were made and the licensor is not represented as endorsing the use made of the work. The full details of the license are available at http://creativecommons.org/licenses/by/4.0.

CC BY NC SA: The CC BY-NC-SA license allows users to copy, to create extracts, abstracts and new works from the Article, to alter and revise the Article, provided this is not done for commercial purposes, and that the user gives appropriate credit (with a link to the formal publication through the relevant DOI), provides a link to the license, indicates if changes were made and the licensor is not represented as endorsing the use made of the work. Further, any new works must be made available on the same conditions. The full details of the license are available at http://creativecommons.org/licenses/by-nc-sa/4.0.

CC BY NC ND: The CC BY-NC-ND license allows users to copy and distribute the Article, provided this is not done for commercial purposes and further does not permit distribution of the Article if it is changed or edited in any way, and provided the user gives appropriate credit (with a link to the formal publication through the relevant DOI), provides a link to the license, and that the licensor is not represented as endorsing the use made of the work. The full details of the license are available at http://creativecommons.org/licenses/by-nc-nd/4.0. Any commercial reuse of Open Access articles published with a CC BY NC SA or CC BY NC ND license requires permission from Elsevier and will be subject to a fee.

Commercial reuse includes:

- Associating advertising with the full text of the Article
- Charging fees for document delivery or access
- Article aggregation
- Systematic distribution via e-mail lists or share buttons

Posting or linking by commercial companies for use by customers of those companies.

20. **Other Conditions**: Posting of the full chapter online is not permitted. You may post a summary of the book with a link to the Elsevier website www.elsevier.com , or to the chapter on ScienceDirect if it is available on that platform.

v1.10

Questions? customercare@copyright.com or +1-855-239-3415 (toll free in the US) or +1-978-646-2777.

Dry powders containing chitosan-based nanocapsules for pulmonary administration: Adjustment of spray-drying process and in vitro evaluation in A549 cells

Author:
Estefanía Fernández-Paz,Cristina Fernández-Paz,Sheila Barrios-Esteban,Irene Santalices,Noemi Csaba,Carmen Remuñán-López

Publication: Powder Technology

Publisher: Elsevier

Date: February 2022

Journal Author Rights

Please note that, as the author of this Elsevier article, you retain the right to include it in a thesis or dissertation, provided it is not published commercially. Permission is not required, but please ensure that you reference the journal as the original source. For more information on this and on your other retained rights, please visit: https://www.elsevier.com/about/our-business/policies/copyright#Author-rights

BACK CLOSE WINDOW

NHS
National Research Ethics Service

NRES Committee East Midlands - Nottingham 2
The Old Chapel
Royal Standard Place
Nottingham
NG1 6FS

Telephone: 0115 8839428 (Direct Line)
Facsimile: 0115 9123300

05 May 2011

Professor Richard Grundy
Professor of Paediatric Neuro-oncology and cancer biology
The University of Nottingham
Children's Brain Tumour Research Centre
Queens Medical Centre
Medical School
Nottingham NG7 2UH

RECEIVED
12 MAY 2011

Dear Professor Grundy

Study title: **Comparative molecular analysis of childhood brain tumours in relation to adult brain tumours and normal brain**

REC reference: **11/EM/0076**

The Research Ethics Committee reviewed the above application at the meeting held on 18 April 2011. Thank you for attending to discuss the study.

Ethical opinion

- The committee members asked you who was making the initial approach to potential participants and how this was being done. You informed the committee the research team have been doing tumour banking for 10 years now and that a consultant will discuss the study with any new participants, usually it will be that same consultant taking consent. In cases where a consultant is not available to inform participants and take consent, Lis Whiles, a research nurse who has been taking consent for 5 years will approach the participants after discussing with the chief investigator beforehand. You felt that Lis Whiles has the experience to handle the situation sensitively.

- The committee members queried how long potential participants or their parents have to decide whether to give consent. You informed the committee that potential participants or the parents are able to have as long as they like. They have the option of taking the information away and giving consent on their return. They also have the option to give consent on the day and if they change their mind they can inform you and the sample will be removed.

- The committee members queried how long personal data is to be stored for. The IRAS application form states at A.43 that personal data will be stored for less than 3 months however the samples are linked anonymised so the personal data will need to be kept. You informed the committee that this is an error on the form and that the personal data will be stored indefinitely as the study is continued.

- The committee informed you that the indemnity is not adequate as it does not cover children under 5 who are to be included in the study. You informed the committee that this matter will be rectified.

The members of the Committee present gave a favourable ethical opinion of the above research on the basis described in the application form, protocol and supporting documentation, subject to the conditions specified below.

Ethical review of research sites

NHS Sites

The favourable opinion applies to all NHS sites taking part in the study, subject to management permission being obtained from the NHS/HSC R&D office prior to the start of the study (see "Conditions of the favourable opinion" below).

Conditions of the favourable opinion

The favourable opinion is subject to the following conditions being met prior to the start of the study.

Management permission or approval must be obtained from each host organisation prior to the start of the study at the site concerned.

Management permission ("R&D approval") should be sought from all NHS organisations involved in the study in accordance with NHS research governance arrangements.

Guidance on applying for NHS permission for research is available in the Integrated Research Application System or at http://www.rdforum.nhs.uk.

Where a NHS organisation's role in the study is limited to identifying and referring potential participants to research sites ("participant identification centre"), guidance should be sought from the R&D office on the information it requires to give permission for this activity.

For non-NHS sites, site management permission should be obtained in accordance with the procedures of the relevant host organisation.

Sponsors are not required to notify the Committee of approvals from host organisations

Additional conditions

- The committee request that suitable indemnity is in place which covers all participants.

It is responsibility of the sponsor to ensure that all the conditions are complied with before the start of the study or its initiation at a particular site (as applicable).

You should notify the REC in writing once all conditions have been met (except for site approvals from host organisations) and provide copies of any revised documentation with updated version numbers. Confirmation should also be provided to host organisations together with relevant documentation

Approved documents

The documents reviewed and approved at the meeting were:

Document	*Version*	*Date*
Protocol	Final Version 1.0	21 February 2011
Investigator CV		01 March 2011
Evidence of insurance or indemnity		22 July 2010
Covering Letter		01 March 2011
Letter from Sponsor		02 March 2011
REC application	46123/193182/1/723	28 February 2011

Membership of the Committee

The members of the Ethics Committee who were present at the meeting are listed on the attached sheet.

Martin Hewitt declared that he was a close colleague of the chief investigator of this study and that he would prefer to leave the room whilst the discussion and decision were carried out. Frances Game took over as chair while Martin Hewitt left the room.

Statement of compliance

The Committee is constituted in accordance with the Governance Arrangements for Research Ethics Committees (July 2001) and complies fully with the Standard Operating Procedures for Research Ethics Committees in the UK.

After ethical review

Now that you have completed the application process please visit the National Research Ethics Service website > After Review

You are invited to give your view of the service that you have received from the National Research Ethics Service and the application procedure. If you wish to make your views known please use the feedback form available on the website.

The attached document "After ethical review – guidance for researchers" gives detailed guidance on reporting requirements for studies with a favourable opinion, including:

- Notifying substantial amendments
- Adding new sites and investigators
- Progress and safety reports
- Notifying the end of the study

The NRES website also provides guidance on these topics, which is updated in the light of changes in reporting requirements or procedures.

We would also like to inform you that we consult regularly with stakeholders to improve our service. If you would like to join our Reference Group please email referencegroup@nres.npsa.nhs.uk.

11/EM/0076 **Please quote this number on all correspondence**

With the Committee's best wishes for the success of this project

Yours sincerely

pp **Dr Martin Hewitt**
Chair

Email: heather.harrison@nottspct.nhs.uk

Enclosures: *List of names and professions of members who were present at the meeting and those who submitted written comments*
"After ethical review – guidance for researchers"

Copy to: *Mr Paul Cartledge – University of Nottingham*

R&D office for NHS care organisation at lead site - NUH

GOBIERNO DEL PRINCIPADO DE ASTURIAS

CONSEJERÍA DE SALUD

Dirección General de Calidad, Transformación y Gestión del Conocimiento

Comité de Ética de la Investigación del Principado de Asturias

Hospital Universitario Central de Asturias

N-1, S3.19

Avda. de Roma, s/n
33011 Oviedo

Oviedo a jueves, 23 de marzo de 2020

El Comité de Ética de la Investigación con Medicamentos del Principado de Asturias ha evaluado el Proyecto nº 2020.050, titulado: "OBTENCION DE ORGANOS Y TEJIDOS HUMANOS EN EL LABORATORIO ÚTILES EN INVESTIGACION BIOMÉDICA PARA REDUCIR O ANULAR COMPLETAMENTE LA EXPERIMENTACION CON ANIMALES", Investigador Principal, Dr. ALVARO MEANA INFIESTA. Instituto Universitario Fernandez-Vega (Universidad de Oviedo .

El Comité ha tomado el acuerdo de considerar que el citado Ensayo reúne las condiciones éticas necesarias para poder realizarse y, en consecuencia, emite su autorización.

Le recuerdo que deberá guardar la máxima confidencialidad de los datos utilizados en este Proyecto; les aconsejamos que el Consentimiento Informado se firme por duplicado y que el Investigador guarde una copia en el archivo.

Le saluda atentamente.

Fdo: MAURICIO TELENTI ASENSIO

Secretario/a del Comité de Ética de la Investigación del Principado de Asturias

CONSEJERÍA DE SANIDAD
COMITÉ DE ÉTICA DE LA INVESTIGACIÓN CON MEDICAMENTOS DEL PRINCIPADO DE ASTURIAS

XUNTA DE GALICIA
CONSELLERÍA DO MEDIO RURAL

Xefatura territorial de Lugo
Servizo de Gandaría
Ronda da Muralla, 70
Lugo

galicia

RESOLUCIÓN DE AUTORIZACIÓN DE PROXECTOS DE EXPERIMENTACIÓN ANIMAL

Expediente núm.: 01/20/LU-003
Interesado: **Ana Quelle Regaldie**
Procedemento: RESOLUCIÓN DE AUTORIZACIÓN DE PROXECTOS DE EXPERIMENTACIÓN ANIMAL
Data de inicio: 1 de marzo de 2020
Forma de inicio: solicitude da interesada

ANTECEDENTES

A interesada, como responsable do proxecto "**El pez cebra y su aplicación en biomedicina, acuicultura y medio ambiente"** presentou con data 12 de febreiro de 2020 solicitude para a realización do proxecto de experimentación animal cuxos datos se detallan a continuación:

Denominación do proxecto : El pez cebra y su aplicación en biomedicina, acuicultura y medio ambiente
Nome do centro usuario: Animalario da Facultade de veterinaria(AE-LU-003).
Persoa responsable do proxecto: Ana Quelle Regaldie
Establecemento onde se realizarán os procedementos do proxecto (ou lugar xeográfico no caso de traballos de campo) Animalario da Facultade de veterinaria(AE-LU-003).
Clasificación do proxecto : **Tipo III.**

CONSIDERACIÓNS LEGAIS E TÉCNICAS

Real decreto 53/2013, de 1 de febreiro (BOE núm. 34, do 8 de febreiro), polo que se establecen as normas básicas aplicables para a protección dos animais utilizados en experimentación e outros fins científicos, incluíndo a docencia, establece no seu artigo 33 as condicións de autorizacións dos proxectos con animais de experimentación.

Artigo 88 da Lei 39/2015, do 1 de outubro, do procedemento administrativo común das administracións públicas (BOE núm. 236, do 2 de outubro) establece que a resolución que poña fin ao procedemento decidirá todas as cuestións formuladas polos interesados e aquelas outras derivadas del.

Esta xefatura territorial é competente para ditar resolución de conformidade co artigo 11 do Decreto 245/2009, do 30 de abril, polo que se regulan as delegacións territoriais da Xunta de Galicia e o Decreto 149/2018, do 5 de decembro, polo que establece a estrutura orgánica da Consellería do Medio Rural. O Servizo Provincial de Gandería de Lugo revisou a documentación presentada coa solicitude e visto o informe favorable da avaliación do proxecto, de data 30 de xaneiro de 2020 emitido polo órgano habilitado, e o Comité de Ética da Universidade de Santiago de Compostela, esta xefatura territorial resolve AUTORIZAR o proxecto solicitado.

Xacobeo 2021

A autorización deste proxecto terá unha duración de 5 ANOS e unha vez que transcorran deberán renovala.

A autorización é unicamente válida nas condicións que figuran no expediente. Ante calquera cambio significativo no proxecto que poida ter efectos negativos sobre o benestar dos animais, deberá solicitar a confirmación da autorización ao Servizo Provincial de Gandería.

Esta autorización poderá ser suspendida no caso de que o proxecto non se leve a cabo de acordo coas condicións de autorización e retirala previo expediente tramitado ao que se lle dará audiencia.

Contra a presente resolución, que non pon fin á vía administrativa, poderá interpor recurso de alzada ante o conselleiro de Medio Rural da Xunta de Galicia no prazo dun mes contado a partir da recepción da notificación da presente resolución, conforme cos artigos 121 e 122 da Lei 39/2015, do 1 de outubro, do procedemento administrativo común das administracións públicas.

Documento asinado electronicamente á marxe

Glioblastoma and uveal melanoma are tumors without high incidence rate, but they are characterized by being one of the most aggressive tumors with a life expectancy between 6 and 14 months. Their standard treatment combines surgical resection, radiotherapy and chemotherapy, triggering several severe side effects. Consequently, the search for new therapeutic approaches is required, where gene therapy stands out. However, genetic medicines require delivery systems for the protection and transport of nucleic acids to target cancer cells. Nanomedicine plays an important role to the design of polymeric non-viral vectors, being very promising in gene therapy. The present work is focused on the development of tunable gene delivery nanosystems and their evaluation in different advanced preclinical cancer models.